e-ISSN : 2320-0847
p-ISSN : 2320-0936

American Journal of Engineering Research (AJER)

Volume 3 Issue 1 – January 2014

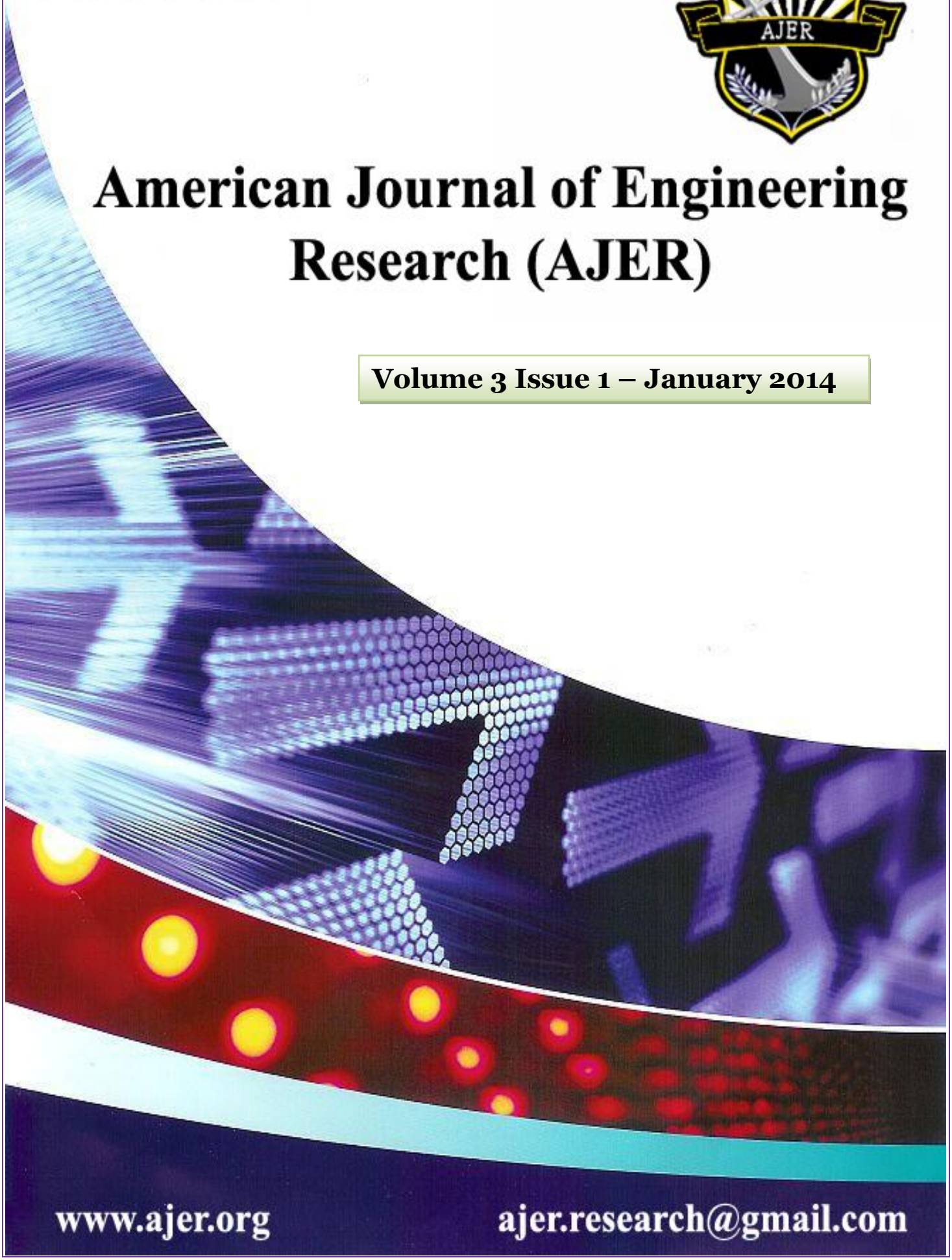

www.ajer.org ajer.research@gmail.com

Editorial Board

American Journal of Engineering Research (AJER)

Volume-3 Issue-1

American Journal of Engineering Research (AJER)
e-ISSN : 2320-0847 p-ISSN : 2320-0936
Volume-03, Issue-01, pp-01-08
www.ajer.org

Research Paper Open Access

Performance and Analysis of Modular Multilevel Converter

T.Yuvaraja[1], Somnath Mazumder[2]
[1](*Research Scholar, Department of Electrical & Electronics, Meenakshi Academy of Higher Education &Research, MAHER UNIVERSITY, India)*
[2](*Assistant Professor, Department of Electronics & Communication, Shirdi Sai Engineering College, India)*

Abstract: - The Modular Multilevel Converter (MMC) represents an emerging topology with a scalable technology making high voltage and power capability possible. The MMC is built up by identical, but individually controllable sub modules. The Modular Multilevel Converter (MMC) is a new topology for multilevel converters with potential for medium voltage and high voltage applications. Equivalent Circuit models and dynamic models for the MMC that provide a faithful representation of system behavior are quite complex given the large number of energy states and control variables. They are not particularly useful in studying the terminal behavior of the converter and for the development of an intuitive control approach to regulate power transfer. A control scheme with a new sub module capacitor voltage balancing method is also proposed in this paper. Modular multilevel converters, based on cascading of half bridge converter cells, can combine low switching frequency with low harmonic interference. They can be designed for high operating voltages without direct series connection of semiconductor element.

Keywords: - *Modular Multilevel Converter (MMC), Voltage Source Converter (VSC), Harmonic Analysis, Terminal model, high voltage direct current.*

I. INTRODUCTION

The introduction of the paper should explain the nature of the problem, previous work, purpose, and the contribution of the paper. The contents of each section may be provided to understand easily about the paper. With new renewable energy production, HVDC is more applicable than ever. More stochastic energy production calls for solutions that can transport power from areas with high generation to areas with lower generation. Offshore wind farms far from the coast require HVDC transmission to the shore and compact and reliable converter technology with large power capability. Connecting the converter to a DC grid should be feasible and the converter should be able to handle fault situations. To gain compactness, the need for filters should be minimized. The emerging topology, the Modular Multilevel Converter (MMC) might address these aims. The newest generation of voltage source converters (VSCs) is the main driver for the latest evolutionary step in the EMT software community due to their use of a very high number of power electronic devices. This technology, known as modular multilevel converters (MMCs) or cascaded two-level converters (CTLCs), generates voltages with very low harmonic content and presents loss levels much closer to those of "classic" thyristor line-commutated converters [1] [2] [3]. A MMC consists of multiple cascaded sub-modules (SM), the internal structure of which can be a half-bridge, a full bridge, or a clamp-double SM [8]. This work is dedicated to mathematical model which can be useful in the analysis and design of structures and control strategies of MMCs This paper studies the modular multilevel STATCOM using full-bridge SM. Due to its topology, MMC offers some advantages and unique features:

1. Its AC voltage and current have low harmonics. A passive filter becomes unnecessary.
2. MMC arm currents are continuous, and there is no longer a single bulky capacitor in a DC link.
3. The PWM carrier frequency is low, and consequently the losses are reduced.
4. Short-circuit of one sub-modules (SM) capacitor has little effect on others, and the system has fast recovery.
5. The modular structure provides redundancy to temporarily tolerate breakdown of some SM.

In MMC, there is a strong harmonic content in the arm current, although this is not reflected in the load current. This essentially controls the dynamic behavior of the converter. It is necessary to understand and predict the harmonic content of the arm current because transient behavior of this system depends on the current harmonics. In addition, to evaluate the abnormal operation of the converter; such as the failure of a module's control system or failure of the module itself, it is necessary to derive a well-defined model based on frequency domain methods.. However, in the available literature, no analytical frequency domain description of the MMC could be found that focused on harmonic interaction of the converter.

In general, power converters are nonlinear and time varying devices. It is well known that a small-signal model in the frequency domain can be used to predict the dynamic performance and stability of an MMC. Such a model is generally advantageous because it requires less computational time compared with time-domain simulation. It also provides more insight and understanding of the interaction between the AC and DC sides caused by the converter. To some extent, the harmonic distortion difficulties experienced with the previously used two-and three-level topologies are replaced by harmonic fluctuation challenges in the cell capacitors which require attention with regard to the dimensioning and control of the system.

An analytical study is made in Ref. [6] of the impact of capacitor voltage ripple, under simplified assumptions with regard to the control and modulation of the converter. To date however, there has been no comprehensive frequency-domain model of this topology and the analysis has generally relied on extensive simulation studies. In this paper a steady-state harmonic model is presented which can explain the relationship between the operating point variables, the pulse pattern used in the cells, and the harmonics of the cell capacitor voltages and the circulating currents. A power rating of 1 GW and above now becomes possible. Although the MMC topology has been presented in earlier literature [9],[10], the discussion on control methods is sparse. This paper discusses control approaches and investigates their performance using electromagnetic transients (EMT) simulation. The paper also investigates the control and performance of a HVDC transmission scheme feeding to a weak ac system.

1.1 Structure of Modular Multilevel Converter

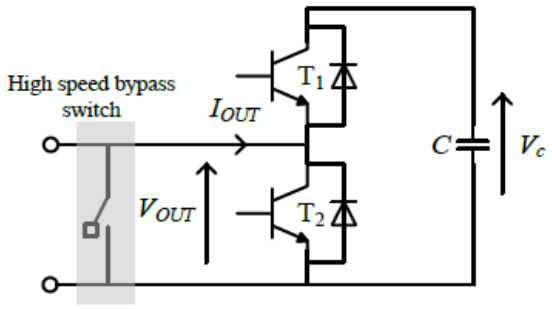

"Fig."1 Basic MMC Converter

The SM terminal voltage is determined by the states of the four switches. For a SM, there are three operating modes, namely PWM mode, natural rectifying mode, and forbidden mode. In the PWM mode, four IGBT, T1 to T4 receive PWM gating signals. The pair of T1 and T2 has complementary signals, as well as the pair of T3 and T4. The SM terminal voltage is either equal to its capacitor voltage, or the negative of capacitor voltage, or zero. When there is at least one pair of IGBT being blocked, the SM is in the natural rectifying mode. The terminal voltage is determined by the current direction which forces certain anti parallel diodes to conduct. When there is no current, the SM has high impedance and the terminal voltage is determined by the external circuit. Two IGBT in one pair cannot have ON signals at same time. This mode will short circuit the capacitor and damage the device and therefore is forbidden.

1.2 Control Schemes

To some extent, the harmonic distortion difficulties experienced with the previously used two-and three-level topologies are replaced by harmonic fluctuation challenges in the cell capacitors which require attention with regard to the dimensioning and control of the system. An analytical study is made in Ref. [6] of the impact of capacitor voltage ripple, under simplified assumptions with regard to the control and modulation of the converter. To date however, there has been no comprehensive frequency-domain model of this topology and the analysis has generally relied on extensive simulation studies. In this paper a steady-state harmonic model is presented which can explain the relationship between the operating point variables, the pulse pattern used in the cells, and the harmonics of the cell capacitor voltages and the circulating currents.

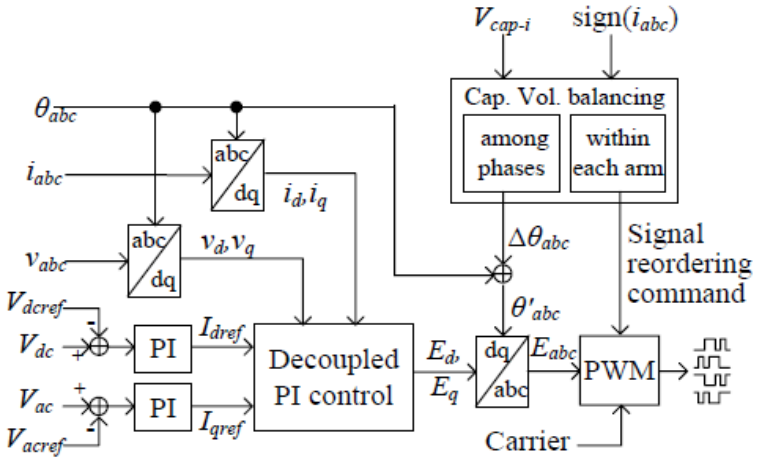

"Fig."2 Control Schemes

Several recent publications provide analytical models suitable for studying the behavior of MMC. One MMC averaged equivalent circuit that assumes all the sub modules to be identical is illustrated in Fig. 2, where the internal converter arm currents *iBij* and arm-level capacitor voltages *vSij* of the *i*th row and *j*th column may be described via (1)–(3) using an averaged duty ratio *dBij* [9], [12]. Rows and columns in this context refer to the arm position a sub module in the circuit schematic of the MMC. Each arm possesses *n* sub modules and *x* denotes the sub module number within the arm. Further nomenclature detail of the variables is illustrated in Fig. 2, and more details may be found in [9], [15], and the nomenclature.

The dynamic model that represents the coupling between the various quantities are expressed in (1)–(3), where *v*NSB is defined as the bridge neutral voltage, which is nominally zero under balanced operating conditions. While this equivalent circuit model provides a faithful representation of system behavior, it still is not particularly useful in studying the terminal behavior of the converter, because it consists of 12 coupled differential equations, even if all the sub modules are identical to each other. This section further reduces the complexity of the MMC analytical model to an equivalent boost–buck converter circuit. The transformation is performed in a step-by-step process beginning with the model defined in Fig. 2 and manipulation of (1)–(3).

II. PARAMETER REPRESENTATION

2.1 Dual capacitance selection

In the voltage source converters the energy is stored in DC-link capacitors. The maximum energy stored in capacitors *E*Cmax is determined by the rated converter power *S*n and the energy-power ratio. This ratio varies depending on the converter application and typically is *EP* = 10 J/kVA to 50 J/kVA Lower values mean a reduction of the converter cost but higher voltage ripples in the DC-link circuit. In this paper it is assumed that the same energy-power ratio is applicable to the modular multilevel converter. At the beginning of the AC-DC converter design stage two main converter parameters are set. It is the rated converter power *S*n and rms value of the line-to-line voltage *V*acll, rms at the ac side of the converter or the voltage *V*dc at the dc side of the converter. Assuming that in the MMC there are no redundant Sub modules, the relation between ac side and dc side voltages.

2.2 Power conversion within the cell strings

In the previous section it was assumed that the cell strings of the phase legs can be treated as voltage sources. Due to the presence of low-frequency voltage and current harmonics in the cell capacitors this assumption is only applicable with few qualifications. To gain a better understanding of the behavior of the cells and cell strings when the cell capacitor ripple cannot be neglected a frequency-domain model is derived in this section. Throughout the section as well as the next section, only one phase leg is considered since the treatment of all phase legs is identical. For this reason the index *i*, related to the phase leg number is dropped.

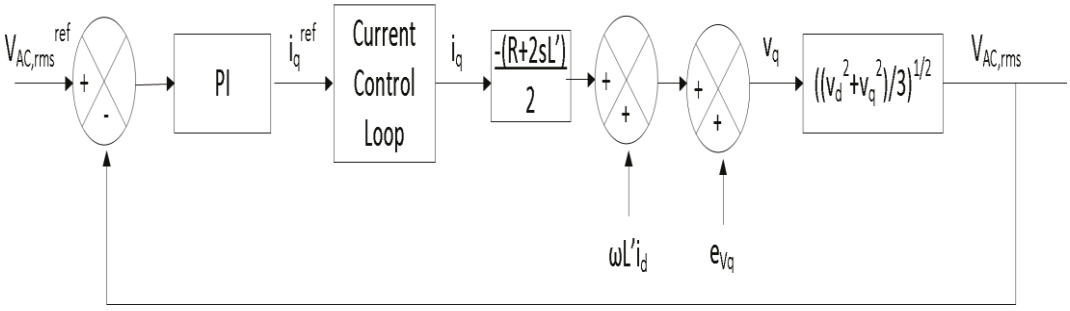

"Fig."3 Closed loop conversion

2.3 Arm inductance selection

The role of the arm inductors *L*arm in the MMC is to suppress any high frequency components of the arm currents caused by differences in upper and lower arm voltages. These differences can exist for example, due to different switching times of converter switches. From Table I it can be seen that different arm inductances *L*arm have been chosen in different references. The exact value of the arm inductance depends on the sub module capacitor voltage *V*dc/*n*, the modulation technique, the switching frequency and an additional controller optionally used for suppressing the circulating current.

In this paper only direct modulation is considered as a modulation technique and the circulating current is not suppressed by any other control methods. It means that the circulating current has to be suppressed only by proper selection of the arm inductance *L*arm. This can be done by avoiding resonances (11) that occur in the circulating current for the previously given arm capacitance *C*arm, thus shows a cell, numbered *n*, with the relevant electrical quantities indicated. The signal *s{u,l}n* is the switching function which assumes the value 0 when the valve in parallel to the cell terminal conducts and the value 1 when the valve in series with the capacitor conducts. Firstly, the equations relating the cell capacitor voltage and current to the voltage and current at the cell terminal.

Every phase-leg is composed of two arms where each arm has a number of n sub modules. In turn, in every sub module there is a DC capacitor charged with the voltage Vdc . Note that during any moment, half the modules are connected and half the modules are bypassed. This is necessary since the sum of all connected modules in a phase-leg must be Vdc.

$$V_{SM}(t) = I_{SM}(t)\frac{R_2(R_1+R_C)}{R_2+R_1+R_C} + V_{CEQ}(t-\Delta T)\frac{R_2}{R_2+R_1+R_C} \quad (1)$$

$$R_{SMEQ}(t) = \frac{R_2(R_1+R_C)}{R_2+R_1+R_C}$$

$$V_{SMEQ}(t-\Delta T) = V_{CEQ}(t-\Delta T)\frac{R_2}{R_2+R_1+R_C} \quad (2)$$

III. FREQUENCY –MODULAR MODELING METHOD

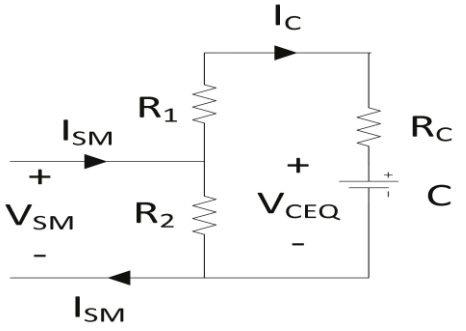

"Fig."4 Voltage source converter

With VSCs, both active power flow and reactive power flow can be controlled, independently, and accordingly no reactive compensation is needed. A VSC station is therefore more compact than a LCC station as

the harmonic filters are smaller and no switch yards and capacitor banks are needed. Other advantages with the VSC is that the converter can be connected to weak systems and even to networks lacking generation, and as no phase shift is needed, the VSC can use ordinary transformers.

A disadvantage is that the VSC has larger losses than LCC, typically 1.7 % per converter. Using LCC, the current direction is fixed and power reversal is done by changing the voltage polarity. With VSCs power reversal is done by changing of the current direction. This makes the VSC technology more suitable for a DC grid application. Cross-linked polyethylene (XLPE) cables can be used with VSCs, but cannot handle the stress from a polarity change. XLPE cables are advantageous as they are less costly, lighter, and smaller in diameter than traditional mass impregnated cables.

The power reversal with VSCs can be done gradually because the full range of active power is available, even zero active power can be combined with a positive or negative reactive power. Because both active and reactive power can obtain positive and negative values, the converter is said operate in all four quadrants of the PQ plane. LCCs normally have a minimum active power output 5% below rated power. This makes VSC more favorable for power transmission with varying power e.g. power generated from a wind farm. But an advantage with LCC HVDC is that DC pole to pole short circuit faults can be cleared in the converter station. This is not the case with classical VSC HVDC where in most cases the fault currents must be suppressed by opening the AC breaker feeding the converter.

$$V_{MV}(t) = \sum_{i=1}^{N} V_{SM_i}(t) = I_{MV}(t) \sum_{i=1}^{N} R_{SMEQ_i}(t) + \sum_{i=1}^{N} V_{SMEQ_i}(t - \Delta T) = I_{MV} R_{EQ} + V_{EQ}(t - \Delta T) \tag{3}$$

$$i_U + i_L = i_v$$

$$i_U = I_{s1} + i_{diff}$$

$$i_L = I_{s2} - i_{diff} \tag{4}$$

IV. SIMULATION RESULTS

In this section, a point to point MMC based HVDC transmission system; feeding to a weak ac network has been simulated. The dc link is connected to the two ac systems. The sending end ac system has a short circuit ratio (SCR) of 2.5, and is relatively strong. The receiving end system is weak, with an SCR of 1.0. The simulated system is schematically shown in Fig. 10. In the simulation, MMC1 acts as the rectifier and MMC2 acts as the inverter. The dc system is rated at 400MW, ±200kV. Each MMC has 100 sub-modules in a multi-valve; hence the sub-modules were rated at 4.0kV.

Parameters used for MMC

Parameter name	Symbol	Value
Voltage at the converter dc side	V_{dc}	5.0 kV
Output current amplitude	I_V	100 A
Fundamental frequency	f_m	50 Hz
Modulation index	m_a	1.0
Output phase shift angle	φ	0 deg
Arm capacitance	C_{arm}	0.02, ..., 2 mF
Arm inductance	L_{arm}	0.05, ..., 5 mH
Arm resistance	R_{arm}	0.1 Ω

As there is a total of 2400 switches in the two converters, it is practically impossible to model the converters using the traditional approach using individual switches in EMT programs. Therefore, computationally fast model discussed in section IV, was used for modeling the system [8]. HVDC System controls. The direct control strategy [7] was selected for the higher level controllers of the system. The

controllers output the desired phase shift angle δ and the magnitude M of the reference signal (Vref). The reference for measuring the angle is the ac converter bus-bar (Bus 1 for MMC1 and Bus 2 for MMC2). The angle of this bus voltage is tracked by a phase locked loop (PLL) which provides the synchronizing reference. The details of the individual rectifier and inverter side controllers are given below.

4.1 Rectifier Side Controller

The MMC1, rectifier is responsible for regulating the dc side voltage and ac side Bus1 voltage. Proportional-integral controllers derive magnitude, M1, and phase, δ1, of the reference waveform to regulate the ac bus-bar voltage and the dc bus voltage respectively. Using these, three phase reference waveforms are generated and sent to the firing control system.

4.2 Inverter Side Controller

At the inverter, a similar control strategy is used, with the difference that the magnitude, M2, and phase, δ2, of the reference waveform are the outputs of proportional-integral controllers that regulate ac bus voltage and real power. The above HVDC transmission system where a power order change from full power (400 MW) to half power (200 MW) is applied at 0.4 s. The real and reactive power at the receiving end with the inverter side rms ac voltage and three phase bus voltage waveforms shown respectively. From the simulation, it can be seen that when the load is reduced, the voltage is immediately controlled to the rated value of 115kV and no significant overvoltage is seen, even though the inverter side ac system is weak. The control of voltage is obtained by rapid control of the reactive power to follow the real power change, as shown in the trace of reactive power. The change in power to (to 90% of final setting) is seen to be achieved in approximately 60 ms. The converter output ac voltage waveforms are shown during this transient and are indeed sinusoidal even though no ac filters are used.

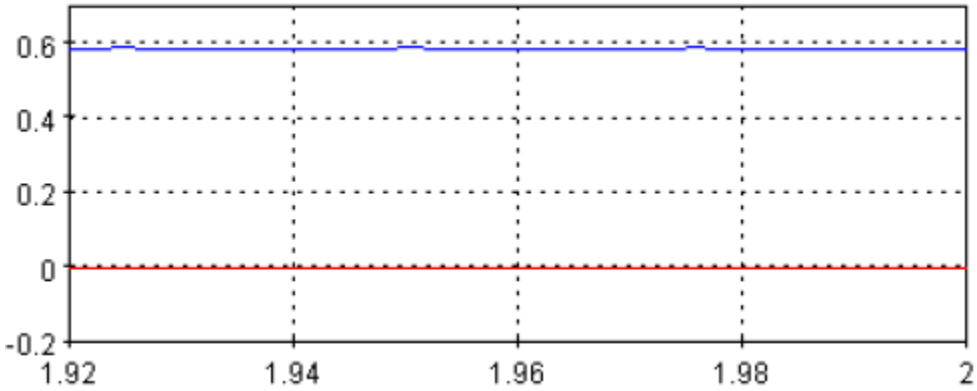

"Fig."5 Voltage Representation

From the similarity of these two equations, it can be seen that the active power controller and the reactive power controller will have the same structure and parameters. The reactive power control loop will contain the q axis current control loop. This loop has the same closed loop transfer function as the d axis current control loop. Due to these similarities only the active power control loop is shown here (Fig. 7). It consists of a PI controller, the d axis current control loop, and a gain given by equation (34). Tuning of the PI controller must be done to ensure a sufficiently large phase margin combined with a high crossover frequency. Plotting of the transfer function shows that the gain must be kept under a certain value and that the integral time constant, *TiP*, must be kept a number of times higher than the time delay in the converter *Ta*.

The nonlinearity of the switching function in the cells provides a few challenges for the derivation of a frequency domain model. According to Eq. (3) the capacitor current, and hence the capacitor voltage ripple, will contain modulation products of the switching function and the phase branch currents. On the other hand, Eq. (4) shows that the capacitor voltage ripple will influence the voltage at the cell terminals, and hence also the phase-branch currents, according to the discussion in the previous section. Thus, the branch currents influence the capacitor voltages which in turn affect the cell output voltages that together contribute to the phase-branch currents etc. For this reason, it is not trivial to obtain a closed analytical solution to the harmonic problem in the general case. A possible approach is to iterate between calculations of the capacitor harmonics on the one hand, and the phase-branch currents on the other hand until a solution is found. Such an algorithm is outlined in Figure 5, and Described in detail below. Starting from an estimate of the phase-branch current, the harmonic components of the current injected into cell capacitor *n* can be obtained as shown

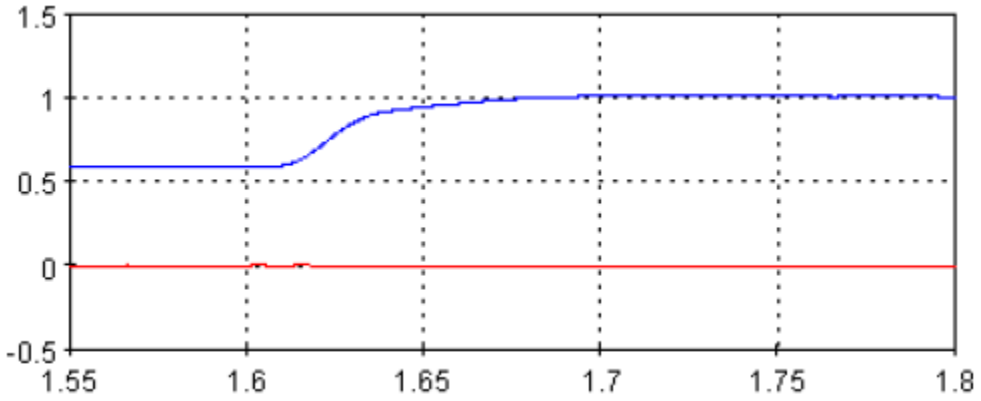

"Fig."6 Current Representation

The Current Control Loops. Fig. 6 shows the d axis current control loop. It consists of a PI controller, a time delay representing the converter and a block representing the electrical system given by equation (3). From the symmetry of equations (1) and (2) it can be seen that the q axis current control loop will have the same structure and parameters and this loop is therefore not shown here. The PI controller in the control loop can be tuned using modulus optimum [18]. Using modulus optimum, the PI controller's zero should cancel the largest time constant in the system transfer function. In this case that will be the time delay in the block representing the electrical system

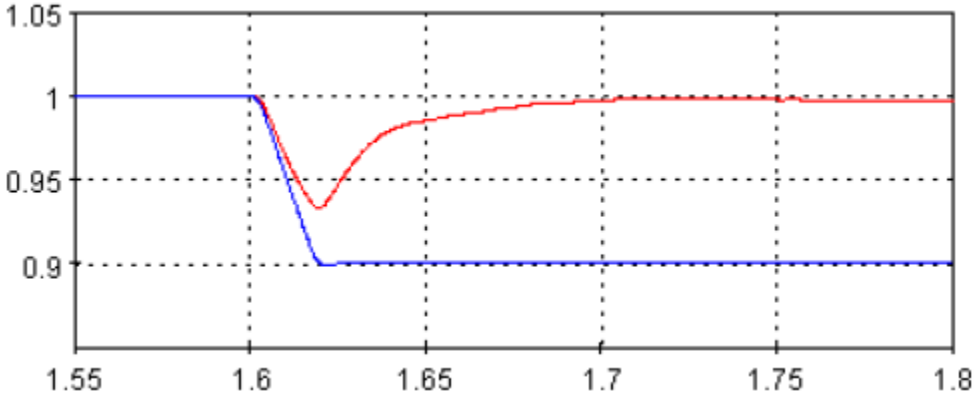

"Fig."7 Magnitude Displacement

As regards the average cell capacitor voltage, a few alternatives are possible, depending on the control of the considered converter. If, on the one hand, a control algorithm is implemented to maintain the average voltage at a certain set point, this value is used since this would be the steady-state value. If, on the other hand, the converter is connected to a dc bus bar with constant pole-ground voltage *Udc*, the cell capacitor voltage will adapt to the bus bar voltage and this corresponding capacitor-voltage dc. For the steady-state operation of the MMC converter it is vital to maintain energy balance between the dc and ac sides. In the previous chapter it was mentioned that the frequency-domain model does not give any direct guidance as to the dc components of the cell capacitor voltages and the converter dc-side current, both of which are related to the energy balance of the system. In this section the considerations necessary for choosing these variables in each iteration are discussed.

V. CONCLUSION

A benefit of the method is that it allows for a clear separation of steady-state and dynamic Effects which is not always possible by time-domain simulation. A weakness of the studied method is that no dynamic phenomena can be modeled, so that it is less useful as a tool for designing and evaluating closed-loop control systems, for instance. In this paper, the methodology was employed to solve the problem where the converter is connected to fixed ac and dc circuits and a fixed pulse pattern applied for the cells. However, also other problems may be solved by the studied model, which will be the topic of coming work. Furthermore, the methodology has been applied to the MMC converter with half bridges. However it could with modifications also be applied to other similar cell-based topologies, such as converters employing full bridges, where similar cell capacitor ripple effects are present For the simulation model, a The equivalent was introduced to obtain a

voltage value for each multivalve at every instant. This model must be combined with a capacitor voltage balancing algorithm. The equivalent is important as it reduces the computational efforts a lot, and hence makes realistic simulations possible. Regarding control, the MMC has the same advantages as two-level and three-level VSCs, d axis and q axis control can be done independently. This can be used to control either DC voltage or active power and either AC voltage magnitude or reactive power. The presented control loops use a cascaded structure with a fast inner current loop and an outer loop controlling active power and reactive power or the AC voltage magnitude.

REFERENCES

Journal Papers:

[1] M Ozaki, Y. Adachi, Y. Iwahori, and N. Ishii, Application of fuzzy theory to writer recognition of Chinese characters, *International Journal of Modelling and Simulation, 18(2),* 1998, 112-116. (8)

[2] S. S. Gjerde and T. M. Undeland, "The best suitable multilevel converters for offshore wind power generators without transformers," in *Proc. Int. Power Electron. Conf.*, 2010, pp. 2398–2404.

[3] S. Allebrod, R. Hamerski, and R. Marquardt, "New transformerless, scalable modular multilevel converters for HVDC-transmission," in *Proc. IEEE Power Electron. Spec. Conf.*, 2008, pp. 174–179.

[4] J. K. Reed and G. Venkataramanan, "Fault tolerant MVDC-HVAC power converter for wind farm applications," presented at the CIGRE HVDC Colloq., San Francisco, CA, USA, 2012.

[5] A. L. P. de Oliveira, C. E. Tiburcio, M. N. Lemes, and D. Retzmann, "Prospects of voltage-sourced converters (VSC) applications in DC transmission systems," in *Proc. Transmiss. Distrib. Conf. Expo.: Latin Am.*, 2010, pp. 491–495.

[6] U. N. Gnanarathna, S. K. Chaudhary, A. M. Gole, and R. Teodorescu, "Modular multi-level converter based HVDC system for grid connection of offshore wind power plant," in *Proc. IET Int. Conf. AC DC Power Transmiss.*, 2010, pp. 1–5.

[7] G. P. Adam, O. Anaya-Lara, and G. Burt, "Multi-terminal DC transmission system based on modular multilevel converter," in *Proc. 44th Int.Universities Power Eng. Conf.*, 2009, pp. 1–5.

[8] D. Soto-Sanchez and T. C. Green, "Control of a modular multilevel converter-based HVDC transmission system," in *Proc. 14th Eur. Conf. Power Electron. Appl.*, 2011, pp. 1–10.

[9] D. C. Ludois, J. K. Reed, and G.Venkataramanan, "Hierarchical control of bridge-of-bridge multilevel power converters," *IEEE Trans. Ind. Electron.*, vol. 57, no. 8, pp. 2679–2690, Aug. 2010.

[10] J. Reed, G. Venkataramanan, and F. Martinez, "Complex phasor modeling and control of modular multilevel inverters," in *Proc. IEEE Energy Convers. Congr. Expo*, 2011, pp. 4013–4020.

[11] S. Rohner, J. Weber, and S. Bernet, "Continuous model of modular multilevel converter with experimental verification," in *Proc. IEEE Energy Convers. Congr. Expo.*, 2011, pp. 4021–4028.

[12] K. Ilves, A. Antonopoulos, S. Norrga, and H.-P. Nee, "Steady-state analysis of interaction between harmonic components of arm and line quantities of modular multilevel converters," *IEEE Trans. Power Electron.*, vol. 27, no. 1, pp. 57–68, Jan. 2012.

American Journal of Engineering Research (AJER)
e-ISSN : 2320-0847 p-ISSN : 2320-0936
Volume-03, Issue-01, pp-09-13
www.ajer.org

Research Paper Open Access

Preservation of Concrete Shell Structures

J. Mundo-Hernandez[1], M. C. Valerdi-Nochebuena[2], J. Sosa-Oliver[2]
[1]*Associate Professor at Universidad de las Americas Puebla, Sta. Catarina Martir, Cholula, Puebla, Mexico, 72810,*
[2] *Professors at Universidad Autonoma de Puebla, Mexico.*

Abstract: - This paper aims to analyse current people's perception towards concrete shell structures located in the main campus of the University of Puebla, in central Mexico. We are interested in knowing the perception of building academics and architecture and engineering students regarding the use, value and current conditions of concrete shells. This will help us to understand what kind of actions can be taken to preserve those structures, and what factors should be considered during the design of new spatial structures.

***Keywords*: -** *concrete shell structures, lightweight buildings, users' perception, building heritage, sustainability, 20th Century architecture.*

I. INTRODUCTION

Concrete shell structures have defined an important moment in the design of space structures during the 20th century. Concrete lightweight structures continue to impact in the design of new buildings. In Mexico there are still a great number of examples of concrete shell structures, mainly built during the 1950´s and 60´s, by Felix Candela. He and designers Fernando and Raúl Fernández-Rangel, established in 1950 a Company called "Cubiertas Ala" (that name translates as Wing Shells); which built around 800 thin concrete shell buildings until the company closed in 1976 [1].

Despite the architectural significance of thin concrete shells, some of them built in the city of Puebla in Mexico have been demolished, hence, the importance of finding and developing strategies to preserve them. This paper aims to analyse current people's perception towards those structures. We are interested in knowing the perception of building professionals and students regarding concrete shell structures located in the main campus of the University of Puebla in central Mexico. A broader project intends to develop a catalogue of concrete shell structures and other lightweight structures (mainly fabric structures) built since the construction of the University Campus in 1969.

The University campus in Puebla was built during the second half of the 20th Century, hence, an important number of concrete shell structures were built, for instance: the Cultural Centre of the Architecture Faculty designed by architect Miguel Pavón Rivero (Fig. 1), and a lab building of the Engineering Faculty (Fig. 2).There are alsoconcrete hyperbolic paraboloid umbrella shells that cover exterior corridors for rain and solar protection (Fig. 3). Recently, some of those structures were demolished in order to build a new entrance to the campus, which has no architectural value. This fact raised concern among members of the Architecture Faculty, especially academic staff members, who have studied and worked for several years in that campus.

Knowing current users´ perception towards those structures would help to raise awareness about the importance of preserving examples of fine architecture that could help us to understand the life cycle of buildings and consider certain factors in the design of new structures. Those factors are: lifetime, life-cycle analysis, interior environmental quality, users' role, climate, aesthetics, flexibility, comfort, building systems and materials. Valuable lessons can be learnt from past architecture examples. In addition, preserving usable buildings contribute to sustainability: avoiding the construction of unnecessary new structures or buildings, preserving land for other use, saving natural resources such as energy, water and wood, reducing waste; whilst decreasing the production of $CO_2$and air pollution generated by the extraction, transport and manufacturing of building materials, and the use of construction equipment.

Figure 1. La Monja Cultural Centre, Architecture Faculty, BUAP (2012).

Figure 2. Lab building, Engineering Faculty, BUAP (2013).

Figure 3. Corridor covered by a concrete shell, University Campus, BUAP (2013).

II. MATERIALS AND METHODS

A questionnaire with 16 questions was designed to answer the following main queries: **Do current users value concrete shell structures? How do they use them? And how those structures respond to present spatial needs? Are concrete shell structures worth preserving?** The questionnaire was distributed between February and April 2013, among students and academic members of the Architecture and Engineering Faculties of the University of Puebla (BUAP). In total, 117 answered questionnaires were received and analysed using the statistical software SPSS v18.0.

III. RESULTS AND DISCUSSION

Respondents are mainly 5th year students (44%), 18% are 4th year students and 17% are 3rd year students, the rest are 1st and 2nd year students. Most of them (88%) are architecture students, and the rest are Engineering students (12%). Only 4 academic staff participated in the survey, therefore, their comments will be included in the discussion but not considered in the data analysis. 85% of respondents are between 17 and 23 years old, and 15% are between 24 and 30 years old.Hence, their use of the university campus and the concrete shell buildings is limited to 5 years.

Respondents were asked about their general opinion regarding the university concrete shell buildings. People who have a positive opinion are 74% of respondents, they believe those buildings are useful, interesting and innovative in their design. On the other hand, people who believe concrete shell buildings are ugly, not

useful, boring and dated represent 26% of participants. Regarding the concrete shell umbrellas that cover the exterior corridors (Fig. 3), 82% of respondents think they fulfil their functional objective of solar and rain protection; and 77% believe they must be preserved. Reasons for that include: the structures are an icon of the Architecture Faculty and the University Campus, it is more expensive and not sustainable to demolish them in order to build new structures, they are part of the architectural history of Mexico and those structures are useful for sun and rain protection and to lit the corridors at night.

Figure 4 shows users' perception regarding their mood when using the university´s concrete shell buildings. Their answers were grouped into two categories: comfortable and uncomfortable; however, people´s responses included feelings such as being: warm, cold, bored, happy, distracted, active, etc. It is interesting to observe their opinions,51% of respondents feel comfortable while the other half (49%) feel uncomfortable.

Users were asked if they believe the concrete shell structures look integrated with the whole campus architecture. 39% of respondents agreed that the concrete shells integrate with the rest of the university buildings, while 38% said they do not integrate, and 22% stated that they do not know (Figure 5). Moreover, people were questioned about their perception towards the level of maintenance of these buildings. The majority of respondents (almost 54%) said maintenance is fair, 12% answered maintenance is good and almost 34% responded maintenance is bad and very bad (Fig. 6). Open comments from people included:

- "Maintenance to concrete shell buildings is poor;
- it seems that they are going to fall down;
- they are functional buildings but need good and continuous maintenance;
- they need painting, especially on facades;
- include green roofs and natural ventilation for thermal control in lecture rooms located in La Monja building (figure 1);
- some lecture rooms are flooded in the raining season;
- they need immediate attention and renovation;
- it is important to preserve these buildings for historical reasons;
- It would be better to restore them than to build new buildings".

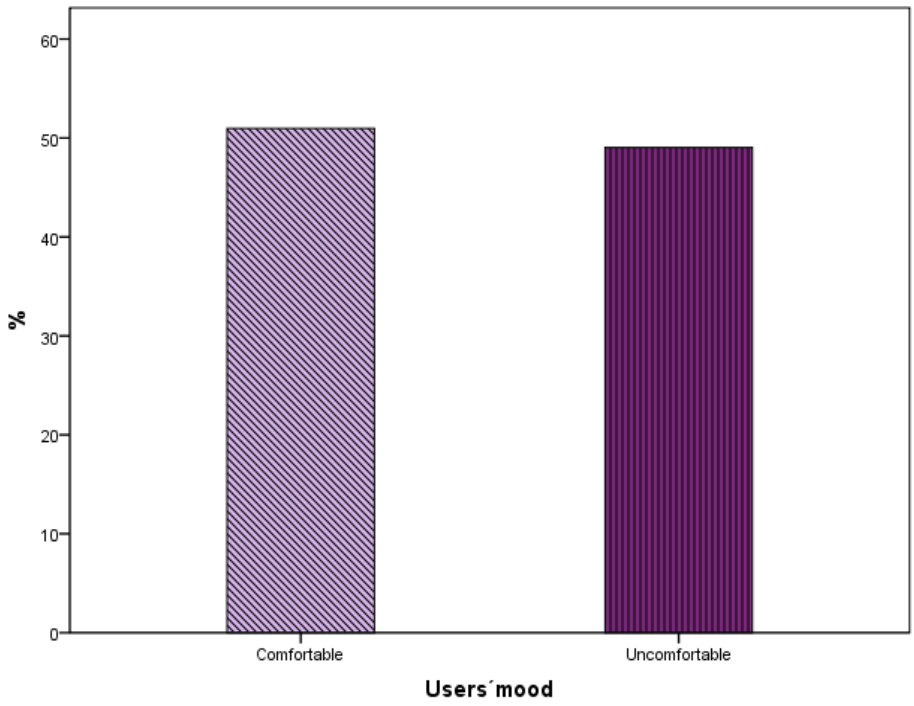

Figure 4. Users' mood originated by using thin concrete shell buildings.

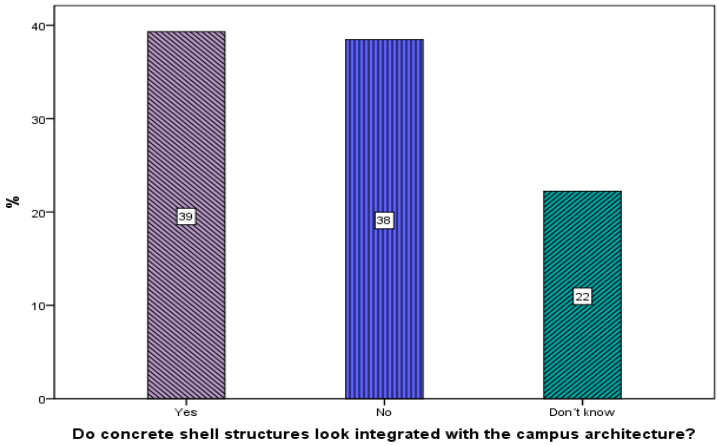

Figure 5. Users' perception regarding concrete shell integration with other Campus buildings.

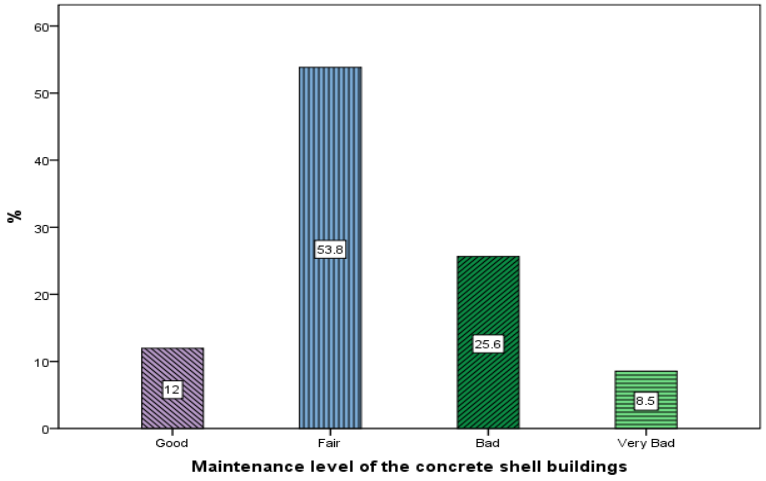

Figure 6. Users' perception towards maintenance of the concrete shell buildings.

When users were asked about the value of concrete shells and the importance of preserving those structures, students pointed out that they look dated and poorly maintained. They also mentioned that it would be necessary to restore them in order to preserve them. Some people mentioned the need to demolish them in order to build new and modern buildings. Staff members value more the architectural significance of concrete shells, and the importance of preserving them as part of the university´s architectural heritage.

IV. CONCLUSION

We believe the key to preserve thin concrete shell structures relies mainly on the education of future building professionals. If they recognise their architectural value and engineering advantages such as lightweight, minimum use of materials and the ability to cover large span buildings, those shellscould be saved from demolition.According to Draper et al [2] one of the reasons for rarely finding today designers building such structures is the lack of technical expertise to properly understand their structural behaviour.

In addition, few approximations to study thin concrete shells environmental behaviour have been carried out. Previous research developed at the University of Puebla was focused on studying the interior environment of La Monja building [3, 4]. Results of that project pointed out some major environmental problems of the building: lack of natural ventilation, elevated interior temperature and the presence of glare. Those factors have made people to leave the building and even to suspend lectures or conferences being held in there.

Preserving functional concrete shell buildings would allow future generations to use, see and admire space structures designed and built during the 20th Century. Concrete shell structures represent an important contribution to engineering, technology and architecture. Recently some researchers have proposed and tested

the use of fabric and pneumatic formwork for the construction of thin concrete shells and other type of concrete buildings [5, 6]. These procedures could make possible to design and build innovative and modern building shapes, without the stiffness and flatness of traditional wood or steel formwork. Moreover, they could contribute to reduce building costs since the construction would be simpler and more efficient. Cauberg et al [5] have done a review of the possibility of replacing traditional steel reinforcement for textile reinforcement, allowing to build the same double curvature and elegant concrete shells with more flexible and lighter materials.

Moreover, preserving existing buildings is a sustainable approach of the building industry. Reusing buildings avoids the construction of new ones, and this contributes to preserving farm land, forests and natural habitats. It also avoids the use of water and energy necessary to build new structures. The quantity of construction material used to build new buildings is far greater than the amount of material used to restore an existing building. The same can be said about the production of waste in building sites, and air pollution with CO_2 and dust generated by construction machinery and other demolition and construction activities.

Particularly to this case study, it is recommended to take the following actions:

- To introduce topics related to the design and construction of concrete shell buildings in Mexico and the rest of the worldin the contents of Architecture and Civil Engineering courses.
- To organise university study trips to visit concrete shell buildings and other innovative structures.
- To make emphasis among university students and building professionals of the design possibilities and construction advantages of thin concrete shells,their current use and building technology and materials available.
- To encourage the preservation of existing concrete shell structures with the University planners and central administration.
- To propose innovative and energy efficient lighting systems to be integrated into the umbrella type concrete shell structures, in order to enhance their shape while illuminating the university corridors.

REFERENCES

[1] Garza-Usabiaga, D., *Félix Candela*, (Ed. Del Cueto, J. Spain: Acción Cultural Española, 2011, pp. 10-17).

[2] Draper, P., Garlock, M., and Billington, D.,Optimization of concrete hyperbolic paraboloid umbrella shells, *Proceedings of the 6th International Conference on Computation of Shell and Spatial Structures*, Ed. Abel, J. and Cooke, J., IASS-IACM, Acapulco, Mexico, 2008, pp. 16-32.

[3] Mundo, J., Valerdi, M., Sosa, J. and Romero, E.**,** Iluminación y confort ambiental: La percepción de los usuarios del Centro Cultural La Monja, BUAP, Puebla. *Revista Legado de Arquitectura y Diseño*, *No. 7*, *Year 5*, pp. 63-74.

[4] Mundo, J., Valerdi, M., Sosa, J. and Arenalde, B.,Occupants' environmental perception of a concrete shell building: a case study in Mexico. *Book of Abstracts and Proceedings of the IASS-SLTE Symposium*, Ed. Oliva-Salinas, J., IASS, Acapulco, Mexico, 2008, p. 189-190.

[5] Cauberg, N., Tysmans, T., Adriaenssens, S., et al.,Shell elements of textile reinforced concrete using fabric formwork : a case study. *Advances in Structural Engineering, Vol. 15, No. 4*, 2012, pp. 677-689.

[6] Lusis, V.,Production technology for concrete shells using pneumatic formwork with variable elevation.*Scientific Journal of Riga Technical University, Vol. 12*, 2011, pp. 35-39.

American Journal of Engineering Research (AJER)
e-ISSN : 2320-0847 p-ISSN : 2320-0936
Volume-03, Issue-01, pp-14-17
www.ajer.org

Research Paper Open Access

Glaucoma Distribution in major Religious Communities of Rural Gangetic Delta

Dr Chandrima Paul, Prof Himadri Datta, Prof Gautam Bhaduri
Address : HA 274, Saltlake, Kolkata – 700097 .West Bengal. India
Affiliation : Regional Institute of Ophthalmology, Medical College and Hospitals, Kolkata
Acknowledgement : The West Bengal University of Health Sciences.

Abstract: **- Aim:** To study the pattern of glaucoma distribution among the patients in rural Gangetic Delta **Materials and Methods:** A retrospective analysis of 1800 glaucoma patients was done, who were recruited by a door to door field survey and brought to a rural Base Eye Hospital in the Hooghly district of West Bengal, India between January 2010 and December 2012 . The subtypes of glaucoma in different religious groups(mainly among Hindus and Muslims) along with the age and gender distribution were studied. **Results:** The mean age of the glaucoma patients was 54.6 years. Glaucoma was diagnosed in 972(54%) Muslim and in 632(35.1%) Hindu patients. The prevalence of POAG (35.0%) was close to that of PACG (33.1%). POAG was the most common type of glaucoma in males (15.2%), while PACG was very common among females (16.4%). In Hindu patients, POAG (42.4%) was the commonest form of glaucoma, while in Muslims, PACG (41.8%) was the highest form of glaucoma.

Conclusion: *Glaucoma distribution in the Muslim population is the highest among all religious groups of the rural Gangetic Delta .*

I. INTRODUCTION

The blindness caused by glaucoma is expected to reach alarming proportions. [1] It is the second most common cause of world's blindness and majority of them reside in Asia [2, 3]. India accounts for 12.9% of the Primary Open Angle Glaucoma (POAG) cases and 12.7% of the Primary Angle Closure Glaucoma (PACG) cases in the world [4].

There were studies which account for the different subtypes of glaucoma and showed the varying predominance of glaucoma types in different regions of India in urban [5] and rural populations [6–8]. There is only little data on the distribution of these glaucoma subtypes according to the religion of the patients, as India has complex patterns of migration and this contributes to the marked ethnic diversity between the different regions and religions.

As the data on the distribution of these glaucoma subtypes according to the religion of the patients, is small and India has complex patterns of migration and this contributes to the marked ethnic diversity between the different regions and religions, we conducted this study, to further contribute in this regard, West Bengal, India.

According to the Census of India 2001,Hugly (12),West Bengal (19)C District Hugli (12), 1.Hindus 4,216,701
2.Muslims 763,471
3.Others 49,075
The Hindu population accounts for 35.1% of the glaucoma cases in rural Gangetic Delta, which is much lower than that in the state of Uttar Pradesh (80.62%)

II. MATERIALS AND METHODS

The rural study area consists of 28 contiguous villages from the district of Hugli in West Bengal which are about 20kms surrounding the Rural base hospital located at Dhobapara,in Village Bakulia of this District.

A three year retrospective analysis (January 2010-December2012) of the records of 12000 patients was done.1800 patients , aged >30 years, who were diagnosed as having glaucoma in one or both the eyes were included.

Exclusion criteria :

Incomplete data

Congenital and Developmental glaucoma

Patients lost to follow up

A previous glaucoma surgery

The work up of the history and the ophthalmic examination included:

The Best Corrected Visual Acuity (BCVA)

The IOP which was obtained by using a Goldman applanation tonometer. Slit lamp examination .gonioscopy, with the use of a Goldman four-mirror lens, was done in all the patients. The occludability was assessed by using a dim ambient and a slit lamp illumination, with the patient looking straight ahead. The anterior chamber angle was classified by using Shaffer's grading [9]. Grade 2 or less was considered as occludable, and grade 3 or more was considered as open. The eyes with occludable angles and no glaucoma were labelled as latent ACG.

Optic disc examination was done with a+90 dioptres (D) lens at 16 × magnification without a pupillary dilatation. The Vertical Cup-to-Disc Ratio (VCDR) was used as the index for the structural glaucomatous change. If the stereo view was not satisfactory due to the opacity of the lens or due to the restrictions of the pupil size, the pupil was dilated by using 0.5% tropicamide and 0.5% phenylephrine hydrochloride. The fundus changes which were suggestive of glaucoma included focal notching of the disc, deepening of the cup, thinning of the neuroretinal rim, a laminar dot sign, overpass cupping, saucerization of the cup, asymmetrical cupping in the two eyes and Retinal Nerve Fibre Layer (RNFL) defects.

A field examination was done by using automated perimetry (the Humphrey Field Analyzer 24-2 Sita Standard) if the fundus findings were suggestive of glaucoma. The unreliable fields [10] with the typical glaucomatous visual field damage (i.e. nasal step, or paracentral, Seidel's or arcuatescotoma, or deep diffuse depression) were repeated twice [11].

A glaucomatous visual field defect was considered to be present if the following were found:

A Glaucoma Hemifield Test (GHT) result which was outside the normal limits, and

A cluster of three or more nonedge, contiguous points, which were not crossing the horizontal meridian, with a probability of 5% of the age-matched normals on the pattern deviation plot, on two separate occasions.

Some components of the examination could not be carried out on the patients who refused such an examination, those with cataracts, or those with corneal opacities.

PAOG was defined as a condition in a subset of patients with open angles, a raised IOP which was associated with either a glaucomatous cupping of the optic nerve head or visual field changes which were suggestive of glaucoma [12]. The patients who were less than 35 years of age, with a clinical picture which was similar to that of POAG, were labelled as having Juvenile Open Angle Glaucoma (JOAG) [12].

PACG was said to exist when a person had, in the same eye or in both eyes (a) a pressure of >21 mm Hg and (b) an anterior chamber angle which was two-thirds obstructed. The angle closure was considered to be either appositional or synechial. The chronic appositional angle closure was diagnosed in the presence of a raised intraocular pressure and with closed angles on gonioscopy, in the absence of peripheral anterior synechiae (PAS). The presence of glaucomatous field defects or optic disc changes was not considered as mandatory for the diagnosis of angle closure glaucoma [12], [13]. The latent ACG comprised of asymptomatic patients with occludable angles [12].

The normal tension glaucoma patients were classified as having open angles, and progressive optic nerve head changes or a visual 500field loss which was suggestive of glaucoma in the absence of an elevated IOP [12]. The glaucoma suspects included (a) a subset of patients with open angles, an IOP of less than 22 mmHg and absence of field changes but with optic nerve head changes; and (b) patients with a strong family history of glaucoma in the absence of optic nerve head changes or a high IOP [12].

III. RESULTS

A door to door survey was conducted in the 28 villages of the Hugli district in West Bengal . Of the 4,216,701 .Hindus and 763,471 Muslims , there were 1800 diagnosed glaucoma patients.

Glaucoma was diagnosed in 972(54%) Muslim and in 632(35.1%) Hindu patients. The prevalence of POAG (35.0%) was close to that of PACG (33.1%). POAG was the most common type of glaucoma in males (15.2%), while PACG was very common among females (16.4%). In Hindu patients, POAG (42.4%) was the commonest

form of glaucoma, while in Muslims, PACG (41.8%) was the highest form of glaucoma. 1800 (2.03%) glaucoma patients were identified. The mean age was 54.6 years with an S.D. of 11.3.
The mean IOP recorded in RE was 25.8 mm Hg with S.D of 11.14 [Table/Fig-1] and in LE it was 26.4 mm Hg with S.D. of 11.36 [Table/Fig-2]. By matching the IOP with the slit lamp examination findings and the field defects, the patients were categorized into various glaucoma subtypes.
Primary Open angle glaucoma was diagnosed in the maximum number of patients (35%), followed by Primary angle closure glaucoma (33.1%)

Further analysis was done to find out the pattern of glaucoma which was present in the two major religious population.. They included Hindus (GroupA) and Muslims (Group B). POAG (42.4%) was found to be leading form of glaucoma among the Hindu patients [Table/Fig-3] while PACG was the most common type of glaucoma (41.8%) among the Muslim patients [Table/Fig-3]

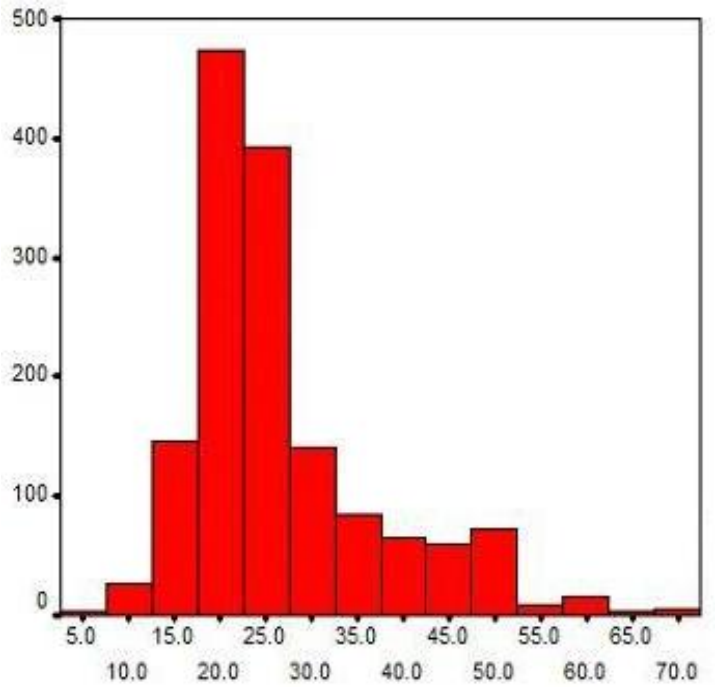

Table/Fig 1 : Right Eye IOP(Intra Ocular Pressure) N= 1800; Mean IOP 25.8 ; SD 11.14

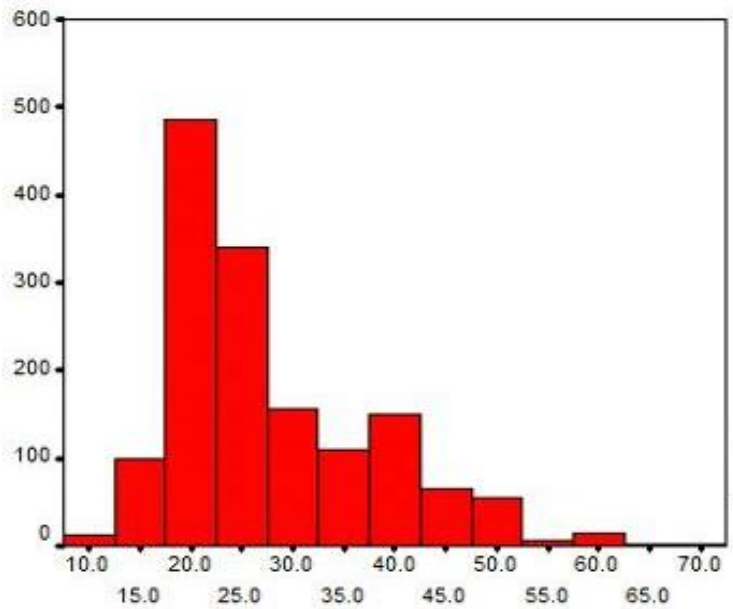

Table/Fig 2 : Left Eye IOP(Intra Ocular Pressure) N= 1800; Mean IOP 24.6 ; SD 11.36

Subtype	Group A	Group B
Juvenile open angle glaucoma	15 (2.5%)	26 (2.7%)
Primary open angle glaucoma	267 (42.4%)	447 (46.2%)
Primary angle closure glaucoma	205 (32.6%)	406 (41.8%)
Normal tension glaucoma	24 (3.8%)	40 (4.2%)
Secondary glaucoma	13 (2.2%)	27 (2.8%)
Ocular hypertension	64 (10.2%)	31 (3.2%)
POAG suspect	55 (8.8%)	17 (1.8%)

Table/Fig 3: Showing distribution of various glaucoma subtypes

IV. DISCUSSION

We studied the data of 1800 glaucoma patients following a door to door survey of rural patients in the hugli district of West Bengal , India. The mean age of presentation was 54.6 years. The mean age of presentation of glaucoma varies from 30 to 60 years, as was seen in various studies [13], [14].

In our study, we tried to find the pattern of the prevalence of glaucoma in a Population based data . The prevalence of glaucoma was found to be higher among Muslim patients, 972 (54%) as compared to 632 (35.1%) Hindu patients. This was despite the fact that overall Hindu patients were 4,216,701 of the population , more as compared to Muslims 763,471. POAG was found to be most common type of glaucoma (40.8%) among the Hindu patients, followed by PACG(20.7%). Whereas PACG was reportedly highly prevalent among the Muslim patients (42.4%) as compared to PAOG (32.6%). The difference which we found, might be due to some cultural practices which are more common in the Muslim population, like consanguineous marriages [15]. An important aspect of our study is that, this is the first study in Eastern India, which has highlighted the prevalence of glaucoma and its subtypes, based on religious factors in a population database.

REFERENCES

[1] Smita Agarwal, M. A Shamshad, Dishanter Goel, Maryem Ansari Distribution of Glaucoma in the Major Religious Communities of a North Indian Town: A Hospital Survey *JCDR/2013/ Volume : 7, Issue : 3,Page : 499 – 502*

[2] Quigley HA, Broman AT, The number of people with glaucoma worldwide in 2010 and 2020 *Br J Ophthalmol* 2006; 90262:267.267

[3] Resnikoff S, Pascolini D, Etya'ale D, Global data on visual impairment in the year 2002 *Bull World Health Organ* 2004 Nov; 82(11):844-51.

[4] Thylefors B, Negrel AD, The global impact of glaucoma *Bull World Health Organ* 1994; 72:323-26.

[5] Dandona L, Dandona R, Mandal P, Angle-closure glaucoma in an urban population in southern India. The Andhra Pradesh Eye Disease Study *Ophthalmology* 2000; 107:1710-16.

[6] Ramakrishnan R, Nirmalan PK, Krishnadas R, Glaucoma in a rural population of southern India: the Aravind comprehensive eye survey *Ophthalmology* 2003; 110:1484-90.

[7] Vijaya L, George R, Paul PG, Prevalence of open-angle glaucoma in a rural south Indian population *Invest Ophthalmol Vis Sci* 2005; 46:4461-67.

[8] Raychaudhuri A, Lahiri SK, Bandyopadhyay M, Foster PJ, Reeves BC, Johnson GJ, A population based survey of the prevalence and types of glaucoma in rural West Bengal: the West Bengal Glaucoma Study. Br J Ophthalmol.2005; 89:1559–1564 *Br J Ophthalmol* 2004; 88:1493-97.

[9] Shaffer RN, A suggested anatomic classification to define the pupillary block glaucomas *Invest Ophthalmol* 1973; 12:540-42.

[10] Sommer A, Enger C, Witt K, Screening for glaucomatous visual field loss with automated threshold perimetry *Am J Ophthalmol* 1987; 103:681-84.

[11] Katz J, Sommer A, Screening for glaucomatous visual field loss: the effect of patient reliability *Ophthalmology* 1990; 97:1032-37.

[12] Das J, Bhomaj S, Chaudhuri Z, Sharma P, Negi A, Dasgupta A, Profile of glaucoma in a major eye hospital in North India *Indian J Ophthalmol* 2001; 49:25-30.

[13] Jacob A, Thomas R, Koshi SP, Braganza A, Muliyil J, Prevalence of primary glaucoma in an urban South Indian population *Indian J Ophthalmol* 1998; 46:81-86.

[14] Vijaya L, George R, Baskaran M, Arvind H, Raju P, Ramesh SV, Prevalence of primary open-angle glaucoma in an urban south Indian population and comparison with a rural population. The Chennai Glaucoma Study *Ophthalmology* 2008 Apr; 115(4):648-54.

[15] Bittles AH, Endogamy, consanguinity and community genetics *Journal of Genetics* 2002 Dec; 81(3):91-98.

American Journal of Engineering Research (AJER)
e-ISSN : 2320-0847 p-ISSN : 2320-0936
Volume-03, Issue-01, pp-18-26
www.ajer.org

Research Paper Open Access

The Densification and Diametral Compression Strength of Isi-Ogwuta Clay

J. E. O. Ovri* and A. I. Ndukwe[+]
Department of Materials and Metallurgical Engineering, Federal University of Technology Owerri, Nigeria.

Abstract: - The diametral compression strength of clay was investigated. The clay sample was analyzed to ascertain its chemical composition and mineralogical constituent. The diametral clay discs were produced using a uniaxial cold pressing hydraulic press and sintered at a predetermined temperature and time (1200℃ and 15 minutes). Two diameters (D) of discs of 23mm and 29mm were used with varying thicknesses (3mm-10mm). The effect of disc thickness with intent to qualitatively define the plane stress and the plane strain fracture conditions of the clay was undertaken. The plane stress condition was obtained by discs with thickness $\leq 1/4\,D$ for 23mm and 29mm whilst the plane strain condition was obtained by testing discs of thickness $> 1/4\,D$. The diametral compression strength of discs of thicknesses $3-10$mm gave a range of $14.6-5.5$MPa for samples of 23mm diameter whilst a range of $5.8-2.2$MPa was obtained for samples of 29mm diameter. Greater numbers of 29mm diameter samples failed in the normal tensile fracture mode whilst more samples of 23mm diameter failed in the triple-cleft fracture mode. 23mm diameter discs gave higher values of Weibull moduli in comparison with the values obtained for discs of 29mm diameter indicating the flaws sampled in the 23mm diameter were of the same severity. Pores were observed to be singularly effective as initiation sites for failure as shown by the negative slope of the effect of porosity on the strength of clay.

Keywords: - *Diametral Compression Strength, Plane Stress, Plane Strain, Fracture mode, Discs, Weibull moduli.*

I. INTRODUCTION

It is frequently inconvenient to measure the tensile strength of brittle materials by employing the direct conventional method of pulling apart a suitably shaped specimen owing to the difficulty of preparing such specimens from the materials concerned [1]. The use of briquettes, bobbins and cylinders or prisms with embedded studs, tested in direct tension have all suffered from local stress concentrations [2]. Therefore to overcome these problems, the strength of a brittle material is measured indirectly. Some of the indirect methods are the equi-biaxial tension test, the diametral compression disc test and the flexure bending test.

In the diametral compression disc test according to [3], a right circular cylindrical specimen is compressed diametrally between two flat platens as shown in Fig 1. The diametral compression disc test is a convenient method for determining the tensile strength of brittle materials because of the fact that the specimen is simple to prepare and to load.

Previous studies have been carried out using the diametral compression disc test and the test method appears to give a reasonable result for the tensile strength of brittle materials. In their work[3]on diametral compression of silicon nitride, stated that the volume effect was mainly responsible for the difference observed between the strength obtained using diametral compression disc test and that obtained using bending flexure test for sintered silicon nitride. on the other hand, [4] investigated the tensile strength of disc and annuli by diametral compression test and pointed out that the diametral compression test was capable of giving a good measure of uniaxial tensile test for *Griffith's* type materials.

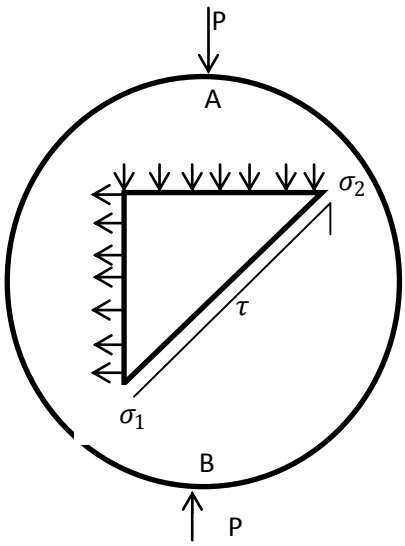

Fig.1: Stress distribution across the loaded diameter for a disc compressed between two uniaxial loading points[3].

In addition, [5] in their research on the tensile measurements of frangible bullets using the diametral compression test at quasi-static $1\mu m/s$ and high $12.5m/s$ displacement rates discovered that the tensile strength was not strongly sensitive to the displacement rate.

The thickness of a brittle material is critical when investigating the material's response to mechanical forces. Plane stress and plane strain conditions are phenomena which describe the stress states for thin and thick discs during fracture. It is believed that the plane stress condition is valid when the disc thickness is less than or equal to one quarter of the disc diameter but if the disc thickness is greater than one quarter of the disc diameter, a condition which deviates substantially from the ideal plane stress exists (plane strain).

The diametral compression test has some stringent requirements which include[6]: (i) material must be ideally linearly elastic,(ii) elastically isotropic,(iii)elastically homogeneous, and (iv) have shear and compression strengths appreciably higher than its tensile strengths.Not many materials will satisfy these conditions and consequently the application of the test result has limited applicability. As a matter of fact the first and last requirements made the test inapplicable to ductile materials in which the specimens would simply flatten out under the influence of the high shear and compression stresses at the loading points.

The fundamental aims for which this work was embarked upon were to:
(i) ascertain the applicability of the diametral compression disc test for the clay, and to
(ii) define more closely the plane stress and the plane strain fracture conditions of the clay.

II. EXPERIMENTAL PROCEDURE

2.1 Materials Characterisation and sample Production

The particle size analysis commenced with the sieving operation. Wet sieving was first carried out on about $60g$ of the clay using a sieve of $200\mu m$ mesh size. Both the filtrate and the residue were collected. Dry sieving was conducted on the residue whilst the filtrate was poured into a glass cylinder where the hydrometer reading was taken. The essence the hydrometer analysis was to obtain additional information on the fine particle nature of the clay.

The examined clay was obtained from Unwana in Afikpo-North Local Government Area of Ebonyi State, Nigeria. "The clay is popularly known as Isi-Ogwuta clay".

The clay lumps, as sourced, were crushed to smaller sizes, dried and finally ground into fine clay particles. All clay particles passed through a $-425\mu m$ mesh and were retained on a $212\mu m$ mesh. No water was added to the clay before cold forming. Several weights of the powdered clay i.e., 4g, 6g, 9g, 10g, 11g, 12g, 13.5g, 15g and 16.5g were measured out using the electronic precision balance (ConTECH model CA223) with 220g maximum and 0.1g minimum capacity. Using a hand operated hydraulic press at a pressure of 8MPa with tungsten carbide-lined interior steel dies, the powdered clay samples were compressed to discs of various thicknesses.

The cold pressed samples were fired in a muffle furnace at approximately $120°C$ per hour up to $600°C$ in order to burn off combustible materials. Finally, the samples were fired at approximately $150°C$ per hour up to $1200°C$ and held at this temperature for 15 $minutes$. The fired samples included discs of nominally 23mm and 29mm diameters with each diameter disc having different thicknesses of 3mm, 5mm, 7mm, 8mm, 9mm and 10mm.

2.2 Mechanical Test Procedure

All mechanical strength tests were carried out at room temperature on the sintered clay discs using TQ Sm1000 Universal Material Testing Machine of maximum capacity 100KN at a cross-head speed of $0.5mm/min$ in the Materials and Metallurgical Engineering(MME) laboratory, Federal University of Technology, Owerri. Prior to the mechanical strength test, the platens were tightly screwed into the two internally threaded hollows at the central points of the upper and lower sections of the mechanical tester. Subsequently, the test pieces were diametrally compressed between the two platens. In all cases, the frictional effects were assumed to be negligible.

III. RESULTS

3.1 Clay Characterisation Result

The result of the particle size analysis of the clay are given in Tables 3.1.1 and 3.1.2

Table 3.1.1: Sieve Analysis of the Clay

Sieve size (μm)	*Mass retained* (g)	*Mass passing* (g)	*% passing* (%)
75	0.1	59.2	98.7
150	0.1	59.3	98.8
300	0.2	59.4	99.0
425	0.3	59.6	99.3
600	0.1	59.9	99.8
850	0.0	60.0	100.0
1180	0.0	60.0	100.0

Table 3.1.2: Hydrometer Reading of Clay

Date	*Time* (min)	*Hydro — meter reading*	*True reading*	*Effect — ive depth* (mm)	*Fully correct —ed reading*	*Particle diameter D* (mm)	*% finer than* (%)
7/4/11	0	0	0	0	0	0	0
	1	23.5	24.0	115.60	23.3	0.044	62.4
	3	21.0	21.5	125.85	20.8	0.026	55.7
	6	19.5	20.0	132.00	19.3	0.019	51.7
	10	17.5	18.0	140.20	17.3	0.015	46.3
	16	16.0	16.5	146.35	15.8	0.012	42.3
	31	13.5	14.0	156.60	13.3	0.009	35.6
	60	6.0	6.5	187.35	5.8	0.007	15.5
8/4/11	1440	1.0	1.5	207.85	0.8	0.002	2.1

3.2 Sintered Densities

The sintered densities of the clay specimen are given in Table 3.2.1 and were evaluated by direct measurements of the physical dimensions of the disc using a vernier calliper. The effect of sintered density on the diametral compression strength is shown in Fig. 3.1.

Table 3.2.1: Sintered Densities of the Clay

Diameter D (mm)	*Thickness t (mm)*	*Average strength σ(MPa)*	*Sintered density SD (Mgm^{-3})*
23	3	14.607	2.362
	5	12.140	2.166
	7	9.278	2.294
	8	7.876	2.246
	9	6.417	2.217
	10	5.507	2.203
29	3	5.756	2.300
	5	5.239	1.989
	7	4.515	1.968
	8	3.924	2.004
	9	3.010	2.012
	10	2.239	2.026

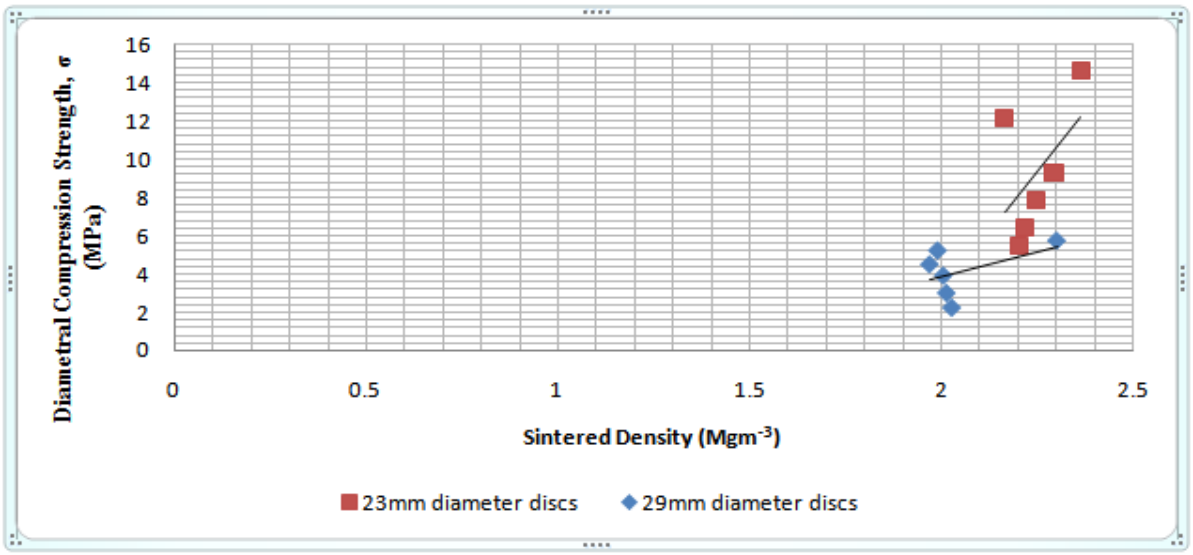

4.1: Effect of Sintered Density on the Diametral Compression Strength of the Clay.

3.3 Diametral Compression Test Result of the Clay

Equation (3.1) [3] was used to compute the diametral compression strengths and the results including the average, standard deviations, *(S)* and the coefficient of variations, *(cv)* are given in Table 3.3.1 and displayed in Fig. 3.2.

$\sigma_t = \frac{2P}{\pi Dt}$ ..... (3.1)

Where;

σ_t (MPa) is the maximum tensile stress,

P (N) is the applied load at fracture,

D (mm) is the disc diameter, and

t (mm) is the disc thickness.

Table 3.3.1: Effect of Disc Thickness on the Diametral Strength of the Clay.

D (mm)	t (mm)	σ_t (MPa)	S (MPa)	P (%)	cv (%)	*Weibull modulus, m*	
23	3(30)	14.607	±2.453	11.60	16.8	6.27*	6.61**
	5(30)	12.140	±1.585	13.89	13.1	8.44*	8.47**
	7(30)	9.278	±1.632	12.42	17.6	5.85*	6.31**
	8(30)	7.876	±1.550	16.91	19.7	5.60*	5.63**
	9(30)	6.417	±0.961	20.55	15.5	7.00*	7.16**
	10(30)	5.507	±0.991	18.47	24.2	3.25*	4.59**
29	3(30)	5.756	±2.058	14.78	35.8	2.28*	3.10**
	5(30)	5.239	±1.123	15.50	21.4	5.52*	5.19**
	7(30)	4.515	±1.620	23.23	35.9	2.56*	3.09**
	8(30)	3.924	±0.839	21.55	21.4	5.00*	5.19**
	9(30)	3.008	±0.716	25.15	23.4	5.22*	4.66**
	10(30)	2.239	±0.664	28.64	29.7	3.90*	3.74**

The number in parenthesis represents the number of specimen that was tested.

* Indicates the Weibull modulus obtained using the graphical method proposed by [6]

* * Indicates the Weibull modulus calculated using the relation, m = $\frac{1.11}{cv}$ proposed by [7]

$d(mm) = Disc\ diameter,$
$t(mm) = Disc\ thickness,$
$\sigma_t(MPa) = Average\ diametral\ Strength,$
$S(MPa) = Standard\ deviation,$
$P(\%) = Apparent\ Porosity$
$cv(\%) = Coefficient\ of\ variation$

Table 3.3.2: Plane Stress and Plane Strain Fracture Conditions for the Clay

Clay discs of nominally 23mm diameter						
	Plane stress condition		*Plane strain condition*			
Disc thickness, t(mm)	3(30)	5(30)	7(30)	8(30)	9(30)	10(30)
Average strength, σ(MPa)	14.607	12.140	9.278	7.876	6.417	5.507
Standard deviation, S	±2.453	±1.585	±1.633	±1.549	±0.961	±0.991
Clay discs of nominally 29mm diameter						
	Plane stress condition				*Plane strain condition*	
Disc thickness, t(mm)	3(30)	5(30)	7(30)	8(30)	9(30)	10(30)
Average strength, σ(MPa)	5.756	5.239	4.515	3.924	3.010	2.239
Standard deviation, S	±2.058	±1.123	±1.620	±0.839	±0.716	±0.664

The numbers in parentheses represent the numbers of specimen tested.

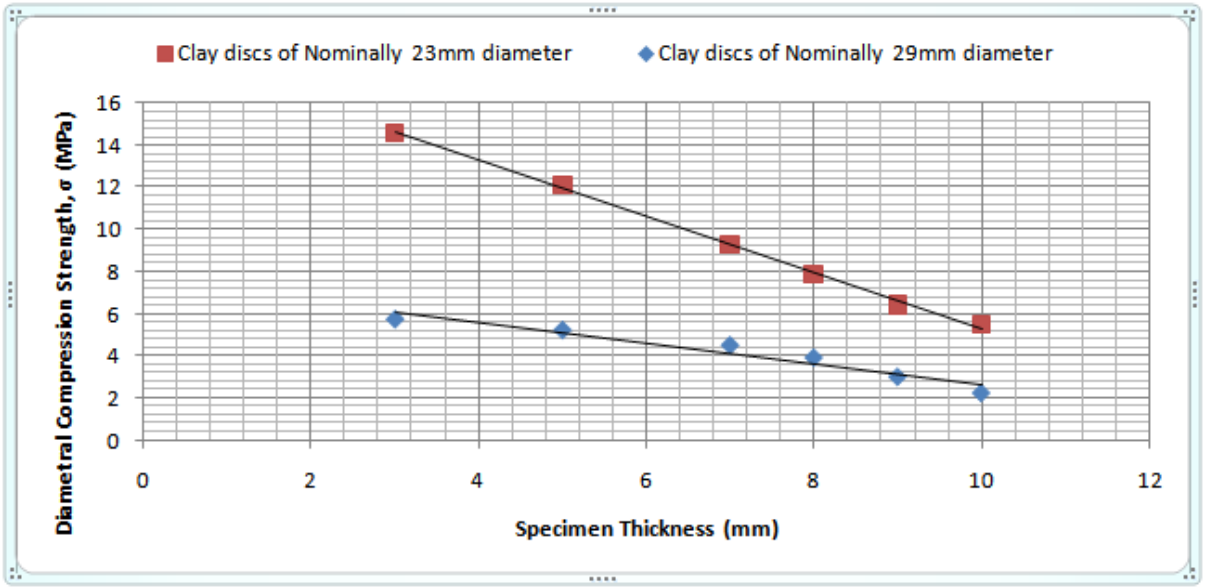

Fig. 3.2: Effect of Disc Thickness on the Diametral Compression Strength of the Clay

3.3.3 The Fracture Mode

The fracture modes (normal tensile and triple-cleft) are displayed in plate 3.1.

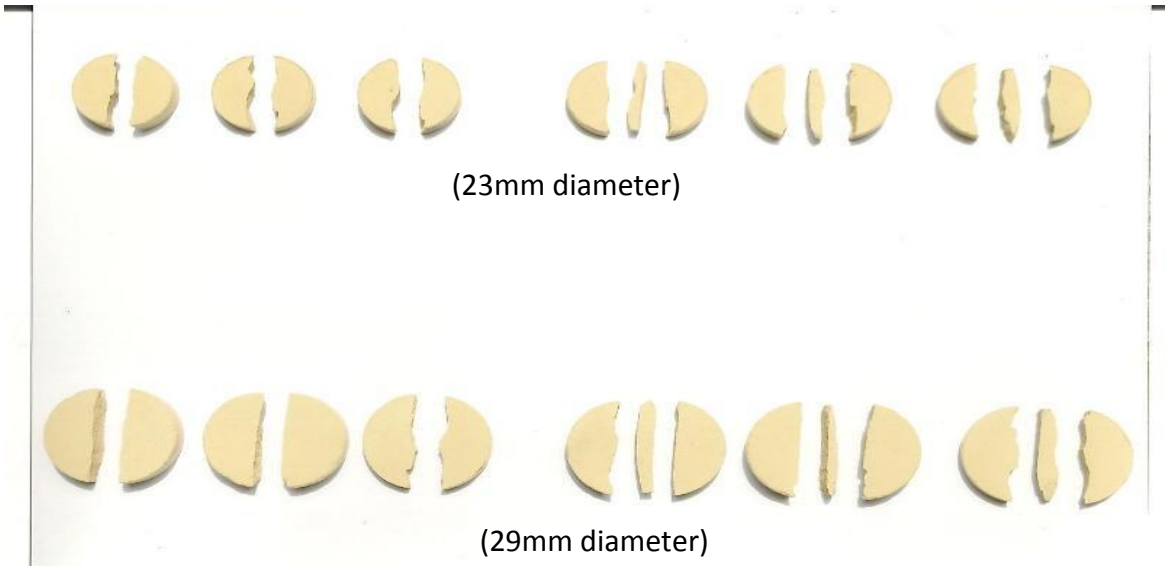

Plate 3.1: Room Temperature Fracture Modes for the Clay.

3.3.3 Effect of Porosity on the Diametral Compression Strength of the Clay

Table 3.4: Effect of Porosity on the Diametral Strength of the Clay.

Symbol	*Gradient*	*Disc diameter (mm)*
	−0.042	23
	−0.061	29

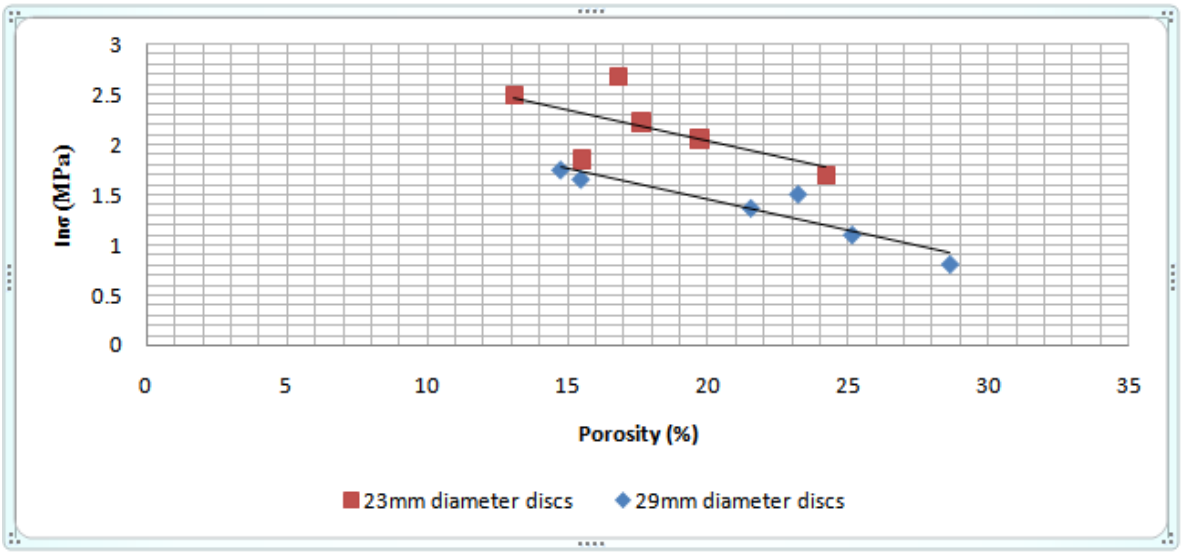

Fig. 3.3: Effect of Porosity on the Diametral Compression Strength of the Clay.

IV. DISCUSSION OF RESULTS

4.1 Clay Characterization Result

The sieve analysis showed that 98.7% of the clay particles passed through $-75\mu m$ mesh allowing about $0.1g$ of the clay to be retained in the mesh. Up to 99.0% of the clay particle passed through the $-300\mu m$ mesh whilst about $0.2g$ of the clay was retained in the mesh. A higher weight of about $0.3g$ was retained in the $425\mu m$ mesh whilst 99.3% of the clay particle was able to pass through the mesh. All clay particles were observed to pass through $-850\mu m$ and $-1180\mu m$ mesh sizes. The result of the hydrometer analysis of the clay revealed that the particle size diameter, D of the clay was about $0.04mm$ at 1 $minute$, $0.019mm$ at 6 $minute$, $0.009mm$ at 31 $minutes$ and about $0.002mm$ after 1440 $minutes$. The result of the particle size analysis of the clay was in agreement with the previous report on the particle size of clay by [9,10]. However, the essence the hydrometer analysis was to obtain additional information on the fine particle nature of the clay.

4.2 Sintered Densities

Clay discs of 23mm and 29mm diameters attained end-point densities of $2.36Mgm^{-3}$ and $2.30Mgm^{-3}$ respectively. A sintered density range of $2.17Mgm^{-3}$ to $2.36Mgm^{-3}$ was obtained for samples of nominally 23mm diameter whilst for samples of nominally 29mm diameter, a sintered density range of $1.97Mgm^{-3}$ to $2.30Mgm^{-3}$ was obtained. In general, the densification trend for the clay was observed to slightly differ in incremental order as the disc thickness decreased for the 23mm diameter specimen whilst the 29mm diameter specimen revealed an erratic densification trend with decreasing disc thickness. This observation may be due to the presence of different severity of flaws in discs of 29mm diameter.

4.3 Diametral Compression Test Result of the Clay

4.3.1 Effect of Thickness on the Diametral Strength of Clay

For both clay discs i.e., 23mm and 29mm diameters, a decrease in the average diametral compression strength was observed with increase in specimen thickness with clay discs of nominally 23mm diameter having the highest average strength values. This observation was in agreement with the statistical theory of brittle fracture which predicted lower strength value for larger specimen [11]. The reason for the observation may be due to a number of factors such as (1) the stress state, (2) porosity, (3) the fracture mode and (4) sintered density. The stress state contributed a reduction in the measured diametral compression strength such that the plane stress condition aided a decrease of *9-12%* in the diametral compression strength whilst the plane strain condition contributed a reduction of *25.4-27%* in the diametral strength for discs of 23mm and 29mm diameters. Pores were found to be effective as initiation sites for failure. The discs that failed in the triple-cleft fracture mode recorded higher strength values in comparison with the strength values obtained for the normal tensile fracture mode. An increase in diametral compression strength was observed with increase in sintered density.

The coefficient of variation, *cv* (which provides a normalized measure of the dispersion of test data) was observed to be larger for discs of nominally 29mm diameter having a range of $21-36\%$ whilst a range of $13-24\%$ was obtained for discs of nominally 23mm diameter. This observation revealed that discs of 29mm diameter indicated more scatter in the measured strength data.

The investigation of the plane stress and the plane strain fracture conditions of the clay showed that for the specimen of nominally 23mm diameter, the trend of fracture strength for the disc thickness below one quarter of the disc diameter (i.e., < *5.75mm*) was obtained as follows: for *3-5mm* disc thickness, a range of average fracture strength of *14.61±2.45MPa* to *12.14±1.59MPa* (about *9.2%* decrease in the diametral strength) was obtained whilst the mean fracture strength for the disc thickness above one quarter of the disc diameter (i.e., >*5.75mm*) for *7-10mm* disc thickness gave a range of *9.28±1.63* to *5.51±0.99MPa* (i.e., about *25.4%* decrease in the diametral strength). With regard to the specimen of nominally *29mm* diameter, the trend of fracture strength for the disc thickness below one quarter of the disc diameter (i.e., < *7.25mm*) was obtained as follows: for *3-7mm* disc thickness, a range of average fracture strength of *5.76±2.06 to 4.52±1.62MPa* (i.e., about *12%* decrease in the diametral strength) was observed whilst the average fracture strength for the disc thickness above one quarter of the disc diameter (i.e., >*7.25mm*) for *8-10mm* disc thickness gave a range of *3.92±0.84 to 2.24±0.66MPa* (i.e., about *27%* decrease in the diametral strength).

It is reasonable to conclude that within limits of experimental errors, the plane stress condition aided a decrease of *9-12%* in the diametral compression strength whilst the plane strain condition contributed a reduction of *25.4-27%* in the diametral compression strength for clay discs of 23mm and 29mm diameters.

To further establish the variability in the measured diametral compression strength, statistical tests ($F\ test\ and\ t\ test$) were carried out. The F distribution test was employed to test the null hypothesis that the data under consideration were drawn from populations that have the same standard deviation. The t distribution test was used to evaluate sample differences by using means and the distribution of sample scores around the mean. The t distribution test with a significant level of *0.01* revealed a significant statistical difference in the average diametral compression strengths between discs of nominally; *23mm* diameter by *5mm* thick and *23mm* diameter by *7mm* thick. The same statistical disparity in the diametral compression strength was obtained between discs of nominally; *29mm* diameter by *7mm* thick and *29mm* diameter by *9mm* thick. This implied that the plane stress condition was obtained for *3mm (14.61MPa)* and *5mm (12.14MPa)* disc-thicknesses for samples of *23mm* diameter whilst for discs of *29mm* diameter, the plane stress condition was obtained for *3mm (5.76MPa), 5mm (5.24MPa), 7mm (4.52MPa),* and *8mm (3.92MPa)* disc-thicknesses. On the other hand, the plane strain condition was obtained for *7mm (9.28MPa), 8mm (7.88MPa), 9mm (6.42MPa), and 10mm (5.51MPa)* disc-thicknesses for samples of *23mm* diameter whilst for samples of *29mm* diameter, the plane strain condition was obtained for 9mm (*3.01MPa), and 10mm (2.24MPa)* disc-thicknesses.

The result of the statistical test enabled the assertion that the plane stress condition was obtained for clay of *3-8mm* disc thickness for samples of *29mm* diameter. However, this condition did not extend to the thickness of *7mm (9.28MPa)* for samples of nominally *23mm* diameter.

4.3.2 The Fracture Mode

The fracture modes observed for the test were the normal tensile in which the specimen fractured into two almost equal pieces along the loaded diameter and the triple-cleft fracture which involved the splitting of the specimen into three or more pieces with fracture consisting of a central normal tensile and two nominally collinear fractures on either side of the central fracture. The observed fracture modes were similar to those previously reported by [3] for silicon nitride and [12] for sintered mullite samples.

Clay discs of 23mm diameter by 3mm thick produced the highest number of specimens (8 discs) that failed in the triple-cleft fracture mode. In general, greater numbers of the tested discs failed in the normal tensile mode with discs of 29mm diameter by 8mm thick and 29mm diameter by 10mm thick having the highest number of samples (29 discs) that failed in the normal tensile fracture mode. This observation was due to the high strength recorded for 23mm diameter samples. The reason wherein more discs of 23mm diameter failed in the triple-cleft fracture mode may be as a result of stronger particle contact areas throughout the specimen.

4.3.3 Weibull Statistical Treatment of the Strength of Clay

To test the variability in the fracture strengths for clay, the Weibull moduli, m of all the tested samples were calculated using the formula, $m = \frac{1.11}{cv}$ ($cv = coefficient$ of variation obtained from the strength data) proposed by [8] and the graphical method proposed by [7]**.** The relationship proposed by [8] gave more consistent values of Weibull moduli for both disc-diameters in comparison with the values of Weibull moduli obtained using the graphical method proposed by [7]**.**

Clay discs of nominally 23mm diameter generally gave higher values of Weibull moduli vis a' vis the values obtained for discs of nominally 29mm diameter regardless of the fact that both test-diameter discs indicated scatter in the strength value, "which is common for brittle materials". The reason for the high values of Weibull moduli obtained for samples of nominally 23mm diameter may be due to the presence of minimal clustering of flaws throughout the sample. On the other hand, inconsistent clustering of flaws which engender weak and variable strength may be responsible for the low values of Weibull moduli obtained for samples of

nominally 29mm diameter. Flaws of similar severity were perhaps sampled in the 23mm diameter discs hence the higher Weibull moduli obtained.

4.3.4 Effect of Porosity on the Diametral Strength of Clay

A slope of -0.042 was obtained for samples of 23mm diameter whilst samples of 29mm diameter gave a slope of -0.061 for the plot of $In\sigma_t$ against $porosity$ (%) as shown in Fig. 3.3. The negative slope obtained for the plot of $In\sigma_t$ against $porosity$ (%) showed that pores were singularly effective as initiation sites for failure.

The negative gradient obtained for the plot of $In\sigma_t$ against $porosity$ (%) shows that the clay obeys the relationship proposed by [13, 8]. It indicated that pores were singularly effective as initiation sites for failure (i.e., pores were non-uniformly distributed); in contrast to the result previously reported by [3] for silicon nitride.

V. CONCLUSIONS

1. A decrease in the diametral compression strength of clay was observed during this investigation and this was found to be thickness dependent.
2. Plane stress condition was obtained for clay of 3-8mm disc thickness for samples of nominally 29mm diameter. However, this condition did not extend to the thickness of 7mm (9.28MPa) for samples of nominally 23mm diameter.
3. Greater numbers of the 29mm diameter samples failed in the normal tensile fracture mode while more samples of the 23mm diameter failed in the triple-cleft fracture mode.
4. In general, 23mm diameter samples gave higher values of Weibull moduli vis-à-vis the values obtained for discs of 29mm diameter, which indicated that flaws of similar severity were sampled in the 23mm diameter discs.
5. Pores were found to be effective as initiation sites for failure.
6. It has been shown that the diametral compression disc test is a simple test method for providing tensile strength for clay economically.

REFERENCES

[1] R. Berenbaum, and I. Brodie, (1958): Measurement of the Tensile Strength of Brittle Materials. Mining Research Establishment, National Coal Board, Worton, Isleworth, Middlesex, p. 281.

[2] J. E. O. Ovri, (1999): Determination of the Mechanical Strength of Plain Concrete. GJPAS, Vol. 6, No. 2. Nigeria: Bachudo Science Company, p. 295-300.

[3] J. E. O. Ovri, and Davies, T. J. (1987): Diametral Compression of Silicon Nitride. Jour, Mater. Sci. And Eng. Netherland: Elsevier Sequoia, P. 109-116.

[4] I. Hawkes, And M.Molcolm, (1971): Measurement of Tensile Strength by Diametral Compression of Discs and Annuli: Jour, Eng. Geo, USA: Science direct Elsevier, p.173- 225.

[5] R. Rhorer, S. Mates, Banovic, S., Whiteton, E., and Fields, R. (2007): Tensile Measurements of Frangible Bullets Using Diametral Compression Disc Test. Jour, Eng. Vol. 35, Issue 6, p. 511-520.

[6] J.E.O. Ovri, Ph.D Thesis, University of Manchester, Oct. 1986 (Unpublished).

[7] M.W.Barsoum, (1997): Fundamentals of Ceramics. Singapore: McGraw-Hill Book, p. 426-428.

[8] J. E. O. Ovri, (1997): Sintering and Mechanical Strength of a Nigerian Clay. Jour, vol. 5, No. 2. Lagos: Faculty of Engineering, University of Lagos, P. 53-63.

[9] G. S. Brady,H.R. Clauser, and J. Vaccari, (1979): Materials Handbook, Eleventh Edition. New York: McGraw Hill.

[10] B.Head, (1980): Manual of Soil Laboratory Testing. Britain: Briddles Ltd.

[11] R. W.Davidge, (1979): Mechanical Behaviour of Ceramics. London: Cambridge University Press, p.32-35, 133- 138.

[12] P. M. Souto, and T. A. G. Martinez, (2011): High Temperature Diametral Compression Strength of Microwave-Sintered Mullite. Jour. Ceram Soc. Vol. 31, P. 2819.

[13] W. H. Duckworth, and E. Rhyschkewitsch, (1953): Jour, Am. Ceram. Soc., vol. 36, p. 68.

American Journal of Engineering Research (AJER)
e-ISSN : 2320-0847 p-ISSN : 2320-0936
Volume-03, Issue-01, pp-27-34
www.ajer.org

Research Paper Open Access

Feasibility of Natore Rubber Dam on Mahanonda River in Bangladesh and its Performance on Irrigation

Md. Sazadul Hasan[1], Md. Imran Kabir[1]
[1](*Faculty, Department of Civil Engineering, Stamford University Bangladesh, Bangladesh)*

Abstract: - Low rainfall in winter causes a great problem on irrigation. Bangladesh Agricultural Research Council (BARC) started research on this problem from 1974. In 1994-95, Rubber Dam projects have been taken by BIC (Beijing IWHR Corporation) in Bangladesh as it is very convenience and effective in both irrigation and cultivation of crops in winter. After installing, it is very important and challenging task to study the suitability and effect of Rubber Dam on agriculture. In this research work, the analysis of Rubber Dam in Natore, Bangladesh and its suitability on Mahanonda River has been analyzed and also studied its performance on irrigation. Also Bakkhali and Idgaon Rubber Dam were analyzed for the performance evaluation of Rubber Dam projects in Bangladesh for irrigation development. Then, feasibility of Natore Rubber Dam was studied and briefly discussed about its probable effect and benefit on agriculture. Reservoir capacity was also determined on the basis of a theoretical concept known as flow mass curve. Results of performance evaluation in irrigation were expressed in three groups: hydraulic, agricultural and socio-economic. Results of the analyses of hydraulic indicators showed that water supply is available. Agricultural performance, evaluated in terms of irrigated area was satisfactory. Analyses of socio-economic indicators showed that the Rubber Dam projects were financially viable in terms of profitability of farmers. Finally results were found that, it has a great probable effect on national economic and thus an alteration method of irrigation instead of uses of ground water. Thus, a comparative capital and operation and management cost analyses of different irrigation technologies has been carried out to ascertain the viability of Rubber Dam technology in irrigation development.

Keywords: *- Effect of Dam on Irrigation, Irrigation technologies, River water, Rubber Dam, Water Reservoir.*

I. INTRODUCTION

Rubber Dams being deflectable to open the full passage way of the river channel during monsoon floods are ideally feasible water conservation structures for many small and medium rivers and will thus play a vital role in enhancement of irrigation capacity. Rubber Dams can be used to conserve water in channel storages of small and medium rivers and streams in flat areas and in small reservoirs in hilly areas for the principal purpose of irrigation.

In Bangladesh, there is very low rainfall in winter. So, the requirement of water for winter irrigation must be met from groundwater source and by conserving a part of monsoon surface water in suitable storage. To use the river water in winter, Rubber Dams were introduced as a cost effective technology for retention and conservation of surface water in river channels, reservoirs and lakes for the purpose of supplying irrigation water to winter crop cultivation and Natore Rubber Dam is the most important one. It is ideally feasible for conservation of water in channel storages of rivers and channels in north zone as the Dams can be inflated to retain river flows and deflated fully to allow passage of flood flows without any obstruction whatsoever. Conservation of surface water is of immense importance to many countries to sustain growth of agriculture through better water and irrigation management in face of nature's uneven distribution of water throughout the year in one hand and prevent its environment and eco-system from plunging below dangerous level of degradation in face of artificial shortage of water in its rivers and streams created by unlawful withdrawal of lean season flow by the upstream country or region on the other. It is therefore necessary to exploit possible ways and means of surface water retention and conservation, especially the ones which are cost effective and suitable for the low and flat physiographic of some countries. Rubber Dam is one of such means of promise to retain and conserve water in reservoirs, lakes and channel storages of small and medium rivers of the countries.

II. LITERATURE REVIEW

2.1 BIC Constructed Dam in Bangladesh

The 84 m long 3.5 m high water filled Bakkhali Rubber Dam in Bangladesh was built by BIC as a two-side water retaining rubber dam. The Bakkhali River at the dam site is in a tidal environment not far from the Sea and separates downstream saline water as it impounds upstream sweet water flow in the river and tributary channels.

TABLE 1: BIC constructed Dam in Bangladesh.

No.	Rubber Dam	Construction Time
1	Bakkhali, Cox's bazar	May 1995
2	Idgaon, Cox's bazar	May 1995
3	Bhogai, Sherpur	March 1998
4	Tankhabti, Chittagong	April 2001
5	Kakhara, Dinajpur	April 2001
6	Kaoraid, Dinajpur	May2002
7	Matikata, Dinajpur	May 2002
8	Sonai, Hobigonj	May 2002
9	Atrai, Natore	May 2002
10	Brahmaputra, Narayanganj	April 2003
11	Bahara, Narayangonj	April 2003
12	Khasiamara, Sunamgonj	August 2003
13	Netai, Mymensing	February 2004
14	WRS, Dinajpur	February 2004
15	Someswari, Sherpur	March 2004
16	Sonaichari, Cox's bazar	May 2004
17	Baro Jungchhari Khal	March 2005
18	Khutakhali, Ramu	March 2005
19	Tetang khal, Ramu	March 2005
20	Talma, Panchagar	June 2006
21	Gopla, Panchagar	June 2006

The dam conserves fresh water in the upstream side and prevents flow of saline tidal water from downstream. The conserved water will be used for irrigation by lifting through low lift pumps. The dam will be operated in winter for cultivation of 6000ha Boro rice in January to May. BIC has constructed 14 Rubber Dams in Bangladesh. The construction has recommended that Rubber Dams are appropriate and cost effective water conservation structures in small and medium rivers of Bangladesh both in non-tidal and tidal locations.

2.2 Construction procedure of Rubber Dam

The rubber bag of the dam is attached with the concrete floor. At the beginning of the construction sheet pile wall or cut off wall is constructed at both the upstream and downstream side for controlling soil corrosion due to seepage. After that, the upstream, downstream, and the rubber bag is cast with concrete. At last, abutment wall, block, pump house, valve chamber etc. are constructed. But the main attached concrete structure of rubber bag is constructed very carefully. By using M.S. pipe, pad and platen; rubber bag is anchored with the floor bed.

2.3 Working principle of Rubber Dam

The main part of the Rubber Dam is rubber bag, pump house and concrete floor (with which rubber bag is attached with steel pad and platen). The water coming from the upstream side is directly entered to the pump house. Then with the help of different valve and pump motor, the water is used to inflate the rubber bag. After the use of water for irrigation purposes, the bag is then emptied by valves and the bag is sinking at the river bed. Generally gravity drainage system is used for emptied of the rubber bag. So, it does not create obstruction for the passing of water in rainy season and also passage of boat freely through the River.

2.4 Checking of Rubber Dam operation and recoding

There will be a checking routine of Rubber Dam. Before the rubber bag is inflated, complete checking must be done. Such as:

1) Is there any serious damage in Rubber Dam?
2) Is there any nut of the anchorage part become loose or not?
3) Are the inlet and outlet pipes blocked or not?

4) Is there any mechanical and electrical problem in the pump system?
5) Is there any damage and erosion in the preventive work?
6) Are any foundation settlement, water swelling and water stop and reverse filter damage or not?

2.5 Operation and maintenance of Rubber Dam

1) Before inflating the rubber bag, the pump, motor, valve, pipe line and other system which are used to make the bag emptied and inflated; should be checked well that it can function properly.
2) Anchorage part and other key point should be checked and damaged part will be repaired.
3) In front of the Dam site, the silt and sand will be removed from pipe line.
4) At the time of inflating the bag, extra pressure of water inside the bag will be abandonment and when the height of the Dam is reached at the surface level of the river, at that time inflating operation must be stopped.
5) The past flooded time will be under observation so that the Dam will be emptied at the highest flood time for the bag, air mouth of the top will be opened. For that, the inside air will be exerted fully.
6) At inflated condition, if the overflow depth exceeds a definite height (generally 20% of the Dam) then vibration effects. The Dam height and overflow depth must be maintained within 20% of the Dam height by increasing or decreasing the Dam height. But, never exceed the design Dam height.
7) The dam design for one side preservation of water should never use for two side storage. If, the downstream water level rises above the upstream level at that time the rubber bag must be emptied.

2.6 Repair of Rubber Dam

2.6.1 Repair of rubber bag

The main component of the Rubber Dam is rubber bag. After the bag is inflated by water or air it is used as Dam. The Rubber Dam bag may be cut off bluest out or defected due to different causes and may damage many part of the Dam.

The defect area and extra area around it will be cleaned by rubbed with zhama brick or other material used for the same purpose. A piece of rubber sheet (provided for repair of rubber bag) cut according to cut area is cleaned by the same procedure. Best quality glue is applied on the both cleaned area and paste on the defected area. At the time of repair the bag by glue it should never be wetted. If repair is essential in wetted condition, at that time the defected area is cut sufficiently in addition of some extra area of the defected places. Hole will be done at the outside of the Rubber Dam bag at some suitable points. Same hole will be done also at the cut rubber sheet. Bolt will be place in the hole of Rubber Dam bag by using gasket and the cut rubber sheet is placed and then nut is fixed on the bolt water tightly.

2.6.2 C.C. block

C.C. block will be provided after the end of main sub-base structure of the Rubber Dam. Because, it prevent erosion of river bed due to flow of river water. There may be openings at downstream side and after the sheet pile. Thus, C.C. block also provides side slope and river bed to prevent erosion.

Sometimes, C.C. block is displaced from their position for the action of the river stream. Many times, small sizes C.C. block is also displaced from sides slope due to water action. If the soil at the slope of side slope is displaced then settlement of slope will occur. For, all the above reason it is necessary to repair C.C. blocks.

2.6.3 Repair of C.C blocks

Useless C.C. blocks should be removed and new C.C. blocks will be placed at their position. Displaced C.C. blocks should be settled at their right position levelly. Firstly the settled C.C. block will be picked up from their position. The settled places will fill with soil and sand and then, completed and level. After leveling and compacting C.C block will set at the position.

2.6.4 Sedimentation

While the flowing water gets contact with the Dam section, the velocity of water reduces. The silt will be take place at the upstream side for decreasing river flow. Thus, problem may occur in operation process of the Dam. This sedimentation of silt will removed by pipe, at the time of inflated of the rubber bag. Observe that no damage occur in the Dam.

III. FEASIBILITY OF NATORE RUBBER DAM

3.1 Location

The Rubber Dam is set up in the River Atrai at Jogendra Nagor village under Gurudaspur upozila in Natore.

3.2 Short description of the project

The rubber dam structure is composed of four parts: rubber bag, anchorage, filling and emptying system (pump house) and foundation, as shown in Figure 1. Water is impounded by inflating the rubber bag with water. When deflated, the body of the dam lies flat on the river bottom without causing any obstruction to the river flow. As there are no gates or lifting structures, the operation and maintenance (O&M) of the dam are simple and cheap. The span of the dam can be as long as 100 m without any dividing piers and the height of the dam can be adjusted to regulate the flow.

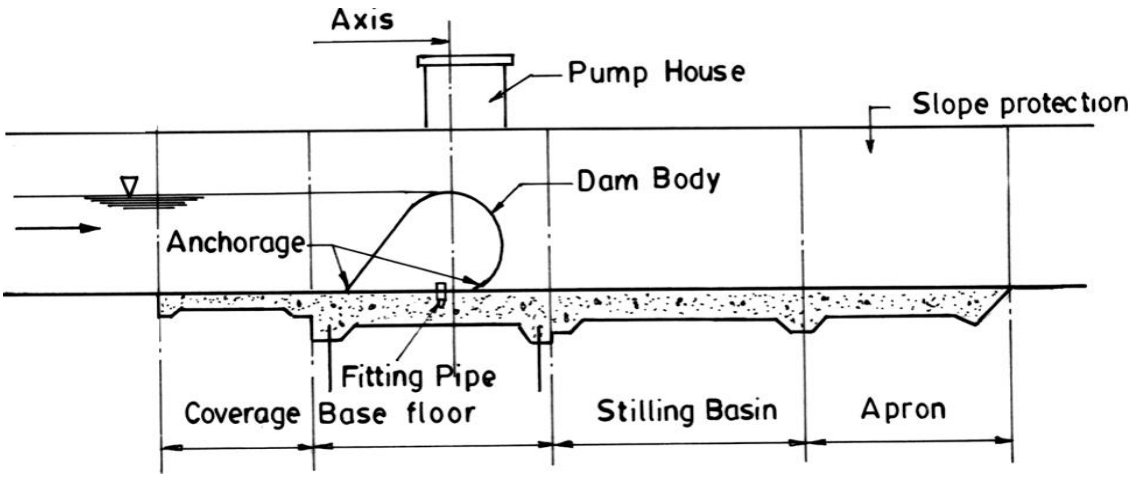

Figure 1: Cross section of a Rubber Dam

At the Natore Rubber Dam project the river is tidal and the dam conserves fresh water at upstream. It was estimated that about 25 million-m3 of water would be conserved by the Rubber Dam during January which would be lifted by LLPs and delivered through to irrigate 2500 ha of Boro (winter) rice. Two rice crops are given in both the project Irri and Boro.

3.3 Principle of the project

1) The main purpose of project supply of irrigation water by construction of Rubber Dam at Atrai River.
2) Whole operation and maintenance, arrangement of water, collection of irrigation tax etc. are operated by the beneficial community of this Dam project.
3) By accumulating the farmer at the projected area opportunity will create by giving share and money of water controlling co-operative organization.

3.4 Summary and socio-economic condition of the project

3.4.1 Structure related to the project

1) Rubber Dam- Length 45m* Height 4.5m : preserve water during dry season.
2) Construction of bridge- Length 45m : create opportunity with the people living on both side of the river.

3.4.2 Engineering parameters of the project

1) Length of the rubber bag : 45m
2) Height of the rubber bag : 4.5m
3) Thickness of rubber bag : 8mm
4) Construction procedure of rubber bag : attached above the concrete casting with Steel pad anchored bolt and nut.
5) Life time of the bag : 15-20 years
6) Duration of water filling in the bag : 12-15 hour
7) Pump capacity : 100 m3/s
8) Engineering concern of construction of rubber bag : IWHR, China.
9) Establishing committee : Local Government Engineering Department
10) Financing organization : Agriculture Department of Bangladesh Department
11) Operation & maintenance : The water maintenance committee from the beneficial community.

3.4.3 Socio-economic condition of the project

1) Name of the project : Atrai river Rubber Dam project.
2) Location of the project : Union-Subgari,upazila-Gurudaspur
District- Natore
3) The number of union under the project : 3
4) The number of village under the project : 21
5) The number of beneficial family under the project : 2900
6) The area under the project : 2500 ha (Net: 2460 ha)
7) The beneficial area under the project : 2257 ha
8) Irrigation type : Low lift pump + Gravity flow
9) Target of extra crop production : 2500 metric ton (yearly)

IV. DATA COLLECTION AND ANALYSIS

4.1 Collection of Data

Data has been collected from Local Government Engineering Department, Water Development Board, local people, projects farmers, etc. Information about structural and socio economic was collected from L.G.E.D and information to determine the capacity of the Dam was collected from Water Development Board. Benefit from Rubber Dam project was collected from local farmers.

4.2 Analysis of Data

4.2.1 Determination of Reservoir Capacity

TABLE 2: Mass flow

Year	Mass inflow in (100 ha-MTs)
1997	21.52
1998	45.22
1999	83.04
2000	90.84
2001	109.74
2002	134.54
2003	140.31

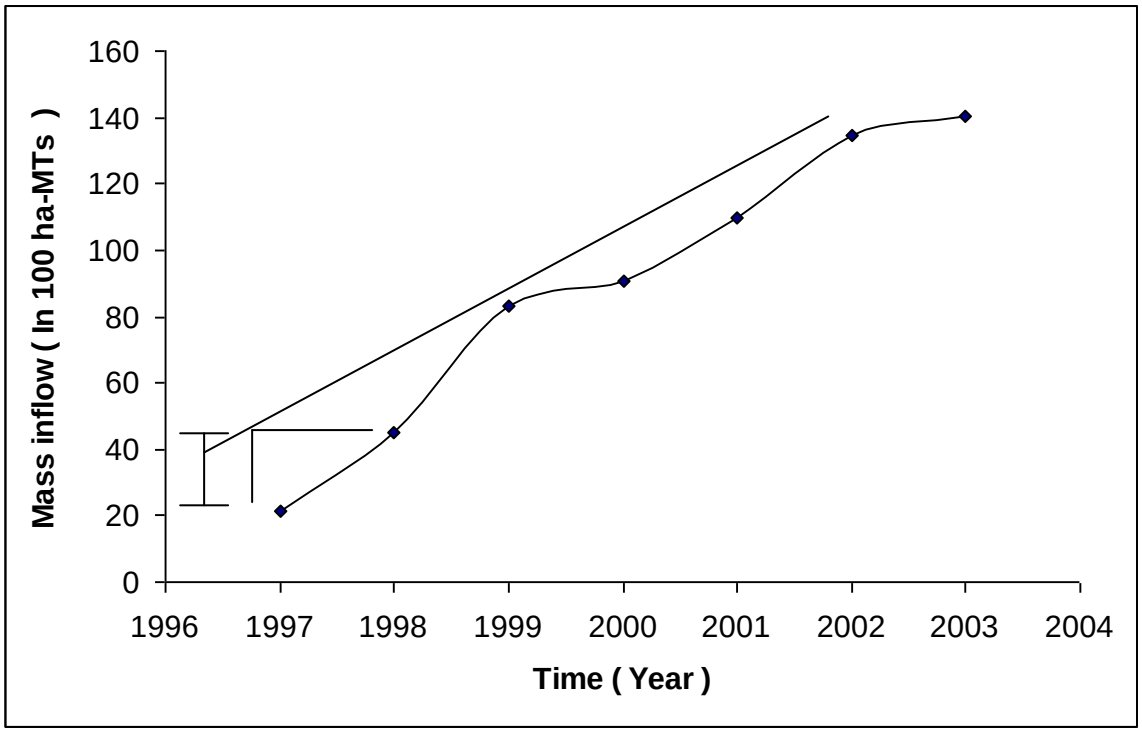

FIGURE 2: Mass inflow curve.

The capacity of the reservoir is founded from the flow mass curve shown in fig-2. From the triangle of the curve we get the capacity of the reservoir. The vertical distance of the triangle is the reservoir capacity and thus capacity is 2200ha-m.

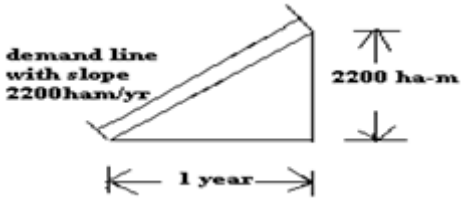

FIGURE 3: Triangular portion of Mass inflow curve.

4.2.2 Performance evaluation in agriculture

1) Hydraulic indicators

Hydraulic indicators deal with lifting/diversion and conveyance of irrigation water from the source to the farmers' fields by management of irrigation facilities. The hydraulic indicators used in the performance evaluation were as follows.

II) Water delivery performance

This indicator determines the extent to which water is delivered (total volume) as planned during the irrigation season and is defined as: Water delivery performance = Actual volume delivered / Target volume

The average discharge of the LLPs was 40litres per second (lps). Data on LLP operating hours during different months of the 2002-2003 Boro seasons were collected from the block managers. The pump discharge was multiplied by the operating hours to obtain lifted volume and hence total lifted volume (7.2 million m3). To compute water delivery performance, the target volumes of water planned for lifting/diversion were taken as 25 million m3. The water delivery performance of Natore Rubber Dam was found as 0.29 respectively and was very low.

III) Agricultural indicators

Agricultural indicators measure the contribution of the irrigation activity to the economy in relation to consumption of the increasingly scarce resource, water. The main outputs (actual irrigated area, crop yield) of the major inputs (water, land and finances) in an irrigated agricultural system are directly reflected by these indicators. The agricultural indicators used in the performance evaluation were as follows.

IV) Irrigated area performance

This indicator becomes more important where water is a limiting resource towards irrigation development. The indicator is expressed as:

$$\text{Irrigated area performance} = \frac{Actual\ irrigated\ area}{T\ \text{arg}\ et\ area}$$

The actual command areas of Natore Rubber Dam project during the 2002-2003 Boro seasons were 3200 ha. The target command areas were 2500 ha. Irrigated area performance was found 0.78. Thus, the irrigated area performance of the project was good.

V) Socio-economic indicators

TABLE 3: Cost and benefit (tk ha-1) of crop production from farmers' perspectives in the Natore Rubber Dam project.

Name of item	Natore Rubber Dam project
Total input cost (a)	12,550
Total labour cost (b)	2,600
Labour cost excluding family labour (c)	1,500
Irrigation fee (d)	2,500
Total cost (d)	15,150
Gross benefit (e)	22,500
Net benefit (e-a-b)	7,350
Net benefit excluding family labour (e-a-c)	8,450

VI) Profitability of farmers

This indicator deals with the profitability of farmers at the individual farm level. The indicator is expressed as:

Profitability of farmers = Benefit of irrigation per Ha / Irrigation fee per Ha

The cost and benefit of Boro production from farmers' perspectives are given in TABLE 3. The profitability of farmer was found dividing net benefit by the corresponding irrigation fee. Thus, profitability of farmers was found to be 2.94. The higher profitability in Natore was due to the lower irrigation fee in the former project.

TABLE 4: Comparison the condition of projected area before and after construction of the Rubber Dam.

Item	Previous irrigation facilities (Earth Dam)	Present irrigation facilities (Rubber Dam)
Construction authority	Water Development Board	Local Government Engineering Department
Construction time	1984	2002
Cultivated area	1000 ha	2500 ha
Extra crop production	6,350 ton	10,000 ton
Irrigation cost per bigha	1.000 tk	300 tk
Beneficial family	987	2900
Condition during rainy season	Flooded at upstream side.	No risk of flooded.
No of villages under project	5	12
Economical increasing rate	No absolute information.	7%
Crops grow in years.	Only one crop in a year.	More than one crops
Adverse effects of dam.	Sand covered huge area causes of damaging the dam in rainy season.	It has no as few adverse effects.

V. RESULTS AND DISCUSSION

The target volume of water availability, as mentioned earlier, estimated in feasibility reports were 25 million m3 for Natore Rubber Dam projects. It was found from reanalysis of the discharge data of the Atrai River that this estimation was probably based on 75% dependability, which has no risk of uncertainty in the available water availability.

TABLE 5: Comparative costs (tk ha-1) of irrigation development by Rubber Dam and previous technology.

Project	Capital cost	O&M cost	O&M fee
Previous Earth Dam in Natore	60,000	1000	300
Present Rubber Dam in Natore	90,000	500	150

A comparison of the costs of irrigation development by Rubber Dam and the previous technology in Natore was made and the costs are given in Table-6.1. The earlier technology has command areas of 1000 ha and present technology has 2500 ha. It is evident from the Table- that per hectare irrigation development costs using a Rubber Dam are better than the previous Earth Dam technology. The table- 5.1 also shows that the operation and maintenance cost of Rubber Dam is low compared to Earth Dam technology and also have large irrigated area under the Rubber Dam project. Thus, if found technically feasible and considering the lower operation & management cost, Rubber Dam technology is more economically viable option than the other irrigation technologies adopted in the small and medium river projects of Bangladesh.

VI. CONCLUSIONS AND RECOMMENDATIONS

6.1. CONCLUSIONS

The performance of Natore Rubber Dam projects in terms of socio-economic, agriculture and hydraulic indicators can be considered satisfactory. Considering both the capital and the lower operation and management costs of irrigation development, Rubber Dam technology is more economically viable than the previous traditional technology and if found technology feasible, the technology is recommended in the small and medium river projects of Bangladesh.

To consider all sides of rubber dam project we can say that rubber dam project on Mahanonda River will have to a great step to change socio-economic condition of that region.

6.2. RECOMMENDATIONS

I) Continuing study of Rubber Dam analysis and updating results will be proved to be useful, as more data become available in future.

II) During such study special attention may be paid for evaluation of Rubber Dam project in irrigation.

III) Possible of this project on the entire irrigated area the surrounding environment and also on the river may also be studied.

IV) If all the studied are done attentively then it may be a great project having vast effect on agriculture evaluation in the entire area.

REFERENCES

[1] LGED, Feasibility of Rubber Dam in Bangladesh. Institute of Water Conservancy and Hydraulic Power Research, China and Technical Design Unit, Local Government Engineering Department, Natore, Bangladesh, 2002.

[2] Bangladesh Bureau of Statistics, Statistical Yearbook, Dhaka, Bangladesh Bureau of Statistics, 1995.

[3] Chakma, H., Chakma, T., Dewan, P. & Ullah, M., Bara Parang: The Tale of the Development Refugees of the Chittagong Hill Tracts, Dhaka, Center for Sustainable Development, 1955.

[4] Government of Bangladesh, Chittagong Hill Tracts District Gazetteer, Dhaka, BG Press, 1975.

[5] Hutchinson, R.H.S., An account of Chittagonj Hill Tracks, Calcutta, Bengal Secretariat Press, 1906.

[6] Johnson, B.C.L, Ahmed. N., Geographical record: the Karnafuli Project,Oriental Geographer, 1(2), pp. 159-164.

[7] PDB, Karnafuli Hydro Station, Dhaka, Bangladesh Power Development Board, 1985.

[8] Rashid, H., The Geography of Bangladesh, Dhaka, University Press Ltd, 1991.

[9] Samad, S., Dams caused environmental refugees of the ethnic minorities in Chittagong, report presented at the WCD Regional Consultation Meeting held in Sri Lanka, 10–11 December, 1998.

[10] NOMAN, N.S., Optimal operation of the Karnafuli reservoir, Bangladesh, Master of Engineering thesis, School of Civil Engineering, Asian Institute of Technology, Bangkok, Thailand, (1997).

American Journal of Engineering Research (AJER)
e-ISSN : 2320-0847 p-ISSN : 2320-0936
Volume-03, Issue-01, pp-35-42
www.ajer.org

Research Paper Open Access

Fast Fourier Transformation Processing Method for Wheel Speed Signal

Wang Liqiang[1], Meng Hui[2], Han Zongqi[1]
[1](*College of Vehicle and Energy Engineering, Yanshan University, China)*
[2](*College of Electrical Engineering, Yanshan University,China;*

Abstract : - At high speed, there are two problems for safety and effective control of vehicles. One is that Signal-to-noise of wheel speed sensors are reduced, and the other is the data calculated by wheel speed signal is emanative. In this paper, wheel speed sensor signal was transformed into a frequency domain by using Fast Fourier Transformation (FFT) or Inverse Fast Fourier Transform (IFFT), waveform features of true signal and noise were studied in a frequency domain. Based on a narrow frequency domain and high energy of true signal, and wide-band signal and low energy of noise spectrum, a new method to process wheel speed signal was presented by using FFT and IFFT algorithms. Namely, transforming wheel speed signal into frequency domain using FFT firstly, "filtering" the wide-band noises in a frequency domain using polynomial fitting method secondly, and transforming waveforms of the noise spectrum into real signal inversely thirdly. The effects of three filtering methods which are electronic current filter, Karman filter and FFT/IFFT filter were compared to each other by road test of automotive vehicle. The test indicates that it can get rid of noises efficiently； improve signal-to-noise ratio clearly by using the processing method of FFT/IFFT filter.

Keywords: - *Wheel speed signal, Filter, Signal-to-noise, Fast Fourier Transform*

I. INTRODUCTION

At high speed, collection and procession wheel speed signal of automotive vehicle real-timely and precisely，which are bases of indirect Tire Pressure Monitoring System (TPMS), Anti-lock Brake System (ABS), Acceleration Slip Regulation (ASR), Active Yaw Control (AYC), Electronic Stability Program (ESP), Dynamic Stability Control (DSC) and other active safety control systems. In these safety control systems, processed wheel speed signal are used to calculate vehicle speed, acceleration or deceleration, wheel slip ratio or slip rate, yaw rate, understeer correction, and other important automotive motion parameters. And these parameters are used as a basis for safety control systems estimating vehicle driving state and generating control commands. Therefore, when a car is operated at high speed, it is an important guarantee for safe driving that collection and procession wheel speed signal real-timely and precisely.

However, due to the facts that Signal-to-noise of wheel speed sensors are reduced, and the data calculated by wheel speed signal is emanative when vehicle driving in high-speed, the active safety control systems mentioned above face with a common problem [1]. Traditional Karman filter, noise reduction using wavelet filter, digital Wiener filter and other measures, although these measures are able to reduce noises in wheel speed signal appropriately, and decrease the divergence of vehicle motion parameters based on wheel speed signal, but noises can not be eliminated completely. In order to improve the situation, many domestic and foreign researchers have carried out a lot of work widely and deeply. Including using Karman filter and genetic iterative algorithm to suppress sensor signal errors [2], using fault-tolerant manner based on analytica redundancy to solve the distortion problem of oscillation type sensor signal [3], using adaptive enhancer based on minimum mean square error in a frequency domain to predict wheel speed sensors mean square error in a frequency domain to predict wheel speed sensor signal, and enhance Signal-to-noise [4]. Some domestic scholars had studied in-depth researches about measurement error and filtering techniques of wheel speed signal, in their approach, digital variable gain filter of Karman filter structure was proposed [5]. In addition, during the researches had studied anti-interference processing method of wheel speed signal, the method for

smoothing processing data was proposed [6], and the method for processing wheel speed signal by using wavelet algorithm mean squared error threshold quantization based on improved threshold, analyzing wheel speed signal both in time domain and frequency domain at the same time was achieved, the filtering effect of this method is excellent [7].

In this paper, the cause of noises and the problem of signal acquisition were analyzed starting from wheel speed signal in high-speed. Based on narrow frequency domain and high energy of true signal, and wide-band signal and low energy of noise signal, a new method to process wheel speed signal was presented by using FFT (Fast Fourier Transform) and IFFT (Inverse Fast Fourier Transform) algorithms. Namely, transforming wheel speed signal which in a time domain into frequency domain using FFT firstly, "filtering" the wide-band noises in a frequency domain using polynomial fitting method secondly, and transforming waveforms of the noise spectrum into real signal inversely thirdly [8].

II. CHARACTERISTICS OF WHEEL SPEED SIGNAL AND CAUSES OF GENERATING NOISE

In the process of driving vehicles, with increasing speed, stronger signal noises are generated by the interference inside and outside a vehicle. Fig. 1 to Fig. 2 are the output signal waveforms which were collected by magnetic sensors installed in a given vehicle segment in the conventional method, and the three figures correspond to the vehicle speeds at 80 km/h and 160 km/h. Signal frequency and average amplitude increased with speed increasing, but the changes of the waveforms were irregular. The waveform was regular sine wave when the vehicle speed was 80km/h, but the evident distorted waveform which was the superposition of a sine wave and the noise signal, was relatively disorder at the speed of 160km/h.

The waveforms above show wheel speed signal at high speed have following characteristics: (1) Wheel speed signal was prone to appear the situations of pseudo impulses (increasing pulse) or missing impulse signal; (2) The amplitude and the phase position of Signal impulses which was no longer a sine wave had changed obviously; (3) Generation of the case that noise signal was superimposed on normal signal generating was strong randomness.

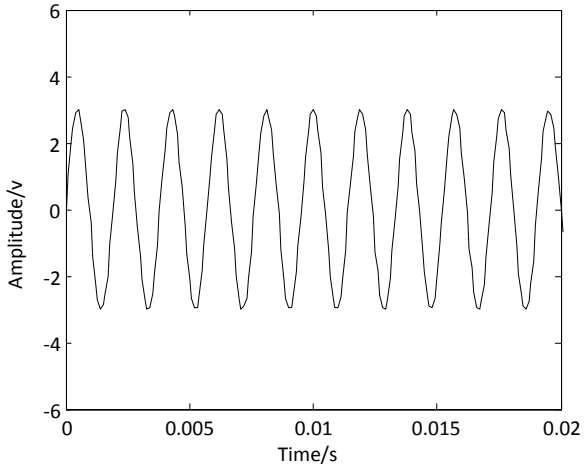

Fig. 1. The wheel speed sensor signal(80km/h)

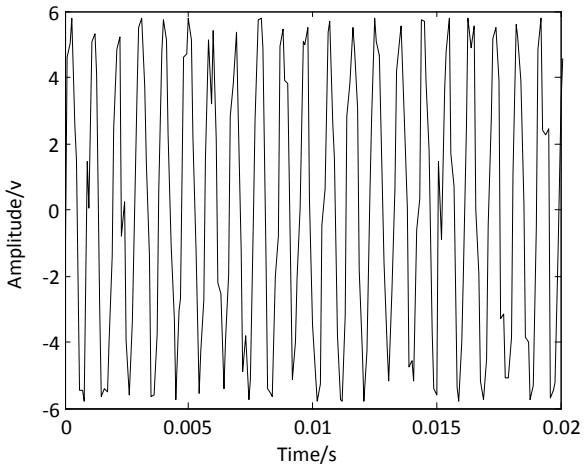

Fig. 2. The wheel speed sensor signal(160km/h)

There are three main causes result in generating wheel speed noise [9]: The first causes are pseudo impulse signal, missing impulse signal and other gross errors, which are caused by wheel vibration or sensor vibration. A change of relative position of the wheel and the sensor is caused at the same time, and the change occurs in the time of the sensor facing to tooth space or tooth crest of the fluted disc. In this situation, pseudo impulses and missing impulse signal are generated possibly. The second cause is narrow band noise whose frequency is low and frequency range is narrow, which is the superposition of normal wheel speed signal and the signal which is caused by the wheel torsional vibration. Road excitation and driveline excitation cause the wheel torsional vibration. The third is wide band noise, which is caused by circuit outside interference and environmental interference. Circuit boards on-vehicle are equipped with a variety of relays, transformers, solenoids and other inductive circuit devices. These devices work frequently in the circuit, thus generate induced noises. Besides, a variety of electromagnetic waves in the atmospheric environment also make induction sensors inducing broadband but small amplitude induced noises.

The noises in the signal make it difficult to obtain the instantaneous wheel speed signal precisely. By

acquiring imprecise wheel speed signal, calculated wheel slip ratio or slip rate, yaw rate and other motion parameters also will appear a larger divergence and a larger errors, and thus affecting the effect of security control [10].

III. FAST FOURIER TRANSFORM OF WHEEL SPEED SIGNAL

According to the analysis of collected wheel speed signal and noise signal on the real vehicle, we can see the real wheel speed signal are strong (large amplitude), the change of frequency is small during a relatively short time (for example, an acquisition cycle). On the contrary, noises are small amplitude, the frequency of which ranges in a wide range. Because the features mentioned above of wheel speed signal, processing method for wheel speed signal based on FFT/IFFT was designed, "filtering" noises in a frequency domain, eliminating noises and transforming waveforms of the noise spectrum into a time domain inversely, as shown in Fig. 3.

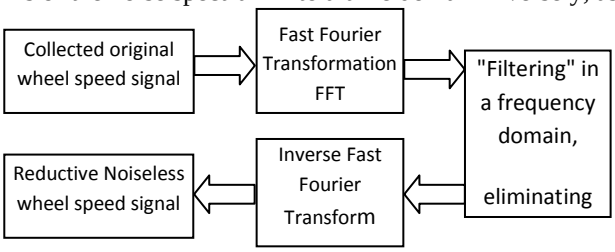

Fig. 3. FFT / IFFT filtering flow

FFT is a fast algorithm of DFT (Discrete Fourier Transform). According to odd, even, true, real and other characteristics of the discrete Fourier transform, FFT is a improved discrete Fourier transform algorithm. FFT is divided to the FFT algorithm by the time and the FFT algorithm by the frequency. The former is decomposing the sequence into two shorter sequences based on the sequence number is odd or even; the latter is dividing the sequence into before and after two sequences, and the numbers of two parts are equal. FFT algorithm is used in this paper [11].

Data collected by electromagnetic induction wheel speed sensors are time data sequence and the voltage value sequence of its corresponding wheel speed signal:

to,t1,t2,…,tn, …,tN

xo,x1,x2,…,xn…,xN

Where N is the total number of collected data, n is a data in the sequence. By the DFT transform above equation:

$$X(k)=DFT[x(n)]=\sum_{n=0}^{N-1} x(n)W_N^{nk} \quad (1)$$

Where $0 \le k \le N-1$, WNnk is twiddle factor.

By dividing x(n) into two groups according to the parity of n, each of whose variable substitution is easy to get:

$$x(2r)=x1(r)\ x(2r+1)=x2(r) \quad (2)$$

Where r=0,1,2,…,N/2-1

Substituting Eq. (2) into Eq. (1) gives the following equation:

$$X(k)=\sum_{r=0}^{N/2-1} x_1(r)W_N^{2rk}+W_N^k\sum_{r=0}^{N/2-1} x_2(r)W_N^{2rk} \quad (3)$$

thus:
$$W_N^{2n}=e^{-j\frac{2\pi}{N}2n}=e^{-j\frac{2\pi}{N/2}2n}=W_{N/2}^{2n} \quad (4)$$

By Eqs. (3), (4), we can get:

$$X(k)=X_1(k)+W_N^k X_2(k) \quad (5)$$

According to the cyclical nature of the coefficient of WN :

$$W_{N/2}^{r(N/2+k)}=W_{N/2}^{rk} \quad (6)$$

$$X_1(N/2+k)=\sum_{r=0}^{N/2-1} X_1(r)W_{N/2}^{rk} \quad (7)$$

then:

therefore: X1(N/2+k)=X1(k) (8)

Similarly: X2(N/2+k)=X2(k) (9)

According to the symmetry of WNk :

$$W_N^{r(N/2+k)} = W_N^{N/2}\ W_N^k = -W_N^k \tag{10}$$

therefore: $$X(k) = X_1(k) + W_N^k X_2(k) \tag{11}$$

$$X(N/2+k) = X_1(k) - W_N^k X_2(k) \tag{12}$$

Where k=0,1,2,…,N/2-1

The operations of Eqs. (11) and (12) are usually named after butterfly operation, the operation process as shown in Fig. 4.

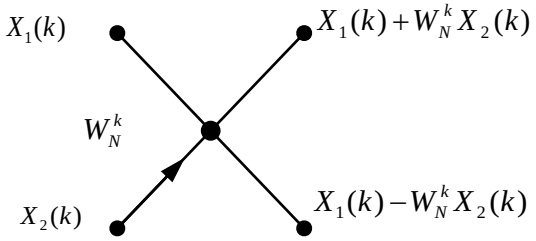

Fig. 4. Butterfly operation

In Fig. 4, the two lines on the left are inputs, and the two lines on the right are outputs. Inputs and outputs are separated by a small circle which represents addition or subtraction (the upper right road for the added output, the lower right road for the subtraction output). If the signal in a branch needs a multiplication, it is a necessary to mark arrows on the branch, and mark the multiplication coefficient on the side. Fig. 5 describes wheel speed signal was transferred into a frequency domain by using FFT in this expressive method.

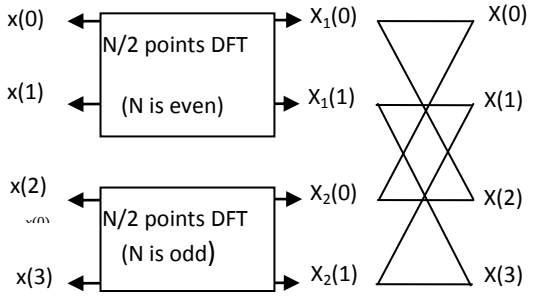

Fig. 5. The algorithm principle of FFT/IFFT (N=4)

By transferring wheel speed signal data in the time domain to the frequency domain using FFT, obtain its corresponding frequency spectrum. Fig. 6 to Fig. 7 are the frequency spectrums, and the three figures correspond to the vehicle speeds at 80 km/h, 120 km/h and 160 km/h.

IV. ELIMINATING SIGNAL NOISES IN FREQUENCY DOMAIN

By analyzing the speed signal spectrums after FFT transform, we can get the conclusion that the real wheel speed signal are narrowband and high-energy signal, while the noises are broadband and low-energy signal. A process of "filtering" in frequency domain means keeping the energy amplitude of the signal frequency components, and attenuating the energy amplitude of the noise components.

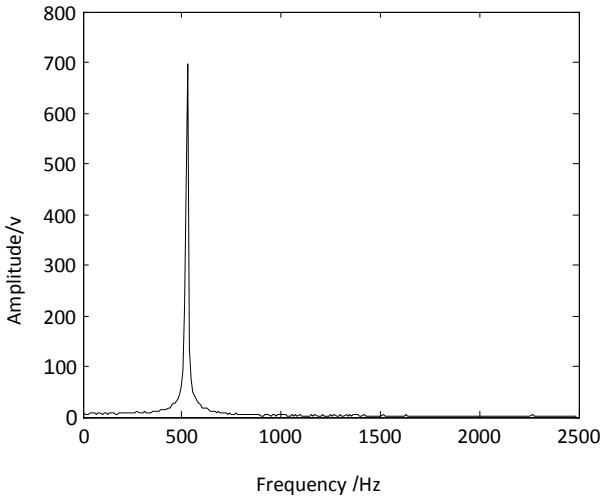

Fig. 6. The spectrums (80Km/h)

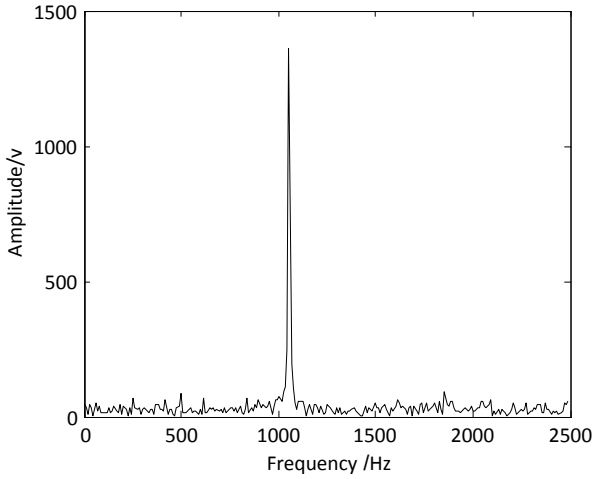

Fig. 7. The spectrums (160Km/h)

Table 1 gives out each frequency component of wheel speed signal sequence which is transferred by using FFT and the corresponding energy amplitude sequence.

Table 1 The frequency of signaland the corresponding energy amplitudes

Frequency/ f	f0	f1	…	fi	…	fn
Energy amplitude/X	X0	X1	…	Xi	…	Xn

The appropriate upper and lower cutoff frequency that the "binding site" of the frequencies of original signal and noise signal, are determined according to the difference of energy between the two signal. The selection of the upper and lower cutoff frequencies are about the frequency range of the real signal, and therefore the highest energy value and the corresponding center frequency should be determined.

At first, the center frequency of signal that is fi, the corresponding energy amplitude Xi is the maximum amplitude, Xmax= Xi; then determining the appropriate coefficients a and b of the amplitude of Signal-to-noise:

Xs/Xmax=a Xx/Xmax=b

The two correspond to the energy amplitude of the upper and lower cutoff frequency respectively, namely, each of the upper and lower cutoff frequency fs and fx is corresponded to the frequency of Xs and Xx. The pass band of wheel speed signal is fs ~ fx, both ends of the band are bands which need to filter noises. As shown in Fig. 8.

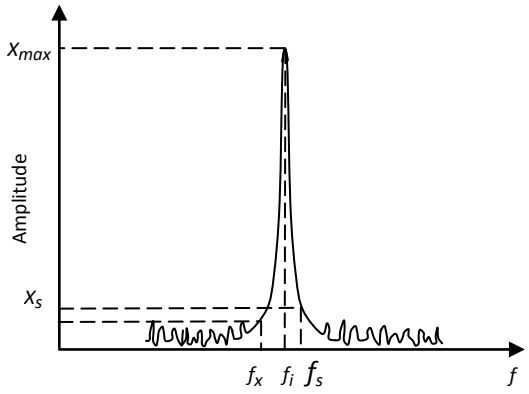

Fig. 8. The division of filtering bands

As you can see by the principle of Fourier transform, any continuous periodic signal can be made up of an appropriate combination of a set of sine curves. Therefore, for the fitting of spectrum curve correctly, it would be necessary to restore the real time domain signal. The principle of curve fitting is constructing new

spectrum curve, using the fitted function to reduce the amplitude of the noise component, meanwhile make every frequency component of the new fitted function to satisfy the relationship of Fourier transform, and restore every frequency component to real wheel speed signal after IFFT processing.

Table 1 shows the corresponding relationship of frequency and signal energy; Eq. (13) expresses the function of after curve fitting:

$$[X0,X1,\ldots,Xn]=F[f0,f1,\ldots,fn] \quad (13)$$

Generally, Eq. (13) is a first-order polynomial or quadratic polynomial. After fitting the signal energy, the noise component of which is suppressed, substituting the frequency value into Eq. (13) again, the sequences of the fitted values of frequency and energy are:

$$f0, f1, f2 ,\ldots\ldots,fi , \ldots\ldots,fn$$
$$X1',X2',X3',\ldots,Xi',\ldots,Xn'$$

The process of filtering in domain frequency of wheel speed signal at speed of 160km/h is shown for illustrating. Looking at the curve within cutoff frequency in Fig. 9, the number of fitting is determined to 2 with a preliminary. The fitted spectral curve and the time domain curve of after IFFT reduction are shown in Fig.9 and Fig.10 respectively.

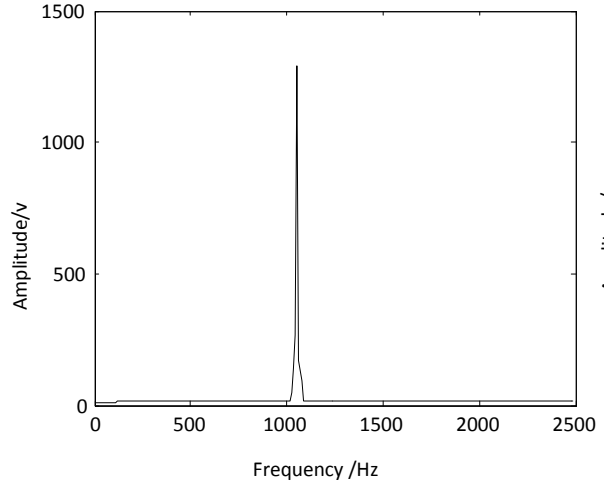

Fig. 9. The spectral curve after filtering in frequency domain

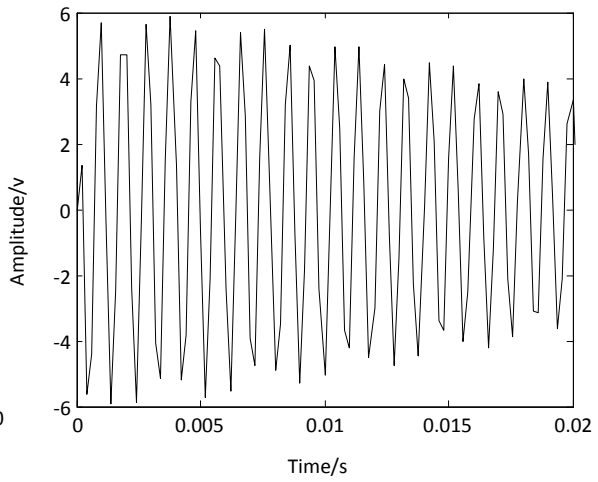

Fig. 10. The time domain graph after IFFT inverse transform

As shown in Fig. 10, the noise signal after fitting in time domain is eliminated substantially, periodic is uniform, but the amplitude of the signal is distortion. The continuous but not differentiable points, that operate in the situation of the fitting part of the spectrum curve at the transition is more abrupt, contribute to a reason why the distorted signal occurs. The noise band is divided into two sections, the section near the center frequency needs a higher order polynomial fitting, so that each section of the curve in continuous conduction. The spectral curve after piecewise fitting and the time domain graph of wheel speed signal after IFFT inverse transform are as shown in Fig.11and Fig.12 respectively.

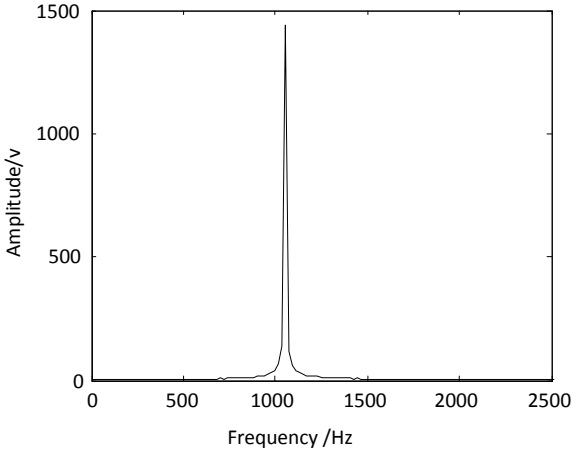

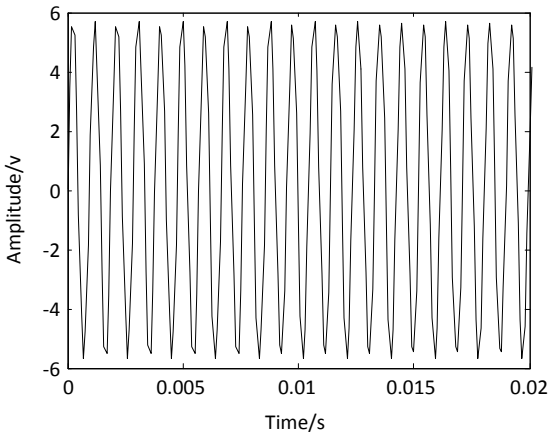

Fig. 11. The spectral curve after piecewise fitting

Fig. 12. The time domain graph of wheel speed signal after IFFT inverse transform

According to the plot in Fig.12, the correct spectral curve can be fitted after piecewise fitting, the fitting out of, a true wheel speed signal is restored by using IFFT.

V. ROAD TEST

In order to verify the ultimate effects of processing wheel speed signal using FFT and IFFT, road comparison tests with Jetta sedan are done. The wheel speed sensor signal is directly connected to the number 1 analog channel of data acquisition system; the wheel speed sensor outputs after low-pass filtering and Karman filtering are connected to the number 2 counting channel of the data acquisition system; the output of the true corner which was measured by grating wheel angle / speed sensor wheel in every turn 1000 pulses within a certain distance traveled is connected to the number 3 digital counting channel of the data acquisition system. The frequency of the data acquisition system is 100 KHz. After processing the wheel speed signal collected by analog channel by using FFT and IFFT, writing down the pulse number.

The pulse coefficient of the grating sensor is 0.36°in every pulse. The wheel turned angle φ can be calculated by the pulse number recorded by the counter. The fluted disc of wheel speed sensor has 44 teeth, each pulse corresponds to the wheel rotation of 9 °. The real number of pulses Nz can be calculated according to the rotation angle of four wheels. Comprising the pulse number ND recorded after circuit filtering, the pulse number NK recorded after Karman filtering and the pulse number NF recorded after the processing of FFT/IFFT to Nz respectively, each of filtering effects is judged based on respective corresponding relative error.

Road test chooses three kinds of speed of 80 km/h,120 km/h and 160 km/h as the test speeds, the average of two driven wheels as the collecting data, 200 meters as the collection distance, and when the grating sensor counts to reach 100000, test is over. Actual wheel turns 100 rpm, the number of real wheel speed sensor pulse Nz is 4000. Each of the counted errors after three filters was shown in Table 2.

Table 2 The effects comparison of three kinds of filtering

Items	Units	Wheel speed(km/h) 80	120	160
the pulse number of grating sensor	thousand piece	100	100	100
the pulse number of real wheel speed sensor Nz	piece	4000	4000	4000
the count pulse number after circuit filtering ND and error	piece	3998	3994	3990
	%	0.05	0.15	0.25
the count pulse number after Karman filtering and error	piece	4000	3997	3995
	%	0	0.075	0.083
the count pulse number after FFT filtering NF and error	piece	4000	4000	3999
	%	0	0	0.025

From Table 2 above, compared to hardware circuit filtering and Karman filtering, the error of FFT filtering in frequency domain is smaller, more precise, the filtering effect is obvious.

VI. CONCLUSION

The wheel speed signal of the vehicle and the data based on calculate of the wheel speed signal are foundations for automotive effective security control. However, at high speed, the noise of wheel speed signal and the divergence of calculated data make the control effect reducing.Though using conventional software and hardware filtering in time domain to reduce the wheel speed signal noise can have an effect, but can not eliminate the noise completely.Based on the differences of frequency distribution and energy amplitude of true signal and noise signal, wheel speed sensor signal was transformed from a time domain into a frequency domain for processing by using FFT, then "filtering" the noise frequency by using polynomial fitting method for noise band data, and restoring the filtered noise frequency into time domain to eliminate noise in the signal effectively. Road test shows that the effect of eliminating the noise is quite good.In process of frequency filtering, the selections of cutoff frequency and polynomial fitting method for noise band data have a certain effect on frequency filtering.The processing method of FFT/IFFT for wheel speed signal has a obvious effect on reducing gross error and improving the accuracy of acquisition and other aspects, true signal is well restored. In this paper, the effect of applying the processing method was only carried on the preliminary attempt, the method and technique about frequency domain filtering are still need to conduct a more in-depth discussion.

VII. ACKNOWLEDGEMENTS

This work was financially supported by the National Natural Science Foundation (51175450), Hebei Province Natural Science Foundation (E2012203046).

REFERENCES

[1] Li Pu, Song Jian, Yu Liangyao. Treatment method of anti-interference of ABS wheel speed signal.*Automobile Technology*, 2001, 5. 15-18.

[2] T. Hsiao, M. Tomizuka. Sensor fault detection in vehicle lateral control systems via switching karman filtering . *ACC'05*, 2005. 209-222.

[3] Li Xu, H. E. Tseng. Robust model-based fault detection for a roll stability control system . *IEEE Transaction on Control System Technology*, 2007, 15(3):519-528.

[4] Wilmar Hernández. Improving the response of a wheel speed sensor using an adaptive line enhancer. *Measurement*, 2003, 33(3):229-240.

[5] Liu Guofu, Wang Yueke, Zhang Qi, Zheng Weifeng. Study on the filer technique in ABS wheel speed signal. *Automotive Technology*, 2004, 22 (3).22-24.

[6] Li Pu, Song Jian, Yu Liang-yao A preconditioning algorithm of singular point rejecting for wheel speed signal processing in anti-lock brake system.*Journal of Higyway and Transportation Research and Development*, 2001,8(4):119-123.

[7] Jiang Kerong, Tang Xiangqing, Zhu Dequan. Automobile wheel speed signal processing based on wavelet algorithm of improved threshold. *Journal of Scientific Instrument*, 2010,31(4). 736-740

[8] Cheng Peiqing. *Digital signal processing tutorial*. Beijing：Journal of Tsinghua University, 2007.

[9] Fang Yugu, Ding Nenggen, Pan Weimin. Analysis of the distort of wheel speed pulse signal and the processing of software anti-interference. *Automotive Engineering (Suppl.)*，2003,10：119-120.

[10] Sun Shangzhi, Chen Yanfu, Sun Jun. Study on SNR of wheel speed sensor signal in ABS. *Automobile Parts*, 2010, (12):59-60.

[11] Fang Jie, Zhang Ke, Wang Rui, et al. Study on improved FFT algorithm and Applications. *Sichuan Electric Power Technology*, 2007, 6(30):9-11.

American Journal of Engineering Research (AJER)
e-ISSN : 2320-0847 p-ISSN : 2320-0936
Volume-03, Issue-01, pp-43-49
www.ajer.org

Research Paper Open Access

Analysis of the impact of anthropic activities on the water chemistry of weathered layer aquifer of M'bahiakro locality (Center of Côte d'Ivoire).

Dibi Brou[1], Konan Kouakou Séraphin[1], Konan-Waidhet Arthur Brice[1], Savané Issiaka[2] and Gnakri Dago[1]

1 : University Jean Lorougnon Guedé, Daloa - Côte d'Ivoire, BP 150 Daloa
2 : University Nangui Abrogoua, Abidjan – Côte d'Ivoire, 02 BP 801 Abidjan 02

Abstract: - Water wells are one of the main sources of drinking water for the population of the town of M'bahiakro. However, their quality is very threatened by the behavior of these people themselves. This study aims to improve knowledge of groundwater and to determine the origin of the mineralization of groundwater in the region from a combination of hydro- chemical methods and Principal Component Analysis. The results obtained show that the water is slightly acidic and highly mineralized (832 µS / cm on average). Nitrate levels remain very high with an average higher than the WHO standard (52 mg / L). Hydrochemical classification of water from the diagram Piper and Stiff showed that the waters are divided into two main hydrofacies. It is calcium bicarbonate water (58 %) and calcium chloride- water (42 %). The Principal Component Analysis normalized showed three main classes that are rock dissolution, water salinization and infiltration from surface. Comparative analysis of three classes indicates that the mineralization of groundwater could be controlled by the intrusion of brackish water probably from latrines nearby septic systems.

Keywords: - *Anthropic activities, hydrofacies, mineralization, water resources, M'bahiakro*

I. INTRODUCTION

Groundwater is a major source of drinking water for many people around the world. They may be contaminated from natural sources or many types of human activities such as residential, municipal, commercial, industrial and agricultural. This sensitivity of groundwater pollution due to these activities is a major problem [1]. To help solve this problem, two types of methods have been used. The prevention methods represented by the vulnerability to pollution and curative methods that are statistical tests or biostatistics. In this study, where we have a case of proven pollution, curative methods (statistical tests, biostatistics, hydrofacies characterization and transfer of pollutants) are considered as the most appropriate. Combinations of statistical tests and multivariate analyzes were often used [2]. A multivariate statistical technique is an effective tool for the interpretation of the relationship between water chemistry and the origin of the samples. Works of [3] have used principal component analysis to explore the relationship between trace element hydrochemistry and host rock samples. Multi-criteria analysis was adopted to characterize the geochemical data samples and explain the origin of water sources [4]. These methods allow a better characterization of water quality and determining the likely origin of pollutants in these waters. In Côte d' Ivoire, the application of these methods has already yielded quite interesting results as the works of [5] are shown. However, their importance in a study depends on the objectives.

This study aims to characterize the groundwater resources of this locality and determine the mechanism at the basis of the presence of these parameters in waters. It considers only the water consumed in the locality. The importance of this study lies in the fact that the sectors where contamination is already observed as is the case of M'bahiakro, determining the origin of these pollutants and the main hydrofacies could allow attempts to propose of solution. Indeed, in this area, we note the presence of many individual sanitation and garbage that meet throughout the city.

II. MATERIALS AND METHODS

II-1. Study area

M'Bahiakro locality is in the central part of Côte d'Ivoire between 4°19 and 4°21 W and 7°27 and 7°29 N (Figure1). Geological formations encountered in the area are composed of volcano- sedimentary rocks. The terrain is generally flat plains with altitudes that vary between 120 and 137 m. The hydrographic network is less dense. The average annual rainfall is relatively low at about 1000 mm / year, distributed over four seasons. These are two great seasons with the dry (December to March) and one other rainy (April - July) and 2 small seasons composed of one dry (August - September) and one rainy (October - November). The thickness of the weathered layer are often large, often reaching 70 m. The recharge remains significant at the weathered layer aquifers where it often exceeds 100 mm per season.The local population is estimated at 40,000 inhabitants.

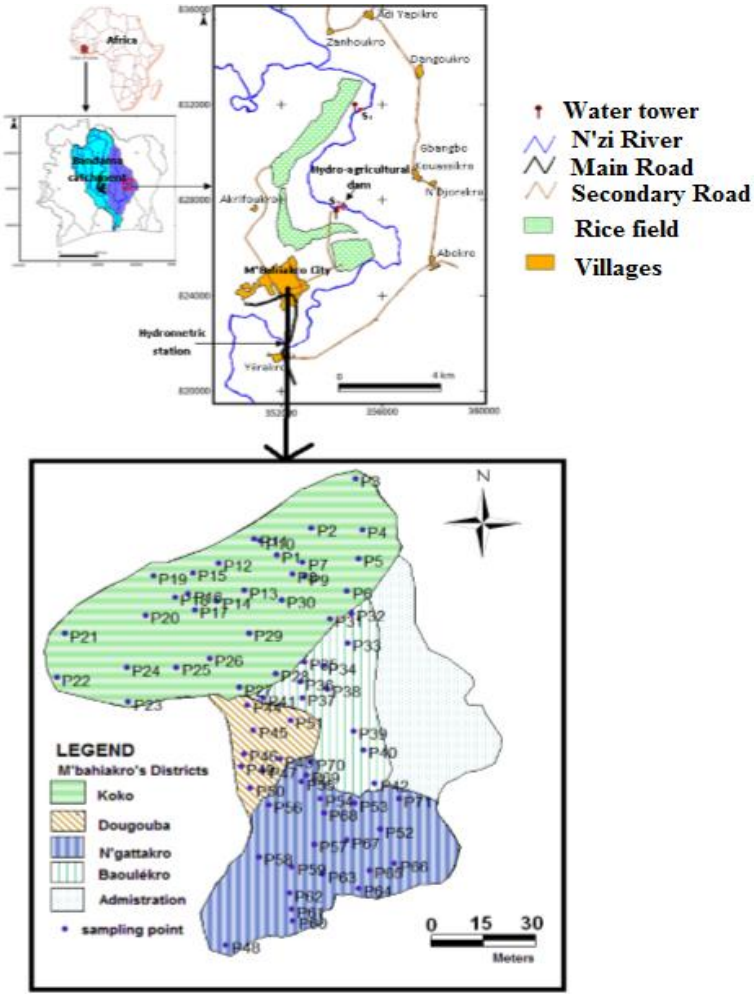

Figure 1. Study area

II-2. Materials

The material is composed of laboratory equipment used for the analysis of samples collected and field equipment consisting of a probe multiparameters, pots of sampling and a GPS. The physico-chemicals data collected during the campaign are composed of physical parameters (pH and electrical conductivity) measured in situ using a multiparameters probe. Samples were then collected on 21 sites and stored at 5 °C in a cooler for a laboratory analysis of the Research Center for Oceanography (CRO) in Abidjan (Côte d'Ivoire). Analytical methods vary depending on the chemical elements, Ca^{2+}, Mg^{2+}, Cl^{-} and HCO_3^{-} by titration (acid titration), Na^{+} and K^{+} by atomic absorption flame SO_4^{2-} and NO_3^{-} spectrometry molecular absorption.

II-3. Methods

In order to characterize these water resources and to determine the probable origin of these pollutants in water resources of the locality of M'bahiakro, hydrogeochemical facies were thirst used to describe the bodies of

groundwater in an aquifer that differ in their chemical composition. The hydrochemical study required the use of two types of diagrams that are Piper and Stiff for the characterization of hydrofacies. The use of these diagrams in the field of water chemistry by [6] often gave very good results. Indeed, the facies are function of the lithology, solution kinetics and flow patterns of the aquifer [7]. Classification of waters depends on the principles of the IAH (International Association of Hydrogeologist) 1979. In these principles, total equivalents of cations and anions were taken as 100 % and ions, as more than 20% (meq/l), were evaluated in the classification. Knowing these key hydrofacies will contribute to the determination of the uses of these water wells that may be agriculture, industry or drinking water.

Then, in order to know the probable origin of pollutants observed in groundwater, statistical tests were performed. Thirst, we adopted standard methods [8 - 10] like spatial analysis to assess spatial variation. The statistical approach that was used to study phenomena at the origin of the mineralization of water is based on Principal Component Analysis. Its application in the study of hydrochemical water was carried out by several authors in other the world and in Africa with very significant results [11]. Statistical analysis was performed from 21 samples and 12 variables (Temperature, pH, conductivity, HCO_3^-, SO_4^{2-}, Cl^-, Ca^{2+}, Mg^{2+}, K^+, Na^+ and NO_3^- and NO_2^-). The application of the methods allowed knowing the mechanism of mineralization of water of weathered layer aquifers of locality of M'bahiakro and the probable origin of the pollutants found in these waters. The method of Principal Component Principal Analysis Standardized (PCAS) used for this study is based on the interpretation of the various factors as well as the correlation matrix obtained as a result of data processing. The software used is the NCSS (Number Cruncher Statistic System) version 6.0. The point cloud resulting from this treatment was projected in different factorial plans which are determined in the space of variables

III. RESULTS AND DISCUSSION

The simplified analysis of the different parameters shows that groundwater from subsurface aquifers exploited by traditional wells have generally higher levels to WHO standards. The values of nitrate levels remain very high with an average (52 mg / L) higher than the WHO standard. These values vary between 2.1 and 114.8 mg / L. They are very low in the water surface where they remain below 10 mg / L, whereas in the wells they remain very high. For other parameters, the levels are still relatively low with the exception of some peaks obtained concerning nitrites and sulfates. For the physical parameters, the conductivity remains high also varying from 30 to 1400 µs/cm with an average of 832 µs/cm. As for pH, there is generally normal with values ranging from 5.5 to 7.5.

Hydrochemical classification of water in the Piper diagram highlights two main hydrofacies (Figure 2). The bicarbonated and calcite waters (58%) and sulfated and chlorited waters (42%). The proportions obtained are virtually identical despite a slight dominance of bicarbonated and calcite waters.

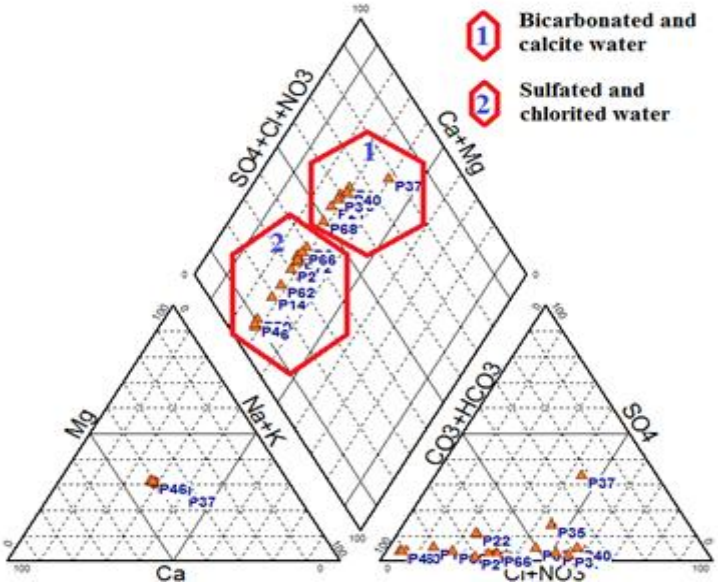

Figure 2. Waters classification by piper diagram

These results are confirmed by the Stiff diagram (Figure 3). This graph shows the influence of bicarbonated and calcite waters on the water resources of this locality, although levels generally remain low. These results show that the hydrochemical characteristics of the water from the wells of M'bahiakro are variable

in space and time. Indeed, given the nature of these formations generally from weathered layers and exposed to seasonal fluctuations, the residence time of water in contact with these rocks is very limited. Water therefore has not enough time to exchange with some parameters of the host rocks. The phenomenon of mineralization is very low as also indicated concentrations of ions from the mineralization that are especially Ca^{2+} and Mg^{2+}. Thus, the pollutants found in the groundwater could come from either diffuse or accidental pollution. The influence of lithology may be limited in contrast to the works of [12; 13] respectively in the synclinal Kourimat in Morocco and in the region of Bondoukou in Côte d'Ivoire.

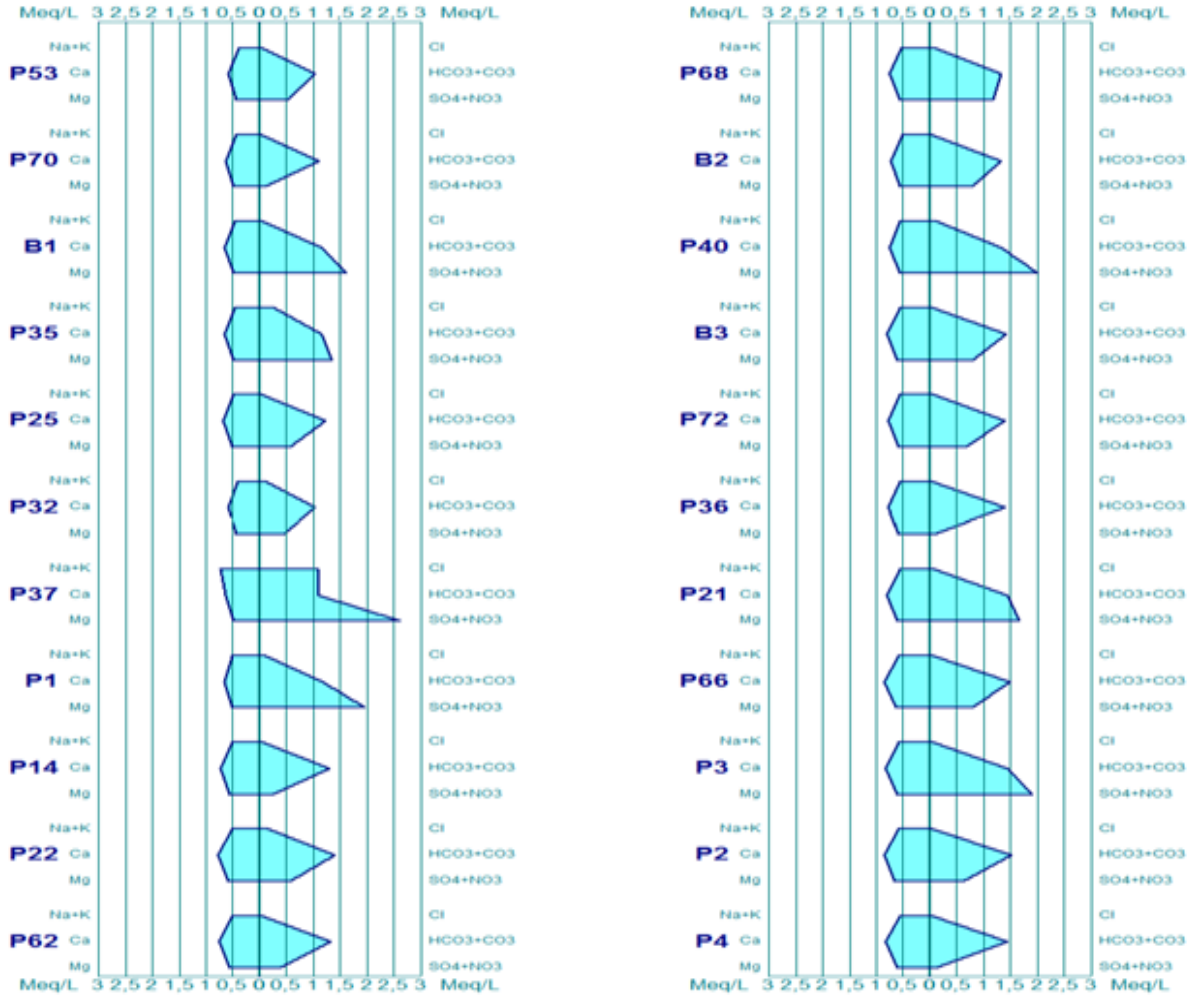

Figure 3: Waters classification by stiff diagram

Groundwaters in these areas also have mixed chemical facies bicarbonate and calcite waters and sulfated and chlorited waters very varied depending mainly on the lithology of the crossed fields. It is the same for the works of [2]. Indeed, in these areas the samples analyzed are dominated by water wells that are generally deep and seasonal influence is weaker.

The results of the statistical analysis give numerous tables which some are summarized in this study. Table of eigenvalues (Table 1) shows that the first three factors represent 71.43% of the variance expressed. They include the maximum variance expressed and are sufficient to translate exactly the information required.

Table1: Table of eigenvalues and percent of principals factors

No.	Eigenvalue	Percent individual	Percent cumulative
1	3.83	31.94	31.94
2	2.83	23.62	55.56
3	1.90	15.86	71.43

The correlation matrix shows the differents correlations necessary for the understanding of the phenomena studied variables is presented in Table 2.

Table 2: Correlation matrix

Temp	pH	Cond	Ca^{2+}	Mg^{2+}	Na^{+}	K^{+}	HCO_3^{-}	Cl^{-}	SO_4^{2-}	NO_3^{-}	NO_2^{-}	Variables
1	-0.44	0.48	0.04	0.05	0.31	0.44	0.04	0.30	0.30	0.59	0.06	**Temp**
	1	-0.4	0.11	0.09	-0.42	-0.37	0.11	0.05	0.05	**-0.33**	-0.18	**pH**
		1	-0.3	-0.3	0.05	0.18	-0.3	0.12	0.12	0.46	-0.01	**Cond**
			1	**0.96**	0.15	0.17	**0.94**	0.28	0.28	0.14	-0.01	**Ca^{2+}**
				1	0.16	0.18	**0.94**	0.28	0.28	0.15	0.01	**Mg^{2+}**
					1	**0.76**	0.15	0.04	0.04	0.63	-0.04	**Na^{+}**
						1	0.17	0.48	0.48	0.45	0.02	**K^{+}**
							1	0.28	0.28	0.14	0.01	**HCO_3^{-}**
								1	**0.96**	-0.03	0.07	**Cl^{-}**
									1	-0.03	0.07	**SO_4^{2-}**
											-0.12	**NO_3^{-}**
											1	**NO_2^{-}**

This matrix highlights significant correlations between Mg^{2+}, Ca^{2+} and HCO_3^{-} (0.94) on the one hand and other parts between Cl^{-} and SO_4^{2-} (0.96). There is also to a lesser degree a correlation between variables such as Na^{+} and K^{+} (0.76). These correlations reflect the influence of each parameter in the mineralization of water into alterites of M'bahiakro. Indeed, the correlation between Mg^{2+}, Ca^{2+} and HCO_3^{-} reflects the dissolution of rocks related to the residence time of water in the aquifer. However, low levels obtained for these parameters show that groundwater has not passed a sufficient residence time in contact with these formations that they could have released these ions during alteration of crystalline or cristallophyllienne rocks. The correlation between K^{+} and Na^{+} could highlight salinization due to the proximity of latrines and other places bathroom. These two parameters are logically in its natural state in water, but in very small proportions. However, when the levels become important as in the case of potassium, another origin may be mentioned. In this study, the origin could be wastewater from latrines usually located near these wells. Regarding the correlation between SO_4^{2-} and Cl^{-}, it is explained by an intrusion from surface. This infiltration from surface could also be justified by lack of correlation between these and the NO_3^{-} that could possibly come from latrines near septic tanks [14].

The analysis in the space of variables of different factorial can design highlight three main groupings of variables (Figure 4). This is the main factor F1 (31.94%), gathering the parameters HCO_3^{-}, Mg^{2+} and Ca^{2+}, which represent the dissolution. The factor F2 (23.62%) gathering the variables K^{+} and Na^{+} which represent the salinization of water and F3 factor (15.86%) are made up Cl^{-} and SO_4^{2-} designating from surface infiltration. These groups confirm the results of the correlation matrix.

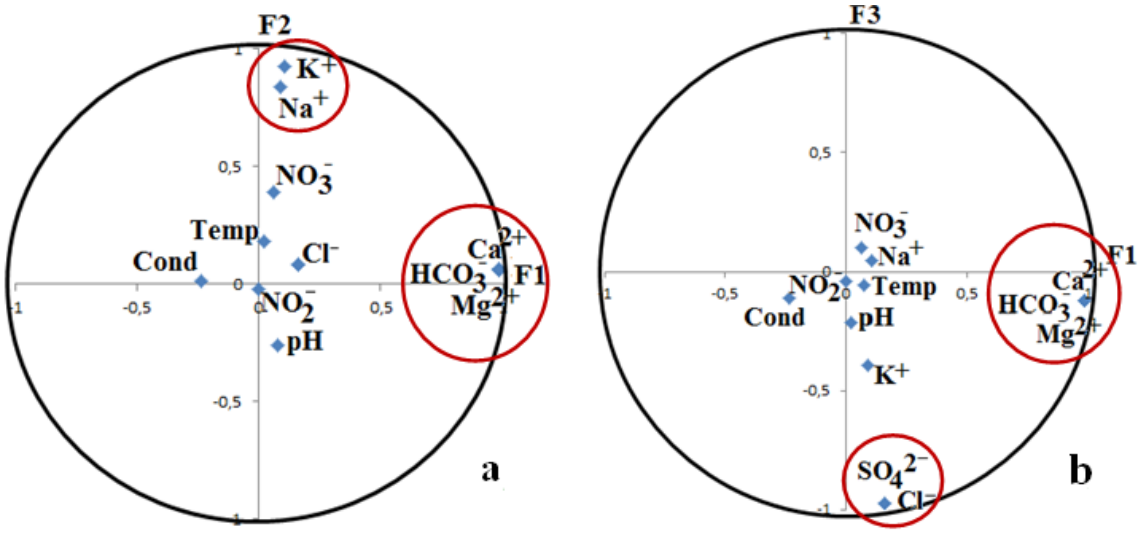

Figure 4: Analysis of factorial plans (a) F1 - F2 and (b) F1 - F3

Analysis of the results of these factorial plans shows that the main parameters that control the factor F1 reveal the existence of a phenomenon of dissolution of rocks considering the combination of these around this axis. However, the levels of these parameters remain very low in the groundwater of the area. Indeed, the presence of Mg^{2+} and Ca^{2+} in groundwater indicates the existence of dissolution rocks in relation to a sufficiently long residence time which may allow the water that was in contact with the rock to dissolve them and into solution. However, within this study we worked on wells where groundwater contained in weathered layer aquifers are vulnerable to seasonal fluctuations and do not have time to dissolve the rocks to get the ions in solution. In addition, the lack of correlation between these parameters and the conductivity is further shown that the presence of these ions in groundwater is not due to dissolution of rocks related to the residence time as indicated by the work of [15]. According to [16], it is called dissolution of rocks related to the residence time when there is a positive correlation between these ions from the dissolution of rocks (Mg^{2+} and Ca^{2+}) and conductivity. This is not the case in this study. The results of the analysis of factors 2 and 3 respectively indicate salinization and water infiltration from surface suggest a superficial pollution. The importance of salinization in groundwater in the area has already been indicated by [17]. However, nitrates are the most representative of a surface origin parameter is correlated with any of the axes. This lack of correlation in one hand with one of the axes and on the other hand with SO_4^{2-} and Cl^- as well as the high levels of nitrates show that the mineralization of the water is probably not the fact to an infiltration from surface. It is due to the intrusion of brackish water which may come from septic systems often located near wells. This could still be explained by the high levels of nitrates obtained in wells located nearby latrines.

IV. CONCLUSION

The analysis of physical and chemical parameters of water from wells and streams in the area of M'bahiakro allowed knowing the main hydrofacies that characterize these water resources and the likely origin of the ions in these waters. The results of this analysis show that groundwater is slightly acidic with pH ranging between 5.5 and 7.5. These waters have a very varied mineralization in all between 30 and 1400 µS/cm with an average of 832 µS/cm. Nitrate levels remain very high with an above average of WHO standard (52 mg / L). Hydrochemical classification of water from the diagram Piper and Stiff showed that the waters are divided into two main hydrofacies that are calcium bicarbonate water (58%) and calcium chloride-water (42%). The Principal Component Analysis normalized highlighted three main classes of water that are rock dissolution, salinization and water infiltration from surface. Comparative analysis of three classes indicates that the mineralization of groundwater could be controlled by the intrusion of brackish water probably from latrines nearby septic systems.

V. ACKNOWLEDGEMENTS

We thank the International Foundation for Science (IFS) for funding this research. We also thank the people of M'bahiakro for their availability and understanding.

REFERENCES

[1] Thirumalaivasan D., Karmegam M., and Venugopal K., (2003). AHP-DRASTIC: Software For Spesific Aquifer Vulnerability Assessment Using DRASTIC Model And GIS, Journal of Modelling and Software, 18, 645-656.

[2] Jang C.S., Chen J.S., Lin Y.B. and Liu C.W. (2012). Characterizing hydrochemical properties of springs in Taiwan based on their geological origins. Environ Monit Assess 184:63–75 DOI 10.1007/s10661-011-1947-4.

[3] Kreamer D.K., Hodge V.F., Rabinowitz I., Johannesson K.H. and Stetzenbach K.J. (1996). Trace element geochemistry in water from selected springs in Death Valley National Park, California. Ground Water, 34, 95–103.

[4] Swanson S.K., Bahr J.M., Schwar M.T. and Potter K.W. (2001). Two-way cluster analysis of geochemical data to constrain spring source waters. Chemical Geology, 179, 73–91.

[5] Ahoussi K.E., Oga Y.M.S., Koffi Y.B., Kouassi A.M., Soro N. et Biémi J. (2011). Caractérisation hydrogéochimique et microbiologique des ressources en eau du site d'un Centre d'Enfouissement Technique (CET) de Côte d'Ivoire : cas du CET de Kossihouen dans le District d'Abidjan (Côte d'Ivoire). International Journal of Biological and Chemical Sc iences, 5(5), 2114-2132.

[6] Kouassi A.M., Yao K.A., Ahoussi K.E., Seki L.C., Yao N.A. et Biémi J. (2010). Caractérisation hydrochimique des aquifères fissurés de la région du N'zi-Comoé (Centre-Est de la Côte d'Ivoire). International Journal of Biological and Chemical Sciences, 4(5), 1816-1838.

[7] Back W. (1966). Hydrochemical facies and groundwater flow pat- tern in northern part of Atlantic Coastal Plain. US Geological Survey Professional Paper 498-A.

[8] Kouassi A. M., Ahoussi K. E., Koffi Y. B., Aké Y. A., Biémi J. (2012). Caractérisation hydrogéochimique des eaux des aquifères fissurés de la zone Guiglo-Duekoué (Ouest de la Côte d'Ivoire). International Journal of Biological and Chemical Sciences, 6(1), 504-518.
[9] Oga M. S., Lasm T., Yao T. K., Soro N., Saley M. B., Kouassi D., Gnamba F., (2009). Caractérisation chimique des eaux des aquifères de Fracture: Cas de La Région de Tiassalé en Côte d'Ivoire. European Journal of Scientific Research, 31 (1), 72-87.
[10] Yidana S.M., Ophori D. and Banoeng -Yakubo B. (2008). A multivariate statistical analysis of surface water chemistry data – The Ankobra Basin, Ghana. Journal of Environmental Management, 86, 80-87.
[11] Thilagavathi R., Chidambaram S., Prasanna M.V., Tivya C. and Singaraja C.A. (2012). study on groundwater geochimistry and water quality in layered aquifèrs system of pondicherry region, southeast India. Applied Water Science, 2, 253-269.
[12] Bahir M., Carreira P., Oliveira D.S.M., Fernandes P. (2008). Caractérisation hydrodynamique, hydrochimique et isotopique du système aquifère de Kourimat (Bassin d'Essaouira, Maroc). Estudios Geológicos, Vol. 64 (1), pp. 61-73.
[13] Ahoussi K. E., Youan T. M., Loko S., Adja M. G., Lasm T. et Jourda J. P. (2012). Étude hydrogéochimique des eaux des aquifères de fractures du socle Paléo- protérozoïque du Nord-Est de la Côte d'Ivoire : Cas de la région de Bondoukou. Afrique Science 08(3) 51 – 68.
[14] Dibi B., Kouassi K.L., Kouamé K.I., Konan K.S., Soumahoro M., Konan-waidhet A.B. et Gnakri D. (2013). Evaluation de la vulnérabilité à la pollution des aquifères des formations altérites à partir des méthodes DRASTIC et SYNTACS: Cas de la ville de M'bahiakro, Centre de la Côte d'Ivoire. International Journal of Innovation and Applied Studies ISSN 2028-9324 Vol. 2 No. 4 Apr. 2013, pp. 464-476.
[15] Dibi B., Inza D., N'go Y. et Gone D. L. (2006). Origine et mécanisme de la minéralisation des eaux souterraines de la région de Dabou, Côte d'Ivoire. Apport de l'Analyse en Composantes Principales Normées. BIOTERRE, Rev. Inter. Sci. De la Vie et de la Terre, Vol.5 (1): 5-16.
[16] Goné D.L. (2001). Contribution des paramètres physico-chimiques à la compréhension du fonctionnement du système hydrauliques en milieux fi ssurés de la région semi- montagneuse de Man (Ouest de la Côte d'Ivoire). Thèse de Doctorat 3ème cycle, Uni. Abobo- Adjamé, 177 p.
[17] Kouamé K.I., Konan K.S., Kouassi K.L., Dibi B., Soumahoro M., Savané I., Gnakri D. (2012) : Assessment of wells water quality and their suitability for drinking in M'bahiakro city (Côte d'Ivoire). International Journal of Conservation Science, Volume 3, Issue 4, October-December 2012: 289-300.

American Journal of Engineering Research (AJER)
e-ISSN : 2320-0847 p-ISSN : 2320-0936
Volume-03, Issue-01, pp-50-56
www.ajer.org

Research Paper Open Access

Security in Wireless Sensor Networks using Cryptographic Techniques

Madhumita Panda
*Sambalpur University Institute of Information Technology(**SUIIT**)Burla, Sambalpur, Odisha, India.*

Abstract: **-**Wireless sensor networks consist of autonomous sensor nodes attached to one or more base stations.As Wireless sensor networks continues to grow,they become vulnerable to attacks and hence the need for effective security mechanisms.Identification of suitable cryptography for wireless sensor networks is an important challenge due to limitation of energy,computation capability and storage resources of the sensor nodes.Symmetric based cryptographic schemes donot scale well when the number of sensor nodes increases.Hence public key based schemes are widely used.We present here two public – key based algorithms, RSA and Elliptic Curve Cryptography (ECC) and found out that ECC have a significant advantage over RSA as it reduces the computation time and also the amount of data transmitted and stored.

Keywords: *-Wireless Sensor Network,Security, Cryptography, RSA,ECC.*

I. WIRELESS SENSOR NETWORK

Sensor networks refer to a heterogeneous system combining tiny sensors and actuators with general-purpose computing elements. These networks will consist of hundreds or thousands of self-organizing, low-power, low-cost wireless nodes deployed to monitor and affect the environment [1]. Sensor networks are typically characterized by limited power supplies, low bandwidth, small memory sizes and limited energy. This leads to a very demanding environment to provide security.

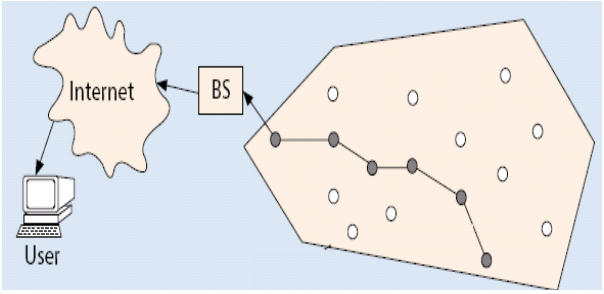

Figure 1:Wireless Sensor Network

11.SECURITY REQUIREMENTS IN WIRELESS SENSOR NETWORK

The goal of security services in WSNs is to protect the information and resources from attacks and misbehaviour. The security requirements in WSN include:

Confidentiality:

Confidentiality is hiding the information from unauthorized access. In many applications, nodes communicate highly sensitive data. A sensor network should not leak sensor reading to neighbouring networks.Simple method to keep sensitive data secret is to encrypt the data with a secret key that only the intended receivers'possess, hence achieving confidentiality.As public key cryptography is too expensive to be

used in the resource constrained sensor networks,most of the proposed protocols use symmetric key encryption methods.For symmetric key approach the key distribution mechanism should be extremely robust.

Authentication:

Authentication ensures the reliability of the message by identifying its origin.In a WSN,the issue of authentication should address the following requirements:[1] communicating node is the one that it claims to be(ii)the receiver should verify that the received packets have undeniably come from the actual sensor node**.**For Authentication to be achieved the two parties should share a secret key to compute message authentication code(MAC) of all communicated data.The receiver will verify the authentication of the received message by using the MAC key.

Integrity:

Integrityis preventing the information from unauthorized modification.Data authentication can provide data integrity also.

Availability:

Availability ensures that services and information can be accessed at the time they are required. In sensor networks there are many risks that could result in loss of availability such as sensor node capturing and denial of service attacks**.**

III.OBSTACLES OF SENSOR SECURITY

A wireless sensor network is a special network which has many constraintscompared to a traditional computer network. Due to these constraints itis difficult to directly employ the existing security approaches to the areaof wireless sensor networks. Therefore, to develop useful security mechanismswhile borrowing the ideas from the current security techniques, it isnecessary to know and understand these constraints first [2].

3.1 Very Limited Resources

All security approaches require a certain amount of resources for the implementation,including data memory, code space, and energy to power thesensor. However, currently these resources are very limited in a tiny wirelesssensor.

• Limited Memory and Storage Space:

A sensor is a tiny device withonly a small amount of memory (few KB) and storage space for the code. Inorder to build an effective security mechanism, it is necessary to limitthe code size of the security algorithm.

• Power Limitation:

A Sensor node has to economize with the shipped battery,i.e.the supplied energy must outlet the sensor's life.This is resulting from the fact that the sensor's battery can neither be replaced nor recharged,once deployed in a difficult access area or hostile environment.The energy of a sensor node is consumed by mainly three essential components:the sensor unit,the communication unit and the computation unit.Because of the limited energy reserves,energy is often one of the primary metrics in WSNs routing algorithms[3].Many Operating systems for WSNs provide certain features to preserve energy[4].

- **Transmission range:**

To minimize the energy needed for communication it is very common that sensor nodes use a rather small transmission range.This results in the necessity of using multiple-hops to transfer data from a source to a destination node through a large network.

3.2 Unreliable Communication

Certainly, unreliable communication is another threat to sensor security.The security of the network relies heavily on a defined protocol, which inturn depends on communication.

• Unreliable Transfer:

Normally the packet-based routing of the sensor network is connectionless and thus inherently unreliable. Packetsmay get damaged due to channel errors or dropped at highly congestednodes. The result is lost or missing packets. Furthermore, the unreliablewireless communication channel also results in damaged packets.Higher channel error rate also forces the software developer to devoteresources to error handling. More

importantly, if the protocol lacksthe appropriate error handling it is possible to lose critical securitypackets. This may include, for example, a cryptographic key.

• **Conflicts**:

Even if the channel is reliable, the communication may stillbe unreliable. This is due to the broadcast nature of the wireless sensor network. If packets meet in the middle of transfer, conflicts will occurand the transfer itself will fail. In a crowded (high density) sensornetwork, this can be a major problem. More details about the effectof wireless communication can be found at [5].

• **Latency:**

The packet-based multihop routing in WSNs increases the latency due to congestion in the network and additionally require processing time. Besides, the routing process in WSNs is often causing delays:For example, if a routing algorithm uses different paths between a source and a destination to distribute energy load, not always the shortest path is used so that additional delays are predictable.

3.3 Unattended Operation

Depending on the function of the particular sensor network, the sensor nodesmay be left unattended for long periods of time. There are three maincaveats to unattended sensor nodes:

• **Exposure to Physical Attacks:**

The sensor may be deployed in anenvironment open to adversaries, bad weather, and so on. The likelihoodthat a sensor suffers a physical attack in such an environmentis therefore much higher than the typical PCs, which is located in asecure place and mainly faces attacks from a network.

• **Managed Remotely:** Remote management of a sensor network makesit virtually impossible to detect physical tampering (i.e., through tamperproofseals) and physical maintenance issues (e.g., battery replacement).

• **Lack of Central Management Point:**

A sensor network should be adistributed network without a central management point. This willincrease the vitality of the sensor network. However, if designed incorrectly,it will make the network organization difficult, inefficient, andfragile.Perhaps most importantly, the longer that a sensor is left unattended themore likely that an adversary has compromised the node.

IV.CRYPTOGRAPHY

Cryptography schemes are often utilized to meet the basic security requirements of confidentiality and integrity in networks. But as the sensor nodes are limited in their computational and memory capabilities,the well-known traditional cryptographic techniques cannot be simply transferred to WSNs without adapting them.

4.1Symmetric Cryptography

Symmetric encryption(also called as secret-key cryptography) uses a single secret key for both encryption and decryption as shown in Figure 2.

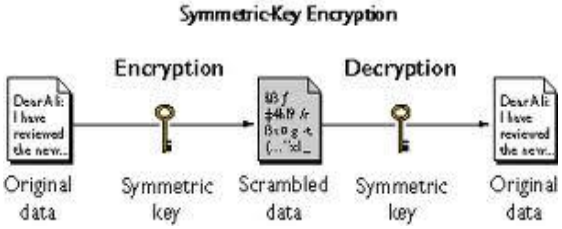

Figure 2:Symmetric -Key Cryptography

This key has to be kept secret in the network, which can be quite hard in the exposed environment where WSNs are usedto achieve the security requirements, several researchers have focused on evaluating crypto graphical algorithms in WSNs and proposing energy efficient ciphers. Symmetric key algorithms are much faster computationally than asymmetric algorithms as the encryption process is less complicated. Examples are AES,3DES etc.

We first focus on Symmetric Cryptography due to the assumption that symmetric cryptography has a higher effectiveness and require less energy consumption, in contrast to public key cryptography.

According to [6]public key is used in some applications for secure communications eg.SSL(Secure Socket Layer) and IPSec standards both use it for their key agreement protocols.But it consumes more energy and it is more expensive as compared to symmetric key.

[7] has given a reason that public key consumes more energy due to great deal of computation and processing involved ,which makes it more energy consumptive as compared to symmetric key technique e.g. a single public key operation can consume same amount of time and energy as encrypting tens of megabits using a secret key cipher.

According to [8],the more consumption of computational resources of public key techniques is due to the fact that it uses two keys. One of which is public and is used for encryption ,and everyone can encrypt a message with it and other is private on which only decryption takes place and both the keys has a mathematical link, the private key can be derived from a public key.In order to protect it from attacker the derivation of private key from public is made difficult as possible like taking factor of a large number which makes it impossible computationally.Hence,it shows that more computation is involved in asymmetric key techniques thus we can say that symmetric key is better to choose for WSN.

According to [9] the cost of public key is much more expensive a s compared to symmetric key for instance, a 64 bit RC5 encryption on ATmega 128 8 MHZ takes 5.6 milliseconds,and a 160 bit SHA1 function evaluation takes only 7.2 millisecond's.These symmetric key algorithms are more than 200 times faster than Public key algorithms.

Public Key cryptography is not only expensive in computation but also it is more expensive in communication as compared to symmetric key cryptography.According to [10] to send a public key from one node to another, at least 1024 bits required to be sent if the private key is 1024 bits long.

Two types of symmetric ciphers are used: block ciphers that work on blocks of a specific length and stream ciphers that work bitwise on data. A stream cipher can be seen as a block cipher with a block length of 1 bit.

Law et al. [11] investigate in their survey in the evaluation of block ciphers for WSNs, based on existingliterature and authoritative recommendations. The authors do not only consider the security properties of thealgorithms, but additionally they try to find the most storage- and energy-efficient ones. To compare the differentblock ciphers, benchmarks are conducted on the 16-bitRISC-based MSP430F149 considering different cipher parameters, such as key length, rounds and block length; anddifferent operation modes, such as cipher-block chaining(CBC), cipher feedback mode (CFB), output feedback mode(OFB) and counter (CTR). Based on a review of differentcryptographic libraries, such as OpenSSL, Crypto++,Botan and Catacomb, most of the code was adapted fromOpenSSL [12]. Ciphers without public implementationswere implemented based on the original papers. For thecompilation of the sources the IAR Systems' MSP430 CCompiler was used. The evaluation results of the conductedbenchmarks show that the most suitable block ciphers forWSNs are Skipjack, MISTY1, and Rijndael, depending onthe combination of available memory and required securitylevel. As operating mode "Output Feedback Mode (OFB)"for pair wise links, i.e. a secured link between two peers, issuggested. In contrast, "Cipher Block Chaining (CBC)" isproposed for group communications, for example, to enablepassive participation in the network.

Fournel et al. [13] investigate in their survey streamciphers for WSNs. The chosen stream cipher algorithms(DRAGON, HC-256, HC-128, LEX, Phelix, Py and Pypy,Salsa20, SOSEMANUK) are all dedicated to software usesand were originally submitted to the European ProjectEcrypt in the eStream call (Phase 2). To extend the selectionof stream ciphers, the famous RC4, SNOWv2 and AESCTRwere considered for evaluation. The performedbenchmarks on an ARM9 core based ARM922T aimedat finding the most storage-efficient and energy-efficientstream ciphers for this platform. Based on the methodologyof the eStream testing framework [14], four performancemeasures were considered: encryption rate for long streams,packet encryption rate, key and IV setup, and agility.Furthermore, the code size required for each algorithm onthe ARM9 platform was investigated. The used streamcipher algorithms, originally developed in C for thetraditional PC platform, were executed on the ARM9platform without any optimizations. The results of thebenchmarks show that the stream ciphers Py and Pypy, thetwo most efficiently running algorithms on traditional PCplatforms, do not work as fast on the ARM9 architecture. Incontrast, SNOWv2, SOSEMANUK and HC-128 performed similarly fast on both

platforms. For SOSEMANUK, thekey setup was very huge in comparison to the key setup onthe traditional PC platform.

4.2Asymmetric Cryptography

Asymmetric encryption (also called public-key cryptography) uses two related keys (public and private) for data encryption and decryption, and takes away the security risk of key sharing. The private key is never exposed.

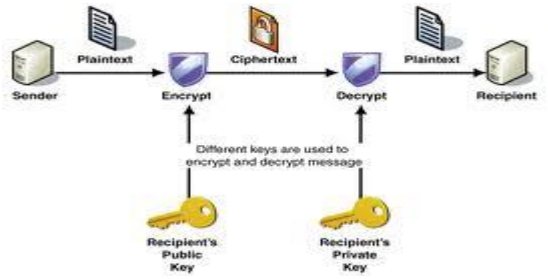

Figure 3:Asymmetric Key Cryptography.

A message that is encrypted by using the public key can only be decrypted by applying the same algorithm and using the matching private key. Likewise, a message that is encrypted by using the private key can only be decrypted by using the matching public key. Examples are RSA,ECC etc.

Public key Cryptography was omitted from the use in WSN because of its great consumption of energy and bandwidth which was very crucial in sensor network. Now a days a sensor become powerful in terms of CPU and memory power so, recently there has been a change in the research community from symmetric key cryptography to public key cryptography. Also symmetric key does not scale well as the number of nodes grows[15].

Arazi et al. [16] describe the efficiency of public-key cryptography for WSNs and the corresponding issues that need to be considered. Particularly, ECC is highlighted as suitable technique forWSN which provides a good trade-off between key size and security.

Liu and Ning [17] also emphasize that ECC is oneof the most efficient types of public key cryptographyin WSNs. The steps of design, implementation andevaluation of TinyECC, a configurable and flexible libraryfor ECC operations in WSNs, are presented. The libraryprovides a number of optimization switches that can becombined according to the developer's needs for a certainapplication, resulting in different execution times andresource consumptions. The TinyECC library was alsoevaluated on several sensor platforms; including MICAz,Tmote Sky, and Imotel; to find the most computationally efficient and the most storage efficient configurations.

In Public key Cryptography mostly two algorithms RSA and ECC use. The ECC is offer equal security for a far smaller key size than any other algorithm.So that it reducing processing and communication overhead. For example, RSA with 1024 bit keys (RSA-1024) provides a currently accepted level of security for many applications and is equivalent in strength to ECC with 160 bit keys (ECC-160) .To protect data beyond theyear 2010, RSA Security recommends RSA-2048 as the new minimum key size which is equivalent to ECC with 224 bit keys (ECC-224)[18].

[19]described the efficiency of public-key cryptography for WSNs and the corresponding issues that need to be considered. Particularly, ECC is highlighted as suitable technique for WSN which provides a good trade-off between key size and security. Lopez, 2006 focused on the security issues by analysing the use of symmetric cryptography in contrast with public-key cryptography. The author also discussed the important role of elliptic curve cryptography in this field.

A.RSA algorithm

A method to implement a public key cryptosystemwhose security is based on the difficulty of factoringlarge prime numbers was proposed in [20].*RSA* standsfor Ron Rivest, Adi Shamir and Leonard Adleman, whofirst publicly described the algorithm in 1977. Throughthis technique it is possible to encrypt data

and createdigital signatures.It was so successful that today *RSA*public key algorithm is themost widely used in theworld.

Key generation:
1. Choose two distinct prime numbers, p and q.
2. Compute modulus n = pq
3. Compute phi, φ= (p - 1)(q - 1) where φ is Euler's Totient Function.
4. Select public exponent *e* such that 1 < e < φ and gcd(e, φ) = 1
5. Compute private exponent d = $e^{-1} \bmod \varphi$
6. Public key is {n, e}, private key is d

Encryption: $c = m^e \pmod n$.
Decryption: $m = c^d \pmod n$.
Digital signature: $s = H(m)^d \bmod n$, Verification: $m' = s^e \bmod n$, if m' = H(m) signature is correct. H is a publicly known hash function.

***B.*ECC(Elliptic curve cryptography)**[21]

This algorithm is mainly depend on the algebraicstructure of elliptic curves.The difficulty in problemis ,the size of the elliptic curve. The primary benefitpromised by ECC is a smaller key size, reducingstorage and transmission requirements—i.e., that anelliptic curve group could provide the same level of security afforded by an RSA-based system with alarge modulus and correspondingly larger key—e.g., a 256bit ECC public key should providecomparable security to a 3072bit RSA public key(see #Key sizes).For current cryptographicpurposes, an *elliptic curve* is a plane curve whichconsists of the points satisfying the equation***:*** $y^2=x^3+ax+b$***,***

Compared to RSA,ECC has small key size,low memory usage etc.Hence it has attracted attention as a security solution for wireless networks [22].

4.3 Hybrid Cryptography

Symmetric key algorithm has a disadvantage of keydistribution[23] and asymmetric algorithm needmuch computation so the power of the sensor iswasted in it[23] and it is not feasible to use as poweris wasted then sensor will be of no useThus the algorithm which combines both thealgorithm i.e. asymmetric and symmetric so theadvantages of both the algorithm can be utilized in it.
A hybrid cryptosystem is a protocol using multiple ciphers of different types together, each to it's best advantage. One common approach is to generate a random secret key for a symmetric cipher, and then encrypt this key via an asymmetric cipher using the recipient's public key. The message itself is then encrypted using the symmetric cipher and the secret key. Both the encrypted secret key and the encrypted message are then sent to the recipient.
The recipient decrypts the secret key first, using his/her own private key, and then uses that key to decrypt the message. This is basically the approach used in PGP. Some of the hybrid algorithm like DHA+ECC[24] is described in detail.

V.CONCLUSION

The wireless sensor networks continue to grow and become widely used in many applications. So, the need for security becomes vital. However, the wireless sensor network suffers from many constraints such as limited energy, processing capability, and storage capacity, etc. There are many ways to provide security, one is cryptography. Selecting the appropriate cryptography method for sensor nodes is fundamental to provide security services in WSNs. Public Key based cryptographic schemes were introduced to remove the drawbacks of symmetric based approaches.We have compared two schemes in this paper ECC, and RSA and found out that ECC is more advantageous compared to RSA,due to low memory usage,low CPU consumption and shorter key size compared to RSA.ECC 160 bits is two times better than RSA 1024 bits when code size and power consumption are the factors of consideration. Tests were performed in 8051 and AVR platforms as in[25].ECC 160 bits use four times less energy than RSA 1024 bits in Mica2dot as in[26].Recently a new scheme called Multivariate Quadratic Almost Group was proposed which showed significant improvements over RSA and ECC.

REFERENCES

[1]. Matt Welsh, Dan Myung, Mark Gaynor, and Steve Moulton "Resuscitation monitoring with a wireless sensor network", in Supplement to Circulation: Journal of the American Heart Association, October 2003.

[2] D. W. Carman, P. S. Krus, and B. J. Matt. Constraints and approaches for distributed sensor network security. Technical Report 00-010, NAI Labs,Network Associates, Inc., Glenwood, MD, 2000.

[3]. K.Akkaya and M.Younis,*A survey on routing protocols for wireless sensor networks*,Ad Hoc Networks,3(2005),325-349.

[4]. M.Healy,T.Newe,andE.Lewis. *Power management in operating systems for wireless sensornodes*, in Proc. of the IEEE Sensor Applications Symposium(SAA'07),San Diego,CA,2007,1-6.

[5]. I. F. Akyildiz, W. Su, Y. Sankarasubramaniam, and E. Cayirci. A survey on sensor networks.*IEEE Communications Magazine*, 40(8):102–114, August 2002.

[6]. Ning P, Wang R and Du W (2005), "An efficient scheme for authenticating public keys in sensor networks", Proceedings of the 6th ACM international symposium on Mobile ad hoc networking and computing, Chicago, IL, USA, pp. 58-67.

[7]. Goodman J and Chandrakasan P (2001), "An Energy Efficient Reconfigurable Public Key Cryptography Processor ", IEEE journal of solid state circuits, pp. 1808-1820, November 2001.

[8]. RSA Security (2004), "Cryptography ", Available at: http://www.rsasecurity.com/rsalabs/node.asp?id=2152.

[9]. Ganesan P, Venugopalan R, Peddabachagari P, Dean A, Mueller F and Sichitiu M (2003), "Analyzing and modelling encryption overhead for sensor network nodes ", In Proceeding of the Ist ACM international workshop on Wireless sensor networks and application, San Diego, California, USA, September 2003.

[10]. Ling Tan, Shunyi Zhang, and Yanfeng Sun, Jing Qi "Application of Wireless Sensor Networks in Energy Automation", Sustainable Power Generation and Supply, 2009. Supergen '09.International conference.

[11]. Y.W.Law,J.Doumen,andP.Hartel,*Survey and benchmark of block ciphers for wireless sensor networks*,ACM Transactions on Sensensor Networks(TOSN),2(2006),65-93.

[12]. E.A.Young,T.J.Hudson,and R.S.Engelschall,*OpenSSL*.Availableonline:http://www.openssl.org/,2010.

[13]. N. Fournel, M. Minier, and S. Ub´eda, *Survey and benchmark of stream ciphers for wireless sensor networks*, in Information Security Theory and Practices: Smart Cards, Mobile and Ubiquitous Computing Systems, D. Sauveron, K. Markantonakis,A. Bilas, and J.-J. Quisquater, eds., vol. 4462 of Lecture Notes in Computer Science, Springer-Verlag, Berlin, 2007, 202–214.

[14]. C. De Canni`ere, *eSTREAM Optimized Code HOWTO*. Available online: http://www.ecrypt.eu.org/stream/perf/, 2005.

[15]. IAN F.Akyildiz, Weilian Su, YogeshSankarasaubramaniam,ArdialCayirci,"A Survey on Sensor Networks",IEEE Communications Magazine,August 2002,pages 102-114.

[16]. B. Arazi, I. Elhanany, O. Arazi, and H. Qi, *Revisiting public-key cryptography for wireless sensor networks*, Computer, 38 (2005),103–105.

[17]. A. Liu and P. Ning, *TinyECC: a configurable library for elliptic curve cryptography in wireless sensor networks*, in Proc. of the International Conference on Information Processing in Sensor Networks (IPSN '08), St. Louis, MO, 2008, 245–256.

[18]. The Scheme of Public Key Infrastructure for improving Wireless Sensor Networks Security Zhang Yu.

[19]. Arazi,B.,Elhanany,L.,Arazi,O.,Qi,H.,2005:Revising public –key cryptography for wireless sensor networks. IEEE Computer,38(11):103-105.

[20]. R.L.Rivest,A.Shamir,and L.Adleman,"A method for obtaining digital signatures and public-key cryptosystems",Communications of the ACM,21(2):120-126,1978.

[21]. Kristin Lauter, Microsoft Corporation , ―The Advantages Of Elliptic CurveCryptography For Wireless Security IEEE Wireless Communications ,Vol 3,pp 22-25,February 2004.

[22]. Dona Maria Mani,Nishamol P H,"A Comparision Between RSA And ECC In Wireless Sensor Networks",International Journal of Engineering Research & Technology,Volume.2 Issue 3,March-2013.

[23] Yong Wang, GarhanAttebury, Byrav Ramamurthy,―A Survey of Security Issues In Wireless SensorNetworks‖ , IEEE Communications Surveys & Tutorials •,pp223-237 2nd Quarter 2006.

[24] Mohd. Rizwan beg1 and Shish Ahmad ―EnergyEfficient PKI Secure Key ManagementTechnique in Wireless Sensor NetworkusingDHA & ECC‖ International Journal of Ad hoc,Sensor& Ubiquitous Computing (IJASUC) Vol.3, No.1,pp 256- 262,February 2012.

[25]. Nils Gura, ArunPatel,ArvinderpalWander,HansEberle,andSheueling Chang Shantz,"Comparing Elliptic Curve and Cryptography and RSA on 8-bit CPUs"In Proceedings of the 2004 Workshop on Cryptographic Hardware and Embedded Systems(CUES 2004),Boston Marriott Cambridge(Boston)August,2004.

[26]. Shish Ahmad,Mohd.Rizwanbeg,andQamarAbbas,"Energy Saving Secure Framework for Sensor Network using Elliptic Curve Cryptography",IJCA Special Issue of Mobile Ad-hoc Networks,pages 167-172,2012.

American Journal of Engineering Research (AJER)
e-ISSN : 2320-0847 p-ISSN : 2320-0936
Volume-03, Issue-01, pp-57-63
www.ajer.org

Research Paper Open Access

Implementation of Machinery Failure Mode and Effect Analysis in Amhara Pipe Factory P.L.C., Bahir Dar, Ethiopia

Yonas Mitiku Degu[1], R. Srinivasa Moorthy[2]
[1, 2]: *School of Mechanical and Industrial Engineering, BiT, Bahir Dar University, Bahir Dar, Ethiopia.*

Abstract: - Failure Mode and Effect Analysis (FMEA) is a pro-active quality tool for evaluating potential failure modes and their causes. It helps in prioritizing the failure modes and recommends corrective measures for the avoidance of catastrophic failures and improvement of quality. In this work, an attempt has been made to implement Machinery FMEA in UPVC pipe production unit of Amhara Pipe Factory, P.L.C., Bahir Dar, Ethiopia.
The failure modes and their causes were identified for each machine, the three key indices (Severity, Occurrence and Detection) we reassessed and the analysis was carried out with the help of MFMEA Worksheet. Finally, the necessary corrective actions were recommended.

Keywords: - Detection, MFMEA, Occurrence, RPN, Severity.

I. INTRODUCTION

Amhara Pipe Factory P.L.C., Bahir Dar, Ethiopia specializes in the production of UPVC, HDPE and threaded casting pipes of various diameters and geo-membrane sheets for domestic, construction and industrial needs. They currently follow breakdown maintenance for the machinery which results in a considerable machine downtime, disrupting the continuous production of pipes. The identification and elimination or reduction of the problems inherent in the UPVC pipe production unit using a continuous process improvement tool will be substantially beneficial in the grounds of reduced MDT (machine down time), minimized scrap, lessened cost of replacing spare parts and higher productivity.

Failure Mode and Effect Analysis (FMEA) is one such quality tool which gives a clear description of the failure modes so that the catastrophic failure possibilities can be readily identified and eliminated or minimized through corrective actions in design or operating procedure.
Among the different types of FMEA, Machinery FMEA has been chosen for implementation in UPVC production unit of Amhara Pipe Factory P.L.C. The methodology, the results of MFMEA analysis and the recommended corrective actions for quality improvement were detailed in this work.

II. FAILURE MODE AND EFFECT ANALYSIS (FMEA)

Murphy's Law states, "Everything that can fail shall fail". FMEA addresses the elimination of premature failure due to faulty design or process.

Failure Mode and Effect Analysis (FMEA) is defined as a systematic process for identifying potential design and process failures before they occur, with the intent to eliminate them or minimize the risk associated with them. FMEA procedures are based on standards in the reliability engineering industry, both military and commercial [1]. FMEA provides an organized critical analysis of potential failure modes of the system being defined and identifies the associated causes. It uses occurrence and detection probabilities in conjunction with severity criteria to develop a risk priority number (RPN) for ranking corrective action considerations [2].

FMEA can also be defined as a group of activities intended to "recognize and evaluate the potential failure of a product or process and its effects and identify actions that could eliminate or reduce the chance of potential failures" [3].

2.1 Objectives of FMEA

The main objectives of FMEA are to:

- identify the equipment or subsystem and mode of operation

- recognize potential failure modes and their causes
- evaluate the effects of each failure mode on the system and
- identify measures for eliminating or reducing the risks associated with each failure mode [1].

2.2 Major types of FMEA

The following major types of FMEA are commonly used, based on the application:

- Design FMEA (DFMEA) – focuses on potential failure modes of products caused by design deficiencies.
- Process FMEA (PFMEA) - focuses on potential failure modes of products caused by manufacturing or assembly process deficiencies.
- Machinery or Equipment FMEA (MFMEA) – focuses on designs that improve the reliability and maintainability of the machinery for long-term plant usage [4].

2.3 Key parameters of FMEA

Any type of FMEA involves the following key parameters for prioritizing the corrective action:

2.1.1 Severity

It is an assessment of seriousness of the effect of a failure mode on the customers.

2.1.2 Occurrence

Occurrence is an assessment of the likelihood that a particular cause will happen and result in a failure mode.

2.1.3 Detection

It is an assessment of the likelihood that the current controls will detect the cause of the failure mode thus preventing it from reaching the customer.

2.1.4 Risk Priority Number (RPN)

It is a mathematical product of Severity (S), Occurrence (O) and Detection (D). It serves in fixing the priority for the process / item to focus for corrective action. It is computed as:

$$\boldsymbol{RPN = S \times O \times D} \qquad \textbf{(1)}$$

The three indices (Severity, Occurrence and Detection) are individually assessed on a 1 to 10 scale basis for each failure mode, using the standard guidelines specifically tailored for Design, Process and Machinery FMEA's, to address the objectives and requirements of the selected type of FMEA. Then RPN is calculated using **(1)** for each process/system/sub-system to rank and prioritize the corrective action plan.

2.4 General benefits of FMEA

- Prevention planning
- Identifying change requirements
- Cost reduction
- Increased through-put
- Decreased waste
- Decreased warranty costs
- Reduced non-value added operations

III. MACHINERY FMEA

MFMEA is a standardized technique for evaluating equipment and tooling during its design phase to improve the operator safety, reliability and robustness of the machinery. MFMEA provides an opportunity to prioritize the design improvement actions through identification of corrective actions to prevent or mitigate possible failures.

Machinery FMEA should be started early in the design process (best practice) when the equipment and tooling is able to take advantage of design revisions. Normally MFMEA's are targeted for long-term, repetitive cycles, where wear-out is a prime consideration. The specifically tailored criteria for ranking MFMEA parameters of Severity, Occurrence and Detection are given in TABLES I, II and III [4].

The key benefits of MFMEA are to:

- improve safety, reliability and robustness of equipment / tooling
- allow design changes to be incorporated early, to minimize machinery cost and delivery delays and
- reduce overall life-cycle costs.

Owing to the fact that Amhara Pipe Factory P.L.C. is continuous pipe production industry and that the current problems in UPVC pipe production unit are more machine-centric, MFMEA was selected among the three major types of FMEA for implementation.

IV. PROFILE OF AMHARA PIPE FACTORY P.L.C., BAHIR DAR, ETHIOPIA

Amhara Pipe Factory P.L.C., Bahir Dar, Ethiopia is the biggest producer of plastic products in Ethiopia. The major products of the factory are Un-plasticized Polyvinyl Chloride (UPVC) pipes, High Density Poly Ethylene (HDPE) pipes, Geo-membrane sheets and Threaded casing pipes.

UPVC pipe unit has the capacity to produce pipes of diameters ranging from 16 mm to 630 mm for various nominal pressures from 3 bar to 16 bar, as per the Ethiopian standards identical to ISO standards. UPVC pipes are used for water sewerage system, potable water transportation, industrial waste disposal system, irrigation and for making electric conduits.

HDPE unit has two lines – one for producing pipes of outer diameter in 16 mm – 63 mm range which can be coiled in lengths from 100 m to 300 m as rolls; the other line produces pipes in 75 mm - 250 mm diameter range for 12 m length or as per the customer requirements. HDPE pipes, made to withstand four different nominal pressure capacities from 6 bar to 25 bar, are used for industries, marine mining, potable water transport, waste water disposal, slurry/chemical and compressed gas transport.

Geo-membrane sheets are produced in the range of thickness 0.5 mm to 2.0 mm, width 6.2 m to 6.3 m, and lengths up to 140 m. They are used for land fill project sites, banking dam, channel irrigation, tunnel, highway and railway construction, river way, etc.

Threaded casing pipes are produced for standard diameters from 75 mm to 315 mm for two nominal pressures (10 bar and 16 bar), confirming to international standards.

V. PRODUCTION OF UPVC PIPES

The UPVC pipe production is carried out in eight distinct stages, right from raw materials to finished pipe of required dimensions.

5.1 Mixing Unit

This unit comprises of Hot and Cold chambers. The raw materials are thoroughly mixed in the Hot chamber first and are automatically transferred to the Cold chamber. The output of the Cold chamber is a homogenous mixture of the raw materials in proper proportion.

5.2 Helical Spring Conveyor Unit

The output of Mixing unit is conveyed to Extruder unit through a helical spring conveyor enclosed in a flexible PVC pipe.

5.3 Extruder Unit

A threaded feeder thrusts the mixture into a die set with a concentric mandrel and sleeve of required size to extrude the pipe. The mandrel and sleeve heaters impart the required temperature, thus giving uniform temperature distribution in the pipe cross-section.

5.4 Vacuum Pass

The extruded pipe is made to pass through a vacuum unit. This facilitates the extruded pipe to sustain the dimensions without any wrinkling and improves cleanliness and hardness of the pipe surface.

5.5 Cooling Pass

In this unit water is used for spray cooling to ensure the pipe quality and high speed stable extruding.

5.6 Haul-off Unit

The chain drive with an endless wooden gripper belt is used to provide traction to pull the extruded pipe.

5.7 Planetary Cutter Unit

A motor-driven circular saw cutter enables high-speed cutting operation of the pipes. A chamfer tool is also incorporated along with the cutter.

5.8 Belling Unit

This unit performs the bulging operation on one end of the cut pipes to facilitate joining of pipes.

VI. RESULTS AND DISCUSSION

MFMEA of the UPVC pipe production unit was done based on the MFMEA Severity, Occurrence and Detection criteria outlined in TABLES I, II and III respectively, by the MFMEA team comprising of the authors, Mr. Adem Dawud, Production and Technical Process Owner and the workers of each machine.

The results summarized in MFMEA Worksheet (TABLE IV) revealed that the Risk Priority Number was the highest (RPN = 168) for Mixer unit, mainly owing to the degree of severity of the failure in disrupting the entire production, excessive mean-time-between-failures (MTBF) and difficulties in detection. Hence, utmost priority should be given to the corrective measures for Mixer unit to eliminate the failure. The next priority should be given to the Extruder unit (RPN = 120), mainly because of its criticality in affecting further processing. For the Planetary cutter unit ranking three with an RPN of 42, the sole reason for failure was found to be the breakage of screw shaft in the minor diameter section.

The RPN values of the other units were found to be less critical and substantially low when compared to Mixer and Extruder units. Nevertheless, the required corrective actions were recommended for all the eight units in the MFMEA Worksheet.

VII. CONCLUSION

The failure problems in UPVC production unit of Amhara Pipe Factory P.L.C. was analyzed using MFMEA technique and corrective actions for quality improvement were documented and presented to the authorities of the factory. The vibration problem inherent in the Mixer unit was found to pose a major threat. Since MFMEA implementation involves preventive maintenance as a control to ensure reliability, the authorities were insisted to keenly follow the preventive maintenance guidelines for each machine, documented in the Maintenance Catalogue given by the suppliers of the machinery, in addition to the recommended corrective actions.

Once the recommended actions for reducing machine vibrations and other corrective measures mentioned in MFMEA Worksheet were implemented along with a strict adherence to the preventive maintenance schedule, then the RPN values can be recomputed, which are sure to show a marked decrease in its value, owing to reduced severity, occurrence and detection indices, thus improving the life of machines and the overall productivity of Amhara Pipe Factory P.L.C. The authorities were suggested to keep track of the MFMEA documents in future, since it is a continuous quality improvement tool.

Use of FTA (Fault Tree Analysis), a deductive top-down failure analysis technique, will compliment this attempt. The work can be extended by using FMECA (Failure Mode, Effect and Criticality Analysis) which additionally charts the probability of failure modes against the severity of their consequences.

VIII. ACKNOWLEDGEMENTS

The authors wish to register their heartfelt gratitude to Mr. Adem Dawud, Production and Technical Process Owner in particular and all the authorities, management staff and workers of Amhara Pipe Factory P.L.C., Bahir Dar, Ethiopia for supporting us with necessary technical information and giving feedback about the failure modes of each machinery of UPVC production unit.

IX. REFERENCES

[1] Guidance of Failures Modes and Effects Analysis, International Marine Contractors Association, April 2002.

[2] Failure Mode and Effects Analysis (FMEA): A Guide for Continuous Improvement for the Semi-conductor Equipment Industry, Sematech, September 30, 1992.

[3] Veeranna D. Kenchakkanavar and Co., Failure Mode and Effects Analysis: A Tool to Enhance Quality in Engineering Education, *International Journal of Engineering (IJE), Vol. 4: Issue 1.*

[4] Failure Mode and Effects Analysis, Cayman Business System (Rev: Q), May 31, 2011.

TABLES

TABLE I: Criteria for Ranking Severity (S) in MFMEA [4]

Effect	*Severity Criteria*	*Ranking*
Hazardous without warning	Very high severity ranking: Affects operator, plant or maintenance personnel; safety and/or effects non-compliant with government regulations.	10
Hazardous with warning	High severity ranking: Affects operator, plant or maintenance personnel; safety and/or effects non-compliant with government regulations.	9
Very high downtime or defective parts	Downtime of more than 8 hours .	8
High downtime or defective parts	Downtime of more than 4-7 hours.	7
Moderate downtime or defective parts	Downtime of more than 1-3 hours.	6
Low downtime or defective parts	Downtime of 30 minutes to 1 hour.	5
Very low	Downtime up to 30 minutes and no defective parts	4
Minor effect	Process parameters variability exceed upper/lower control limits; adjustments or process controls need to be taken. No defective parts.	3
Very minor effect	Process parameters variability within upper/lower control limits; adjustments or process controls need to be taken. No defective parts.	2
No effect	Process parameters variability within upper/lower control limits; adjustments or process controls not needed or can be taken between shifts or during normal maintenance visits. No defective parts.	1

TABLE II: Criteria for Ranking Occurrence (O) in MFMEA [4]

Probability of Failure Occurrence	*Possible Failure Rates Criteria*	*Ranking*
Very high: Failure is almost inevitable	Intermittent operation resulting in 1 failure in 10 production pieces or MTBF of less than 1 hour.	10
	Intermittent operation resulting in 1 failure in 100 production pieces or MTBF of less than 2 to 10 hours.	9
High: Repeated failures	Intermittent operation resulting in 1 failure in 1000 production pieces or MTBF of 11 to 100 hours.	8
	Intermittent operation resulting in 1 failure in 10,000 production pieces or MTBF of 101 to 400 hours.	7
Moderate: Occasional failures	MTBF of 401 to 1000 hours.	6
	MTBF of 1001 to 2000 hours.	5
	MTBF of 2001 to 3000 hours.	4
Low: Relatively few failures	MTBF of 3001 to 6000 hours.	3
	MTBF of 6001 to 10,000 hours.	2
Remote: Failure unlikely	MTBF greater than 10,000 hours.	1

TABLE III: Criteria for Ranking Detection (D) in MFMEA [4]

Detection	*Likelihood of Detection by Design Controls*	*Ranking*
Absolute uncertainty	Machine controls will not and/or cannot detect potential cause/mechanism and subsequent failure mode; or there is no design or machinery control.	10
Very remote	Very remote chance a machinery/design control will detect a potential cause/mechanism and subsequent failure mode.	9
Remote	Remote chance a machinery/design control will detect a potential cause/mechanism and subsequent failure mode. Machinery control will prevent an imminent failure.	8
Very low	Very low chance a machinery/design control will detect a potential cause/mechanism and subsequent failure mode. Machinery control will prevent an imminent failure.	7
Low	Low chance a machinery/design control will detect a potential cause/mechanism and subsequent failure mode. Machinery control will prevent an imminent failure.	6
Moderate	Moderate chance a machinery/design control will detect a potential cause/mechanism and subsequent failure mode. Machinery control will prevent an imminent failure and will isolate the cause. Machinery control may be required.	5
Moderately high	Moderately high chance a machinery/design control will detect a potential cause/mechanism and subsequent failure mode. Machinery control will prevent an imminent failure and will isolate the cause. Machinery control may be required.	4
High	High chance a machinery/design control will detect a potential cause/mechanism and subsequent failure mode. Machinery control will prevent an imminent failure and will isolate the cause. Machinery control may be required.	3
Very high	Very high chance a machinery/design control will detect a potential cause/mechanism and subsequent failure mode. Machinery controls not necessary.	2
Almost certain	Design control will almost certainly detect a potential cause/mechanism and subsequent failure mode. Machinery controls not necessary.	1

TABLE IV: MFMEA Worksheet for PVC Pipe Production Unit of Amhara Pipe Factory P.L.C.

Sub-system	*Function*	*Potential Failure Mode(s)*	*Potential Effect(s) of Failure*	*S*	*Potential Cause(s) of Failure*	*O*	*Current Design / Machine Control(s)*	*D*	*RPN / Rank*	*Recommended Action(s)*
Mixer	To mix the raw materials homogenously	Premature Bearing failure Crushing of key	The respective production line is disrupted	7	Undue vibration of the equipment	3	Replacing bearing Replacing key	8	168 / I	Providing vibration isolation with elastic pads; laying foundation beds
		Burning of motor coil			Overload due to coagulation		Rewinding motor coil			Monitoring of Hot chamber temperature
Helical Spring Conveyor	To transport Mixer unit output to Extruder unit	Breakage of spring	Disrupts further processing	5	High inertia torque	4	Welding the broken spring	1	20 / V	Limiting the radius of curvature
		Feed motor failure			Overload due to coagulation					Monitoring of Cold chamber temperature
Extruder	To get the reqd. pipe dimensions	Burning of mandrel and sleeve heaters	Prolonged uneven temperature distribution causing scrap	8	Improper handling of die sets	3	Replacing resistors	5	120 / II	Use of material handling equipment for die sets
Vacuum Pass	To prevent pipe wrinkling	Noisy operation	Reduced vacuum pressure causing pipe wrinkling	3	Accumulation of foreign particles	2	Cleaning of vacuum pump, when noisy	1	6 / VI	Supplying clean filtered water for recycling
Cooling Pass	To cool the pipe	Leakage of water	Reduces the cooling effect	2	Poor maintenance of pipe joints	2		1	4 / VII	Periodic maintenance of cooling pipes
Haul-off	To pull the extruded pipe	Accelerated wear and tear of rubber gripper	Disrupts further processing	6	Inadequate gripping and slippage	3	Replacing damaged grippers	2	36 / IV	Periodic grease lubrication of the chain sprocket
		Breakage of roller chain					Replacing broken pins			
Planetary Cutter	To cut and chamfer the pipe	Breakage of screw shaft	Necessitates manual cutting	6	Stress concentration in screw shaft shoulder	7	Replacing the screw shaft	1	42 / III	Avoiding abrupt change in screw diameter
Belling	To bulge the pipe	Burning of 0.5 A	Delivery affected till repair	1	Variation of supply voltage	6	Changing fuse	1	6 / VI	Using 1 A fuse

AUTHORS' BIBLIOGRAPHY

Yonas Mitiku Degu received his B.Sc. in Mechanical Engineering from Bahir Dar University, Bahir Dar, Ethiopia in 2005; pursued M.Sc. in Applied Mechanics (Mechanical Design) Addis Ababa University, Addis Ababa, Ethiopia graduated in 2008; currently working as Assistant Professor and Director of School of Mechanical and Industrial Engineering, Bahir Dar Institute of Technology, Bahir Dar University, Bahir Dar, Ethiopia.

R. Srinivasa Moorthy obtained his Masters Degree in Mechanical Engineering Design from Kongu Engineering College, Perundurai, Tamilnadu, India; has 17+ years of teaching experience; worked in Erode Sengunthar Engineering College, Erode, Tamilnadu, India, for 10 + years; worked in Eritrea Institute of Technology, Eritrea, North-East Africa, for 4 years; currently working as a Lecturer in School of Mechanical and Industrial Engineering, Bahir Dar Institute of Technology, Bahir Dar University, Bahir Dar, Ethiopia.

American Journal of Engineering Research (AJER)
e-ISSN : 2320-0847 p-ISSN : 2320-0936
Volume-03, Issue-01, pp-64-67
www.ajer.org

Research Paper Open Access

Effect of Oxygen Concentration on Corrosion Rate of Carbon Steel in Seawater

A.Ismail[1], N.H. Adan[2]
Faculty of Mechanical Engineering & Manufacturing
UniversitiTun Hussein Onn Malaysia (UTHM) Batu Pahat, Johor

Abstract: - Carbon steel is widely used in engineering applications and comprises about 85% of the annual steel production worldwide. With considering the cost of product, carbon steel has been widely employed as a construction material in oil and gas production. However, one of the major problems related to its use is its low corrosion resistance in this environment. An investigation has been carried out to evaluate the corrosion behaviour of AISI 1040 steel in artificial seawater and different sulphate (SO_4^{2-}) to chloride (Cl^-) ratio. The experimental was run under static conditions with controlled temperatures and the changes of weight loss, morphology and hardness was identified before and after corrosion attack. The materials experience extremely weight loss after corrosion attack and this indicate that uniform corrosion developed on AISI 1040. The Open Circuit Potential (OCP) shifted to more negative value in the non-oxygen solution which indicate that metals are susceptible to corrosion attack in high oxygen content. Morphology observation supports the corrosion product growth in oxygen content solution.

Keywords: - *AISI 1040, Carbon Steel, Dissolved Oxygen and Corrosion Rate*

I. INTRODUCTION

Rusting is an important phenomenon accompanied with the corrosion of carbon steel and the formation of corrosion products such as iron oxides is an a biotic process of chemical reactions. It was generally agreed by most of the researches that carbon steels are generally attacked by uniform corrosion or general corrosion. The term ‘uniform’ or ‘general’ corrosion is used to describe the corrosion damage that proceeds in a relatively uniform manner over the entire surface of an alloy. It is an even rate of metal loss over the exposed surface. It also characterised by a chemical or electrochemical reaction or metal loss due to chemical attack or dissolution that proceeds uniformly over the entire exposed surface or over a large area. During this process, the material becomes thinner as it corrodes until its thickness is reduced to the point at which failure occurs. Corrosion attack of metal in seawater is dependent mainly on the salt content (which increase the electrical conductivity) and its oxygen content. A number of variables can influence and complicate the course of corrosion in different ways such as chloride, sulphate and temperature.

Experimental Procedures

Linear polarisation tests were carried out in static conditions. Specimens with an electrical connecting wire were embedded in a non-conducting resin and the exposed surface with known area was subsequently ground using SiC sandpaper and diamond polished to a 6-micron finish. The sample was held in each solution for 5min before starting the experiment to stabilize the surface. This method makes use of a three-electrode electrochemical cell consist of reference electrode silver/saturated-silver-chloride (Ag/AgCl) half cell, the potential of which, versus normal hydrogen electrode (NHE), is +0.197 V. The working electrode is the sample and platinum is used as the counter electrode. This accelerated test method facilitates analysis of the kinetics of the corrosion reactions by controlling the potential between the reference and the working electrode and maintaining the current in the external cell between the counter and the working electrode. The potential is controlled by a computer-controlled potentiostat and is shifted at a constant rate in the anodic direction from the open circuit potential (OCP), causing the working electrode to become the anode and causing electrons to be

withdrawn from it. For linear polarisation, the measurement begins at approximately -20mV and scan in the positive direction to +20mV from OCP. The data are obtained from a linear plot of the potential versus current density graph. The slope of the graph was then calculated to obtain the corrosion rate by using the Stern and Geary equation.

Results and Discussion

The Tafel constants, β_a and β_c generally used were 120 mV/decade. It is strongly agreed by Hinds (2006) that any values between 60 and 120 mV/decade, a maximum error of only 20% can be expected [1]. To be sure, this value was identified by the Tafel polarization run for AISI 1040. In anodic polarisation tests, the electrode potential of the material is scanned from the free corrosion potential (E_{corr}), also known as the Open Circuit Potential (OCP), in the more positive direction at a fixed rate. The preliminary test begins with identified the hardness of carbon steel before corrosion attack. However, the overall objectives of experiment was conducted is to quantify the effect of oxygen and anions to corrosion attack on carbon steel. Figure 1 shows anodic and cathodic polarisation of carbon steel in 3.5% NaCl in with and without oxygen content whereas Figure 2 and 3 presents the electrochemistry behaviour of carbon steel in higher sulphate content compared to seawater but same salinity and higher chloride content respectively. The OCP shifted to more negative value in the solutions with oxygen content which indicates that material's resistance to corrosion attack reduced [2]. The corrosion resistance of carbon steel depends on the oxygen activities combines with metal's composition to form a strong, protective oxide film on metal surface [3]. Figure 4 summarised the corrosion rate for AISI 1040 in all solutions. It is clearly presents that the corrosion rate is higher in solution with oxygen compared to without oxygen content. However, the corrosion rate in without oxygen content has shown no significant effect in every solution. The corrosion rate increased drastically in HCl (high chloride content) compared to in 3.5% NaCl and in H_2SO_4 (sulphate); all solutions has same salinity, pH and temperature. This indicates that chloride accelerate corrosion attack on carbon steel drastically compared to sulphate.

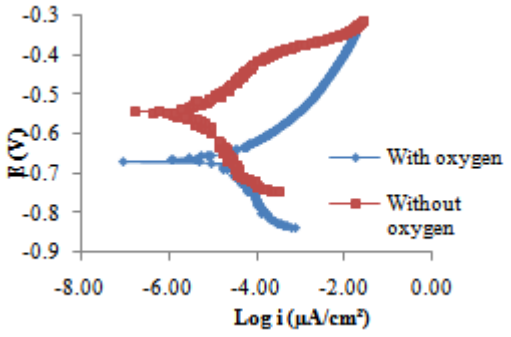

Figure 1: Carbon steel in 3.5%NaCl

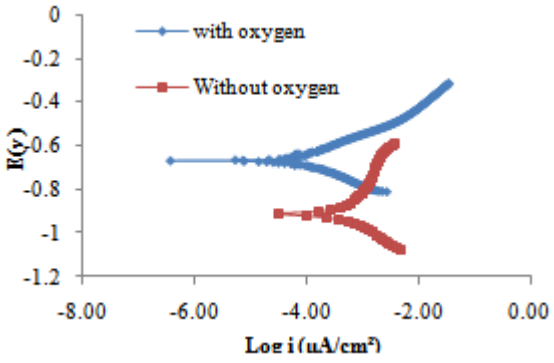

Figure 2: Carbon steel in sulphate content

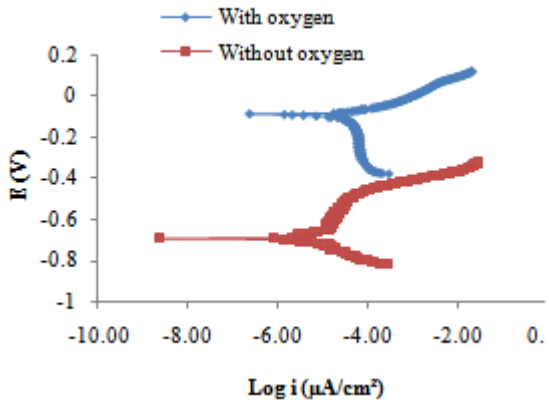

Figure 3: Carbon steel in 3.5%NaCl

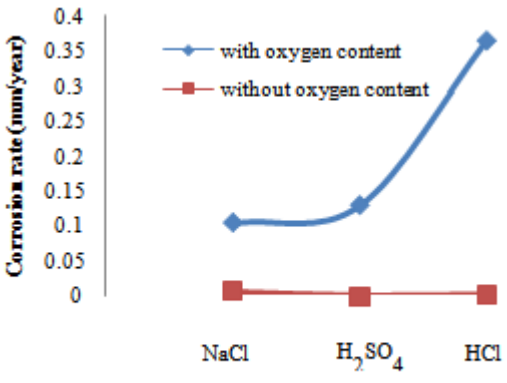

Figure 4: Carbon steel in sulphate content

The preliminary test begins with identified the hardness of carbon steel before and after corrosion attack. In all solutions, the hardness reduced after corrosion attack and carbon steel in high chloride content shows the highest reduction as shown in Figure 5. As the different hardness of the sample reduce, the resistance

of a material will increased which make the material less susceptible to corrosion. The weight loss also was determined before and after corrosion attack. The results are significant to hardness reduced in all solutions and chloride shown the highest weight loss compared to carbon steel in NaCl and H_2SO_4 (Figure 6).

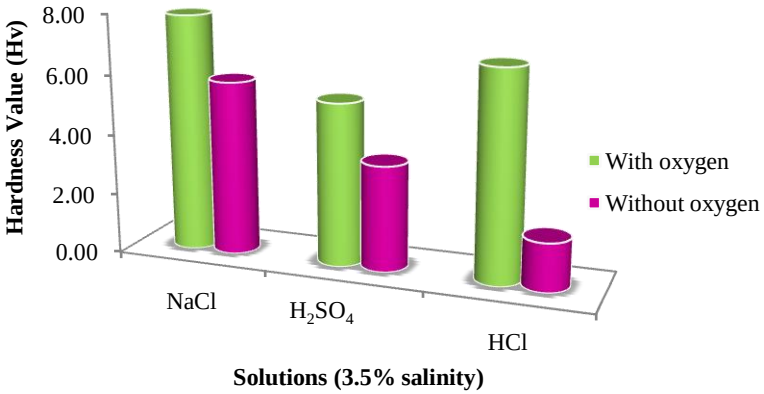

Figure 5: The hardness value for carbon steel in different solutions

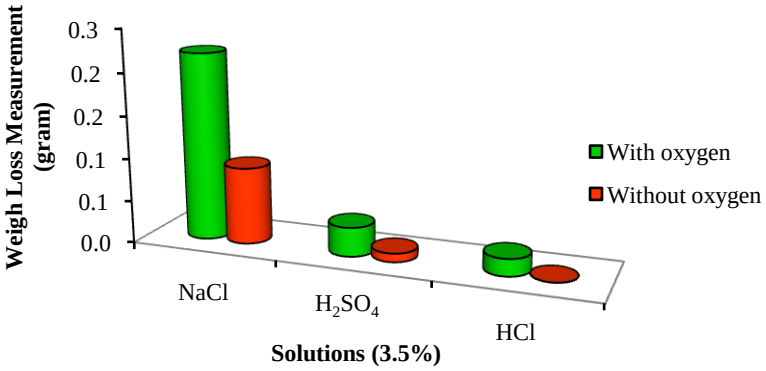

Figure 6: Weight loss of carbon steel in different solutions

The changes of the surface microstructure before and after the corrosion attack were observed by using optical microscope to show that the sample surface damaged due to corrosion attack. From the observation (Table 1), it showed that carbon steel corrodes severely in solutions with oxygen content and it form of small holes all over the surfaces. The holes of the corrosion product was observed using SEM to get a clearer image of the hole.

Table 1: Optical observation on corrosion attack

Before corrosion attack			
Solutions	NaCl	H_2SO_4	HCl
Oxygen	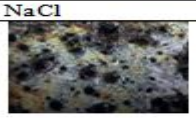		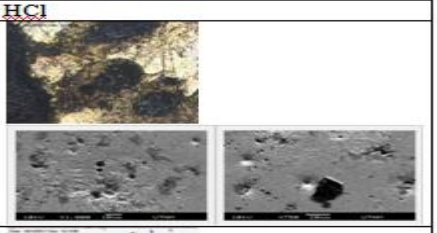
No oxygen			

II. CONCLUSIONS

The conclusion has been made according to corrosion rate of carbon steel in NaCl as compared to corrosion rate in different sulphate and chloride content in with and without oxygen content. The corrosion rates are higher in solutions with oxygen content in all solutions. The hardness properties of carbon steel reduced after corrosion attack significant to weight loss of the materials. Furthermore, the weight loss value and hardness reduced is directly proportionate to corrosion rate. Figure 7 presents the corrosion rate performance of AISI 1040 in three different solutions namely; chloride (by using hydrochloric acid), sulphate (sulphuric acid) and sodium chloride (3.5% NaCl). All the solutions are in the same salinity and temperature. The corrosion rate increased as oxygen content increased as expected. However, the corrosion rate increased drastically (critical point) in sulphate and chloride solution which clearly explained that aggressive anions accelerate corrosion attack on carbon steel. Nevertheless, the corrosion rate is higher in chloride solution compared to sulphate which elucidate that chloride is more aggressive than sulphate in the same pH. The material's performance was classified according to Equivalent Metric Rate Expression as showed in Table 2. It can be concluded that AISI 1040 can be categorized in the range of outstanding, excellent and good relative corrosion resistance material. The surface of samples AISI 1040 steel at highest dissolved oxygen concentration in solution more corrode than sample in the solution of the lowest dissolved oxygen concentration.

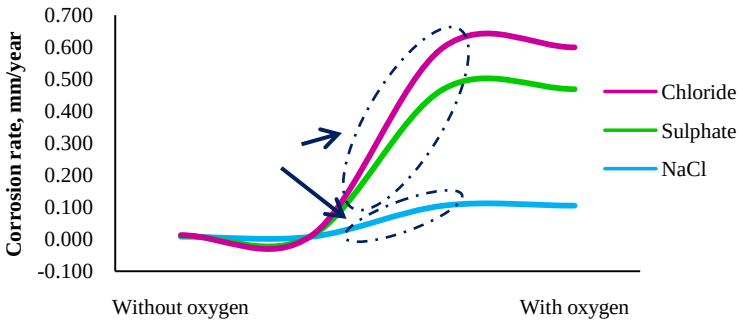

Figure 7: The critical corrosion rate

Table 2: Performance ranking of carbon steel

Solution	Oxygen content	Hardness Value (Hv)	Weight Loss (g)	Corrosion Rate (mm/y)	Relative Corrosion Resistance
NaCl	With	7.900	0.220	0.150	Good
	Without	5.800	0.090	0.008	Excellent
H_2SO_4	With	5.400	0.034	0.364	Good
	Without	3.500	0.010	0.0034	Excellent
HCl	With	6.900	0.020	0.1301	Good
	Without	1.600	0.000	0.0011	Outstanding

III. ACKNOWLEDGEMENT

The authors would like to acknowledge the Office for Research, Innovation, Commercialization and Consultancy Management (ORICC) Universiti Tun Hussein Onn Malaysia for financial support.

REFERENCES

[1] Hinds G., *The electrochemistry of corrosion*,[online]. 2006. [Accessed 2012], Available from: http ://www.npl.co.uk/upload/pdf/the_electrochemistry

[2] P. R. Roberge (2008). *Corrosion Engineering: Principle and Practice* Retrieved on March 23 from http://www.corrosion-doctors.org

[3] H. Uhlig, D. Triadis and M. Stern (1955). Uhlig's Corrosion Handbook. *Journal of The Electrochemical Society, 102, 59*

American Journal of Engineering Research (AJER)
e-ISSN : 2320-0847 p-ISSN : 2320-0936
Volume-03, Issue-1, pp-68-79
www.ajer.org

Research Paper Open Access

Geotechnical Properties of Mixed Marine Sediments on Continental Shelf, Port Sudan, Red Sea, Sudan

Al-Imam, O. A. O.; Elzien, S. M.; Mohammed A. A.; Hussein A.A. Kheiralla, K. M. & Mustafa A.A.

Faculty of Petroleum & Minerals, Al-Neelain University, Khartoum, Sudan

Abstract: **-** Samples from eleven boreholes have been taken from Dama Dama area, which is a part of Sudanese continental shelf. Physical and mechanical properties were investigated with SPT to obtain the bearing capacity and safety factor for engineering properties. The area consists of two facies, which are alluvial mixed with marine deposits and highly to extremely weathered limestone. The computation of effective overburden pressure, N-values were used to predict ultimate and allowable bearing capacity from which the safety factor was calculated and equal 2.5 with final settlement of 2.54mm.

I. INTRODUCTION

The Red Sea region is interesting for geologists, and geotechnical engineers in mining and constructions. The regional geology (Fig. 1) was carried out by Vail (1983, 1989); Babikir (1977); Al Nadi (1984) and Koch (1996). Felton (2002) reported that the modern rock shoreline sedimentary environment is a hostile one and range of high – energy processes characterize these shorelines. The designation of weathering depositional companion model of the karst formation in the Red Sea coast of Sudan had been done by Al-Imam et al., (2013). For solving engineering, geological, hydrogeological and environmental tasks, geo-electrical methods are routinely applied. However, almost the investigations were used the geo-electrical methods in different types of coast formations (Olayinka et al., 1999; Limbrick, K.J. 2003). In contrast, several geotechnical characteristics of soil could be evaluated by using electric resistivity and the correlated with depth and other parameters (Giao et al. 2003).

Very rare geotechnical publications in Sudanese coast on continental shelf even hazard map for engineering purposes, planning and/or development never take any researcher interest. In contrast, intensive investigations have been done on the eastern Red Sea coast. Geotechnical problems as chemical stabilization in Sabkha and formations were studied by Al-Imoudi (1995).

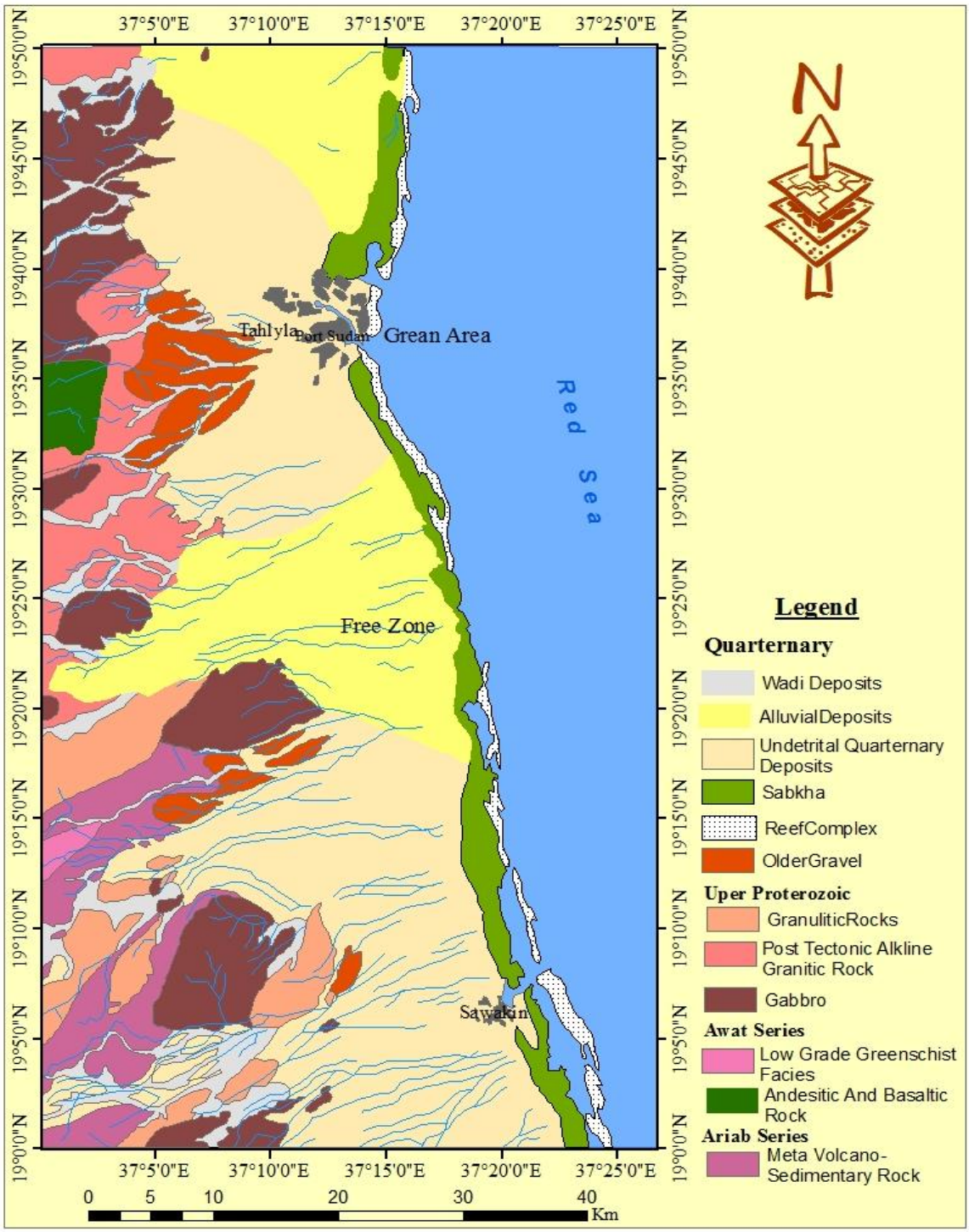

Fig. 1: Regional geological map of the study area

II. LOCATION AND SAMPLING

Dama Dama is located about 7.0km southern Port Sudan (Fig. 2). The site was selected by the Administration of Engineering Projects Department-Sudan Ports Corporation. Eleven boreholes were drilled in mixed alluvial marine deposits on continental shelf (Table 1) using rotary x-y rig on mobile platform. The sampler have thick wall of 89mm thickness, 200mm length and the hammer weight is 63.5kg with length of 810mm. Drop distance is 760mm, tube 51mm and penetration pen 300mm.

Five as sampling boreholes and six for exploration, disturbed and undisturbed samples from different levels were collected and obtained for physical and mechanical tests.

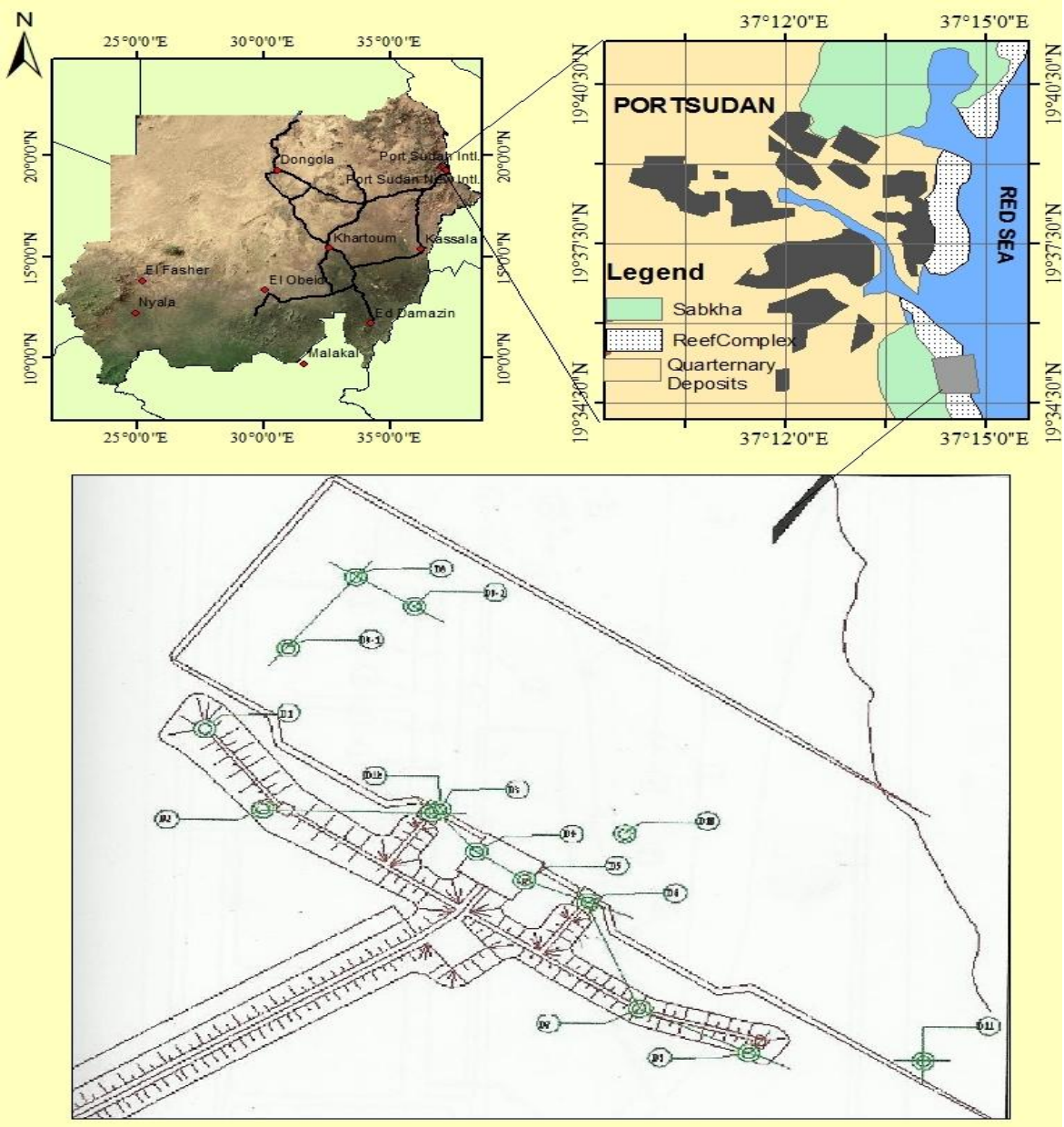

Fig. 2: Location map, shows the boreholes positions

Table 1: Location of boreholes

BH NO.	BH type	Depth (m)	Elevation (m)	Location	
				D (m)	C (m)
1	Explorer	21.70	-18.60	7657.60	11414.70
2	Sampling	22.80	-4.00	7612.00	11439.70
3	Sampling	33.10	-2.70	7610.30	11517.70
4	Explorer	36.00	-0.70	7588.50	11535.90
5	Sampling	34.80	-0.70	7572.10	11557.10
6	Explorer	30.50	-4.60	7560.20	11585.00
7	Sampling	26.00	-0.75	7500.10	11608.60
8	Explorer	24.80	-0.70	7475.80	11657.70
9	Sampling	15.50	-0.80	7741.50	11481.30
10	Explorer	09.25	-7.00	7597.80	11601.40
11	Explorer	06.50	-6.50	7470.60	11735.90

III. METHODOLOGY

Different designations were carefully selected from American Standard Test Methods (ASTM) and BS-59-30 for weathering grade. All data were processed by Rock wares 2004 software in two and three dimensions.

IV. OBJECTIVES

To investigate the marine deposits which consists of mixed alluvial carbonate forming the sea bed by using physical and mechanical properties for stable foundation under prevailing oceanographic conditions.

V. MARINE CONDITIONS

The sea level change is higher from November to May with the maximum in March and lower during June-October with minimum in August (Alzain and Al-Imam, 2002). The regional drop in the sea level (June-September) due to NNW wind which blow over the entire length of the sea (Osman, 1984a). The hydrodynamic condition prevailed and the generated waves towards the shoreline reach heights of order of 30.0cm. The wind velocities occasionally attain gale force producing up to one meter high. The tidal amplitude is 0.3- to 0.4m placing the shore zone in micro tidal environment (Alzain and Al-Imam, 2002).

VI. CORAL REEF LIMESTONE

Before the last regression, the sea level rose by perhaps as much as 20.0m and both positive and negative changes have occurred in the area (Alzain and Al-Imam, 2004). Pliocene and Tertiary deposits exposed to weathering and erosion during marine regression. Braithwaite (1982) suggested that at such times, limestone would have been sculpted into the complex karsts topography. However, the outcrops coral reef limestone in the area almost indicates to synchronous deposition of fossiliferous limestone followed by oolitic and then lime mud. The variability of the shore and shoreline in the area caused by seasonal changes in the climate, oceanographic conditions and drainage system which become active in the interseasonal periods. With the help of the concept of morphologic states the seasonal and interseasonal variability can be assessed qualitatively. Obviously, beach mobility increases with increasing temporal variability of the beach state observed. The alluvial deposits reach the sea floor within the reef area by hydrological process and mixed with reefal sediments.

VII. RESULTS AND DISCUSSION

Values of some representative samples reflect the environment deposition and grain size. The boreholes consist of two types of facies, carbonate and mixed alluvial with marine depositsexcept BH10 and BH11 whichare carbonate as a resultant of variations of environmental conditions. BH1 and BH2 almost are alluvial and the carbonate appears at depth at 22.20m. The Carbonate facies in BHs thickness between 3to8m at depth range between 9.80m to 13.80m. The coral reef of grow stopped at mentioned depths due to intensive accumulation of alluvial deposits by drain system pattern direct to the sea. The thickness of these deposits varies from 6.88m in BH6 to 11.3m in BH3. The marine environment was changed to be suitable for coral reef growing at depth in range of 1.6m to 3.6m up to the bottom surface. Two cycles of mixed deposits appear in BH9 cutting by carbonate facies which have 1.2m thickness. The thickness of the first cycle which overlain the coral reef is 5.6m between depths of 10.6m to 5.0m and the second cycle which covered by coral reef have 2.0m thickness between depths 3.8m to 1,8m. These environmental variations encouraged to weathering of soils and directly affected on its properties, and created a new stratification with the facies according to weathering degree.

1.1. Physical Properties

Table 2 shows some physical properties and consistency of some representative samples. Moisture contents values are indicator for coarse grain soil as well as the apparent specific gravity (Ga) which recorded a relative high values. Wet densityγ_{wet} was determined for each facies and the relative density was empirical value according to Bowles (1984). The distribution of wet density by 2D model (Fig.3a) appeared the weakness zones in the area and it was confirmed by 3D model. Refer to the software scale, where to avoid the values which are less than 1.98 sinkholes like appear due to chemical dissolving for carbonate minerals by sea water (Fig. 3b).

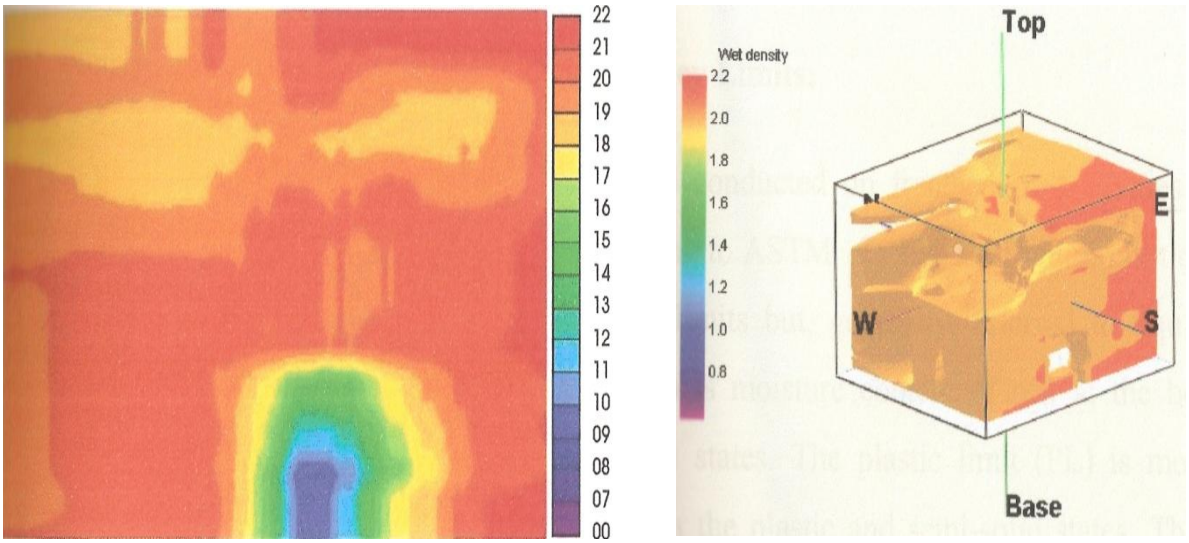

Fig. 3 (a): 2D models of distributions of wet density with depth and (b) 3D bulk model after removing densities less than 1.89, shows sinkhole like in the area

Saturation degree, void ratio values (Table2) were depend on the particle size and show that the alluvial deposits never subjected to high overbarding pressure. However, consistency values liquid limit (LL) and plasticity (PI) were calculated to predict the compression index (C_C) by using the formula:
$C_C = 0.009(L_L - 10)$ for normal consolidation clay. According to the plasticity index (P_I) values show that samples have a values greater than 1.0 means that they are solid clay with $P_I > 17$ which referred to high plastic clay. The relative plasticity index (Rr) was determined for soil condition and moisture content by:
Moisture content- plastic limit/ liquid limit- plastic limit
The application of this formula shows that the values are less than 1.0 in soft state.

Table 2: Physical properties of soil samples

Sample No	Physical properties						Consistency			
	Moisture Content	Specific Gravity	Wet Density	Dry Density	Saturation	Void Ratio	Liquid Limit	Plastic Limit	Plastic Index	Cc
DB2-1	20.9	2.65	1.98	1.46	89.6	0.618				
DB2-4	21.0	2.65	1.87	1.55	77.9	0.715				
DB2-8	20.8	2.65	1.98	1.50	78.5	0.761	22.2	15.6	6.6	0.11
Db2-9							45.3	41.7	3.6	0.32
DB2-10							43.7	30.2	13.5	0.18

1.2. Mechanical Properties

1.2.1. Direct Shear Test

Is adopted from ASTM D3080-72 and samples from BH-2 were obtained to test (Table3). Graph of shear strength versus normal stress (Fig.4) was drowning to predict the cohesion (C) and angle of internal friction (Ø). However, the (C) values are 38.2KPa, 25.5KPa and (Ø) values are 37.4^o and 39.6^o respectively. The results clarify that these types of soils have high internal fraction between particles affected the cohesion intercept (C) and reflected on the internal friction angle. The results confirmed that the friction angle (Ø) of these mixed soils increasing towards the finest particles.

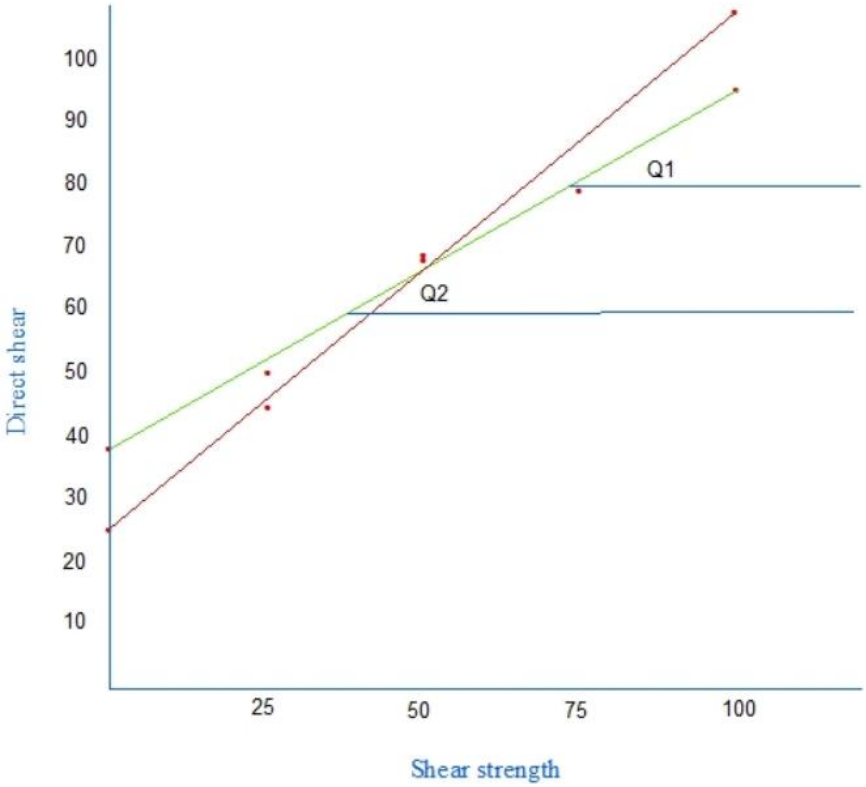

Fig. 4: Shear stress vs direct shear

1.2.2. Compressibility

ASTM D2435-80 has been used for consolidation. The samples were subjected to applied compressive load and allowed to act until equilibrium is reached with corresponding time (24h) and the data graphically presented to evaluate:

- Void ratio versus the load (e-p curve) (Fig. 5a) and (Fig. 5b).
- Time versus deformation (time curve) (Fig. 6a) and (Fig.6b).
- Void ratio versus the log of the pressure after converted to short tour (e-log p).
- Consolidation coefficient versus the log pressure (C_C-log P) curve.

Even more, the e-p curve was used for settlement evaluation and the CC-log P for estimation the time rate of settlement.

The compressibility coefficient (av) obtained from the equation:

$$av = {e_0 - e_1}/{\sigma_1 - \sigma_0}$$

Where: e_o is an initial void ratio, e_1 is a void ratio at 200KPa, σ_1 is 200KPa and σ_o is 100KPa.

Then av equal:

$$av_1 = \frac{0.9908 - 0.978}{200 - 100} = 2 \times 10^{-4} MPa$$

and

$$av_2 = \frac{10 - 0.9753}{200 - 100} = 2.3 \times 10^{-4} MPa$$

The values of (av) can be use to obtain the coefficient of volume change or compressibility (mv) from the formula:

$$mv = {av}/{1 + e_0}$$

Hence:

$$mv_1 = \frac{2 \times 10^{-4}}{1.998} = 1.0 MPa$$

$$mv_2 = \frac{2.3 \times 10^{-4}}{1.998} = 1.15 MPa$$

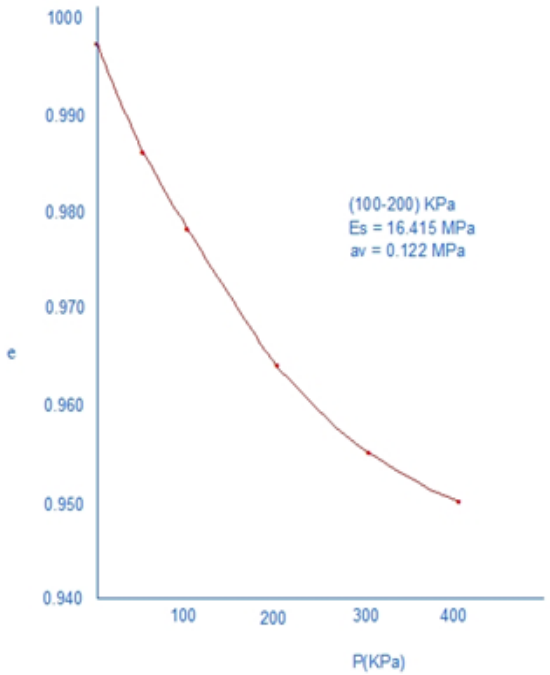

Fig. 5a: e-p curve sample # D2-1

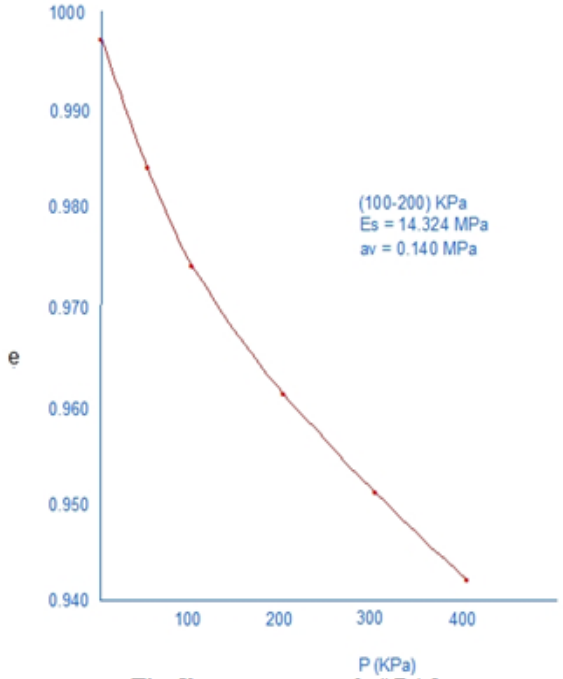

Fig. 5b: e-p curve sample # D4-2

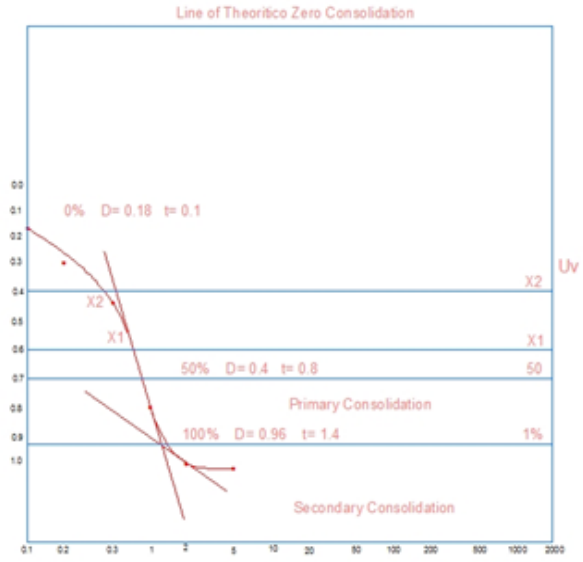

Fig. 6a: Time –consolidation curve, sample # D2-1

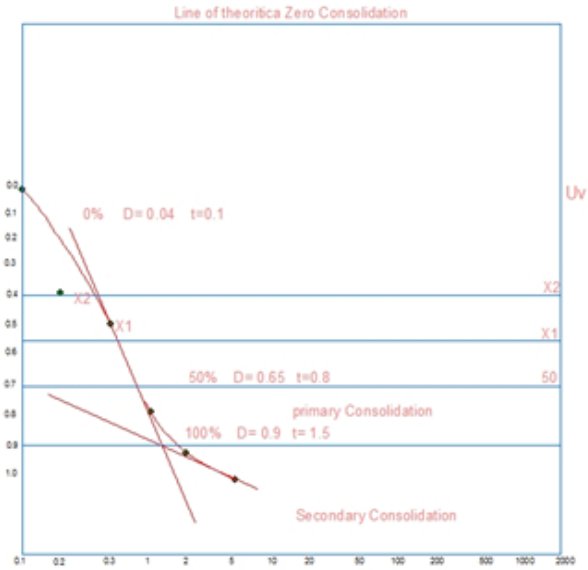

Fig. 6b: Time –consolidation curve, sample # D4-2

Table 3: Mechanical properties of soil samples

Sample No	Direct shear test		Direct shear strength				Compressibility Mode				Compressibility coefficient			
	C KPa	Φ	KPa 25	KPa 50	KPa 75	KPa 100	KPa	KPa	KPa	KPa	KPa	KPa	KPa	KPa
DB2-1	38.2	36.4	50.44	68.39	79.52	95.14	8.14	12.53	16.42	25.73	0.245	0.159	0.122	0.078
DB2-4	25.5	39.6	44.88	69.11		107.7	7.74	10.62	14.32	21.87	0.296	0.188	0.140	00.91

1.2.3. Consolidation Index (CC)

It is a slope of straight line of void ratio versus log load in tannage as shown in Fig (7) which equal 0.05 and 0.02 respectively.

Void ratio and variation in samples height are corresponding to deformation which can compute from height of solids, void ratio, before and after test. By applied load the initial water height, thickness of the sample and void ratio are decrease. The formula is:

$$H_s = \frac{W_s}{A} G_s \gamma_w = H_s = G_s W_s$$

Where,
H_s = Height of initial water.
W_s = weight of dry sample
A = are of specimen
G_s = specific gravity
γ_w = unit weight of water

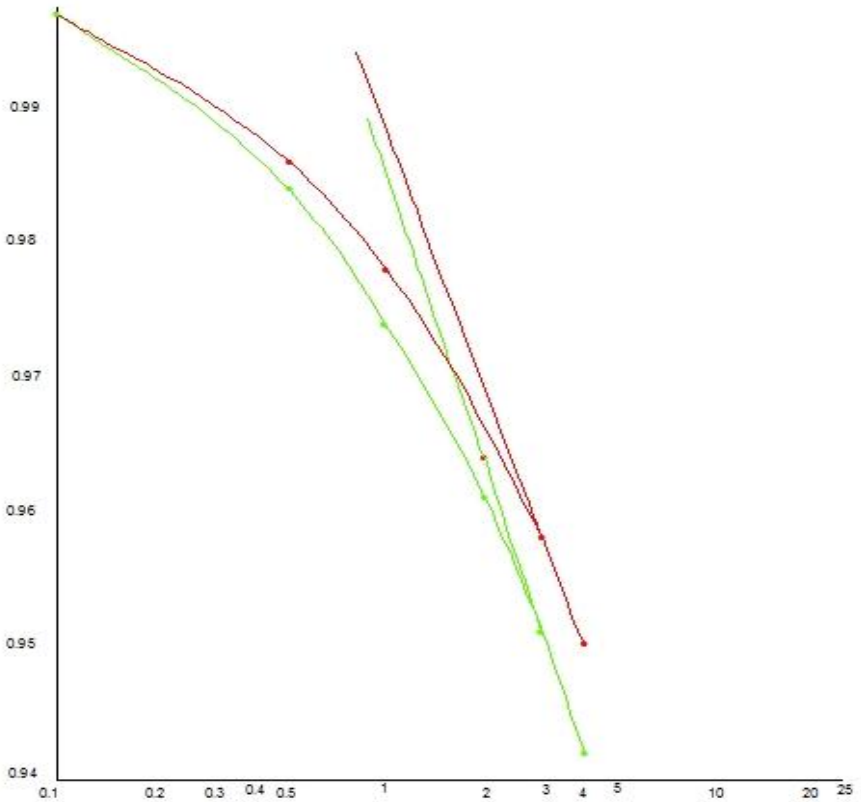

Fig. 7: Void ration vs log load in tonnage to obtained the consolidation index

By calculation the (H_s) equal 20mm before test and (e_o) equal 0.9908 (Fig. 5a) after test. The actual height of the sample after test is:

$$e_0 = H_s - \frac{\Delta H}{H_s}$$

$$0.9908 = 20 - \frac{\Delta H}{20}$$

$$\Delta H = 0.184$$

The results of accumulation ΔH versus time shown in Fig (6a) and Fig (6b) respectively, which can be concentrated into a time – consolidation curve, from which:
For sample (I):
100% deformation (D) = 0.96 at time (t) = 1.4 min.
50% deformation (D) = 0.40 at time (t) = 0.80 min
0.0% deformation (D) = 0.183 at time (t)
For sample (II):
100% deformation (D) = 0.87 at time (t) = 1.5 min
50% deformation (D) = 0.60 at time (t) = 0.70 min
0.0% deformation (D) = 0.0 at time (t)

1.2.4. Consolidation coefficient (Cv)

It is obtained from time-curve by using the formula:

$$C_y = \frac{T_y d^2}{t}$$

Where, T_v was determined from the relation between consolidation degree (U_v) and the time factor from time table which designed by Tarzagiki and Peck (1967).
d^2 = ½ samples thickness (H)
t = time
For sample (I)

	X_2	X_1	D_{50}
U_v	0.50	0.60	0.70
T_v	0.197	0.287	0.403
t	0.40	0.0	0.80
1/2H	10	10	10

By the application of consolidation equation the average value of (C_v) as follow:

$$X_2 = \frac{0.197 \times 10^2}{0.40} = 49.25\ mm^2/min$$

$$X_1 = \frac{0.197 \times 10^2}{0.60} = 47.80\ mm^2/min$$

$$D_{50} = \frac{0.197 \times 10^2}{0.80} = 50.37\ mm^2/min$$

$$C_v(average) = 49.14\ mm^2/min$$

The same procedure was followed to predict the average value of (C_v) of sample (II) which was 69.9mm^2/min.

1.2.5. Settlement

Settlement is stress induced but is statistical time dependent accumulation of particle rolling and slipping which results in permanent soil skeleton change (Bowles, 1984). The sum of immediate settlement (Pi) and consolidated settlement (Pc) is the final settlement (Pf) which can be computed by semi-empirical method based on Standard Penetration Test(SPT) values or from (e-p) curve by using the equation

$$Q_{ud} = \frac{H}{1 + e_1(e_1 - e_2)}$$

Or by using the consolidation index (C_c) by the following equation:

$$H/1 + e_1 \times log_{10} P_0 \sigma_2 / P_0$$

The application of Fig (5a and 5b) using the last equation, the settlement in the area as follow:

Sample	P_i (mm)	P_c (mm)	P_f (mm)
1	0.13	2.41	2.54
2	0.13	0.10	0.23

The variation in (P_c) values refer to the different (C_v) values

1.2.6. Standard Penetration Test (SPT)

The (SPT) was used for its simplicity and availability of variety for correlation with other data. When SPT is performed in soil layers containing shell, coral fragments or any other similar material, the sampler may be plug. This will cause the SPT N-value to be much greater than unplugged sampler and therefore, not representative index of soil layer properties. In this circumstance, a realistic design requires reducing the N-values which do not appear distorted (st. of Florida, 2004). The field N-values were corrected by equation depends on the effective overburden pressure proposed by Bazaraa (1967) as follow:

$$P_0 =\geq 75\ KPa \ldots N = \frac{4N}{3.25 + X_2 P_0}$$

Where:
X_1 = 0.4 for SI units.
X_2 = 0.01 for SI units.
P_0 = effective overburden pressure.
The SPT profile of the area (Fig. 8a) shows medium N-values trend to low except small surface area due to the weathering grade. According to the relation between N-values and densities and when to avoid N-values which less than 20 the weakness of the strata appear in 3D model (Fig. 8b).

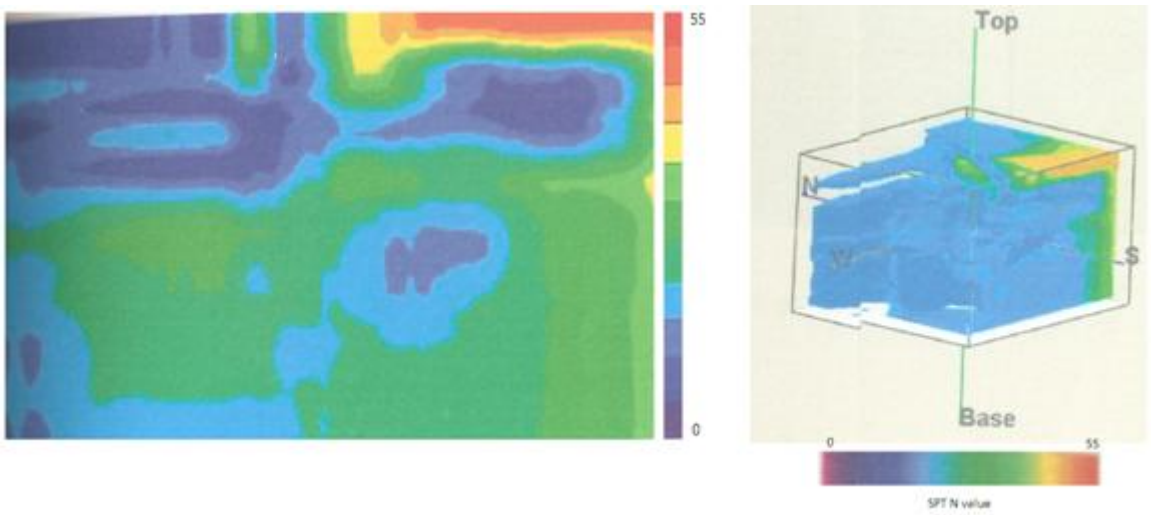

Fig. 8 (a):. 2D models of N value and (b) 3D of N value >20

1.2.7. Bearing Capacity by (SPT)

The general equation of bearing capacity depends on both, angle of internal friction (Ø) and total overburden pressure (TOP). To determine the (Ø) value the standard curve of the relationship between SPT (N-values) and angle of shear resistance (Peak, Hanson and Thorburn, 1967) have been used. The general equation of ultimate bearing capacity is:

$$q_{ult} = q'\{(1 + sin\emptyset)/(1 - sin\emptyset)\}^2$$

The values increasing with depth (Fig. 9a) and when avoid values less than 4000 which equal one third of the total value, the strata became as in Fig. (9b).The (q_{ult}) divided by safety factor to obtain the allowable bearing capacity (q_{all}). However, the safety factor depends on type of foundation, load such as dead load (DL) , live load (LL), wind load (WL) and earth pressure (EP) (Bowles, 1984), and he suggested that the values of safety factors between 1.2 to 5.0. In this study, the safety factor is one third of (q_{ult}) and then divided by (3) because the dominant weathering grade is grade III. Subtract another one third and divided the maximum (q_{ult}) by the result as follows, after application of RW software and the safety factor (F) has been change to 4.5:

(q_{ult}) = 10.000

Divide by 3 = 10.000/3 = 3.33

= 3.33/3 = 1.11

3.33-1.11= 2.22

Hence: 10.000/2.22 = 4.5 = F

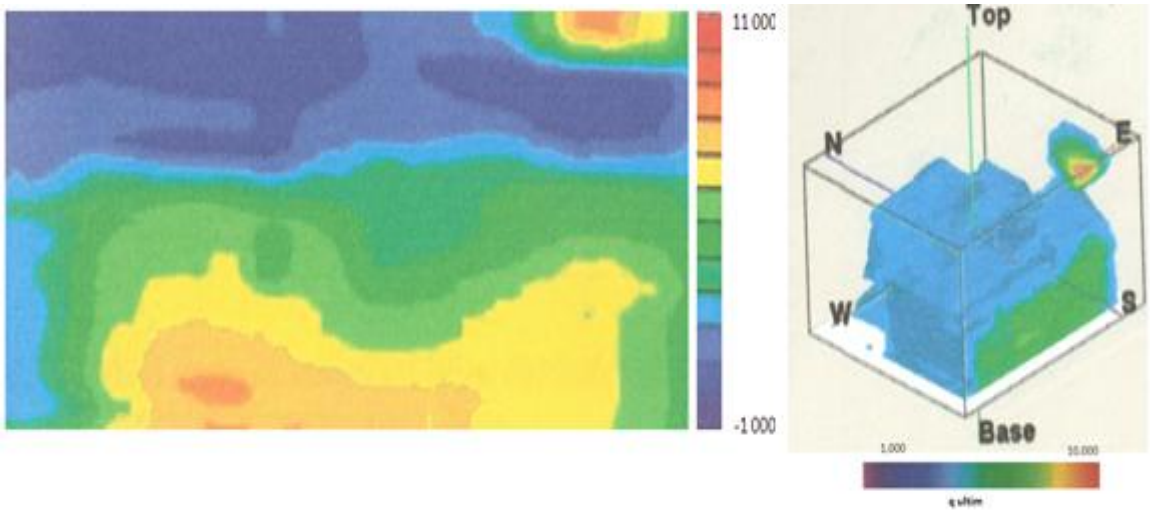

Fig. 9 (a): 2D ultimate bearing capacity and (b) 3D ultimate bearing capacity less than 4000

The (q_{all}) have the same shape with slightly less in value (Fig. 10) comparing with Fig. (9b).This confirmed the results and the relation between density and N-value.

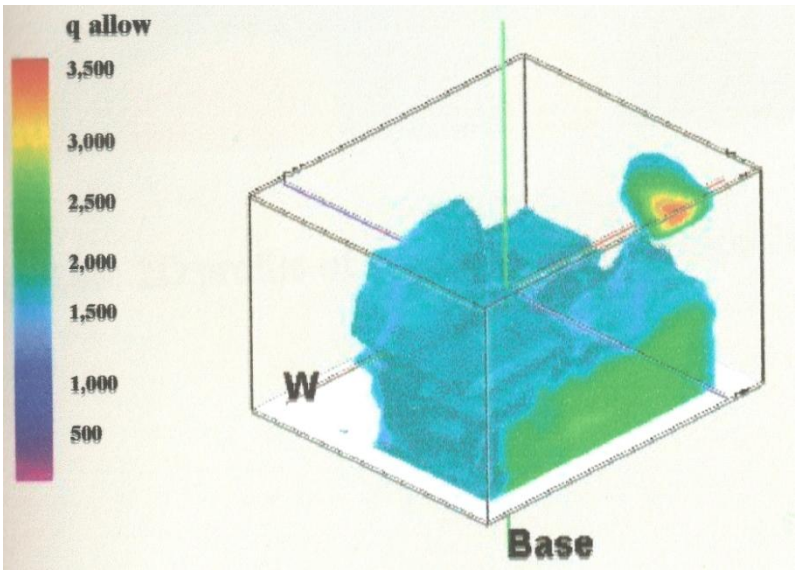

Fig. 10.3D: allowable bearing capacity

VIII. CONCLUSION

The sea water is a geotechnical system having direct efficiency on soil and reef limestones causing weathering and corrosion by chemical reactions. The reef limestones in the region are completely and extremely weathered, having varies bearing capacity. Both specific gravity (G_s) and dry density (γ_{dry}) values in contrast of wet density (γ_{wet}) and saturation values give an indication of mixture of alluvial marine deposits. The intensive cavities are characteristic the region and can be developed to be sink holes. Although, the mechanical parameters values give an encouragement for engineering construction, all foundation in the area and/or which like must be pilling design with taken case in soil geotechnical profile.

REFERENCES

[1] **Al-Amoudi, O.S.B., (1993).** Chemical Stabilization of Sabkha soils at high moisture contents. Eng. Geol., 36:279-291.

[2] **Al-Imam O.A.O; ElsayedZeinelabdein, K.A., and Elsheikh A.E.M. (2013).** Stratigraphy and subsurface weathering grade investigation for foundation suitability of Port-Sudan-Suakin area, Red Sea region, NE Sudan. SJBS, Series (G), U of K, Sudan (in press).

[3] **Al-Zain, S.M.& Al-Imam, O.A.O., (2002).** Carbonate Minerals diagenesis in Towaratit Coastal Plain, south Port-Sudan, Red Sea, Sudan. Nile Basin Research Journal .Alneelain University, Khartoum, Issue No. 4, Vol. II p35 – 58.

[4] **Al-Zain, S.M.& Al-Imam, O.A.O., (2004).**Sea Level Changes and Evolution of Towaratit Coastal Plain south Port-Sudan, Red Sea, Sudan. Nile Basin Research Journal Alneelain University, Khartoum, Issue No. 6, Vol.III, p 32-54.

[5] **Babikir, I.M., (1977).**Aspects of the Ore Geology of Sudan. Ph.D. Thesis. University College of Cardiff. U.K.

[6] **Bazaraa A. R. (1967).** Use of stander Penetration Test of estimating settlements of shallow foundation on sand.PhD. Thesis. Uni. Illinois, Urban, pp. 379.

[7] **Bowles. J. E. (1984).** Foundation analysis and design. 3rd ed McGraw-Hill International, London.

[8] **Braithwaite, C. J. R. (1982).** Geomorphology accretion of reef in the Sudanese Red Sea. Mar. Geol., 46:297-325

[9] **El Nadi, A.H., (1984).**The geology of the Precambrian metavolcanics. Red Sea Hills, NE Sudan. PhD. Thesis. University of Nottingham, England, UK.

[10] **Felton, E.A. (2002).** Sedimentology of rocky shorelines: 1. A review of the problem, with analytical methods, and insights gained from the Hulopoe gravel and the modern rocky shoreline of Lanai, Hawaii. Sedimentary Geology 152, 221–45.

[11] **Giao, P.H., Chung, S.G., Kim, D.Y., Tanaka, H. (2003).** Electrical imaging and laboratory resistivity testing for geotechnical investigation of Pusan clay deposits. Journal of Applied Geophysics 52, 157–175.
[12] **Koch.W.(1996).**Analyseund Visualisie runggeo wissen schaftlicher Datenmit Hil fedigitaler Bildverar beitung und eines Geo-Informations systems: Beitrag zurregionalen Geologie der Red Sea Hills, Sudan: geologischeKarte Port Sudan 1:250 000 und Blatt Jebel Hamot 1:100 000. Berliner GeowissenschaftlicheAbhadlungen, Reiche D Band 12.
[13] **Limbrick, K.J. (2003).** Baseline nitret concentration in groundwater of ckalk in south desert, UK. The Sci. of the total environ. 314-316. 89-98
[14] **Olayinka, A. I.; Abimbola, A. F.; Isibor, R. A.; Rafiu, A. R. (1999).** Ageo-electrical hydrothermal investigation of shallow groundwater occurrence in Ibadan, Southwest Nigeria,. Environ. Geol. Vol. 37:31-39
[15] **Osman, M. M. (1984a).** Evaporation off water in port Sudan. Jour of the Fac. Mar. Sci., KAU. S Arabia. 4:29-37
[16] **Peak, Hanson and Thorburn.(1967).** Foundation design engineering 2ed ed. John Willey, New York. P310.
[17] St. of Florida. (2004). Soils and foundations handbook: Dept. of Transportation, State Materials office, Gainesvlle, Florida, USA.
[18] **Tarzagiki K: Peck, R. B. (1967).** Soil mechanics in engineering practices 2ed ed. John Willy New York. Pp 341-347.
[19] **Vail, J. R. (1983).** Pan- African Crustal Accretion in NE Africa. Jour. Earth Society, 1:285-294
[20] **Vail, J. R. (1989).** Tectonic and evolution of the Proterozoic Basement of NE Africa. In: Elgaby, S. and R. O. Greiling (Eds). The Pan-African belts of NE Africa and adjacent areas. Fried Uieweg and Sohu: 185-226.

American Journal of Engineering Research (AJER)
e-ISSN : 2320-0847 p-ISSN : 2320-0936
Volume-03, Issue-01, pp-80-88
www.ajer.org

Research Paper Open Access

Anaerobic Co-Digestion of Cattle Slurry with Maize Stalk at Mesophilic Temperature

A.O. Adebayo[1*], S.O. Jekayinfa[1] & B. Linke[2]
1. Department of Agricultural Engineering, Ladoke Akintola University of Technology, P. M. B. 4000, Ogbomoso, Oyo State, Nigeria
2. Leibniz-Institute for Agricultural Engineering (ATB), Max-Eyth-Allee 100, D - 14469 Potsdam, Germany.

Abstract: - Anaerobic digestion from batch digester containing varying ratio of mixture of cow slurry and maize stalk was studied at mesophilic temperature (37^{o}C). Cattle slurry and maize stalks were co-digested at ratios 3:1, 1:1 and 1:3 using the percentage volatile solid of each substrate. The experiment was carried out in a laboratory scale batch digester. The digester was fed with cattle slurry-maize stalks mixtures calculated for the selected ratios based on the volatile solid (VS) concentration of the selected substrates. Co-digestion of cattle slurry with maize stalks at ratios 3:1, 1:1 and 3:1 at mesophilic temperature gave biogas yields of 0.426, 0.385 and 0.391m^3/kgoDM respectively while the methane yields were 0.297, 0.270 and 0.262m^{3}CH$_4$/kgoDM respectively. From the fresh mass of the substrate, biogas yields of 0.052, 0.059 and 0.090 m^3/kgFM were obtained for cattle slurry-maize stalks ratios of 3:1, 1:1 and 1:3 respectively while the methane yields from the fresh mass for the same ratios were 0.036, 0.043 and 0.060 CH$_4$/kgFM respectively. Co-digestion of cattle slurry with maize stalks was found to have methane concentrations of 69.66, 70.24 and 66.98% at cattle slurry/maize stalks combinations of 3:1, 1:1 and 1:3 respectively. The highest biogas yields (oDM) of 0.426 m^3/kgoDM was obtained at the mixing ratio of 3:1; therefore the mixing ratio of 3:1 is recommended as the optimal for the co-digestion of cattle slurry with maize stalks at mesophilic temperature.

Keywords: - *Co-digestion, cattle slurry, maize stalks, batch experiment, mesophilic temperature*

I. INTRODUCTION

The conventional energy sources in the world such as liquefied petroleum gas (LPG), benzene fuel, diesel fuel, and fire wood are rapidly reducing due to industrial and urban development. Renewables such as solar, wind, hydropower, and biogas are potential candidates to meet global energy requirements in a sustainable way [1, 2]. Also, there is a global energy crisis as a consequence of declining quantity of fossil fuels coupled with the unprecedented rising crude oil prices. The crisis demands greater attention to alternative energy sources and revision of existing technologies.

Biogas, the gas produced when organic matter of animal or plant ferments in an oxygen-free environment (anaerobic condition) occurs naturally in swamps and spontaneously in landfills containing organic waste. Anaerobic digestion (AD) offers a very attractive route to utilize certain categories of biomass for meeting partial energy needs. Also, proper functioning of AD systems can provide multiple benefits to the users and the community resulting in resource conservation and environmental protection [3]. It can also be induced artificially in digestion tanks to treat sludge, industrial organic waste, and farm waste [4]. The product of AD primarily are methane (CH_4) and carbon dioxide (CO_2), with varying amounts of water, hydrogen sulphide (H_2S), oxygen and other compounds [5, 6].

Millions of cubic metres of methane in the form of swamp gas or biogas are produced every year by the decomposition of organic matter, in form of both animals and vegetables. It is almost identical to the natural gas pumped out of the ground by the oil companies and used by many people for heating houses and cooking meals. In the past, however, biogas has been treated as a dangerous by-product that must be removed as quickly as possible, instead of being harnessed for any useful purposes. It is only in very recent times that a few people have started to view biogas, in an entirely different light, as a new source of energy for the future. High biogas yield can be achieved through co-digestion of manure with energy crops and / or their residues.

According to Agunwamba [7], co-digestion is the simultaneous digestion of more than one type of waste in the same unit. Co–digestion is the simultaneous digestion of a homogenous mixture of two or more substrates. The most common situation is when a major amount of a main basic substrate (e.g. manure or sewage sludge) is mixed and digested together with minor amounts of a single, or a variety of additional substrates. Better digestibility, enhanced biogas production/methane yield arising from availability of additional nutrients, improved buffer capacity with stable performance as well as a more efficient utilization of equipment and cost sharing have been highlighted as part of the advantages of co-digestion [7, 8, 9,10, 11,12,13] Researchers have shown that co-digestion of banana and plantain peels, spent grains and rice husk, pig waste and cassava peels, sewage and brewery sludge, among many others, have resulted in improved methane yield by as much as 60% compared to that obtained from single substrates [14,15,16,17]. A wide variety of substrates, animal and plant wastes, as well as industrial wastes such as carbonated soft drink sludge and brewery wastes have been used for biogas production [18, 19, 20, 21, 22, 23, 24].

Also, the addition of readily biodegradable organic matter into animal manure digester could significantly increase biogas production due to the changes of feedstock characteristics. Co-digestion of cassava peels with poultry, piggery and cattle waste has been found to result into increase in biogas production [25]. Several researchers have studied biogas generation from animal and agricultural wastes [26, 27, 28]. According to Callaghan *et al*. [29], co-digestion of cattle slurry with fruit and vegetable waste yielded more cumulative biogas production than the digestion of cattle slurry alone. This work studied the effect of co-digestion on anaerobic digestion of cattle slurry with maize stalks at mesophilic temperature (37^{o}C).

II. MATERIALS AND METHODS

2.1 Sources of organic materials

Maize plants were harvested from the Institute for Animal Breeding and Animal Husbandry (ABAH), Ruhlsdorf / Grosskreutz, Germany and the stalks were separated for experimentation. Cattle slurry was also obtained from the same institute (ABAH).

2.2 Methodology

All samples were kept in the laboratory at a temperature of +3°C after size reduction prior to feeding into the digester. The amount of substrate and seeding sludge weighed into the fermentation bottles were determined in accordance to German Standard Procedure VDI 4630 [30] using the equation 1:

$$\frac{oTS_{substrate}}{oTS_{seeding\,sludge}} \leq 0.5 \qquad (1)$$

Where:

oTS $_{substrate}$ = organic total solid of the substrate and;

oTS $_{seeding\ sludge}$ = organic total solid of the seeding sludge (the inoculum)

Biogas production and gas quality from maize stalks (MS) and cattle slurry (CS) were analyzed in batch anaerobic digestion test at 37°C according to German Standard Procedure VDI 4630 (2004). Batch experiments were carried out in lab-scale vessels with two replicates as described by Linke and Schelle [31]. A constant temperature of 37°C was maintained through a thermostatic cabinet heater (Plate 1). Characteristic chemical and thermal properties of the substrates used are summarized in Table 1. Vessels (0.9 litre capacity) were filled with 800g of the stabilized inoculum. Two bottles were used for each of the combinations and the average yields found at the end of the experiment.

Plate 1: Experimental set up for batch digestion

Table 1: Chemical and thermal properties of substrates

Parameter	Analysis	
	Cattle Slurry	Maize Stalks
Dry Matter, DM (105°C)-%	11.77	45.54
Organic Dry Matter (oDM, %DM)	84.05	90.75
Organic Dry Matter (%FM)	9.89	41.33
NH_4-N (g/kgFM)	1.22	<2
Crude Fibre (%DM)	26.75	39.07
Fat (% DM)	-	1.61
Potassium (% DM)	2.05	1.22
Ethanol (g/l)	0.12	<0.04
Propanol	<0.04	<0.04
Total Acetic Acid	0.88	0.17
Ph	6.56	6.40
Conductivity (mS/cm)	9.98	0.744

At the beginning of the experiment, anaerobically digested material from a preceding batch experiment was used as inoculums for this study. The substrates fed into the digestion bottles were calculated using equation (2) and found to be 80.46g CS / 0MS (100% Cattle slurry with no maize stalk), followed by 41.53g CS / 3.31g MS (75%CS and 25%MS), 25.08gCS/ 6.00g MS (50%CS and 50%MS), 13.85gCS/9.94gMS and (25%CS and 75%MS). The calculated amount of the substrates (using equation 1) was added to 800g inoculum to ensure compliance of the $oDM_{feedstock}$ to $ODM_{inoculum}$ ratio being less or equal 0.5 as it is recommended in VDI 4630 (equations 1 and 2). Two digestion vessels were also filled with 800g of inoculums only as control.

The biogas produced was collected in scaled wet gas meters for 35 days. This duration of the test fulfilled the criterion for terminating batch anaerobic digestion experiments given in VDI 4630 (daily biogas rate is equivalent to only 1% of the total volume of biogas produced up to that time). The volume of the gas produced was measured daily. Besides, other gas components, methane (CH_4) and carbon dioxide (CO_2) contents were determined at least eight times during the batch fermentation test using a gas analyser GA 2000. The tests were conducted in two replicates. Plate 1 shows the set up of the batch experiment conducted at mesophilic temperature (37°C).

Quantitative evaluation of the results gained in batch anaerobic digestion tests included the following steps: standardizing the volume of biogas to normal litres (1_N); (dry gas, t_0=273 K,p_0=1013hPa) and correcting the methane and carbon dioxide contents to 100% (headspace correction, VDI 4630). Readings were analysed using Microsoft Excel spread sheet together with "Table curve" computer software. Accumulated biogas yields over the retention time were fitted by regression analysis using Hill-Kinetic equation in order to determine the maximum biogas and methane potentials of the selected substrates.

The amount of substrate fed into the digester was calculated using equation (1).

$$\frac{oTS_{substrate}}{oTS_{seeding\ sludge}} \leq 0.5 \qquad 1$$

Where:

$oTS_{substrate}$ = organic total solid of the substrate and;

$oTS_{seeding\ sludge}$ = organic total solid of the seeding sludge (the inoculum)

Equation (1) can be modified to read

$$p_i = \frac{m_i . c_i}{m_s c_s} \qquad (2)$$

Where

p_i= mass ratio=2 ; m_i= amount of inoculum, g

c_i=Concentration of inoculum, oDM in % Fresh mass

m_s= amount of substrate,g

c_s= Concentration of substrate, oDM in % fresh mass

Readings of the gas production (ml), air pressure (mbar), gas temperature (°C) and time of the day were taken on daily basis throughout the period of the experiment. The gas was analysed at least twice per week for the four

weeks of the experiments. The gas factor was calculated as well as the fresh mass biogas and methane yield with the volatile solid biogas and methane yields also determined on daily basis. The amount of gas formed was converted to standard conditions (273.15 K and 1013.25 mbar) and dry gas. The factor was calculated according to equation 3.

$$F = \frac{(p - P_{H_2O}).T_o}{(t + 273.15).p_o} \quad (3)$$

Where
T_o= 273.15 ^oC (Normal temperature)
t= Gas temperature in ^oC
P_o= 1013.25 mbar (standard pressure)
P= Air Pressure

The vapour pressure of water P_{H_2O} is dependent on the gas temperature and amounts to 23.4 mbar for 20^{o}C. The respective vapour pressure of water as a function of temperature for describing the range between 15 and 30^{o}C is given as in equation 4

$$P_{H_2O} = y_o + a.e^{b.t} \quad (4)$$

Where:
y_o = -4.39605; a = 9.762 and b= 0.0521
The normalized amount of biogas volumes is given as

$$Biogas[N\,ml] = Biogas[ml] \times F \quad (5)$$

Normalized by the amount of biogas, the amount of gas taken off of the control batch is given as

$$Biogas[N\,ml] = (Biogas[Nml] - Control[Nml]) \quad (6)$$

The mass of biogas yield in standard liters / kg FM fresh mass (FM) is based on the weight
The following applies:
1 standard ml / g FM=1 standard liters / kg FM = 1 m^3 / t FM

$$Mass\,of\,biogas\,yield = \sum \frac{Biogas[N\,ml]}{Mass\,[g]} \quad (7)$$

The oDM biogas yield is based on the percentage of volatile solids (VS) in substrate

$$oDM\ biogas\,yield = \sum \frac{Biogas[N\,ml).100]}{Mass[g].VS[\%FM]} \quad (8)$$

$$CH_{4corr.} = \frac{CH_4[vol\%].100}{(Mass\,[g] + CO_2[vol\%])} \quad (9)$$

$$Fresh\ Mass\ Methane\,yield = \frac{Fresh\ mass\ biogas\,yield \times CH_{4corr.}}{100} \quad (10)$$

$$oDM\ Methane\,yield = \frac{oDM\ biogas\,yield \times CH_{4corr.}}{100} \quad (11)$$

2.3 Substrates and Analytical Procedures

Sample of maize stalks (MS) was investigated for Fresh matter (FM), organic Dry Matter (105^{o}C), Organic Dry Matter in % fresh mass, Volatile fatty acids (VFA), pH, NH_4-N, Conductivity (EC), Organic dry matter in % of fresh mass (oTS). All analyses were performed according to German standard methods [31].

2.4 Model Formulation

Models were formulated for the prediction of the biogas and methane yields at selected ratios of the substrates co-digested using the design expert computer software.

III. RESULTS AND DISCUSSION

Table 1 shows the results of the chemical and thermal properties of the selected substrates before digestion. The cumulative biogas and methane productions obtained from batch digesters are shown in Figures 1-4.

3.1 Substrates

The dry matter (DM), organic dry matter (oDM), NH_4-N, Crude Fibre, N, P, K, pH, and the conductivity of the selected substrates determined are as shown in Table 1 [32,33].

3.2 Co-Digestions of Cattle Slurry with Maize Stalks

Figures 1-4 show the fresh mass biogas yields, fresh mass methane yields, organic dry matter biogas yields and organic dry matter methane yields from the co-digestion of Cattle Slurry (CS) with Maize Stalks (MS) respectively. In the co-digestion of cattle slurry with maize stalk under mesophilic condition (37^{o}C), the fresh mass biogas yields at ratios 3:1, 1:1 and 1:3 were found to be 0.052, 0.059 and 0.090 m^3/kg_{FM} respectively while the fresh mass methane yields for the same combinations were found to be 0.036, 0.043 and 0.060 m^3CH_4/kg_{FM} respectively (Figures 1 and 2). In the same vein, the biogas yields (oDM) of cattle slurry co-digested with maize stalk at the same ratios were found to be 0.426, 0.385 and 0.391 m^3/kg_{oDM} while the methane yields (oDM) were respectively found to be 0.297, 0.270 and 0.212 m^3/CH4/kg_{oDM} when experimented at mesophilic temperatures (Figs. 3 and 4).

Higher biogas and methane yields were obtained at ratio 3:1 (75% VS of cattle slurry co-digested with 25% VS of maize stalk). The reason for this is that higher mixing ratios meant higher quantity of maize stalks in the mixture which also implied increased lignin content and this made digestion activities to be more difficult for the anaerobic bacteria. Thus, co-digestion of cattle slurry with maize stalks showed increase in the yields both from fresh mass and the organic dry matter contents of the selected substrates. This agrees with the results of previous researches that co-digestion aids biogas and methane yields [25, 29, 13, 11].

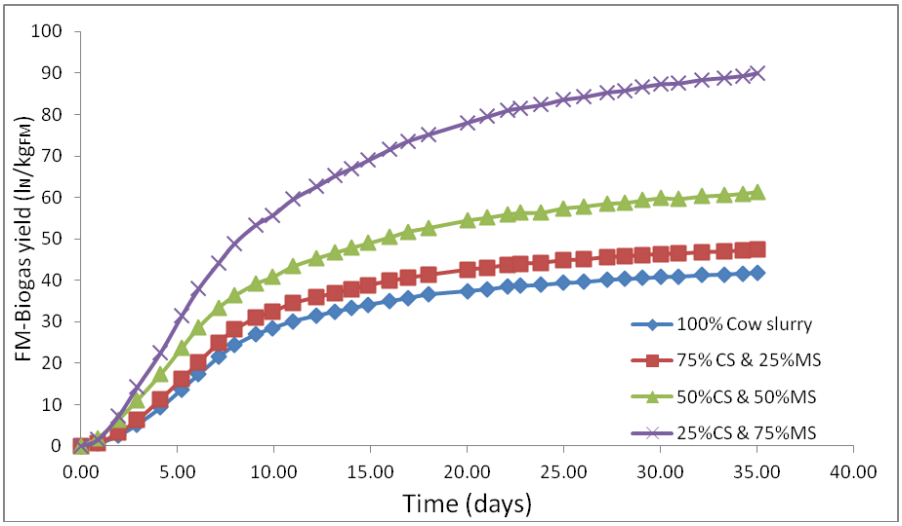

Figure 1: Fresh-Mass biogas Yields of Co-digestion of Cattle slurry with Maize-Stalks

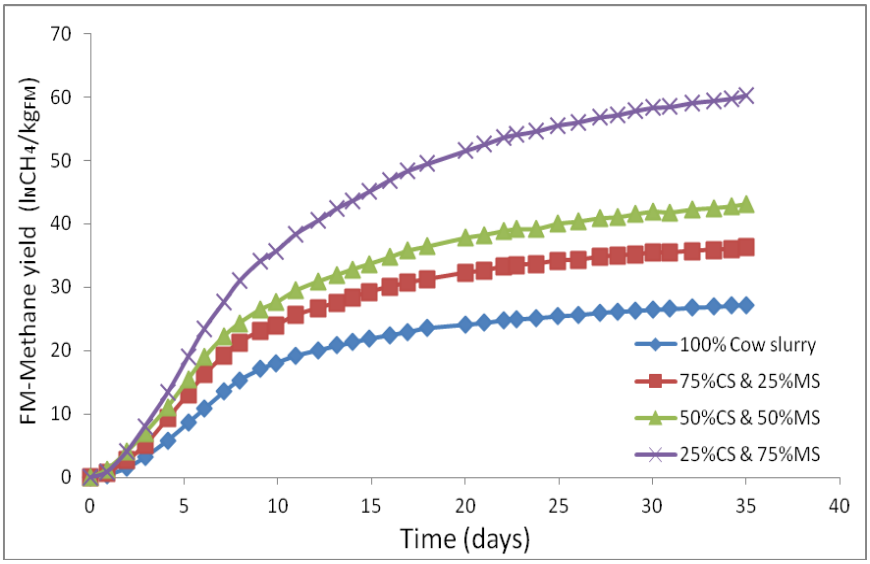

Figure 2: Fresh-mass methane yields of cattle slurry co-digested with maize-stalks

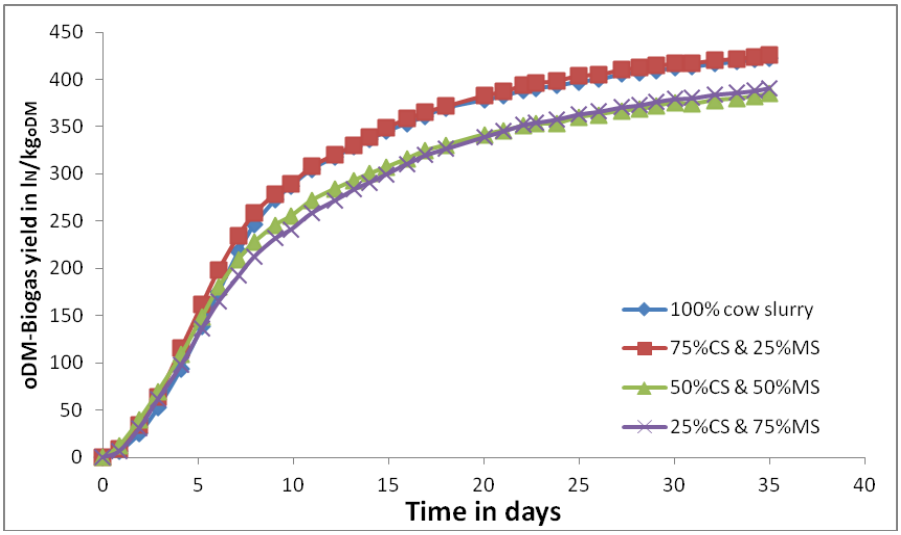

Figure 3: oDM biogas yields of cattle slurry co-digested with maize-stalks

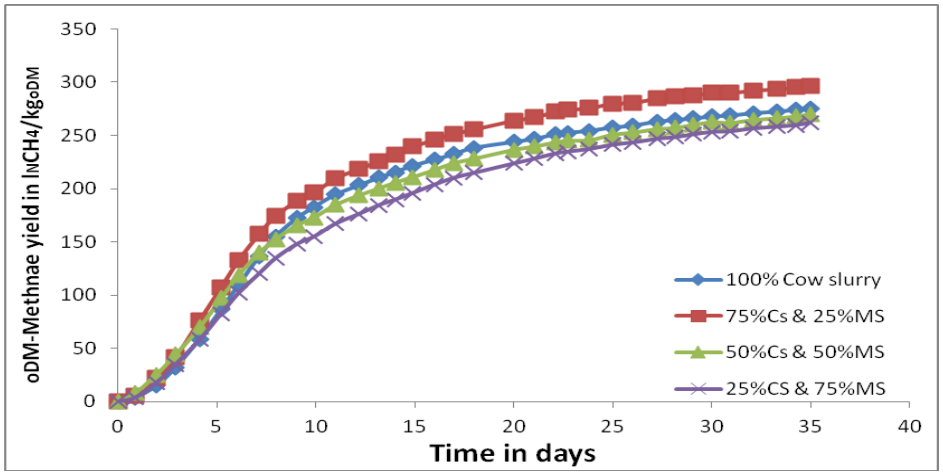

Figure 4: oDM methane yields of cattle slurry co-digested with maize-stalks

Also, since the biogas yield of maize stalk (0.357 m^3/kg_{oDM}) was lower than the results obtained from all the co-digestions at the selected ratios [34], it means that co-digestion has lowered the C/N ratio of maize stalk and thus enhancing biogas production. For biogas production from the co-digestion of cattle dung and maize stalk, mixing in ratio 3:1 will be adequate for enhanced biogas production. Also, the analysis of the results of the co-digestion of cow slurry with maize stalks revealed that there was a significant difference between the yields at 95% level of significance while the substrate ratios indicated no significant difference (Table 2).

Figures 5 and 6 show the relationships and interactions between the biogas and methane yields of the selected substrates when co-digested at different ratios. From the response surface methodology (RSM), it can be deduced that increase in %VS of CS and MS resulted in a corresponding increase in biogas yield.

Table 2: Anova: Two-Factor Without Replication at 95% Confidence Limit for Co- Digestion 2

SUMMARY	*Count*	*Sum*	*Average*	*Variance*
Row 1	4	878.84	219.71	42800.43
Row 2	4	856.2	214.05	34118.6
Row 3	4	930.12	232.53	29445.62
Column 1	3	218.93	72.97667	646.7294
Column 2	3	1299.6	433.2	339.1804
Column 3	3	165.55	55.18333	373.5977
Column 4	3	981.08	327.0267	38.41003

ANOVA

Source of Variation	*SS*	*Df*	*MS*	*F*	*P-value*	*F crit*
Substrate ratios	717.1979	2	358.5989	1.035098	0.410962	5.143249
Yields	317015.3	3	105671.8	305.0222	6.03E-07	4.757055
Error	2078.637	6	346.4396			
Total	319811.1	11				

Response: Methane

ANOVA for Response Surface 2FI Model

Analysis of variance table [Partial sum of squares]

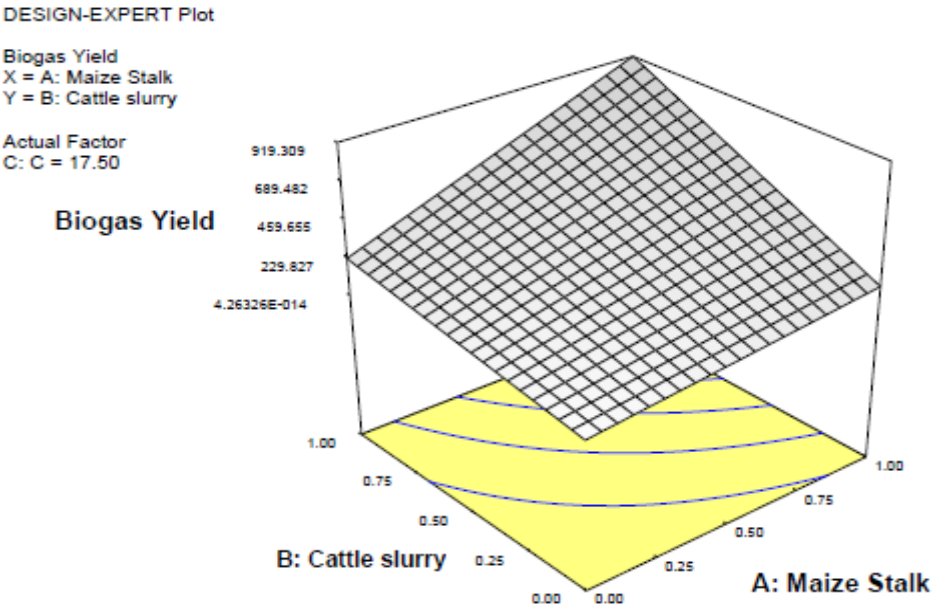

Figure 5: Interactions between cattle slurry and maize stalks (biogas yields)

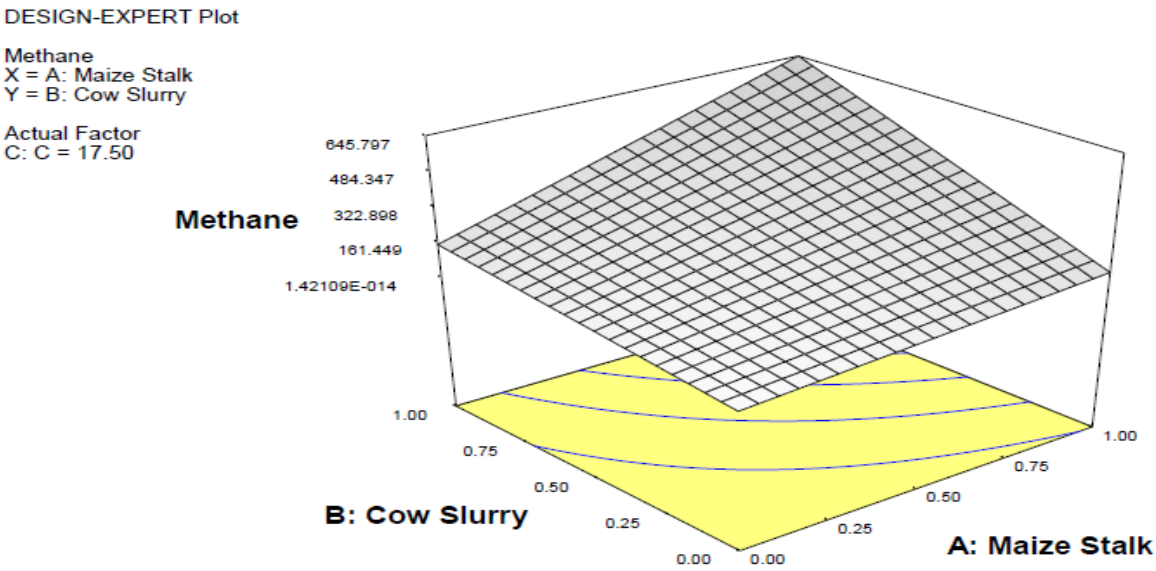

Figure 6: Interactions between cow slurry and maize stalks (methane yields)

The model developed from the RSM for the prediction of biogas and methane yields of cow slurry and maize stalks when co-digested are different ratios are as shown in equations 12 and 13.

Final Equation in Terms of Coded Factors:

$$Biogas\,Yield = +332.33 + 218.00 * A + 241.66 * B + 191.72 * C + 127.33 * A * B + 85.29 * A * C + 106.42 * B * C \quad (12)$$

$$Methane\ Yield = +228.03 + 150.97 * A + 171.93 * B + 125.82 * C + 94.87 * A * B + 53.61 * A * C + 72.21 * B * C \quad (13)$$

Where A=Maize stalks
B= Cow Slurry
C= Time (days)

IV. CONCLUSION

The study has shown that co-digesting cattle slurry with maize stalks at different ratios result into an increase in both biogas and methane yields.

ACKNOWLEDGMENTS

The first author is grateful to the Deutscher Akademischer Austauschdienst (DAAD) Germany for her financial support through the award of Research Scholarship for Doctoral Candidates and also to the entire staff and management of the Leibniz- Institute for Agricultural Engineering, Potsdam-Bornim, Germany where this research was carried out.

REFERENCES

[1] T. Muneer, S. Maubleu and M. Asif, (2006). Prospects of solar water heating for textile industry in Pakistan. Renew. Sustain. Energy Rev. 10:1–23.
[2] H. Balat (2007). A renewable perspective for sustainable energy development in Turkey: The case of small hydro-power plants. Renew. Sustain. Energy Rev. 11:2152–2165.
[3] Y. Santosh, T.R. Sreekrishnan, S. Kohli, and V. Rana (2004). Enhancement of biogas production from solid substrates using different techniques—A review. Biores. Technol. 95:1–10.
[4] A.H. Igoni, M. J. Ayotamuno, C.L. Eze, S.O.T. Ogaji and S.D. Probert (2008): Designs of anaerobic digesters for producing biogas from municipal solid-waste, *Applied Energy* 85: 430–438.
[5] C. Madu and O. A. Sodeinde. 2001. Relevance of biomass in the sustainable energy development in Nigeria. In Proc. National Engineering Conference and Annual General Meeting of the Nigerian Society of Engineers, 220 - 227.
[6] D.M. Keefe and D.P. Chynoweth (2000). Influence of phase separation. Leachate recycle and aeration on treatment of municipal solid waste in simulated landfill cells. *Bioresource Techno* 72, 55-66.
[7] J. C. Agunwamba (2001) "Waste Engineering and Management Tool" Immaculate Publication Limited, Enugu.
[8] A.M. Mshandete and W. Parawira (2009). Biogas technology research in selected sub-Saharan African countries - A review. Afr. J. Biotechnol. 8: 116-125
[9] W. Parawira, M. Murto, R. Zvauya and B. Mattiasson (2004). Anaerobic digestion of solid potato waste alone and in combination with sugar beet leaves. Renew. Energy 29: 1811-1823.
[10] P. Sosnowski, A. Wieczorek and S. Ledakowicz (2003): Anaerobic co-digestion of sewage sludgeand organic fraction of municipal solid wastes. Adv. Environ. Res. 7:609–616.
[11] M. Murto, L. Björnsson and B. Mattiasson (2004). Impact of food industrial waste on anaerobicco-digestion of sewage sludge and pig manure. J. Environ. Manage. 70:101–107.
[12] A. Mshandete, A. Kivaisi, M. Rubindamayugi and B. Mattiasson (2004). Anaerobic batch codigestion of sisal pulp and fish wastes. Biores. Technol. 95:19–24.
[13] K. Umetsu, S. Yamazaki, T. Kishimoto, J. Takahashi, Y. Shibata, C. Zhang,T. Misaki, O. Hamamoto, I. Ihara and M. Komiyama (2006). Anaerobic co-digestion of dairy manure and sugar beets. Intl. Congr. Ser. 1293:307–310.
[14] V.A. Ezekoye and C.E. Okeke (2006). Design, construction and performance evaluation of plastic bio-digester and the storage of biogas. The Pacific J. Sci. Technol. 7: 176-184
[15] M.O. Ilori, A. Adebusoye, A.K. Lawal and O.A. Awotiwon (2007). Production of biogas from banana and plantain peels. Adv. Environ. Biol. 1: 33-38.

[16] A.A. Adeyanju (2008). Effect of seeding of wood-ash on biogas production using pig waste and cassava peels. J. Eng. Appl. Sci. 3: 242-245.
[17] S. Babel, J. Sae-Tang and A. Pecharaply (2009). Anaerobic co-digestion of sewage and brewery sludge for biogas production and land application. Int. J. Environ. Sci. Tech. 6: 131-140.
[18] R.I. Mackie and M.P. Bryant (1995). Anaerobic digestion of cattle waste at mesophilic and thermophilic temperatures. Appl. Mocrobiol. Biotechnol. 43: 346-350.
[19] R. Zhang and Z. Zhang (1999). Bio-gasification of rice straw with an anaerobic-phased solids digester system. Bioresour. Technol. 68: 235-245.
[20] E.T. Iyagba, E.T., Mangibo, I.A. and Y.S. Mohammad (2009). The study of cow dung as co-substrate with rice husk in biogas production, Scientific Research and Essay Vol.4 (9), pp. 861-866.
[21] A.K. Kivaisi, (2002). Pretreatment of Robusta coffee hulls and codigestion with cow dung for enhanced anaerobic digestion. Tanz. J. Sci. 28:1-10.
[22] E.O. Uzodima, A.U. Ofoefule, J. I. Eze and N.D. Onwuka (2007). Biogas production from blends of agro-industrial wastes. Trends Appl. Sci. Res. 2: 554-558.
[23] B. Nagamani and K. Ramasamy (2007) "Biogas Production Technology: An Indian Perspective" Fermentation Laboratory, Department of Environmental Sciences, Tamil Nadu Agricultural University, Coimbatore 641 003, India.
[24] E.O. Uzodima, A.U. Ofoefule, J. I. Eze, I. Mbaeyi and N.D. Onwuka (2008). Effect of some organic wastes on the biogas yield from carbonated soft drink sludge. Sci. Res. Essay, 3(9): 401-405.
[25] Adelekan , B.A. and Bamgboye, A. I. (2009): Comparison of Biogas Productivity of Cassava Peels Mixed in Selected Ratios with Major Livestock Waste Types, *African Journal of Agricultural Research* Vol. 4 (7), pp. 571-577.
[26] C.E. Dunlop (1978). *In Single Cell Protein II*, Tannenbaum S.R. and Wans D.LC. (Eds) MIT Press CambrIdge, Massachusetts, pp 244-262.
[27] O. L. Momoh, N. Yusuf and L. Ify (2008): Effect of Waste Paper on Biogas Production from Co-digestion of Cow Slurry and Water Hyacinth in Batch Reactors J. Appl. Sci. Environ. Manage. *December*, 2008 Vol. 12 (4) 95 – 98.
[28] T. Jash and S. Basu (1999). Development of a Mini- Biogas Digester for Lighting in India, ENERGY 24; 409-411.
[29] F.J. Callaghan, D.A.J. Wase, K. Thayanithy, and C.F. Forster (1999): Co-digestion of waste organic solids: batch studies. Biores. Technol. 67:117–122.
[30] Verein Deutscher Ingenieure, VDI 4630 Entwurf. (2004): Vergarung organischer Stoffe (Green paper: Fermentation of organic materials). Beuth Verlag GmbH, D-10772 Berlin.
[31] B. Linke and H. Schelle (2000). Solid State Anaerobic Digestion of Organic Wastes. Agricultural Engineering into the Third Millenium.*AgEng Warwick 2000. Paper Number 00-AP*-025, 101-102, 2-7 July 2000.
[32] M. Kirchgeßner (1997). Tierernährung. 10th edition, Verlags Union Agrar, Frankfurt a. M., 582 p.
[33] P.M. Mähnert, M. Heiermann, Pöch, H, Schelle and B. Linke (2002). Alternative Use for Grassland Cuts - Forage Grasses as Biogas Co-substrates (Verwertungsalternativen für Grünlandbestände – Futtergräser als Kosubstrat für die Biomethanisierung). Landtechnik; 5: 260-261.
[34] A.O. Adebayo (2012). Effect of Some production parameters on anaerobic digestion of selected crop and animal residues, An unpublished Ph.D thesis in the Department of Agricultural Engineering, Ladoke Akintola University of Technology, Ogbomoso, Nigeria.

American Journal of Engineering Research (AJER)
e-ISSN : 2320-0847 p-ISSN : 2320-0936
Volume-03, Issue-01, pp-89-95
www.ajer.org

Research Paper Open Access

Alternative Source of Cooking Gas – Conversion of Crop Waste to Energy

Ajoko, Tolumoye John
Department of Mechanical/Marine Engineering, Faculty of Engineering.
Niger Delta University, Wilberforce Island, Bayelsa State, Nigeria.

Abstract: - The research is aimed to reduce the total dependence on cooking gas refined from petroleum product for rural dwellers due to the difficult terrain and challenges of transportation system encountered. Study was carried out in Igbedi Community of Kolokuma/Opokuma Local Government Area in Bayelsa State, Nigeria; to procure an alternative source of cooking gas for indigenes.
The sample used for this research work is waste materials collected from arable crops predominantly cultivated by indigenes of this community. They are such as waste from cassava, sugar cane and grains (maize). Study unveils at the end of test duration that high performance rate recovered for average energy and moisture content, density, pressure and temperature for domestic cooking gas as obtained from cassava piles waste is 7.2391KJ/Kg, 45.56%, 842.4kgm-3, 6098Nm-2 and 3.37℃ respectively with the support of using Waste Transformation Techniques. Hence, waste from cassava piles satisfying the real properties of cooking gas from petroleum product as revealed in the review literature is the major source of alternative cooking gas from crop waste.
Therefore, to maintain sustainability this reliable and effective proven gas from crop wastes is aided with the provision of a larger waste disposal tank for waste collection at an affordable rate, design to recover at least a good quantity of cooking gas for every home. Thus, a consistent follow up with the lay down procedure to convert waste to energy will give rise to the availability of the gas.

Keywords: - *Crop waste, cooking gas, moisture and Energy content, biogas.*

I. INTRODUCTION

The usefulness of energy has led to its conversion from household domestic non-recyclable waste materials into useable biogas for cooking, electricity, heat supply, etc. This process is often called Waste – to – Energy (Marie, 2007). Such unwanted wastes are substances derived from human activities which are as follows; garbage, paper refuse, plastic/rubber and glass waste, textiles and leather waste, plant/food crop refuse, etc (Marie, 2007; Nolan, 2001). These heterogeneous mass of throwaways from residences and commercial activities is traceable to ancient time and has caused lots of epidemic of plagues in the world (Alaa et al., 2012).
Research reveals that biomass can be derived from the cultivation of dedicated energy crops such as Short Rotation Coppice (SRC), Perennial grasses and other plant residues; and biomass waste like organic industrial waste and organic domestic waste (Peter, 2001; Abdulkareem, 2005). Similar studies unveils Biomethanisation technology as an acceptable and proven technology for Bio-energy generation from domestic wastes which uses different types of anaerobic bacteria/microbes in a concealed chamber or digester to help treat degradable waste for easy conversion process and usage (Saji Das, 2011). Marie, 2007; Peter, 2001; Abdulkareem, 2005; reported that Waste – to – energy process is a source of reducing carbon/No_x emissions by offsetting the need for energy from fossil sources and reduces methane generation from landfills. Meanwhile, a paper presented by (Saji Das, 2011) stated some advantageous facts that energy from waste is more suitable for eco-friendly waste disposal and also good source of energy generation. Hence, the merit of turning to this alternative source of energy are numerous, they are such as low cost in production and easy methodology, readily available, more economical, etc (Abdulkareem, 2005).

Therefore, the idea of providing an alternative source of cooking gas for rural dwellers and other future potential users has become very imperative. Thus, this paper presentation will help in reducing excessive

spending for the importation of kerosene, and other cooking gas; however minimizing the risk of transporting the product through water means to local and interior communities.

II. METHODOLOGY

The method employed for this research work is simply known as ***Waste Transformation Techniques.*** This technology is simple, users friendly and capable of generating energy such as cooking gas with the aid of simple waste disposal tank connected to an energy reservoir (gas cylinder). Large quantity of degradable waste materials from arable crops is deposited inside the tank for effective and sustainable recovery of energy (cooking gas) for the use of every rural dweller. However, dung from cow and other domestic animals are injected into the waste disposal tank for quick and easy decomposition. It also serves as a chemical catalyst which fastens the reactions. Thus, the recovered energy is a good substitute for the cooking gas from petroleum product.

Meanwhile, for the purpose of this research a sample experimental bed is set as shown in figure 1. Waste materials from crop such as cassava pile, grain chaffs and sugar cane waste were disposed into three separate waste collection bins respectively with equal and corresponding dung added to the bins which is connected to an energy tank. In order to estimate the amount of energy in either of the waste reservoir; the other two will be shut with the help of the stop cork arrangement which regulate the flow of fluid from the waste reservoir to the energy tank. This is preceded with an analytical manipulation to determine the corresponding energy content and other parameters to obtain the properties of the gas in question.

However, the experiment is conducted in the presence of direct sun light of temperature variation of 25℃ - 31°C for a period of 23 – days to serve as means of drier [a replacement of oven drying method (Alaa, 2001; Peter, 2001)] to enable determine the moisture content of the waste materials.

Figure 1:- Pictorial illustration of waste collection bins and energy collection tank

The importance and function of the sun light with respect to the temperature and the period of the experiment is to facilitate complete dehydration of the waste products; and limiting the vaporization of volatile materials.

III. MOISTURE CONTENT

Moisture content is a depended variable to the mass composition of the waste which determines the quality of waste products. It is presented mathematically in equation 1 (Alaa et al., 2012) as:

$$\text{Moisture Content } (\%) = \frac{Mi - Md}{Mi} \times 100\% \qquad 1$$

Where M_i = Initial mass of the sample

M_d = Dry mass of the sample after 23 – days.

A tabulation of samples of waste materials collected with respect to their wet and dry mass and moisture content in percentage in the test duration is presented in table 1.

Table - 1 Sample of Waste Materials

Test Duration (days)	Cassava Piles			Grain Chaffs			Sugar Cane Waste		
	Wet Mass (Kg)	Dry Mass (Kg)	Moisture Content (%)	Wet Mass (Kg)	Dry Mass (Kg)	Moisture Content (%)	Wet Mass (Kg)	Dry Mass (Kg)	Moisture Content (%)
1	3.8	3.8	0	1.2	1.2	0	1.4	1.4	0
2	3.8	3.8	0	1.2	1.2	0	1.4	1.4	0
3	3.8	3.799	0.026315789	1.2	1.2	0	1.4	1.4	0
4	3.799	3.79	0.236904449	1.2	1.2	0	1.4	1.4	0
5	3.79	3.75	1.055408971	1.2	1.2	0	1.4	1.399	0.07142857
6	3.75	3.7	1.333333333	1.2	1.2	0	1.399	1.3976	0.10007148
7	3.7	3.64	1.621621622	1.2	1.198	0.16666667	1.3976	1.396	0.11448197
8	3.64	3.56	2.197802198	1.198	1.1958	0.1836394	1.396	1.3942	0.12893983
9	3.56	3.47	2.528089888	1.1958	1.1935	0.19233986	1.3942	1.3902	0.28690288
10	3.47	3.37	2.88184438	1.1935	1.1911	0.20108923	1.3902	1.3802	0.71932096
11	3.37	3.27	2.96735905	1.1911	1.1871	0.33582403	1.3802	1.3602	1.44906535
12	3.27	3.17	3.058103976	1.1871	1.1791	0.67391121	1.3602	1.3352	1.83796501
13	3.17	3.07	3.154574132	1.1791	1.1631	1.35696718	1.3352	1.3052	2.2468544
14	3.07	2.97	3.25732899	1.1631	1.1381	2.14942825	1.3052	1.2742	2.37511492
15	2.97	2.87	3.367003367	1.1381	1.1131	2.19664353	1.2742	1.2422	2.51137969
16	2.87	2.77	3.484320557	1.1131	1.0881	2.2459797	1.2422	1.2092	2.65657704
17	2.77	2.67	3.610108303	1.0881	1.0621	2.38948626	1.2092	1.1752	2.81177638
18	2.67	2.57	3.745318352	1.0621	1.0361	2.44798042	1.1752	1.1412	2.89312457
19	2.57	2.47	3.891050584	1.0361	1.0101	2.50941029	1.1412	1.1062	3.06694707
20	2.47	2.37	4.048582996	1.0101	0.9831	2.67300267	1.1062	1.0702	3.25438438
21	2.37	2.27	4.219409283	0.9831	0.9561	2.7464144	1.0702	1.0342	3.36385722
22	2.27	2.17	4.405286344	0.9561	0.9291	2.82397239	1.0342	0.9972	3.57764456
23	2.17	2.07	4.608294931	0.9291	0.9021	2.9060381	0.9972	0.9572	4.01123145

An estimation of moisture content of the selected waste sample by percentage and amount of water loss in each case is analyzed as 45.56%, 37.56% and 28.20%; and 1.73, 0.44 and 0.3 for cassava piles, sugar cane waste and grain chaffs respectively for the period of the experiment.

DENSITY

Previous studies disclose the relationship between moisture content and the density of the wet waste material (Kraszewski et al., 1998; Mohammad et al., 2010; Laurent et al., 2005). The density, ρ is a reliable tool in the determination of the properties of fluid which is presented mathematically in equation 2 (Rajput, 2004; John et al., 2011) is significant to the study as it is used to analyze the amount of temperature of the gas, as in equation 3;- a standard value of maximum density of water as bench mark for the most dense fluid which equals $1000kgm^{-3}$ at 4℃; knowing that density of any fluid is temperature dependent (Rajput, 2004; John et al., 2011).

$$\rho = MV^{-1} \qquad 2$$

$$1000kgm^{-3} = 4℃ \qquad 3$$

ENERGY CONTENT

The energy content of the waste products was established by the use of some simple dimensional analytical procedures in terms of M-L-T fundamental system. The energy extracted is a function of the pressure and volume of the gas with respect to its mass.

Thus, the governing equation for this expression is given in equation 4-5 as:

$$\text{Energy Content } E_{con} = \frac{\text{Pressure} \times \text{Volume}}{\text{Mass}} \qquad 4$$

Dimensionally;

$$E_{con} = \frac{ML^{-1}T^{-2} \times L^3}{M} \qquad 5$$

Where;

$ML^2 T^{-2}$ = Newton × Metre = Joule

So that E_{con} is expressed in J/Kg or KJ/Kg.

Meanwhile, statistical data concerning density, energy content and other useful parameters to obtain the properties of the cooking gas is presented on table 2 based on equations stated above and other sensitive mathematical expressions.

Table - 2 Data Presentation for Sample Waste Materials

Test Duration (days)	Empty Mass (ME) of Energy Container (Kg)	Empty Mass of Energy Container & Fluid (MEF) - (Kg)	Mass of Fluid (MEF-ME) (Kg)	Density of the Fluid (KgM-3)	Temp. of Fluid (°C)	Weight of Fluid (MEF-ME)g N	Press. (Nm-2)	Energy Content (KJ/Kg)
Cassava Piles								
1	0.1	0.5	0.4	173.91304	0.6957	3.928	1259	7.2391
2	0.1	0.5	0.4	173.91304	0.6957	3.928	1259	7.2391
3	0.1	0.625	0.525	228.26087	0.913	5.1555	1652.4	7.2391
4	0.1	0.696	0.596	259.13043	1.0365	5.85272	1875.9	7.2391
5	0.1	0.802	0.702	305.21739	1.2209	6.89364	2209.5	7.2391
6	0.1	0.897	0.797	346.52174	1.3861	7.82654	2508.5	7.2391
7	0.1	0.995	0.895	389.13043	1.5565	8.7889	2817	7.2391
8	0.1	1.023	0.923	401.30435	1.6052	9.06386	2905.1	7.2391
9	0.1	1.195	1.095	476.08696	1.9043	10.7529	3446.4	7.2391
10	0.1	1.323	1.223	531.73913	2.127	12.00986	3849.3	7.2391
11	0.1	1.437	1.337	581.30435	2.3252	13.12934	4208.1	7.2391
12	0.1	1.568	1.468	638.26087	2.553	14.41576	4620.4	7.2391
13	0.1	1.667	1.567	681.30435	2.7252	15.38794	4932	7.2391
14	0.1	1.698	1.598	694.78261	2.7791	15.69236	5029.6	7.2391
15	0.1	1.856	1.756	763.47826	3.0539	17.24392	5526.9	7.2391
16	0.1	1.904	1.804	784.34783	3.1374	17.71528	5678	7.2391
17	0.1	1.999	1.899	825.65217	3.3026	18.64818	5977	7.2391
18	0.1	2.357	2.257	981.30435	3.9252	22.16374	7103.8	7.2391
19	0.1	2.675	2.575	1119.5652	4.4783	25.2865	8104.6	7.2391
20	0.1	2.892	2.792	1213.913	4.8557	27.41744	8787.6	7.2391
21	0.1	3.015	2.915	1267.3913	5.0696	28.6253	9174.8	7.2391
22	0.1	3.255	3.155	1371.7391	5.487	30.9821	9930.2	7.2391
23	0.1	3.575	3.475	1510.8696	6.0435	34.1245	10937	7.2391
Grain Chaffs								
1	0.1	0.12	0.02	20.202	0.081	0.1964	20.67	1.023
2	0.1	0.12	0.02	20.202	0.081	0.1964	20.67	1.023
3	0.1	0.12	0.02	20.202	0.081	0.1964	20.67	1.023
4	0.1	0.12	0.02	20.202	0.081	0.1964	20.67	1.023
5	0.1	0.12	0.02	20.202	0.081	0.1964	20.67	1.023
6	0.1	0.12	0.02	20.202	0.081	0.1964	20.67	1.023
7	0.1	0.175	0.075	75.7576	0.303	0.7365	77.53	1.023
8	0.1	0.225	0.125	126.263	0.505	1.2275	129.2	1.023
9	0.1	0.232	0.132	133.333	0.533	1.29624	136.4	1.023
10	0.1	0.255	0.155	156.566	0.626	1.5221	160.2	1.023
11	0.1	0.275	0.175	176.768	0.707	1.7185	180.9	1.023
12	0.1	0.295	0.195	196.97	0.788	1.9149	201.6	1.023
13	0.1	0.315	0.215	217.172	0.869	2.1113	222.2	1.023
14	0.1	0.324	0.224	226.263	0.905	2.19968	231.5	1.023
15	0.1	0.345	0.245	247.475	0.99	2.4059	253.3	1.023
16	0.1	0.365	0.265	267.677	1.071	2.6023	273.9	1.023
17	0.1	0.385	0.285	287.879	1.152	2.7987	294.6	1.023
18	0.1	0.398	0.298	301.01	1.204	2.92636	308	1.023
19	0.1	0.42	0.32	323.232	1.293	3.1424	330.8	1.023
20	0.1	0.435	0.335	338.384	1.354	3.2897	346.3	1.023
21	0.1	0.445	0.345	348.485	1.394	3.3879	356.6	1.023
22	0.1	0.46	0.36	363.636	1.455	3.5352	372.1	1.023
23	0.1	0.485	0.385	388.889	1.556	3.7807	398	1.023

Sugar Cane Waste								
1	0.1	0.325	0.225	40.9091	0.164	2.2095	232.6	5.685
2	0.1	0.325	0.225	40.9091	0.164	2.2095	232.6	5.685
3	0.1	0.325	0.225	40.9091	0.164	2.2095	232.6	5.685
4	0.1	0.325	0.225	40.9091	0.164	2.2095	232.6	5.685
5	0.1	0.352	0.252	45.8182	0.183	2.47464	260.5	5.685
6	0.1	0.385	0.285	51.8182	0.207	2.7987	294.6	5.685
7	0.1	0.395	0.295	53.6364	0.215	2.8969	304.9	5.685
8	0.1	0.405	0.305	55.4545	0.222	2.9951	315.3	5.685
9	0.1	0.445	0.345	62.7273	0.251	3.3879	356.6	5.685
10	0.1	0.565	0.465	84.5455	0.338	4.5663	480.7	5.685
11	0.1	0.675	0.575	104.545	0.418	5.6465	594.4	5.685
12	0.1	0.795	0.695	126.364	0.505	6.8249	718.4	5.685
13	0.1	0.985	0.885	160.909	0.644	8.6907	914.8	5.685
14	0.1	1.05	0.95	172.727	0.691	9.329	982	5.685
15	0.1	1.265	1.165	211.818	0.847	11.4403	1204	5.685
16	0.1	1.465	1.365	248.182	0.993	13.4043	1411	5.685
17	0.1	1.795	1.695	308.182	1.233	16.6449	1752	5.685
18	0.1	1.855	1.755	319.091	1.276	17.2341	1814	5.685
19	0.1	2.015	1.915	348.182	1.393	18.8053	1980	5.685
20	0.1	2.235	2.135	388.182	1.553	20.9657	2207	5.685
21	0.1	2.655	2.555	464.545	1.858	25.0901	2641	5.685
22	0.1	2.805	2.705	491.818	1.967	26.5631	2796	5.685
23	0.1	2.955	2.855	519.091	2.076	28.0361	2951	5.685

IV. RESULT PRESENTATION

Figures 2-7 illustrates the variation of energy and moisture contents of the sample waste materials for the research with a corresponding rate of density, temperature and mass of the fluid recovered with respect to the test duration. Meanwhile, the chart presentation were generated from tables 1 and 2 which shows the practical ways of obtaining domestic cooking gas for rural communities from waste products of arable crops. Result plots also describe and explain the relationship, behavior and properties of the cooking gas and its raw material. However, the trend of energy content, temperature and Pressure change of the gas for the waste sample such as cassava piles, grain chaffs and sugar cane waste is best demonstrated on a histogram in figures 5 – 7.

V. DISCUSSION

Established results in the test duration of moisture content is obvious and clear that cassava piles is of the highest moisture content of 45.56%, followed by sugar cane waste with 37.56% and grain chaffs yielding 28.19%. This indicates a speedy decay of the reactions it undergoes in the experimental test duration. The reason for this might be the high level of sugar content in its waste product which is a component of carbohydrates. However, the analyzed result for energy content of the waste materials is 7.2391KJ/Kg, 1.023KJ/kg and 5.685KJ/Kg for cassava Piles, grain chaffs and sugar cane waste respectively. Other subsequent results obtained in the process for an overall average density, pressure and temperature of the gas in terms of Cassava piles, grain chaffs and sugar cane waste is 842.4kgm-^{3}, 6098Nm^{-2}, 3.37℃; 204.55kgm-^{3}, 209.34Nm^{-2}, 0.82℃ and 280kgm-^{3}, 1591.8Nm^{-2}, 1.12℃ respectively.

Result comparison with estimated properties of a cooking gas from petroleum product of 7.379KJ/Kg and 46.54% energy content and moisture content respectively from review sources (Alaa et al., 2012, Propane, 2013) is used to validate the result obtained from this paper.

VI. CONCLUSION

After critical evaluation of the properties of crop waste with that of cooking gas from petroleum product, energy derived from crop waste is considerably potential substitute for its counterpart.

Thus, it shows that waste product from carbohydrates class of food with animal dung is prompt to decay faster to produce energy capable of cooking.

For the purpose of validation of the established Waste Transformation Techniques used for this research, result comparison was a measure to establish a bench-mark for the sustained energy for the cooking gas.

In order to maintain sustainability of this derived energy from crop waste is the provision of a larger waste disposal tank at an affordable rate for every house hold in rural communities to help generate a larger quantity of the gas.

Therefore, massive production of animal dung will lead to rearing of animal for reliability and effectiveness of this alternative source of cooking gas for rural dwellers.

VII. ACKNOWLEDGEMENT

The author wishes to acknowledge all colleagues in the department of Mechanical/Marine Engineering, Niger Delta University, Wilberforce Island, Bayelsa State. Nigeria.

REFERENCES

[1] Abdulkareem A. S. (2005). "Refining Biogas Produced from Biomass: An Alternative to Cooking Gas".

[2] Alaa Husaeen Wadie, Jawad Kadhim Abbood, Riyad Hassan Hadi (May, 2012). "Residential Solid Wastes Characteristics and Energy Content in Al-Mussaib City in the Middle of Iraq", *ICEBS*, PP. 38-43.

[3] John F. Douglas, Janusz M. Gasiorek, John A. Swaffield, Lynne B. Jack (2011). "Fluid Mechanics, (5th Ed)", Dorling Kindersley (India): PVt. Ltd., ISBN: 978-81-317-2140-7.

[4] Kraszewski A. W.,Trabelsi S., Nelson S. O. (1998). "Simple Grain Moisture Content Determination from Microwave Measurements", *Transactions of the ASAE*, Vol.4 (1), PP. 129-134.

[5] Laurent J. P., Olivier F., Goure J. P. (March, 2005). "Monitoring Moisture Content in Municipal Solid Waste: Results of a Preliminary test under Laboratory Conditions", *International Workshop "Hydro-Physico- Mechanics of Landfills.*

[6] Marie Lariviere (May, 2007). "Methodology for Allocating Municipal Solid Waste to Biogenic and Non-Biogenic Energy", EI-52, Washington, DC.20585.

[7] Mohammad Reza Seifi, Reza Alimardani (December, 2010). "The Moisture Content Effect on some Physical and Mechanical Properties of Corn (SE 704)", *Journal of Agricultural Science*, Vol. 2, No. 4, PP. 125-134. ISSN 1916-9752 E-ISSN1916-9760.

[8] Nolan Itu Pty Ltd., TBU Environmental Engineering Consultants (March, 2001). "Guideline for Determining the Renewable Components in Waste for Electricity Generation", Ref: 3082-01.

[9] Peter Mckendry (July, 2001). "Energy Production from Biomass (Part 2) Conversion Technologies", *Applied Environmental Research Centre Ltd, UK*.

[10] Propane (2013). Properties of Propane, available at http://en.wikipedia.org/wiki/propane, Accessed on the 20th August, 2013.

[11] Rajput R. K. (2004). "A Text Book of Fluid Mechanics and Hydraulic Machines, (Reprint-2nd Ed)", Ram Nagar, New-Delhi: S.Chand and Company Ltd., ISBN:81-219-1666-6.

[12] Saji Das A. (August, 2011). "Generation of Energy through Decentralized Waste Treatment", Biotech Renewable Energy PVt. Ltd., Thiruvananthapuram-14, Kerala.

LIST OF FIGURES

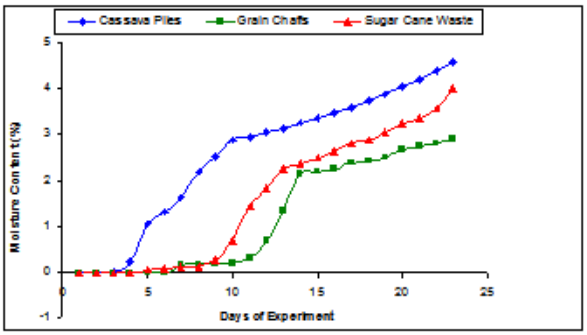

Figure 2:- Moisture Content Percentage Performance of Waste Materials

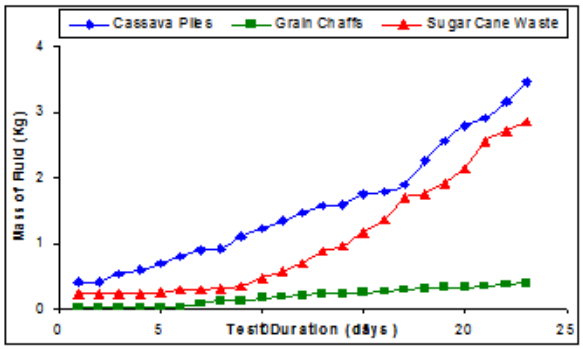

Figure 3:- Deviation of Mass of Fluid with Days of Experiment

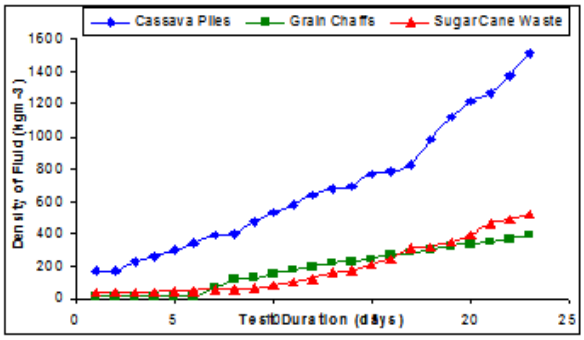

Figure 4:- Rate of Density Change with Time

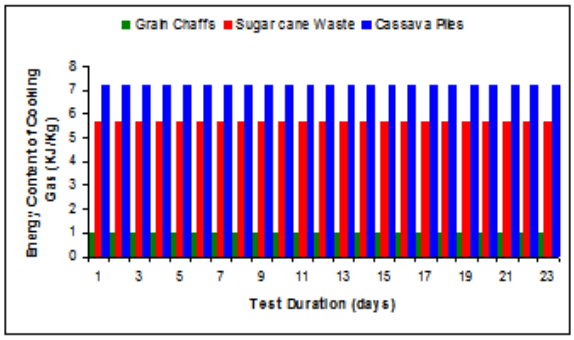

Figure 5:- Variation of Energy Content for Waste Materials

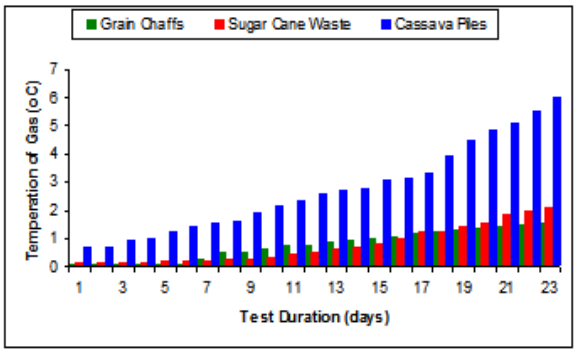

Figure 6:- Variation of Temperature with Time

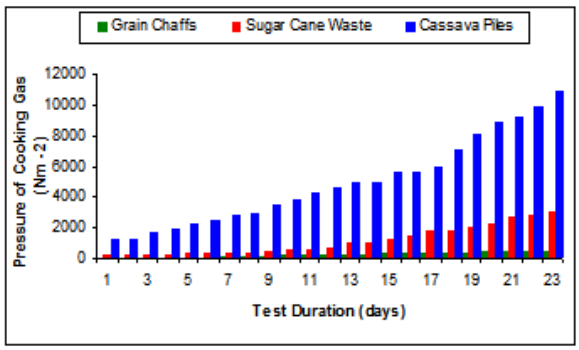

Figure 7:- Variation of Pressure with Test Duration

American Journal of Engineering Research (AJER)
e-ISSN : 2320-0847 p-ISSN : 2320-0936
Volume-03, Issue-01, pp-96-105
www.ajer.org

Research Paper Open Access

A comparison of the Voltage Enhancement and Loss Reduction Capabilities of STATCOM and SSSC FACTS Controllers

[1]Aborisade, D.O., [2]Adebayo, I.G., and [3]Oyesina, K.A.
[1,2,3] *Department of Electronic and Electrical Engineering,*
Ladoke Akintola University of Technology, PMB 4000, Oyo State, Ogbomoso, Nigeria

Abstract: - Power systems deteriorate with time as load grows and generation is added. The transmission system is also usually subjected to a number of steady-state and transient problems. This leads to voltage instability and increased system losses. This work addressed the problems of voltage instability, active and reactive power losses. Presented in this paper is a comparison of the voltage enhancement and loss reduction capabilities of Static Synchronous compensator (STATCOM) and Static Synchronous Series Compensator (SSSC) at low voltage buses in the Nigerian 330kV grid. Power flow equations involve solution to nonlinear algebraic equations using reliable mathematical algorithms. In this work, the Newton Raphson iterative algorithm was adopted due to its ability to converge after a few iterations. Simulation of power flow solutions without any Flexible Alternating Current Transmission System (FACTS) device (STATCOM and SSSC) and with STATCOM and SSSC were done using a MATLAB based program. Where voltage drops were noticed, STATCOM and SSSC were incorporated in turn and the new voltage magnitudes were computed. The voltage enhancement capability of the devices is thus demonstrated. The system losses were also computed for each case. Such low voltage buses are buses 9(Ayede), 13(New-Haven), 14(Onitsha) and 16(Gombe). The results obtained from the incorporation of both devices into the grid system were satisfactory. The voltage magnitudes at these buses were sufficiently improved to maintain it at or above 1.0pu with both STATCOM and SSSC. The active power and reactive power losses also reduced by 0.171% and 1.009% respectively when STATCOM was applied while the incorporation of SSSC into the Nigerian grid system reduced active power and reactive power loss by 1.078% and 10.326% respectively.

Keywords: - *Voltage stability, Power Flow, Line Flow, FACTS devices, STATCOM, SSSC*

I. INTRODUCTION

Electrical energy is the most popular and widely used form of energy because it can be transported easily and relatively efficiently at lower cost. [1] [2]. The transmission system which connects the generation and the consumers are however always subjected to disturbances in one form or the other which consequently affects the power system adversely.

The ability of the transmission system to transmit power becomes impaired by a number of steady-state and dynamic limitations [3]. These steady-state and transient problems usually affect the power system negatively. This can culminate in limited power transfer and system instability and in some critical cases it may result into total system collapse [4],[5]. This implies that the relative advantage of the use of electrical energy is threatened in the form of reduced efficiency and higher cost of transmission. In addition, the Nigerian network topology is such that the generating stations are located far from major load centres, resulting in low bus voltages [6] [7]. Voltage instability is directly associated with reactive power imbalance [8].

As a result of this, there exists a continuous challenge to improve stability of power systems [9]. Control in power systems is thus of tremendous importance. Power flow control has traditionally relied on generator control, voltage regulation (by means of tap-changing and phase-shifting transformers) and reactive power plant compensation switching. Phase-shifting transformers have been used for the purpose of regulating active power in alternating current (AC) transmission networks. In practice, some of them are permanently operated with fixed angles, but in most cases their variable tapping facilities are actually made use of [10] [11] and [12].

However, with the rapid advances in power electronics area, it has become possible to apply power electronics to power system. Flexible Alternating Current Transmission System (FACTS) devices are based on the rapid development of power electronics technology to improve stability of power system. FACTS devices can be categorized in two groups. The first group of FACTS devices uses the Thyristor to control the reactors or capacitors (i.e. the Thyristor-based devices). The second group of FACTS devices uses more advanced power electronics to control power flow of power system. [9] . [13] further divided FACTS devices into three groups based on their switching technology viz, mechanically switched (such as phase shifting transformers), thyristor switched and fast switched, using IGBTs. While some types of FACTS, such as the phase shifting transformer (PST) and the static VAR compensator (SVC) are already well known and used in power systems, new developments in power electronics and control have extended the application range of FACTS. The stability of power system can be much better improved by coordination control of FACTS devices.

Simply put, Flexible AC Transmission System (FACTS) controllers are essentially power electronics based controllers. With the applications of FACTS technology, bus voltage magnitude and power flow along the transmission lines can be more flexibly controlled [14].

Furthermore, intermittent renewable energy sources and increasing international power flows provide new applications for FACTS. The additional flexibility and controllability of FACTS allow to mitigate the problems associated with the unreliable of supply issues of renewable [9]. Meanwhile, [17] had worked on steady state voltage stability enhancement using SSSC considering Nigerian grid power system as a case study. However, [17] did not place emphasis on the loss reduction capability of the SSSC, and above all, STATCOM FACTS controller device was not considered in the paper.

This paper therefore focused on the application of STATCOM (a shunt controller) and SSSC (a series controller) at low voltage buses in the Nigerian 330kV grid to compare the voltage enhancement and loss reduction capabilities of Static Synchronous compensator (STATCOM) and Static Synchronous Series Compensator (SSSC).

II. STRUCTURE OF 28-BUS 330KV NIGERIAN TRANSMISSION SYSTEM

The single line diagram of the Nigerian 330kV network is as shown in figure 3. It consists of nine generating stations and twenty-six load stations. The system may be divided into three major sections: - North, South-East and the South-West sections, as shown in Figure 1. The North is connected to the South through one triple circuit lines between Jebba and Osogbo while the West is linked to the East through one transmission line from Osogbo to Benin and one double circuit line from Ikeja to Benin.

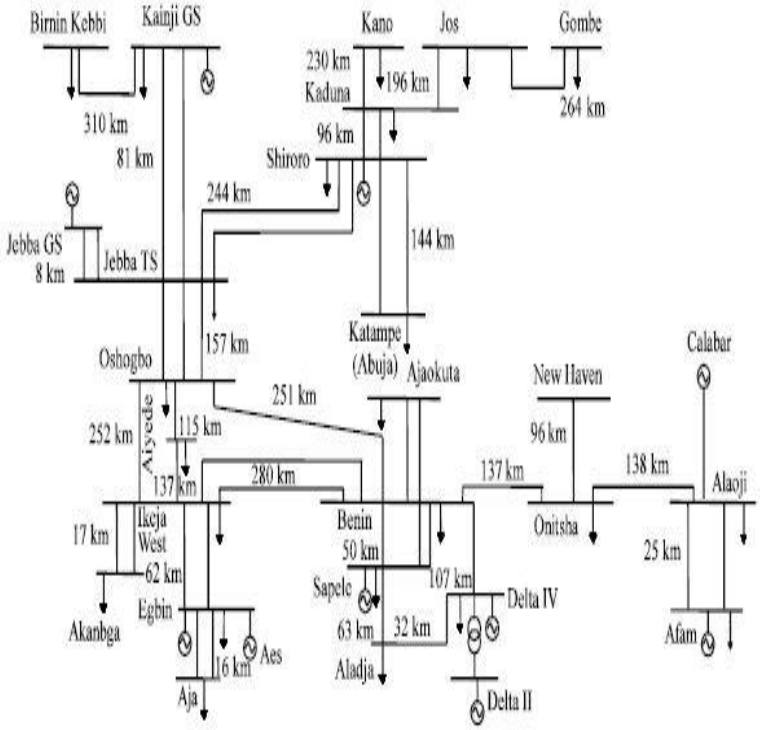

Figure 1: 28-bus 330kV Nigerian transmission system Source: [15]

III. STATIC SYNCHRONOUS SERIES COMPENSATOR

A static synchronous compensator (STATCOM) is a regulating device used on alternating current electricity transmission networks. It is based on a power electronics voltage-source converter and can act as either a source or sink of reactive AC power to an electricity network. If connected to a source of power it can also provide active AC power.

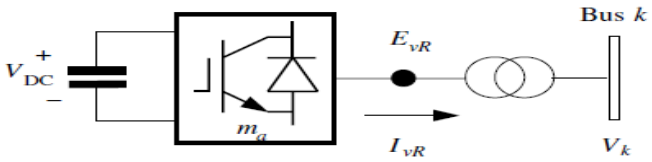

Figure 2: STATCOM schematic diagram Source: [11]

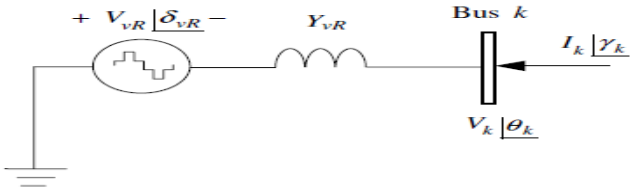

Figure 3: STATCOM equivalent circuit Source: [11]

IV. STATIC SYNCHRONOUS SERIES COMPENSATOR

This device works in a similar manner to the STATCOM. It has a voltage source converter serially connected to a transmission line through a transformer. It injects voltage in quadrature with one of the line end voltages in order to regulate active power flow. It does not draw reactive power from the AC system; it has its own reactive power provisions in the form of a DC capacitor.

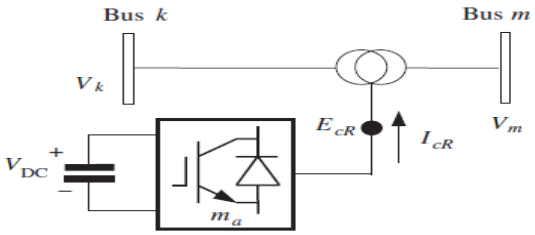

Fig. 4 : Schematic representation of SSSC [11]

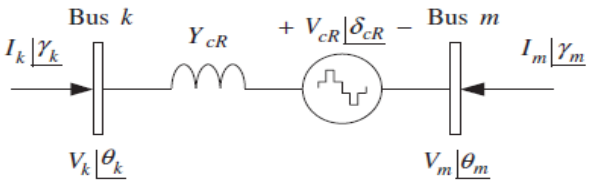

Figure 5 : SSSC equivalent circuit Source: [11]

V. PROBLEM FORMULATION

A Power flow Equations

A typical bus of a power system network is as shown in Figure (6). Transmission lines are represented by their equivalent π model where impedance has been converted to per unit admittances on common MVA base. [1]

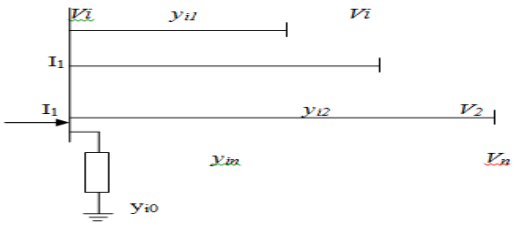

Figure 6: Typical bus

In any system, the active and reactive power are given by equations (1) and (2)

$$P_i = \sum_{j=1}^{n} |V_i||V_j||Y_{ij}|\cos(\theta_{ij} - \delta_i + \delta_j) \quad (1)$$

$$Q_i = -\sum_{j=1}^{n} |V_i||V_j||Y_{ij}|\sin(\theta_{ij} - \delta_i + \delta_j) \quad (2)$$

Expanding equation (1) and (2) in Taylor's series about the initial estimate and neglecting all higher order results in the following set of linear equations. Details of this equation is presented in [1].

The linearized form of this equation is as shown in equation (3)

$$\begin{bmatrix} \Delta P_2^{(k)} \\ \vdots \\ \Delta P_n^{(k)} \\ \Delta Q_2^{(k)} \\ \vdots \\ \Delta Q_n^{(k)} \end{bmatrix} = \left[\begin{array}{ccc|ccc} \frac{\partial P_2^{(k)}}{\partial \delta_2} & \cdots & \frac{\partial P_2^{(k)}}{\partial \delta_n} & \frac{\partial P_2^{(k)}}{\partial |V_2|} & \cdots & \frac{\partial P_2^{(k)}}{\partial V_n} \\ \vdots & \ddots & \vdots & \vdots & \ddots & \vdots \\ \frac{\partial P_n^{(k)}}{\partial \delta_2} & \cdots & \frac{\partial P_n^{(k)}}{\partial \delta_n} & \frac{\partial P_n^{(k)}}{\partial V_2} & \cdots & \frac{\partial P_n^{(k)}}{\partial V_n} \\ \hline \frac{\partial Q_2^{(k)}}{\partial \delta_2} & \cdots & \frac{\partial Q_2^{(k)}}{\partial \delta_n} & \frac{\partial Q_2^{(k)}}{\partial V_2} & \cdots & \frac{\partial Q_2^{(k)}}{\partial V_n} \\ \vdots & \ddots & \vdots & \vdots & \ddots & \vdots \\ \frac{\partial Q_n^{(k)}}{\partial \delta_2} & \cdots & \frac{\partial Q_n^{(k)}}{\partial \delta_n} & \frac{\partial Q_n^{(k)}}{\partial V_2} & \cdots & \frac{\partial Q_n^{(k)}}{\partial V_n} \end{array}\right] \begin{bmatrix} \Delta \delta_2^{(k)} \\ \vdots \\ \Delta \delta_n^{(k)} \\ \Delta |V_2^{(k)}| \\ \vdots \\ \Delta |V_n^{(k)}| \end{bmatrix} \quad (3)$$

VI. STEADY-STATE MODEL OF STATCOM

From first principles and assuming the voltage source representation: [11]:

$$E_{vR} = V_{vR}(cos\delta_{vR} + jsin\delta_{vR}) \quad (4)$$

From the STATCOM equivalent circuit of figure 3;

$$S_{vR} = V_{vR}I_{vR}^* = V_{vR}Y_{vR}^*(V_{vR}^* - V_k^*) \quad (5)$$

Solution for the active and reactive converter powers yields equations (6) and (7) ;

$$P_{vR} = V_{vR}^2 G_{vR} + V_{vR}V_k[G_{vR}\cos(\delta_{vR} - \theta_k) + B_{vR}\sin(\delta_{vR} - \theta_k)] \quad (6)$$

$$Q_{vR} = V_{vR}^2 B_{vR} + V_{vR}V_k[G_{vR}\sin(\delta_{vR} - \theta_k) - B_{vR}\cos(\delta_{vR} - \theta_k)] \quad (7)$$

Active and reactive powers at bus k are given by equations (8) and (9);

$$P_k = V_k^2 G_{vR} + V_k V_{vR}[G_{vR}\cos(\theta_k - \delta_{vR}) + B_{vR}\sin(\theta_k - \delta_{vR})] \quad (8)$$

$$Q_k = -V_k^2 B_{vR} + V_k V_{vR}[G_{vR}\sin(\theta_k - \delta_{vR}) - B_{vR}\cos(\theta_k - \delta_{vR})] \quad (9)$$

Using these power equations, the linearized STATCOM model is given in equation (10), where the voltage magnitude V_{vR} and phase angle δ_{vR} are taken to be the state variables [11];

$$\begin{bmatrix} \frac{\partial P_k}{\partial \theta_k} & \frac{\partial P_k}{\partial V_k}V_k & \frac{\partial P_k}{\partial \delta_{vR}} & \frac{\partial P_k}{\partial V_{vR}}V_{vR} \\ \frac{\partial Q_k}{\partial \theta_k} & \frac{\partial Q_k}{\partial V_k}V_k & \frac{\partial Q_k}{\partial \delta_{vR}} & \frac{\partial Q_k}{\partial V_{vR}}V_{vR} \\ \frac{\partial P_{vR}}{\partial \theta_k} & \frac{\partial P_{vR}}{\partial V_k}V_k & \frac{\partial P_{vR}}{\partial \delta_{vR}} & \frac{\partial P_{vR}}{\partial V_{vR}}V_{vR} \\ \frac{\partial Q_{vR}}{\partial \theta_k} & \frac{\partial Q_{vR}}{\partial V_k}V_k & \frac{\partial Q_{vR}}{\partial \delta_{vR}} & \frac{\partial Q_{vR}}{\partial V_{vR}}V_{vR} \end{bmatrix} \quad (10)$$

Steady-State Model of SSSC

The SSSC voltage source is given by the equation (11) [16];

$$E_{cR}^{\rho} = V_{cR}^{\rho}\left(cos\delta_{cR}^{\rho} + jsin\delta_{cR}^{\rho}\right) \quad (11)$$

The boundary condition for V_{cR} and δ_{cR} are as given by equations (12) and (13);

$$V_{cR.min} \le V_{cR} \le V_{cR.max} \quad (12)$$

$$0 \le \delta_{cR} \le 2\pi \quad (13)$$

Considering the SSSC Thevenin equivalent circuit and equation, the expressions for the active and reactive powers at bus k are as in equations (14) and (15) [16];

$$P_k = V_k^2 Q_{kk} - V_k V_m[G_{km}cos(\theta_k - \theta_m) - B_{km}\sin(\theta_k - \theta_m)] - V_k V_{cR}[G_{km}\cos(\theta_k - \delta_{cR}) - B_{km}\sin(\theta_k - \delta cR \quad (14)$$

$$Q_k = -V_k^2 B_{kk} - V_k V_m[G_{km}sin(\theta_k - \theta_m) - B_{km}\cos(\theta_k - \theta_m)] - V_k V_{cR}[G_{km}sin(\theta_k - \delta_{cR}) - B_{km}cos(\theta_k - \theta cR \quad (15)$$

The active and reactive power relations for the converter are given in (16) and (17);

$$P_{cR} = V_{cR}^2 G_{mm} - V_{cR}V_k[G_{km}cos(\delta_{cR} - \theta_k) - B_{km}sin(\delta_{cR} - \theta_k)] - V_{cR}V_m[G_{mm}cos(\delta_{cR} - \theta_m) - B_{mm}sin(\delta_{cR} - \theta_m)] \quad (16)$$

$$Q_{cR} = -V_{cR}^2 B_{mm} - V_{cR} V_k [G_{km} \sin(\delta_{cR} - \theta_k) - B_{km} \cos(\delta_{cR} - \theta_k)] - V_{cR} V_m [G_{mm} \sin(\delta_{cR} - \theta_m) - B_{mm} \cos\delta_{cR} - \theta_m] \quad (17)$$

The linearized SSSC model is thus shown in equation (18) [16];

$$\begin{bmatrix} \frac{\partial P_k}{\partial \theta_k} & \frac{\partial P_k}{\partial \theta_m} & \frac{\partial P_k}{\partial V_k} V_k & \frac{\partial P_k}{\partial V_m} V_m & \frac{\partial P_k}{\partial \delta_{cR}} & \frac{\partial P_k}{\partial V_{cR}} V_{cR} \\ \frac{\partial P_m}{\partial \theta_k} & \frac{\partial P_m}{\partial \theta_m} & \frac{\partial P_m}{\partial V_k} V_k & \frac{\partial P_m}{\partial V_m} V_m & \frac{\partial P_m}{\partial \delta_{cR}} & \frac{\partial P_m}{\partial V_{cR}} V_{cR} \\ \frac{\partial Q_k}{\partial \theta_k} & \frac{\partial Q_k}{\partial \theta_m} & \frac{\partial Q_k}{\partial V_k} V_k & \frac{\partial Q_k}{\partial V_m} V_m & \frac{\partial Q_k}{\partial \delta_{cR}} & \frac{\partial Q_k}{\partial V_{cR}} V_{cR} \\ \frac{\partial Q_m}{\partial \theta_k} & \frac{\partial Q_m}{\partial \theta_m} & \frac{\partial Q_m}{\partial V_k} V_k & \frac{\partial Q_m}{\partial V_m} V_m & \frac{\partial Q_m}{\partial \delta_{cR}} & \frac{\partial Q_m}{\partial V_{cR}} V_{cR} \\ \frac{\partial P_{mk}}{\partial \theta_k} & \frac{\partial P_{mk}}{\partial \theta_m} & \frac{\partial P_{mk}}{\partial V_k} V_k & \frac{\partial P_{mk}}{\partial V_m} V_m & \frac{\partial P_{mk}}{\partial \delta_{cR}} & \frac{\partial P_{mk}}{\partial V_{cR}} V_{cR} \\ \frac{\partial Q_{mk}}{\partial \theta_k} & \frac{\partial Q_{mk}}{\partial \theta_m} & \frac{\partial Q_{mk}}{\partial V_k} V_k & \frac{\partial Q_{mk}}{\partial V_m} V_m & \frac{\partial Q_{mk}}{\partial \delta_{cR}} & \frac{\partial Q_{mk}}{\partial V_{cR}} V_{cR} \end{bmatrix} \quad (18)$$

VII. IMPLEMENTATION

A MATLAB based program was developed for the power flow analysis of electrical power systems without and with steady-state model of the FACTS controllers, STATCOM and SSSC. The flow chart algorithm is presented in figure 6.

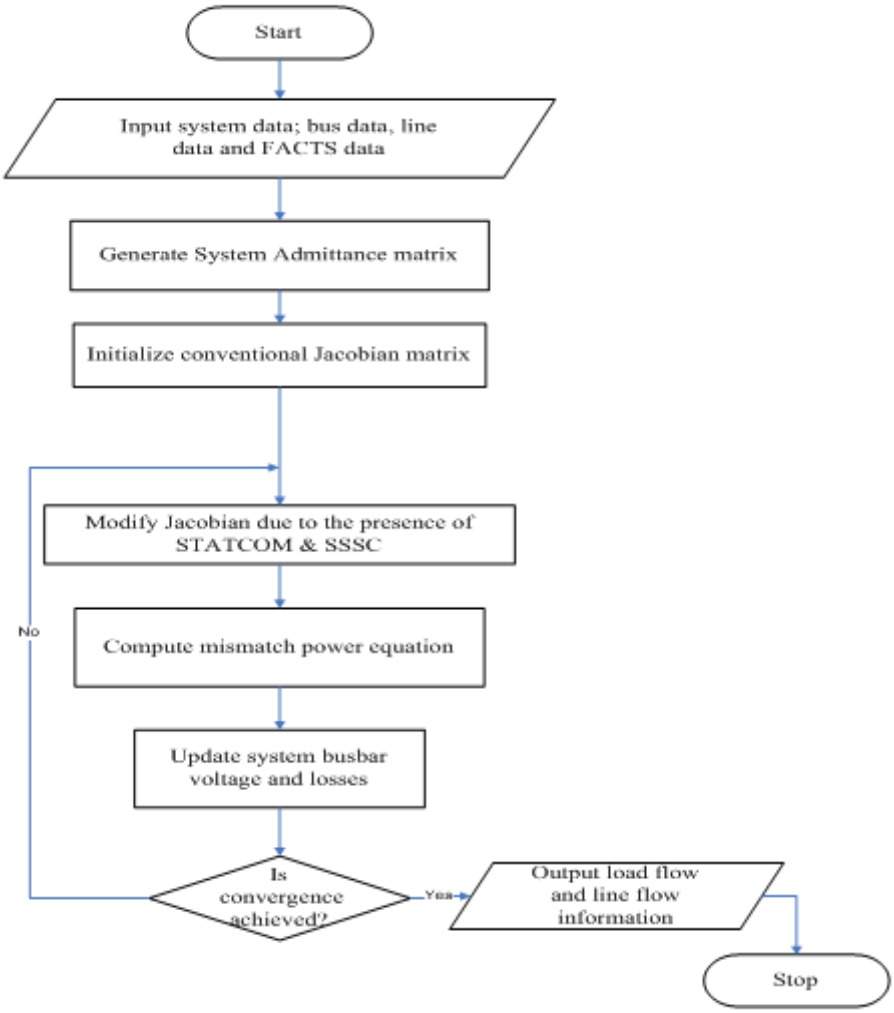

Figure 6: Flow Chart for the implementation

VIII. RESULTS AND DISCUSSIONS

This section presents the results of the power flow analysis for 330kV Nigerian 28-bus system under the various conditions i.e. with and without the application of FACTS devices. Bus 1 is taken as the reference bus which caters for losses on the other buses. Its phase angle is 0.
The Power Flow solutions, Line Flow and Losses were subsequently presented.

A. Power Flow Results

Case A: Power Flow solution without the Incorporation of STATCOM and SSSC

The result of the Power Flow Solutions for the system under consideration is as presented in Table 1. The accuracy is 1.000*e*-012 as specified in the power flow program while the maximum power mismatch has a value of 3.47417*e*-013. Convergence was achieved after 6 iterations.

Table 1: Power Flow Solution without SSSC and STATCOM using Newton-Raphson iterative technique

Bus No	Bus Name	V mag	Angle	Load		Generation	
				MW	MVAR	MW	MVAR
1	Egbin	1.050000	0	68.9	51.7	157.0774	534.3012
2	Delta	1.050000	11.8396	0	0	670	-20.0718
3	Aja	1.045002	-0.284	274.4	205.8	0	0
4	Akangba	1.018570	0.640607	344.7	258.5	0	0
5	Ikeja	1.025957	1.064812	633.2	474.9	0	0
6	Ajaokuta	1.061519	5.964331	13.8	10.3	0	0
7	Aladja	1.045662	10.27407	96.5	72.4	0	0
8	Benin	1.041416	6.322001	383.3	287.5	0	0
9	**Ayede**	**0.989663**	**1.970789**	**275.8**	**206.8**	**0**	**0**
10	Osogbo	1.031274	7.598416	201.2	150.9	0	0
11	Afam	1.050000	10.22838	52.5	39.4	431	317.5332
12	Alaoji	1.038084	9.568155	427	320.2	0	0
13	**New Heaven**	**0.976528**	**2.44244**	**177.9**	**133.4**	**0**	**0**
14	**Onitsha**	**0.993851**	**3.765763**	**184.6**	**138.4**	**0**	**0**
15	Benin-Kebbi	1.064558	13.60785	114.5	85.9	0	0
16	**Gombe**	**0.993725**	**3.685152**	**130.6**	**97.9**	**0**	**0**
17	Jebba	1.050483	13.29239	11	8.2	0	0
18	Jebbag	1.050000	13.55467	0	0	495	-101.197
19	Jos	1.050656	9.796701	70.3	52.7	0	0
20	Kaduna	1.03954	5.939198	193	144.7	0	0
21	Kainji	1.050000	16.46001	7	5.2	624.7	-267.215
22	Kano	1.010139	1.968138	220.6	142.9	0	0
23	Shiroro	1.050000	8.10979	70.3	36.1	388.9	55.22139
24	Sapele	1.050000	7.870247	20.6	15.4	190.3	113.8765
25	Abuja	1.049254	13.63136	110	89	0	0
26	Okpai	1.029469	6.031589	290.1	145	0	0
27	AES	1.050000	25.28002	0	0	750	-106.81
28	Calabar	1.050000	3.274312	0	0	750	319.2044
Total				**4371.8**	**3173.2**	**4456.977**	**844.8423**

In this case, the voltage profile for the unfortified system shows buses 9(Ayede), 13(New-Haven), 14(Onitsha) and 16(Gombe) to be having voltages below 1.0pu and thus has to be reinforced in order to maintain the bus voltage magnitudes at 1.0pu.

Case B: Power Flow Solution with the incorporation of STATCOM

This section presents the power flow solution when the system has been reinforced by the incorporation of STATCOM. Improvement in voltage magnitude at the four low voltage buses that is , buses 9(Ayede), 13(New-Haven), 14(Onitsha) and 16(Gombe) were presented in Table 2.

Table 2: Power Flow solution with STATCOM

Bus No	Bus Name	V mag	Angle	Load		Generation	
				MW	Mvar	MW	Mvar
1	Egbin	1.050000	0	68.9	51.7	166.2599	521.114
2	Delta	1.050000	11.6819	0	0	670	-23.3005
3	Aja	1.045002	-0.284	274.4	205.8	0	0
4	Akangba	1.019565	0.589399	344.7	258.5	0	0
5	Ikeja	1.026945	1.012784	633.2	474.9	0	0
6	Ajaokuta	1.062528	5.803115	13.8	10.3	0	0
7	Aladja	1.045663	10.11687	96.5	72.4	0	0
8	Benin	1.042400	6.160435	383.3	287.5	0	0
9	**Ayede**	**1.000000**	**1.797337**	**275.8**	**206.8**	**0**	**0**
10	Osogbo	1.034286	7.366748	201.2	150.9	0	0
11	Afam	1.050000	9.967147	52.5	39.4	431	375.3341
12	Alaoji	1.036044	9.320848	427	320.2	0	0
13	**New Heaven**	**1.000000**	**2.085903**	**177.9**	**133.4**	**0**	**0**
14	**Onitsha**	**1.000000**	**3.510967**	**184.6**	**138.4**	**0**	**0**
15	Benin-Kebbi	1.064558	13.32334	114.5	85.9	0	0
16	**Gombe**	**1.000000**	**2.862205**	**130.6**	**97.9**	**0**	**0**
17	Jebba	1.050649	13.00717	11	8.2	0	0
18	Jebbag	1.050000	13.27031	0	0	495	-118.64
19	Jos	1.000000	9.709066	70.3	52.7	0	0
20	Kaduna	1.029477	5.526562	193	144.7	0	0
21	Kainji	1.050000	16.17549	7	5.2	624.7	-268.667
22	Kano	1.000000	1.473855	220.6	142.9	0	0
23	Shiroro	1.050000	7.695393	70.3	36.1	388.9	129.7094
24	Sapele	1.050000	7.714093	20.6	15.4	190.3	99.95579
25	Abuja	1.028255	13.60363	110	89	0	0
26	Okpai	1.029469	5.617192	290.1	145	0	0
27	AES	1.050000	25.33482	0	0	750	-32.6636
28	Calabar	1.050000	3.227603	0	0	750	301.7016
Total				**4371.8**	**3173.2**	**4466.16**	**984.5439**

Case C: Power Flow Solutions with the incorporation of SSSC

Presented in this case is the power flow solutions when SSSC was incorporated in the system.There is a significant improvement in the voltage magnitude at the four low voltage buses that is , buses 9(Ayede), 13(New-Haven), 14(Onitsha) and 16(Gombe) as shown in Table 3.

Table 3: Power Flow solution with SSSC

Bus No	Bus Name	V mag	Angle	Load		Generation	
				MW	Mvar	MW	Mvar
1	Egbin	1.050000	0	68.9	51.7	-119.909	581.1085
2	Delta	1.050000	15.77806	0	0	670	-20.9867
3	Aja	1.045002	-0.284	274.4	205.8	0	0
4	Akangba	1.018395	1.966547	344.7	258.5	0	0
5	Ikeja	1.025784	2.390896	633.2	474.9	0	0
6	Ajaokuta	1.061805	9.90179	13.8	10.3	0	0
7	Aladja	1.045663	14.21267	96.5	72.4	0	0
8	Benin	1.041695	10.25936	383.3	287.5	0	0
9	**Ayede**	**1.000000**	**5.692264**	**275.8**	**206.8**	**0**	**0**
10	Osogbo	1.032672	11.37605	201.2	150.9	0	0
11	Afam	1.050000	16.78539	52.5	39.4	431	374.8972
12	Alaoji	1.036060	16.13899	427	320.2	0	0
13	**New Heaven**	**1.000000**	**9.17094**	**177.9**	**133.4**	**0**	**0**
14	**Onitsha**	**1.000000**	**10.399**	**184.6**	**138.4**	**0**	**0**
15	Benin-Kebbi	1.064558	17.89175	114.5	85.9	0	0
16	**Gombe**	**1.000000**	**12.9235**	**130.6**	**97.9**	**0**	**0**
17	Jebba	1.050548	17.57602	11	8.2	0	0
18	Jebbag	1.050000	17.83863	0	0	495	-107.994
19	Jos	1.000000	16.45181	70.3	52.7	0	0
20	Kaduna	1.029907	11.8995	193	144.7	0	0
21	Kainji	1.050000	20.7439	7	5.2	624.7	-267.781
22	Kano	1.000000	8.921075	220.6	142.9	0	0
23	Shiroro	1.050000	13.55912	70.3	36.1	388.9	118.9867
24	Sapele	1.050000	11.80914	20.6	15.4	190.3	109.9318
25	Abuja	1.028261	20.38124	110	89	0	0
26	Okpai	1.029469	11.48092	290.1	145	0	0
27	AES	1.050000	32.11241	0	0	750	-32.6868
28	Calabar	1.050000	4.599461	0	0	750	322.2772
		Total		**4371.8**	**3173.2**	**4179.991**	**1077.753**

Table 4 shows a comparison of the voltage magnitude at the low voltage buses with and without FACTS devices

Table 4: Voltage profile with and without FACTS devices

Bus No	Bus Name	Voltage Magnitude		
		NO FACTS	WITH STATCOM	WITH SSSC
9	Ayede	0.989663	1.000	1.000
13	New Heaven	0.976528	1.000	1.000
14	Onitsha	0.993851	1.000	1.000
16	Gombe	0.993725	1.000	1.000

Buses 9(Ayede), 13(New-Haven), 14(Onitsha), 16(Gombe) are the low voltage buses as shown in case A. To enhance the voltage magnitude at each of those buses, it therefore becomes necessary to reinforce the system by incorporating STATCOM and SSSC into it as in cases B and C. The updated voltages are shown in

Table 6. A comparison of the voltage improvement at the reinforced low voltage buses expressed as a percentage is presented by Table 5.

Table 5: Voltage improvement at reinforced buses

Bus No	% increase using STATCOM	% increase using SSSC
9	1.044	1.044
13	2.404	2.404
14	0.619	0.619
16	0.631	0.631

B. **Line flow and Losses**

The total active and reactive power losses is calculated by the power flow programme using Newton-Raphson iterative techque. The total active power loss and reactive power loss obtained for the base case (i.e without the incorporation of STATCOM and SSSC) are 85.177MW and 2328.358MVAR respectively. However, after the incorporation of STATCOM, the total active power loss is reduced to 85.031MW while the total reactive power loss reduced to 2304.868MVAR. Similarly, the total active power loss and reactive power loss obtained after the incorporation of SSSC are 84.259MW and 2087.875MVAR respectively. This is shown in Table 6. The effect of these devices expressed as a percntage decrease in losses is also presented in Table 7.

Table 6: Active and Reactive power Losses

Power Loss	No FACTS Controller	With STATCOM incorporated	With SSSC incorporated
Active Power(MW)	85.177	85.031	84.259
Reactive Power(MVAR)	2328.358	2304.868	2087.875

Table 7: Effect of STATCOM and SSSC on Active and Reactive Power Losses

	% decrease with STATCOM incorporated	% decrease with SSSC incorporated
Active Power Loss (MW)	0.171	1.078
Reactive Power Loss (MVAR)	1.009	10.326

IX. CONCLUSION

In this research work, a power flow analysis was carried out using MATLAB and the buses with low voltages were identified. The effect of the application of SSSC and STATCOM for enhancing voltage stability and loss reduction was demonstrated and compared. Both devices gave satisfactory result, raising the magnitude of the voltage at the buses where they were applied and at other load buses sufficiently to maintain the voltage at 1.0pu, thereby reinforcing the grid. The system losses were also significantly reduced. Active power and reactive power losses reduced by 0.171% and 1.009% respectively when STATCOM was applied. Also the incorporation of SSSC into the Nigerian grid system reduced active power and reactive power losses by 1.078% and 10.326% respectively. STATCOM and SSSC provided approximately the same effect on the voltage. However, SSSC gives a higher reduction in losses compared to STATCOM.

REFERENCES

[1] Saadat, H. (1999). *Power System Analysis*. United State of America: The McGraw-Hill Companies Inc.

[2] Metha, V.K. and Metha,R (2008) Principles of power System. New Delhi: S. Chand and Company Ltd

[3] Song and Johns

[4] Rambabu, C., Obulesu, Y. P. and Saibabu, C. (2011). Improvement of Voltage Profile and Reduce System Losses by using Multi Type Facts Devices. *International Journal of Computer Applications.* Vol. 13, pp 37-41

[5] Kalaivani, R. and Kamaraj, V. 2011. Modelling of Shunt FACTS Devices for Voltage Stability Enhancement . European Journal of Scientific Research. 61 (1) : 144-154.

[6] Komolafe, O. A. and Omoigui, M. O. (2000). *An Assessment of Reliability of Electricity Supply in Nigeria*. Conference Proceedings of the 4th International Conference on Power Systems Operation and Planning (ICPSOP), Accra, Ghana. 89 – 91.

[7] Komolafe, O. A., Adepoju, G. A. and Aborisade, D. O. (2011).Reinforcing the Nigerian 330kV transmission system to improve voltage profile and reduce power losses. *International Journal of Applied Science and Technology.* 1(5) : 186-200

[8] Kamarposhti, M. A. and Lesani, H. (2011) "Effects of STATCOM, TCSC, SSSC and UPFC on Static Voltage Stability" Electr Eng Vol 93 pp 33-42
[9] Kumkratug Prechanon(2010) "Coordination of Series and Shunt Flexible AC Transmission System Devices Based Voltage Source Converter for Improving Power System Stability" *American Journal Applied Sciences* Vol 8 (5) pp 495-498
[10] Adebayo, I.G., Adejumobi, I.A., and Adepoju, G.A (2012) Application of Load Tap – Changing Transformer (LTCT) to the Optimal Economic Dispatch of Generation of the Nigerian 330kV grid System *International Journal of Emerging Technologies in Sciences and Engineering* Vol.5(03), pp 40-50
[11] Acha, E., Fuerte-Esquivel, C. R., Ambriz-Pe´rez, A. and Angeles-Camacho, C. (2004). *FACTS; Modeling and Simulation in Power Networks.* England: John Wiley and Sons Ltd.
[12] Grainger, J. J. and Stevenson, W. D. (1994). *Power System Analysis.* New York: McGraw-Hill Inc.
[13] Alok, K. M. and Amar, K. B. (2006). Power System Stability Improvement using FACTS devices. *International Journal of Modern Engineering Research (IJMER).* Vol 01, pp. 666-672.
[14] Adepoju, G. A. and Komolafe, O. A. 2011. Analysis and Modelling of Static Synchronous Compensator (STATCOM): A comparison of Power Injection and Current Injection Models in Power Flow Study. *International Journal of Advanced Science and Technology.* 36 : 65- 76
[15] Onohaebi, O. S. (2009). "Power Outages in the Nigerian Transmission Grid" *Research Journal of Applied Sciences.* Vol. 04, pp 1-9.
[16] Seifi, A.R., Gholami S., and Shabanpour, A. 2010. "Power Flow Study and Comparison of FACTS: Series (SSSC), Shunt (STATCOM), and Shunt-Series (UPFC)". *Pacific Journal of Science and Technology*. 11(1):129-137.
[17] Adebayo, I.G., Aborisade, D.O. and Oyesina, K. A. (2013) ' Steady State stability Enhancement Using Static Synchronous Series Compensator (SSSC) : A case study of Nigerian 330kV grid Sytem', Research Journal in Engineering and Applied Sciences, 2 (1), pp. 54-61, USA.

American Journal of Engineering Research (AJER)
e-ISSN : 2320-0847 p-ISSN : 2320-0936
Volume-03, Issue-01, pp-106-111
www.ajer.org

Research Paper Open Access

Wavelet Based Medical Image Compression For Telemedicine Application

Neha S. Korde[1], Dr. A. A. Gurjar[2]
(Electronics & Telecommunication, Sipna College Of Engineering & Technology, Amravati /SGBAU, Amravati, India)
(Electronics & Telecommunication, Sipna College Of Engineering & Technology Amravati /SGBAU,Amravati, India)

Abstract: - In this paper, we discuss about a simple and lossless compression method for compression of medical images. Method is based on wavelet transform of medical application. Wavelets provide a mathematical way of encoding information in such a way that it is layered according to level of detail. These approximations can be stored using a lot less space than the original data. Here a low complex 2D image compression method using wavelets as the basis functions and the approach to measure the quality of the compressed image are presented. By using this coding method the compressed bit stream are all embedded and suited for progressive transmission. The reconstructed image is synthesized using the estimated detail matrices and information matrix provided by the Wavelet transform. In this paper, different wavelets have been used to perform the transform of a test image. The compressed image can be accessed and sent over telemedicine network.

Keywords: - *Medical Images, Progressive Transmission, Telemedicine Network, Wavelet Transform, 2D Image Compression.*

I. INTRODUCTION

Medical images are very important in the field of medicine. Every year, terabytes of medical image data are generated through advance imaging modalities such as magnetic resonance imaging (MRI), computed tomography (CT), digital subtraction angiography (DSA), positron emission tomography (PET), X-rays and many more recent techniques of medical imaging. But storing and transferring these huge voluminous data could be a tedious job. some of the medical images are shown in fig. 3.

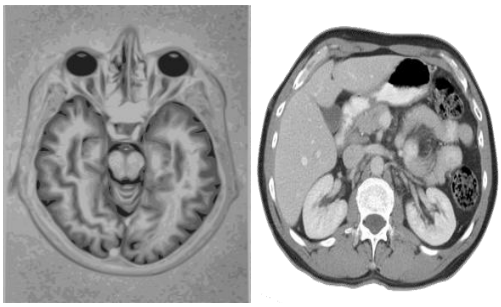

Fig 1. MRI IMAGE OF BRAIN CT IMAGE OF ABDOMEN

A compression of medical imagery is an important area of biomedical and telemedicine. In medical image compression diagnosis and analysis are doing well simply when compression techniques protect all the key image information needed for the storage and transmission. As in telemedicine, videos and the medical images are transmitted through advanced telecommunication links, so the help of medical image compression to compress the data without any loss of useful information is immense importance for the faster transfer of the information. There are many medical image compression techniques are available. Technically, all image data

compression schemes can be broadly categorized into two types. One is reversible compression, also referred to as "lossless." A reversible scheme achieves modest compression ratios of the order of two, but will allow exact recovery of the original image from the compressed version. An irrreversible scheme**,** or a "lossy" scheme, will not allow exact recovery after compression, but can achieve much higher compression ratios. To avoid the above problem, there may be third option that the diagnostically important is transmission and storage of the image is lossless compressed. This is the case of lossless compression.

Telemedicine is the use of telecommunication and information technologies in order to provide clinical health care at a distance. It is the use of medical information exchanged from one site to another via electronic communications. Telemedicine includes a growing variety of applications and services using two-way video, email, smart phones, wireless tools and other forms of telecommunications technology. The other popular technology is the two-way interactive television (IATV). This is used when a 'face-to-face' consultation between the health expert and the patients become mandatory. It is usually between the patients and their provider in one location and a specialist in another location.

II. FRAME WORK OF OUR PROPOSED METHOD

2.1 EXISTING METHODS

2.1.1. **Medical Image Compression Using Integer Multi Wavelets Transform**

In the proposed method integer wavelet transform is used in compressing the image. The compressed image is decomposed by the multiwavelet transform. The encoding is done based on maximum value of image pixel, original value is reduced based on the neighboring pixel value. The final image obtained by this process is an encoded bit stream image which is in binary image (i.e 0's and 1's). Receiver decodes the incoming bit stream value, decompress it and reconstructs the original image. Major advantage of this method is that the mean square error is reduced when compared to other transforms and the compression ratio is significantly increased.

The original image is taken as a test images as shown in fig 1.Input image of size is 256 x 256

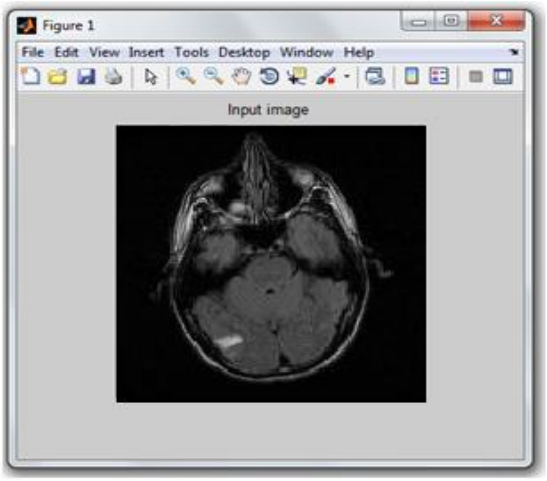

Fig 2.Input Image

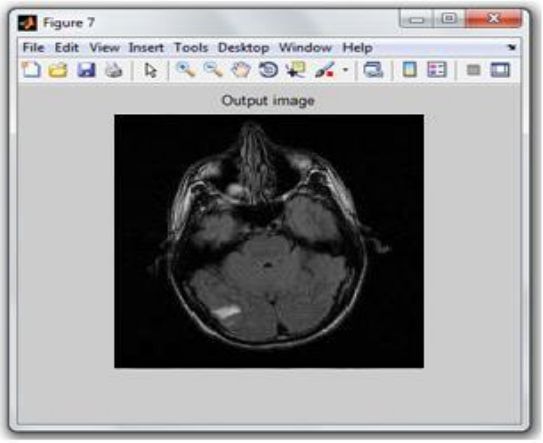

Fig 3.Reconstructed Image

Table 1: Performance Metric Measurements of PSNR, MSE,CR

S. no	Technical parameter	Existing technique	Proposed technique
1	PSNR	26.50	37.32
2	MSE	65.50	57.50
3	CR	80.50	87.50

2.1.2. ROI-based DICOM image compression for telemedicine

Many classes of images contain spatial regions which are more important than other regions. For medical images, only a small portion of the image might be diagnostically useful, but the cost of a wrong interpretation is high. Hence, Region Based Coding (RBC) technique is significant for medical image compression and transmission. A CT or MRI image contains three parts, ROI (the diagnostically important part), Non-ROI image part, and the background (part other than image contents) .The ROI is selected by expert radiologists. Depending on the selected part ROI-mask is generated in such a way that the foreground is totally included and the pixel values in the background are made zero. The background regions though they appear to be black in colour, they do not have zero grey level values.

Algorithm is implemented on a group of MR DICOM images. SPIHT is proved to be the best. But for ROI-based compression computational complexity is also one of the important issues to be considered, while addressing real time applications. A new and simple algorithm as explained above is used to encode the image. Original image formatted in DICOM format of size 256 X 256 with 8 bit resolution is input to software. The 'compressed image' is the image which is generated at the decoder side after reconstruction process. The output of encoder is a bit stream of numbers arranged in a manner so as to support the progressive transmission, with initial part as a ROI compressed with run length encoding. This bit stream is transmitted over the telemedicine network using GSM mobile device.

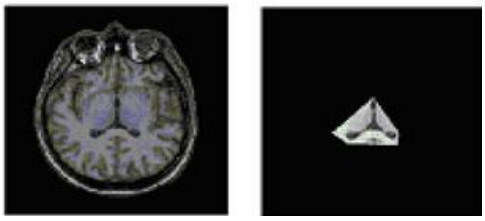

Fig 4. Original image Region of interest

2.1.3. Medical Image Compression using Wavelet Decomposition for Prediction Method

Method is based on wavelet decomposition of the medical images followed by the correlation analysis of coefficients. The correlation analyses are the basis of prediction equation for each sub band. Predictor variable selection is performed through coefficient graphic method to avoid multicolinearity problem and to achieve high prediction accuracy and compression rate. The method is applied on MRI and CT images.

Two MRI and two CT gray scale standard test images as shown in figure 2 of size128*128 have been taken from world wide web for experiments and comparisons. MATLAB 7.0 has been used for the implementation of the proposed approach and results have been conducted on Pentium-1V, 3.20 GHz processor with a memory of 512 MB. BPP (Bits Per Pixel) metric is evaluated to compile compression result. Every image was decomposed into three scales with 10 wavelet sub bands.

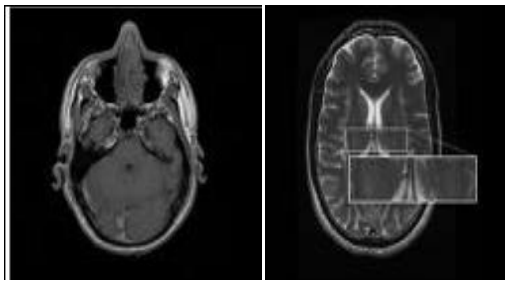

Fig 5. MRI 1 MRI 2

Table 2: Comparison of Compression Rate In Bits/Pixel Of Different Methods With Proposed Method

Type	Method		
	SPHIT	JPEG 2000	Proposed
MRI -1	2.53	2.42	1.45
MRI -2	3.11	3.12	1.51
MRI Average	2.82	2.77	1.48

2.2 PROPOSED METHOD

In the proposed work wavelet transform is the tool which we are going to use for medical image compression Wavelet transform has some of the advantages over the traditional transforms like

1. More robust under transmission and decoding errors.
2. Better matched to the HVS characteristics.
3. Good frequency resolution at lower frequencies, good time resolution at higher frequencies – good for natural images.

2.2.1 Basics Of Wavelet Transform

The wave is an infinite length continuous function in time. In contrast, wavelets are localized waves. A wavelet is a waveform of an effectively limited duration that has an average value of zero. Wavelet transform of a function is the improved version of Fourier transform. It provides the time-frequency representation. . The fundamental idea of wavelet transforms is that the transformation should allow only changes in time extension, but not shape. This is effected by choosing suitable basis functions that allow for this Changes in the time extension are expected to be conform to the corresponding analysis frequency of the basis function. Wavelet transforms are based on small wavelets with limited duration.

The Continuous Wavelet Transform or CWT formally it is written as:

$$\gamma(s,r)=\int f(t)\ \psi^{*}_{s,r}(t)dt \qquad (1)$$

where * denotes complex conjugation. This equation shows how a function $f(t)$ is decomposed into a set of basis functions $\psi s,-(t)$, called the wavelets. The variables s and - are the new dimensions, scale and translation, after the wavelet transform. equation (2) gives the inverse wavelet transform

$$f(t)=\iint\gamma(s,r)\psi s,r(t)drds \qquad (2)$$

The wavelets are generated from a single basic wavelet $\psi(t)$, the so-called mother wavelet, by scaling and translation:

$$\Psi_{s,r}(t)=1/\sqrt{s}\ \psi(t-r/s) \qquad (3)$$

In (3) s is the scale factor, - is the translation factor and the factor s-1/2 is for energy normalization across the different scales.

2.2.2 DISCRETE WAVELET TRANSFORM

Discrete wavelets are not continuously scalable and translatable but can only be scaled and translated in discrete steps. This is achieved by modifying the wavelet representation (3) to create

$$\Psi_{j,k}(t)=1/\sqrt{s_0^{j}}\psi(t-kr_0s_0/s_0^{j}) \qquad (4)$$

Although it is called a discrete wavelet, it normally is a (piecewise) continuous function. In (10) j and k are integers and $s0 > 1$ is a fixed dilation step. The translation factor -0 depends on the dilation step. The effect of discretizing the wavelet is that the time-scale space is now sampled at discrete intervals. We usually choose $s0 = 2$ so that the sampling of the frequency axis corresponds to dyadic sampling. This is a very natural choice for computers, the human ear and music for instance. For the translation factor we usually choose -0 = 1 so that we also have dyadic sampling of the time axis. In the analysis of both numerical and functional methodologies, a Discrete Wavelet Transform (DWT) can be used. DWT is a kind of wavelet transform for which the wavelet functions are discretely sampled by the other wavelet transforms. A major advantage of discrete wavelet transform over the Fourier transform is the effect of temporal resolution.

Different types of wavelets are given below these all types of wavelets are used for image compression for telemedicin application

1. Harr wavelet
2. BNC wavelet
3. Coiflet wavelet
4. Daubechies wavelet
5. Bionomial wavelet
6. Mathieu wavelet
7. Legendre wavelet
8. Beta wavelet
9. Hermitian wavelet
10. Hermitian Hat wavelet
11. Meyer wavelet
12. Maxican Hat wavelet
13. Shannon wavele

3. FIGURE

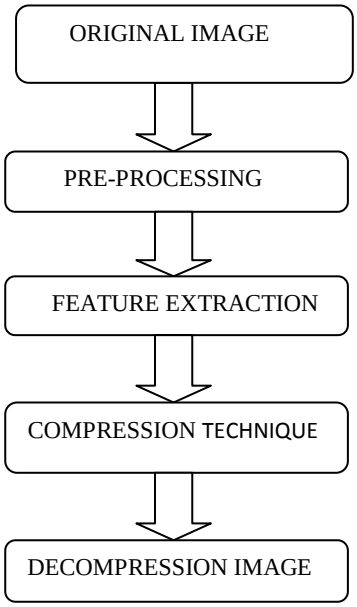

Fig 6.Flow Diagram of The Proposed Method.

Steps involved in the process:

Step 1: Consideration of Original Image

Initially the input image is fed to the system, the input image may be a highly non stationary one, hence we convert the size of the input image to 256 x 256. In gray scale coding even if the input image is a colour image it will be converted into gray scale image using RGB converter.

Step 2:Pre-Processing

After the input image is taken, in the Pre-processing step each and every neighborhood pixel of an input image should have a new brightness value corresponding to the output image. Such pre-processing operations are also known as filtration. Types are enhancement (image enhancement for shape detection), image restoration (aim to stem degradation using knowledge about its nature of an image; i.e. relative motion of camera image and object, wrong lens focus etc.), image compression

Step 3: Feature Extraction

In the extraction process the input image data is segmented and then the input data will be transformed into a reduced represented set of features. It is useful on a selection of situations Where it helps to stem data information that is not important to the specific image processing task (i.e. background elimination).Transforming the input data into a particular set of features is called as feature extraction.

Step 4: Compression technique

Basically, there are two types of image compression techniques used with digital image and vedio, lossy and lossless. Lossy compression methods include DCT (Discrete Cosine Transform), Vector Quantization and Huffman coding. Lossless compression method include RLE scheme (Run Length Encoding), string-table compression and LZW (Lempel Ziv Welch). Here we will use wavelet transform for compress the medical image.

Step 5: Decompressed Image

In the decompression process, the original image is extract.

III. CONCLUSION

Medical image compression is the current research area of interest. In this paper focus is on the implementation of lossless image data code, when the input image data is encrypted before using compression technique. Hence this is more suitable for the transmission of Medical images for Telemedicine application. We are using different types of wavelet based compression which has much better coding efficiency and less computational complexity.

IV. ACKNOWLEDGEMENTS

I am very much thankful to Dr.A.A.Gurjar sir, faculty of Electronics & Telecommunication ,Sipna COET,for their valuble guidance.

REFERENCES

Journal Papers:

[1] Mr. E. PraveenKumar, Dr. M. G. Sumithra, Medical Image Compression Using Integer Multi Wavelets Transform For Telemedicine Applications, *International Journal Of Engineering And Computer Science ISSN:2319-7242 Volume 2 Issue 5 May, 2013.*

[2] S. M. Ramesh, Dr. A. Shanmugam, Medical Image Compression using Wavelet Decomposition for Prediction Method, *International Journal of Computer Science and Information Security,Vol. 7, No. 1, 2010.*

[3] Anuja P Parameshwaran, Manisha Gaonkar, DCT And DWT In Medical Image Compression, *International Journal on Advanced Computer Theory and Engineering, Volume-2, Issue-3, 2013.*

[4] Zixiang Xiong, Kannan Ramchandran, Michael T. Orchard, and Ya-Qin Zhang, A Comparative Study of DCT- and Wavelet-Based Image Coding, *Ieee Transactions On Circuits And Systems For Video Technology, Vol. 9, No. 5, August 1999.*

[5] Karen Lees " Image Compression Using Wavelets" *May 2002.*

American Journal of Engineering Research (AJER)
e-ISSN : 2320-0847 p-ISSN : 2320-0936
Volume-03, Issue-01, pp-112-118
www.ajer.org

Research Paper Open Access

Modified Tj's Method for Yield Line Analysis and Design of Slabs

Orumu S.T., Nelson T.A.
Department of Civil Engineering and Hydrology
Niger Delta University Wilberforce Island, Nigeria

Abstract: - The Yield line method is widely used for the analysis and design of reinforced, concrete slabs. The method here described relies on three parameters - the Geometry of the plate, the length of Yield lines & the orientation of the Yield lines. Here the governing equation is broken into integrable parts such that the internal work is taken as the sum of all Yield lines including the negative Yield lines multiplied by (2 + number of nodal moments) and the average moment (ḿ). The external work is taken as the product of the load and the sum of the volume of each integral part with the deflection taken as the length of the positive Yield lines at the segment. The solution for the average bending moment over the Yield lines reduces the solution of plates to simple geometry. Results from the method compares to those of the work method and equilibrium method.

Keywords: *- Equilibrium method, Nodal moments, Pyramidal factor and Prism factor, Yield lines, Work method.*

I. INTRODUCTION

Studies in the yield- line theory of concrete slabs which have largely avoided the question of the distribution of the support reaction were addressed by Johnarry [1]. A great deal of researchers [2],[3],[4],[5]and [6] has worked extensively on Johansen discovery with the aim of tying the yield line theory with more classical plastic theory. It appears that none of the researchers has used or considered the length of the yield line in each segment as having all the characteristics required to determine the internal work and external work which in turn gives the load or carrying capacity of the slab. The work of Johnarry[1] gave an insight into further research which revealed that the Geometry of the plate and the length of the yield lines are just enough for the analysis and design of slabs.

II. METHOD

A review of Johnarry's work [1] (referred in the proposed method as the TJ's method) has the yield-line as the s-axis and its normal n-axis. The yield –line method equation is

$$\int md\left(\frac{dw}{dn}\right) = \int qdsdndw..... (1)$$

Where dw is the elemental deflection
dividing through by (dw/dn), we have

$$\int mds = \int qdsdn\int dn.....(2)$$

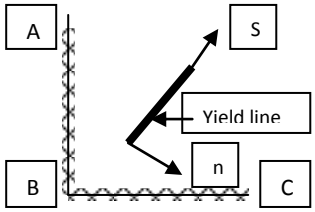

Fig 1-Analysis axes s & n

Equation (2) requires the slab to be divided into continuously integrable components, which must be the same rigid components produced by the yield – lines. The length of the yield lines in each component will be relied, upon to achieve this.

Integration is implied in equation (2) and this must be carried out along the yield lines for example, in fig 1 the yield – line BD relates to the support axes AB and BC. For areas A_1 and A_2 on both sides of the yield – line

$M_F = 2mL_{BD} = q\ A_1\ (a_R - a_q)_1 + qA_2\ (a_R - a_q)_2$ ……(3)

Where M_F is the total amount of forces on both sides of a yield line, a_R is the lever arm to the load centre and a_R is the lever – arm to the reaction centre. Note that the yield – line length L_{BD} is used twice in equation 3. For the case of a UDL called q, the reaction R_j is

$R_j = qA_j$……(4)

2.1 Theoretical formulation of proposed method

This study has shown that it is unnecessary to begin to look for a_R and a_q as proposed by the TJ's method rather the value of $(a_R - a_q)$, should always be taken as the length of the yield line at the segment divided by the pyramidal factor or prism factor. In case of a Udl. this means that eqn 3 is modified as

$$M_F = qA1\left(\frac{LBD}{F1}\right) + qA_2\left(\frac{LBD}{F_2}\right) + \ldots\ldots\ldots + qA_n\left(\frac{Lij}{Fn}\right) \ldots\ldots(5)$$

For pyramidal factor F = 3 , eqn 5 becomes

$$M_F = qA_1\frac{LBD}{3} + qA_2\frac{LBD}{3} \ldots\ldots\ldots\ldots\ldots\ldots(6)$$

For prism factor F = 2

$$M_F = qA_1\frac{LBD}{2} + qA_2\frac{LBD}{2} \ldots\ldots\ldots\ldots\ldots\ldots(7)$$

In the method here described the equations 6 & 7 are used in combination in most cases

2.1.1 Pyramidal factor

The volume of a rectangular pyramid is given by

$$vol = \frac{1}{3}lbh = \frac{l}{3}area$$

The volume of a right angle triangular pyramid is given by

$$vol = \frac{1}{2}Lb\frac{h}{3} = \frac{lbh}{6}$$

2.1.2 Prism factor

The volume of a prism is given by

$$vol = lb\frac{h}{2} = \frac{lbh}{2} = \frac{h}{2}area$$

In fig 2 below

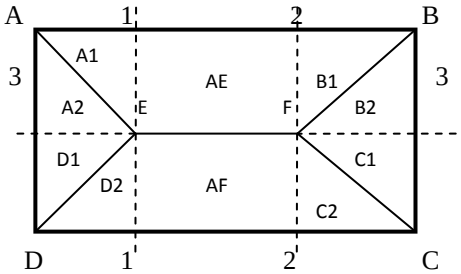

Fig. 2 Segments A1E 3, D1E3, B2F3 and C2F3 are pyramids, while segment 1221 is a prism.

$$M_F = q\left[\frac{LAE}{3}(A_{A1}+A_{A2}) + LDE\left(\frac{AD_1+AD_2}{3}\right) + LBF\left(\frac{AB_1+AB_2}{3}\right) + LCF\left(\frac{AC_1+AC2}{3}\right) + \frac{LEF}{2}(AE+AF)^3\right] \ldots\ldots\ldots\ldots(8)$$

The left hand side

$MF = 2ML_{BD}$ ……..(9)

Needs modification as reported by researchers [1][2]. Here it has been established that when a yield –line meets a free edge, a nodal moment will occur at the dip. This fact is employed in this method to mean than equation 9 should be modified to carter for cases with free ends. Thus it becomes.

M_F = M (2 + no of free edges) L_{BD} ……(10)

Equation 10 is the required internal work in the slab, while the right hand side of equations (5), (6), (7) & (8) are the external work done in the slab.

2.2 Point Loads

In the case of point loads, the internal work remains the same, but the external work needs to be modified as follows equation 8 becomes.

$$M_F = \frac{P}{L}\left[LAE\left(A_{A_1} + A_{A_2}\right) + LBD\left(A_{D_1} + A_{D_2}\right) + \ldots\ldots\ldots LEF\left(A_{A_E} + A_{A_E}\right)\ldots\ldots\ldots\ldots\ldots(11)\right]$$

2.3 Clamped Edges and Re-Entrant Corners

Here the internal work shall include the sum of positive and negative Yl, but the external work shall only deal with volume displaced by the positive Yl alone.

III Results of Interest

It is assumed that, the user of the proposed method is familiar with the theory of yield lines and so should be able to draw yield lines for a given supported slab using the rules of Yl postulation[5][6].

3.1 Simply Supported Square Slab Loaded Uniformly

solution:

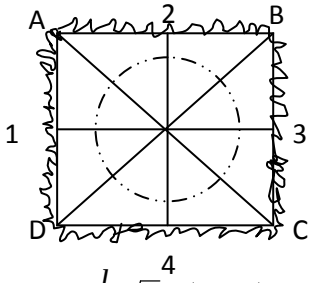

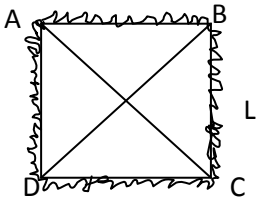

FIG 3

Internal Work $M_{f_m} = m\frac{l}{2}\sqrt{2}.4(2+0) = 4ml\sqrt{2}$

External Work $M_{F_E} = q\left[\frac{l}{2}.\frac{l}{2}.\frac{l}{2}\sqrt{2}.\frac{1}{3}X4\right] = \frac{qL^3\sqrt{2}}{6}$

Equating internal work to external work

$$m = \frac{ql^2}{24}$$

$M=0.0417ql^2$

$m_{classical}=0.0479ql^2$

3.2 Case 2: Clamped square slab loaded uniformly

$$M_{F_{internal}} = m\left[\frac{l\sqrt{2}}{2}x4 + 4l\right][2+0]$$

$$= 8ml\left(1+0.5\sqrt{2}\right)$$

$$M_{f_{external}} = q\left(\frac{l}{2}.\frac{l}{2}\sqrt{2}.\frac{1}{3}x4\right) = \frac{ql^3\sqrt{2}}{6}$$

Equating

$$m = \frac{ql^2}{48}\frac{\sqrt{2}}{\left(1+0.5\sqrt{2}\right)} = 0.0172589ql^2$$

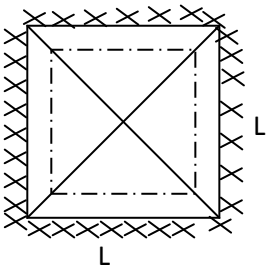

Fig 4

$$m = \frac{ql^2}{57.941}$$

3.3 Case 3: Simply supported rectangular slab loaded uniformly

Solution

Internal work

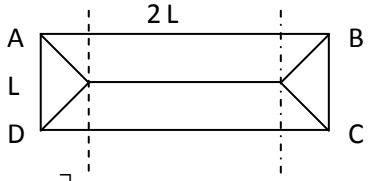

$$M_{f\,\text{int}} = m\left[4\frac{l}{2}\sqrt{2} + l\right](2+0) = 2ml\left(1+2\sqrt{2}\right)$$

$$M_{ext} = q\left(\frac{1}{2}.\frac{l}{2}.\frac{l}{2}\sqrt{2}.\frac{l}{3}x4 + l.l.\frac{l}{2}\right) = \frac{ql^3}{6}\left(3+\sqrt{2}\right)$$

Equating internal work to external work

$$m = \frac{ql^2}{12}\frac{\left(3+\sqrt{2}\right)}{\left(1+2\sqrt{2}\right)} = 0.09608414ql^2$$

$$m = \frac{ql^2}{10.408}$$

Mclassical = 0.10397ql^2

3.4 Case 4 All round clamped rectangular slab loaded uniformly

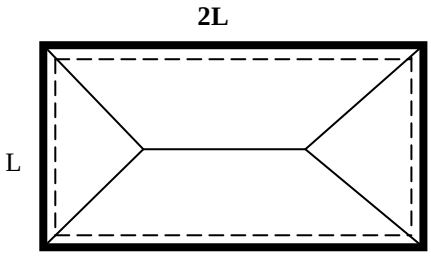

Internal work $= M\left[4.\frac{1}{2}\sqrt{2} + L + L + L + 2l + 2l\right][2+0]$

$$= 4ML\left[\sqrt{2} + 3.5\right]$$

External work same as that in case 4

External work $= \frac{ql^3}{6}\left(3+\sqrt{2}\right)$

Equating

M = 0.0374273ql^2

$$m = \frac{ql^2}{26.9185}$$

$$M_{dassical} = 0.0365\,ql^2$$

3.5 Case 5: Simply supported square slab loaded with a point

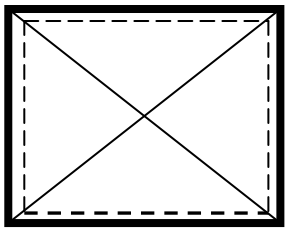

$$M_{f\,\text{int}ernal} = ml\frac{\sqrt{2}}{2}x4(2+0) = 4l\sqrt{2}m$$

$$M_{fexternal} = \frac{p}{l}\left(\frac{l}{2}.\frac{l}{2}\right)x4x\frac{l\sqrt{2}}{2}$$

Equating

$$m = \frac{pl2\sqrt{2}}{2x42\sqrt{2}} = \frac{pl}{8}$$

3.6 Case 6: Simply supported rectangular slab loaded with a Point load

$$M_{F\,internal} = M\left[\frac{l\sqrt{2}}{2}x4 + L\right][2+0]$$

$$= 2ml\left(2\sqrt{2}+1\right)$$

$$M_{F\,external} = \frac{P}{l}\left[\frac{l}{2}.\frac{l}{2}\right]4.\frac{l}{2}\sqrt{2} + \frac{p}{l}.lll$$

$$= Pl^2\left(1+0.5\sqrt{2}\right)$$

Equating

$$m = \frac{pl}{2}\frac{\left(1+0.5\sqrt{2}\right)}{\left(1+2\sqrt{2}\right)}$$

$$m = \frac{pl}{4.4852}$$

M = 0.222951pl

3.7 Case 7: Clamped square plate loaded with a point load

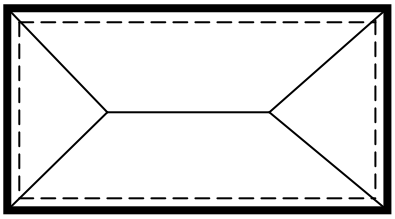

$$M_{F\,internal} = M\left[\frac{L\sqrt{2}}{2}x4 + 4L\right][2+0]$$

$$= 8ml\left(1+0.5\sqrt{2}\right)$$

$$Mext. = \frac{Pl^2\sqrt{2}}{2}(fromcase5)$$

Equating

$$m = \frac{Pl^2}{16l}\frac{\sqrt{2}}{\left(1+0.5\sqrt{2}\right)}$$

M = 0.051777pL

M = pl/19.31371

3.8 Case 8: Clamped rectangle plate loaded with a point load.

$$\text{M}_{\text{finternal}}\ M\left[\frac{L\sqrt{2}}{2}X4 + L + l + l + 2l + l\right][2+0]$$

$$= 4ml\left(\sqrt{2}+3.5\right)..... (case4)$$

$$M_{fexternal} = Pl^2\left(1+0.5\sqrt{2}\right)..... (case6)$$

Equating

$$m = \frac{pl}{4}\frac{\left(1+0.5\sqrt{2}\right)}{\left(3.5+\sqrt{2}\right)}$$

= 0.08685pl

$$m = \frac{pl}{11.5147}$$

3.9 Case 9: Square plate s- s on three sides with one edge free acted upon by a UDL q

Solution

Internal work $= \left[\frac{2l}{2}\sqrt{2} + L\right][2+1]$

$$= 3ml\left[\sqrt{2}+1\right]$$

$$= 3ml\left(1+\sqrt{2}\right)$$

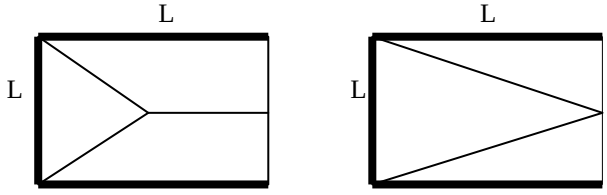

Case A

Case B

External work

$$= q\left[\frac{l}{2}.\frac{l}{2}.\frac{l\sqrt{2}}{2}.\frac{1}{3}.2 + l.\frac{l}{2}.\frac{l}{2}.\frac{1}{2}\right]$$

$$= \frac{ql^3}{24}\left[3+2\sqrt{2}\right]$$

Equating

$$m = \frac{ql^2}{72}\left[\frac{3+2\sqrt{2}}{1+\sqrt{2}}\right]$$

$m = 0.0498025ql^2$

$$m = \frac{ql^2}{20.0793}$$

Case B

$$m_{\text{int.}} = m.2.\sqrt{l^2} + \frac{l^2}{4}x[2+1]$$

$$= 6ml\sqrt{1.25}$$

$$m_{ext} = ql.l\frac{l\sqrt{1.25}}{3} = \frac{ql^3\sqrt{1.25}}{3}$$

Equating

$$m = \frac{ql^2}{18}$$

$M = 0.05556ql^2$

The results for case A and Case B for plate S-S on three sides with one edge free acted upon by a Point load Using the described method are respectively

$$m = \frac{pl}{12} \text{ and } m = \frac{pl}{6}$$

3.10 Case 10 Irregular plates

A typical example, which was earlier solved using the work method and the reaction method shown below, shall be solved using the described method

Solution

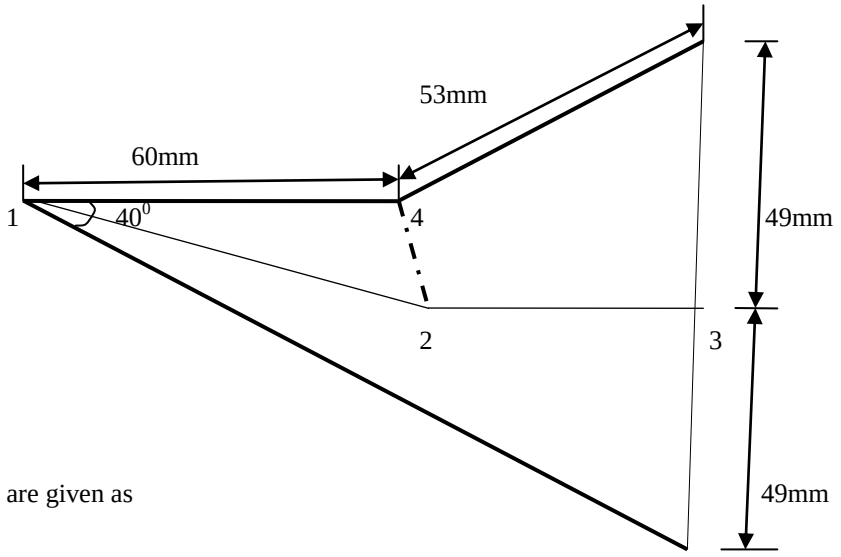

The lengths of the line measured are given as

YL 1-2 = 69mm
YL 2.3 = 37. 5mm
YL 2-4 = 24

Internal Energy $= (69+37.5+24)(2+1)m = 391.5m$

To obtain the external Energy, three cases where considered to demonstrate the method. The sharing of the area of influence each line such that the division line is perpendicular to yield line 2-3 for case 1; perpendicular to yield line 1-2 for case 2 and the simplest form was sharing the area equally to both yield line 2-3 and yield line 1-2. Remember that yield line 2-4 is a negative one and does not influence the external energy as described earlier.

3.10.1 case 1

$$\text{External Energy} = \left(\frac{1}{2}.68.51.5.\frac{1}{2}.7.3.5\right)\frac{69}{2}q + \frac{(55+98)}{2}.37.5.\frac{37.5}{2}q$$

$$= 114621.11875q$$

Equating

$$m = 292.77q$$

3.10.2 case 2 perpendicular to YL 1-2 = 69m

$$Mext = \left(\frac{1}{2}.69.51 + \frac{1}{2}.14.6\right)\frac{69}{2}q + \left(\frac{45+30}{2}\right).\left(\frac{98+55}{2}\right).\frac{37.5}{2}q$$

$$= 62151\ .75q + \left(\frac{45+30}{2}\right).\left(\frac{98+55}{2}\right).\frac{37.5q}{2}$$

= 115940.8125

$$m = \frac{115940.8125}{391.5} = 296.145115q$$

M = 296.15q

M=313.6q (work method)

% diff = - 5.57%

3.10.3 case 3 equal half area

$$mext = \left[\frac{1}{2}.69.51 + \frac{1}{2}.14.6 + \frac{75}{2}.\frac{153}{2}\right]\frac{1}{2}\left[\frac{69}{2} + \frac{37.5}{2}\right]q$$

= 124345.4063q

M_{int} = 391.5m

Equating

$$m = \frac{124345.4063}{391.5}$$

M = 317. 6q

% diff = + 1.28%

IV CONCLUSION

The reliable results obtained from the method herein described when compared to classical methods have given an insight to another view of yield line analysis. The main advantage of the proposed method is in the ease with which it can handle irregular plates. The example treated in case 10 is a clear case which could be handled with such ease and accuracy. Several plates in Engineering practice have shown serious yield lines which is beyond the realm of elastic analysis. The existing methods of handling this which is in fracture mechanics are not easily comprehended by those in practice who need simple but accurate hand method to handle such problems. The work can be extended to solving problems of cracks in structural walls and slabs, highway pavements, earth roads and bond walls around storages with high temperature gradients among others. This is possible because only the lengths of the yield lines and the geometry of the plate are required for their solutions. The work is limited to the average moment required to create the mechanism and by extension the maximum moment in each of the yield lines. The deflection of the plates are not discussed in this paper but can be researched into.

REFERENCES

[1] Johnarry T. Support reaction and its implication for orthotropy in the yield line method-Magazine of concrete research, ICE London, vol. 44, N161 1992

[2] Johnarry T. –Simpler nodal forces for yield line analysis-Magazine of concrete research, ICE London, vol. 37, N131 1984

[3] Timoshenko S.P. and Woinowsky-Krieger S. –Theory of Plates and Shells, McGraw-Hill Kogakusha Ltd.-1959

[4] British Standards Institution BS 8110, 2008-Structural use of Concrete

[5] Johansen K.W.- Yield line formular for slab- Cement and Concrete Association London-English Edition 1972

[6] Reynolds C.E., Steedman J.C.- Reinforced concrete designers handbook 10th edition 1988

American Journal of Engineering Research (AJER)
e-ISSN: 2320-0847 p-ISSN : 2320-0936
Volume-03, Issue-01, pp-119-127
www.ajer.org

Research Paper Open Access

Flexural Behaviour of Reinforced Concrete Beams with Partial Replacement of GGBS

S.P.Sangeetha[#1], P.S Joanna[#2]
[#1(]*Research Scholar, Civil Engineering Department, Hindustan University, Chennai, India)*
[#2] *(Professor, Civil Engineering Department, Hindustan University, Chennai, India)*

Abstract: **-** The present study focuses on the structural behavior of reinforced concrete beam with Ground Granulated Blast furnace Slag (GGBS).It is an inexpensive replacement of Ordinary Portland Cement (OPC) used in concrete, and it improves fresh and hardened properties of concrete. Experimental investigation included testing of eight reinforced concrete beams with and without GGBS. Portland cement was replaced with 40% GGBS and Glenium B-233 was used as superplastisizer for the casting of beams. The results of laboratory investigation on the structural behavior of reinforced concrete beams with GGBS are presented. Data presented include the load-deflection characteristics, cracking behavior, strain characteristics and moment- curvature of the reinforced concrete beams with and without GGBS when tested at 28 days and 56 days. The investigation revealed that the flexural behaviour of reinforced GGBS concrete beams is comparable to that of reinforced concrete beams.

Keywords: **-** *Ordinary Portland cement, Ground Granulated Blast furnace Slag, Reinforced concrete beams, moment- curvature*

I. INTRODUCTION

GGBS concrete is a type of concrete in which a part of cement is replaced by ground granulated blast furnace slag, which is an industrial waste. As a result of its low environmental impacts, using GGBS can reduce significantly many of the environmental burdens associated with concrete. If concrete is mixed with ground granulated blast furnace slag as a partial replacement for Portland cement, it would provide environmental and economic benefits and the required workability, durability and strength necessary for the structures. The cementitious efficiency of ground granulated blast furnace slag (GGBS) at 28 days was tested in concrete at various replacement levels and concluded that it is possible to design GGBS concrete for a desired strength upto an optimum replacement percentage of 50% [1].The characteristics of M_{30} concrete with partial replacement of cement with GGBS was studied and it was found that the partial replacement of cement with GGBS improves the strength of the concrete substantially compared to normal concrete[2]. The behavior of concrete with GGBS at different curing period was tested and found that its strength at early ages is less but continues to gain strength over a long period [3].Experimental studies on the geometric characteristics of concrete with 50% replacement of GGBS proved that the strength of concrete with GGBS increased with age[4]. Studies on the effect of using GGBS as partial replacement in producing a engineered cementitious composites, a ductile cementitious composite reinforced with steel fibers and experimentally proved that addition of slag not only increased the strength of concrete but also increased the binding property of steel[5].The stress strain behavior of concrete made with different cementitious admixtures like GGBS, flyash was experimented and found that the addition of these mineral admixtures reduces the strain in reinforced concrete[6]. Extensive research has been done on the compressive strength and durability of GGBS concrete. Not many investigations were reported on the flexural behavior of concrete beams with GGBS. This paper presents the behavior of reinforced concrete beams with 40% GGBS at 28 and 56 days curing. Data presented include the load-deflection characteristics, cracking behavior, strain characteristics and moment- curvature of the reinforced concrete beams with and without GGBS when tested at 28 days and 56 days.

II. EXPERIMENTAL INVESTIGATION

2.1 Materials

The materials used in the mix design were Ordinary Portland Cement (OPC), river sand, GGBS and potable water. Beam specimens were made with M_{30} grade concrete Water binder ratio of 0.45 and 0.4% of Glenium B233 superplasticiser was used to impart better workability. Fe 500 grade steel was used for longitudinal reinforcement and for stirrups**.**

2.2 Preliminary Investigation

To optimize the percentage replacement of cement with GGBS, preliminary Investigations on were conducted on cube specimens of 150 mm size with 0%,30%, 40% ,50% and 60% GGBS. The specimens were tested at 28 and 56 days in a compression testing machine of capacity 100 T. Compressive strength of concrete with GGBS was less than the ordinary concrete specimens when tested at 28 days, but after 28 days the concrete specimens with 30% and 40% was more than the ordinary concrete specimens when tested at 56 days. Beyond 40% there was gradual decrease in the compressive strength of concrete. Hence beam specimens were casted with 40% GGBS.

2.3 Test specimen details

Eight numbers of reinforced concrete beams with and without GGBS were cast and tested. The span of the beam was 2500 mm and of size 150 mm x 250 mm**.** Out of the 8 specimens tested, four specimens were cast without GGBS and four specimens were cast with 40% GGBS as replacement for cement. Four specimens were tested at 28th day and four specimens were tested at 56th day from the date of casting. Reinforcement details of the specimens tested are given in Table I. A five lettered designation is given to the specimens. First 2 letters represents the type of beam (Controlled and GGBS beams), 3rd one % of GGBS, 4th one identity of specimen in a particular series as two specimens were tested in each series and the last one indicates the day on which the specimen is being tested.

TABLE I Test beam details

S.No	Specification	Testing of Beams (Days)	Reinforcement in Beams			
			Longitudinal		Stirrups (mm)	
			Top	Bottom	Diameter	Spacing
1	CB0% 1-28	28	2#10	3#12	8	160
2	CB0% 2-28		2#10	3#12	8	160
3	GB40%1-28		2#10	3#12	8	160
4	GB40%2-28		2#10	3#12	8	160
5	CB0% 1- 56	56	2#10	3#12	8	160
6	CB0% 2- 56		2#10	3#12	8	160
7	GB40%2-56		2#10	3#12	8	160
8	GB40%2-56		2#10	3#12	8	160

2.4 Test set-up

The testing was carried out in a loading frame of 40T capacity. All the specimens were white washed in order to facilitate marking of cracks. Strain gauges of 20 mm were fixed to the reinforcement to measure the strain and LVDTs were used for measuring deflections at several locations one at midspan, two directly below the loading points and two near the end supports as shown in Figure 1.Strain gauges and LVDTs were connected to a data logger from which the readings were captured by a computer at every load interval until failure of the beam occurred. The beams were subjected to two-point loads under a load control mode. The development of cracks was observed and the crack widths were measured using a hand-held microscope with an optical magnification of X50 and a sensitivity of 0.02 mm. Figure 2(a) and 2(b) shows the arrangement of LVDT and Strain gauges in the experimental setup.

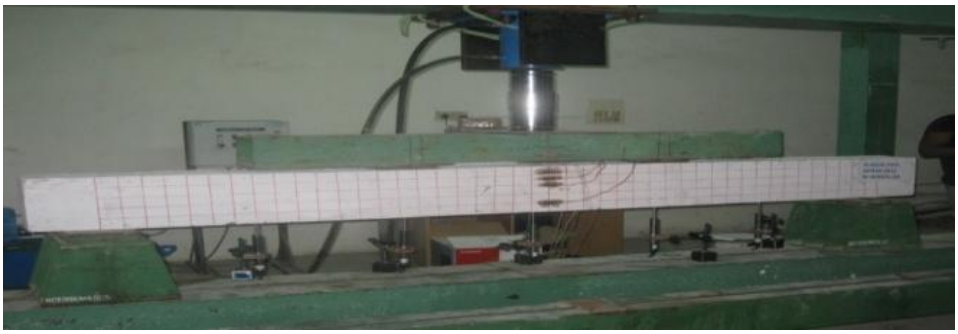

Fig.1 Experimental set-up for the test specimens

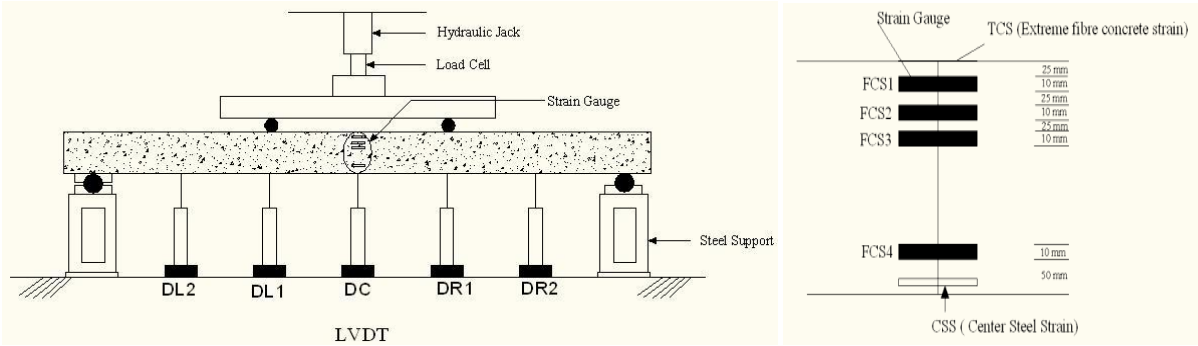

Fig 2: Position of LVDT's and Position of Strain gauges

III. RESULTS AND DISCUSSION

3.1 General observations

Vertical flexural cracks were observed in the constant-moment region and final failure occurred due to crushing of the compression concrete with significant amount of ultimate deflection. When the maximum load was reached, the concrete cover on the compression zone started to fall for the beams with and without GGBS. Figure 3 shows the failure pattern of the test specimens. Crack formations were marked on the beam at every load interval at the tension steel level. It was noticed that the first crack always appears close to the mid span of the beam. The crack widths at service loads for GGBS concrete beams ranged between 0.16mm to 0.2mm

Fig. 3: Failure Pattern of the beams with 40% GGBS

3.2 Load-deflection curve

The experimental load-deflection curves of the RC beams with 0% and 40% GGBS when tested at 28th day and 56th day are shown in Figure 4 & 5 respectively. The average ultimate loads for controlled beams and 40% GGBS concrete beams are 144 kN and 135 kN respectively at 28^{th} day and it is 164 kN and 178kN at 56^{th} day. Though the ultimate loads for the Beams with 40% GGBS is less than that of the controlled beams at 28^{th} day, its ultimate load increases at 56^{th} day.

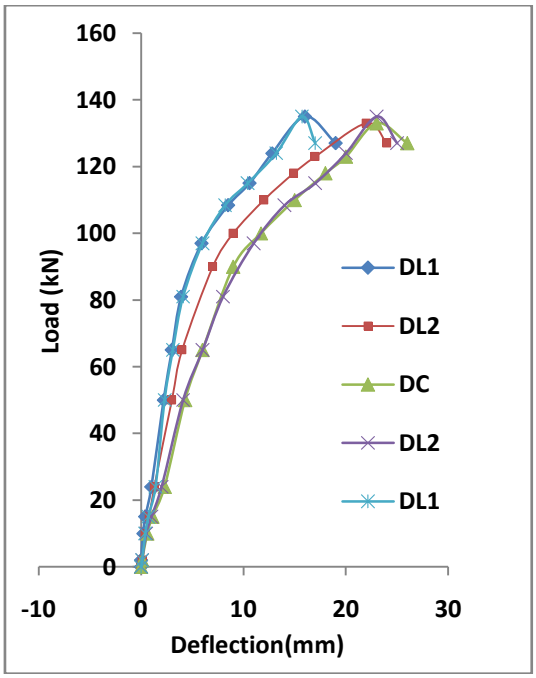

Fig. 4.(a) CB 0% 1-28

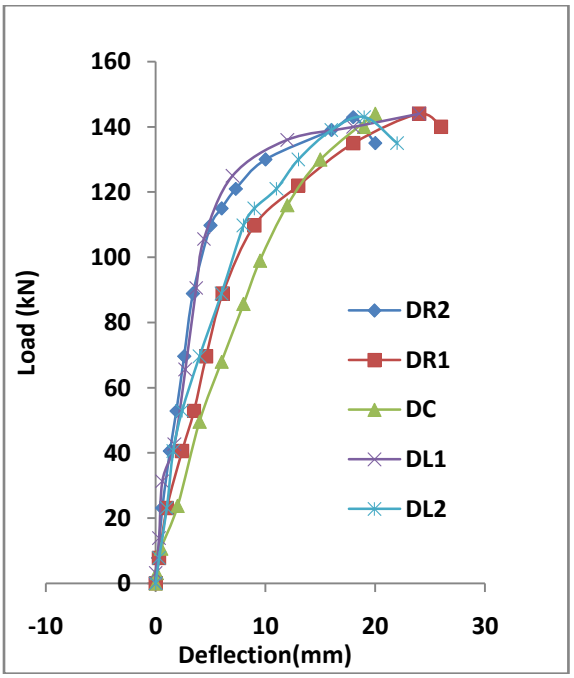

Fig.4. (b) CB 0% 2-28

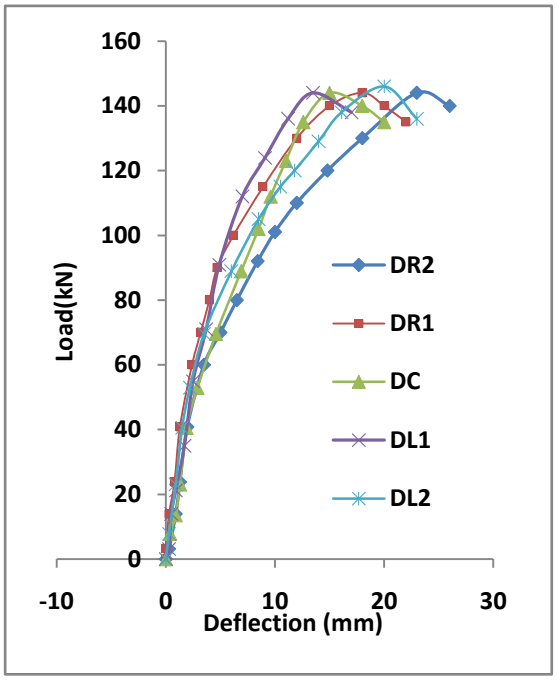

Fig.4. (c) GB 40% 1- 28

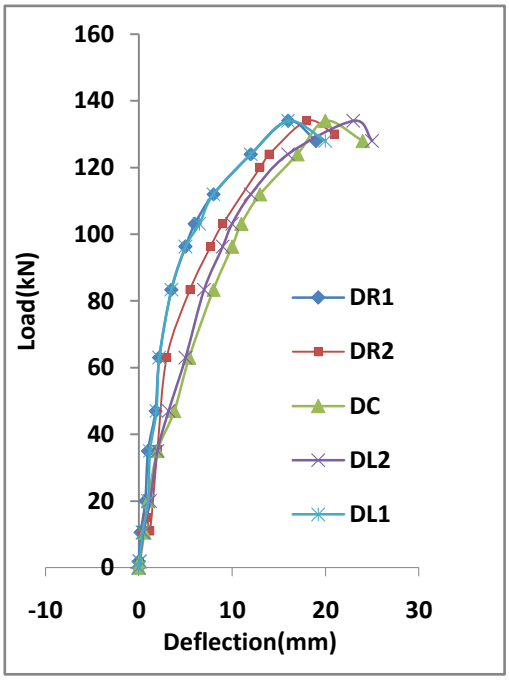

Fig. (d) GB40% 2- 28

Fig 4: Load- Deflection curves for the beams tested at 28 days

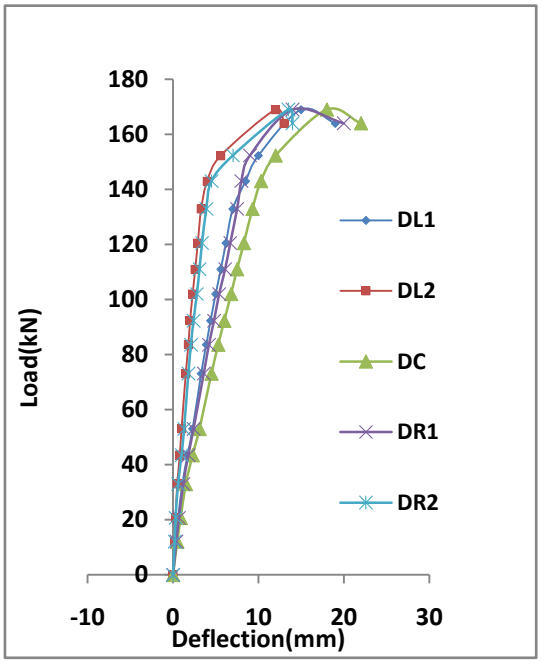

Fig.5 (a) CB0% 1-56

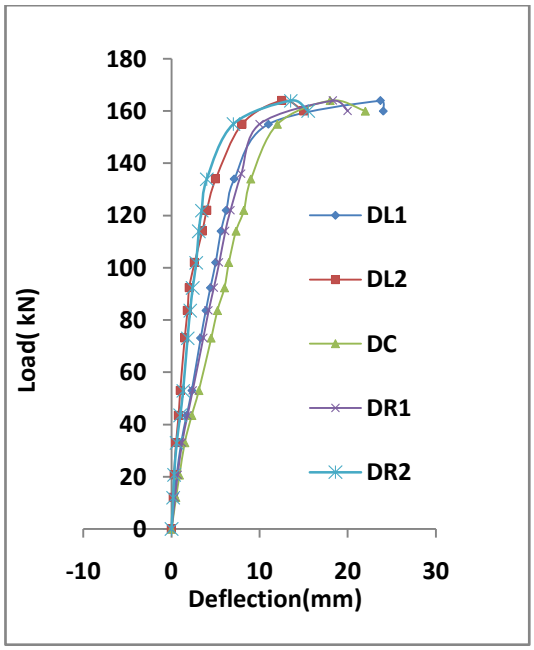

Fig.5. (b) CB0% 2-56

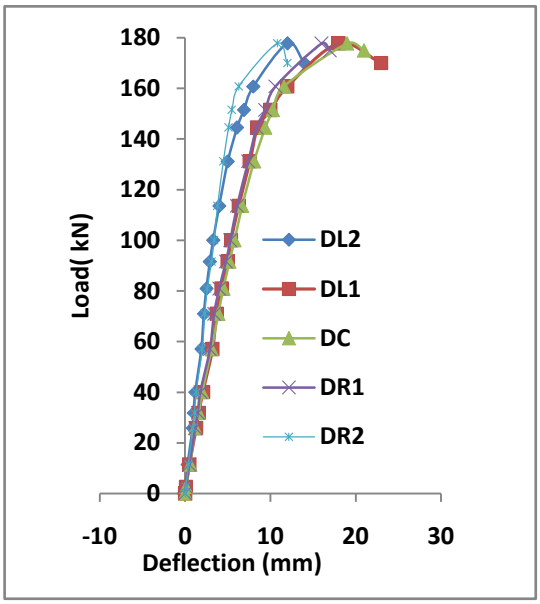

Fig.5 (c) GB 40% 1- 56

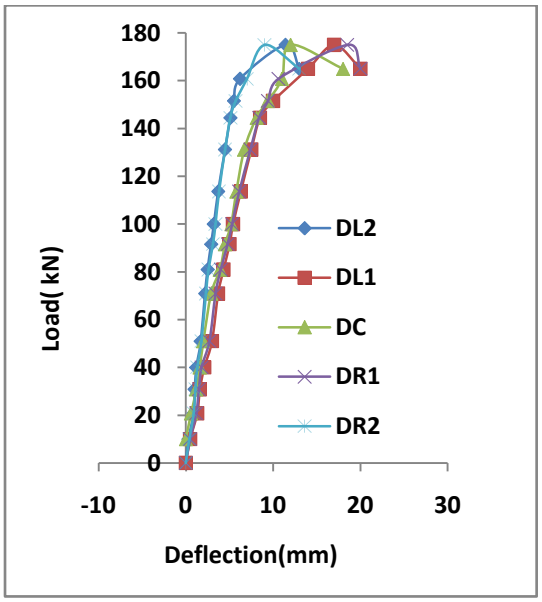

Fig.5. (d) GB 40% 2- 56

Fig. 5: Load- Deflection curves for the beams tested at 56 days

3.3 Concrete and Steel Strain

The concrete and steel strains measured at every load increments at 28th day and 56th day are presented in Figure.6 and Figure 7.The positive strain value represents the tensile strain and the negative strain value indicates the compressive strain. Fig.8 shows the comparison of concrete strain at the top surface and steel strain for all the beams at 28 and 56 days. These results revealed that GGBS concrete is able to achieve its full strain capacity under flexural loading.

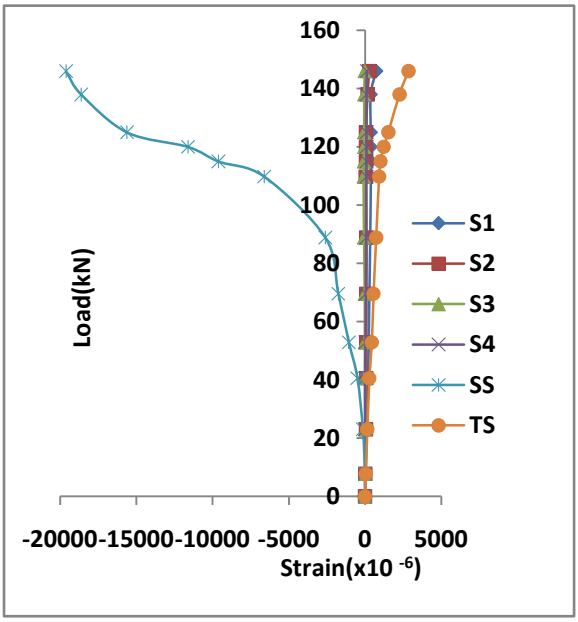

Fig.6. (a) CB 0% 1-28

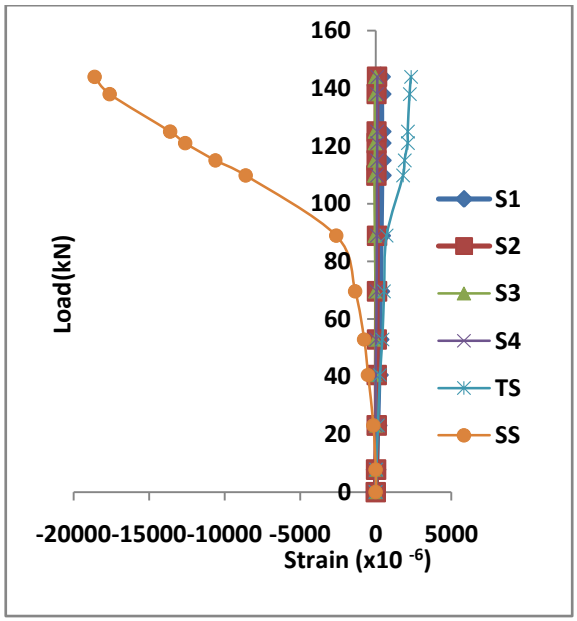

Fig.6 (b) CB 0% 2-28

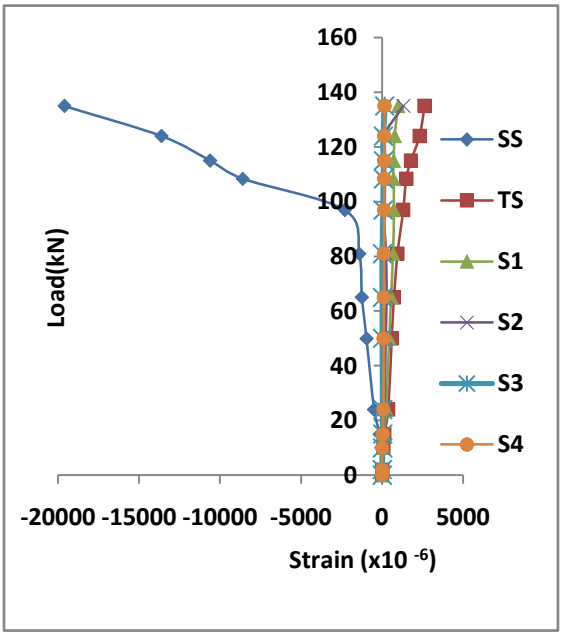

Fig.6 (c) GB 40% 1-28

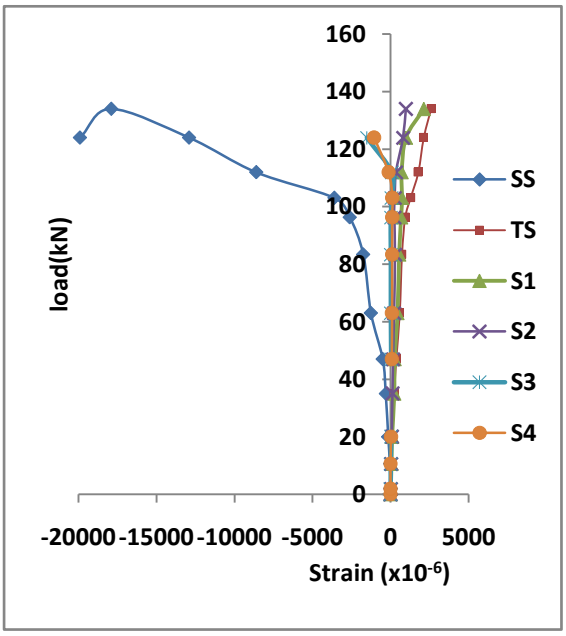

Fig.6 (d) GB4 0% 2-28

Fig.6: Load- Strain curves for beams tested at 28 days

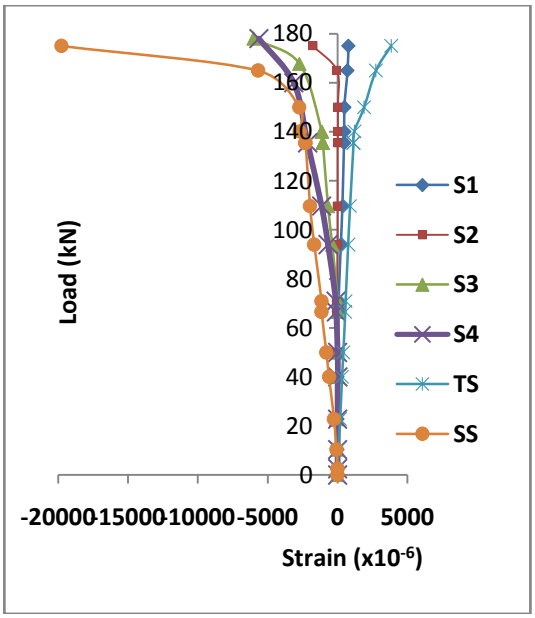

Fig.7 (a) CB0% 1-56

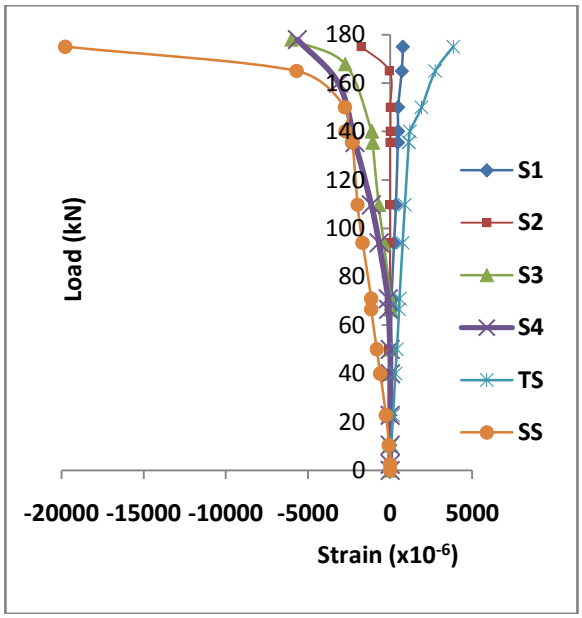

Fig.7 (b) CB0% 2-56

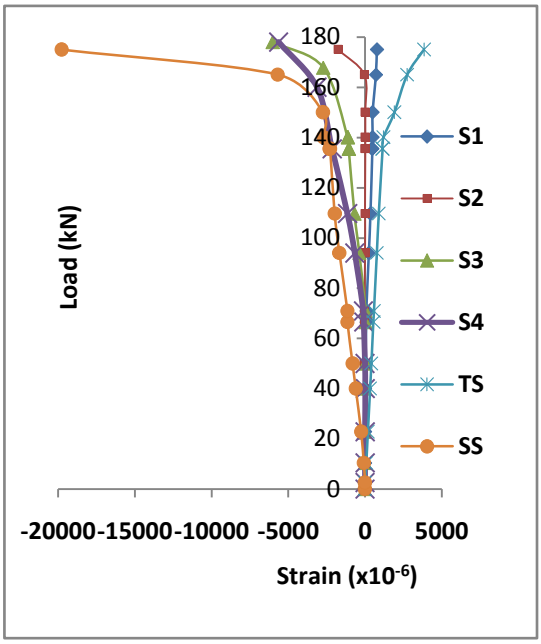

Fig.7 (c) GB 40% 1-56

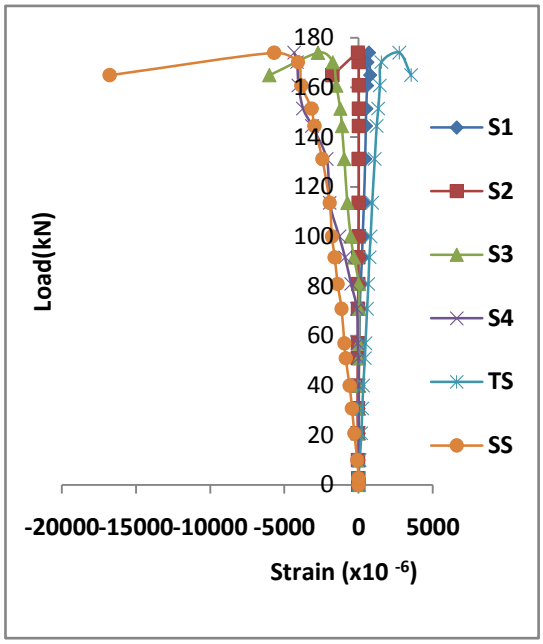

Fig.7 (d) GB 40% 2-56

Fig. 7: Load- Strain curves for beams tested at 56 days

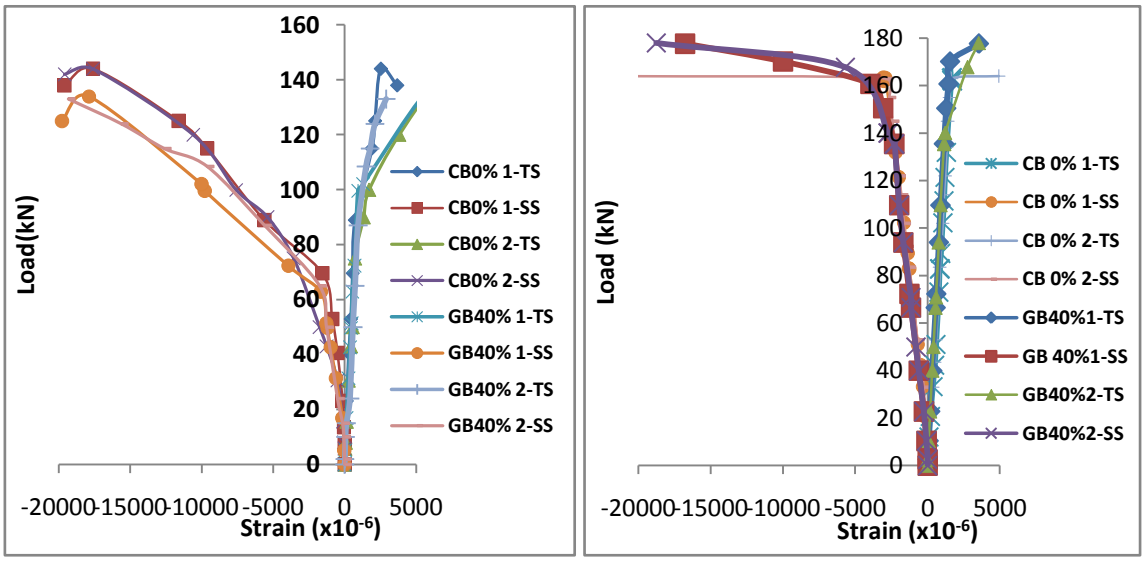

Fig.8 (a) At 28 days Fig.8 (b) At 56 days

Fig. 8: Comparison of Steel and Concrete Strain

3.4 Moment Curvature

Moment-Curvature diagrams were generated for all the beams based on the concrete strain and steel strain. Curvature is computed from the average longitudinal compressive and tensile strains at the middle of the flange and centroid of the bottom reinforcement assuming a linear strain profile cross the cross section using the formula

$$\text{Curvature, } \Phi = \frac{\varepsilon_c + \varepsilon_s}{d}$$

Where, ε_c = Average longitudinal compressive strain in at the concrete fibre at the center of the flange

ε_s = Average longitudinal tensile strain at the centroid of the tension steel

d = Distance between the compression and tension strain locations considered

Figure 9 shows the moment-curvature of the beams at 28th day and 56th day respectively. From the results the curvature of the beam with GGBS is found to be comparable with OPC concrete beams.

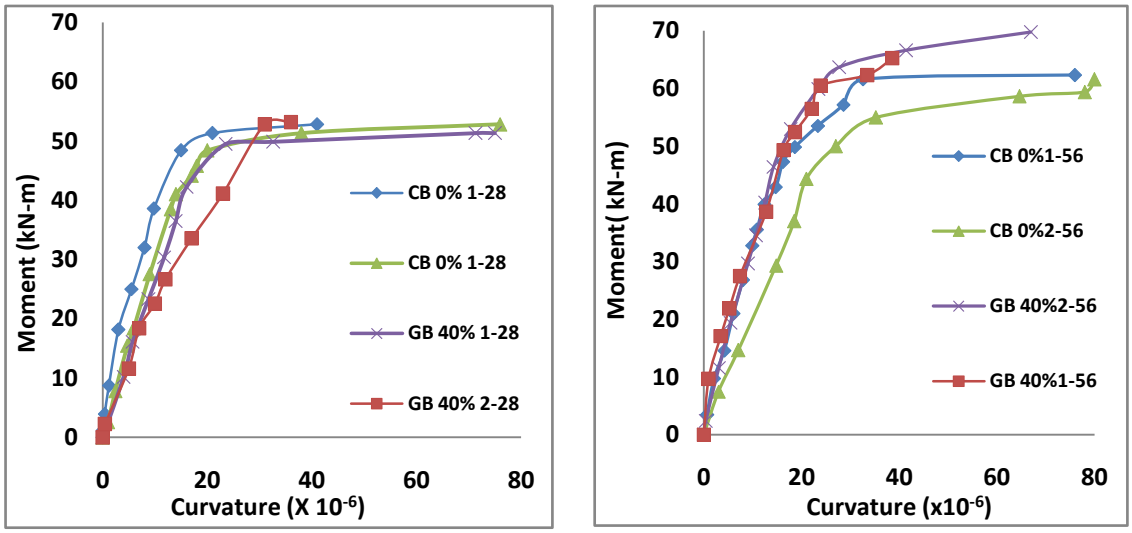

Fig.9 (a) At 28 days Fig.9 (b) At 56 days

Fig. 9: Moment Curvature for beams at 28 and 56 days

IV. CONCLUSION

On the basis of experiments conducted on eight beam specimens the following observations and conclusions are drawn:

1. The ultimate moment capacity of GGBS was less than the controlled beam when tested at 28 days, but it increases by 21% at 56 days.
2. The deflections under the service loads for the concrete beams with 40% GGBS were same as that of the controlled beams at 28 days testing and it was quite less than controlled beams when tested at 56 days.
3. The measured crack width at service loads ranged between 0.17 to 0.2 mm and this is within the allowable limit prescribed by IS 456-2000.
4. The structural behavior of Reinforced concrete beams with GGBS resembled the typical behavior of Reinforced cement concrete beams and there is increase in load carrying capacity of GGBS beams with age. Hence results of this investigation suggest that concrete with 40% GGBS replacement for cement could be used for RC beams.

REFERENCES

[1] K.Ganesh Babu,V. Sree Rama Kumar,"Efficiency of GGBS in concrete", Cement Concrete Research, Volume 30(7), pp.1031–1036,2000.

[2] VenuMalagavelli,P.N.RAO,"High performance concrete with GGBS and Robo sand", International Journal of Engineering Science and Technology, Vol. 2(10),pp.5107-5113,2010.

[3] K. Suvarna Latha, M V Seshagiri Rao, Srinivasa Reddy V," Estimation of GGBS and HVFA Strength Efficiencies in Concrete with Age", International Journal of Engineering and Advanced Technology (IJEAT) ,Vol 2(2): ISSN: 2249 – 8958,2012.

[4] Huiewn Wan and Zhonge Shui,"Analysis of geometric characteristics of GGBS particles and their influences on cement properties", Cement and Concrete Research.Vol.34(1),pp.133-137,2004.

[5] Ing Lim, Jenn-Chuan Chern, Tony Liu, and Yin-Wen Chan," Effect of ground granulated blast furnace slag on mechanical behavior of PVA-ECC", Journal of Marine Science and Technology,vol.20,pp. 319-324,2012.

[6] T. Suresh Babu, M.V. Seshagiri Rao and D. Rama Seshu," Mechanical Properties and stress- strain behaviour of self compacting concrete with and without glass fibres", Asian Journal of Civil Engineering (building and housing),vol. 9(5),pp. 457-472,2008

American Journal of Engineering Research (AJER)
e-ISSN : 2320-0847 p-ISSN : 2320-0936
Volume-03, Issue-01, pp-128-131
www.ajer.org

Research Paper Open Access

Experimental Investigation of Bamboo Reinforced Concrete Slab

Dinesh Bhonde[1], P. B. Nagarnaik[2], D. K. Parbat, U. P. Waghe
[1]*Research Scholar, Yeshvantrao Chavhan College of Engineering, Nagpur, India*
[2] *Professor, Department of Civil Engineering, G.H. Raisoni College of Engineering, Nagpur, India*
[3] *Department of Civil Engineering, Government Polytechnic, Sakoli, India*
[4]*Principal, Yeshvantrao Chavhan College of Engineering, Nagpur, India*

Abstract: - Bamboo is a perennial, renewable, eco friendly, green, fast growing natural material found in almost all part of the world. Bamboo is a lightweight material with good tensile strength. The tensile strength specific weight ratio of bamboo is 20 times more than that of steel. Researchers are working on bamboo as a substitute to steel reinforcement in concrete. An experimental investigation of bamboo reinforced concrete slab cast in the laboratory and subjected to concentrated load at mid span is presented in this paper. The crack pattern, load-elongation curve and the experimental values were investigated. Bamboo reinforced concrete may be a feasible alternative to Steel Reinforced Cement Concrete Structural elements

Keywords: *- bamboo, bamboo composites, bamboo reinforced concrete, brc slab*

I. INTRODUCTION

The depletion of natural resources has posed a serious problem of existence before the next generations. Researchers are working on replacement of conventional materials of building construction with eco friendly material for sustainable development. Bamboo has been in use of mankind for various purposes since a long time. There are more than 1000 species of bamboos and are used for more than 1500 uses all over the world. Bamboo regenerates and can be used within four years, Bamboo has, therefore, acquired a place in the list of material of green technology and renewable source. Bamboo has been used for building construction in different parts of world. Various techniques have been developed for housing. Walls, Roofs, Trusses, Doors, Ccomposite laminates made up of bamboo have been used.

Use of bamboo as a reinforcing material in concrete was first investigated by US Naval Civil Engineering Laboratory, California and have published report in 1966 to assist the construction personnel in design and construction of bamboo reinforced concrete structural members. Some design charts and working stress method is suggested. Yet elaborate standards on bamboo as a structural material have not been developed in many countries. ISO-22156 for Bamboo Structural Design and ISO-22157 for Determination of physical and mechanical properties of bamboo have been published by International Standards. Indian Standards have published several codes on bamboo, however, there are only few for bamboo as a structural material. Bamboo as a reinforcement in concrete slab has been investigated by the authors in the laboratory and the results are presented.

II. LABORATORY PROGRAM

Laboratory Mix design of M20 concrete was used for the experiment. Bamboo samples were collected from the farm Lohgad, 40 km away from Nagpur (India). The species of bamboo was Dendrocalmus Strictus which is predominantly found in India. The age of bamboo used was 5 years. The bamboo splints of width 15 mm were prepared as reinforcement. The water absorption capacity of bamboo split is upto 32% and it swells when water is absorbed. In green concrete, bamboo splints absorb water and swells. When the concrete becomes dry, the bamboo splints contracts and leave spaces between the contacts. The bond strength decreases and the members fail in bond. To overcome this limitation various sealant materials were tested and asphalt was found to be the best economical alternative. All bamboo reinforcements were embedded in asphalt, sand was sprinkled on those to improve bond and were dried. Bamboo splints were tied about 10 cm c/c to form a reinforcing mesh. Binding

wire was used to tie the reinforcements. A slab of 600x600x120 mm was cast with clear cover of 15 mm to reinforcement grid. The slab was cured with water and tested under computerized universal testing machine after 28 days.

Table 1: Test Data for BRC slab

Particulars	Values
Specimen Type	Bamboo Reinforced Slab
Concrete Grade	M20
Size of slab	600x600x120 mm
Effective depth	99 mm
Effective span	490 mm
Reinforcement	Bamboo splints of Dendrocalmus Strictus
Area of reinforcement along span	1154.03Sqmm
Tensile strength of reinforcement	95.81MPa
Ultimate Load	16.200 KN
Eb	18600 MPa
Ec	22361 MPa

Figure 1: BRC slab under test

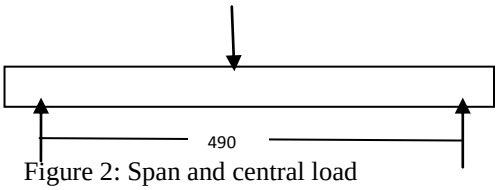

Figure 2: Span and central load

2.1 Experimental Observations and Output

The slab was placed under UTM and load was applied at a constant rate. A visible crack was observed at a load of 15.65 KN at the mid span and the machine paused and did not take any load however the load started dropping up to 9.8 KN. Again the slab took load; the peak load observed was 16.200 KN. At this stage the crack widened and the load started dropping down up to 7.8 KN. Again the slab took load and reached to another lower peak of 10.65 where the crack widen further, After this peak the load dropped continuously and the slab failed.

Figure 3: BRC slab failure

III. RESULTS AND DISCUSSION

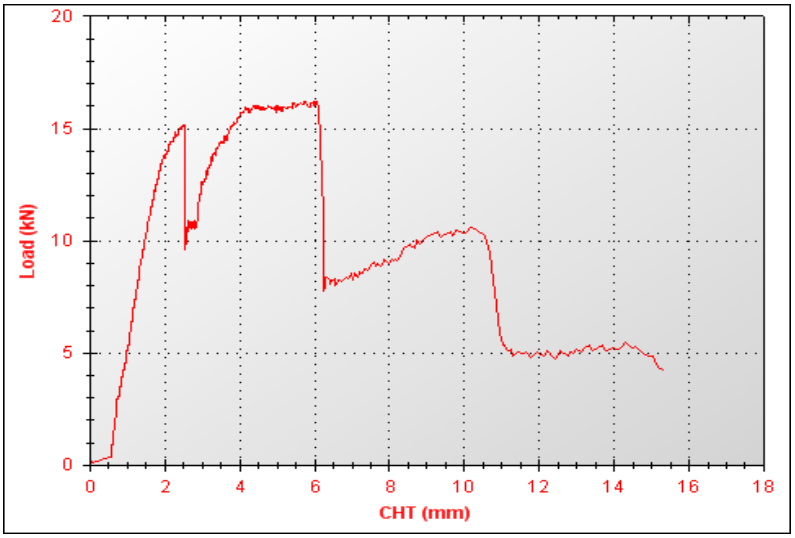

Figure 3: Load Elongation Chart till failure

Dead load= w=24000x0.12=2880 N/m
Point load per unit length= 27000 N/m

Maximum Bending Moment at the peak load= $\frac{WL}{4} + \frac{wl^2}{8} = \frac{27000\ x0.49}{4} + \frac{2880x0.49^2}{8}$
=3393.94 N.m = 3.394 KNm/ m

As per ISO 22156, allowable stresses in bamboo reinforcement are
sall = Rk x G x D / S and allowable stress is 1/7 of characteristics stress
= 13.69 MPa
As per IS-456, Table 21, allowable stress in concrete= 7 MPa
Modular ratio = n = $\frac{Eb}{Ec}$= 0.8
r = $\frac{\text{fb allow}}{\text{fc allow}} = \frac{13.69}{7.0}$ = 1.956
k= $\frac{n}{n+r} = \frac{0.8}{0.8+1.956}$
j= $1 - \frac{k}{3} = \left(1 - \frac{0.29}{0.3}\right)$=0.90
Mdr= fb.j.d.At
Mdr= 13.69x0.90x99x1154.03= 1.408 KNm/ m
Mu/Mdr = 2.41

Design moment of resistance M_{dr} is 2.41 times less than Experimental ultimate moment M_u.

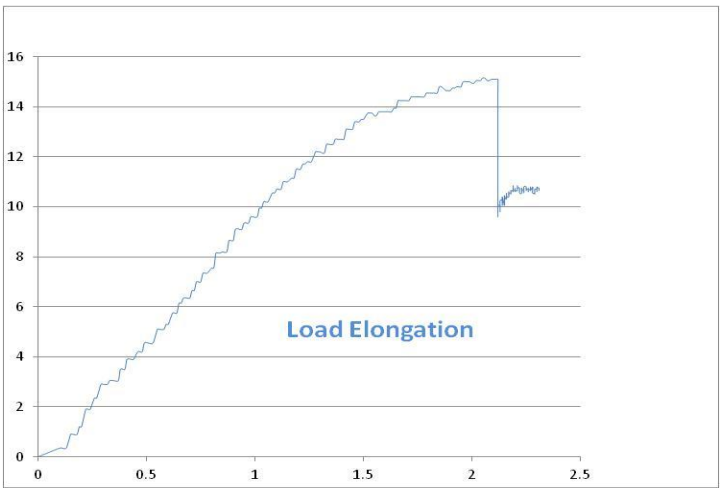

Figure 3: Load Elongation graph up to first crack

IV. RESULTS AND DISCUSSION

The slab under uniformly increasing testing load under UTM was carefully observed. The first crack appeared at a load of 15.65 KN, at this point the concrete surrounding bamboo reinforcement fails and the curve drops sharply, however the reinforcements again start taking load up to a peak load of 16.2 KN and the reinforcement fails in bending along with concrete surrounding it, again other reinforcement and their failure can be visualized from the graphs. The stress strain relationship is linear up to certain limit. The maximum bending moment was at mid section and the crack develops under the load and extends along the horizontal line. Comparing the designed moment of resistance and the ultimate BM at failure, the design moment using working stress method is half of ultimate moment.

V. CONCLUSION

BRC elements follows same pattern as those in steel RCC structural members. The design moment is found less than experimental ultimate moment and thus working stress method can be used to design BRC structural members safely. However, proper sealant such as asphalt shall be used to conceal the reinforcement from water absorption so that they may not swell and degrade the bond.

VI. ACKNOWLEDGEMENTS

The experiment and the testing of bamboo were carried out at Government Polytechnic, Nashik, India and thanks are due to the Head of Institute Dr. Nandanwar, faculty members, laboratory staff and the students.

REFERENCES

[1] Eiichi Obataya, Æ Peter Kitin, Æ Hidefumi, Yamauchi Bending characteristics of bamboo (Phyllostachys pubescens) with respect to its fiber–foam
[2] composite structure, Springer-Verlag 2007
[3] Wu Yao, Zongjin Li Flexural behavior of bamboo–fiber-reinforced mortar laminates, Cement and Concrete Research 33 (2003) 15–19
[4] Dinesh Bhonde, P. B. Nagarnaik, D. K. Parbat, U P Waghe Tension Test on Male Bamboo (Dendrocalmus Strictus), International Journal of Advanced Technology in Civil Engineering ISSN: 223 –572 Volume 2, Issue-1, 2013
[5] International Standards ISO 22157 Bamboo - Determination of physical and mechanical properties
[6] Wan Tarmeze Wan Ariffin Numerical Analysis of Bamboo and Laminated Bamboo Strip Lumber
[7] Punmia B. C., Ashok Kumar Jain, Comprehensive RCC Deigns
[8] R. Srinivasan and K. Sathiya Flexural Behavior of Reinforced concrete Beams using finite element analysis (elastic analysis), Bul. Inst. Polit. Iaşi, t. LVI (LX), f. 4, 2010
[9] Dinesh Bhonde, P. B. Nagarnaik, D. K. Parbat, U P Waghe, Experimental Analysis of Bending Stresses in Bamboo Reinforced Concrete Beam

American Journal of Engineering Research (AJER)
e-ISSN : 2320-0847 p-ISSN : 2320-0936
Volume-03, Issue-01, pp-132-139
www.ajer.org

Research Paper Open Access

Knowledge Based RobotSystem for Diagnosis and Troubleshooting of Personal Computer Using Artificial Intelligence Rete Algorithm

Abrham Debasu Mengistu[1] Dr.Vuda Sreenivasarao[2]
[1]*M.Sc. (Computer Science), School of Computing and Electrical Engineering, IOT, Bahir Dar University, Ethiopia.*
[2]*Professor, School of Computing and Electrical Engineering, IOT, Bahir Dar University, Ethiopia.*

***Abstract*: -** In the information and artificial intelligence age personal computer is the most popular communicating device that can be used in our day to day life. In fact most of the computer users are not skilful enough when it comes to the area of troubleshooting a problem occurred. Using knowledge based robot will save our time and money and also provides a rapid solution and will overcome the need of a computer expert. In this paper,develop a knowledge based robot system that can assists computer users to troubleshoot and maintain their personal computer using artificial intelligence algorithms. After the prototype implemented, ultimately every knowledge-based system must be tested and evaluated to ensure that whether the performance of the system is accurate and the system is usable by the end-users.

Keywords: - *artificial intelligence, knowledge-based system and troubleshoot.*

I. INTRODUCTION

Artificial intelligence can be defined as making an intelegent machine which were previusly done by human beings for example previusly inorder to troubleshoot a computer problem there are things that we identify and it takes time but now a days with the help of artificial intelegence it is easy to identify the problem.Artificial intelligence is a field of since and enginneering mainly concerned with making machine for assisting a day to day activity of humans. But inorder to say an intelegent the following are the basic things.

- Learn or understand from experience.
- Make sense out of ambiguous or contradictory messages.
- Respond quickly and successfully to new situations.
- Use reasoning to solve problems.
- Apply knowledge to manipulate the environment.
- Think and reason.

A robot is a mechanical or virtual agent that contains sensors, control systems, manipulators, power supplies guided by a computer program or software that perform a task which were done previusly by humans guided by a computer program like AI and others.Artificial Intelligence have a direct role in robotics for making the robot to be intellegent. artificial Intelligence addresses the the critical questions of: what knowledge is required in any aspect of thinking; how should that knowledge be represented; and how should that knowledge be used.

Human Intelligence	***Artificial Intelligence***
➢ *Intuition, Common sense, Judgment, Creativity, Beliefs etc*	➢ *Ability to simulate human behavior and cognitive processes*
➢ *The ability to demonstrate their intelligence by communicating effectively*	➢ *Capture and preserve human expertise*
➢ *Plausible Reasoning and Critical thinking*	➢ *Fast Response. The ability to comprehend large amounts of data quickly*

Table I:Human Intelligence VS Artificial Intelligence

❖ We achieve more than we know. We know more than we understand. We understand more than we can explain (Claude Bernard, 19th C French scientific philosopher).

Human Intelligence	***Conventional Computing***
➢ *AI software uses the techniques of search and pattern matching*	➢ *Conventional computer software follow a logical series of steps to reach a conclusion*
➢ *Programmers design AI software to give the computer only the problem, not the steps necessary to solve it*	➢ *Computer programmers originally designed software that accomplished tasks by completing algorithms*

Table II.Artificial Intelligence VS Conventional Computing

II. ARTIFICIAL INTELLIGENCE IN ROBOT

With the enhancement of intelligent technology robot plays an important role in our day to day activity. An artificial intelligent based robot is a machine that has a capability to extract information from its environment and use knowledge about its world to move safely in a meaningful and purposeful manner. With an intelligent technology robot plays an important role in our day to day activity. For the given problem wehave a means for checkinga proposed solution and caused that problem,and then we can solve the problem by testing allpossible answers. But this method this always takes a long period of time to handle the given problem. If we handle the same problem with the help of intelligent machine let's say robot it takes a minimal time because intelligent machine like robots have higher processing speed than that of human beings

2.1. Components of AI for Robots:

A rule-based system of robots is composed of three components: an interpreter (or inference engine), a knowledge base and a fact database.

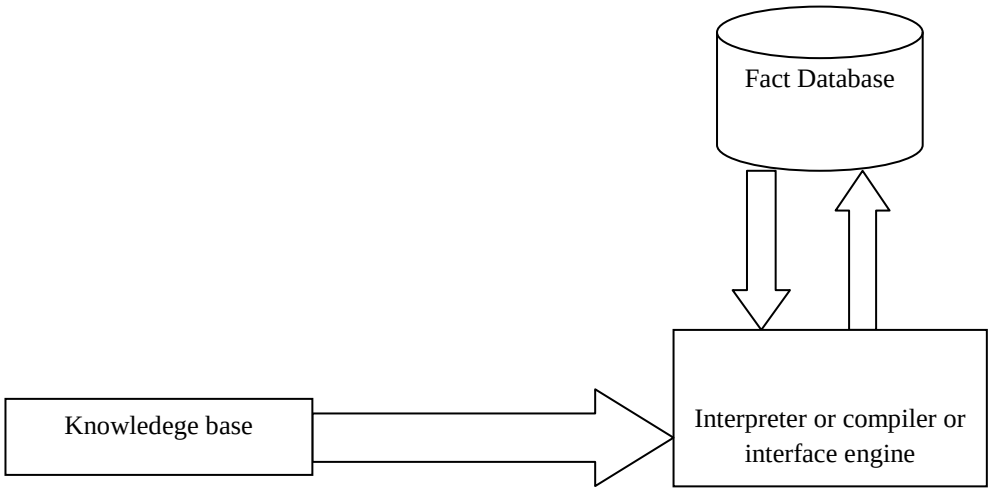

Figure 1. Components of AI robot.

A fact database consists of consists of facts, concepts, theories, heuristic methods, procedures, and relationships and Knowledge base is the collection of knowledge related to a problem used in an AI system Knowledge is also information organized and analyzed for understanding and applicable to problem solving or decision making. The interpreter part is responsible for generating rule depending on the fact and knowledge base and also giving decision.

III. STATEMENT OF THE PROBLEM

A computer system is composed of both hardware and software. Hardware like different subsystems including CPUs, primary and secondary storage, peripherals, and several type of software like general purpose software and application software. Each of these subsystemsprovide their own functionality in order to provide the whole system as oncebut there are only very few maintenance tools and established diagnostic strategieswhich give attention at identifying faults on the system or subsystem level. As a result, identification of single or multiple faults from systemic sign remains a difficult task. The non-specialist field service engineer is trained to use the existing component specific tools and, as a result, is often unable to attack the failure at the systemic level. Expert assistance is then required, increasing both the time and cost required determining and repairing the fault. The design of a knowledge based system reflects the expert's ability to take a systemic

viewpoint on problems and to use that viewpoint to indict specific components, thus making more effective use of the existing maintenance capabilities.

As we know the present period is the information and artificial intelligence age, where faster transfer and retrieval of information is the most important need. However, using an expert system like knowledge based system this scenario will be an economic and rapid solution and will overcome the need of a computer troubleshooting expert. This will help to increase individual's efficiency by reducing the time spend by the expertise.

IV. ARCHITECTURE OF THE SYSTEM

Architecture is a blueprint that shows how the components of the prototype of knowledge Knowledge based Robot for diagnosis and troubleshooting of personal computer using Rete algorithm. The figure shown below illustrates the architecture of the prototype system.

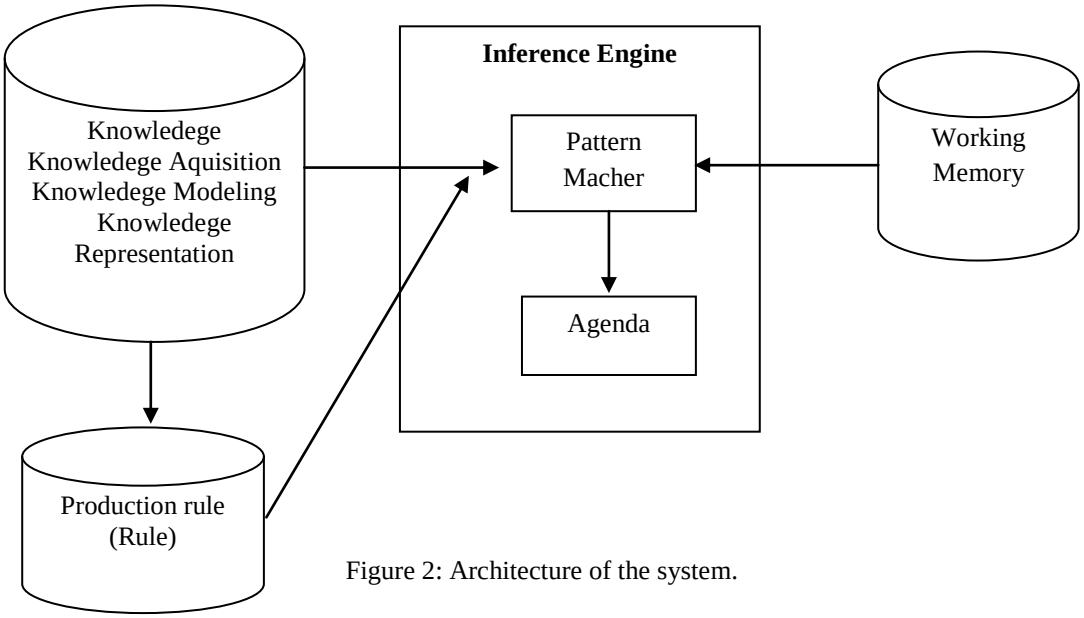

Figure 2: Architecture of the system.

V. PROPOSED METHODOLOGY

The methodology for using Knowledge based Robot for diagnosis and troubleshooting of personal computer is using artificial intelligence by Rete algorithm.The Rete algorithm is a best known pattern matching algorithm which is designed by Dr Charles L. Forgy of Carnegie Mellon University. Rete is a Latin word which has a meaning means net. It is a very efficient algorithm for matching facts against the patterns in rules. Understanding of the Rete algorithm will make one easier to understand why writingrules one way is more efficient than writing them another way.The Rete algorithm is based on the fact that only a few facts are added, changed or removed at every step in the process of inference. Instead of doing all these comparisons every time only new facts added can be taken into consideration which is the approach taken in Rete algorithm. Rete looks for changes to match in each cycle.

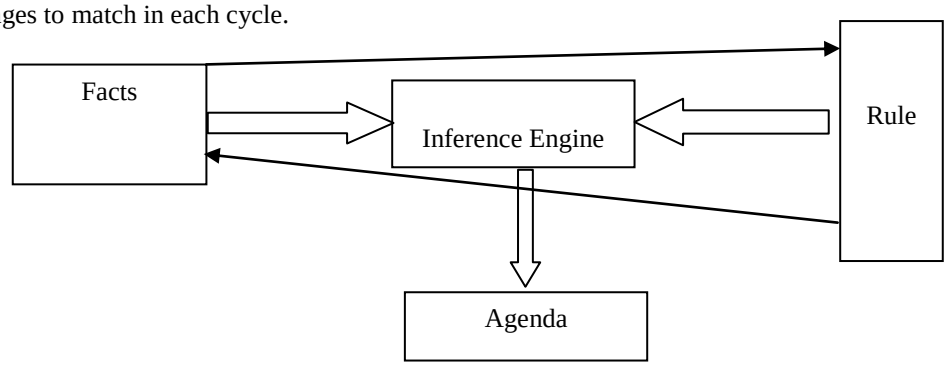

Figure3. Rete algorithm.

If two of the three premises of a rule are satisfied in one cycle, there is no need to check them again in the next cycle. Only the third premise is of interest. The matching process is updated when new facts are added or removed. This will speed up the process of matching if the number of new facts is small. Information about

the premises of each rule which are satisfied partial matches must be stored.The Rete algorithm is implemented by building a network of nodes. It is designed in such a way that it saves the state of the matching process from cycle to cycle and re computes changes only for the modified facts. The state of the matching process is updated only as facts are added and removed. If the facts added or removed are less in number then the matching process will be faster.

For instance, suppose we have one rule on troubleshooting, ifproblem is HDDand Problem is Black screenandsymptom is NTLDR then the following rete network can be created.

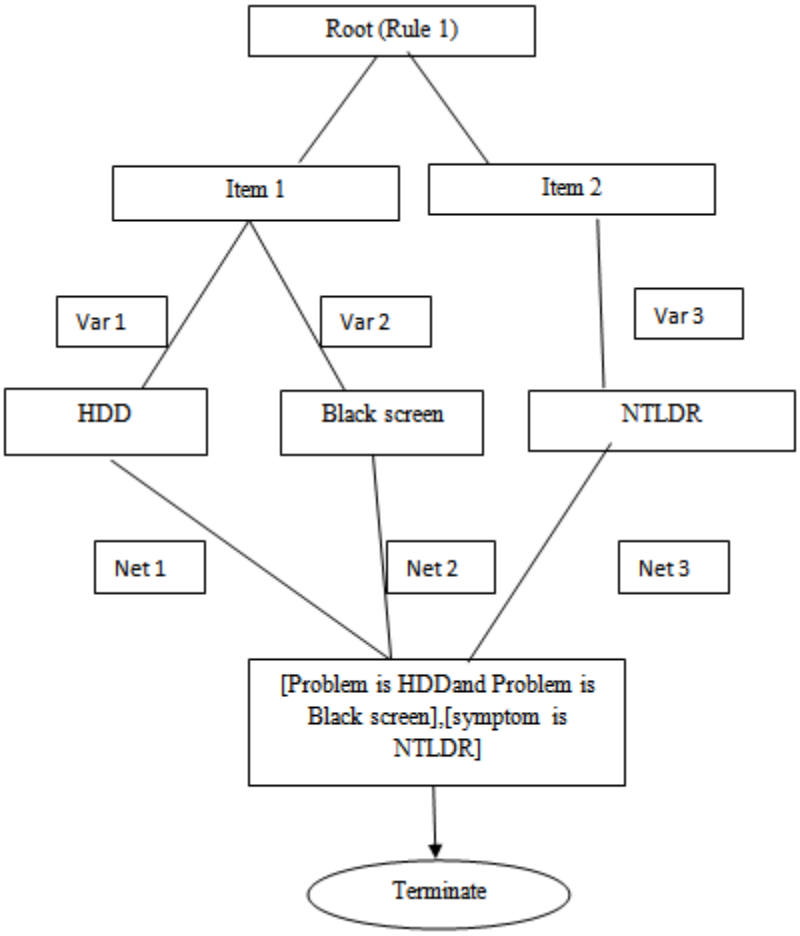

Figure4. A simple Rete network for a single rule.

In the above rete network, there are two kind nodes as there are two types of facts: item 1 type and item 2 type. As there are three patterns:problem is HDDand Problem is Black screenandsymptom is NTLDRthree alpha nodes will be created. var 1 and var 2 representing the first two var nodes are joined by net 1. The third alpha node and beta 1 joined by net 2.

When a value for age enters the root a token will be created. Copies of this token will be passed to item nodes. Item 1 will accept it as the fact type. This token will be passed onto var1 and var 2. If the value satisfies the constraint then the token will be passed onto net1 and then to net2. In the meantime value of symptom enters the root and then accepted by item 2. var 3 receive it and checks if the value satisfies the constraint, symptomis NTLDR. If yes then it allows the token passing onto item 2. If the fact, that is the values, match with the condition in the item2 then the rule will be added to a list for firing.

5.1. Rete Algorithm:

1. Each of these facts is first parsed through the network. The network will then look as in the hand-out.
2. Every time a fact is added or removed the network is updated.
3. Using the network, rules that can execute can be determined quickly in a forward reasoning system using Rete
4. Because sometimes several rules can execute, they will all have to be put on the agenda. Conflict resolution is then necessary to determine the rule to fire or execute.

In order to acquire the desirable knowledge both secondary and primary (documented and undocumented) source of knowledge are used. Primary knowledge is gathered from help desk computer technicians by using interviewing and critiquing knowledge elicitation methods. In the same way secondary source of knowledge are collected by using document analysis. Both unstructured and structured interview were used to collect tacit knowledge from domain experts. In addition critiquing (analyzing) elicitation methods are used to purify the collected knowledge. The acquired knowledge is refined with the consultation of the expert. Moreover, secondary sources of knowledge are gathered from the internet, computer maintenance books, research papers and articles by using document analysis technique.

VI. TESTING AND EVALUATION

After the prototype implemented, ultimately every knowledge-based system must be tested and evaluated to ensure that whether the performance of the system is accurate and the system is usable by the end-users. As the aim of testing and evaluation of the knowledge-based system is to assure that the prototype system does what it is required to do, we can test and evaluate a knowledge-based system as long as we already understand what to expect. Therefore, in this article we try to show the performance testing. In system performance testing section, a number of computers selected in order to test the accuracy of the prototype system. The correct and incorrect outcomes are identified by comparing decisions made by domain experts and with the conclusions of the prototype system.

6.1.Forward chaining rule:

Problem	Algorithms	Solved	Not solved
HDD & Software Related	Forward chaining	7	3
Memory Related	Forward chaining	5	5
Monitor Related	Forward chaining	6	4
Port Related	Forward chaining	6	4
Processor Related	Forward chaining	4	6

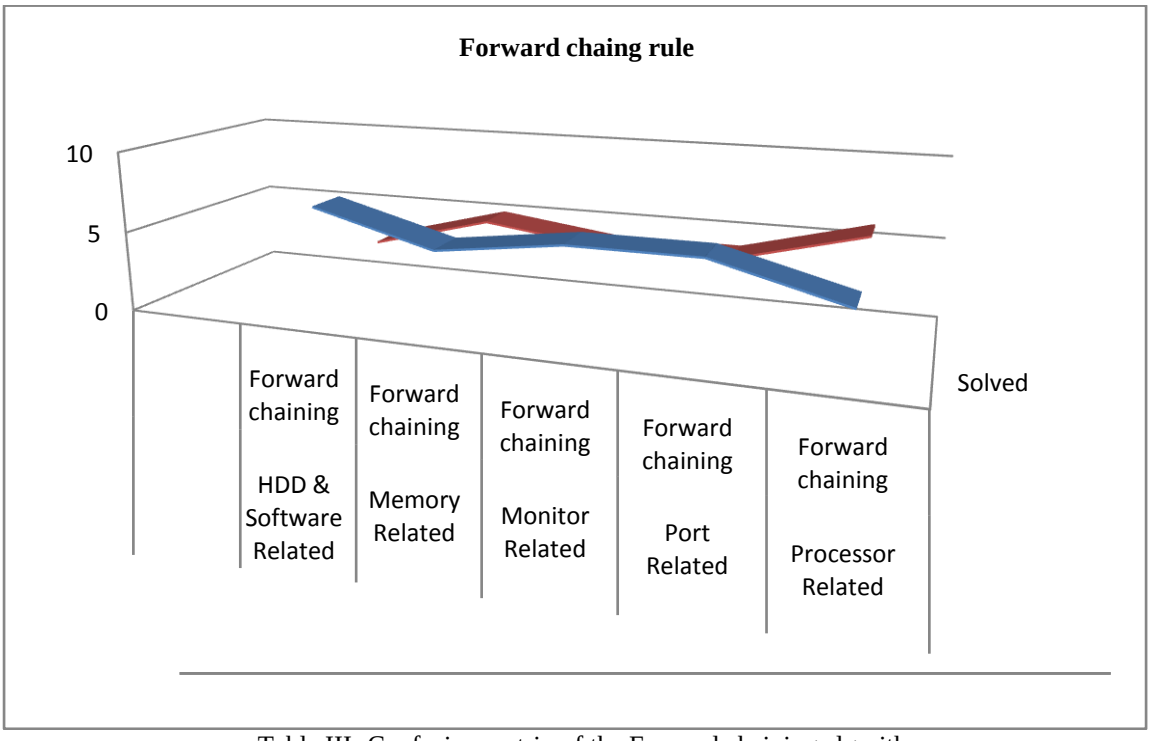

Table III**:** Confusion matrix of the Forward chaining algorithms.

6.2. Rate Algorithms:

Problem	Algorithms	Solved	Not solved
HDD & Software Related	Rete algorithm	10	0
Memory Related	Rete algorithm	7	3
Monitor Related	Rete algorithm	9	1
Port Related	Rete algorithm	9	1
Processor Related	Rete algorithm	7	3

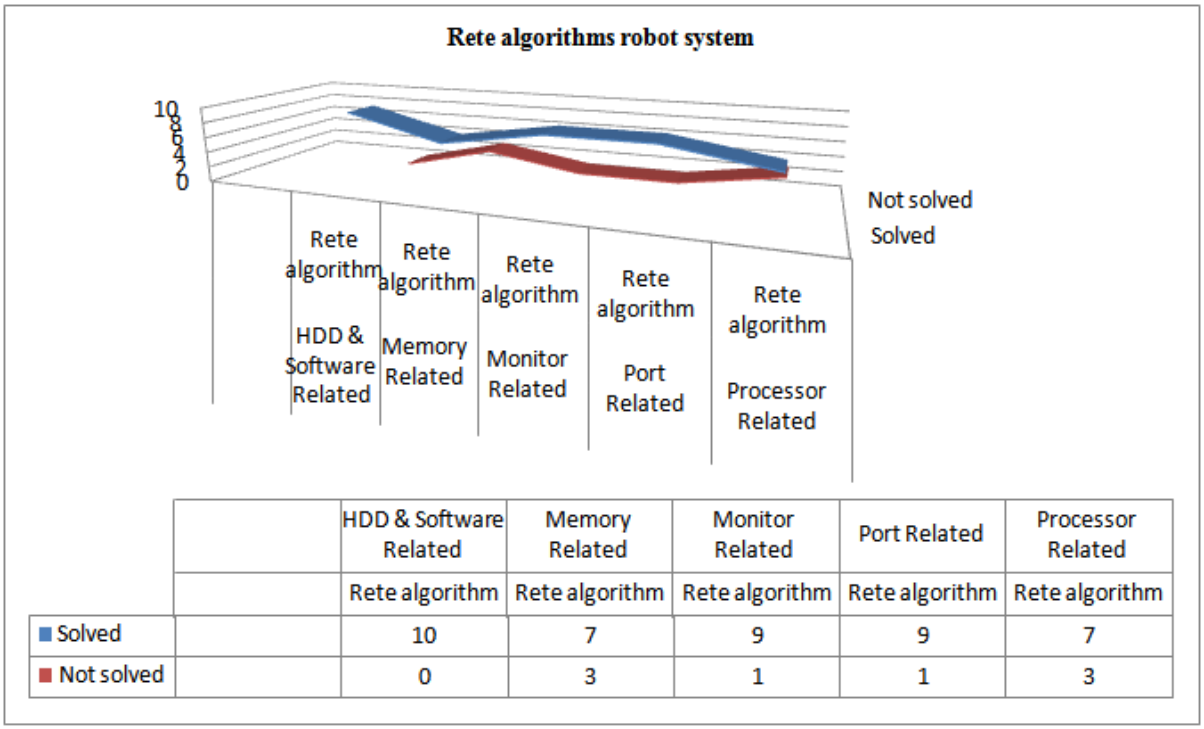

		HDD & Software Related	Memory Related	Monitor Related	Port Related	Processor Related
		Rete algorithm	Rete algorithm	Rete algorithm	Rete algorithm	Rete algorithm
Solved		10	7	9	9	7
Not solved		0	3	1	1	3

Table IV: Confusion matrix of the Rete algorithmsrobot system.

VII. RESULTS:

1.
The first thing that display on the system is menu.

```
  ================================================
@@@@@@@@@@@@@@@@@@@@@@@@@@@@@@@@@@@@@@@@@@@@@@@@@@@@
@ NOTE:- whenever write on the system put dot(.) at the end and press enter key

@ ማሳሰቢያ:- የሚፈለገውን ቃል ካስገቡ በኋላ ነጥብ(.) ያስቀምጡና ኢንተር ቁ ይጫኑ።
@          To start the program write ጀምር followed by period(.)at the end and press
ENTER.
@          ፕሮግራሙን ለመጀመር ጀምር የሚፈለገውን ቃል ካስገቡ በኋላ ነጥብ(.)ያስቀምጡና ኢንተር ይጫኑ።
@@@@@@@@@@@@@@@@@@@@@@@@@@@@@@@@@@@@@@@@@@@@@@@@@@@@
% f:/Abrham Debasu/Rete Algorithm implimented.pl compiled 0.00 sec, 76 clauses
1 ?-  start.
                    ሜኑ/MENU CHOICE .
  1 ን ያስገቡ ቅድመ መረጃ ለማግኘት/ Enter 1 to get general information
  2 ን ያስገቡ ቅድመ መከላከል መረጃ ለማግኘት/ Enter 2 to know prevention  mechanism
  3 ን ያስገቡ ጥገና አገልግሎት ለማግኘት/ Enter 3 to get maintenance service
  4 ን የስገቡ ለመውጣት/ Enter 4 to close prolog
```

2. Select any one from the menu for example select number 2 which means that about preventive maintenance.

```
==========================================================================
                  Preventive maintenance
                  ቅድመ ጥንቃቄ
                  ----------------------------------------
Using power protection devices(like UPS)
የፓወር መከላከያ ይጠቀሙ
Ensure  to clean your computer
ኮምፒተርወትን ያፅዱ
Performing back up
ባክፕ ያድርጉ
Install Antivirus and anti-spy ware and scan
አንቲ ቫይረስ ይጫኑ
Install updates
አፕዴት ያድርጉ
Disk clean up
ዲስክ ክለን አፕ ያድርጉ
Disk defragmenter
ዲስክ ዲፍራግመንት ያድርጉ
Examine the operating systems
ኮምፒተርዎን ይፈትሹ
Using Antistatic wrist-grounding strap
አንቲ ስታቲክ ሪስት ትራፕ ይጠቀሙ
Shutdown properly
ኮምፒተርዎን በአግባቡ ይዝጉ
==========================================================================
Do you want to continue ? መቀጠል ይፈልጋሉ ? (yes/no)
```

3. If you want to continue type yes and then press enter this will lead to the main menu that appears before.

```
Do you want to continue ? መቀጠል ይፈልጋሉ ? (yes/no)yes.
                    ሜኑ/MENU CHOICE .
 1 ን ያስገቡ ቅድመ መረጃ ለማግኘት/ Enter 1 to get general information
 2 ን ያስገቡ ቅድመ መከላከል መረጃ ለማግኘት/ Enter 2 to know prevention  mechanism
 3 ን ያስገቡ ጥገና አገልግሎት ለማግኘት/ Enter 3 to get maintenance service
 4 ን የስገቡ ለመውጣት/ Enter 4 to close prolog
 | :
```

VIII. CONCLUSION

Now we are in the age of information and artificial intelegence, and use of computers, fault diagnosis is becoming crucial in the field of computer engineering and information technology, particularly in personal computer troubleshooting; however, acquiring the troubleshooting knowledge from expert computer technicians is limited as it requires continuous learning, training, and practice in maintenance skills which on the long run can dramatically increase organization operating costs, decrease their net productivity, and proliferate their revenue leakage and losses. Basically, PC troubleshooting covers a wide spectrum of problems including hardware problems, software problems, network problems, server problems, operating system problems, and application software problems.

In developing the prototype system, knowledge is acquired using both structured and unstructured interviews with domain experts and from relevant documents by using documents analysis method to find the solution of the problem. The acquired knowledge is modeled using decision tree that represents concepts and procedures involved in diagnosis and troubleshot of computer. Then, the validated knowledge is represented using rule-based representation technique and codified using SWI-Prolog editor tool for building the knowledge-based system

Also in testing and evaluation of the prototype system, ten cases of computer problem are selected using purposive sampling method in order to test the accuracy of the prototype system. The correct and incorrect results are identified by comparing decisions made by the domain experts on the cases of patients and with the conclusions of the prototype system. This permits end-users to test the prototype system by actually using it and evaluating the benefits received from its use. As the testing result show, the overall performance of the prototype system registers 85.9%.

Knowledge based system for troubleshooting personal computer handles computer faults. The knowledge base contains the knowledge about the different causes and solutions of a personal computer.

REFERENCES

[1]. Kaushik, Akhil, and Satvika Manoj Barnela. "Printer Troubleshooting ExpertSystem." *International Journal* 2.10 (2012).

[2]. K.Soundararajan, Dr.S.Sureshkumar, C.Anusuya, Diagnostics Decision Support System for Tuberculosis using Fuzzy Logic,International Journal of Computer Science and Information Technology & Security (IJCSITS), Vivekanandha, June 2012.

[3]. Ahmad Fazrul, Expert system for PC maintenance and troubleshooting, MSc. Thesis , Universti Utara Malysia , 2008.
[4]. AN Ramesh , C Kambhampati, JRT Monson , PJ Drew Artificial intelligence in medicine.
[5]. Peter V. Homeier and Thach C. Le An Extended CLIPS For Backward Chaining and Goal-Directed Reasoning.
[6]. Andrews, Jean. *A+ Guide to Managing & Maintaining Your PC*. Cengage Learning, 2013.
[7]. Eryk Lagun ,Evaluation and Implementation of Match Algorithms for Rule-based Multi-Agent Systems using the Example of Jadex.
[8]. Forgy, C.: Rete: A fast algorithm for the many pattern/many object pattern match problem. Articial Intelligence 19(1), 17-37 (1982).

AUTHORS BIBLIOGRAPHY:

Abrham Debasu Mengistu received his B.Sc. Degree in Computer Science from Bahir Dar University. Currently perusing M.Sc. in Computer Science, School of Computing and Electrical Engineering, IOT, Bahir Dar University, Ethiopia. He has published 01 research papers in international journal(IJSEAT). His main research interest is Image processing and Robotics. He is a life member of professional societies like MSDIWC.

Dr. Vuda Sreenivasarao received his M.Tech degree in computer science and engineering from Sathyabama University from 2007.He received PhD degree in computer science and engineering from Singhania University, Rajasthan, India from 2010. Currently working as Professor in School of Computing and Electrical Engineering, IOT, Bahir Dar University, Ethiopia. His main research interests are Data mining, Fuzzy logic, Mobile communication and Network Security. He has got 13 years of teaching experience. He has published 36 research papers in various international journals and one Springer international conference paper. He has 124 Editorial Board / Reviewers memberships in various international journals. He is a life member of various professional societies like IEEE, ACM, MAIRCC, MCSI, SMIACSIT, MIAENG, MCSTA, MAPSMS, MSDIWC, SMSCIEI, SNMUACEE and MISTE.

American Journal of Engineering Research (AJER)
e-ISSN : 2320-0847 p-ISSN : 2320-0936
Volume-03, Issue-01, pp-140-148
www.ajer.org

Research Paper Open Access

3D Scene Reconstruction from Video Camera for Virtual 3D City Modeling

Surendra Pal Singh[1], Kamal Jain[1], V. Ravibabu Mandla[2]
[1]*Department of Civil Engineering, Indian Institute of Technology (IIT) -Roorkee, India*
[2]*School of Mechanical and Building Sciences, Vellore Institute of Technology (VIT)-University, India*

Abstract: The main purpose of this study is to explore the potential of normal digital video camera for virtual 3D City modeling. For any photogrammetric project work, image acquisition is the main issue. Cost, time, and success of any close range photogrammetric project is mainly dependent on image acquisition method. Video recording is an easy way to capture the large city area in less time. In the present study a simple method for 3D scene reconstruction by using digital video camera is developed for virtual 3D City modeling. The digital video camera used was Sony DSC HX7V camera for video recording. From this video data, image frames created and identified for suitable image frames for image based modeling. After processing some intermediate products were obtained and finally textured 3D model of area was created. Study area was Civil engineering department, IIT-Roorkee, India. Agisoft Photoscan software was used for this work. This paper covers the methodology, result, discussion, conclusion, advantages and limitations of the method.

Keywords: *- 3D scene, Computer vision techniques, Image based modeling, Virtual 3D City modeling,*

I. INTRODUCTION

The Virtual 3-D city model generation is a very hot research topic to engineering and non-engineering scientist. 3D city models are basically a computerized or digital model of a city contains the graphic representation of buildings and other objects in 2.5 or 3D. Demand of Virtual 3D City models is increasing day by day for various engineering and non-engineering fields. Now days, various methods are available to create Virtual 3D City model. Laser scanning and Photogrammetry are the main techniques. For 3D City modeling, Automatic and Semiautomatic; the two main techniques are used for data acquisition, [1]. For 3D City modeling, Image based techniques are more suitable than Laser based techniques due to cost and availability of data. For 3D City modeling, the main problem comes for image acquisition. To find the suitable position for capturing the image is a very important issue for Image based 3D city modeling. Due to this, there is a very high demand for suitable image acquisition system. Images are easily available to everybody at nominal cost. Handling of image based project is very cost effective and accuracy is also good.

For 3-D city modeling, Video recording is the main techniques for image acquisition. It has many advantages. Video is an easy obtainable and low cost data acquisition system, now a days; many researchers are showing interest in this field.

Some of the important previous works are summarized here:

Videogrammetry is a measurement technique which is mainly based on the principles of 'Photogrammetry, [2]. Videogrammetry refers to video images taken using camcorder or movie function on digital still camera. Video movie consists of sequences of images (or frames). If video speed is 25 fps (frame per second) and taken for 1 minute (i.e. 60 seconds), there are 25 frame per second or overall 1500 image.

Kawasaki et al., (1999), also worked for automatic modeling of a 3D city map from real-world video. They proposed an efficient method for making a 3D map from real-world video data. The proposed method was an automatic organization method by collating the real-world video data with map information using DP matching. They also made a system which can generate a 3D virtual map automatically in VRML format. [3]

Clip et al., (2008), designed a Mobile 3-D City Reconstruction system. It is an efficient flexible capture and reconstruction system for the automatic reconstruction of large scale urban scenes. This system is both backpack

and vehicle mounted allowing capture of interior or less accessible areas as well as large outdoor scenes. In this work, they propose an efficient system to capture the 3D-geometry of existing cities through computer vision techniques. This system can deliver 3D reconstructions of large urban scenes in near real time. This system is modular and man portable, it is able to record both from a backpack mounting for interior areas and from an automobile for exterior recording. GPS and INS was also used in this product. [4]

Figure1. 3D reconstruction from Video only with the back pack system (Source: [4])

Tsai et al., (2006), [5] developed a method for texture generation and mapping by using video sequences for 3D building models.

Gael et al., (2007), [6] explained a system for computing geo-referenced positions and orientations for non calibrated videos images of buildings. This method is based on the fusion of multimodal datasets, namely GPS measures, video sequences and rough 3D models of buildings. This is a method for registration of GPS, GIS, and Video data for urban scene modeling.

Pollefeys et al., (2000), [7] gave a method for 3-D model generation using video image sequence.

In 2008, M. Pollefeys and his team created a detailed real time urban reconstruction from Video. They used video data and GPS/GNS data. In this method, there were two main processing components. One was for video data input and another was computing component. After video data input, the data reading or data preparation is a processing component. In computing component, 2-D tracker (GPU) and 3-D tracker/Geo-location are the main track. Geo-located camera was used in this process. By using sparse scene analysis and multi-view stereo, depth map was generated which is very useful to create 3-D model of an area. After this triangular mesh texture map was generated which give a photorealistic textured 3-D model of that area. [8]

Fulton and Fraser, (2009), explained a method for automatic reconstruction of building by using a hand held video camera. In this method, a video recording was done for the building of interest. Video sequence were transferred into computer and saved as individual JPEG frames. Blurred frames were removed and non-blurred key frames were selected. Registered of these non-blurred key frames was done using phase correlation method, after this feature extraction was done. [9]

Zhang et al., (2009), gave a concept for consistent depth maps recovery from a video sequence. Video image sequence frames were used and depth maps from these frames were created. In this method, they used the Structure From Motion (SFM) to recovered the camera parameters, Disparity Initialization, Bundle optimization, and Space-Time fusion techniques was used to create depth maps. These depth maps are useful to create virtual 3-D model of an area or object. [10]

Tian et al., (2010), gave a concept of knowledge-based building reconstruction from terrestrial video sequence. They gave an automatic method for the reconstruction of building models from video image sequences. Building structure knowledge is used as a key factor. [11]

Hengel et al., (2007), developed a method and system, (named as Video Trace). VideoTrace is a system for interactively generating realistic 3D models of objects from video. The combination of automated and manual reconstruction allows VideoTrace to model parts of the scene not visible, and to succeed in cases where purely automated approaches would fail. In this system initially a frame from the input video sequence is taken and a partial tracing of the model takes place then the final model is overlaid on the video, and the result of rendering the final model is brought back into the original sequence. [12]

Singh et al., (2013), developed a multi-camera setup and method for camera calibration from video image frames. From video data, image frames were created for close range photogrammetric work. [13]
In India, Prof. Bharat Lohani and his team, (2012) from IIT-Kanpur, developed an Indigenous technique for Laser based mobile mapping system for 3D modeling. It creates a basic, simple and good 3D model of an area. [14]
Singh et al. (2013), [15] explains about techniques and applications of virtual 3D city modeling. 3D city model is also useful for e-Governance. [16]. Image based modeling is also suitable for building modeling for Virtual 3D City model generation. [17], [18], [19], [20].

Thus, it can be concluded that till now, there is no cost effective and easy to use system available for 3D City modeling. And there is a need for a method, which can be helpful for 3D City modeling by using video data. The main purpose of this work is to explore the potential of normal digital video camera for virtual 3D City modeling. In the present work, it is tried to develop a method for 3D scene reconstruction for 3D City modeling by using video data. For this work, the Agisoft Photoscan software was used for 3D scene reconstruction.

The main contribution of this research paper is to explore the potential of normal digital video camera for Virtual 3D scene reconstruction mainly for virtual 3D city modeling. This method is very fast and processing of image frames is automatic. So it is very easy to use for any kind of image based 3D modeling.

II. METHODOLOGY

Flow diagram of overall methodology can be seen in Figure. 2.

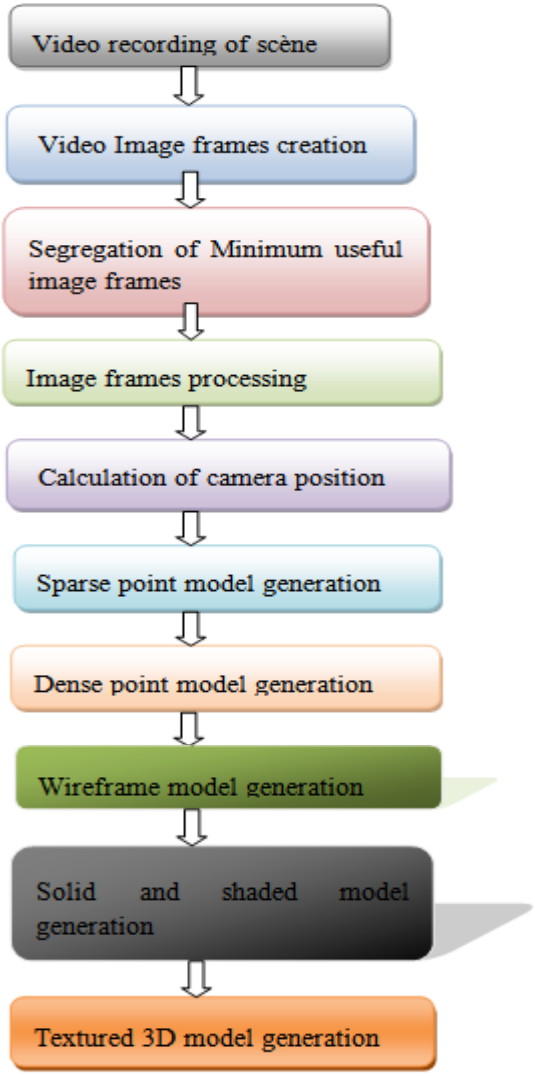

Figure 2. Flow diagram of methodology for 3D scene reconstruction from video camera.

To create the 3D scene reconstruction from video camera, following steps are followed:

1- Video recording of scène
2- Video frame creation
3- Segregation of Minimum useful image frames
4- Image frames processing
5- Calculation of camera position by SfM
6- Sparse point model generation
7- Dense point model generation
8- Wireframe model generation
9- Solid and Shaded model generation
10- Textured model creation

2.1. VIDEO RECORDING OF SCENE

Video recording of Department of Civil Engineering was done using multi camera set up. This multi camera set up is developed by Singh et al. (2013) [13]. Video recording should be taken with slow moving speed. The direction of camera should be parallel for façade modeling. In this research work, the Sony DSC HX 7V, camera was used.

Figure 3. Sony DSC HX7V Digital Camera

The Sony DSC HX7V digital camera is 16.2 mega pixel resolution for image and has Exmor R CMOS Image sensor. It has 10x optical zoom. This digital camera can record full HD video at 1920×1080 resolution. It has capacity to create 50 frames per second (FPS).

2.2. VIDEO FRAME CREATION

After video recording of a scène, the video frames were created. All video camera has the feature "frames per second" (FPS) or "Frame Rate". It is the characteristic feature of any video camera. It defines the frequency (or rate) at which the camera device produces unique consecutive images called frames.

In this work, free software "Free Video to JPG Converter" was used. This software also has the capacity to control the frame rate. It means, if Video recording time is for 5 minutes, (5×60= 300 seconds) and camera has 50 FPS. So in five minutes video (300×50=15000), 15000 images fames are created. With this software, one can change the frame rate. According to user requirements, one can choose every 10, 30, 50,100, 500, 1000 frames, or in every 1,2,5,10,20 seconds. One can also choose total number of frames as 10, 20, 50,100,200,500, or one can also extract every frame from video.

Figure 4, is showing some video image frames created by this software.

Figure 4. Some video image frames

2.3. SEGREGATION OF MINIMUM USEFUL IMAGE FRAMES

After extraction of video image frames, the minimum useful image frames for 3D image modeling was selected. One can use all created image frames, but computer system will heavy loaded during processing and create problem during image frames processing. Consecutive images or frames have more overlapping area. Therefore images frames after some interval were selected; depending on overlapping of area in image frames.

2.4. IMAGE FRAMES PROCESSING

For 3D model generation, these image frames were used for 3D point creation. After processing of these video image frames, 3D points and model was obtained. Image alignment is a main processing for this work.

2.5. CALCULATION OF CAMERA POSITION

After Image Alignment, camera position obtained for each video image frame. Fundamental matrix (3×3 matrix, which relates the corresponding points in stereo images) used and the intrinsic parameter of camera were calculated. After that, a solution for camera position was obtained. [21], [22].

Figure 5. Building façade with video frame positions

2.6. SPARSE POINT CLOUD GENERATION

3D point cloud created by using Structure from Motion (SfM) techniques. Feature detection and feature matching is the key concept to produce sparse 3D point cloud from image sequence [23]. Figure 6, is showing the sparse point cloud model of an area from Civil Engineering department of IIT-Roorkee.

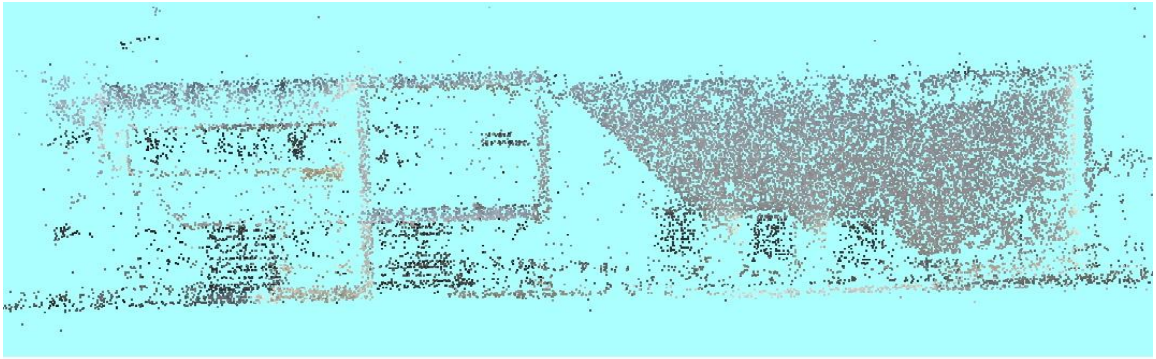

Figure 6. Sparse Point cloud model

2.7. DENSE POINT CLOUD GENERATION

The number of point cloud increased using more efficient methods of feature matching techniques and dense point cloud model of an area were created. It produces more details of area.
Figure 7, showing the dense point cloud model of area.

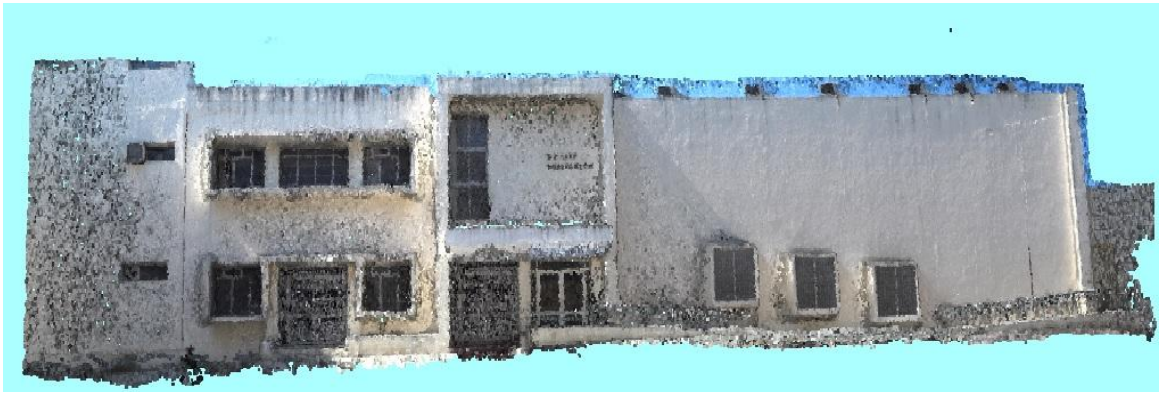

Figure 7. Dense Point cloud model

2.8. WIREFRAME MODEL GENERATION

Wireframe model also created with the help of these 3D points. Wireframe model is useful to produce exploded and perspective view more easily. This model is also useful for viewing the model from any desired point by changing line of sight. Figure-8, showing the wireframe model of an area.

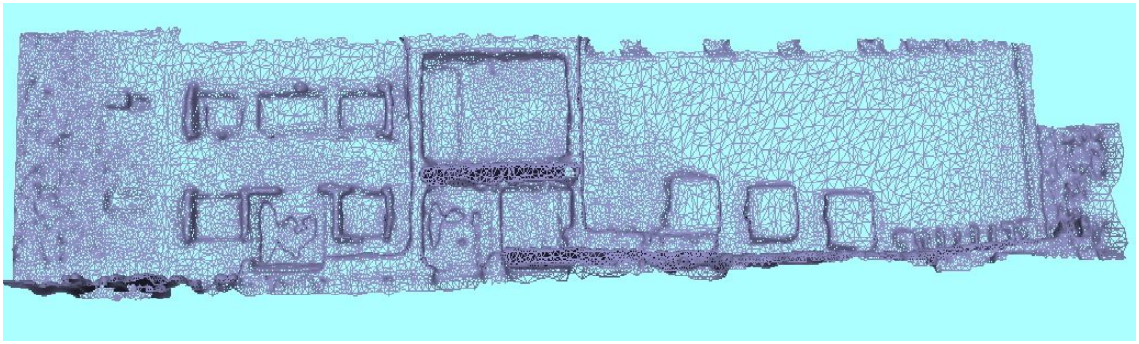

Figure 8. Wireframe model

2.9. SOLID AND SHADED MODEL GENERATION

Wireframe model does not represent an actual solid and has no surface and volume information. Thus, solid model and shaded surface model created. Solids model is a complete and unambiguous representation of a precisely enclosed and filled volume. Shaded model gives near about actual model of an area.
Figure 9, and Figure 10 is showing the Solid model and Shaded model.

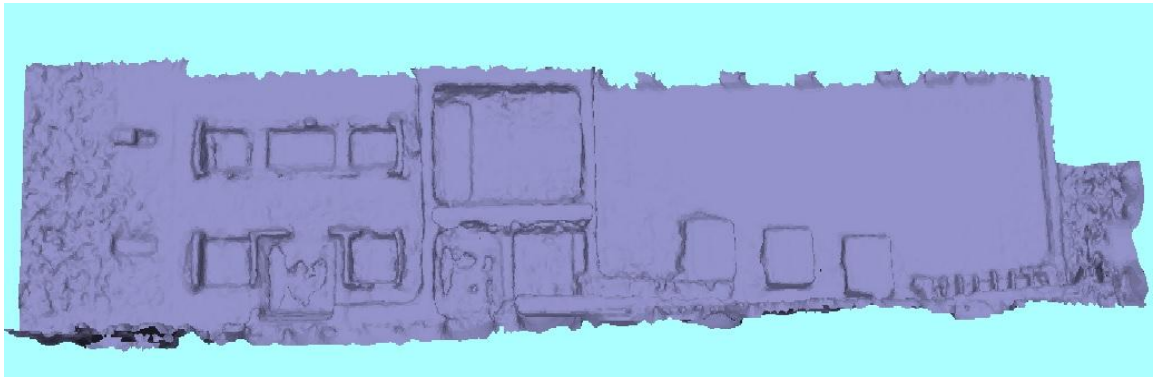

Figure 9. Solid model generation

Figure 10. Shaded model generation

2.10. TEXTURED MODEL GENERATION

At finally, generic texture method applied, which allows parameterization of texture atlas for arbitrary geometry and make final textured 3D model of an area. It gives photo-realistic representation of a scene.

Figure 11. Textured 3D model of O.P.Jain Auditorium building of Civil Engineering Department, IIT-Roorkee, India.

III. RESULT AND DISCUSSION

By using this proposed method, 3D scene obtained of O.P.Jain Auditorium side of Department of Civil Engineering, Indian Institute of Technology, Roorkee, India. Our main goal was to show the feasibility of 3D scene reconstruction from hand held digital video camera. This proposed method will be very useful for image based virtual 3D city modeling by using normal digital video camera. Normal digital video camera is very cheap source of image acquisition and easily to handle by user. In less time, more data can be obtained. So project cost will reduce. In this way, it can conclude that this method will be helpful for 3D city reconstruction.
In Indian city, this technique will be very useful to make virtual model of any city. This technique is very cost effective to create virtual 3D City model, compare to any other Geomatics techniques such as Aerial Photogrammetry, Satellite Photogrammetry or Laser scanning based techniques.

IV. CONCLUSION

Advantages and Limitations of this method can be summarized as given below:
Advantages: The main key advantages for this method:

- Automatic processing,
- Photo-realistic 3D scene,
- Time and Cost of project will reduce.
- Image frames created by video; can be used for any kind of Image based 3D modeling software.

Limitations: The main limitations are given below:

- For Video recording of a City, weather conditions and light condition should be favorable.
- Crowd conditions should be avoided.
- Video camera quality should be high for good quality of 3D model.
- Higher resolution camera gives good photo-realistic 3D model.
- All video image frames are not useful.
- Processing time depends on number of video image frames.
- Speed of video recording is also play important role for image frames quality.
- If the building façade is large then camera is kept at large distance from the building.

The possible application of this research work is also very important. Video recording of any city will be very easy and cost of project will reduce. Anyone can use multi camera set up for 360^0 recording of area. Camera configuration can be change according to software requirements. Integration of GPS/INS is also possible in this research work. For future work, video camera based mobile mapping vehicle is also possible for fast 3D City modeling.

Virtual 3D city modeling has many important applications. 3D city model is useful to identify the encroachment in municipality, Virtual tourism, Historical fort and building conservation etc. So the demand of 3D city modeling is increasing day by day. Normal digital video camera has the good potential to create virtual 3D city model. Finally, it concluded that, this proposed method will be very useful to create 3D city model by using video camera in less cost and less time. Texture quality of 3D model is also very good. This method is fully automatic and very easy to use.

V. ACKNOWLEDGEMENT

This work was supported by the MHRD grant (also called as Institute Fellowship; duration From Jan.-2009 to Dec.-2012) given by Indian Institute of Technology, Roorkee, Uttarakhand, India. Also thanks to my friends and staff of Civil Engineering Department of IIT-Roorkee for support us during this work.

REFERENCES

[1] Forstner, W., “3-D City Models: Automatic and Semi-automatic Acquisition methods”, Photogrammetric week, Wichmann, Karlsruhe. 1999.
[2] Gruen, Armin. "Fundamentals of videogrammetry—a review”, Human movement science, 1997, Page-155-187.
[3] Kawasaki Hiroshi, Yatabe Tomoyuki, Ikeuchi Katsushi, Sakauchi Masao, “Automatic Modeling of a 3D City Map from Real-World Video”, 1999, Institute of Industrial Science, University of Tokyo, Japan.
[4] Clipp Brian, Raguram Rahul, Frahm Jan-Michael, Welch Gregory, Pollefeys Marc, “A Mobile 3D City Reconstruction System”, 2008, UNC Chapel Hill, ETH, Zurich.

[5] Tsai Fuan, Chen Cheng-Hsuan, Liu Jin-Kim and Hsiao Kuo-Hsing, "Texture Generation and Mapping Using Video Sequences for 3D Building Models", Innovations in 3D Geo Information Systems, 2006, 429-438.
[6] Gael Sourimant, Luce Morin,Kadi Bouatouch, "GPS, GIS and Video fusion for urban modeling". CGI, May 2007.
[7] Pollefeys M., Koch R., Vergauwen M., Van Gool L., "Automated reconstruction of 3D scenes from sequences of images", ISPRS Journal of Photogrammetry & Remote Sensing, 55, 2000, 251–267.
[8] Pollefeys M., Nistér D., Frahm J.M., Akbarzadeh A., Mordohai P., Clipp B., Engels C., Gallup D., Kim S.J., Merrell P., Salmi C., Sinha S., Talton B., Wang L., Yang Q., Stewénius H., Yang R., Welch G., Towles H., "Detailed Real-Time Urban 3D Reconstruction from Video", International Journal of Computer Vision, 78: 2008, 143–167.
[9] Fulton J.R. and Fraser C.S., "Automated Reconstruction of Buildings using a Hand Held Video Camera", S. Jones, K. Reinke (eds.), Innovations in Remote Sensing and Photogrammetry, Lecture Notes in Geoinformation and Cartography, Springer-Verlag Berlin Heidelberg, 2009, 393-404.
[10] Zhang Guofeng, Jia Jiaya, Wong Tien-Tsin, and Bao Hujun, "Consistent Depth Maps Recovery from a Video Sequence", IEEE Transactions on pattern analysis and machine intelligence, Vol. 31, No. 6, June, 2009, 974-988.
[11] Tian Yixiang, Gerke Markus, Vosselman George, and Zhu Qing, "Knowledge-based building reconstruction from terrestrial video sequence", ISPRS Journal of Photogrammetry and Remote Sensing, 65, 2010, 395-408.
[12] Hengel Anton van den, Dick Anthony, Thormahlen Thorsten, Ward Ben, Philip H, and Torr S., "VideoTrace: Rapid interactive scene modelling from video", ACM Transactions on Graphics, Vol. 26, No. 3, 2007, 86.
[13] Singh, Surendra Pal, Mandla, V.Ravibabu, Jain, Kamal, "Design and Calibration of Multi Camera setup for 3D City modeling,", International Journal of Engineering Research & Technology (IJERT), Vol. 2, Issue 5, May 2013.
[14] Salil Goel , Manohar Yadav, Anjani K. Singh and Bharat Lohani, "An Indigenous development of land based mobile mapping system", India Geospatial Forum, Hyderabad, 22-24, Jan, 2013.
[15] Singh, Surendra Pal, Mandla, V.Ravibabu, Jain, Kamal, "Virtual 3D City Modeling : Techniques and Applications", International Archives of the Photogrammetry, Remote Sensing and Spatial Information Sciences, Volume XL-2/W2, ISPRS 8th 3DGeoInfo Conference & WG II/2 Workshop, 27 – 29 November, 2013, Istanbul, Turkey.
[16] Singh, Surendra Pal, Mandla, V.Ravibabu, Jain, Kamal, "Virtual 3-D City Model for G-Governance", Regional Conference on Geomatics for Good-Governance (G-Governance-2011) (13-14 Sep, 2011), Indian Society of Geomatics and Kashmir University, Srinagar, (J&K), India.
[17] Shashi M. and Jain Kamal, "Use of Photogrammetry in 3D Modeling and visualization of buildings", Asian Research Publishing Network (ARPN) - Journal of Engineering and Applied Sciences, Vol. 2, No. 2, April 2007, ISSN 1819-6608.
[18] Singh, Surendra Pal, Mandla, V.Ravibabu, Jain, Kamal, "3-D Building Modeling from Close Range Photogrammetry", Geomatrix'12 , An International Conference on Geo-spatial technologies and Applications, 26-29, February 2012, CSRE, Indian Institute of Technology Bombay (IITB).
[19] Singh, Surendra Pal, Mandla, V.Ravibabu, Jain, Kamal, "Image Based 3D Modeling of Campus (Department of Civil Engineering, IIT Roorkee, Uttarakhand, India) by Using SketchUp", International Journal of Advanced Civil Engineering and Architecture Research, Volume 2, Issue 1, pp. 65-71, Article ID Tech-168. September, 2013.
[20] Singh, Surendra Pal, Mandla, V.Ravibabu, Jain, Kamal, "Virtual 3D Campus Modeling by using Close Range Photogrammetry", American Journal of Civil Engineering and Architecture, Vol.1, No.6, 2013, Page 200-205, doi: 10.12691/ajcea-1-6-9.
[21] Richard Hartley, "Estimation of relative camera positions for uncalibrated cameras", Proceedings of European Conference on Computer Vision, 1992.
[22] Richard Hartley and Andrew Zisserman, "Multiple View Geometry in computer vision", Cambridge University Press, 2003, ISBN 0-521-54051-8.
[23] Noah Snavely, Steven M. Seitz, Richard Szeliski, "Photo tourism: Exploring photo collections in 3D," ACM Transactions on Graphics (SIGGRAPH Proceedings), 25(3), 2006, 835-846.

American Journal of Engineering Research (AJER)
e-ISSN : 2320-0847 p-ISSN : 2320-0936
Volume-03, Issue-01, pp-150-162
www.ajer.org

Research Paper Open Access

Hydrogeology Of Nsukka Southeast, – A Preliminary Approach To Water Resources Development.

[1]uzoije A.P [2]onunkwo – A, A,
[1]*department Of Environmental Technology*
[2]*department Of Geosciences Federal University Of Technology, Owerri*

Abstract: - The hydrogeology of Nsukka SE has been carried out as a preliminary approach to water resources development of the region. Topographic, maps, data from meteorological stations, and other departments, Geological maps, aerial photograph, fracture maps and satellite images of Anambra drainage basin were employed in the study. Inorganic analysis were undertaken using Atomic absorption spectroscophy, spectrophotometer, flame photometer, spekker absorption meter and turbimetric methods, while organic analysis was done using the most probable number Technique (MPN).
The result shows that the average precipitation of the area is 2.09 x 10^8 m^3 a year, while the rainfall intensity gives 0.15/year. Runoff for the area was calculated to be 1.06 x 10^7 m^3 / year, amounting to 5.07% of the total precipitation. Potential evapotranspiration amounts to 1057.98mm/year giving 8.112% of the water available from precipitation.
Depth to water table ranges from 106.70m to 9.15 from recharge area of the watershed to the farmland discharge low lying area. Aquifer type ranges from unconfined , semiconfined to confined. The average transmissivity values was calculated to be 3.25 x $10^{-2}m^2/s$, while hydraulic conductivity gives 2.3 x 10^{-3} m/hr. Specific discharge is 2.24 x 10^{-4} m/yr, average groundwater linear velocity is 4.98 x 10^{-4} m/yr. The chemical constituents of deep and shallow aquifer waters show that iron concentration is on the high side. The deep aquifer waters show no pathogens while the shallow aquifers of the low lying discharge environment show heavy coliform presence. The water class for deep aquifer indicates magnesium and a no dominant anion and plotted on a transition between salt and fresh water, while the shallow aquifer water is Magnesium sulphate (hard water) and plots within the zone of salt water. The water meets the consumption standard, and industrial needs though acidic and of high iron content. The water is excellent for irrigation, and requires minor treatment. These information are ideal for reference during the water resources development of the region.

Keywords: *- Hydrogeology, Nsukka SE, Anambra basin, Southeastern Nigeria, Water Resources, development.*

I. INTRODUCTION

The primary objective of this study is to evaluate the hydrogeology of Nsukka SE within the Anambra basin of south-eastern-Nigeria; as a preliminary approach for the development of the water resources of the region. This evaluation consisted of physical, chemical and biological reconstruction of the properties of the underground water and aquifer systems, the total precipitation calculated for water years from gauging stations, the hydraulic head distribution, hydraulic connections between the available lakes / rivers and the aquifers, accessibility of the groundwater through the correlation of lithologs obtained from Vertical Electrical Soundings of the aquifer lithology, estimation of ground water movement direction as a prelude to contaminant migration and waste disposal siting (Viesman, 2004), distribution of geochemical constituents and classification of aquifer / water types. Hydrologic information collected from sources ranging from gauging stations to available literature were integrated to formulate recommendations for optimum development of aquifer system and to help facilitate maximum utilization of the available water resources of the study area. The areas affected by this study include Opiuno, Opi Agu, Ekwegbe Uno, Ekwegbe Agu Orba, Ehalumona and Ehandiagu. The area covers about 160km^2 and lies within latitudes 6.42° N to 6.42° N and longitudes 7° 26′ to 7 36′ E (Iloeje, 1981). The 2006 population figure for the zone is about 100, 000 and this is likely to reach 1,000000 by the year 2010. (NPC, 2006). This calls for water resource development . Water table is very deep at the areas

bordering the water divide (Opi Uno, EkwegbeUno and Eha-Alumona). Water table is relatively shallow at Ekwegbe Agu, Opi Agu and Eha Ndi-Agu low lying areas. This probably accounts for the few number of boreholes at the areas bordering the water shade and the relative abundance of hand dug wells at the low 'Agu' discharge or farmland areas. (Egboka, 1996).

II. METHOD OF STUDY

Description of Study

The study area falls within the Anambra basin of South-eastern Nigeria and lies within latitudes 6° 42′ N and 6° 48′ N, Longitudes 7° 26′E and 7° 36′E and encloses an area of about 160km^2 fig I.

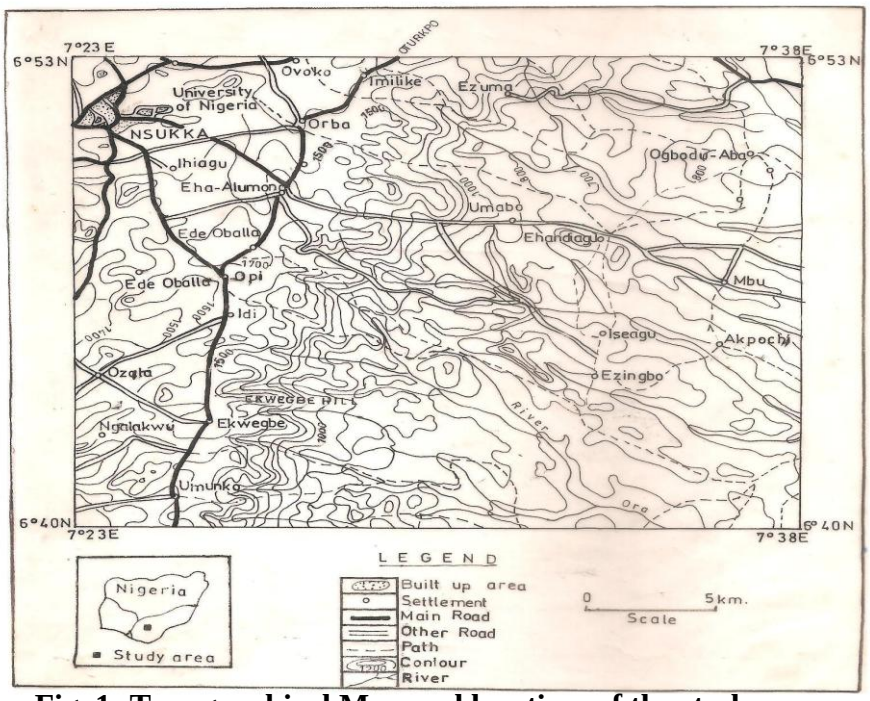

Fig. 1: Topographical Map and location of the study area

Geologically, the area is a part of Anambra basin whose rocks are upper cretaceous in age. The stratigraphic succession in Anambra basin is shown in table 1.

Table I: Generalized Sedimentary Sequence in South-eastern Nigeria (Reyment, 1965).

Age	Sequence	Formation	Lithology
Tertiary	Miocene-recent	Benin Formation	Medium-coarse grained, poorly consolidated sands with clay lenses and stringers.
	Oligocene-miocene	Ogwashi Asaba Fm.	Unconsolidated sands with lignite seams.
	Eocene	Ameki Fm	Grey clayey sandstone and sandy clay stones.
	Paleocene	Imo Shale	Laminated clayey shales
Upper Cretaceous	Upper Maaastritchian	Nsukka Fm	Sandstones intercalating with shales
		Ajali sst	Poorly consolidated sandstone, typically cross beded with minor clay layers.
	Lower Maastritchian	Mamu Fm	Shales, sandstones, mudstones and coal seams.
	Campanian	Nkporo/Enugu Shale	Dark grey shale, clayey shale with clay lenses
	Santonian	Awgu Fm	Bluish grey shale with clay lenses.
	Turonian	Ezeaku Fm	Black shale with clay and limestone lenses.

The three geologic formations which outcropped in the area include Mamu Formation (lower Maastritchian), Ajali sandstone (upper Maaastritchian) and Nsukka Formation (Damian) Fig. 2. Nsukka Formation is described as cap rock previously known as upper coal measures (Simpson, 1954, Reyment 1965). The Mamu Formation consists of mudstone, sandy shales and fresh water sandstones. Reyment (1965) noted the presence of ammoniferous shales in some parts of the formation. The formation strikes N-S and dips west wards, with the average dip between 4° to 8° (Umeji, 1980). Mamu Formation has fine grained sandstone and provides the shaley impermeable base on which the waters of Ajali aquifer are trapped, as the later is

conformably underlain by shaley units of Mamu Formation. The Ajali Sandstone (upper Maastritchian) is about 451m thick (Agagu et al 1985). Lithologically the Ajali sandstone consists of medium to coarse –grained, poorly consolidated white sands with characteristic cross bedding and clay intercalations. Agagu et al (1985) have reported presence of such ostracods as cytherella, ovocytherides and a few foraminifera such as Hyplophragmoids and Ammobaculites. Overlying Ajali sandstone sequence is Nsukka Formation. The formation is related to Mamu Formation in many aspects only that Nsukka Formation has no coal seams in the study area. Outliers of Nsukka Formation dot the area with Ajali sandstone providing the base (Egboka, 1996).

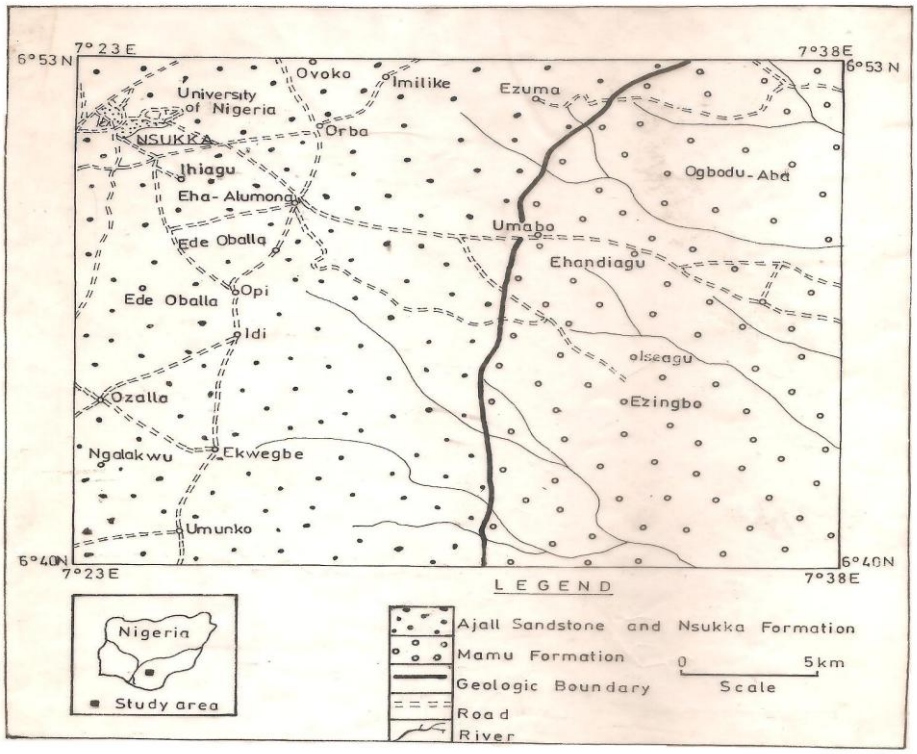

Fig. 2: Geological map of the Study Area (Reyment 1965)

Two climatic seasons characterize the study area – the dry and wet seasons. According to Udo (1978), the dry season generally begins about the middle of October and ends around March, while the rainy season sets in April and ends in early October (Iloeje 1995). According to the author, the mean annual rainfall is 1304.2mm, while the mean monthly maximum temperature is 28.73°C. Also the mean annual relative humidity is 58.28% mean vapour pressure is 21.68, pitche evaporation is 4.32 and mean monthly minimum temperature is 21.26°C. According to Ogbukagu (1976), the physiography is dooted by numerous cone shaped hills that are laterite capped and are the outliers of Nsukka Formation. The conical hills are often separated by low lands and broad valleys. The surface run off on these valleys is virtually nil due to the high permeability of the red earth mantle and soil as well as the thick underlying Ajali Sandstone. The most prominent topographical features in the study are the North- South trending cuesta over Ajali sandstone. The dip slope of the cuesta is generally South-east wards (Edokwe, 1976).

The vegetation and soil types are related. The study area lies within the tropical rain forest / Guinea Savannah belt of Nigeria (Iloeje, 1978). The author classified the soil as the rain forest and lateritic soils. The rainforest soils are rich in humus derived from rainfall in the forest, unfortunately the soils are highly leached by heavy rainfall. Soils underlying savannah type of vegetation have low organic matter content and low cation exchange capacity. Their pH values are very low (3.3 to 4.3) and this may be due to excessive leaching ((Edokwe, 1976). The major characteristic of the vegetation of this area is the abundant combination of varied plant groups whose branches intertwine to form a continuous canopy of leaves. The major plant and grass species include iroko, palm tree, obeche, Eupatorium Odoratum and imperata sylindrica.

Method of Study:

The work was carried out in stages and involved literature review and reconnaissance work. Topographic and geologic maps were employed in the identification of rock formations and in establishing their stratigraphic / structural relationships also detailed surface / subsurface geologic and hydrogeologic studies were carried out. Activities involved the determination of volume mean annual recharge measurement of static

water levels, collection of water samples from streams, springs, hand dug wells and bore holes. The final phase was used for laboratory studies in which chemical analysis of water samples and sieve analysis of aquifer sands were carried out. From sieve analysis data, aquifer hydraulic properties were determined.

Data Acquisition: The instrument used for data acquisition include topographic map of the area, geologic map, aerial photograph, fracture maps, satellite images of Anambra drainage basin. Hydrogeological investigations were carried out by identifying areas of ground water seepage. Lithological logs of three bore holes in the area were obtained from Enugu state water corporation GSN BH 3131 (OPI), GSN BH 3146 (Ehaalumina and GSN BH 2020 (Ekwegbe). The aim of the lithologs is to identify geologic stratification of the sub surface materials, hence the aquifers.

A total of seven water samples were collected for organic and inorganic analysis using Atomic absorption sepectrocopy for Ca^{2+}, Na^{+}, Mn $^{2+}$, Cl^{-} Pb, Cd Zn, copper was analysed with the aid of spectrophotometer, while K^{+} was determined using flame photometer method. pH was measured with standard pH meter concentrations of total iron (Fe^{2+}) were determined calorimetrically using Spekker absorption meter. Total dissolved Solids (TDS) was determined using glass fiber filter. The concentrations of $Ca^{2+,}$ Mg^{2+} and Na^{2+} in milliequivalent per litre were used to obtain sodium absorption ratio. (SAR). Turbimetric method was used to assess turbidity. Physical parameters like pH and dissolved oxygen were measured insitu in the field with appropriate standard meters, while anions like HCO_3^{-} were estimated by titrimetric method water levels were estimated using calibrated tape. Clean plastic containers were used to contain the water samples, they were rinsed several times with the same water samples to be analysed, then covered with air tight cork, carefully labeled and sent to the laboratory for chemical analysis within 24 hours of collection. All details of analytical procedures are reported in Omidiran (2000).

III. RESULTS

Result from all available water resources records of the area Hydrology, and borehole logs were presented and all necessary calculations made.

Tables 2 (a-f) shows Average Hydrological data for six water years (1985-1990) obtained from University of Nigeria Nsukka (UNN) Meteorological Station

Table 2 Average Hydrological data for 1985/86 Water Year

<<<<

(a)

Average	Max. Temp.	Min. Temp.	Rel. Humidity	Vapour Pressure	Piche Evap.
	29.86	19.61	74.58	25.18	4.0

Average Hydrological data for 1986/87 Water Year

(b)

Average	Max. Temp.	Min. Temp.	Rel. Humidity	Vapour Pressure	Piche Evap.
	28.9	19.80	74.32	22.23	4.04

Average Hydrological data for 1987/88 Water Year

(c)

Average	Max. Temp.	Min. Temp.	Rel. Humidity	Vapour Pressure	Piche Evap.
	28.74	21.2	68.56	29.1	4.0

Average Hydrological data for 1988/89 Water Year

(d)

Average	Max. Temp.	Min. Temp.	Rel. Humidity	Vapour Pressure	Piche Evap.
	28.30	20.27	73.69	21.88	4.09

Average Hydrological data for 1989/90 Water Year

(e)

Average	Max. Temp.	Min. Temp.	Rel. Humidity	Vapour Pressure	Piche Evap.
	27.97	27.27	72.61	23.68	3.92

Average Hydrological data for 1990/91 Water Year

(f)

Average	Max. Temp.	Min. Temp.	Rel. Humidity	Vapour Pressure	Piche Evap.
	27.97	27.27	72.61	23.68	3.92

Lithological logs from the 3 available boreholes of the area is shown in fig. 3

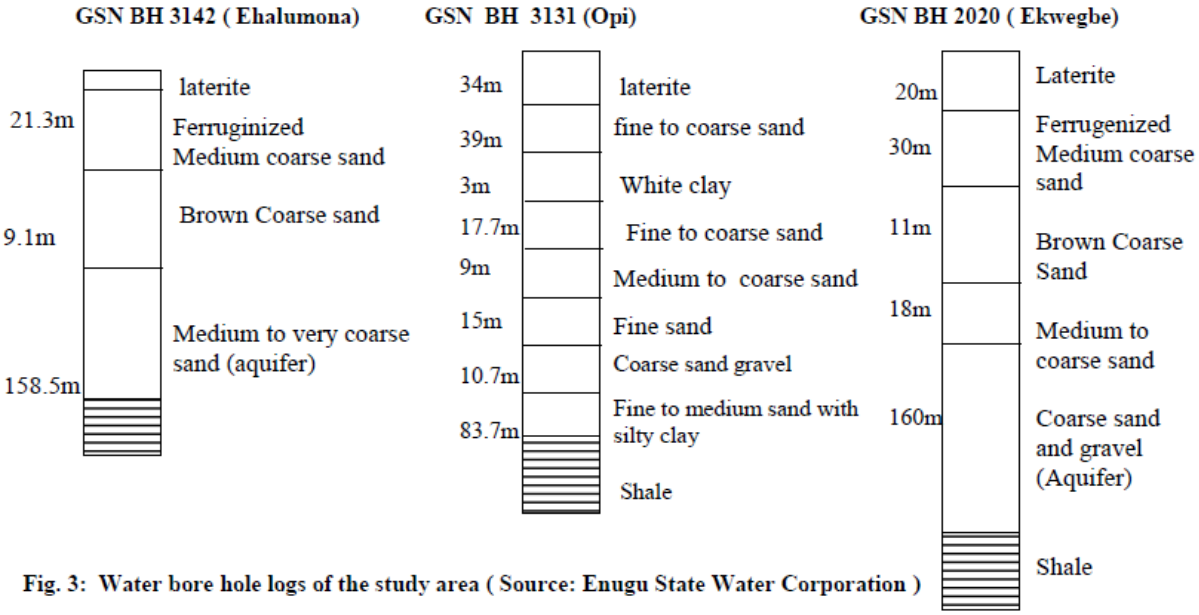

Fig. 3: Water bore hole logs of the study area (Source: Enugu State Water Corporation)

Table 3: result of Rain fall data (mm) for the years 1985-91

Months	1985/86	86/87	87/88	88/89	89/90	90/91
April	60.61	90.4	14.5	107.9	62.4	60.5
May	266.8	212.2	115.6	128.7	250.8	248
June	11.3	230.1	172.4	202	104.3	105.2
July	298.3	312.6	153.7	374	264.5	238.4
August	151.4	179.5	100.5	285	150.7	140.8
Sept.	239.8	255.5	242.3	249.7	225.5	220
Oct	193.7	54.5	48.2	125	135	160
Nov.	0.0	18.5	34.2	103.5	12.4	18.5
Dec.	0.0	0.0	0.0	0.0	0.0	0.0
Jan.	17.5	0.0	0.0	0.0	0.0	0.0
Feb.	48.3	0.0	0.0	4.5	0.0	5.3
March	5.5	12.4	47.5	30.5	50.3	40.8
Total	1454	13.35	928.9	1614.8	1255	1237.5
Monthly Av.	121.17	111.31	77.41	134.57	104.60	103.13

The result obtained from meteorological stations in table 2 and 3 were used to compute the hydrological balance equation as:

$P = 1 + R + E$ ……..(1)

Where P = precipitation, 1 = infiltration, R = Runoff

E = Evapotranspiration . The above equation helps in the estimation of the amount of water leaving or entering a basin. (Iloeje , 1995). The mean annual rainfall from University of Nigeria Nsukka rain guage station gives 1304.2mm, while the area of study was measured from ordinance survey map of Nigeria (1990), and this gives 160k m^2. The amount of water available from precipitation (p) gives 2.09 x $10^8 m^3$ year (1304mm x 160km^2). Viessman (1972) gave a formular for estimating the quantity of water which occurs as runoff from the relation:
Q = C. I.A……(2)

Where Q = Peak discharge or runoff coefficient.
I = Rainfall intensity in mm/ hr, A = Catchment area in Km^2 Scoup (1978) gave the average runoff coefficient (c) for Anambra basin as 44% (0.44). The rainfall intensity (I) calculated for the area gives 0.15mm/yr. Therefore with catchment area of 160km^2, the peak discharge in terms of runoff was calculated to be 1.06 x $10^7 m^3$/yr. Table 4 gives potential Evapotranspiration of Nsukka area

Table 4: Prefeasibility report on the Anmabra River basin (Source: Skoup 1978)

Jan	Feb	March	April	May	June
4.5	5.5	4.9	4.7	4.3	3.7
July	**August**	**Sept.**	**Oct.**	**Nov.**	**Dec**
3.5	3.3	3.5	3.9	4.2	4.3

From table 3, the actual evapotranspiration for a year is taken as 70% of potential evapotranspiration (Skoup 1978) and amounts to 1057.98mm/yr and represents 8.112% of water available from precipitation.

Infiltration (I) is calculated from the following:

Infiltration (I) = p - R - E……..(3)

Where P (Precipitation) = 2.09 x $10^8 m^3$ or 100%

R (Runoff) = 1.06 x $10^7 m^3$ or 5.07%

E (Evapotranspiration) or 8.112%

The percentage of water infiltrating down to the groundwater table (13.182%) shows that the area has a relatively high recharge potential (Ofomata 1985). The runoff of 5.07% is significantly low because of the high permeability of the underlying soil mantle and Ajali sandstone that directly underlie the soil over much of the are (Agagu et al. 1985). The result from the three (3) available well logs and field investigations of the lithologies within the gorges reveal the aquifer systems. It was observed that Nsukka Formation provides perched aquifer units trapped by the basal shale units on the flanks of its outliers (Tattam, 1981) Ajali sandstone consists of thick, poorly, consolidated medium to coarse

Grained sands inter layered with thin white clay bands, silty clays and fine grained sands. The mode of occurrence of clay is significant in the area. The clays have greater thickness when they occur as silty clays. This formation some what confines the Ajali aquifer waters stored between the silty clay and the upper limit of the imperious shale unit of Mamu Formation. This shows that the waters of Ajali aquifer in the area is unconfined to semi confined to confined. Generally, the basal shale unit of Nsukka Formation and upper limit of Mamu Formation confined the Ajali waters. In all the head waters (Gorges) visited the underground water flows under a thick deposit of silty white sand about 60 m thick. This water is confined between the underlying Mamu Shale and overlying Nsukka shale unit. However, from observations where white clay units occur near the surface, the Ajali sandstone furnishes perched water. The Ajali sandstone which is predominantly aquiferous has aquitard units (Nwankwor et al, 1988). The medium to coarse grained sand units of the formation from the aquifers, while the thin clays, silty clays and fine grained sand units of the formation form the aquitards. Aquitards in the area are not prominently developed at the upper horizons. They rather occur in discontinuous bands that trap some perched water especially during the rainy seasons, this perched aquifers (springs) dry up during dry seasons Uma (1989). The base flow for the area therefore occurs above the shale unit of Mamu Formation. The average measured water table in the recharge environment of the watershed gives 106.7om, while at discharge environment (OpiAgu, Ekwegbe Agu, Ehandiagu), the average value is 9.15m, indicating a progressive decrease from the recharge to the discharge zones of the area. The shallowness of the static water table at the farmland lowlying discharge environment likely shows that those areas are

located at the shallow Ajali sandstone – Mamu Formation boundary and shallow wells tap the aquifers which are likely to be polluted (Freeze and Cherry 1979).

Aquifer characteristics : The characteristics of the aquifer of the area were obtained from the work of Egboka and Uma (1986). The data are shown in table 5 and 6.

Table 5: transmissivity Values for the Ajali aquifer system computed from pumping analysis (Source: Egboka and Uma, 1986).

S/No	Location	Step Draw down T (m^2h^{-1})	Recovery T (m^2h^{-1})	Jacobs T(m^2h^{-1})	Logans T (m^2h^{-1})
1	Ibeawaka	3.10	25.64	-	19.2
2	Udi	1.46	-	-	7.79
3	Ekwegbe	4.16	35.26	-	48.99
4	Ohafia	0.83	1.55	-	5.75
5	Ighere	0.28	1.79	6.16	2.68
6	IhaAlumona	0.35	2.19	2.62	4.44
7	AkpugoEze	0.57	0.75	-	-
8	Opi	0.40	0.12	0.22	0.55
9	Ezimo	0.80	5.58	3.36	6.05
10	Ngwo	0.51	2.29	3.60	13.74
11	Ovim	0.41	2.58	2.45	3.95
12	Amiyi	-	0.26	2.33	1.00
13	Okpuje	1.48	12.95	-	38.87
	Average	4.5×10^2	3.158×10^3	1.11×10^3	4.96×10^3

Table 6: Hydraulic Conductivity values for the Ajali Aquifer sytem (Egboka and Uma, 1986)

S/No	Location	Stepdraw down (mh^{-1})	Recovery (mh^{-1})	Jacob (mh^{-1})	Logans (mh^{-1})	Statistical Methods		
						Haleman (mh^{-1})	Hazen (mh^{-1})	Masch and Denny
1	Ighere	0.17	0.119	0.411	0.179	1.07	1.66	0.30
2	Obinofia	0.023	0.146	9.175	0.296	0.831	1.30	0.648
3	Ohafia	0.055	0.103	-	0.383	0.5540	0.864	0.518
4	Akpugoeze	0.035	0.045	-	0.328	0.749	1.166	0.559
5	Udi	0.09	-	-	0.48	0.576	1.166	0.551
6	EhaAlumma	0.053	0.372	0.224	0.403	1.066	0.90	0.421
7	Ngwo	0.034	0.153	0.24	0.249	1.066	1.663	0.6345
8	Ovim	0.027	0.172	0.163	0.26	1.4	1.663	0.794
9	Amiyi	-	0.017	0.022	0.066	1.4	-	-
10	Ekwegbe	0.26	2.18	-	3.30	-	-	-
11	Akpuje	0.097	0.85	-	2.55	-	-	-
12	Opi	0.003	0.008	0.015	0.036	-	-	-
13	Ngwo	0.19	1.59	-	1.19	-	-	-
	Average	0.126	0.480	1.457	0.748	-	-	-

IV. RESULT FROM STATISTICAL METHODS

The data obtained from sieve analysis of aquifer samples of Ajali sandstone are presented in table 7. The statistical method applied are those of Hazen (1993), Harleman et al (1963), Masch and Denny (1966). The statistical methods are based on size analysis of Ajali aquifer samples. From table 6, it is possible to use the various statistical methods to calculate hydraulic conductivity (k) Transmissivity

Table 7: Grain Size Calculation from statistical using sieve analysis method

Location	Dmm_{10}	Dmm_{50}	Q_5	Q_{80}	Q_{95}
Opi	1.0	.43	-.4	1.0	1.6
OpiAgu	1.8	.91	-1.1	1.95	2.9
EhaAlumona	1.2	.48	- .9	2.25	3.6
Ekwegbe	1.60	.65	.95	-	-
Orba	1.44	.50	.07	2.1	2.9

(T) values for the aquifer system (Todd 1979). The average screen length in the three bore holes of the area is 20m. The transmissivity was calculated based on this . Transmissivity (T) is defined as the ease with which an aquifer transmits water through its entire thickness and has been defined mathematically by Freeze and Cherry (1979) as

$$T = kb \ (m^2/s\ldots\ldots\ldots) \quad (4)$$

Where k = hydraulic conductivity (m/s), b = saturated thickness of the aquifer (Screen length). The average T value obtained using 20m Screen length (b) is 3.25×10^{-2} m^2/s.

Specific Discharge and Average linear velocity: The hydraulic gradient of the area computed from difference in head in static water level in borehole between EhaAlumona and Opi gives 0.00975 specific discharge from Freeze and Cherry 1979 is computed as vd = ki ……(5)

Where vd = Specific discharge , k = hydraulic conductivity, i = hydraulic gradient . From equation 5, the average hydraulic conductivity for the area is 2.3 x 10^{-3} m/h. This value is then multiplied by the average hydraulic gradient (0.00975). The specific discharge is obtained as 2.24 x 10^{-4}. The average linear groundwater velocity Va can then be computed from equation 6 given as

$$Va = \frac{vd}{n} \quad \ldots\ldots\ldots\ldots 6$$

Where n = Porosity. The porosity of the aquifer which consists of medium to coarse grained sand is estimated from Table 8

Table 8: Porosity of various sand sizes (Source: Petijohn 1974)

Size of material	Porosity (in Percentage)
Coarse Sand	39-41
Medium Sand	41-48
Fine Sandy Loam	50-59
Fine Sand	44-49

For the study area, the mean estimated porosity is 45%. The average linear ground water velocity (va) is obtained as 4.98 x 10^{-4} m/yr . The measurements of water quality obtained from various stations are shown in table 9 for inorganic constituents of deep aquifer and table 10 for shallow aquifers.

Table 9: Chemical constituents of water samples from deep aquifer in mg/L for the recharge area of water shed.

Table 10: Chemical Constituents if water samples from shallow aquifer- hand dug wells and springs of the discharge farm land settlement

Location	pH	Hardness	Colour	Alkalinity	SO_4^{2-}	Nitrate	Phosphate	Iron	Calcium	Magnesium	Ca^{2+}/Mg^{2+}	Sodium	Chloride	Tds	K^+
Ehakumona	6.9	20	4	10	11	2.7	.76	1.7	4.7	14.6	.3	0	4	92	0
Orba	6.8	20	3.2	3.2	8	2.7	.8	2.1	4.7	14	.3	.1	4	76	0
Opi	6.3	20	10	10	8	2.7	.8	2.1	6.3	14.6	.4	1.2	7	44	10
Opi Agu	7.2	20	5	10	8	1.1	2	2.2	1.2	9	.5	.4	4	68	0
Orba Agu	4.7	12	10	8	15.2	-	2.3	2.7	6.3	9.7	.2	2.7	4	40	8
Ekwegbe	6.1	12	12	10	15	-	2.2	1.1	4	9.0	.2	.2	5.7	53	0
Average	6.3	17.3	7.37	8.53	10.97	2.3	1.48	1.98	4.53	11.8	.32	0.92	6.67	62.17	3
WHO 1984	6.5 -8.5	250		250	250	45	10	0.3	75	50	-	200	250	500	200

Table 11: Coliform analysis of selected shallow aquifer of the area

Location	pH	Hardness	Colour	Alkalinity	SO_4^{2-}	Nitrate	Phosphates	Iron	Magnesium	Ca+/Mg2+	Sodium	Chloride	Tds	K+	Calcium
EhaAlumona	6.6	12	5	25	-	-	-	.38	12	.33	97`	15	-	0	4
Opi I	5.6	12	5	10	15.2	2.7	2.2	1.68	9.7	.41	.4	17	56	0	4
Ekwegbe (I)	6.7	20	5	10	11.6	3.7	.92	1.68	14.6	.32	0	4	60	0	4.7
Orba (I)	5.4	20	10	10	16	3.6	1.84	.68	9.7	0.86	.80	12	4.8	6	7.8
Ekwegbe (II)	5.5	8	8	10	11.6	3.2	1.84	1.68	9.7	.22	.8	6	24	0	3.2
Opi (II)	6	16	4	8	15.2	1.5	1.8	2.7	14.6	.22	0.1	1.5	0.24	4	3.2
Orba (II)	5.4	12	4	10	15.2	2.7	1.5	2.1	9.7	.32	.5	4	56	0	3.2
Average	6.3	17.3	7.37	8.53	10.97	2.3	1.48	1.98	11.8	0.32	0.92	6.67	62.17	3.0	4.53
WHO 1984	6.5-8.5	250		250	250	45	10	0.3	50	-	200	250	500	200	75

The result of the Biochemical examination of the shallow aquifer is shown in table 11. From analysis , the deep aquifers show no pathogenic presence. However, the shallow aquifers have anthropogenic infestations as table 11 clearly indicates.

EhandiAgu		**1/3**	**0/3**	**0/3**	**MPN 4/100ml**
Opi Agu		**0/3**	**1/3**	**0/3**	**MPN 3/100ml**
Ekwegbe Agu	**1/3**	**0/3**	**1/3**	**MPN**	**7/100ml**

Sawyer and Mc Carty (1967) indicated that pathogenic micro-organisms survival can be expected to be greater when Normal biological activity is the least such as under low temperature and anaerobic conditions. In the analysis of table 11, the coliform count ranged from 3/100ml to 7/100ml. From the table of drinking water standard water with more than 1 per 100ml bacterial content is not good for drinking (Who 1984). Therefore this geological environment of the study area has excessive quantity of coliform bacteria . Freeze and Cherry (1979) indicated that coliform presence is due to wastes of humans and farm animals. The water chemistry of the area for both the shallow and deep aquifer was classified using pipers' diagram as shown in figures 4 and 5

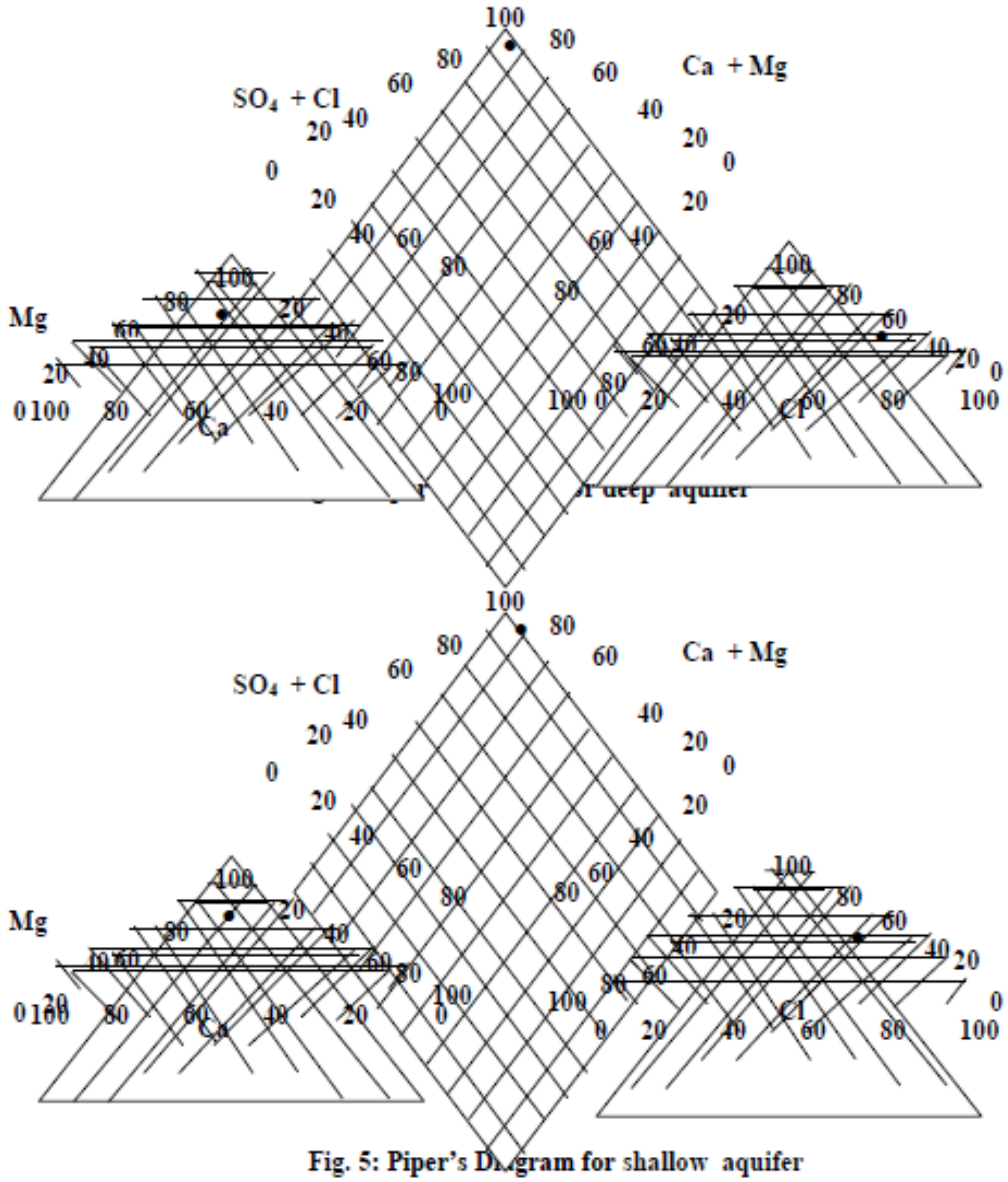

Fig. 5: Piper's Diagram for shallow aquifer

Table 12: Cations and anions computations in milliequivalent per litre for deep aquifer waters

Cations	Conc (mg/L)	Atom Wt (g)	Charge	Conversion factor	Conc Mg/L	Miliequivalent per litre
Ca^{2+}	4.3	40.08	2	.04990	0.2	16.67
Mg^{2+}	11.43	24.31	2	.08226	.94	74.60
Na^{+}	1.7	22.98	1	.04350	.07	5.56
K^{+}	1.43	39.10	1	.02557	.04	3.17
Total					1.26	100
Anions						
HCO^{3-}	0.32	61.02	1	0.01639	.005	0.900
No^{3-}	2.73	62.0	1	0.01613	.04	7.21
$SO4^{2-}$	13.18	96.06	2	1.02082	.27	48.65
Cl^{-}	8.5	35.45	1	0.02821	.24	43.24
TOTAL					0.555	100.00

Table 13 : Cations and anions computations in milliequivalent per litre for shallow aquifer waters

Cations	Conc (mg/L)	Atom Wt (g)	Charge	Conversion factor	Conc Mg/L	Miliequivalent per litre
Ca^{2+}	4.53	40.08	2	0.0499	0.23	17.42
Mg^{2+}	11.80	24.31	2	0.08226	0.97	73.48
Na^{+}	0.92	22.98	1	0.04350	0.04	3.03
K^{+}	3.0	39.10	1	0.02557	0.08	6.06
Total					1.32	100
Anions						
HCO^{3-}	0.25	61.02	1	0.01639	0.004	0.72
No^{3-}	2.3	62.0	1	0.01613	0.04	7.22
$SO4^{2-}$	15.17	96.06	2	0.02082	0.32	57.76
Cl^{-}	6.67	35.45	1	0.02821	0.19	34.30
TOTAL					0.554	100

Tables 12 and 13 were also used to classify the deep and shallow aquifers using pipers' diagram (Pipers 1944). From the plots the deep aquifer classification fig 4 show that the water falls within Mg^{2+} type and a no dominant anion class and plotted between salt and fresh water while the shallow aquifer classification – fig 5 shows a magnesium sulphate water and plots on the right side of the diamond shape of the pipers plot indicating salt water (Pipers 1944). The shallow ground water is therefore hard with $MgSO_4$ (Edward 1978). From the stiff diagram fig 6 and 7, it is clear that there is more dissolved constituents in the deep aquifer waters.

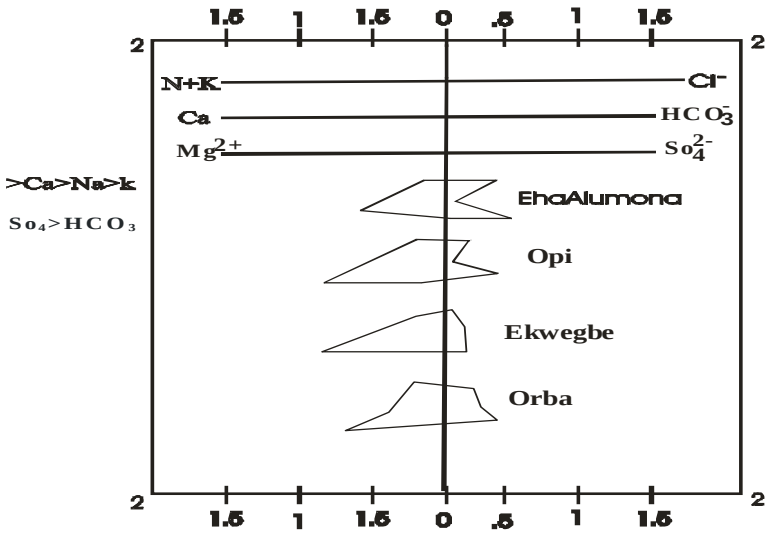

Cations (Meq/L) Anions (Meq/L)

Fig. 6: Stiff diagram for deep aquifer

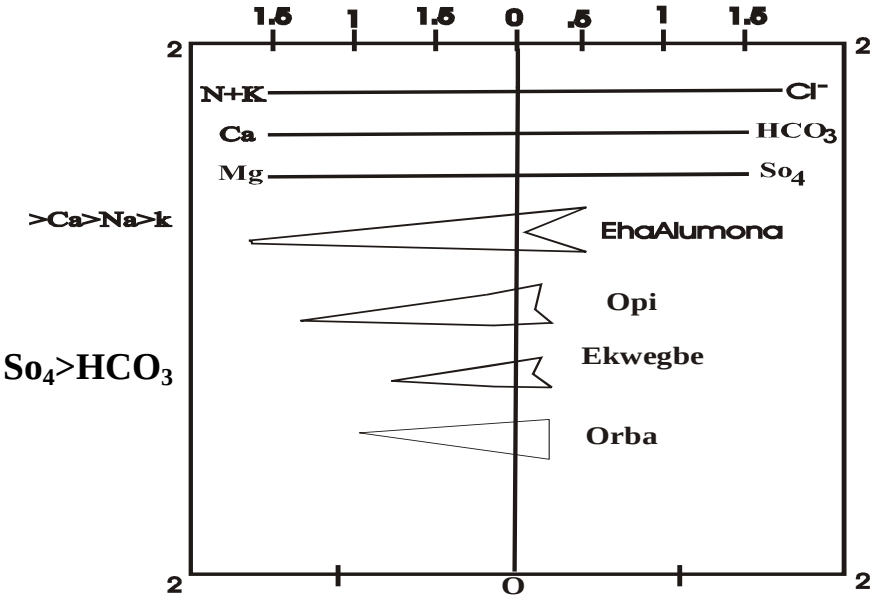

Fig. 6: Stiff diagram for deep aquifer

Calcium content was used to classify water quality of the area for irrigation purpose because of its reaction with soil to reduce permeability (Etu Efeotar 1981). Thus the relation sodium Absorption Ration (SAR).

$$SAR = \frac{Na+\ (Meq/L)}{(Ca^{2+} + Mg^{2+})^{1/2}} \quad \ldots\ldots\ldots\ldots\ldots\ldots\ 5$$

Equation 5 was employed to determine the suitability of the water for irrigation purposes. According to Etu Efeotor 1981, water class based on SAR is classed as 0-10 – excellent, 10-18 – Good , 18-26- Fair , while > 26 is poor. Using equation 5, The average SAR for components derived from tables 12 and 13 gives 0.58 for deep aquifer and 0.32 for shallow aquifer indicating water excellent for irrigation in both cases (EtuEfeotor, 1981). The ground water resources of the area was compared with American water works association (AWWA) as to assess their usability in industries. This is shown in tables 14 and 15

Table 14: Ground water analysis result compared with American water works association (AWWA) for deep aquifer.

Parameters	Average Value of sample analysed mg/L	AWWA (1991) Accepted Standard Mg/L
Tds	37.46	50-500
Total Hardness	14.29	0.250
Iron (Fe2+)	2.27	0.1-10
pH	5.09	6.5-8.3
Chloride (Cl-)	8.5	20- 250
Manganese	-	0-0.5

Table 15: Ground water analysis result compared with American water works association (AWWA) for shallow aquifer.

Parameters	Average Value of sample analysed mg/L	AWWA (1991) Accepted Standard Mg/L
Tds	62.17	50-500
Total Hardness	17.30	0.250
Iron (Fe2+)	1.98	0.1-10mg/L
pH	7.5	6.5-8.3
Chloride (Cl-)	6.67	20- 250
Manganese	-	0-0.5

In both cases the water resource of the area is ideal for industrial applications (AWWA, 1991). The pollution Index of Horton (1995) was employed to calculate the pollution index of the deep and shallow aquifer as to assess their extent of pollution. The Harton scale is shown in Fig 8

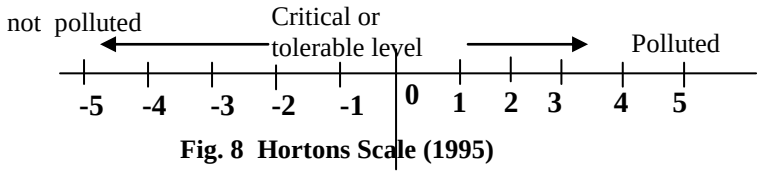

Fig. 8 Hortons Scale (1995)

Unit value (1) indicates tolerable standard, but above this value (1) the water is polluted and below this value the water is not polluted (Harton 1995). The pollution index (piji) was calculated using equation 6 as shown below

$$\frac{(\max Ai/wij)^2 + (\text{mean } Ai/wij)^2}{2} \quad \ldots\ldots\ldots\ldots\ldots\ldots 6$$

Where Ai is the measured parameter and wij is the universal standard

Table 16: Deep Aquifer pollution Index Computation

Parameter	Ai	Wij	Ai / wij	Result
Phat 29°C	5.09	6.50-8.50	0.78	
Turbidity (NTU)	21.50	5.0	5.70	Mean $\frac{Ai}{Wij}$
Conductivity (ms)	30.24	100	0.30	
Tds	37.46	500	0.75	= 1.29
Iron (Fe^{2+})	2.27	0.3	7.57	
Calcium (Ca^{2+})	4.30	50	0.38	
Magnesium (Mg^{2+})	11.43	30	0.38	
Potassium (K^{+})	1.43	50	0.03	Max Ai / wij
Sulphate (SO_4^{2-})	13.18	250	0.05	
Phosphate (PO_4^{2-})	1.68	10	0.17	= 7.57
Nitrate (NO_3^{-})	2.73	45	0.06	
Chloride (Cl^{-})	8.5	250	0.04	
Carbonate (CO_3^{-})	14.29	250	0.06	
Manganese (Mn)	-	0.5	-	
Mean	10.39		1.29	

From equation 6, employing parameters in table 16 and referencing fig 8, the pollution index of deep aquifer is 5.43 in the same way that of shallow aquifer is 4.69. This indicates pollution in both cases.

V. DISCUSSION

The average precipitation of 2.09 x $10^8 m^3$ a year signifies the total water presence which can always be referred to during water budgeting. This is quite high indicating high recharge. High temperature and vegetation of the region bring about high evapotranspiration of 1057.98mm/year amounting to 8.112% of the water available from precipitation. This in essence indicates that during dry periods of intense heat, the underground water is likely to be a function of base flow. The depth of water table of 106.70m to 9.15m from recharge to discharge lowlying areas of farm settlement indicates difficulty and expensive nature of water exploitation of the upland recharge areas, though this water will be free from pathogens due to natural attenuation processes (Raymond, 1979).On the other hand, the waters of the lowlying discharge areas should be easy to exploit though polluted and the terrain would be ideal for commercial agriculture due to high water table. The high values of transmissivity, (3.25 x 10^{-2}, m^2/yr) hydraulic conductivity (2.3 x 10^{-3} m/h). Specific discharge (2.24 x 10^{-2}) and average linear velocity of 4.98 x 10^{-4} m/yr indicate aquifer of high efficiency, specific capacity and yield and would be ideal for water resources development (Hazen, 1993).

Water chemistry indicates for deep water aquifer the order $mg^{2+} > Ca^{2+} > K^{+} > Na^{+}$ for cations and $SO_4^{2-} > Cl^{-} > HCO_3^{-}$ for cations $mg^{2+} > Ca^{2+} > Na^{+} > K^{+}$ with low Ca^{+} / Mg^{2+} ratio. This indicates that Magnesium is the major contribution of water hardness. The high coliform content of the shallow aquifers of the discharge environment is due to indiscriminate pit latrines while the low pH (the acidic environment) is due to the carbonaceous unit of Mamu Formation (Reyment, 1965). The water Chemistry indicates that there is the need for water treatment due to pathogens, high acidity, above all the water is saline, and brackish in nature. The coliform presence is due to waste of humans, farm animals and probable soil erosion (Uma, 1989). The

presence of soluble cations is due to the fact that most metallic elements are soluble in acid ground water (Viesman, 1972). The problem of low Ph (acidic) is that when it is below 5, the hydrogen ion concentration can reactivate some poisons found in sediments (Viesman, 1972) The water hardness is due to $MgSO_4$. This is probably due to presence of pyrite or gypsum in the underlying shales in the area. Water containing 500mg/L of sulphate tastes bitter and may be cartartic , this is the major fear in the area. Saline water may likely lead to saline soil (Nacl and $NaSO_4$). These types of soils will support little or no plant growth. Excess chloride may be due to contamination from excretion products (livestock and human defaecation). The major dissolved solids in the area arise due to calcium and magnesium ions. The average range for the area is 4.3 to 11 mg/L. The high iron content in the area is likely to be due to lateritic nature of the outliers of Nsukka Formation, as the latter contains iron and Aluminum compounds (Reyment , 1965). Removal of iron in groundwater is desirable because it can form rust (iron oxides) deposits causing staining of plumbing fixtures, laundered clothes and manufactured product, as well as imparting metallic taste to the water (Mc. Carty , 2001)

VI. CONCLUSION AND RECOMMENDATION

The water resource of the study area is practically good for every purpose, but the problems of pollution due to pathogens, iron and acidity should be addressed . Removal of iron consists of aeration of raw water in aeration tanks, providing for the oxidation of ferrous to ferric iron Fe^{2+} + ¼ O_2 + OH^+ Fe_3^+ + ½ H_2O. On the other hand, the soil of the area should be made alkaline by the use of alkaline fertilizer, this reduces acidity. Modern toilet facility should replace pit latrines. Above all, deeper water borehole exploitations is recommended for he low lying discharge environment, such bore holes should be over 50 m deep and the upper 30 m cased or properly lined to prevent the ingress of bacteria. For industrial applications, chloride treatment is quite desirable.

REFERENCES

[1] Agagu, O.K., Fayose, E.A. AND Peters S.W.(1985). Stratigraphy and Sedimentation in the Senonian Anambra basin of Southeastern Nigeria. Nigerian Journal of Mining geology v 22(1) pp 25-36

[2] American Water Works Association (1995).

[3] Edokwe, P.C. (1970). Soil variations under forest savanna mosaic of Nsukka area unpublished Ph.D Thesis University of Nigeria Nsukka pp 30-35

[4] Egboka, B.C.E. (1996). Analysis of the groundwater resources, of Nsukka area and environs, Nigerian Journal of Mining Geology V. 20 P 1-6.

[5] Egboka, B.C.E. and Uma, K.O. (1986). Comparative analysis of transmissivity and hydraulic conductivity value, from Ajali aquifer system, Nigeria Journal of Hydrogeology v 83, pp 185-196

[6] EtuEfeotor, J.C. (1981). Preliminary hydrogeochemical investigation of the sub surface waters in parts of Niger Delta, Min. Geol. Pp 103-105.

[7] Hazen, A (1993). Some physical properties of sand and gravels. Mass State board of health 24th annual report pp 8-15

[8] Harleman , D.R.E., Mehlhorn , P.F. and Rumer, RR (1983) dispension – permeability correction in porous media, J. Hydrology Division, American Society of Civil Eng. No. 2, vol. 89 pp 67 and 85.

[9] Iloeje , N.P. (1995). A new geography of Nigeria Revised Ed. Longman Nig. Ltd. pp 45-50

[10] Marsch, F.D. and K.J. Denny (1966). Grain Size distribution and its effect on the permeability of unconsolidated sands. Water resources research vol. 2 pp 615-677.

[11] Mc. Carty (2001). Thirty second annual report of the director of water examinations to the metropolitan water board P. 89, p. 5 King and Son, London pp 35-38.

[12] NPC, 2006. National Population Commission Information 2006.

[13] Ogbukagu, I.N. (1976). Soil erosion in the northern parts of Awka – Orlu uplands Nigeria J. Min. Geol V. 13 No 2, p. 6-19.

[14] Omidiran C.S. (2003). Principles and approach of Geochemical analyses of water resource pp 70-85.

[15] Pettijohn, F.J. (1975). Sedimentary rocks. Harper and Row New York. Pp 36-40.

[16] Reyment, R.A. (1965). Aspects of the geology of Nigeria Ibadan Univ. Press, Nigeria pp 55-70.

[17] Skoup, J.C. (1978). Pre feasibility report on the Anambra River Basin International Conference on Water Resources of Anambra River Basin pp 6-15.

[18] Simpson, A (1974). The Nigerian Coal Field. The geology of part of Onitsha, Owerri and Benue Province Nig. No. 24 pp 15-20

[19] Tattam , C.M. (1994). A Review of Nigeria Stratigraphy Rep. Geol. Survey. Nigeria pp 27-39

[20] Uma, K.O. (1989). Water resources potentials of Owerri area and the environs. Unpublished Ph.D Thesis University of Nigeria Nsukka.

[21] Umeji, A.C. (1980). Tertiary Plantation Surface on the cuesta in South-eastern Nigeria J. Mining Geology V. 17 No 2 p 109-117

[22] Viesman W.T (1972). Introduction to hydrology Mac.Millian Pub. London pp 85-98.

American Journal of Engineering Research (AJER)
e-ISSN : 2320-0847 p-ISSN : 2320-0936
Volume-03, Issue-01, pp-163-173
www.ajer.org

Research Paper Open Access

Optimal Design Of Existng Water Distribution Network Using Genetics Algorithms.

A Saminu[1], I Abubakar[2],H Sani [3]U Tsoho[4] I Suleman 5
**1, 3,4 5 Department of civil Engineering, Nigerian Defence Academy, Kaduna*
2 Department of civil Engineering, Ahmadu Bello University Zaria

Abstract: - In this study EPANET, a widely used water distribution package was linked to OptiGa, a Visual Basic ActiveX control for implementation of genetic algorithm, through Visual Basic programming technique, to modify the computer software called OptiNetwork. OptiNetwork in its modifications, introduced means of selecting options for advanced genetic algorithm parameters (Top mate; Roulette cost; Random; Tournament methods; and one point crossover; two points crossover; uniform crossover methods and random seed number). Using Badarawa/Malali existing water distribution network consisting of 96 pipes of different materials, 75junctions, two tanks, and one overhead reservoir, and a source reservoir (i.e treatment plant) from which water is pumped through a pumping main to the overhead reservoir and later distributed to the network by gravity .The modified software optiNetwork was applied to Badarawa / Malali networks distribution designs. The results obtained were compared with those obtained using commercial software package (OptiDesigner), The modified software has been able to obtained almost equal result with OptiDesigner software for the first optimization i.e before the application of advance GA, after the application of Advance GA It was observed that the least-cost design of $195,200.00 that satisfies the constraints requirements was obtained using optiNetwork, which is much lower than $435,118.00 obtained from OptiDesigner software. The results obtained show that the introduction of the advanced genetic parameters of OptiNetwork is justified. This is because, it has been able to improve the search method in terms of achieving the "least-cost" designed water distribution system that will supply sufficient water quantities at adequate pressure to the consumers.

Keywords: - *Water, distribution, systems, least cost, design, optimization, genetic algorithms,*

I. INTRODUCTION

Pipe network optimization involves the design of new pipe network and rehabilitation of existing network. A water distribution system must sustain two hydraulic requirements: water demand and pressure head at the supply locations. There are three types of optimization models including least cost design, maximum benefit design, and cost-benefit tradeoff design, Wu et al. [1]: (a) least cost optimization searches for the optimal solution by minimizing the cost while satisfying the design constraints. The least cost optimization, however, produces the minimum pipe sizes that reduce the supply capacity and reliability. (b) Maximum benefit design optimization maximizes the return on every dollar spent by searching for the maximum benefit design solution within an available budget while still meeting hydraulic constraints.

Both the least cost and the maximum benefit optimization models identify the optimal or near-optimal solutions at the minimum cost and the maximum benefit (often corresponding to the maximum cost) respectively, using a single objective design model. (c) Cost-benefit tradeoff optimization is achieved using a multi-objective design model to minimize the cost and maximize the benefit while satisfying the constraints. Traditionally, most of the work on the design of water distribution networks has focused on developing optimization procedures for the least cost pipe-sizing problem. Numerous optimization techniques are used in water distribution systems. These
include the deterministic optimization techniques such as linear programming (for separable objective functions and linear constraints), and non-linear programming (when the objective function and the constraints are not all in the linear form), and the stochastic optimization techniques such as genetic algorithms and simulated annealing.

The problem of optimal design of water distribution network has various aspects to be considered such as hydraulics, reliability, water quality, and infrastructure and demand pattern. Though, each of these factors has its own part of the planning, design and management of the system despite the inherent dependence.

II. WHAT IS GENETIC ALGORITHM?

Genetic algorithms (GAs) are optimization techniques based on the concepts of natural selection and genetics. Genetic algorithms are inspired by Darwin's theory of evolution. In this approach, the variables are represented as genes on a chromosome. Solution to a problem solved by genetic algorithms uses an evolutionary process (it is evolved). GAs features a group of candidate solutions (population) on the response surface. Through natural selection and the genetic operators, mutation and recombination, chromosomes with better fitness are found. Natural selection guarantees that chromosomes with the best fitness will propagate in future populations. Using the recombination operator, the GA combines genes from two parent chromosomes to form two new chromosomes (children) that have a high probability of having better fitness than their parents. Mutation allows new areas of the response surface to be explored. This is repeated until some condition (for example number of populations or improvement of the best solution) is satisfied.

2.2. Steps in Using Genetic Algorithms for Network Optimization

The following steps summarize an implementation of a genetic algorithm for optimizing the design of a water distribution network system (based on Simpson, Murphy and Dandy 1993[2]; Simpson, Dandy and Murphy 1994) [3]

1. Develop a coding scheme to represent the decision variables to be optimized and the corresponding lookup tables for the choices for the design variables.
2. Choose the form of the genetic algorithm operators; e.g. population size (say N=100 or 500); selection scheme - tournament selection or biased Roulette wheel; crossover type - one-point, two-point or uniform; and mutation type - bit-wise or creeping.
3. Choose values for the genetic algorithm parameters (e.g. crossover probability – pc; mutation probability - pm; penalty cost factor *K*).
4. Select a seed for the random number generator.
5. Randomly generate the initial population of WDS network designs.
6. Decode each string in the population by dividing into its sub-strings and then determining the corresponding decision variable choices (using the lookup tables).
7. For the decoded strings, compute the network cost of each of the designs in the population.
8. Analyze each network design with a hydraulic solver for each demand loading case to compute network flows, pressures and pressure deficits (if any).
9. Compute a penalty cost for each network where design constraints are violated.
10. Compute the fitness of each string based on the costs in steps 7 and 9; often taken as the inverse of the total cost (network cost plus penalty cost).
11. Create a mating pool for the next generation using the selection operator that is driven by the "survival of the fittest."
12. Generate a new population of designs from the mating pool using the genetic algorithm operators of crossover and mutation.
13. Record the lowest cost solutions from the new generation.
14. Repeat steps 6 to 13 to produce successive generations of populations of designs stop if all members of the population are the same.
15. Select the lowest cost design and any other similarly low cost designs of different configuration.
16. Check if any of the decision variables have been selected at the upper bound of the possible choices in the lookup table. If so, expand the range of choices and re-run of genetic algorithm.
17. Repeat steps 4 to 16 for say, ten different starting random number seeds.
18. Repeat steps 4 to 17 for successively larger and larger population sizes.

The review of application of these techniques in the water distribution systems can be found in (Tospornsampon et al.2007) [4] applied a combination of Tabusearch (TS) and Genetic Algorithm (GA) to solve a problem of split-pipe design of water distribution network.

The first, is the two-loop network which was first introduced by (Alperovits and Shamir 1997) [5]. The system is to supply water to meet the required demand and to satisfy minimum pressure head at each node. Three different values of α are adopted in the study which consist of the maximum and minimum values. The unit of the "Q" (flow rate) and "D" (diameters) maintained in the study are m^3/h and centimeter "C". The results obtained using α = 10.5088 and α = 10.6792, produced a cost of $400, 337.97 and $403, 751.22, lower than that of simulated Annealing (SA) with a cost of $408,035.00.

The second network is the water distribution network in Hanoi, Vietnam, which was first introduced by (Fujiwara and Khang 1990) [6]. The problem is similar to the two-loop network that the network is fed by gravity from a single fixed head source and is to satisfy demands at required pressures. In this problem, six sizes of commercial pipe are available and the cost of each pipe with diameter Di and length Li is calculated from Ci = 1.1 X Di Xli in which cost is in dollars, diameter and length in meters. The Hazen Williams coefficient is fixed at 130 for all pipes. The result obtained shows that combined Tabu search and Genetic Algorithm (TS-GA) provide very

remarkable solutions, after satisfying all the demand and pressure requirements. All solutions obtained using different hydraulic constant α = 10.5088, and α = 10.6823, are superior to those obtained by simulated Annealing (SA) in the work of Tospornsampan et.al (2007) [4]. The total cost obtained by TS-GA are $6.022 and $6.111 for the values of α = 10.5088 and 10.0823 compared to that of SA, within the cost of $6.200 for the value of α 10.9031. The comparison of those solutions shows that the TS-GA has produced significant improvements in the network.

The third network is the New York City water supply network. The data of the New York City water supply tunnels are taken from (Fujirawa and Khang 1990) [6], and (Dandy et.al 1999) [7]. The challenge in the third network is to construct additional gravity flow tunnels parallel to the existing system to satisfy the increased demands at the required pressures. The results obtained from the TS-GA are $36.87 and $38.05 when compared to the work of (Tospornsampan et.al 2007) [4], with a cost of $40.04, after satisfying the demand pressure requirements at all nodes, the result shows that a combination algorithm is better than the SA for the design problem

Schaake and Lai [8] used the New York Tunnel system consisting of 21 pipes, 19 nodes and 1 reservoir. Walski et al. [9] set up the hypothetical Anytown water distribution system (USA) (40 pipes and 22 nodes) as a realistic benchmark to compare and test network optimization software, and has features and problems typical of those found in many real systems. Fujiwara and Khang [6] used the water distribution trunk network in Hanoi consisting of one reservoir, 31 demand nodes and 34 pipes. Halhal et al. [10] studied the optimization of a town in Morocco. The network consisted of 115 nodes, 158 existing pipes to be rehabilitated, and nine new pipelines to be designed (or sized) for the system.

From the previous review, it can be concluded that the application of the GA optimization model to existing network systems demonstrates the capability of the GA to incorporate real design concerns of water system planners, to systems of multiple pressure zones, and potentially identify significant cost savings.

III. METHODOLOGY

3.1 Introduction to Modified Program (OptiNetwork Software)

The modified program (Figure 3.1) is called OptiNetwork software and modified to:

1. Overcome all the shortcomings of the Demonstration Program.
2. It can handle a water distribution network up to 150 pipes.
3. Provide additional design parameters (pressure constrain, velocity constrain and diameter constrain).
4. Open and locate a water distribution network file that needs to be optimized.
5. Provide options for the selection of advanced genetic algorithm parameters (selection methods, crossover methods and random seed number).

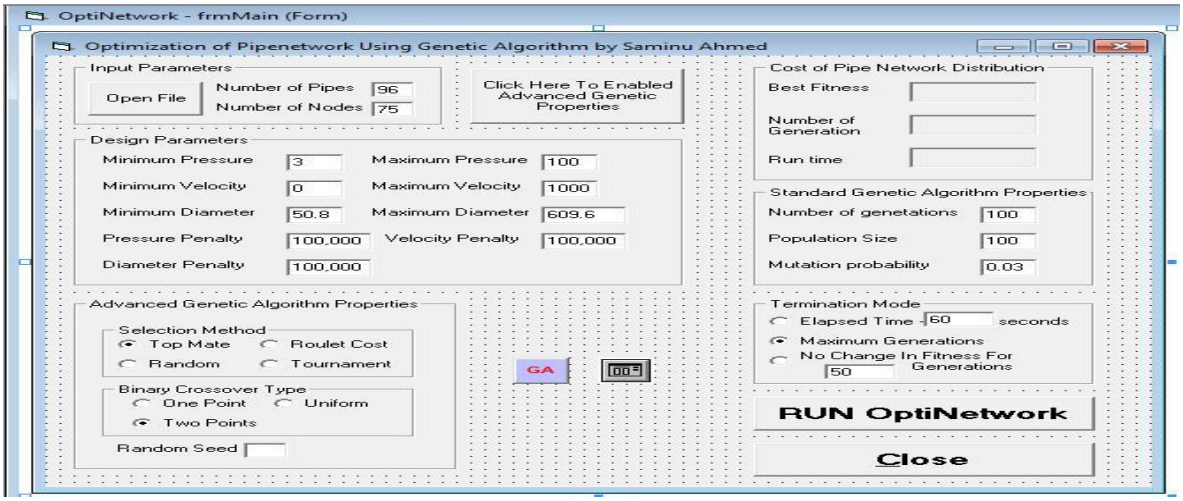

Figure 3.1 Modified Program (OptiNetwork Software)

3.2 Description of the Modified Software (OptiNetwork)

The flow chat for the software modified (OptiNetwork model) is shown in Figure 3.6. It is divided into two main stages, the first stage is hydraulic simulation, which involves the simulation of the water distribution network using the data collected / available. EPANET (Rossman, 2000)[11] a computer program that performs extended period simulation of hydraulic and water quality behavior within pressurized pipe networks is used, when a successful run is obtained, the network is then exported as an input file for optimization process.

The second stage is the implementation of the Genetic Algorithm. This is achieved by the use of EPANET TOOLKIT, which is a dynamic link library of functions that allows developers to customize EPANET's computational engine for their own specific needs, and OptiGA (Visual Basic ActiveX control for implementation of genetic algorithm) Solomons (2001) [12].

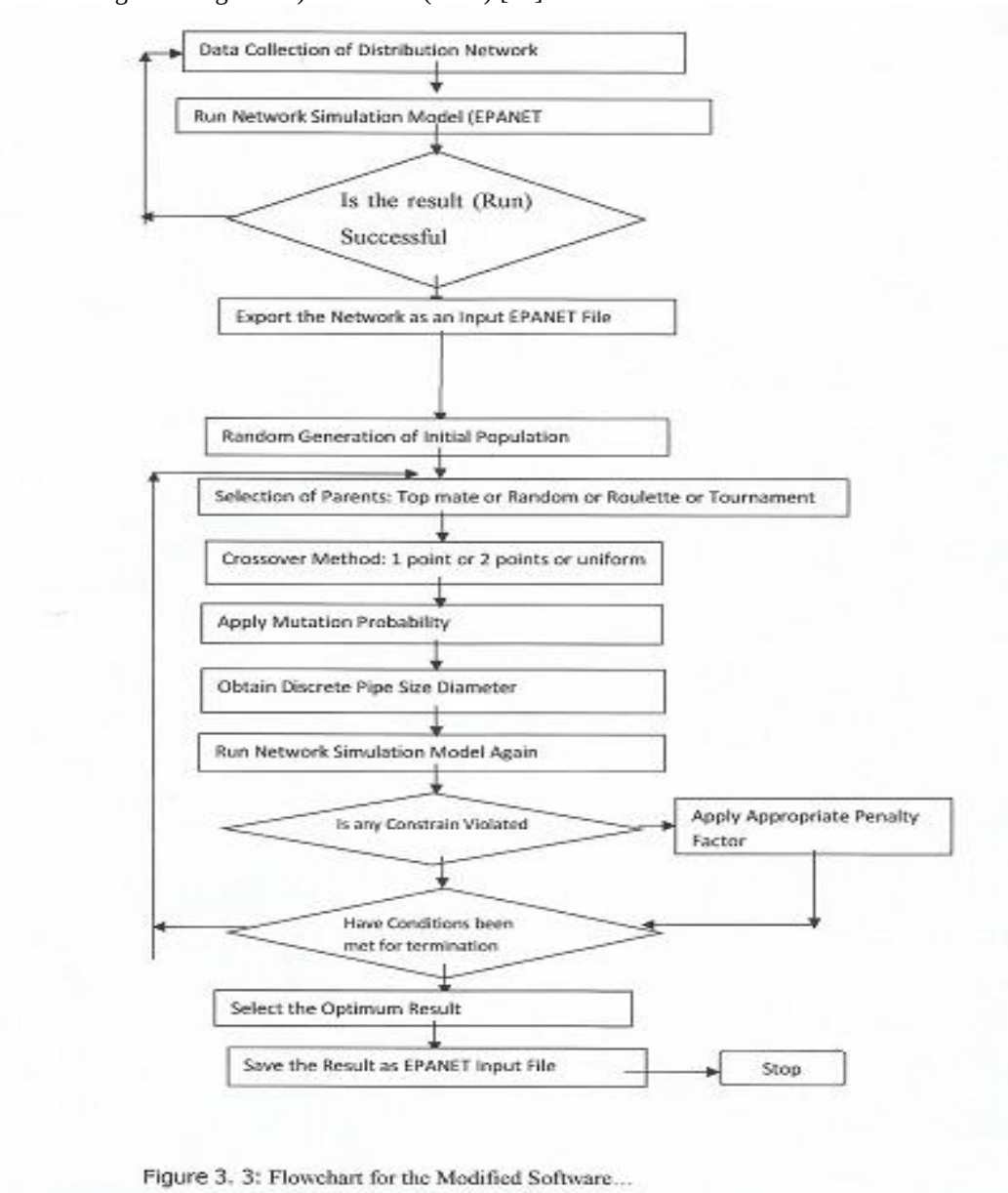

Figure 3. 3: Flowchart for the Modified Software…

3.3 Steps for optiNEtwork software

The following steps are to be taken for the use of OptiNetwork software:

1. Draw the system using EPANET and set system properties.
2. Export the network from EPANET as an INP file to OptiNetwork software directory.
3. Edit the text file called cost.text with appropriate commercial diameters pipes with corresponding cost.
4. Start the program by clicking OPEN, to select the imported file you want to work with and key in the correct number of pipes and nodes in the network.

5. Set constraint that is the design parameters i.e. pressures, velocities and diameters.
6. Set optimization parameters (standard genetic properties), you can change the defaults setting of advanced genetic properties by enabling it.
7. Set the termination mode.
8. Run the simulation.
9. View results using EPANET software.

3.4 THE CASE STUDY AREA

The existing distribution network of Badarawa/ Malali was studied and analyzed. It consists of 96 pipes of different materials,75junctions, two tanks, a source reservoir (i.e treatment plant) from which water is pumped through a pumping main to the overhead reservoir and later distributed to the network by gravity, as shown in (figure 4.1).

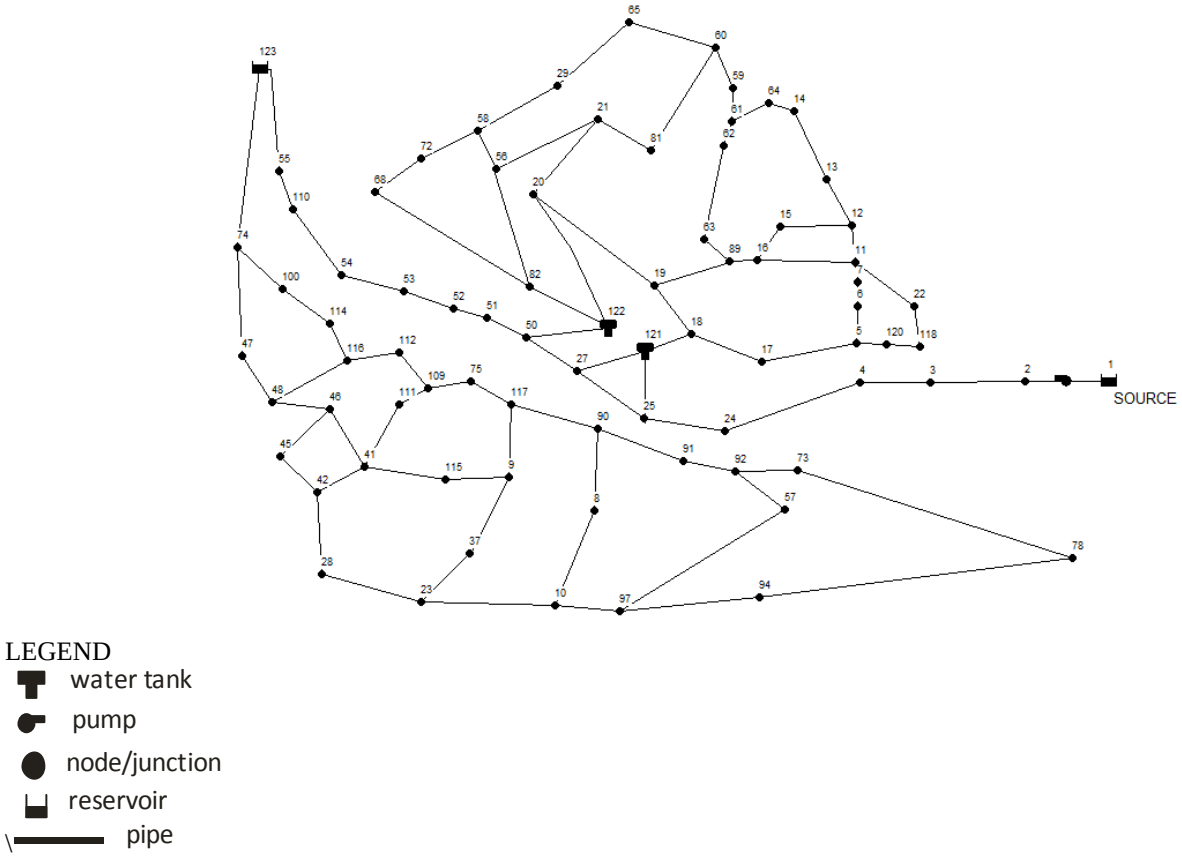

Figure 3.3 Badarawa/ Malali existing water distribution network

IV. RESULTS AND DISCUSSION

After several runs the least-cost obtained from this network using OptiNetwork software under advance genetics algorithm option is $195,200.00, which is much lower than $435,118.00 obtained from OptiDesigner software. Table 4.2 below shows the sample results of first five runs using 3 bits binary representative, different methods of selection and crossover with minimum pressure head of 3m, Pressure penalty of 200,000 and probability of mutation equal to 0.03, commercial diameters 4”, 6”, 8”, 10”, 12”, 14”, 16” 18” 20’’, 22’’and 24’’ d_{min} =4”, d_{max} = 24”. The optimum result from OptiNetwork software was achieved at Topmate selection method, two point crossover method and at mutation probability of 0.03. The commercial available diameters are shown in Table 4.1. And the data for the studied network is shown in Tables 4.3 (in the Appendix).

Table 4.1: Cost of Commercial Available pipe Diameter for Badarawa/ Malali water distribution

Diameter (mm)	Cost per Linear meter ($)
152.40	16
203.20	23
254.00	32
304.80	50
355.60	60
406.40	90
457.20	130
508.00	170
558.80	300
609.60	550

Table 4.2: Cost in $ of Badarawa and Malali Network With two Reservoir using 3 bits binary representative.
One point cross over method

No. of Runs	Top Mate	Roulette Cost	Random	Tournament
1	205,132	201,300	199,500	203,300
2	203,801	203,201	199,700	202,400
3	204,211	203,500	200,800	204,400
4	199,500	205,023	199,200	203,400
5	202,300	207,300	201,800	200,500

Table 4.2: Cost in $ of Badarawa and Malali Network With two Reservoir using 3 bits binary representative (continued).
Two points crossover method

No. of Runs	Top Mate	Roulette Cost	Random	Tournament
1	199,000	200,800	198,200	210,600
2	197,200	199,600	203,800	207,800
3	195,200	198,500	199,500	207,800
4	198,200	197,300	201,000	205,200
5	199,802	199,200	203,200	206,600

Uniform cross over method

No. of Runs	Top Mate	Roulette Cost	Random	Tournament
1	197,900	199,500	200,600	205,205
2	197,600	198,100	201,202	199,406
3	197,600	199,205	200,20.6	199,900
4	198,000	200,700	199,303	201,405
5	198,600	196,700	199,20.9	198,20.5

V. CONCLUSION

This study describes the modification of a computer program, called optiNetwork, which uses Genetic Algorithm for the least-cost design on existing of water distribution system. The modifications provide the options for selection of advanced genetic parameters (Top mate; Roulette cost; Random; Tournament methods; and one point crossover; two points crossover; uniform crossover methods and random seed number).

The performance of the OptiNetwork software was compared with OptiDesigner a commercial software package. The results obtained prove the introduction of the advanced genetics parameters by OptiNetwork is justified, as it has been able to improve the search in terms of achieving least cost of the distribution network.

VI. R ECOMMENDATIONS

Although the present software used only investment cost of pipes in the analysis, it is recommended that further research should be extended to include operational and maintenance cost. Also the use of OptiNetwork software should be encouraged in the design of water distribution network, as it has proved effective in obtaining optimal results satisfying the constraints requirements. Also recommended for solving similar problems in water distribution network

VII. REFRENCES

[1] **Wu, Z.Y., Walski, T.M., Naumick, G., Dugandzic, J., and Nasuti, R.,**"Optimizing Water System Improvement for a Growing Community," *International Conference of Computing and Control in the Water Industry*, Sept.5-7, 2005, Exeter, UK. http://www.genetic-programming.org/hc2005/ OptimalDGN4CCWI05.pdf

[2]. Simpson, A. R., Murphy, L. J., and Dandy G. C. (1993). "Pipe Network Optimization using Genetic Algorithms." Paper presented at ASCE, Water Resources Planning and Management Specialty Conference, ASCE, Seattle, USA.

[3] Simpson, A. R., Dandy G. C., and Murphy, L. J. (1994). "Genetic algorithms compared to other techniques for pipe optimization." J. Water Resour. Plng. and Mgmt., ASCE, 120(4), 423-443.

[4] Tospornsampan J, Kita J. Ishii M. and Kitamura. Y [2007]., Split-pipe Design of Water Distribution Networks using a Combination of Tobu Search and genetic Algorithm. International Journal of Computer, Information and Systems Science, and Engineering.

[5] Alperovists, E. and Shamir, U. [1997]. Design of Optimal water distribution systems. Water Resources Research, 1977, 13 (6), 885 – 900.

[6] Fujirawa, O. and Khang, D. B [1990]., A two phase decomposition method for optimal design of looped water distribution networks. Water Resources Research, 1990, 26 (4) 539 – 549.

[7] Dandy G.C, Simpson A. R, and L.J. Murphy L.J [1999]. An Improved Genetic Algorithm for Pipe Network Optimization. Water Resources Research, vol. 157, pp. 221.

[8] Schaake, J. and Lai, D., "Linear Programming and Dynamic Programming –Application of Water Distribution Network Design," Report 116, 1969 (MIT Press: Cambridge, MA).

[9] Walski, T.M., Brill, E.D., Gessler, J., Goulter, I.C., Jeppson, R.M., Lansey, K., Lee, H.L., Liebman, J.C., Mays, L.W., Morgan, D.R., and Ormsbee, L.E., "Battle of the Network Models: Epilogue," Journal of Water Resources Planning and Management, ASCE, Vol. 113(2), 1987,pp. 191-203.

[10] Halhal, D., Walters, G.A., Ouazar, D., and Savic, D.A**.,** "Water Network Rehabilitation with Structured Messy Genetic Algorithm," *J. Water Resources Planning and Management*, ASCE, Vol. 123(3), 1997, pp. 137-146.

[11] Rossman,L.A .(2000) EPANET2, LISERS MANUAL LI.S. Environmental protection Agency, Cincinnati Ohio.

[12] Salomons E. (2001). OptiDesigner Version 1, User Manual http://www.optiwater.com/optidesigner

Table 4.3: Network Data for Badarawa/Malali Water Distribution Network with two Reservoirs. After Optimization.(Using OptiNetwork)

Link ID	Length m	Diameter mm	Roughness mm	Flow LPS	Velocity m/s	Unit Headloss m/km	Friction Factor
Pipe 3	218.88	609.6	0.005	-38.32	0.13	0.03	0.019
Pipe 11	323.23	254	0.005	-6.64	0.13	0.08	0.023
Pipe 12	120.65	508	0.005	-1.41	0.01	0	0
Pipe 13	250.34	101.6	0.005	-6.09	0.75	5.44	0.019
Pipe 14	350.21	406.4	0.005	2.13	0.02	0	0.038
Pipe 15	230.23	101.6	0.005	-0.67	0.08	0.11	0.033
Pipe 19	388.48	101.6	0.005	-12.55	1.55	20.1	0.017
Pipe 20	145.68	101.6	0.005	-16.43	2.03	32.84	0.016
Pipe 22	151.33	355.6	0.005	30.9	0.31	0.24	0.018
Pipe 23	540.56	101.6	0.005	-40.97	5.05	176.89	0.014
Pipe 24	230.56	508	0.005	-43.32	0.21	0.08	0.018
Pipe 26	202.41	101.6	0.005	-13.38	1.65	22.6	0.017
Pipe 43	170.88	355.6	0.005	-17.25	0.17	0.09	0.02
Pipe 8	123.54	101.6	0.005	-5.24	0.65	4.16	0.02
Pipe 46	535.74	152.4	0.005	-37.16	2.04	20.42	0.015
Pipe 47	118.59	406.4	0.005	-29.27	0.23	0.12	0.018
Pipe 48	175.18	101.6	0.005	-20.18	2.49	47.84	0.015
Pipe 57	240.12	101.6	0.005	10.11	1.25	13.59	0.017
Pipe 58	134.77	101.6	0.005	12.27	1.51	19.29	0.017
Pipe 62	125.76	457.2	0.005	-20.96	0.13	0.04	0.02
Pipe 63	75.43	101.6	0.005	-18.71	2.31	41.67	0.016
Pipe 64	240.25	355.6	0.005	-2.47	0.02	0	0.035
Pipe 66	101.45	101.6	0.005	0.18	0.02	0.01	0.031
Pipe 67	278.9	508	0.005	13.69	0.07	0.01	0.023
Pipe 68	102.33	457.2	0.005	-7.42	0.05	0.01	0.026
Pipe 74	230.79	609.6	0.005	-3.16	0.01	0	0.033
Pipe 75	160.23	508	0.005	-5.51	0.03	0	0.031

Pipe 76	1350.68	203.2	0.005	75.45	2.33	18.51	0.014
Pipe 84	90.22	101.6	0.005	-14.91	1.84	27.52	0.016
Pipe 87	42.84	152.4	0.005	-26.92	1.48	11.33	0.016
Pipe 94	200.12	508	0.005	2.83	0.01	0	0.038
Pipe 16	1400	101.6	0.005	-51.71	6.38	273.03	0.013
Pipe 1	220.23	203.2	0.005	-233.18	7.19	150.89	0.012
Pipe 60	450.43	558.8	0.005	50.37	0.21	0.07	0.017
Pipe 77	250.12	609.6	0.005	48.02	0.16	0.04	0.018
Pipe 95	280.12	152.4	0.005	45.67	2.5	29.82	0.014
Pipe 96	1000	254	0.005	23.79	0.47	0.77	0.017
Pipe 97	200.65	101.6	0.005	21.44	2.64	53.47	0.015
Pipe 98	240.65	406.4	0.005	25.12	0.19	0.09	0.019
Pipe 99	230.65	304.8	0.005	22.67	0.31	0.29	0.018

Table 4.3: Network Data for Badarawa/Malali Water Distribution Network with two Reservoirs. After Optimization.(Using OptiNetwork)(continued).

Link ID	Length m	Diameter mm	Roughness mm	Flow LPS	Velocity m/s	Unit Headloss m/km	Friction Factor
Pipe100	150.77	152.4	0.005	21.94	1.2	7.81	0.016
Pipe101	200.99	406.4	0.005	12.65	0.1	0.03	0.022
Pipe102	200.12	254	0.005	10.3	0.2	0.17	0.021
Pipe103	230.43	254	0.005	4.55	0.09	0.04	0.025
Pipe123	100.54	101.6	0.005	-10.02	1.24	13.35	0.017
Pipe126	350.12	101.6	0.005	-46.76	5.77	226.25	0.014
Pipe127	400.12	101.6	0.005	-49.01	6.04	246.99	0.013
Pipe128	200	304.8	0.005	-6.23	0.09	0.03	0.024
Pipe129	280.79	254	0.005	-8.93	0.18	0.13	0.021
Pipe137	135.35	152.4	0.005	4.13	0.23	0.39	0.023
Pipe138	200.43	609.6	0.005	1.48	0.01	0	0.174
Pipe139	250.35	558.8	0.005	-1.22	0	0	0.131
Pipe140	120.32	254	0.005	3.62	0.07	0.03	0.027
Pipe141	110.11	101.6	0.005	1.07	0.13	0.25	0.029
Pipe142	100.32	101.6	0.005	-1.58	0.19	0.5	0.026
Pipe143	2600.54	203.2	0.005	-0.35	0.01	0	0.032
Pipe144	300.12	254	0.005	-3.05	0.06	0.02	0.028
Pipe 5	70.21	101.6	0.005	-25.03	3.09	71.09	0.015
Pipe 10	80.12	101.6	0.005	-36.16	4.46	140.23	0.014
Pipe 18	70.32	101.6	0.005	-38.86	4.79	160.3	0.014
Pipe 29	100.22	101.6	0.005	-41.66	5.14	182.44	0.014
Pipe 49	210.99	101.6	0.005	18.24	2.25	39.76	0.016
Pipe 51	100.43	558.8	0.005	15.99	0.07	0.01	0.021
Pipe 4	420	203.2	0.005	10.1	0.31	0.48	0.02
Pipe 6	400	406.4	0.005	3.2	0.02	0	0.029
Pipe 9	600	101.6	0.005	-44.11	5.44	202.93	0.014
Pipe 17	220	609.6	0.005	19.43	0.07	0.01	0.022
Pipe 50	220	101.6	0.005	8.47	1.05	9.86	0.018
Pipe 53	110	609.6	0.005	67.57	0.23	0.08	0.017
Pipe 55	110	254	0.005	34.42	0.68	1.5	0.016

Table 4.3: Network Data for Badarawa/Malali Water Distribution Network with two Reservoirs. After Optimization.(Using OptiNetwork) (continued).

Link ID	Length m	Diameter mm	Roughness mm	Flow LPS	Velocity m/s	Unit Headloss m/km	Friction Factor
Pipe 56	380	101.6	0.005	15.64	1.93	30.03	0.016
Pipe 59	89	101.6	0.005	1.53	0.19	0.47	0.026
Pipe 70	150	152.4	0.005	32.49	1.78	15.96	0.015
Pipe 73	260	101.6	0.005	4.5	0.56	3.18	0.021
Pipe 79	200	406.4	0.005	22.43	0.17	0.07	0.019
Pipe 80	380	254	0.005	2	0.04	0.01	0.031
Pipe 81	300	152.4	0.005	0.55	0.03	0.01	0.041
Pipe 82	60	558.8	0.005	10.99	0.04	0	0.027
Pipe 83	270	457.2	0.005	8.54	0.05	0.01	0.025
Pipe 86	200	152.4	0.005	-3.92	0.22	0.36	0.023
Pipe 90	380	101.6	0.005	8.06	0.99	9.01	0.018
Pipe 91	250	101.6	0.005	-1.62	0.2	0.52	0.026
Pipe 92	300	101.6	0.005	4.03	0.5	2.61	0.021
Pipe 93	260	304.8	0.005	6.94	0.1	0.04	0.023
Pipe104	200	101.6	0.005	6.87	0.85	6.77	0.019
Pipe105	300	355.6	0.005	4.17	0.04	0.01	0.027
Pipe106	390	254	0.005	3.31	0.07	0.02	0.027
Pipe107	200	304.8	0.005	4.85	0.07	0.02	0.026
Pipe108	300	203.2	0.005	4.24	0.13	0.1	0.024
Pipe109	1000	101.6	0.005	1.68	0.21	0.56	0.026
Pipe110	280	508	0.005	10.86	0.05	0.01	0.024
Pipe111	200	558.8	0.005	8.21	0.03	0	0.029
Pipe 2	350	152.4	0.005	35.97	1.97	19.23	0.015
Pipe 7	120	101.6	0.005	12.87	1.59	21.06	0.017
Pipe 21	110	609.6	0.005	-10.22	0.04	0	0.026
Pipe 25	200	101.6	0.005	8.95	1.1	10.9	0.018
Pump52	#N/A	#N/A	#N/A	197.21	0	-33.23	0

Table 4.3 Network Data for Badarawa/Malali Water Distribution Network with two Reservoirs. After Optimization.(continued)

Node ID	Elevation m	Demand LPS	Head m	Pressure m
Junc 2	600	0	615.23	15.23
Junc 3	610	2.35	621.96	11.96
Junc 4	611	2.65	621.97	10.97
Junc 5	655	2.35	712.03	57.03
Junc 6	660	2.55	712.03	52.03
Junc 7	665	2.65	712	47
Junc 11	667	2.55	712.05	45.05
Junc 12	650	2.55	712.05	62.05
Junc 13	703	2.45	713.41	10.41
Junc 14	704	2.45	713.41	9.41
Junc 15	700	2.8	712.05	12.05

Junc 16	675	2.7	712.07	37.07
Junc 17	685	2.45	712.23	27.23
Junc 18	710	2.35	720.04	10.04
Junc 19	715	2.35	724.83	9.83
Junc 20	720	2.25	724.99	4.99
Junc 21	700	2.55	724.95	24.95
Junc 22	660	2.7	711.98	51.98
Junc 24	650	2.35	717.59	67.59
Junc 25	700	2.55	717.61	17.61
Junc 27	718	2.7	722.18	4.18
Junc 37	1351	2.35	1404.36	53.36
Junc 41	1351	2.7	1405.14	54.14
Junc 42	1352	2.8	1405.16	53.16
Junc 45	1353	2.35	1405.64	52.64
Junc 46	1355	2.65	1405.66	50.66
Junc 47	1360	2.25	1424.98	64.98
Junc 48	1353	2.45	1416.6	63.6
Junc 50	700	2.65	727.17	27.17
Junc 51	720	2.7	738.41	18.41
Junc 52	730	2.8	749.68	19.68
Junc 53	755	2.45	767.96	12.96
Junc 54	800	2.65	889.72	89.72
Junc 55	1000	2.7	1067.76	67.76
Junc 56	700	2.35	721.69	21.69
Junc 58	700	2.55	719.09	19.09

Node ID	Elevation m	Demand LPS	Head m	Pressure m
Junc 59	690	2.25	716.56	26.56
Junc 60	712	2.45	716.56	4.56
Junc 61	693	2.55	713.42	20.42
Junc 62	685	2.65	713.42	28.42
Junc 63	692	2.65	713.42	21.42
Junc 64	696	2.7	713.41	17.41
Junc 65	713	2.8	716.57	3.57
Junc 68	701	2.55	719.09	18.09
Junc 72	701	2.35	719.09	18.09
Junc 73	1353	2.55	1403.79	50.79
Junc 74	1400	2.65	1424.99	24.99
Junc 75	1354	2.45	1405.08	51.08
Junc 78	1351	2.35	1403.78	52.78
Junc 81	709	2.25	716.57	7.57
Junc 82	700	2.35	722.52	22.52
Junc 89	673	2.8	713.42	40.42
Junc100	1380	2.35	1424.96	44.96
Junc109	1349	2.55	1405.1	56.1
Junc110	880	2.25	968.93	88.93
Junc111	1355	2.7	1405.11	50.11
Junc112	1355	2.35	1415.83	60.83
Junc114	1360	2.35	1424.95	64.95
Junc115	1351	2.65	1405.14	54.14
Junc116	1353	2.45	1416.6	63.6
Junc117	1353	2.35	1405.01	52.01
Junc118	654	2.7	711.98	57.98
Junc120	655	2.65	711.98	56.98
Junc 90	1352	2.35	1403.83	51.83
Junc 91	1351	2.35	1403.83	52.83
Junc 92	1351	2.55	1403.79	52.79
Junc 94	1350	2.7	1403.78	53.78
Junc 97	1349	2.35	1403.79	54.79
Junc 57	1350	2.65	1403.79	53.79
Junc 8	1350	2.7	1403.83	53.83
Junc 9	1352	2.55	1405.14	53.14
Junc 10	1350	2.7	1403.79	53.79
Junc 23	1349	2.55	1403.8	54.8
Junc 28	1350	2.7	1403.81	53.81
Junc 29	703	2.65	716.57	13.57
Resvr123	1450	-127.16	1450	0
Resvr 1	582	35.97	582	0
Tank 122	715	-74.01	725	10

American Journal of Engineering Research (AJER)
e-ISSN : 2320-0847 p-ISSN : 2320-0936
Volume-03, Issue-01, pp-174-179
www.ajer.org

Research Paper Open Access

Investigations on LPG sensing of nanostructured zinc oxide synthesized via mechanochemical method

Richa Srivastava*,
Nanomaterial sensor Research Lab Department of Physics, University of Lucknow, Lucknow-226007, U.P., India.

Abstract: - Present paper reports synthesis of zinc oxide and its application as liquefied petroleum gas sensor. The structural and morphological characterizations of the sample were analyzed by X-ray diffraction (XRD) and Scanning electron microscopy (SEM). The average value of crystallite size of ZnO calculated from Scherrer's formula is found to be 50 nm. SEM images exhibit the porous nature of sensing material with a number of active sites. The LPG sensing properties of the zinc oxide were investigated at room temperature for different vol.% of LPG. The variations in electrical resistance were measured with the exposure of LPG as a function of time. The maximum value of sensitivity was found to be 12.3 for 4 vol. % of LPG. These experimental results show that nanostructured zinc oxide is a promising material for LPG sensor.

Keywords*: - Sensor, morphology, sensitivity, nanomaterial, LPG*

I. INTRODUCTION

Zinc oxide due to the large band gap 3.37 eV and high exciton binding energy of 60 meV shows various useful properties and gives large and diverse range of growth of different type of morphologies such as nanosheets, nanocombs, nanobelts, nanowires and nanorings, which may be used in various applications [1-3]. It is one of the promising materials among metal oxides for use in humidity sensors [4-9] and gas sensors [10-17]. Basic requirement for the sensor is its change in electrical conductivity with exposure of LPG to semiconducting oxides which depends on their band gaps, surface morphology, size, diffusion rate of gas and specific surface area [18]. The semi-conductive properties of metal oxides represent the basis for their use as gas sensors, since the number of free charge carriers within the metal oxide and thus its electrical conductivity reversibly depends on the interactions with the ambient gas atmosphere [19]. For sensor application of nanostructured materials the charge transfer either results from adsorption or chemisorptions of gas molecules at the sensor surface, or from diffusion of the gas into the bulk of the sensor material [20].

The sensing mechanism of the reducing gases consists in the change of the electrical resistance resulting from chemical reaction between the gas molecule and adsorbed oxygen on the metal oxide surface [21-22]. As the sensing phenomenon mainly takes place on the surface of sensing element, the surface morphology has an essential role on the sensitivity of sensor. Also, the sensitivity of the sensor depends on the method used for production of nanoparticles. The efficiency of the chemical sensor increases as particle size decreases [23].

II. EXPERIMENTAL

2.1 Synthesis of material

ZnO is prepared by chemical precipitation method using zinc sulphate and sodium hydroxide. For the preparation of zinc hydroxide, sodium hydroxide solution was mixed drop wise to zinc sulphate and stirred for 1 h. Also some drops of poly ethylene glycol-400 (PEG-400) was added, which works as capping agent and prevents the grain growth. After that the solution is sonicated for 30 minutes using ultrasonic machine. The obtain hydroxides were dried in an electrical oven at 100°C for 8-10 h. In addition, the powder was annealed at 400°C for 2 h, resulting in complete crystallization into powder. The pellet having thickness 4 mm and diameter 10 mm was prepared by using hydraulic pressing machine under pressure 616 MPa at room temperature.

2.2 Characterizations of n-type ZnO

2.2.1 Scanning Electron Microscopy (SEM)

The surface morphology of the synthesized powder in form of the pellet was analyzed using a scanning electron microscope (SEM, LEO-Cambridge) as shown in Fig. 1. SEM images show porous nature of the prepared pellet with clusters of crystallites over the entire surface of the material. The porosity of the material is an imperative parameter regarding gas sensing point of view as the pellet has a number of active sites.

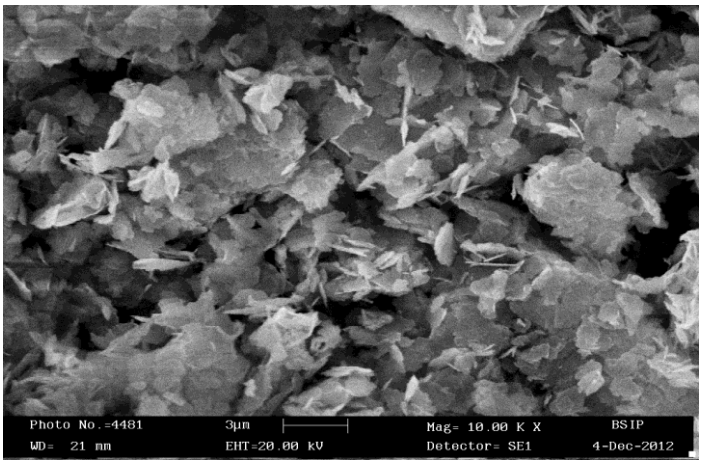

FIGURE 1 Scanning electron micrographs of ZnO pellet.

2.2.3 X-Ray Diffraction

The crystal structure and phase identification of material was analyzed using X-ray Diffractometer (X-Pert, PRO PANalytical XRD system, Nether land) with Cu K_α radiations as source having wavelength 1.5418 Å. X-Ray diffraction pattern show extent of crystallization of the sample. The average crystallite size (D) of the sensing material can be calculated by the Debye-Scherrer's formula, which is given by

$$D = K\lambda / \beta\cos\theta$$

where K= 0.94 is Scherrer's coefficient, which depends on the shape of the crystallite and the type of defects present, λ is the wavelength of X-ray radiation, β is the full width at half maximum (FWHM) of the diffraction peak and θ is the angle of diffraction. Fig. 2 show XRD patterns of the zinc oxide prepared recorded for $2\theta = 30°$ to $90°$ reveal that the sensing material consists of larger peaks of ZnO. The average value of crystallite size of ZnO calculated from Scherrer's formula is found to be 50 nm corresponding to plane (101) having full width half maxima (FWHM) values of 2.460º.

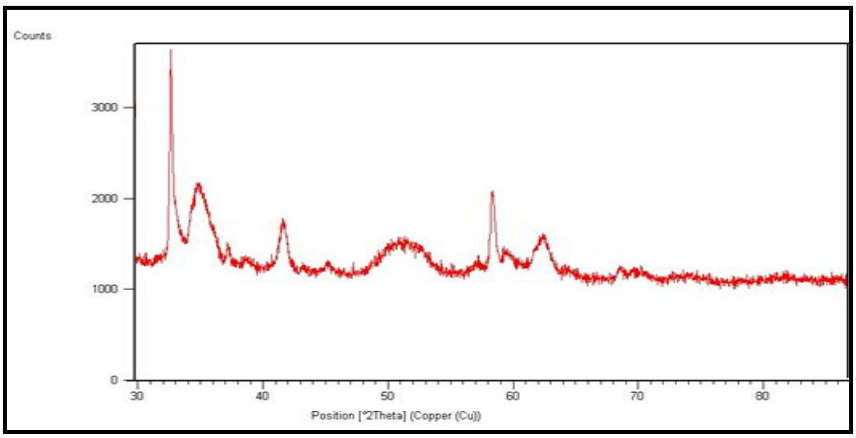

FIGURE 2 X-Ray Diffraction of ZnO powder prepared at room temperature

2.3 Gas Sensing Measurements

Prima facie before the exposition of LPG to the sensing element, the gas chamber was allowed to

evacuate at room temperature for 15–20 min and the stabilized resistance was taken as Ra. For the LPG sensing measurements a special gas chamber was designed which consists of a gas inlet and an outlet knob for LPG exclusion. The schematic diagram of LPG sensing set-up is shown in Figure 3. The sensing pellet was inserted between the two Ag electrodes inside the glass chamber having two knobs. One knob is associated with the concentration measuring system (gas inlet) and other is an outlet knob for releasing of the gas. Now this was exposed with LPG and variations in resistance with the time for different vol % of LPG were recorded by using Keithley electrometer (Model: 6514).

Sensitivity of the LPG sensor is defined as the change in resistance in the presence of gas (R_g) to the resistance in presence of air (R_a) that is

$$S = R_g / R_a$$

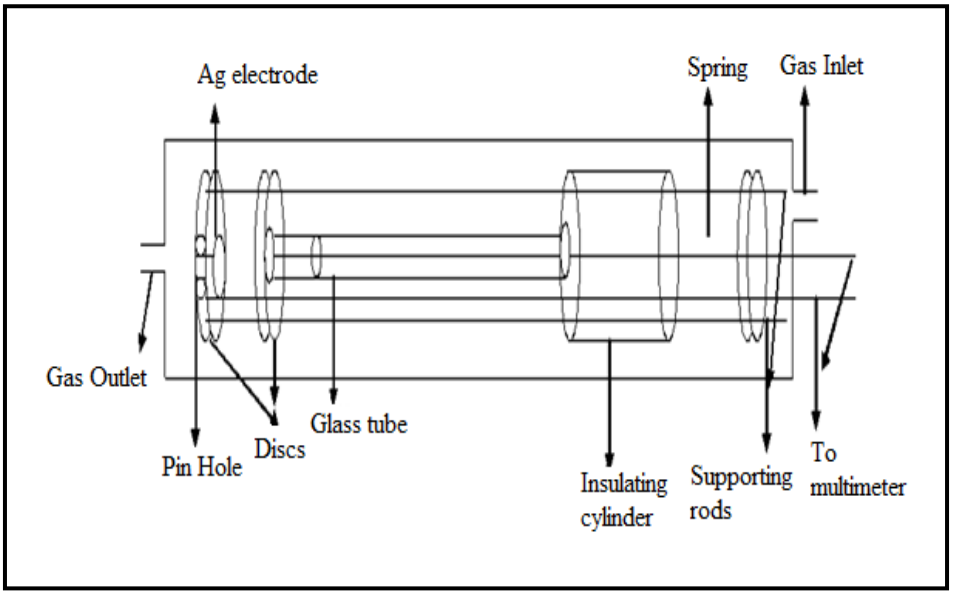

FIGURE 3 Experimental-set-up

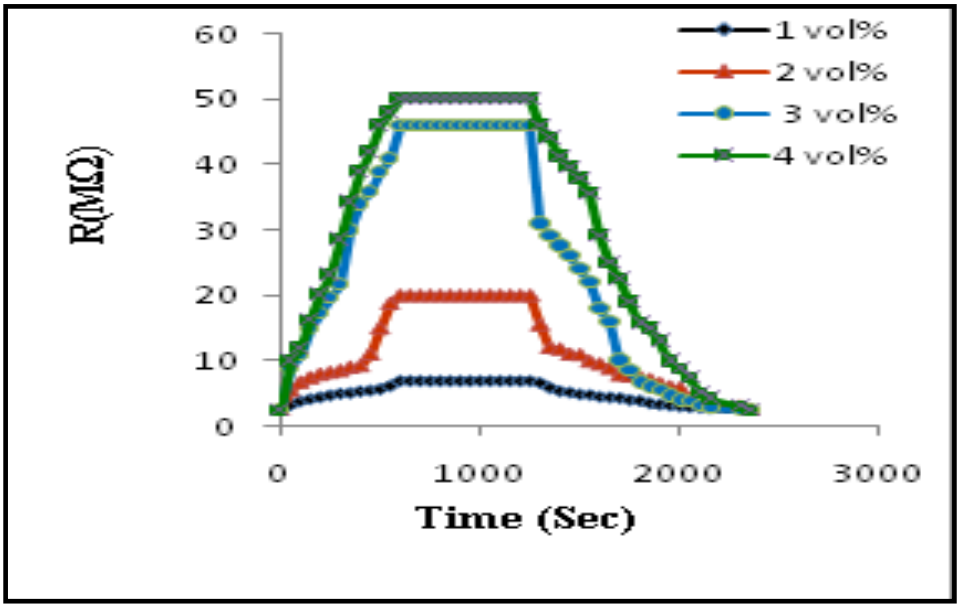

FIGURE 4 Variations in resistance of pellet with time after exposure for different vol% of LPG

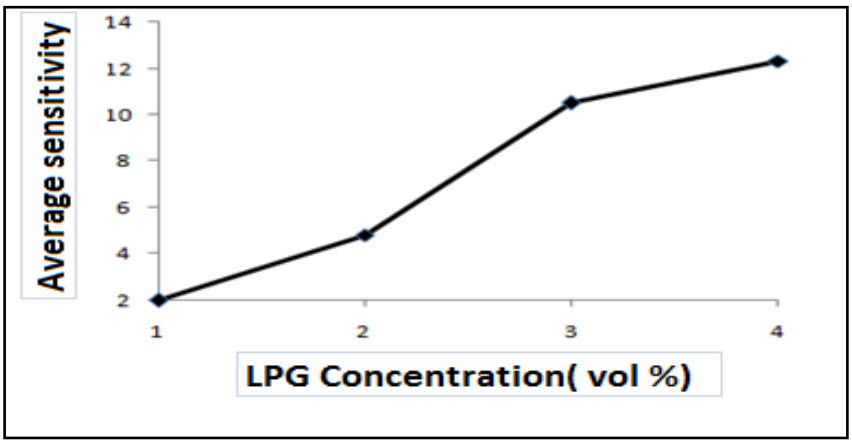

FIGURE 5 Variations of average sensitivity with different concentrations of LPG

Fig. 4 illustrates the variations in resistance of the pellet with time after exposure for different vol.% of LPG at room temperature. Curves for 1 and 2 vol% of LPG show small variation in resistance with time after exposure. Curve for 3 vol% of LPG exhibits improved response and has better sensitivity than 1 and 2 vol% of LPG. Further, for 4 vol% of LPG resistance increases sharply with time after exposure up to 600 s and then become constant.

Fig. 5 exhibits the variations of average sensitivity with different concentrations of LPG and it was found that as the concentration of LPG (in vol.%) increases, the average sensitivity of sensor increases linearly upto 3 vol% of LPG later it increases slowly. The linear increment of the sensitivity of the sensor is a significant factor for device fabrication. The maximum sensitivity was obtained for 4 vol% of LPG and is ~ 12.3.

The gas sensing mechanism of zinc oxide based LPG sensor is a surface controlled phenomenon i.e., it is based on the surface area of the pellet at which the LPG molecules adsorb and reacts with pre-adsorbed oxygen molecules. As mentioned earlier, the pellet is porous. Therefore, the oxygen chemisorptions centers viz., oxygen vacancies, localized donor and acceptor states and other defects are formed on the surface during synthesis. These centers are filled by adsorbing oxygen from air. After some time equilibrium state is achieved between oxygen of zinc oxide and atmospheric oxygen through the chemisorptions process at room temperature. The stabilized resistance at present state is known as resistance in presence of air (R_a). The pellet interacts with oxygen by transferring the electrons from the conduction band to adsorbed oxygen atoms, resulting into the formation of ionic species such as O_2, O_2^-, O^- or O^{2-}. The reaction kinematics may be explained by the following reactions:

$$O_2(gas) \leftrightarrow O_2(ads)$$
$$O_2(ads) + e^- \rightarrow O_2^-$$

The electron transfer from the conduction band to the chemisorbed oxygen results in the decrease in the electron concentration at surface of the pellet. As a consequence, an increase in the resistance of the pellet is observed. The conduction process in gas sensing is electronic and the chemisorptions of atmospheric gases take place only at the surface of the zinc oxide. The overall conduction in a sensing element, which will monitor the sensor resistance, is determined by the surface reactions resulting out from the charge transfer processes with the sensing element. In LPG molecules the reducing hydrogen species are bound to carbon, therefore, LPG dissociates less easily into the reactive reducing components on the pellet surface. When the pellet is exposed to reducing gas like LPG, the LPG reacts with the chemisorbed oxygen and is adsorbed on the surface of pellet then the exchange of electrons between the LPG and oxide surface upon adsorption would be taken place, i.e., a surface charge layer will be formed. When the LPG reacts with the surface oxygen ions then the combustion products such as water depart and a potential barrier to charge transport would be developed i.e., this mechanism involves the displacement of adsorbed oxygen species by formation of water. The overall reaction of LPG with the chemisorbed oxygen may be taken place as shown below:

$$2C_nH_{2n+2} + 2O_2^- \longrightarrow 2C_nH_{2n}O + 2H_2O + 2e^-$$

Where C_nH_{2n+2} represents the various hydrocarbons. These liberated electrons recombine with the majority carriers (holes) of sensing pellet resulting in a decrease in conductivity. The formation of barrier is due to reduction in the concentration of conduction carriers and thereby, results in an increase in resistance of the sensing element with time. As the pressure of the gas inside the chamber increases, the rate of the formation of such product increases and potential barrier to charge transport becomes strong which has stopped the further formation of water constituting the resistance constant. The free charge carriers have to overcome the surface barriers appearing at the surface of the grains.

It was observed that as the concentration of LPG increases, the average sensitivity increases linearly in the beginning and later it becomes saturated. The linear relationship between sensitivity and gas concentration may be attributed to the availability of sufficient number of sensing sites on the pellet to act upon the LPG. The low concentration implies a lower surface coverage of gas molecules, resulting in a lower surface reaction between the surface adsorbed oxygen species and the gas molecules. The increase in LPG concentration increases the surface reaction due to a large surface coverage. Further increase in the LPG concentration does not increase the surface reaction and eventually saturation takes place. Thus, the maximum sensitivity was obtained at higher concentration of LPG i.e. 4 vol.%. The linearity of average sensitivity for the LPG (< 3 vol.%) suggests that the zinc oxide pellet can be reliably used to monitor the LPG over this range of concentration. As the lower explosive limit (LEL) for LPG is 4.0 vol. % [24] therefore, response is measured up to 4.0 vol. % in order to detect the LPG below LEL for safety requirement. Figure 6 shows the reproducibility curve of sensor after two month. It was found that after two month, it performs 90% of its initial performance.

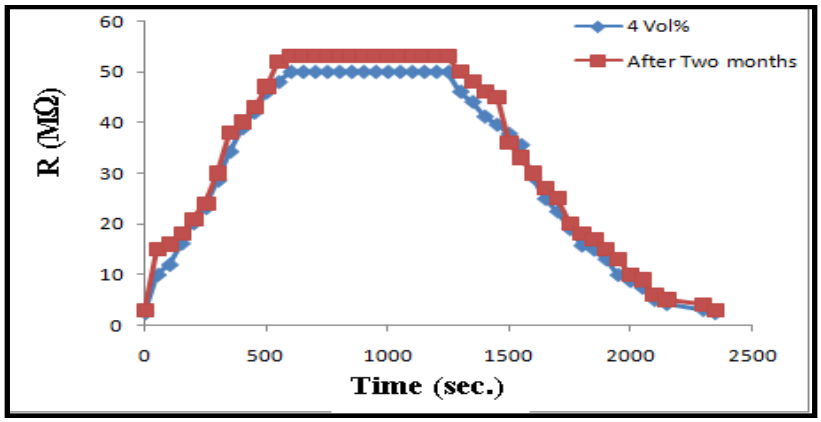

Figure 6 Reproducibility curve of sensor after two months

III. CONCLUSION

We have successfully synthesized nanostructured Zinc oxide via mechanochemical method. It was found that synthesized zinc oxide works as a good LPG sensor at room temperature and average sensitivity of this sensor is found 12.3 for 4 vol % LPG. As detection of Liquefied petroleum gas is very important for disaster management purpose that's why this study is quite appreciable for commercial applications. Good sensitivity, reproducibility and stability demonstrate the promise of this sensor for LPG determination in the industrial and environment monitoring. Thus, this study demonstrates the possibility of utilizing zinc oxide pellet as a sensing element for the detection of LPG.

IV. ACKNOWLEDGEMENT

Dr. Richa Srivastava is highly grateful to University Grants commission Delhi for **'Post Doctoral fellowship for Women'.** No. F.15-79/11(SA-II).

V. REFERENCES

[1] X. Feng, Y. Ke, L. Guodong, L. Qiong and Z. Ziqiang, Synthesis and field emission of four kinds of ZnO nano structure: Nanosleeve-fishes, radial nanowire arrays, nanocombs and nanoflowers, *Nanotech*, 17, 2006, 2855- 2859.

[2] Q. Wei, G. Meng, X. An, Y. Hao and L. Zang, Temperature controlled growth of ZnO nanostructure: Branched nanobelts and wide nanosheets, *Nanotech*, 16(2005), 2561-2566.

[3] C. Xu, M. Kim, J. Chun and D.E. Kim, The selectively manipulated growth of crystalline ZnO nanostructures, *Nanotech*, 16, 2005, 2104-2110.

[4] S.K. Shukla, G.K. Parashar, P. Misra, B.C. Yadav, R.K. Shukla, A. Srivastava, F. Deva and G.C. Dubey, On exploring sol-gel deposited ZnO thin film as humidity sensor: An optical fiber approach, *Chem. Sensors*, Japan, Supplement B, 20, 2004, 546-547.

[5] X. Zhou, T. Jiang, J. Zhang, X. Wang and Z. Zhu, Humidity sensor based on quartz tuning fork coated with sol-gel-derived nanocrystalline zinc oxide thin film, *Sens. Actuators B*, 123, 2007, 299-305.

[6] N. Kavasoglu and M. Bayhan, Air moisture sensing properties of ZnCr2O4, *Turk Phys*, 29, 2005, 249-255.

[7] Q. Wan, Q.H. Li, Y.J. Chen, T.H. Wang, X.L. He, X.G. Gao and J.P. Li, Positive temperature coefficient resistance and humidity sensing properties Cd-doped ZnO nanowires, *App. Phys. Lett*, 84, 2004, 3085-3087.

[8] Y. Zhang, K. Yu, S. Ouyang, L. Luo, H. Hu, Q. Zhang and Z. Zhu, Detection of humidity based on quartz crystal microbalance coated with ZnO nanostructure films, *Physica B: Cond. Matt.*, 368, 2005, 94-99.

[9] B.C. Yadav, R. Srivastava, C.D. Dwivedi and P. Pramanik, Moisture sensor based ZnO nanomaterial synthesized through oxalate route, *Sens. Actuators B*, 131, 2008, 216-222.

[10] C.S. Rout, S. Harikrishna, S.R.C. Vivekchand, A. Govindaraj and C.N.R. Rao, Hydrogen and ethanol sensors based on ZnO nanorods, nanowires and nanotubes, *Chem. Phy. Lett.*, 418, 2006, 584-590.

[11] H. J. Lim, D.Y. Lee and Y.J. Oh, Gas sensing properties of ZnO thin films prepared by microcontact printing, *Sens. Actuators A*, 125, 2006, 405-410.12.

[12] Z.P. Sun, L. Liu, L. Zhang and D.Z. Jia, Rapid synthesis of ZnO nano-rods by one-step room-temperature, solid-state reaction and their gas-sensing properties, *Nanotech.*, 17, 2006, 2266-2270.

[13] B. C. Yadav, R. Srivastava, A. Yadav, Nanostructured Zinc Oxid Synthesized via Hydroxide Route as Liquid Petroleum Gas Sensor *Sensors & Materials*, 21, 2009, 87-94.

[14] B. C. Yadav, R. Srivastava, A. Yadav, V. Srivastava, LPG sensing of nanostructured zinc oxide and zincniobate, *Sensor Letters*,714, 2008, 1-5.

[15] N. Wu, M. Zhao, J.G. Zheng, C. Jiang, B. Myers, S. Le, M. Chyu and S.X. Mao, Porous CuO -ZnO nanocomposite for sensing electrode of high temperature CO solid-state electrochemical sensor, *Nanotech.*, 16, 2005, 2878-2881.

[16] Q. Zhang, C. Xie, S. Zhang, A. Wang, B. Zhu, L. Wang and Z. Yang, Identification and pattern recognition analysis of Chinese liquors by doped nano ZnO gas sensor array, *Sens.Actuators B*, 110(2005), 370-376.17.

[17] V.R. Shinde, T.P. Gujar and C.D. Lokhande, LPG sensing properties of ZnO fims prepared by spray pyrolysis method: Effect of molarity of precursor solution, *Sens. Actuators B*, 120, 2007, 551-559.

[18] S.C. Yeow, W.L. Ong, A.S.W. Wong and G.W. Ho, Template-free synthesis and gas sensing properties of well-controlled porous tin oxide nanospheres, *Sensors Actuators B* 143, 2009, 295–301.

[19] N. Barsan and U. Weimar, Understanding the fundamental principles of metal oxide based gas sensors; the example of CO sensing with SnO_2 sensors in the presence of humidity, *J. Phys. Condens. Matter* 15, 2003, R813-R839.

[20] N. Yamazoe and K. Shimanoe, Receptor function and response of semiconductor gas sensor, Review Article, *J. Sens.*, 2009, 1-27.

[21] N. Barsan, U. Weimar, Conduction model of metal oxide gas sensors, *J. Electrocer*. 7 2000, 143-167.

[22] Y. Xiaojuan, C. Naisheng, S. Shuifa, L. Ersheng and H. Jinling, Preparation, characterization and gas sensitive properties of nano- crystalline Cr_2O_3-Fe_2O_3 mixed oxides, Sci. in China 41, 1998, 442-448.

[23] G. Sberveglieri, L.E. Depero, M. Ferroni, V. Guidi, G. Martinelli, P. Nelli, C. Perego and L. Sangletti, A novel method for the preparation of nanosized TiO_2 thin films, *Advan. Mater.* 8, 1996, 334-337.

[24] B.C. Yadav, A. Yadav, T. Shukla and S. Singh, Experimental investigations on solid state conductivity of cobaltzincate nanocomposite for liquefied petroleum gas sensing, *Sens. Lett.* 7, 2009, 1-5

American Journal of Engineering Research (AJER)
e-ISSN : 2320-0847 p-ISSN : 2320-0936
Volume-03, Issue-01, pp-180-184
www.ajer.org

Research Paper Open Access

The Susceptibility of Austenitic Stainless Steel to Stress Corrosion Cracking in Sodium Chloride

Iliyasu, I, Yawas, D.S. and Aku, S.Y.
Department of Mechanical Engineering, Ahmadu Bello University Zaria, Nigeria.

Abstract: - The stress corrosion cracking (SCC) behavior of type 304 austenitic stainless steel in Sodium Chloride (NaCl) was investigated. This was done by exposing the entire specimen to the corrosives (NaCl) at concentrations of 0.3M,0.5M, 0.7M, and 1M. After every seven days one specimen from each of these corrosives was removed and loaded on a tensometer until fracture. Percentage elongation and percentage reduction in cross sectional area were used to investigate the SCC behavior of the steel.

Keywords: - *SCC, Sodium Chloride, Austenitic Stainless*

I. INTRODUCTION

Stress-corrosion cracking relates to the environmental degradation of the mechanical Integrity of structural components. Stress-corrosion failures are well known in a variety of industries such as aircraft, petrochemical and underground pipeline transmission systems (Ashby and Jones, 1980).
Stress corrosion cracking (SSC) is the process of brittle crack growth in a normally ductile material exposed to conjoint corrosion and straining of a metal due to residual or applied stresses. In order for a component to undergo SCC a combination of three factors must be in place, a susceptible material, a corrosive environment and an appropriate level of tensile stress(Pipe Line research council,2006).

An environment having the presence of dissolved elements such as chlorides, carbon dioxide, hydrogensulphide and oxygen are termed aggressive. In such an environment steel is at high risk from corrosion. Some examples of such environments where processing facilities are found are water and wastewater treatment plants, pulp paper mills, chemical plants, refineries, seawater and brackish water (http://www.outokumpu.com/46874.epibrw).

1.2 Significance of study

The evaluation of the susceptibility to cracking is a basic requirement for safe and economical design of many types of equipment since no one corrosive environment causes stress corrosion in all alloys, and most alloys are subject to attack in only a few specific corrosives. The information that will be obtained from this research is expected to be useful for the process chemical industries, petrochemicals and the water engineer.

II. MATERIALS AND METHODS

2.0 Materials

The material used in this study is a 5mm diameter 304 austenitic stainless steel .The chemical composition and mechanical properties as supplied by the manufacturer are shown in Table 1.0 and 2.0 The tensile specimen were prepared from this material using the lathe machine as shown in Figure 1.0.They were machined from round bars to the required specifications. They were then washed and degreased with acetone. The entire procedure was carried out according to (ASTM, 1989/1990).

Table 1.0 Composition of 304 austenitic stainless steel (wt%)

Element	C	S	Ni	Si	Mo	Mn	Cr	Fe
Wt%	0.06	0.005	8.03	0.45	0.03	1.40	18.95	Bal

Table 2.0 Mechanical properties of Type 304 Austenitic stainless steel at room temperature.(www.aksteel.com)

	UTS Ksi(MPa)	0.2%YS Ksi(MPa)	Elongation %in 2"(50.8mm)	Hardness Rockwell
Type 304	**90(621)**	**42(290)**	**55**	**B82**

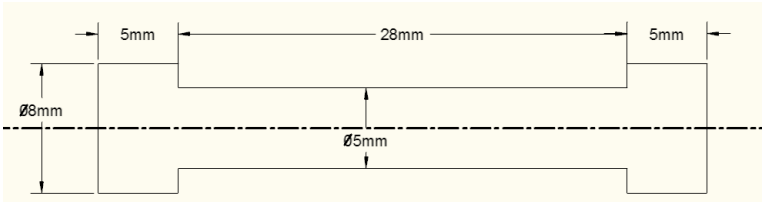

Figure 1.0 Tensile test specimen

2.1 Experimental procedure

All the specimen were immersed at the same time in the experimental media which were sulphuric acid(H_2SO_4) andsodium chloride(NaCl)at concentrations of 0.3M,0.5M,0.7M,1M. A specimen was removed from each of these acids after every seven days and the constant extension rate tensile test (CERT) was performed with a tensometer at a strain rate of 0.003cm/sec. As straining continued, the load extension curves were plotted by intermittently depressing the pin against the rotating drum which bore the graph paper. This operation continued until the specimen fractured. The time to fracture was measured with the aid of a stop watch and the percentage reduction in area of each test piece was recorded. This test was carried out according to the methods of (Le and Ghali,1993),(Rondelli*et al*,1997) and (Yawas,2005).

2.3 Determination of results

To determine the percentage elongation and percentage reduction in cross sectional area the relations 1 and 2 below were used (Afolabi*etal*,2007):

1. The percentage elongation (%EF) of the samples was calculated using the relation

$$\%EF = \frac{L-L_o}{L} \times 100 \qquad \text{.....(7)}$$

$$Where$$
$$L = Length\ after\ fracture\ and$$
$$L_o = Initial\ Length$$

2. The percentage reduction in area (%RA) is given by

$$\%RA = \frac{A_o - A}{A_o} \times 100 \qquad \text{.....(8)}$$

$$Where A_o = Cross\ sectional\ area\ before\ deformation\ and$$
$$A = Cross\ sectional\ area\ after\ deformation$$

III. RESULTS

The results of this work are shown in figures 2.0 to 5.0

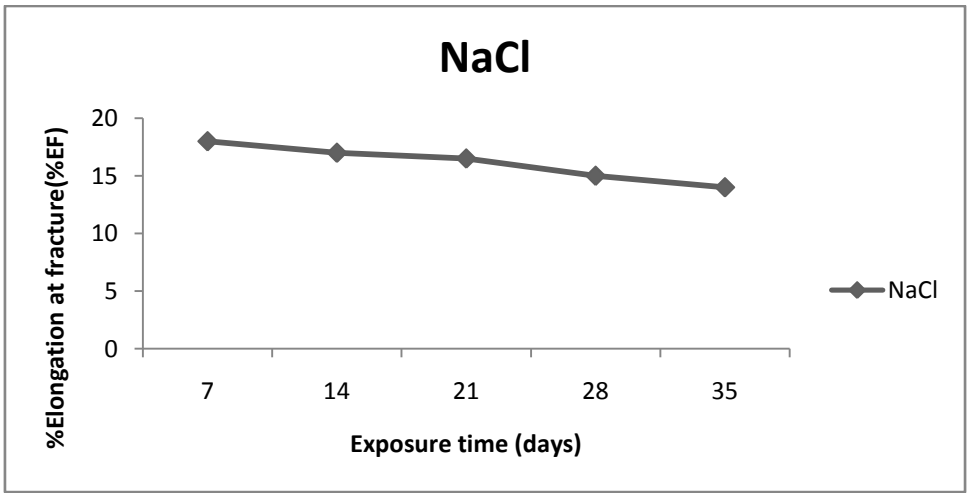

Figure 2.0.Variation of % Elongation to fracture against time for steel immersed in 1M NaCl

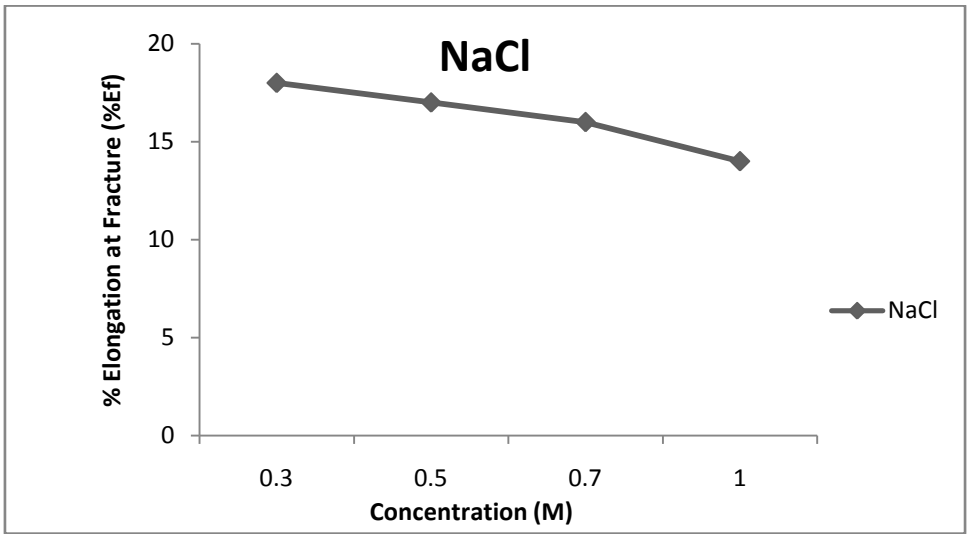

Figure 3.0 Variation of % Elongation to fracture against concentration for steel immersed in NaCl after exposure for 7days

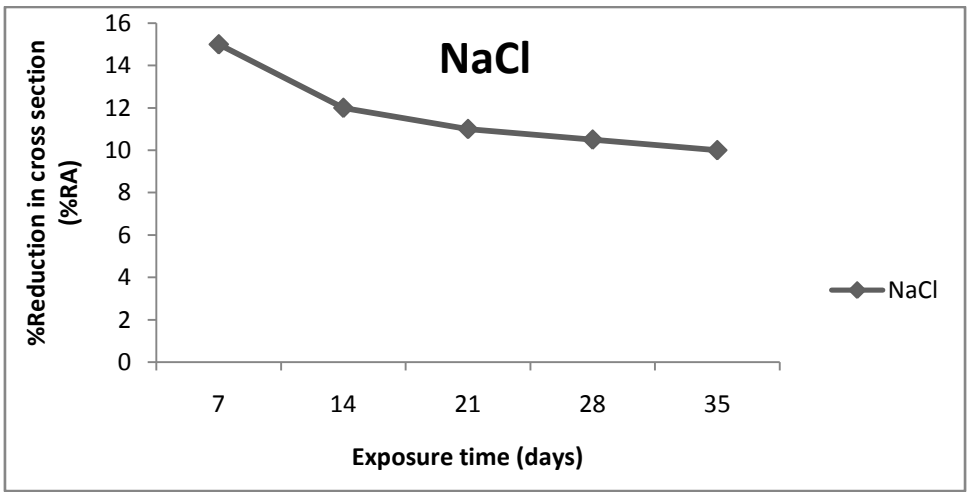

Figure 4.0 Variation of % Reduction in cross sectional area against time for steel immersed in 1M NaCl

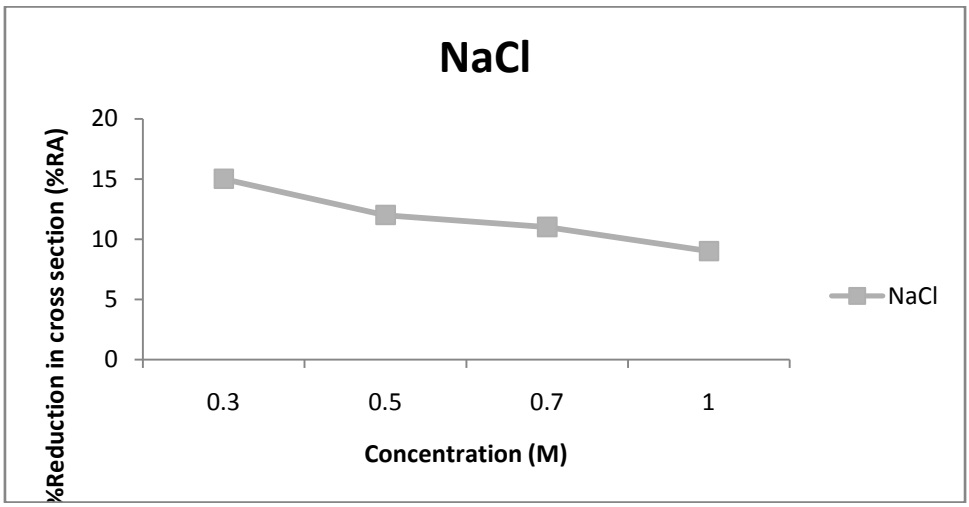

Figure 5.0 Variation of % Reduction in cross sectional area against concentration for steel immersed in NaCl after exposure for 7days

IV. DISCUSSIONS

Figures 2.0,3.0,4.0 and 5.0 show the SCC behaviour of type 304 austenitic stainless steel in NaCl expressed in terms of percentage elongation to fracture and in terms of reduction in cross sectional area. These parameters were derived following the procedures of McIntyre and Dillion(1985) and Beaver and Koch (1994). From the Figures it can be observed that both the percentage elongation and reduction in cross sectional area decreased with increased exposure time and increased concentration,showing a high susceptibility to SCC.This higher susceptibility in NaCl could have been enhanced by the presence of chloride ions in the media. Consequently, the risk of cracking chlorides tends to be most severe for the austenitic steel.

Owing to the low nickel and molybdenum contents austenitic stainless steel type 304 is highly susceptible to stress corrosion cracking in chloride solution(www.sandmeyersteel.com/300-series-austenitic.html).

High-alloyed austenitic stainless steels with suchhigh contents of nickel above 10% and molybdenum above 2% will offer high resistance to SCC (www.avestapolarit.com).

V. CONCLUSIONS

The following conclusions can be drawn on the studies undertaken on SSC of type 304 austenitic stainless steel in dilute H_2SO_4 and NaCl.

i. The ductility of Type 304 Austenitic stainless steel decreased with increased exposure time and concentration, an indication that it is susceptible to stress corrosion cracking in NaCl.
ii. Chloride is a principal agent in environments causing stress corrosion cracking e.g sea water, oil and gas industries
iii. The mechanism of SCC involves the conjoint action of the environment and the presence of a tensile stress.
iv. High-alloyed austenitic stainless steels with such high contents of nickel above 10% and molybdenum above 2% will offer high resistance to SCC.

REFERENCES

[1] Afolabi,A.S.(2007):*Corrosion and stress Corrosion Behaviors of Low and Medium Carbon Steel in Agro-Fluid Media*.Leonard Electronic Journal of Practices and technologies, ISSN 1583-1078,Issue 10,p.55-66.

[2] Afolabi,A.S. and Borode, J.O. (2007):*Stress Corrosion Cracking Suceptibility of Medium Carbon steel in Caustic and Potash Media*. AU Journal of Technology page 165-170.

[3] Ashassi-Sorkhabi H., Ghalebsaz-Jeddi N., Hashemzadeh F. andJahani H.(2006):*Corrosion Inhibition of Carbon Steel in Hydrochloric Acid by Some Polyethylene Glycols*, Journal of ElectrochimicalActa 51, 2006, p. 3848-3854

[4] Ashby,M.F. and Jones,D.R.H.(1980):*Engineering Materials:Introduction to properties and Applications*,VolI,ButterworthHeineman,Oxford.

[5] Austenitic Stainless Steels (n.d).Retrieved July 10, 2011 from www.gowelding.com/met/austenitic.html

[6] Chih-Kuang, L. and I-Lon, L. (NA): *Environmental Effects on the Fatigue Behavior of Austenitic stainless Steel*, Department of Mechanical Engineering, National Central University, Chung-Li 32054, Taiwan

[7] Cliffort,M.(2002):*Engineers Data Book*,SecondEdition.Professional Engineering Publishing Ltd. London and Burry Edmonds.UK. Dillon, C. P .(2001):*Forms of Corrosion*, MPE Engineers Inc.

[8] High Alloy Austenitic Stainless Steel (n.d). Retrieved on August 20,2011from

[9] http://www.valbrunanordic.se/dokument/produktblad/EN1.4539- 0509%20original%20Eng.pdf

[10] International Stainless Steel Forum(ISSF) (2010).*Introduction to Stainless Steel*.Retrieved on August 22,2011 from www.worldstainless.org

[11] Jabeera, B., Shibli S. M. A., Anirudhan T. S.,(2006):*Synergistic Inhibitive Effect of Tartarate and Tunstate in Preventing Steel Corrosion in Aqueous Media*,Journal of Surface Science 252, p. 3520-3524.

[12] AK Steel 304/304L Stainless Steel Data Sheet (n.d).Retrieved July 20, 2011 from www.aksteel.com

[13] McIntye, D.R. and Dillion,C.P.,(1985):*Guidelines for Preventing Stress Corrosion Cracking in the Chemical Process Industres*.MTI Publications No. 15.

[14] National Corrosion Service (NCS) Publication UK(2000):*Guides to good Practice in Corrosion Control*.(www.npl.co.uk)

[15] Newman RC and Procter RPM,(1990):*Stress Corrosion Cracking*:1965-1990,British Corrosion Journal, Vol. 25,no 4,pp 259-269.

[16] Pipe Line Research CouncilInternational (PRCI) Publications(2006):*Stress Corrosion Cracking: Roadmap to Reduce the Cost and Increase the effectiveness of tools for Managing internal and External Stress Corrosion cracking.*

[17] Seifedine, K. (2008):*Corrosion Analysis of Stainless Steel*.European Journal of Scientific Research,ISSN 1450-216X Vol. 22 No.4;pp 508-516.
[18] Shrier, L. L., (2000):*Corrosion Metal / Environment reaction*, Volume 1,printed and bound in Great Britain, Butterworth Hejne Mann.
[19] Staehle,R.W. and other (editors) (1977): *Stress Corrosion Cracking and Hydrogen Embrittlement of iron Base Alloys*,NACE.
[20] Stainless steels in oil and Gas Production (n.d). Retrieved on August 20, 2011 from http://www.outokumpu.com/46874.epibrw
[21] Yawas, D.S. (2005):*Suitability Assessment of Some Plant Extracts and Fatty Acid Vegetable Oils as Corrosion Inhibitors*. Department of Mechanical EngineringABU,Zaria.
[22] Yunan, P., Ibrahim,K. and Wan W. B. (2009): *Effect of pH and chloride concentration on the corrosion of duplex Stainless steel***:**The Arabian Journal for Science and Engineering, Volume 34, Number 2C.

American Journal of Engineering Research (AJER)
e-ISSN : 2320-0847 p-ISSN : 2320-0936
Volume-03, Issue-01, pp-185-199
www.ajer.org

Research Paper Open Access

Effect of Fly Ash Based Soil Conditioner (Biosil) and Recommended Dose of Fertilizer on Soil Properties, Growth and Yield of Wheat

Suhas Tejram Buddhe[1], Mahendra Thakre[2], Pramod R. Chaudhari[3]
[1] *Department of Environmental Science, Sevadal Mahila Mahavidyalaya & Research Academy, Sakkardara Chowk, Umred Road, Nagpur 440009, India*
[2] *Department of Environmental Science, Arts, Science and Commerce College, Tukum, Chandrapur 442401, India*
[3] *Ex-Deputy Director, National Environmental Engineering Research Institute, Nagpur 440020, India*

***Abstract*: -** Fly ash has been used in agriculture for improving the soil health and to increase the crop productivity with very high doses 10% to 80% of fly ash. In order to mitigate the impact of excess dose in terms of boron and heavy metal toxicity, present investigation was undertaken to process fly ash into improved soil conditioner "Biosil" through magnetization and to conduct field trials using wheat (*Triticum aestivum* L.) variety GW-273 with Biosil fortified by recommended dose of chemical fertilizers keeping Vermicompost and recommended dose of chemical fertilizers as control treatments. Very low Biosil doses resulted in improvement in soil quality, fertility, crop growth & productivity. The optimum concentration of Biosil dose was recorded to be in the range of 450 kg/ha to 900 kg/ha which were effective in reducing bulk density and improving organic carbon, phosphorus, potassium, sulphur and zinc which are generally deficient in Indian soils as per the results of national soil survey by Indian Council of Agricultural Research (ICAR). Vermicompost and chemical fertilizers were also effective in improving soil fertility. The Plant height, number of leaves/plant, length of earhead, number of grains/earhead, test weight, grain yield and straw yield showed improvement with the increasing Biosil doses. Vermicompost and chemical fertilizers were next to Biosil in improving the growth and yield of wheat. It is recommended that long term trials with Biosil fortified by chemical fertilizers and Vermicompost would be more beneficial for sustainable agriculture.

***Keywords:* -** *Chemical Fertilizer, Fly ash, Soil, Vermicompost, Wheat*

I. INTRODUCTION

The amount of fly ash produced annually in India was around 90 million tonnes during 1995 and is likely to cross the 140 million tonne barrier during 2020. Its disposal is a major concern. In India, most thermal power plants use bituminous coal as a fuel which contains a high amount of ash (up to 40%). Fly ash possesses unique physicochemical properties and has potential for its reuse in various sectors. There is also ample scope to process fly ash to make it a valuable product in different areas through applying suitable technology. Among all the recycling and reuse method for fly ash, agricultural utilization of fly ash as soil conditioner is now popular and can use huge quantity of fly ash produced in India.

In the past, various research studies evaluated the impact of fly ash on soil and crop productivity [1, 2, 3, 4, 5]. Trace elements in fly ash are found at concentrations which are higher than those in coal that act as source of micronutrients for healthy growth of plants, however the concentrations of biologically toxic elements such as B, Mo and Se greatly exceed their levels in soil [6]. To mitigate these problems, several techniques are being used like use of weathered fly ash or use of physically or chemically modified fly ash.

In order to mitigate the environmental problem, present study is proposed to study the effects of augmentation of soil with magnetized fly ash "Biosil" fortified with recommended dose of chemical fertilizers, keeping Vermicompost and chemical fertilizer as controls, on the growth and yield parameters of wheat and improvement of soil quality and fertility. The results of field trials will be used to optimize the dose of Biosil

and its fortifications for improvement of wheat crops in the black soils of Jabalpur, Madhya Pradesh, India.

II. MATERIALS AND METHODS

The field experiments were conducted in an agricultural field near Jabalpur, Madhya Pradesh, India that comes under Kymore Plateau & Satpura Hills Agroclimatic Region of India. The main crops of the area are wheat, rice, pulses, oil seeds, and maize. Fly ash from Koradi Thermal Power Station at Koradi, District Nagpur, Maharashtra State, India was securely collected and processed to produce novel soil conditioner "Biosil" by the process of magnetization.

Field experiments were conducted during Rabi season (October to March) 2011-2012 using wheat (*Triticum aestivum* L.) variety GW-273. The different doses of soil conditioner "Biosil" ranging from 150 kg/ha to 900 kg/ha, fortified with recommended dose of fertilizers (RDF), was applied to the agricultural field to study the improvement in quality & fertility of soil and growth & yield of wheat crop. The results of (Biosil+RDF) were compared with those obtained from RDF control and Vermicompost (VC) control. Randomised Block Design was used with a total 32 number of plots and 4 replications. Gross and net plot sizes were 6m x 4m and 5.6m x 3.6m respectively. The distance between plots were kept at 1.5 m and the distance between replications was kept at 2 m. Soil samples collected from the test sites were analyzed for physical and chemical characteristics [7, 8]. Surface soil-samples (0-30 cm) collected from three areas, were analyzed and averaged for site characterization. The levels of "Biosil" addition (on an oven-dry basis) were selected on the basis of preliminary field trials conducted earlier.

The details of treatment are given in TABLE I. Wheat cultivar GW-273 was sown with six levels of Biosil along with RDF (120:69:40 kg NPK/ha). Biosil was applied to the soil at the time of sowing. Nitrogen (50% dose), phosphorus (100% dose) and potash (100% dose) were applied as basal dose. Two Nitrogen (25%) doses were applied as top dressing after one and two months. Statistical analyses were carried out to establish the effects of fly ash addition on soil characteristics and crop yields.

Soil samples from the experimental field were analyzed before sowing and after harvest of crop for the parameters namely pH, electrical conductivity (EC), bulk density (BD), nitrogen (N), phosphorus (P), potassium (K), sulphur (S) and zinc (Zn). In case of crops, pre-harvest observations at maturity were recorded on plant population (Number of plants/m2), plant height (cm), and number of leaves/plant, while post-harvest observations were made on number of effective tillers/m2, length of earhead (cm), number of grains/earhead, test weight (g), grain yield (q/ha) and straw yield (q/ha).

III. RESULTS AND DISCUSSION

3.1 Climate and Meteorological Status

Jabalpur has a humid subtropical climate, typical of North-Central India (Madhya Pradesh and Southern Uttar Pradesh). Summer starts in late March and last up to June. May is the hottest month. The total annual precipitation is nearly 55 inches (1386 mm). Jabalpur gets moderate rainfall of 35 inches (889 mm) during July-September due to the southwest monsoon. Winter starts in late November and last until early March. They peak in January. The annual average meteorological status of 3 years is given in TABLE II. The annual average temperature ranged from 25.1 ^{0}C to 26.2 ^{0}C with maximum temperature from 31.5 ^{0}C to 32.5 ^{0}C and minimum temperature from 19.6 ^{0}C to 20.6 ^{0}C. Total annual precipitation ranged from 1375.40 mm with 62 to 86 days with rain, 17 to 33 days with thunderstorm, with fog from 0 to 5 days and with hail from 0 to 1 day. The annual average wind speed ranged from 2.9 to 3.0 km/h.

3.2 Preparation of 'Biosil' Soil Conditioner

Refined magnetized fly ash 'Biosil', imparting magnetic activity and adding economic value to fly ash for use as a soil conditioner was used in present investigation. Biosil was prepared by passing it through a magnetizer under controlled conditions.

3.3 Quality of Soil of Experimental Field before Sowing

A field experiment was conducted during Rabi 2011-12. The soil of Jabalpur region is broadly classified as Vertisol as per norms of US classification of soil. It is medium to deep in depth and black in colour. It swells by wetting and shrink when dries. Thus, it develops wide cracks on the surface during summer season.

The mean values of the surface soil data before sowing are presented in TABLE III. The soil of experimental field showed particulate composition as sand 25.18%, silt 19.18% and clay 55.64% and thus the texture is clayey. The soil pH is 7.1 which is neutral and is in the range 7.0 to 8.5 which is favorable for most crops and most of the essential nutrients are available within this pH range (Table IV; Fig.1). The EC is 0.31 dS/m which is below the desirable level for black soils for most plants (TABLE V). The Bulk Density of Soil is 1.46, which is much higher than the ideal Bulk Density of 1.10 for clayey soils (TABLE VI).

The soil fertility was assessed based on the guidelines for rating the soil fertility indicators (TABLE VII). The qualitative ratings of soil, arising from the comparison between soil data and the indicator's stratification are presented in TABLE VIII that reveals that the organic carbon content was medium, available N medium-low, available P low, and available K medium in soil before sowing. The low to medium nutrient status is due to medium content of organic carbon which plays an important role in binding nitrogen and other nutrients in the soil protecting them from leaching out. Under low organic carbon content in soil, nitrogen is a very dynamic element, susceptible to leaching in high rainfall area; volatilization due to annual vegetal burning and high temperature of the tropical environment; and immobilization in organic pool. Therefore widespread nitrogen deficiency is not surprising.

Overall, the soil of experimental field is said to be of medium fertility with low available P. This is in conformity with the results of National Survey of Soils in India by ICAR. The productivity of Indian soils at present stands at a very low levels in comparison to world soils, due to cumulative effect of multiple factors like scarcity of moisture, deficiency of plant nutrients, and faulty management of soils [9].

3.4 Effect of Treatments on Soil Properties

The initial soil quality before sowing and the final soil quality after harvest in different treatments are presented in TABLE IX.

3.4.1 Soil pH

Soil pH was recorded before sowing as well as after harvest of crop. It did not change significantly neither with the application of Biosil in combination with RDF nor due to the addition of VC or RDF (TABLE IX). Soil pH increased to 7.2 in T3-300 to T4-600 treatments. Indian fly ashes are alkaline due to presence of low sulphur and appreciable content of oxides of Ca, Mg etc. in coals and an increase in the pH of mine spoil after lignite fly ash amendments during field study has been reported [10]. This low response of soil may be due very low application of Biosil as compared to conventional doses given from 10% to 80% of fly ash:soil mixture, where change in pH is reported [11,12,13]. Another reason is that this is first year of application of Biosil and long term treatments are expected to give more desirable results.

3.4.2 Electrical Conductivity

Electrical conductivity of soil was correlated (R: 0.5; R2: 0.25) with Biosil+RDF doses (Table IX, Fig. 2). T2-300 treatment showed maximum 6.45% increase in electricity conductivity of soil, showing Biosil (300kg/ha) as optimum dose for improving electrical conductivity (TABLE XA and XI). RDF also showed equivalent increase in electrical conductivity by 6.45%. Vermicompost was lowest among them with 3.23% increase in electricity conductivity over initial, showing trend as given below, RDF+Biosil>RDF>VC (TABLE XI). Similarly, gradual increases in soil pH and conductivity [13, 14, 15, 16] has been observed with increased application rate of fly ash.

3.4.3 Bulk Density

The initial bulk density of soil 1.46 g/cc decreased due to application of Biosil+RDF in the range of 1.41 g/cc to 1.44 g/cc that is by 1.37% to 3.43% and negatively correlated with Biosil+RDF doses (R: -0.93; R2: 0.86) (TABLE IX; Fig. 2). The reduction was more pronounced due to addition of Vermicompost which had significantly lowest value of bulk density (1.37 g/cc) showing -12.33% reduction. Bulk density did not decrease in RDF treatment (TABLE XA). The Vermicompost (8t/ha) treatment proved superior over the lowest doses of Biosil i.e. 150, 300, and 450 kg/ha and RDF control also. This shows that the application of Biosil @600 kg/ha (T4-600) and vermicomppost @8t/ha are sufficient to keep the soil porous. However, the bulk density is required to be reduced to 1.10 g/cm3 which is ideal for clayey soils (TABLE VI). These changes in soil properties might have been due to modification in macro- and micro-pore size distribution in black soils of Jabalpur and which may have also contributed to the increased crop yield. Reduction of bulk density in these soils is also advantageous for reduced hydraulic conductivity and improved moisture retention at field capacity and wilting point.

Similar observations have been recorded [17] that fly ash addition in soil resulted in lower bulk density, although the differences compared with control plots were not significant. Application of fly ash at 0, 5, 10 and 15% by weight in clay soil significantly reduced the bulk density and improved the soil structure, which in turn improves porosity, workability, root penetration and moisture-retention capacity of the soil [18]. Fly ash treated plots tended to have lower bulk density of surface soil (0-30 cm) by 5.9 percent under 20 t/ha fly ash treatment, though the differences over control were non-significant for both sorghum and wheat crop [19].

3.4.4 Soil Organic Carbon

Organic carbon of soil recorded after harvest of crop showed improvement in Biosil+RDF treatments by 1.56% in T1-150 (0.65% organic carbon) to 7.81% in T4-600 (0.69% organic carbon) over initial value (0.64% organic carbon) as well as over RDF control (0.64% organic carbon). The highest organic carbon (0.73%) (Increase by 14.06%) was noted in the plots receiving Vermicompost @ 8t/ha and it was found at par to higher doses of Biosil (T4-600,T5-750 and T6-900) (Table IX, XA; Fig. 2). These organic carbon levels (0.69% in Biosil+RDF and 0.73% in Vermicompost) are medium as compared to soil fertility classification and are in optimum range for the crops (TABLE VII). Similar observation have been reported [13]wherein increase in organic carbon and electrical conductivity was observed after application of fly ash at 50t/ha in wheat field. Biosil dose of 600kg/ha was optimum for improving organic carbon and the trend was VC>Biosil+RDF>RDF (Table XI).

The importance of organic carbon is due to its positive correlation with nutrient content of soil. The method of analyzing organic carbon of the soil in order to assess nitrogen content of the soil is most commonly adopted. Therefore, there is need to utilize Biosil + RDF as well as Vermicompost in order to get highest benefit with respect to soil fertility and crop productivity. This will be helpful to retain major portion of the soil nitrogen, phosphorus and sulphur in the soil in the organic form. As the organic matter decomposes, these nutrients are released in the soil and absorbed by the plant roots. A soil rich in organic matter is always found rich in nitrogen. However, organic carbon should not be very high that is >1.00% that make the nitrogen less available to the plants.

3.4.5 Nitrogen

Application of Biosil+RDF treatments did not brought any significant change in the content of nitrogen in soil over initial status of soil. Similarly different treatmentsof Biosil+RDF did not exhibit marked variations among the doses (TABLE IX; Fig. 4). The T6-900 treatment showed 1.08% increase in soil nitrogen, while Vermicompost showed 2.15% and T7-RDF showed 0.54%, showing Vermicompost as having best results among the treatments (TABLE XB). T6-900 is the optimum dose of Biosil and the trend of improvement is VC>Biosil+RDF>RDF (TABLE XI). Low level increase in Biosil+RDF Treatments is explained by the initial nitrogen deficiency in the soil and luxury uptake of nitrogen by the wheat crop. It is reported [20] that fly ash incorporation on soil led to uptake of nitrogen, phosphorus and potassium by rich amount and succeeding wheat also increased with increasing fly ash amendment. Better results were recorded with higher doses of fly ash [21] where a distinct increase in the concentrations of N, P, K, S, in soil plus fly ash mixtures was obtained with concomitant increase in fly ash percentage.

3.4.6 Phosphorus

The content of phosphorus markedly increased over initial status of 17.45 kg/ha due to increasing doses of Biosil+RDF (R: 0.94; R2: 0.88) that is T4-600 (17.90 kg/ha), T5-750 (17.9 kg/ha) and T7-900 (18.30 kg/ha) (TABLE IX; Fig. 3), showing 2.58% to 4.87% increase, while Vermicompost and RDF control each showed only 2.58% increase over initial level (TABLE XB). Thus, Biosil+RDF treatment is best to improve the phosphorus content of soil and facilitate the phosphorus mobilization in the edaphic environment. The optimum Biosil dose is 900 kg/ha (T6-900) and the trend of improvement is Biosil+RDF>RDF=VC (TABLE XI). These results indicate that Biosil+RDF treatment facilitate the activity of phosphate solubilizing bacteria in soil. Similar result is obtained by a worker [21] who reported good adaptability of phosphate solubilizing bacteria to fly ash amended soils and better survival exhibiting 36.4% to 86.1% phosphate solubilization, and the population of phosphate solubilizing bacteria in fly ash amended soils mixed with chemical fertilizer was higher in the presence of fly ash, a level as high as 12%. Increase in phosphorus content with increase in fly ash doses is also observed [15].

3.4.7 Potassium (K)

Good improvement in potassium content in Biosil+RDF treatment plots was observed over initial status (R: 0.64; R2: 0.41). The initial potassium content of 297 kg/ha was observed to be increased to 303 kg/ha in T6-900 treatment showing 2.02% increase, while RDF treatment showed 298 kg/ha (0.34% increase) and Vermicompost showed 380 kg/ha (1.68% increase) (TABLE IX & XB, Fig. 4). Thus, Biosil 900 kg/ha is optimum for mobilization of potassium, followed by Vermicompost, the trend being Biosil+RDF>VC>RDF (TABLE XI). Biosil+RDF was 1.34% more effective than T7-RDF and superior than T2-300 treatment. Biosil dose upto T2-300 were less effective than T8-VC but T3-450 to T6-900 treatments were more effective than T8-VC. Similar observation is recorded wherein a distinct increase in the concentrations of N, P, K, S were observed in soil plus fly ash mixtures with concomitant increase in fly ash percentage [21].

3.4.8 Sulphur

The initial sulphur content (9.2 kg/ha) is close to the critical level (10 ppm) and significant improvement was observed due to application of each dose of Biosil+RDF (R: 0.88; R2: 0.77) which proved superior over Vermicompost @ 8t/ha. The Biosil+RDF treatments showed increase in level of sulphur up to 9.5 kg/ha in T6-900 (3.26% increase over initial level), while Vermicompost and RDF controls showed 9.3 kg/ha sulphur (1.09% increase over initial level) (TABLE IX, XC and XI). Thus, the minimum optimum concentration of Biosil+RDF treatment is 600kg/ha, and the trend of improvement is Biosil+RDF>VC=RDF (TABLE XI). Biosil treatment (T6-900) was 3.26% more effective than T7-RDF and 2.15% more effective than T8-VC. This indicates that the Biosil+RDF has capacity to mobilize S from the soil and make it available to the growing crop. Similar observations have been recorded by other authors that the fly ash improves the nutrient status of soil [22].

3.4.9 Zinc

Zinc content also showed the similar improvement over initial status (1.2 kg/ha) of soil in different treatments. The Biosil+RDF treatments showed linear increase (R: 0.84; R2: 0.71) in Zn content as 1.33 kg/ha (T1-150), 1.35 kg/ha (T2-300), 1.45 kg/ha (T3-450) showing percentage increase as 10.83%, 12.50% and 20.83% respectively) (TABLE IX, XC; Fig.3). While Vermicompost and RDF controls, each one with 1.46 kg/ha zinc, showed 21.67% increase over initial level in both, showing trend as VC=RDF>Biosil+RDF (TABLE XI). Thus, all the three treatments are more or less equivalent in improving the zinc content of soil. T3-450 is the optimum Biosil treatment. This is in conformity with [21] who observed that on fly ash addition to agricultural field, micronutrients (Fe, Cu, Zn, Mn and Mo) and heavy metals (Cr, Co) were observed to occur within permissible limits in soil,

It is thus concluded that the Biosil+RDF, Vermicompost and recommended dose of fertilizers are effective in improving the soil fertility by mobilizing the macro- and micro-nutrients in the soil. Biosil+RDF range of T4-600 to T6-900 treatments with Biosil dose of 600 to 900 kg/ha was, in general, observed to be optimum for improving the physicochemical status of black soil of Jabalpur, especially nutrient content and fertility. This shows that magnetized fly ash Biosil at very low doses, has remarkable property of improving the flow of available nutrients to the plant roots, thereby improving the growth of plant. Biosil+RDF and Vermicompost were more or less equally highly effective followed by RDF. Biosil+RDF treatment was more effective for improving electrical conductivity, phosphorus, potassium,, sulphur; Vermicompost was more effective for improving organic carbon, bulk density, nitrogen and zinc; while RDF was suitable for phosphorus, sulphur and zinc. These conclusions are in conformity with other workers [19] who observed that fly ash (5, 10, 20 t/ha) with nitrogen (25, 50, 100 kg/ha) treated plots of wheat and sorghum showed decrease in pH, whereas electrical conductivity increased in accordance with the amounts of fly ash added in the soil. Organic carbon and sodium increased with fly ash addition.

3.5 Effect on Growth and Yield of Wheat

The effects of soil conditioner Biosil+RDF were assessed on wheat crop and compared with Vermicompost and RDF controls (TABLE XII, XIIIA-B, XIV; Fig. 5, 6).

3.5.1 Plant Population

Results revealed that the plant population did not vary much under different treatments; however no reduction was observed in any treatment. This shows that all the treatments are favourable for seed germination, seedling growth and vegetative growth which determine population (TABLE XII; Fig.5). TABLE XIVA indicates more positive effect of Vermicompost over Biosil+RDF treatment in respect of plant population.

3.5.2 Plant Height

Plant height is linearly increasing with the increasing dose of Biosil+RDF. The average plant height increases from 86.2 cm in T1-150 through 87.4 cm in T2-300, 88.0 cm in T3-450, 89.2 cm in T4-600, 89.5 in T5-750 and 89.8 cm inT6-900 and is well correlated with Biosil doses (R: 0.97; R2: 0.94). The plant height in T8-VC (88.2 cm) is next highest to Biosil+RDF treatment, followed by T7-RDF with 85.4 cm plant height (TABLE XII; Fig. 6). The plant height stimulation by Biosil+RDF treatments over RDF treatment range from 0.94% to 5.15%. Vermicompost treatment was superior to Biosil doses upto T3-450, however higher Biosil doses from 600 kg/ha (T4-600) to 900 kg/ha (T6-900) showed 1.13% to 1.81% higher stimulation for plant height (TABLE XIIIA). Optimum Biosil dose for plant height is 900kg/ha and the trend of plant height stimulation is Biosil+RDF>VC>RDF (TABLE XIV).

Similar improvements in the growth parameter of trees were obtained by others [11, 21], but with high doses of normal fly ash. Fly ash at 18% [21] resulted in a 15% increase in the growth of Acacia auriculiformis; and co-addition of chemical fertilizers resulted in significant rise in the collar diameter to 2.6 cm corresponding

to almost a 19% increase. In *Eucalyptus tereticornis* at 12, 18, and 24% fly ash with the co-addition of chemical fertilizer, there was increase up to 26% in the collar diameter and the plant growth was significantly increased with increasing fly ash percentage and the difference was maintained over the years. Fly ash had no negative effect on the mean annual increment (MAI) of both the tree species and it was rather higher in the presence of fly ash. Similarly, the length of root and shoot of Indian mustard Brassica juncea were observed maximum in the amendment in 60% Fly ash (or 2:3, fly ash and soil) as recorded on 30, 60 and 90 days of experiment. The length of root increased gradually from 10% (28.50%) to 60% (28.55%) and then decreased from 80% fly ash (33.34%) to 100% fly ash (44.5%) as compared to control [11]. The height of wheat plant was observed to be significantly higher (89.10 cm) in treatment NPK + farm yard manure (FYM), however, it was at par with RDF+fly ash (FA) 100 t/ha (84.04 cm), RDF 75%+FA 70 t/h +Vermicompost 2 t/ha (86.12 cm), RDF + FA 40 t/ha + VC 1 t/ha (87.15 cm), RDF + FA 20 t/ha + VC 1 t/ha (85.89 cm) and RDF + VC 1 t/ha (85.28 cm), indicating that the application of FYM, VC and FA in combination with recommended dose of NPK for wheat was beneficial[23].

3.5.3 Number of Leaves/Plant

Biosil+RDF treatment was observed to be highly stimulating for number of leaves/plant which gradually increases with the increase in the dose of Biosil+RDF and both are well correlated (R: 1.0; R2: 1.0). The number of leaves/plant was 22.80 in T1-150 which increase through 22.85 in T2-300, 25.60 in T3-450, 28.55 in T4-600, 30.88 in T5-750, and 32.65 in T6-900 (TABLE XII; Fig. 6). Biosil+RDF treatment was 22.51% more effective than Vermicompost and 61.16% more effective than RDF. Vermicompost was 31.54% more effective than RDF treatment (Table XIIIA). The optimum dose of Biosil+RDF was 900 kg/ha and the trend of impact is Biosil+RDF>VC>RDF (TABLE XIV). Vermicompost treatment was superior to T3-450 treatment (TABLE XII, XIIIA). This is in conformity with the observation [23] that significantly higher leaf area (20.10 cm2) was recorded in the treatment RDF + FYM 10 t/ha over absolute control, RDF 50 % + FA 100 t/ha and RDF 75 % + FA 70 t/ha. The reduction in dose of NPK reduced flag leaf area significantly.

Similar observations have been recorded in case of other soil conditioners [24]. It is reported, in Turkey in 2004, that the number of leaves, leaf area, most developed root length, fresh and dry root weight and increasing fresh weight of strawberry plants were increased at an important level ($p<0.01$) in 30% and 45 % pumice amendments in 4-8 mm grade compared to control. The highest number of leaves, leaf area, most developed root length, fresh and dry root weight and increasing fresh weight were also obtained from 45% pumice amendments in 4-8 mm grade. It is observed in case of *Brassica juncea* that the number of leaves and flowers per plant increased from control to 60% fly ash. However, the number of pods showed a 100% increase from control to 40% fly ash (2:3 fly ash and soil). A maximum of twelve pods was observed in 40% fly ash (2:3 fly ash and soil) [11].

3.5.4 Number of Effective Tillers/m2

Biosil+RDF treatments were again very effective in increasing the number of effective tillers/m2 showing linear increase in number with increasing doses of Biosil. The initial number of effective tillers 221.5 in T1-150 increases through 243.8 in T2-300, 245.0 in T3-450, 249.7 in T4-600, 256.8 in T5-750 and 299.4 in T6-900, showing good correlation (R: 0.9; R2: 0.81) (Table XII; Fig. 5) . The next highest number of tillers/m2 was 244.4 in T8-VC followed by 198.9 in T7-RDF. Vermicompost treatment was superior to T2-300 treatment. The Biosil+RDF treatment was 50.53% more effective than RDF and 22.50% more effective than VC. VC treatment was 22.88% more effective than RDF treatment. The optimum Biosil dose was 900 kg/ha (T6-900) and the trend of effective treatment was Biosil+RDF>VC>RDF (TABLE XIV). Similar observation have been noted [23] wherein numerically higher number of tillers (4.61) were obtained by the application of NPK + FA 100 t/ ha over the application of NPK only (3.89)

3.5.5 Length of Earhead

Biosil+RDF treatment was highly stimulative for the length of earhead showing linear increase in the length with increase in the doses of Biosil+RDF. The length of earhead (cm) was 9.4 in T1-150 that increased through 9.5 in T2-300, 9.6 in T3-450, 9.7 in T4-600 and T5-600 each and 9.8 in T6-900 treatment, showing good correlation (R: 0.98; R2:0.96). The next highest length was 9.5 cm in T8-VC followed by 9.1 cm in T7-RDF treatment (TABLE XII; Fig .6). Biosil+RDF treatments were 3.30% to 7.69% more effective than T7-RDF treatment. The T3-450 to T6-900 treatments were effective by 1.05% to 3.16% than T8-VC treatment. T8-VC treatment was 17.8% more effective than T7-RDF treatment and T1-150 treatment (TABLE XIIIB). Biosl 900 kg/ha dose was optimum while the trend was Biosil+RDF>VC>RDF (TABLE XIV).

Similarly the length of spike was higher in RDF + FYM 10 t/ha (9.28 cm) over absolute control, RDF, RDF 50 % + FA100 t/ha and RDF 75 % + FA 70 t/ha indicating that the application of FYM, VC and FA had beneficial effect [23]. It is interesting to note that the application of fly ash along with the recommended dose of NPK and

Vermicompost has beneficial effect on wheat. Further, it was also noticed that the application of fly ash along with NPK had beneficial effect over application NPK only.

3.5.6 Number of Grains/Earhead

There is full correlation between doses of Biosil+RDF and number of grains/earhead (R: 1.0; R2: 1.0). The number of grains/earhead was 53.9 in T1-150 and further increased through 55.7in T2-300, 57.9 in T3-450, 59.8 in T4-600, 61.1 in T5-750, and 63.4 in T6-900 (TABLE XII; Fig. 7), showing percentage increase of 7.8% to 26.8% over T7-RDF. The treatments T4-600 to T6-900 showed 1.53% to 7.64% increase over T8-VC treatment (TABLE XIIIB). Vermicompost treatment was 17.8% effective than RDF treatment and superior to T3-450 treatment.

3.5.7 Test Weight

Test weight is well correlated with the doses of Biosil+RDF (R: 0.9; R2: 0.81). Test weights (g) were recorded to be 42.1, 42.4, 42.6, 43.9, 44.4, 46.5 in T1-150, T2-300, T3-450, T4-600, T5-750 and T6-900 respectively. Next superior treatment was of T8-VC with 44.3 g test weight followed by T7-RDF treatment with 41.8 g test weight (Table XII; Fig.7) with trend Biosil+RDF>VC>RDF. Biosil 900 kg/ha (T6-900) was optimum treatment (TABLE XIV). The Biosil treatments were 0.72% to 11.24% more effective than T7-RDF treatment and the treatments T5-750 to T6-900 were better by 0.23% to 4.97% than VC treatment. VC treatment was 5.98% more effective than T7-RDF treatment and more effective than T4-600 treatment (TABLE XIIIB). Similarly, it has been observed that the application of NPK + Fly ash was found significantly superior over NPK in respect of 1000 grain weight of wheat [23].

3.5.8 Grain Yield

The grain yield and doses of Biosil+RDF were highly correlated (R: 0.97; R2: 0.94). The grain yield (q/ha) was recorded as 47.7, 50.5, 53.8, 57.8, 58.6, 59.4 in T1-150, T2-300, T3-450, T4-600, T5-750 and T6-900 respectively. Next superior treatment was of T8-VC with 56.5 q/ha followed by T7-RDF with 45.5 q/ha grain yield (TABLE XII; Fig.7), with trend as Biosil+RDF>VC>RDF and optimum dose of Biosil as 900 kg/ha (T6-900) (TABLE XIV). Biosil treatments were 4.84% to 30.55% more effective than T7-RDF treatment and the treatments T4-600 to T6-900 were 2.3% to 5.3% more effective than T8-VC. Vermicompost treatment was 24.18% more effective than T7-RDF treatment and was superior over T3-450 treatment (TABLE XIIIB).

The research trials conducted under fly ash mission projects at Farakka [25], revealed that on an average 40 per cent increase in yield of wheat was obtained with the application of fly ash @ 200 t/ha. The results obtained on research conducted at Punjab Agricultural University[26] indicated that, application of fly ash @ 10 t/ha increased the yield of wheat from 21.5 q ha-1 to 24.1 q/ha. It is reported [27] that the soil application of fly ash increased wheat grain yield by 20 percent.

3.5.9 Straw Yield

There was good correlation between straw yield and doses of Biosil+RDF (R: 0.97; R2: 0.94). The recorded straw yields (q/ha) were 70.4, 73.8, 78.5, 86.8, 88.5, 89.6 in treatments T1-150, T2-300, T3-450, T4-600, T5-750 and T6-900 respectively. Next superior treatment was T8-VC with 85.5 q/ha followed by T7-RDF with 74.4 q/ha straw yield (TABLE XII; Fig. 7), with trend as Biosil+RDF>VC>RDF and optimum dose as 900 kg Biosil/ha (T6-900) (TABLE XIV). The Biosil treatments T3-450 to T6-900 were 5.51% to 20.43% more effective than T7-RDF and T4-600 to T6-900 treatments by 1.52% to 4.8% more effective than T8-VC. For the first time, T7-RDF was more superior treatment than T2-300 treatment. T8-VC treatment was superior to T3-450 treatment (TABLE XIIIB).

It is reported that [27] the soil application of fly ash increased wheat grain yield by 2%, and the application of fly ash to soil increased both grain and straw yield in pearl millet (direct) and subsequent wheat (residual) crop significantly at all levels of fly ash [28]. A two year experiment [29] indicated that clay loam soil being higher in CEC, organic matter content, water holding capacity and available nutrients brought an improvement in growth, yield attributes, grain and straw yields and uptake of plant nutrients by wheat when compared with sandy loam soil.

IV. CONCLUSION

These treatments were effective in mobilizing macro and micro nutrients in soil and in improving the soil fertility. Biosil is based on fly ash that generally contains small amounts of C and N, it is medium in available K and high in available P and micronutrients [20], which also form source of nutrients to the soil. Though all the three soil conditioners have some role in mobilizing all the nutrients in soil, it is interesting to see their dominant role in some of them and that Biosil+RDF has better results than RDF as well as vermicompst. This indicates that the potency of RDF (and may be of Vermicompost) may be increased in presence of Biosil.

Similar observation shows [29] that incorporation of fly ash manure and fly ash at 10t/ha, in general, improved cation exchange capacity of soil, organic content, available nutrient status and decrease the soil pH.

Biosil+RDF was highly effective in improving the growth and yield parameters of wheat crop. Next superior treatment was of Vermicompost, which was followed by RDF. This indicates the important contribution of Biosil, Vermicompost and RDF in improving the wheat growth and yield. Biosil (+RDF) in the range of 600 to 900 kg/ha is optimum for stimulating the crop growth and yield in Jabalpur black soils. Overall, it is concluded that the Biosil is very effective at a very low dose of 600 to 900 kg/ha in improving the soil quality and fertility and wheat growth and yield. The promoting effect of Biosil is enhanced by the RDF. Similar observations have been made by other workers [19, 23, 28, 29, and 30]. It is noted [19] that application of fly ash in combination with nitrogen had some advantageous effect on grain and biomass yield of wheat crop irrespective of the variety though the positive effect was non-significant. It is also observed [23] that the application of fly ash @ 100 t/ha along with recommended dose of NPK was found superior over recommended dose of NPK to wheat crop and for soil properties also. A mixture of fly ash and sludge for 4 years [30], each at 26 t/ha, increased the yield of French bean and soybean by 53% and 30%, respectively, over the control treatment that received NPK fertilizers at recommended rates. Unlike sewage sludge or the fly ash-sludge mixture, the application of only fly ash at 52 t ha-1 did not sustain crop yields [28]. Thus it is evident that the fly ash potency can be increased by its combined treatment with RDF and any other organic source.

Thus Biosil may be termed as 'Nuclear Soil conditioner', as it is useful in very low doses to soil. High fly ash doses have been reported to decrease seed germination in Indian mustard as compared to control in very high doses of fly ash from 10% to 100% fly ash [11] and heavy metal and Boron toxicity. This was most likely due to increased impedance offered by the soil / ash matrix to germinating seeds [2].

V. ACKNOWLEDGEMENT

The authors wish to thank the Principal, Sevadal Mahila Mahavidyalaya and Research Academy, Nagpur, India for providing all the facilities for carrying out the present investigation.

VI. REFERENCES

[1] R.N. Garg, G. Singh, N. Kalra, D.K. Das, and S. Singh, Effect of soil amendments on soil physical properties, root growth and grain yields on maize and wheat, *Asian Pacific Journal of Envioronmental Development, 1996, **3**(1):54-59.*

[2] N. Kalra, A. Chaudhary, S.K. Sharma, B.K. Vatsa, V. Kumar,R. Kumar, R.C. Harith, and U. Kumar, Impact of fly ash on agriculture. *ICAR News, 1997, 3(2):20*

[3] D.K Gupta, U.N. Rai, R.D. Tripathi, and M. Inouhe, Impacts of fly ash on soil and plant responses. *Journal of Plant Research, 2002, 115: 401-409.*

[4] Prem Kishor, A.K. Ghosh and Dileep Kumar, Use of fly ash in agriculture: a way to improve soil fertility and its productivity. *Asian Journal of Agricultural Research, 2010, 4:1-14*

[5] S. Singh, D. Gond, A. Pal, B. Tewary, and A. Sinha, Performance of several crops grown in fly ash amended soil. *World Coal Ash Conference*, In Denver, CO, USA, May 9-12, 2011.

[6] N. Kalra, H.C. Joshi, S.K. Sharma, R.C. Harit, and Kishor Brij, Effect of fly ash incorporation on soil and crop productivity, *ICAR News, 1996, 2(2):18.*

[7] J.J. Hanway and H. Heidal, Soil analysis methods used in Iowa state soil testing lab. *Agronomy, 1952, 57: 1-31.*

[8] M.L. Jackson and Phillip Barak, *Soil chemical analysis: advanced course*, UW Madison Libraries Parallel Press, 2005

[9] K.T. Chandy, *Status of plant nutrients in Indian soil.* Online, browsed 2013, Booklet no. 71, (Soil Sci.: SSS – 20. Agric. and Env. Education).

[10] L.C. Ram, N.K. Srivastava, R.C. Tripathi, S.K. Jha, A.K. Sinha, G. Singh, and V. Manoharan, Management of mine spoil for crop productivity with lignite fly ash and biological amendments, *Journal of Environmental Management, 2006a, 79:173–187.*

[11] Sarita Gautam, Annapurna Singh, Jaspal Singh, Shikha, Effect of fly ash amended soil on growth and yield of Indian Mustard (*Brassica Juncea*), *Advances in Bioresearch, 2012, 3(4):39-45*

[12] Im-Erb Rungsun, Noparat Bamroongrugsa, Koji Kawashima, Tomoyuki Amanoand Shigeru Kato, Utilisation of coal ash to improve acid soil, *Journal of Science and Technology, 2004, 26(5):697-708.*

[13] A.S. Tekade, G.N. Kulkarni, S.A. Mohite, Influence of fly ash on soil characteristics of Kharland pond, Ratnagiri (Maharashtra), *Discovery Agriculture, 2013, 1(2):62-66.*

[14] T. Matsi, and V.Z. Keramidas, Fly ash application on two acid soils and its effect on soil salinity, pH, B, P and rye grass growth and composition, *Environmental Pollution, 1999, 104:107-112.*

[15] P.K. Sarangi, D. Mahakur, and P.C. Mishra, Soil biochemical activity and growth response of *Oryza sativa* in fly ash amended soil, *Bioresource Technology, Feb., 2001, 73(3):199-205.*

[16] S.K. Sharma, Naveen Kalra and G.R. Singh, Soil physical and chemical properties as influenced by fly ash addition in soil and yield of wheat. *Journal of Scientific & Industrial Research, 2002, 61:617-620.*

[17] N. Kalra, M.C. Jain, H.C. Joshi, R. Choudhary, R.C. Harith, V.K. Vatsa, S.K. Sharma, and V. Kumar, Fly ash as a soil conditioner and fertilizer. *Bioresource Technology, 1998, 64:163-167*
[18] D.R. Kene, S.A. Lanjewar, B.M. Ingole, and S.D. Chaphale, Effect of application of fly ash on physico-chemical properties of soil, *Journal of Soils and Crops, 1991, 1(1):11-18.*
[19] S. Aggarwal, G.R. Singh and B.R. Yadav, Utilization of fly ash for crop production: effect on the growth of wheat and sorghum crops and soil properties. *Journal of Agricultural Physics, 2009, 9:20-23*
[20] S.K. Sharma, and Naveen Kalra, Effect of fly ash incorporation on soil properties and productivity of crops: a review. *Journal of Scientific and Industrial Research, 2006, 65:383-390*
[21] Sudha Jala, *Fly ash as an amendment agent for soil fertility*. Ph.D. Thesis, 2005
[22] Rautaray, S.K., B.C. Ghosh and B.N. Mittra, 2003. Effect of fly ash, organic wastes and chemical fertilizers on yield, nutrient uptake, heavy metal content and residual fertility in a rice-mustard cropping sequence under acid lateritic soils. Bioresour. Technol., 90: 275-283.
[23] M.R. Yavazadeh, and H. Shamsadini, Safe environment by using fly ash and Vermicompost on wheat. In: *International Conference on Transport, Environment and Civil Engineering (ICTECE2012)*, Kuala Lumpur (Malaysia), August 25-26, 2012.
[24] Sahin Ustun, Selda Ors, Sezai Ercisli, Omer Anapali, Ahmet Esitken, Effect of pumice amendment on physical soil properties and strawberry plant growth. *Journal of Central European Agriculture, 2005, 6(3):361-366.*
[25] Anonymous, Utilization of fly ash in agriculture and revegetation of dumping sites. *Annual Progress Report, 1993.*
[26] Punjab Agriculture University, *Utilisation of fly ash in agriculture and revegetation of dumping sites.* Annual Progress Report, 1993.
[27] D.B. Matte, and D.R. Kene, Effect of application of fly ash on yield performance of Kharif and Rabi crops. *Journal of Soils and Crops 1995, 5(2):133-136.*
[28] K.S. Grewal, D.S. Yadav, S.C. Mehta and M.C. Oswal, Direct and residual effect of fly ash application to soil on crop yields and soil properties, *Journal of Crop Research, 2001, 21(1):60-65.*
[29] K.L. Totawat, G.L. Nagar, S.L. Jat, and R.K. Jangir, Effect of fly ash on the performance of wheat on Ustochrepts of sub-humid plains of India. In*: Symposium no. 24*, Paper no. 215, 2002, Presentation: oral
[30] V.K. Kauthale, P. S. Takawale, P. K. Kulkarni and J. N. Daniel, Influence of fly ash and sewage sludge application on growth and yield of annual crops, *International Journal of Tropical Agriculture, 2005, 23(1-4): Jan-Dec 2005:49-54.*

Table I: Details of Treatments

Code	Treatments
T1-150	RDF (120:60:40 kg NPK/ha) + SOIL conditioner (Biosil@ 150 kg/ha)
T2-300	RDF (120:60:40 kg NPK/ha) + SOIL conditioner (Biosil@ 300 kg/ha)
T3-450	RDF (120:60:40 kg NPK/ha) + SOIL conditioner (Biosil@ 450 kg/ha)
T4-600	RDF (120:60:40 kg NPK/ha) + SOIL conditioner (Biosil@ 600 kg/ha)
T5-750	RDF (120:60:40 kg NPK/ha) + SOIL conditioner (Biosil@ 750 kg/ha)
T6-900	RDF (120:60:40 kg NPK/ha) + SOIL conditioner (Biosil@ 900 kg/ha)
T7-RDF	RDF (120:60:40 kg NPK/ha) alone
T8-VC	SOIL Conditioner Vermicompost @ 8t/ha)

Table II: Meteorological Status and Climate of Jabalpur

Year	**T**	**TM**	**Tm**	**PP**	**V**	**RA**	**TS**	**FG**	**GR**
2010	26.2	32.5	20.6	1470.40	3.0	62	24	5	0
2011	25.1	31.6	19.6	--	2.9	86	33	0	0
2012	25.2	31.5	19.6	1375.40	3.0	75	17	2	1

Note: T: Annual average temperature (^{0}C); TM: Annual average maximum temp (^{0}C); Tm: Annual average minimum temp. (^{0}C); PP: Total annual precipitation of rain (mm); V: Annual average wind speed (km/h); RA: Total days with rain during the year; TS: Total days with thunderstorm during the year; FG: total days with fog during the year; GR: Total days with hail during the year

Table III: Physicochemical Quality of Soil before Sowing

Texture	**Soil pH**	**E.C. (dS/m)**	**Organic Carbon (%)**	**Bulk Density(g/cc)**	**Available Plant Nutrients (kg/ha)**				
					N	**P**	**K**	**S**	**Zn**
Clayey	7.1	0.31	0.64	1.46	372	17.45	297	9.2	1.20

Table IV: Rating Chart for Soil pH

Soil pH	Rating
Less than 6	Acidic
7.0 - 8.5	Normal (all essential nutrients available)
8.6 – 9.0	Tendency to become alkaline
Above 9.0	Alkali

Table V: Soluble Salt Levels Measured by EC for Crops

S. N.	E.C. (dS/m)	Suitability to Crops
1.	0 – 0.25	Very low – indicates probable deficiency
2.	0.25 – 0.75	Suitable for seedlings and salt sensitive plants
3.	0.75 – 1.25	Desirable level for most plants
4.	1.25 – 2.25	Reduced growth, leaf margins burn

Source: Douglas Cox (2014) how to use pH and EC "Pens" to monitor Greenhouse Crop Nutrition. University of Massachusetts, Amherst (online site by Center for Agriculture)

Table VI: General Relationship of Soil Bulk Density to Root Growth Based on Soil Texture

Soil Texture	Ideal Bulk Density (g/cm3) for Plant Growth	Bulk Density (g/cm3) that Restrict Root Growth
Sandy	<1.60	>1.80
Silty	<1.40	>1.65
Clayey	<1.10	>1.47

Source: Arshad M.A., Lowery B., and Grossman B. 1996. Physical Tests for Monitoring Soil Quality. In: Doran J.W.,Jones A.J., editors. Methods for Assessing Soil Quality. Madison, WI., 123-41.

Table VII: Soil Fertility Classification Followed in Maharashtra and Some Other States

Soil Fertility Level	Organic Carbon (%)	Available N (kg/ha)	Available P2O5 (kg/ha)	Available K2O (kg/ha)
Very High	>1.00	>700	>80.0	>360
High	0.81-1.00	561-700	64-80	301-360
Medium	0.61-0.80	421-560	48-64	241-300
Medium Low	0.41-0.60	281-420	32-48	181-240
Low	0.21-0.40	141-280	16-32	121-180
Very Low	<0.20	<140	<16.0	<120

Source: Tandon HLS (2005)

Table VIII: Qualitative Ratings of Soil Nutrients

Organic Carbon	Total N	Avail P	Available K
Medium	Medium Low	Low	Medium

Table IX: Effect of Different Treatments on Soil Properties

Treatment	Soil pH	E.C. (dS/m)	Organic Carbon (%)	Bulk Density (g/cc)	Available Plant Nutrients (kg/ha)				
					N	P	K	S	Zn
Initial Status before sowing	7.1	0.31	0.64	1.46	372	17.45	297	9.2	1.20
After harvest of crop									
T1-150	7.1	0.32	0.65	1.44	374	17.50	298	9.4	1.33
T2-300	7.2	0.33	0.66	1.43	375	17.70	297	9.4	1.35
T3-450	7.2	0.32	0.67	1.43	374	17.80	304	9.4	1.45
T4-600	7.1	0.31	0.69	1.43	375	17.90	306	9.5	1.43
T5-750	7.1	0.31	0.69	1.42	375	17.90	302	9.5	1.44
T6-900	7.2	0.32	0.69	1.41	376	18.30	303	9.5	1.45
T7-RDF	7.1	0.33	0.64	1.50	374	17.90	298	9.3	1.46
T8-VC	7.1	0.32	0.73	1.37	380	17.90	302	9.3	1.46
SEm ±	0.04	0.005	0.005	0.01	32.9	0.31	2.99	0.13	0.09
CD (at 5%)	NS	0.01	0.01	0.03	98.7	0.93	8.97	0.39	0.27
Coefficient of Determination (R^2)	0.01	0.25	0.88	0.86	0.02	0.88	0.41	0.77	0.71
Correlation Coefficient (R)	0.1	0.5	0.94	- 0.93	0.15	0.94	0.64	0.88	0.84

(NS: not significant; SEm: Standard Error around mean; CD: Critical Difference)

Table X A - B - C: Percentage Increase / Decrease in the Growth and Yield of Wheat in Biosil+RDF Treatments over RDF and VC Control A

Treat-ment	Percentage Increase / Decrease in EC			Percentage Increase / Decrease in Organic Carbon			Percentage Increase / Decrease in Bulk Density		
	Over initial Value	Over T7-RDF	Over T8-VC	Over initial Value	Over T7-RDF	Over T8-VC	Over initial Value	Over T7-RDF	Over T8-VC
T7-RDF	6.45	--	3.13	0.0	--	-12.33	2.74	--	9.49
T8-VC	3.23	-3.03	--	14.06	14.06	--	-6.16	8.67	--
T1-150	3.23	-3.03	0.0	1.56	1.56	-10.9	-1.37	-4.0	5.11
T2-300	6.45	0.0	3.13	3.13	3.13	-9.59	-2.06	-4.67	4.38
T3-450	3.23	-3.03	0.0	4.69	4.69	-8.22	-2.06	-4.67	4.38
T4-600	0.0	-6.06	-3.13	7.81	7.81	-5.48	-2.06	-4.67	4.38
T5-750	0.0	-6.06	-3.13	7.81	7.81	-5.48	-2.74	-5.33	3.65
T6-900	3.23	-3.03	0.0	7.81	7.81	-5.48	-3.43	-6.0	2.92

B

Treat-ment	Percentage Increase / Decrease in Nitrogen			Percentage Increase / Decrease in Phosphorus			Percentage Increase / Decrease in Potassium		
	Over initial Value	Over T7-RDF	Over T8-VC	Over initial Value	Over T7-RDF	Over T8-VC	Over initial Value	Over T7-RDF	Over T8-VC
T7-RDF	0.54	--	-1.58	2.58	--	0.0	0.34	--	-1.33
T8-VC	2.15	1.60	--	2.58	0.0	--	1.68	1.34	--
T1-150	0.54	0.0	-1.58	0.29	-2.24	-2.24	0.34	0.0	-1.33
T2-300	0.81	0.27	-1.32	1.01	-1.12	-1.12	0.0	-0.34	-1.66
T3-450	0.54	0.0	-1.58	1.02	-0.56	-0.58	2.36	2.01	0.66
T4-600	0.81	0.27	-1.32	2.58	0.0	0.0	3.03	2.69	1.33
T5-750	0.81	0.27	-1.32	2.58	0.0	0.0	1.68	1.34	0.0
T6-900	1.08	0.54	-1.05	4.87	1.02	1.02	2.02	1.68	0.33

C

Treatment	Percentage Increase / Decrease in Sulphur			Percentage Increase / Decrease in Zinc		
	Over initial Value	Over T7-RDF	Over T8-VC	Over Initial Value	Over T7-RDF	Over T8-VC
T7-RDF	1.09	--	0.0	21.67	--	0.0
T8-VC	1.09	0.0	--	21.67	0.0	--
T1-150	2.17	1.08	1.08	10.83	-8.90	-8.90
T2-300	2.17	1.08	1.08	12.5	-7.53	-7.63
T3-450	2.17	1.08	1.08	20.83	-0.69	-0.69
T4-600	3.26	2.15	2.15	19.17	-2.06	-2.06
T5-750	3.26	2.15	2.15	20.00	-1.37	-1.37
T6-900	3.26	2.15	2.15	20.83	-0.69	-0.69

Table XI: Optimum Dose of Biosil + RDF and Comparison of the Results of Treatments of Biosil+RDF, Vermicompost (VC) and Recommended Dose of Fertilizer (RDF) on Soil Fertility

Parameter of Plant Growth / Yield	Optimum Dose of Borosil with RDF (kg/ha)	Trend of Positive Impact	Remark
EC	T2-300	(Biosil+RDF)>RDF>VC	Improvement in all three treatments
Organic Carbon	T4-600	VC>(Biosil+RDF)>RDF	VC is most effective, followed by (Biosil+RDF) and RDF
Bulk Density	T6-900	VC>(Biosil+RDF)	VC and (Biosil+RDF) only effective
Nitrogen	T6-900	VC>(Biosil+RDF)>RDF	VC treatment superior to all
Phosphorus	T6-900	(Biosil+RDF)>RDF=VC	(Biosil+RDF) highly effective
Potassium	T4-600	(Biosil+RDF)>VC>RDF	VC superior to T2-300
Sulphur	T4-600	(Biosil+RDF)>VC=RDF	All are more or less equally effective
Zinc	T4-600	VC=RDF>(Biosil+RDF)	All are more or less equally effective.

*“ =” more or less as effective as

Table XII: Effect of Different Treatments on Plant Growth and Yield Parameters of Wheat

Treat-ments	Plant Growth Parameters					Crop Yield Parameters			Straw Yield (q/ha)
	Plant Popul-ation (m-2)	Plant Height (cm)	Number of Leaves per Plant	Number of Effective Tillers per m-2	Length of earhead (cm)	Number of Grains/ Earhead	Test Wei-ght (g)	Grain Yield (q/ha)	
T1-150	200.25	86.2	22.80	221.5	9.4	53.9	42.1	47.7	70.4
T2-300	200.38	87.4	22.85	243.8	9.5	55.7	42.4	50.5	73.8
T3-450	200.36	88.0	25.60	245.0	9.6	57.9	42.6	53.8	78.5
T4-600	200.34	89.2	28.55	249.7	9.7	59.8	42.9	57.8	86.8
T5-750	200.40	89.5	30.88	256.8	9.7	61.1	44.4	58.6	88.5
T6-900	200.30	89.8	32.65	299.4	9.8	63.4	46.5	59.4	89.6
T7-RDF	200.32	85.4	20.26	198.9	9.1	50.0	41.8	45.5	74.4
T8-VC	200.35	88.2	26.65	244.4	9.5	58.9	44.3	56.5	85.5
SEm ±	0.33	1.15	2.08	15.41	0.11	0.66	0.61	1.89	3.91
CD at 5%	NS	3.45	6.24	46.23	0.33	1.98	1.83	5.67	9.30
CD (R^2)	--	0.94	1.0	0.81	0.96	1.0	0.81	0.94	0.94
CC (R)	--	0.97	1.0	0.9	0.98	1.0	0.9	0.97	0.97

(NS: not significant; SEm: Standard Error around mean; CD: Critical Difference); CD: Coefficient of Determination; CC: Correlation Coefficient

Table XIII(A) - (B): Percentage Increase / Decrease in the Growth and Yield of Wheat in Biosil+RDF Treatments over Recommended Dose of Fertilizers (RDF) and Vermicompost (VC) Controls

(A)

Treatment	Percentage Increase / Decrease in Plant Population m-2		Percentage Increase / Decrease in Plant Height (cm)		Percentage Increase / Decrease in No. of leaves/ plant		Percentage Increase / Decrease in No. of Effective Tillers/ m-2	
	Over T7-RDF	Over T8-VC	Over T7-RDF	Over T8-VC	Over T7-RDF	Over T8-VC	Over T7-RDF	Over T8-VC
T1-150	-0.035	-0.05	0.94	-2.27	12.54	-14.45	11.36	-9.37
T2-300	0.030	0.015	2.34	-0.91	12.78	-14.26	22.57	-0.25
T3-450	0.020	0.005	3.05	-0.23	26.36	-3.94	23.18	0.25
T4-600	0.01	-0.005	4.45	1.13	40.92	7.13	25.54	2.17
T5-750	0.0004	0.025	4.80	1.47	52.42	15.87	29.11	5.07
T6-900	-0.01	-0.025	5.15	1.81	61.16	22.51	50.53	22.50
T7-RDF	--	-0.015	--	-3.18	--	-23.98	--	-18.62
T8-VC	0.015	--	3.28	--	31.54	--	22.88	--

(B)

Treatment	Percentage Increase / Decrease in Length of Earhead (cm)		Percentage Increase / Decrease in No. of Grains/ Earhead		Percentage Increase / Decrease in Test Weight (gm)		Percentage Increase / Decrease in Grain Yield (q/ha)		Percentage Increase / Decrease in Straw Yield (q/ha)	
	Over T7-RDF	Over T8-VC	Over T7-RDF	Over T8-VC	Over T7-RDF	Over T8-VC	Over T7-RDF	Over T8-VC	Over T7-RDF	Over T8-VC
T1-150	3.30	-1.05	7.8	-8.49	0.72	-4.97	4.84	-15.58	-5.38	-17.66
T2-300	4.40	0.0	11.4	-5.43	1.44	-4.29	10.99	-10.62	-0.81	-13.68
T3-450	5.50	1.05	15.8	-1.70	1.91	-3.84	18.24	-4.78	5.51	-8.19
T4-600	6.59	2.11	19.6	1.53	2.63	-3.16	27.03	2.3	16.67	1.52
T5-750	6.59	2.11	22.2	3.74	6.22	0.23	28.79	3.72	18.95	3.51
T6-900	7.69	3.16	26.8	7.64	11.24	4.97	30.55	5.13	20.43	4.80
T7-RDF	--	-4.21	--	-15.11	--	-5.64	--	19.47	--	-12.98
T8-VC	4.40	--	17.8	--	5.98	--	24.18	--	14.92	--

Table XIV: Optimum Dose of Biosil + RDF and Comparison of the Results of Treatments of Biosil+RDF, Vermicompost (VC) and Recommended Dose of Fertilizers (RDF)

Parameters of Plant Growth and Yield	Optimum Dose of Borosil with RDF (kg/ha)	Trend of Positive Impact	Remark
Plant Population	T1-150	(Biosil+RDF)=VC=RDF	No significant impact
Plant Height	T6-900	(Biosil+RDF)>VC>RDF	VC superior than T2-300
Number of Leaves/plant	T6-900	(Biosil+RDF)>VC>RDF	VC superior than T3-450
Number of Effective Tillers/m2	T6-900	(Biosil+RDF)>VC>RDF	VC superior than T2-300
Length of Earhead	T6-900	(Biosil+RDF)>VC>RDF	VC superior than T1-150
Number of Grains per Earhead	T6-900	(Biosil+RDF)>VC>RDF	VC superior than T3-450
Test Weight	T6-900	(Biosil+RDF)>VC>RDF	VC superior than T4-600
Grain Yield	T6-900	(Biosil+RDF)>VC>RDF	VC superior than T3-450
Straw Yield	T6-900	(Biosil+RDF)>VC>RDF	VC superior than T3-450

*“ =” more or less as effective as

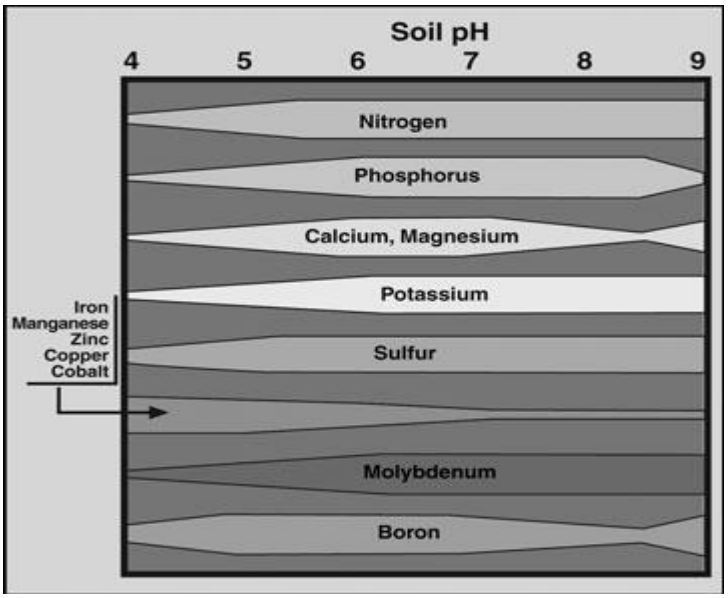

(The width of the band indicates the relative availability of each plant nutrient at various pH levels)

Figure 1: Soil pH Ranges and Nutrient Availability to Plants.

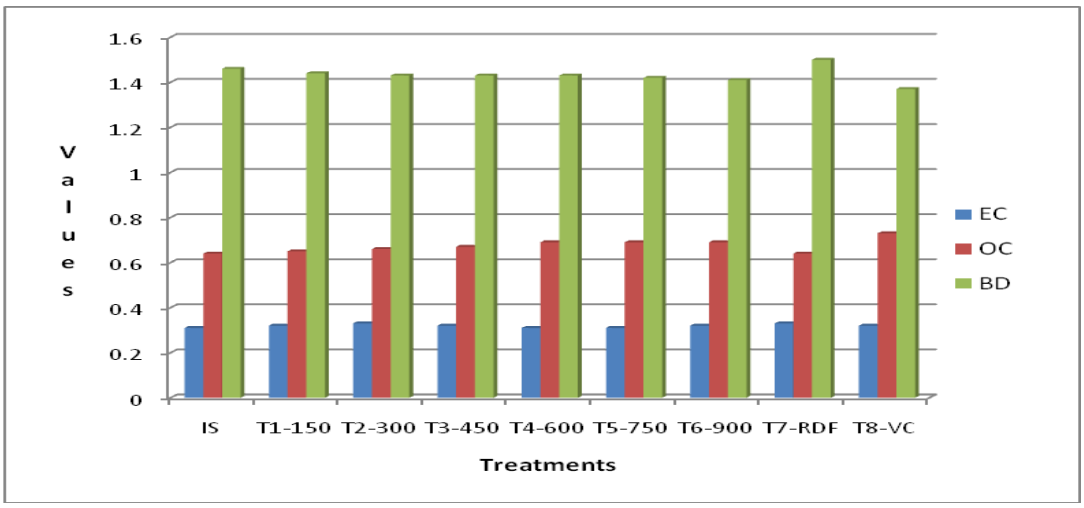

(Electrical Conductivity, EC; Organic Content, OC; Bulk Density, BD)

Figure 2: Effect of Different Treatments on Soil Characteristics

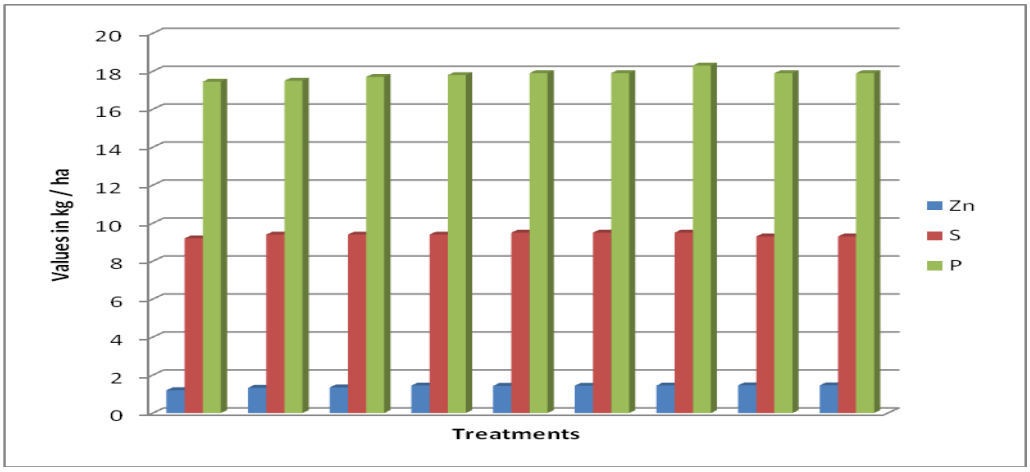

(Zinc, Zn; Suphur, S; Phosphorus, P)
Figure 3: Effect of Different Treatments on Soil Characteristics

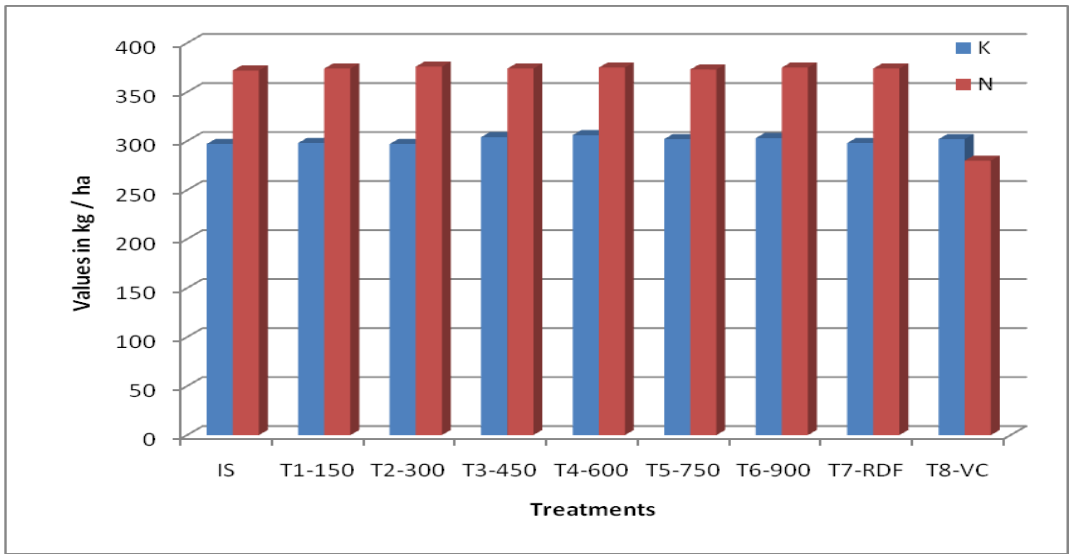

Figure 4: Effect of Different Treatments on Soil Characteristics (Potassium, K; Nitrogen, N)

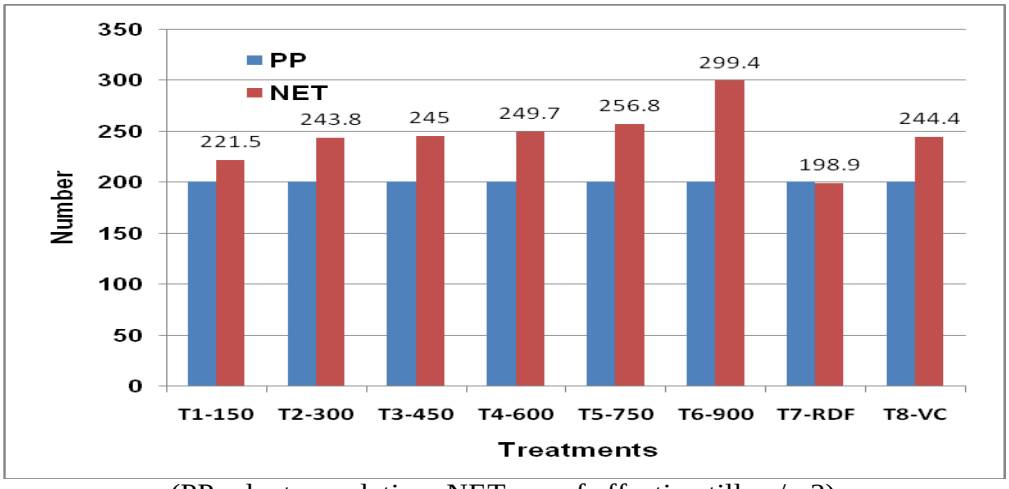

(PP: plant population; NET: no of effective tillers/m2)
Figure 5: Effect of Different Treatments on Plant Growth Characteristics

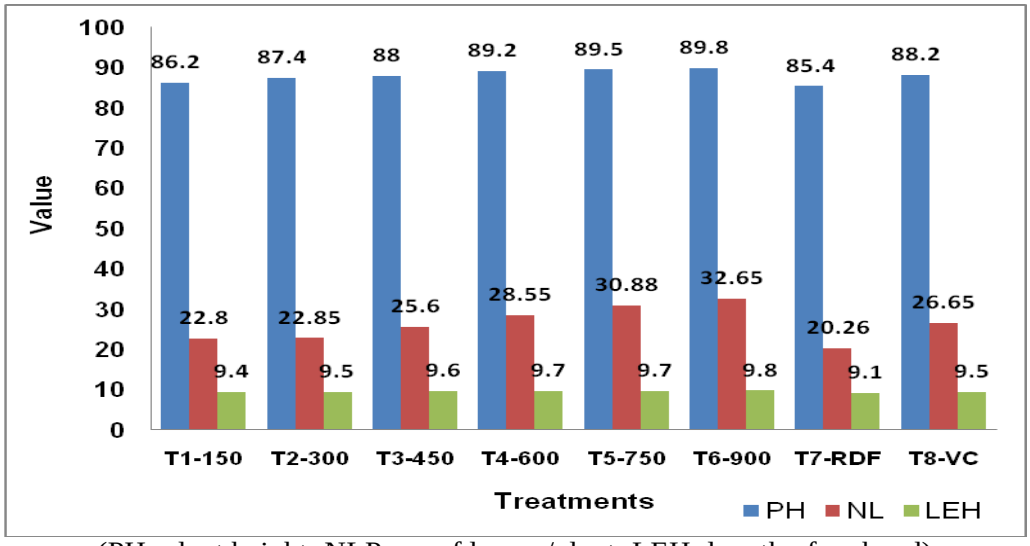

(PH: plant height; NLP: no of leaves/plant; LEH: length of earhead)
Figure 6: Effect of Different Treatments on Plant Growth Characteristics

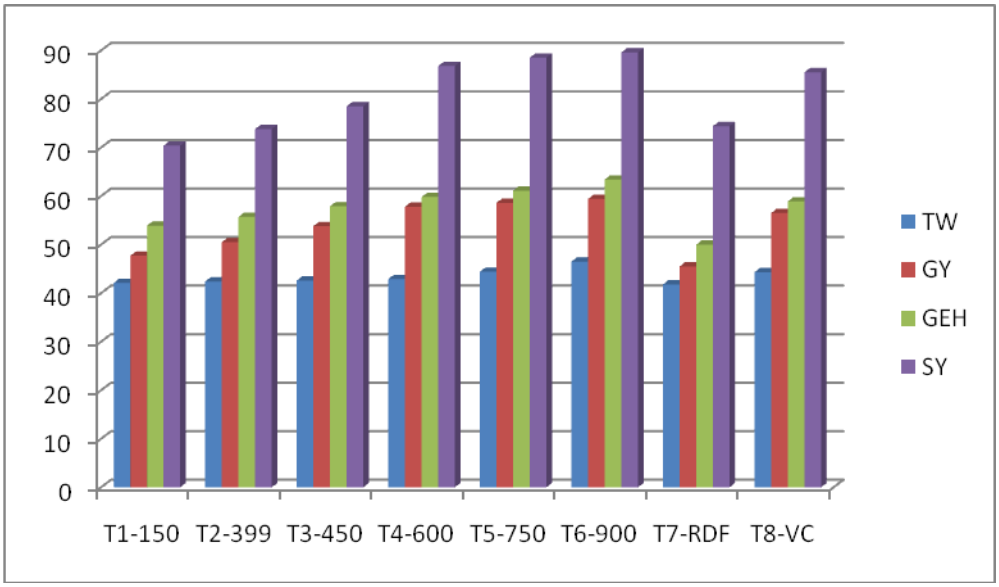

(TW: Test Weight; GY: Grain Yield; GEH: Number of Grains/Earhead; SY: Straw Yield)
Figure 7: Effect of Different Treatments on Plant Growth Characteristics

American Journal of Engineering Research (AJER)
e-ISSN : 2320-0847 p-ISSN : 2320-0936
Volume-03, Issue-01, pp-200-206
www.ajer.org

Research Paper Open Access

Investigation of an Optimum Method of Biodegradation Process for Jute Polymer Composites

Kh. Mumtahenah Siddiquee[1], Dr. Md. Maksud Helali[2], Dr. Md. Abdul Gafur[3], Soma Chakraborty[4]

[1]*Assistant Director (programme),"Fortification of Edible Oil in Bangladesh"-project, Ministry of Industries, Bangladesh.*
[2]*Professor, Department of Mechanical Engineering, Bangladesh University of Engineering and Technology, Bangladesh.*
[3]*Senior Scientific Officer, Bangladesh Council of Scientific and Industrial Research, Bangladesh.*
[4]*Assistant Professor, Department of Mechanical Engineering, Dhaka University of Engineering and Technology, Bangladesh.*

Abstract: - Natural fiber reinforced polymer composites are currently being developed as an alternative for plastic material because of having some environmental benefits such as biodegradability, reduced dependence on non-renewable material, greenhouse gas emissions and enhanced energy recovery. This study focuses on the fabrication of jute polymer composites, biodegradation and the investigation of an optimum method of biodegradation. Polyethylene and Polypropylene were reinforced with 5%, 10% and 15% of fiber. Jute fiber of 1mm and 3mm fiber length were used to fabricate composites using compression molding. Degradation behavior of composites was studied in terms of percentage weight loss. Samples are kept in compost heap and in soil burial to observe the degradation of the specimens. In weather degradation the effect of natural phenomena were observed. The biodegradability of composites was enhanced in compost condition with respect to soil burial and weather degradation. Degradation rate were higher in compost condition considering natural weather and soil and higher fiber reinforced ratio shows higher degradation.

Keywords: - *Jute, Polymer, Composites, Biodegradation*

I. INTRODUCTION

Polymeric materials have gained a wide influence due to their structural versatility, excellent mechanical and thermal properties and high stability [1].

But the non-biodegradability of most commercially available plastic has caused many environmental problems associated with their waste pollution and disposal. These plastics are characteristically inert and resistant to microbial attack and therefore they remain in the nature without any degradation for every long time [2]. However their increasing accumulation in the environment has been a threat to the planet.

Since the end of the nineties, biodegradable polymers have begun to attract interest because of their potential to substitute traditional, non-biodegradable polymers [3]. Biopolymers offer environmental benefits such as biodegradability, greenhouse gas emissions and renewability of the base material [4]. The majority of biodegradable polymers are not widely used because they are too expensive and the range of the material selection suitable for various end-use products is limited [5].

For the purposes of this research, the term “composites” are materials that are comprised of strong load-carrying materials (known as reinforcement) imbedded in a weaker material (known as matrix). Reinforcement provides strength and rigidity, helping to support structural load. The matrix, or binder, maintains the position and orientation of the reinforcement and balance loads between the reinforcements. In this form, both fibers and matrix retain their physical and chemical identities, yet they produce a combination of that cannot be achieved with either of the constituents acting alone.

With the increasing environmental concerns, there has been a significant research interest in the area of natural fiber-based composites [6]. The use of natural fibers as reinforcing material in polymer matrix composites provides positive environmental benefits with respect to ultimate disposability [7]. Degradation tendency in these fiber reinforced composites is also a deciding factor in the use of these materials for various high performance applications and their ultimate disposal at the end of their life cycle [6].

Bangladesh is an agricultural based country and every year it produces a large amount of jute. Based on this, jute fibers have been used as a reinforcing material for composite fabrication in this work.

The improper disposal and treatment of solid waste is one of the gravest environmental problems faced by most of the countries. With the increasing globalization and modernization, generation of waste for disposal is likely to increase still further. Importantly, in many parts of the world proper waste disposal facilities do not exist and the wastes are simply discarded in the surrounding areas [8]. Ultimately, we have to depend on the nature for biodegradation of the materials.

Biodegradation of a polymeric material is chemical degradation brought by the action of naturally occurring microorganisms such as bacteria and fungi via enzymatic action into metabolic products of microorganisms [9]. Biodegradation of the jute polymer composites will encourage increased use in composites and hence capture ever growing market share, boost the agricultural based economy and help the world to make it more environmental friendly.

Yuksel Orhan et al [10] worked on biodegradation of plastic compost bags under controlled soil conditions. Degradation of plastics was determined by the weight loss of sample, tensile strength, carbon dioxide production, chemical changes measured in infrared spectrum and bacterial activity in soil.

Hee-Soo Kim et al [5] carried out experiments on the biodegradability of bio-flour filled biodegradable poly (butylene succinate) (PBS) bio-composites in natural and compost soil. The percentage weight loss and the reduction in mechanical properties of PBS and the bio-composites in the compost soil burial test were significantly greater than those in the natural soil burial test. The biodegradability was enhanced with increasing bio-flour content.

Sanjay K. Nayak [6] studied the degradation and flammability behavior of pp/banana and glass fiber-based composites. Further, BFPP composites exhibited higher degradation tendency as compared with the virgin polymer as well as the hybrid composites. Extent of biodegradation in the irradiated samples showed increased weight loss in the BFPP samples thus revealing effective interfacial adhesion upon hybridization with glass fibers.

J. Chlopec et al [11] studied on the influence of the environment on the degradation of polylactides and their composites. The degradation speed is dependent among others on the viscosity of the applied fluids and thus, their ability of penetration in the polymer's structure and on the interfacial boundaries.

R. Kumar et al [8] carried out experiment on biodegradation of flax fiber reinforced poly lactic acid. Different amphiphilic additives can be added for delayed or accelerated biodegradability.

Prafulla K. Sahoo et al [12] investigated from the experiment on preparation, characterization, and biodegradability of jute-based natural fiber composites super absorbents that the water absorption of the grafted composites with SS was more than 35 times greater than that of the un grafted fiber. The biodegradability of the grafted crosslinked composite with sodium silicate (SS) was lower than the other samples due to dispersed silicate layers in the composite matrix.

II. MATERIALS AND METHODS

The middle parts of jute fibers were taken in this study and to prepare short fibers, the jute fibers were chopped into the lengths of approximately 1 mm and 3 mm. A commercial grade polypropylene (PP) and polyethylene (PE) was used in this study. Melting point of this polypropylene and polyethylene were measured and found to be 170°C and 125°C. In the literature it is mentioned that the melting point of commercial grade polypropylene lies in the range of 160°-170°C and polyethylene lies in the range of 115°-130°C.

2.1Composite fabrication

For the fabrication of the composites polypropylene/Polyethylene matrix and jute fibers were taken in different weight fractions for reinforcing fiber length of 1mm and 3mm (Table 2.1).

2.2 Preparation of composites by *compression* moulding

After loading the mould in the hot press machine (50±5%) KN pressure is applied to get the desired shape and possible homogeneity. *T*he temperature set points were (125°±10^0) C for PE and (170°±10^0) C for PP. About 30 to 40 min is required to reach the desired set points. When the temperature was raised at set points it was kept at those temperatures for 10 min to melt properly. After completion of heating when the pressure down to zero then pressure of (50±5%) KN was applied again to avoid the void and to have a desired thickness.
The composites get from the compression moulding, sized: 126mmx126mmx3mm. (Figure 2.1).

2.3 Biodegradation

Biodegradation is the chemical dissolution or breakdown of materials. It occurs with enzymatic action and involves living organisms (micro/macro). Molecular degradation is promoted by enzymes and can occur under aerobic and anaerobic conditions, leading to complete or partial removal from the environment. Linear polymers are generally more biodegradable than branched polymers. The biodegradability of jute polymer composite has been examined in various environments such as in the soil, compost and weather.

2.3.1 Degradation by Compost

Biodegradability of the samples was studied by weight loss over time in a compost condition. Compost degradation is carried out by following the ASTM D5338. The biodegradation of the specimen was checked after 15 days, 30 days and for 45 days on the compost heap. Samples are placed in 250ml Pyrex bottle containing compost. These bottles were placed in a temperature controlled water bath. To ensure homogeneity of temperature a stirrer was placed in that water bath to create water circulation. For the survival of microorganisms of the compost O_2, temperature and water are required. Water was poured in the bottles in every two days. Water bath provided the temperature. Air compressor was placed to ensure proper O_2 supply in the compost. First day the temperature of the water bath was $(35^0 \pm 5^0)$ C. After that the temperature was maintained at $(58^0 \pm 5^0)$ C for next 4 days. Consecutive 28 days water bath was set to $(50^0 \pm 5^0)$ C and rest days water bath was set to $(35^0 \pm 5^0)$ C. The samples were dug out at 15,30,45 days intervals throughout the time, washed with water, dried in a vacuum oven at 50±1ºC for 24 h before evaluation. The samples were then weighed to determine the weight loss.

2.3.2 Soil Burial Degradation

Soil burial is a traditional and standard method for degradation because of its similarity to actual conditions of waste disposal. Biodegradability of the samples was studied by weight loss over time in a soil environment. Samples were weighed (3.28gm) and then buried in the soil for up to 80 days. The soil was maintained at approximately 20% moisture by injecting water to keep the microorganisms active and samples were buried at a depth of 5 cm. The buried samples were dug out at 30, 60, 80 days intervals throughout the time, washed with water, dried in a vacuum oven at 50±1ºC for 24 h before evaluation. The samples were then weighed to determine the weight loss.

2.3.3 Degradation by weather

Weather testing of composites is the controlled polymer degradation and polymer coating degradation under lab or natural conditions. Just like erosion of rocks, natural phenomena can cause degradation in polymer systems. Both thermoplastics and natural fibers are susceptible to environmental stresses, including temperature, moisture, light [ultraviolet (UV) radiation], and chemical agents such as organic solvents, ozone, acids, and bases, though most polymers are primarily degraded by oxidative reactions. Outdoor weathering is a common case of oxidation enhanced by photochemical reaction, which is referred to as photo degradation. Photo degradation of some thermoplastics can result in changes to polymer morphology because of chemical cross linking or chain scission. Samples were weighed (3.23) and then buried in the natural weather for up to 80 days. The samples were weighed after 30, 60, 80 days to determine the weight loss.

2.4 Percentage Weight loss In Specimen after degradation

The time variation of percentage weight gain (wt) can be measured as:

$$wt = \frac{Wo - W(t)}{W} \; x\, 100$$

Here W(t) is the total weight after time t, W_o is the reference dry weight of the specimen before biodegradation.

III. RESULT AND DISCUSSION

3.1 Percentage weight loss of jute fiber reinforced polypropylene and polyethylene composites (as a function of fiber length and weight fraction) after biodegradation.

Figure 3.1(a) and (b) shows the variation of the percentage weight loss as a function of time for jute fiber reinforced polyethylene and polypropylene composites. The minimum value of % weight loss in weather condition is 0.65, for 5%, 1mm fiber reinforced PP composites after 30 days and the maximum value of % weight loss is 3.67, gain from 15%, 3mm fiber reinforced PE composites after 80 days.

Figure 3.2(a) and (b) shows the variation of the percentage weight loss as a function of time for jute fiber reinforced polyethylene and polypropylene composites. The minimum value of % weight loss in soil burial

condition is 0.62, for 5%, 1mm fiber reinforced PP composites after 30 days and the maximum value of % weight loss is 2.21, gain from 15%, 3mm fiber reinforced PE composites after 80 days.

Figure 3.3(a) and (b) shows the variation of the percentage weight loss as a function of time for jute fiber reinforced polyethylene and polypropylene composites. The minimum value of % weight loss in compost condition is 0.89, for 5%, 1mm fiber reinforced PP composites after 15 days and the maximum value of % weight loss is 6.92, gain from 15%, 3mm fiber reinforced PE composites after 45 days.

Figure 3.4(a) and (b) shows the variation of the percentage weight loss as a function of biodegradation process for jute fiber reinforced polyethylene and polypropylene composites. The maximum degradation rate is 6.92 for compost degradation, 3.67 for weather degradation and 2.21 for soil burial degradation. In case of weight loss, degradation rate is maximum for compost condition. So compost condition enhances the biodegradation rate.

3.2 Optimum method of biodegradation process

- In this research work the degradation rate was observed in weather, compost and soil burial degradation methods in terms of % weight loss.
- Based on above figures degradation rate follows the sequence of:

Compost>Weather > Soil burial

- Compost show better degradation rate because of following reasons
  - Microorganism accelerates the degradation process.
  - Controlled environment.
  - Temperature

IV. CONCLUSIONS

This study has covered the major concerns about the polymers, natural fiber reinforced polymer composites and biodegradability. In this work biodegradability of jute reinforced polymer composites were studied over time in compost, soil burial and weather condition. Degradation rate was designated in terms of weight loss. In the time scale of this study compost showed highest degradation rate and soil was the lowest. The biodegradability in compost condition was almost 60 percent higher considering soil which concludes compost condition as optimum degradation method. In compost condition rate of degradation was accelerated by factors like temperature, water and air. Pure polymers didn't lose their weight due to non biodegradable characteristics. Microorganisms mostly consume the fiber parts. Composites reinforced with larger fiber length showed higher degradation rate. Higher fiber loading gives microorganism's larger surfaces to consume and results higher degradation rate. Over time larger surfaces became smaller and became easier target for microorganisms. This explains reason of higher degradation rate in longer incubation time. Polyethylene showed slightly higher degradation rate concerning polypropylene but not significant.

This study concludes that the opportunities for Bangladesh grown jute fiber reinforced composites is enormous. The method and the rate of biodegradation will encourage increased use in composites and help the world to make it more environmental friendly.

REFERENCES

[1] S Krishna Mohan, Tanu Srivastava, 'Microbial degradation and degradation of polymeric materials'; J Biochem Tech, 2(4), 2010, 210-215.

[2] Dr. Muller. Rolf-Joachim; 'Biodegradability of Polymers: Regulations and Methods for Testing'; Gesellschaft f, r Biotechnologische Forschung mbH, Braunschweig, Germany.

[3] Re Giada Lo, Scaffaro Roberto, Morreale Marco, Manita Francesco Paolo La; 'Mechanical Properties and Biodegradability of Mater-BI®/Wood Flour Ecocomposites'; University of Palermo, Palermo, Italy.

[4] Tao YU, Yan LI, Jie REN; 'Preparation and Properties of Short Natural Fiber Reinforced Poly (lactic acid) Composites'; Trans. Nonferrous Met. Soc. China 19(2009) s651-s655.

[5] Kim Hee-Soo, Kim Hyun-Joong, Lee Jae-Won , Choi In-Gyu; 'Biodegradability of Bio-Flour filled Biodegradable Poly (butylene succinate) Bio-Composites in Natural and Compost Soil'; Polymer Degradation and Stability 91 (2006) 1117e1127.

[6] Nayak Sanjay K.; 'Degradation and Flammability Behavior of PP/ Banana and Glass Fiber-based Hybrid Composites'; Int J Plast Technol 13(1):47–67.

[7] Rashed H.M.M.A., Islam M. A. and Rizvi F. B.; 'Effect of Process Parameters on Tensile Strength of Jute Reinforced Thermoplastic Composites'; Journal of Naval Architecture and Marine Engineering, 2006.

[8] Kumar R., Yakubu M. K., Anandjiwala R. D.; 'Biodegradation of Flax Fiber Reinforced Poly Lactic Acid'; eXPRESS Polymer Letters Vol.4, No.7 (2010) 423–430.

[9] Tokiwa Yutaka, Calabia Buenaventurada P., Ugwu Charles U. and Aiba Seiichi; 'Biodegradability of Plastics'; Int. J. Mol. Sci. 2009, 10, 3722-3742; doi: 10.3390/ijms10093722.
[10] Orhan Yüksel, Hrenović Jasna, and Büyükgüngör Hanife; 'Biodegradation of Plastic Compost Bags Under Controlled Soil Conditions'; Acta Chim. Slov. 2004, 51, 579−588.
[11] Chłopek J., Morawska-Chochół A., Szaraniec B.; 'The Influence of the Environment on the Degradation of Polylactides and their Composites'; JAMME, vol 43, issue 1, november 2010.
[12] Sahoo Prafulla K, Sahu Gobinda C., Rana Pradeep K., Das Aswini K; 'Preparation, Characterization, and Biodegradability of Jute-Based Natural Fiber Composite Superabsorbents'; Utkal University (Department of Chemistry), Vani Vihar, Bhubaneswar, India.

Table 2.1: Relative Amounts of Reinforcing Materials and Polymer Matrix by Weight Fraction.

Reinforcing fiber (Jute) weight fraction (%)	**Polymer matrix (Polypropylene/Polyethylene) weight fraction (%)**	**Composites (Jute : PP/PE)**
None	100	100
05	95	05: 95
10	90	10: 90
15	85	15 : 85

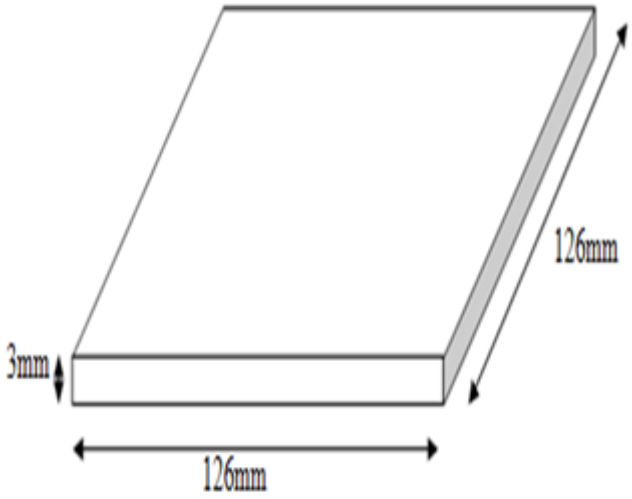

Figure 2.1: Composite after demoulding

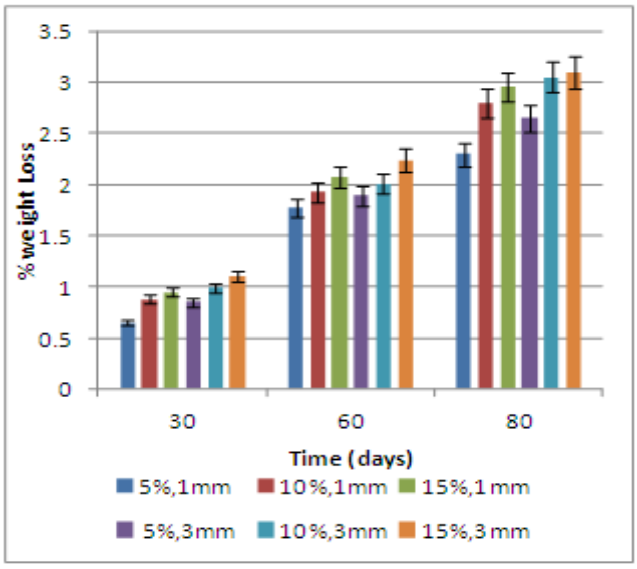

(a)

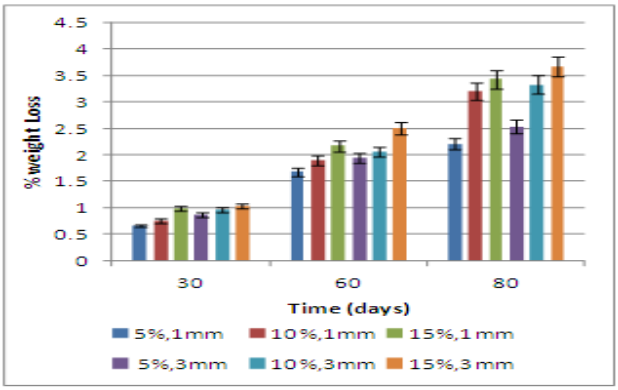

(b)

Figure 3.1: Effect of weather degradation on % weight loss of jute reinforced PP(a) & PE(b) composites

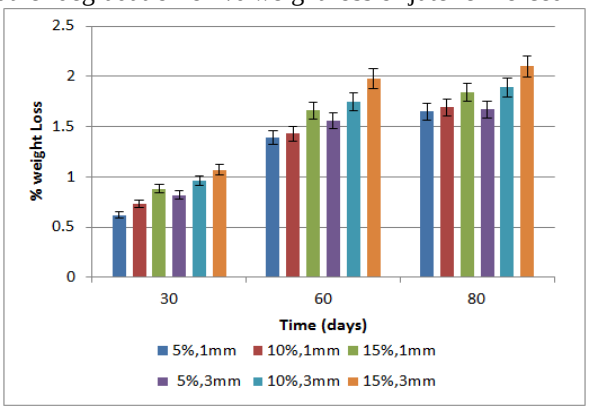

(a)

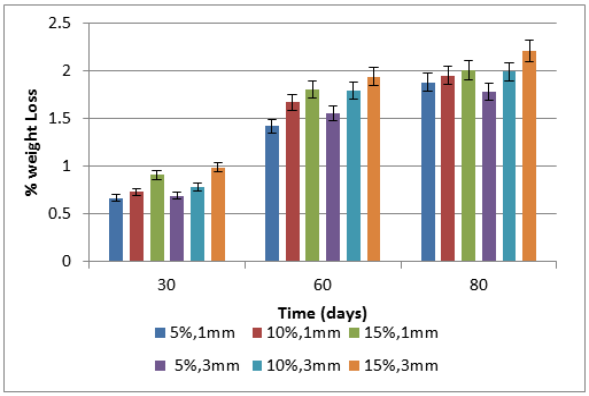

(b)

Figure 3.2: Effect of soil degradation on % weight loss of jute reinforced PP(a) & PE(b) composites

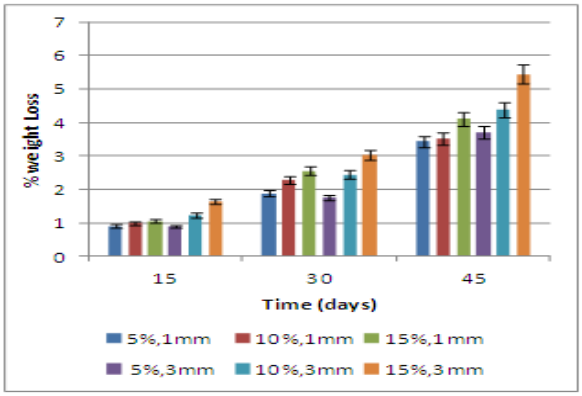

(a)

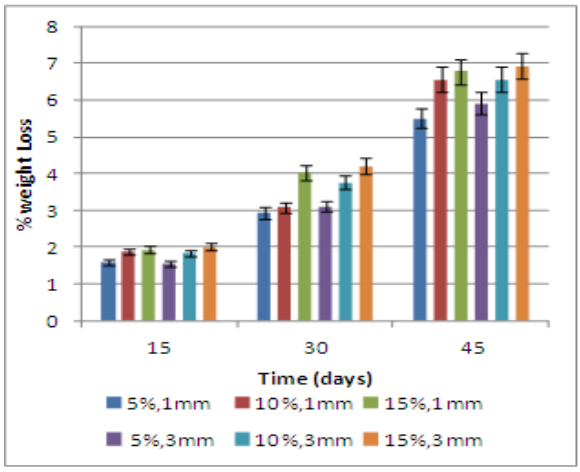

(b)

Figure 3.3: Effect of compost degradation on % weight loss of jute reinforced PP(a) & PE(b) composites

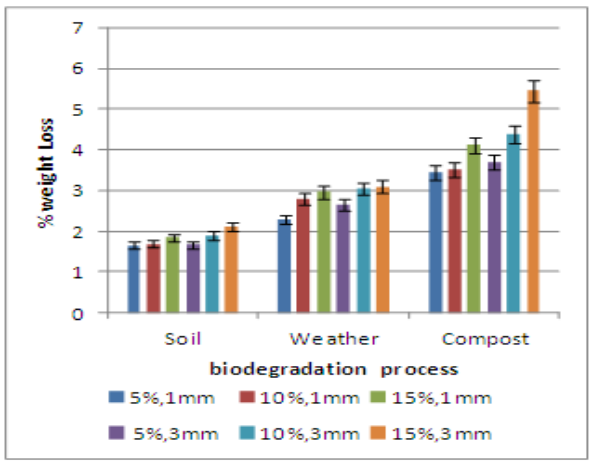

(a)

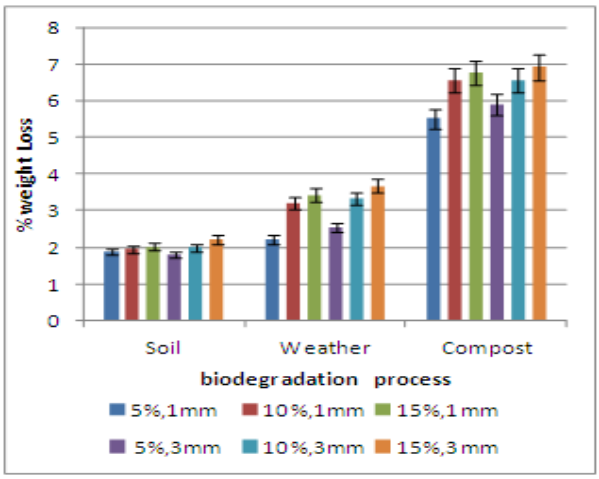

(b)

Figure 3.4: Effect of natural resources (soil, weather & compost) on the biodegradation rate of jute reinforced PP(a) & PE(b) composites in terms of % weight loss

American Journal of Engineering Research (AJER)
e-ISSN : 2320-0847 p-ISSN : 2320-0936
Volume-03, Issue-01, pp-207-221
www.ajer.org

Research Paper Open Access

3D Wavelet Sub-Bands Mixing for Image De-noising and Segmentation of Brain Images

Joyjit Patra[1], Himadri Nath Moulick[2],Shreyosree Mallick[3], Arun Kanti Manna[4]
[1](C.S.E, Aryabhatta Institute Of Engineering And Management,Durgapur,West Bengal,India)
[2](C.S.E, Aryabhatta Institute Of Engineering And Management,Durgapur,West Bengal,India)
[3](B.ech 4th year Student,CSE Dept,Aryabhatta Institute of Engineering and Mangement,Durgapur,W.B,India)
[4](Persuing Ph.D. from Techno India University,W.B.India)

Abstract: - A critical issue in image restoration is the problem of noise removal while keeping the integrity of relevant image information. The method proposed in this paper is a fully automatic 3D block wise version of the Non Local (NL) Means filter with wavelet sub-bands mixing. The proposed a wavelet sub-bands mixing is based on a multi-resolution approach for improving the quality of image de-noising filter. Quantitative validation was carried out on synthetic datasets generated with the Brain Web simulator. The results show that our NL-means filter with wavelet sub-band mixing outperforms the classical implementation of the NL-means filter in of de -noising quality and computation time. Comparison with well established methods, such as non linear diffusion filter and total variation minimization, shows that the proposed NL-means filter produces better de-noising results. Finally, qualitative results on real data are presented. And this paper presents an algorithm for medical 3D image de-noising and segmentation using redundant discrete wavelet transform. First, we present a two stage de-noising algorithm using the image fusion concept. The algorithm starts with globally de-noising the brain images (3D volume) using Perona Malik's algorithm and RDWT based algorithms followed by combining the outputs using entropy based fusion approach. Next, a region segmentation algorithm is proposed using texture information and k-means clustering. The proposed algorithms are evaluated using brain 3D image/volume data. The results suggest that the proposed algorithms provide improved performance compared to existing algorithms.

Keywords: - *Medical Image Analysis, De noising, Segmentation, Redundant Discrete Wavelet Transform.*

I. INTRODUCTION

Image de- noising can be considered as a component of processing or as a process itself. In the first case, the image de- noising is used to improve the accuracy of various image processing algorithms such as registration or segmentation. Then, the quality of the artifact correction influences performance of the procedure. In the second case, the noise removal aims at improving the image quality for visual inspection. The preservation of relevant image information is important, especially in a medical context. This paper focuses on a new de noising method firstly introduced by Buades *et al.* [4] for 2D image de noising: the Non Local (NL) means filter. We propose to improve this filter with an automatic tuning of the filtering parameter, a block wise implementation and a mixing of wavelet sub-bands based on the approach proposed in [17]. These contributions lead to a fully-automated method and overcome the main limitation of the classical NL-means: the computational burden. Section 2 presents related works. Section 3 presents the proposed method with details about our contributions. Section 4 shows the impact of our adaptations compared to different implementations of the NL-means filter and proposes a comparison with well-established methods. The validation experiments are performed on a phantom data set in a quantitative way. Finally, Section 5 shows results on real data. Typically, the field of medical image analysis involves: post-acquisition such as de noising and restoration, segmentation i.e. delineating features of interest, registration, i.e. align captured image with a model or previously captured image, computation i.e physical quantity derivation, visualization, and security. Existing algorithms in medical image analysis, in general, use partial differential equations, curvature driven flows and different mathematical models. Wavelet based methods have also been proposed for medical image analysis. In

1991, Weaver et al. [1] first proposed the use of wavelet theory in medical imaging with the application to noise reduction in MRI images. Thereafter, several algorithms have been proposed for de noising, segmentation, reconstruction, functional MRI, registration, and feature extraction using continuous wavelet transform (CWT), discrete wavelet transform (DWT), and redundant DWT (RDWT). Detailed survey of wavelet based algorithms for medical imaging can be found in [2] [3], [4], and [5]. In this paper, we propose algorithms for brain image de noising and region based segmentation using RDWT for improved performance. RDWT [6], [7], also known as shift invariant wavelet transform, has proven its potential in different signal processing applications but it is not well researched in the field of medical image analysis. The proposed algorithms utilize properties of RDWT such as shift invariance and noise per sub band relationship along with other techniques such as soft thresholding, clustering, and entropy for improved performance. Experimental results on the brain data show the usefulness of the proposed de noising and segmentation algorithms and clearly indicate their potential in medical image analysis. Section 2 briefly explains the fundamentals of redundant discrete wavelet transform. Medical image de noising algorithm is explained in Section 3 and Section 4 describes the proposed image segmentation algorithm.

A. Noise in an Image

It is generally desirable for image brightness (or film density) to be uniform except where it changes to form an image. There are factors, however, that tend to produce variation in the brightness of a displayed image even when no image detail is present. This variation is usually random and has no particular pattern. In many cases, it reduces image quality and is especially significant when the objects being imaged are small and have relatively low contrast. This random variation in image brightness is designated as noise. This noise can be either image dependent or image independent. All the digital images contain some visual noise. The presence of noise gives an image a mottled, grainy, textured or snowy appearance.

1. Random Noise

Random noise revolves around an increase in intensity of the picture. It occurs through color discrepancies above and below where the intensity changes. It is random, because even if the same settings are used, the noise occurs randomly throughout the image. It is generally affected by exposure length. Random noise is the hardest to get rid of because we cannot predict where it will occur. The digital camera itself cannot remove it and it has to be lessened in an image editing program.

2. Fixed Pattern Noise

Fixed pattern noise surrounds hot pixels. Hot pixels are pixel bits that are more intense than others surrounding it and are much brighter than random noise fluctuations. Long exposures and high temperatures cause fixed pattern noise to appear. If pictures are taken under the same settings, the hot pixels will occur in the same place and time. Fixed pattern noise is the easiest type to fix after it has occurred. Once a digital camera realizes the fixed pattern, it can be adjusted to lessen the effects on the image. However, it can be more dubious to the eye than random noise if not lessened.

3. Banding Noise

Banding noise depends on the camera as not all digital cameras create it. During the digital processing steps, the digital camera takes the data produced by the sensor and creates the noise from that. High speeds, shadows and photo brightening will create banding noise. Gaussian noise, salt & pepper noise, passion noise, and speckle noise are some of the examples of this type of noise.

4. Speckle Noise

Speckle noise is defined as multiplicative noise, having a granular pattern. It is an inherent property of ultrasound image and SAR image. Another source of reverberations is that a small portion of the returning sound pulse may be reflected back into the tissues by the transducer surface itself, and generates a new echo at twice the depth. Speckle is the result of the diffuse scattering, which occurs when an ultrasound pulse randomly interferes with the small particles or objects on a scale comparable to that of the sound wavelength. The backscattered echoes from irresolvable random tissue inhomogenities in ultrasound imaging and from objects in Radar imaging undergo constructive and destructive interferences resulting in mottled b-scan image.Speckle degrades the quality of US and SAR images and thereby reducing the ability of a human observer to discriminate the fine details of diagnostic examination. This artifact introduces fine-false structures whose apparent resolution is beyond the capabilities of imaging system, reducing image contrast and masking the real boundaries of the tissue leading to the decrease in the efficiency of further image processing such as edge detection, automatic segmentation, and registration techniques. Another problem in Ultrasound data is that the

received data from the structures lying parallel to the radial direction can be very weak, as where structures normal to the radial direction give a stronger echo.

B. Filtering Techniques

Filtering techniques are used as preface action before segmentation and classification. On the whole speckle reduction can be divided roughly into two categories:

- Incoherent processing techniques
- Image post processing

The first one recovers the image by summing more than a few observations of the same object which suppose that no change or motion of the object happened during the reception of observations. These techniques do not require any hardware modification in the image reconstruction system, and hence have found a growing interest. In this the images are obtained as usual and the processing techniques are applied on the image obtained. Image post processing is an appropriate method for speckle reduction which enhances the signal to noise ratio while conserving the edges and lines in the image.

II. SPECKLE NOISE IN ULTRASOUND IMAGES

These scans use high frequency sound waves which are emitted from a probe. The echoes that bounce back from structures in the body are shown on a screen. The structures can be much more clearly seen when moving the probe over the body and watching the image on the screen. The main problem in these scans is the presence of speckle noise which reduces the diagnosis ability. It provides live images, where the operator can select the most useful section for diagnosing thus facilitating quick diagnoses.

III. WAVELET TRANSFORM AND MULTI-SCALE ANALYSIS

One of the most fundamental problems in signal processing is to find a suitable representation of the data that will facilitate an analysis procedure. One way to achieve this goal is to use transformation, or decomposition of the signal on a set of basis functions prior to processing in the transform domain. Transform theory has played a key role in image processing for a number of years, and it continues to be a topic of interest in theoretical as well as applied work in this field. Image transforms are used widely in many image processing fields, including image enhancement, restoration, encoding, and description {jin_Jain_1989}.Historically, the Fourier transform has dominated linear time-invariant signal processing. The associated basis functions are complex sinusoidal waves *ite*ω that correspond to the eigenvectors of a linear time-invariant operator. A signal ()*ft* defined in the temporal domain and its Fourier transform ˆ()*f*ω, defined in the frequency domain, have the following relationships {jin_Jain_1989; jin_Papoulis_1987}: ˆ()(),*itfftedt*ωω+∞−−∞=∫(1) 1ˆ()().2*itftfe*ω *d* ωωπ+∞−∞=∫ (2)

Fourier transform characterizes a signal ()*ft* via its frequency components. Since the support of the bases function *ite*ω covers the whole temporal domain (i.e infinite support), ˆ()*f*ω depends on the values of ()*ft* for all times. This makes the Fourier transform a global transform that cannot analyze local or transient properties of the original signal()*ft*.In order to capture frequency evolution of a non-static signal, the basis functions should have compact support in both time and frequency domain. To achieve this goal, a windowed Fourier transform (WFT) was first introduced with the use of a window function *w(t)* into the Fourier transform {jin_Mallat_1998}: (,)()().*iSftfwted*ωτωττ+∞−−∞=−∫ τ (3).The energy of the basis function ,()()*itgtwte*ξτξτ−=− is concentrated in the neighborhood of time τ over an interval of size*t*σ, measured by the standard deviation of2*g*. Its Fourier transform is)(,*g*ˆ ( ) *w*ˆ ( )*e iτ* ω ξτ ξ ω = ω −ξ − − , with energy in frequency domain localized aroundξ, over an interval of sizeωσ. In a time-frequency plane(,)*t*ω, the energy spread of what is called the atom is represented by the Heisenberg rectangle with time width,()*gt*ττξ*t*σ and frequency widthωσ. The 4 uncertainty principle states that the energy spread of a function and its Fourier transform cannot be simultaneously arbitrarily small, verifying: 1.2*t*ωσσ≥ (4) Shape and size of Heisenberg rectangles of a windowed Fourier transform therefore determine the spatial and frequency resolution offered by such transform. Examples of spatial-frequency tiling with Heisenberg rectangles are shown in Figure 1. Notice that for a windowed Fourier transform, the shape of the time-frequency boxes are identical across the whole time-frequency plane, which means that the analysis resolution of a windowed Fourier transform remains the same across all frequency and spatial locations.

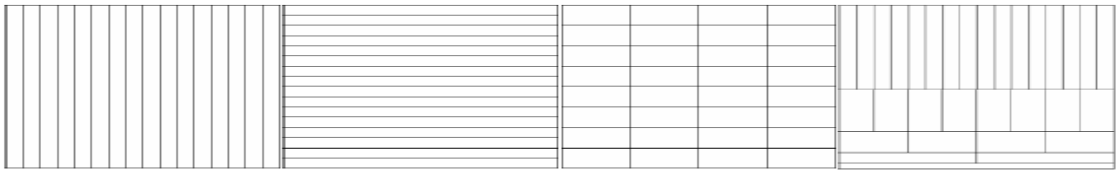

Figure 1: Example of spatial-frequency tiling of various transformations. x-axis: spatial resolution. y-axis: frequency resolution. (a) discrete sampling (no frequency localization). (b) Fourier transform (no temporal localization). (c) windowed Fourier transform (constant Heisenberg boxes). (d) wavelet transform (variable Heisenberg boxes).

To analyze transient signal structures of various supports and amplitudes in time, it is necessary to use time-frequency atoms with different support sizes for different temporal locations. For example, in the case of high frequency structures, which vary rapidly in time, we need higher temporal resolution to accurately trace the trajectory of the changes; on the other hand, for lower frequency, we will need a relatively higher absolute frequency resolution to give a better measurement on the value of frequency.

IV. RELATED WORKS

Many methods for image de noising have been suggested in the literature, and a complete review of them can be found in [4]. Methods for image restoration aim at preserving the image details and local features while removing the undesirable noise. In many approaches, an initial image is progressively approximated by filtered versions which are smoother or simpler in some sense. Total Variation (TV) minimization [21], nonlinear diffusion [2, 19, 24], mode filters [25] or regularization methods [18, 21] are among the methods of choice for noise removal. Most of these methods are based on a weighted average of the gray values of the pixels in a spatial neighborhood [10, 23]. One of the earliest examples of such filters has been proposed by Lee [16]. An evolution of this approach has been presented by Tomasi *et al* [23], who devised the bilateral filter which includes both a spatial and an intensity neighborhood. Recently, the relationships between bilateral filtering and local mode filtering [25], local M-2estimators [26] and non-linear diffusion [1] have been established. In the context of statistical methods, between the Bayesian estimators applied on a Gibbs distribution resulting with a penalty functional [12], and averaging methods for smoothing has also been described in [10]. Finally, statistical averaging schemes enhanced via incorporating a variable spatial neighborhood scheme have been proposed in [13, 14, 20]. All these methods aim at removing noise while preserving relevant image information. The trade-off between noise removal and image preservation is performed by tuning the filter parameters, which is not an easy task in practice. In this paper we propose to overcome this problem with a 3D sub-bands wavelet mixing. As in [17], we have chosen to combine a multi resolution approach with the NL-means filter [4] which has recently shown very promising results. Recently introduced by Buades *et al.* [4], the NL-means filter proposes a new approach for the de-noising problem. Contrary to most de-noising methods based on a local recovery paradigm, the NL-means filter is based on the idea that any periodic, textured or natural image has redundancy, and that any voxel of the image has similar voxels that are not necessarily located in a spatial neighborhood. This new *non-local recovery paradigm* allows to improve the two most desired properties of a de-noising algorithm: edge preservation and noise removal.

C. Methods

In this section, we introduce the following notations:

• $u : \Omega^3 \to \mathbb{R}$ is the image, where Ω^3 represents the image grid, considered as cubic for the sake of simplicity and without loss of generality $(|\Omega^3| = N^3)$.

• for the original voxelwise NL-means approach

– $u(xi)$ is the intensity observed at voxel xi.

– Vi is the cubic search volume centered on voxel xi of size $|Vi| = (2M + 1)3$, M " N.

– Ni is the cubic local neighborhood of xi of size $|Ni| = (2d + 1)3$, d " N.

– $u(Ni) = (u(1)(Ni), ..., u(|Ni|)(Ni))T$ is the vector containing the intensities of Ni (that we term "patch" in the following).

– $NL(u)(xi)$ is the restored value of voxel xi.

– $w(xi, xj)$ is the weight of voxel xj when restoring $u(xi)$.

• for the block wise NL-means approach

– Bi is the block centered on xi of size $|B_i| = (2\alpha + 1)^3, \alpha \in \mathbb{N}$

– $u(Bi)$ is the vector containing the intensities of the block Bi.

– $NL(u)(Bi)$ is the vector containing the restored value of Bi.

– $w(Bi,Bj)$ is the weight of block Bj when restoring the block $u(Bi)$.

– the blocks Bik are centered on voxels xik which represent a subset of the image voxels, equally regularly distributed over "3 (see Fig 2).

– n represents the distance between the centers of the blocks Bik (see Fig 2)

The Non Local Means filter

In the classical formulation of the NL means filter [4], the restored intensity *NL*(*u*)(*xi*) of the voxel *xi*, is a weighted average of the voxels intensities *u*(*xi*) in the "search volume" *Vi* of size (2*M*+1)3:3

$$NL(u)(x_i) = \sum_{x_j \in V_i} w(x_i, x_j) u(x_j) \quad \text{.....(1)}$$

where *w*(*xi*, *xj*) is the weight assigned to value *u*(*xj*) to restore voxel *xi*. More precisely, the weight evaluates the similarity between the intensity of the local

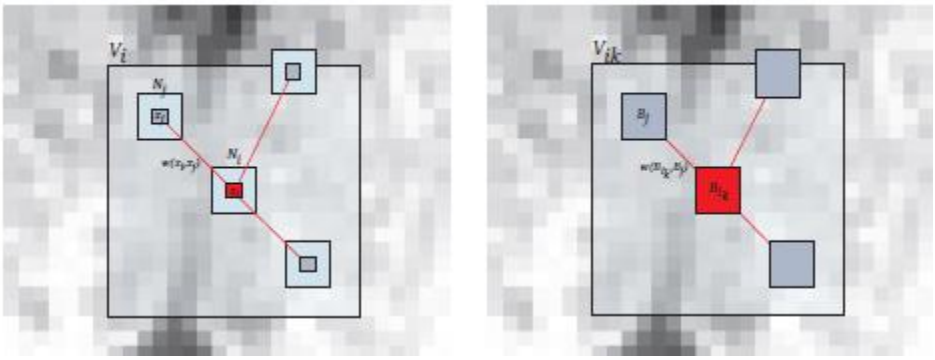

Figure 2: Left: Usual voxel wise NL-means filter: 2D illustration of the NL- means principle. The restored voxel *xi* (in red) is the weighted average of all intensities of voxels *xj* in the search volume *Vi*, based on the similarity of their intensity neighborhoods u(*Ni*) and u(*Nj*). In this example, we set *d* = 1 and *M* = 8. Right: Blockwise NL-means filter: 2D illustration of the block wise NL-means principle. The restored value of the block *Bik* is the weighted average of all the blocks *Bj* in the search volume *Vik* . In this example, we set α = 1 and *M* = 8.

neighborhoods *Ni* and *Nj* centered on voxels *xi* and *xj* , such that $w(x_i, x_j) \in$ " [0, 1] and
"
$\sum_{x_j \in V_i} w(x_i, x_j) = 1$ (cf Fig. 2Left).For each voxel *xj* in *Vi*, the computation of the weight is based on the Euclidean distance between patches u(*Nj*) and u(*Ni*), defined as:

$$w(x_i, x_j) = \frac{1}{Z_i} e^{-\frac{\|u(N_i) - u(N_j)\|_2^2}{h^2}} \quad \text{.....(2)}$$

where *Zi* is a normalization constant ensuring that $\sum_j w(x_i, x_j) = 1$, and *h* acts as a filtering parameter controlling the decay of the exponential function. Automatic tuning of the filtering parameter *h*. As explained in the introduction, de-noising is usually the first step of complex image processing procedures. The number and the dimensions of the data to process being continually increasing, each step of the procedures needs to be as automatic 4 as possible. In this section we propose an automatic tuning of the filtering parameter *h*. First, it has been shown that the optimal smoothing parameter *h* is proportional to the standard deviation of the noise σ [4]. Second, if we want the filter independent of the neighborhood size, the optimal *h* must depend on |*Ni*| (see Eq. 2). Thus, the automatic tuning of the filtering parameter *h* amounts to determining the relationship $h^2 = f(\sigma^2, |N_i|, \beta)$ where # is a constant. Firstly, the standard deviation of the noise σ needs to be estimated. In case of an additive white Gaussian noise, this estimation can be based on pseudoresiduals ϵ_i as defined in [3, 11]. For each voxel *xi* of the volume Ω^3 et us define:

$$\epsilon_i = \sqrt{\frac{6}{7}} \left(u(x_i) - \frac{1}{6} \sum_{x_j \in P_i} u(x_j) \right), \quad \text{.....(3)}$$

Pi being the 6-neighborhood at voxel *xi* and the constant $\sqrt{6/7}$ is used to ensure that $\mathbb{E}[\epsilon_i^2] = \hat{\sigma}^2$] in the homogeneous areas. Thus, the standard deviation of noise $\hat{\sigma}$ is computed as:

$$\hat{\sigma}^2 = \frac{1}{|\Omega^3|} \sum_{i \in \Omega^3} \epsilon_i^2. \quad \text{.....(4)}$$

Based on the fact that, in the case of Gaussian noise and with normalized L2- norm, the optimal de-noising is obtained for $h^2 = 2\sigma^2$ [5]. (2) can be written as:

$$w(x_i, x_j) = \frac{1}{Z_i} e^{-\frac{\|\mathbf{u}(N_i) - \mathbf{u}(N_j)\|_2^2}{2\beta\sigma^2 |N_i|}} \quad \text{.....(5)}$$

where only the adjusting constant β needs to be manually tuned. If our estimation ˆ" of the standard deviation of the noise " is correct, β should be close to
1.The optimal choice for # will be discussed later.
Blockwise implementation
The main problem of the NL-means filter being its computational time, a blockwise approach can be used to 5 decrease the algorithmic complexity. Indeed, instead of de-noising the image at a voxel level, entire blocks are directly restored. A blockwise implementation of the NL-means filter consists in a) dividing the volume into blocks with overlapping supports, b) performing NL-means like restoration of these blocks and c) restoring the voxels values based on the restored values of the blocks they belong to:

2. A partition of the volume Ω^3 into overlapping blocks *Bik* of size (2*!*+1)3 is performed, such as $\Omega^3 = \bigcup_k B_{i_k}$ *k Bik* , under the constraint that each block *Bik* intersects with at least one other block of the partition. These blocks are centered on voxels *xik* which constitute a subset of Ω^3 . The voxels *xik* are equally distributed at positions $i_k = (k_1 n, k_2 n, k_3 n), (k_1, k_2, k_3) \in \mathbb{N}^3$ where *n* represents the distance between the centers of *Bik* . To ensure a global continuity in the de-noised image, the overlapping support of blocks is non empty: $2\alpha \geq n.$
For each block *Bik* , a NL-means-like restoration is performed as follows:

$$\mathbf{NL}(u)(B_{i_k}) = \sum_{B_j \in V_{i_k}} w(B_{i_k}, B_j)\mathbf{u}(B_j), \text{ with } w(B_{i_k}, B_j) = \frac{1}{Z_{i_k}} e^{-\frac{\|\mathbf{u}(B_{i_k}) - \mathbf{u}(B_j)\|_2^2}{2\beta\sigma^2 |N_i|}} \quad \text{.....(6)}$$

where *Zik* is a normalization constant ensuring that $\sum_j w(B_{i_k}, B_j) = 1$ (see Fig. 2(right).

For a voxel *xi* included in several blocks *Bik* , several estimations of the restored intensity *NL*(*u*)(*xi*) are obtained in different NL(*u*)(*Bik*). Theestimations given by different NL(*u*)(*Bik*) for a voxel *xi* are stored in a vector A*i*. The final restored intensity of voxel *xi* is then defined as:

$$NL(u)(x_i) = \frac{1}{|\mathbf{A}_i|} \sum_{p \in \mathbf{A}_i} \mathbf{A}_i(p). \quad \text{.....(7)}$$

where A*i*(*p*) denotes the *pth* element of the vector A*i*.

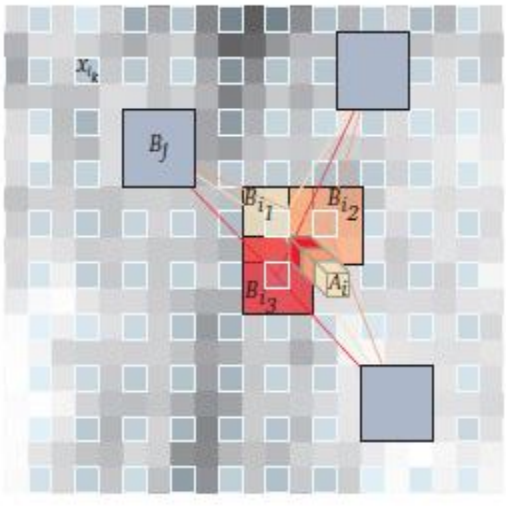

Figure 3: Blockwise NL-means Filter. For each block *Bik* centered on voxel *xik* , a NL-means like restoration is

performed from blocks *Bj* .

In this way, for a voxel *xi* included in several blocks, several estimations are obtained. The restored value of voxel *xi* is the average of the different estimations stored in vector A*i*.In this example $\alpha = 1, n = 2$ and $|\mathbf{A}_i| = 3$.The main advantage of this approach is to significantly reduce the complexity of the algorithm. Indeed, for a volume "3 of size *N*3, the global complexity is $\mathcal{O}((2\alpha+1)^3(2M+1)^3(\frac{N-n}{n})^3)$ .For instance, with *n* = 2, the complexity is divided by a factor 8.Wavelet Sub-bands Mixing.

A. Hybrid approaches

Recently, hybrid approaches coupling the NL-means filter and a wavelet decomposition have been proposed [9, 17, 22]. In [9], a wavelet-based de-noising of blocks is performed before the computation of the non local means. The NL-means filter is performed with de-noised version of blocks in order to improve the de-noising result. In [22], the NL-means filter is applied directly on wavelet coefficients in transform domain. This approach allows a direct de-noising of compressed images (such as JPEG2000) and a reduction of computational time since smaller images are processed. In [17], a multi-resolution framework is proposed to adaptively combine the result of de-noising algorithms at different space-frequency resolutions. This idea relies on the fact that a set of filtering parameters is not optimal over all the space-frequency resolutions. Thus, by combining in the transform domain the results obtained with different sets of filtering parameters, the de-noising is expected to be improved.

V. OVERALL PROCESSING

In order to improve the de-noising result of the NL-means filter, we propose a Multi-resolution framework similar to [17] to implicitly adapt the filtering parameters (*h*, |*Bi*|) over the different space-frequency resolutions of the image. This adaptation is based on the fact that the size of the patches impacts the De-noising properties of the NL-means filter. Indeed, the weight given to a bl depends on its similarity with the block under consideration, but the similarity between the blocks depends on their sizes. Thus, given the size of the blocks, removal or preservation of image components can be favored. In the transform domain, the main features of the image correspond to low frequency information while finer details and noise are associated to high frequencies. Nonetheless, noise is not a pure high frequency component in most images. Noise is spanned over a certain range of frequencies in the image, with mainly middle and high components [17]. In NL-means-based restoration, large blocks and setting # = 1 efficiently remove all frequencies of noise but tend to spoil the main features of the image,whereas small blocks and low smoothing parameter (# = 0.5) tend to better preserve the image components but cannot completely remove all frequencies of noise. De-noising of the original image *I* using wo sets of filtering parameters: one adapted to the noise components removal (i.e. large blocks and $\beta = 1$) and the other adapted to the image features preservation (i.e. small blocks and β = 0.5). This yields two images *Io* and *Iu*. In *Io*, the noise is efficiently removed and, conversely, in *Iu* the image features are preserved.

• Decomposing *Io* and *Iu* into low and high frequency sub-bands. The first level decomposition of the images is performed with a 3D discrete Wavelet Transform (DWT).
• Mixing the highest frequency sub-bands of *Io* and the lowest frequency sub-bands of *Iu*.
• Reconstructing the final image by an inverse 3D DWT from the combination of the selected high and low frequencies.

In this paper, we propose an implementation of this approach using our optimized blockwise NL-means filter and the 3D DWT Daubechies-8 basis. The latter is implemented in Qccpack1 in the form of dyadic sub-band pyramids. This DWT is widely used in image compression due to its robustness and efficiency.

VI. VISUAL ASSESSMENT

Visually, the proposed method combines the most important attributes of a De-noising algorithm: edge preservation and noise removal. Fig.4 shows that our filter removes noise while keeping the integrity of MS lesions (i.e. no structure appears in the removed noise). Fig. 4 focuses on the differences between the Optimized Blockwise NLM and the Optimized Blockwise NLM with WM filters. The de-noising result obtained with the Optimized Blockwise NLM with WM filter visually preserves the edges better than the Optimized Blockwise NLM filter. This is also confirmed by visual inspection of the comparison with the "ground truth". The images of difference between phantom and the de-noised image show that less structures have been removed with the Optimized Blockwise NLM with WM filter. Thus, the multi-resolution approach allows to better preserve the edges and to enhance the contrast between tissues.

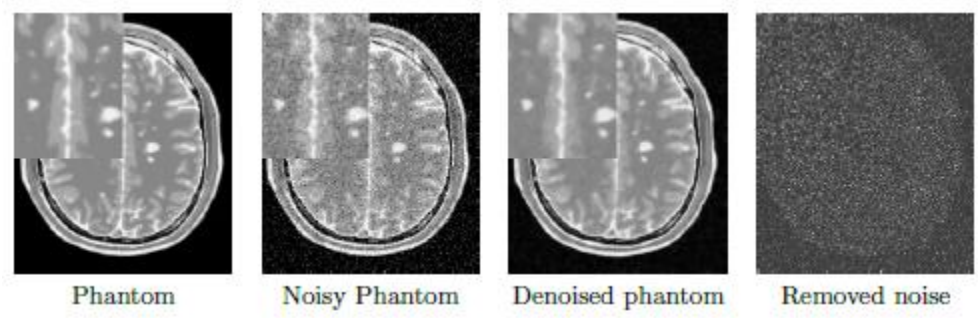

Figure 4: Fully-automatic restoration obtained with the optimized blockwise NL-means with wavelet mixing filter in 3 minutes on a Dual Core Intel(R) Pentium(R) D CPU 3.40GHz. The image is a T2-w phantom MRI with MS of 181 × 217 × 181 voxels and 9% of noise.

VII. ISSUES AND CHALLENGES WHILE PROVIDING IMAGE DE-NOISING TECHNIQUE

Medical imaging technology is becoming an important component of large number of applications such as the diagnosis research and treatment. It enables the physicians to create the images of the human body for the clinical purposes. Medical images like X-Ray, CT, MRI and PET, SPECT have minute information about the heart brain and nerves. These images suffer from a lot of short comings including the acquisition of noise from the equipment, ambient noise from the environment and the presence of background tissue, other organs and anatomical influences such as body fat and breathing motion. Noise reduction therefore becomes very important. The main techniques of image de-noising are filters wavelets and neural networks. The BPNN based approach is a powerful and effective method for image de-noising. Earlier proposed methods suffered from drawbacks such as noise, artifacts and degradation. Although all the spatial filters performs well on the digital images but still suffered from some constraints such as resolution degradation these filters operated by smoothing over a fixed window and it produces artifacts around the object and sometimes caused over smoothing thus causing the blurring of image. Wavelet transform outperforms the filters because of its properties like sparsity, multi resolution and multi scale nature and proved promising as they are capable of suppressing noise while maintaining high frequency signal details. But the limitation with wavelet transform was that the local scale- space information of the image is not adaptively considered by the standard wavelet thresholding methods. Other difficulty was that the soft thresholding function was a piecewise function and does not have high order derivates. A new type of thresholding neural network was presented which outperforms the soft thresholding using wavelet transform but still does not promised a high performance in terms of PSNR, MSE and visual test. Considering and analyzing the drawbacks of the previous methods we propose a new improved BPNN approach and Fuzzy to de-noise the medical images. This approach includes using both mean and median statistical functions for calculating the output pixels of the NN and Fuzzy. This uses a part of degraded image pixels to generate the system training pattern. Different test, images noise levels and

neighborhood sizes are used. Based on using samples of degraded pixels neighborhoods as input, the output of the proposed approach provided a good image de-noising performance which exhibits a promising results of the degraded noisy image in terms of PSNR, MSE and visual test.

VIII. COMPARISON WITH OTHER METHODS

In this section, we compare the proposed method with two of the most used approaches in MRI domain: the Non Linear Diffusion (NLD) filter r [19] and the Total Variation (TV) minimization [21]. The main difficulty to achieve this comparison is related to the tuning of smoothing parameters in order to obtain the best results for NLD filter and TV minimization scheme. After quantifying the parameter space, we exhaustively tested all possible parameters within a certain range. This allows us to obtain the best possible results for the NLD filter and the TV minimization.For the Optimized Blockwise NLM with WM the same set of parameters *Su* = (*!u,MW, #u*) = (1, 3, 0.5) and *So* = (*!o,MW, #o*) = (2, 3, 1) are used for all noise levels. The automatic tuning of *h* adapts the smoothing to the noise level.For NLD filter, the parameter K varied from 0.05 to 1 with a step of 0.05 and the number of iterations varied from 1 to 10. For TV minimization, the parameter & varied from 0.01 to 1 with a step of 0.01 and the number of iterations varied from 1 to 10. The results obtained for a 9% of Gaussian noise are presented , but this screening was performed for the four levels of noise. It is important to underline that the results giving the best PSNR are used, but these results do not necessary give the best visual output. Actually, the best PSNR value for the NLD filter and TV minimization are obtained for a visually under-smoothed image since these methods tend to spoil the edges (see Fig. 5). This is explained by the fact that the optimal PSNR is obtained when a good trade-off is reached between edge preserving and noise removing.

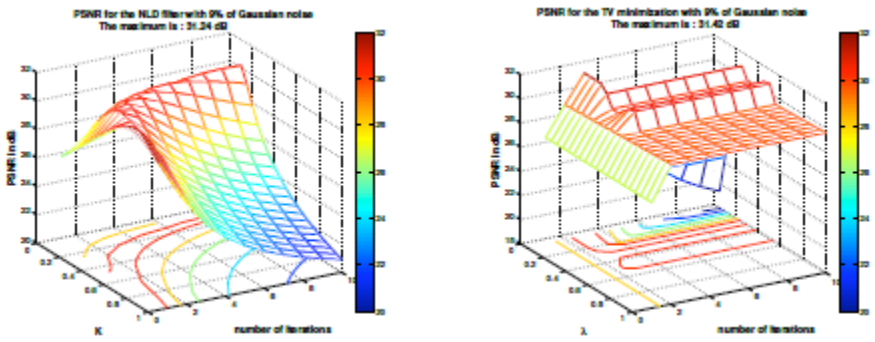

Figure 5: Result for the NLD filter and the TV minimization on phantom images with Gaussian noise at 9%. For the NLD filter, K varied from 0.05 to 1 with a step of 0.05 and the number of iterations varied from 1 to 10. For the TV minimization, & varied from 0.01 to 1 with a step of 0.01 and the number of iterations varied from 1 to 10.

IX. QUANTITATIVE RESULTS

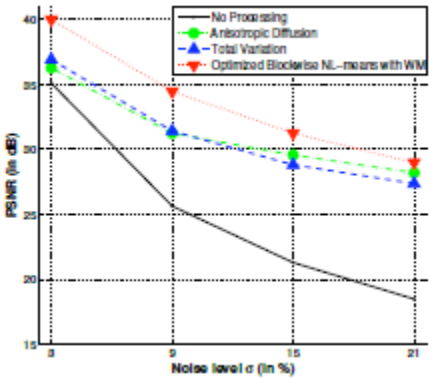

Figure 6: Comparison between Non Linear Diffusion, Total Variation and Optimized Blockwise NL-means with

wavelet mixing denoising. The PSNR experiments show that the Optimized Blockwise NL-means with wavelet mixing filter significantly outperforms the well-established Total Variation minimization process and the Non

Linear Diffusion approach. As presented in Fig. 6, our block optimized NL-means with wavelet mixing filter produced the best PSNR values whatever the noise level.

X. VISUAL ASSESSMENT

The de-noising results obtained by the NLD filter, the TV minimization and our Optimized blockwise NLM with WM. Visually, the NL means- based approach produced the best de-noising. The removed noise shows that the proposed method removes significantly less structures than NLD filter or TV minimization. Finally, the comparison with the "ground truth" underlines that the NL-means restoration gives a result very close to the "ground truth" and better preserves the anatomical structure compared to NLD filter and TV minimization.

XI. EXPERIMENTS ON CLINICAL DATA

The T1-weighted MR images used for experiments were obtained with T1 sense 3D sequence on 3T Philips Gyroscan scanner. The restoration results, presented in Fig. 7, show good preservation of the cerebellum. Fully automatic segmentation and quantitative analysis of such structures are still a challenge, to improve restoration schemes could greatly improve these processings.

Figure 7: Fully-automatic restoration obtained with the optimized blockwise NL-means with wavelet mixing filter on a 3 Tesla T1-w MRI data of 2563 voxels in less than 4 minutes on a Dual Core Intel(R) Pentium(R) D CPU 3.40GHz.

XII. SHIFT INVARIANT REDUNDANT DISCRETE

Wavelet Transform generally, DWT [6], [8] is used in wavelet based medical image analysis as it preserves frequency information in stable form and allows good localization both in time and spatial frequency domain. However, one of the major drawbacks of DWT is that the transformation does not provide shift invariance. This causes a major change in the wavelet coefficients of the image even for minor shifts in the input image. In medical imaging, we need to know and preserve exact location of different information; but shift variance may lead to inaccuracies. For example, in medical image de-noising it is important to preserve edge information and remove noise, but DWT based de-noising may produce specularities along the edges. Several techniques have been proposed to address shift variance in de-noising and segmentation [9]. In this paper, we use RDWT [6], [7], [10] to overcome the shift variance problem of DWT. RDWT can be considered as an approximation to discrete wavelet transform that removes the down-sampling operation from traditional critically sampled DWT, produces an over complete representation, and provide noise per sub band relationship [7]. The shift variance of DWT arises from the use of down-sampling whereas RDWT is shift invariant because the spatial sampling rate is fixed across scale. Similar to DWT, RDWT and Inverse RDWT (IRDWT) of a two dimensional image or three dimensional volume data is obtained by computing each dimension separately where detailed and approximation bands are of the same size as the input image/data

1.Fusion based Two Stage Approach to Medical Image De-noising This section presents a fusion based de-noising algorithm that utilizes the concept of image fusion. In this two stage approach, we first concurrently apply two de-noising algorithms globally and then, in the second stage, generate the quality enhanced image by locally combining the good quality regions from the two de-noised images. In this research, we use Perona Malik's algorithm [11] and RDWT based de-noising algorithm as the two ingredient algorithms and the outputs of these two algorithms are combined using the proposed fusion technique. This section first describes the RDWT based de-noising algorithm followed by the fusion approach. RDWT base Image De-noising Let IT be the true image and N be the noise component. As described by Jin et al. [2], the relationship of noisy image IN corresponding to IT and N can be written as:

$$I_N = I_T + N \quad \text{.....(8)}$$

De-noising IN using wavelet transform to recover the true signal IT can be represented as,

$$I_R = \sum_i W(I_N, l, t) \quad \text{.....(9)}$$

where IR represents the reconstructed signal, W represents the wavelet based de-noising, l represents the level of decomposition, and t is the function that aims at eliminating noise components in the transform domain while preserving the true signal coefficients. In ideal conditions, IR = IT . DWT based de-noising algorithms have been proposed in [12]-[13] using different wavelet basis and thresholding schemes. All these algorithms use some technique to handle shift variance but suffer due to presence of visual artifacts and Gibbs phenomenon. Here, we use RDWT in the proposed de-noising algorithm to address shift invariance and challenges due to artifacts. IN is decomposed at l levels using 3D/2D RDWT. Soft thresholding technique [14] is applied on the RDWT coefficients of sub band Ci (i = 1, 2, · · · , l) with threshold ti to obtain the de-noised sub band C0i .

$$C_i'(x) = \begin{cases} x - t_i, & if \quad x \geq t_i \\ x + t_i, & if \quad x \leq -t_i \\ 0, & if \quad |x| < t_i \end{cases} \quad \text{.....(10)}$$

where the threshold for each sub band ti is computed using Equation 4

$$t_i = \frac{S\alpha_i^2}{\sigma_i} \quad \text{.....(11)}$$

Here, σ_i is the standard derivation for the i^{th} sub band and the noise variance for each sub band α_i^2 i , is computed using Equation 5,

$$\alpha_i^2 = \left[\frac{median(C_i)}{0.6745}\right]^2 \quad \text{.....(12)}$$

The scale parameter S is computed using L_m, i.e length of sub band at m^{th} scale,

$$S = \sqrt{log\left(\frac{L_m}{l}\right)} \quad \text{.....(13)}$$

Finally, the medical volume/image is reconstructed by applying 3D/2D IRDWT on C_i' to get the de-noised medical data.

XIII. MEDICAL IMAGE SEGMENTATION USING RDWT ENTROPY FEATURES

Segmentation of biomedical images is the basis for 3D visualization and operation simulation. Precision in segmentation is critical to diagnosis and treatment. Conventionally, segmentation methods are divided into region based segmentation and edge or gradient based segmentation. Region based segmentation [16], [17] is usually based on the concept of finding similar features such as brightness and texture patterns. Edge based segmentation methods [18] are based on finding the high gradient value in the image and then connect them to form a curve representing a boundary of the object. In this section, we propose RDWT based medical image segmentation algorithm which is a region-based method but inherently provides the features of edge-based segmentation method too. Since the detail bands of RDWT decomposed image provide gradient information, we can use these information for region segmentation. The proposed region based segmentation algorithm is described as follows: Let I be the medical image/volume data to be segmented. This image is decomposed into n levels using RDWT. The proposed approach uses the wavelet energy features computed from the approximation band and all the detailed bands using block size of $x \times x$, where $x \leq 3$ (In our

experiments, we chose the block size as 3×3). fi, the energy features for RDWT sub bands (where i = {a, h, v, d} and a- approximation , v - vertical, d - diagonal, h - horizontal),are computed using Equations 14

$$f_i = \left(\frac{1}{x} \sum_j \sum_k C_{i_{jk}}^2 \right)^2 + \frac{1}{x} \sqrt{\frac{\mu_i^{jk}}{\sigma_i^{jk}}} \quad \text{……..(14)}$$

These energy features, fa, fv, fd, and fh, reflect the texture property of an image, and the wavelet energy features computed from detailed sub bands provide the gradient information which facilitates the robust segmentation. Further, we use k-means clustering based learning algorithm which first learns from the training data and then identifies different feature regions at the testing time. Training data is used to train the k-means clustering algorithm [19] and form different clusters or groups of brain regions such as background, skull, and fat. As shown in Figure 3, we consider six regions present in the brain image namely, background, CSF, grey matter, white matter, skull, and fat. k-means clustering algorithm is trained using the simulated brain data as training data and different colors are assigned to the clusters. For segmentation, the test image is first decomposed into n = 3 levels and wavelet energy features are computed for every level. For the nth level, trained k-means algorithm classifies every feature and assigns a color to each feature. The segmented sub bands are reconstructed to get the n – 1 level of segmented decomposition. At this point of time, approximation band is the segmented image obtained from previous step and detailed sub bands are non-segmented. The same procedure is applied till the reconstruction reaches to 0th level which gives the final segmented image. This algorithm uses the concept of multi-resolution analysis since the results of nth level are used to compute the results of (n −1) th level. Figure 5 shows the segmentation results on the brainweb database.

XIV. EXPERIMENTAL EVALUATION

To evaluate the performance of the proposed de-noising and segmentation algorithms, we use the 3D Brainweb database [15]. This database contains images with different noise factors along with the ground truths. To quantitatively evaluate the de-noising algorithm, Mean Square Error (MSE) and Structural SImilarity Metrics (SSIM) [20] are used. Table 1 delineates the experimental results for the proposed de-noising algorithm.Using the ground truth and noisy images with 7% noise, MSE is 121.4500 and SSIM is 0.5613 whereas with 9% noise, MSE is 189.6959 and SSIM is 0.5040. De-noising algorithm should decrease the MSE and increase the SSIM values. On applying Perona Malik's de-noising algorithm[11] to the 7% noisy brain volume, MSE is reduced to 93.9106 and SSIM is increased to 0.6449 whereas with the RDWT based de-noising algorithm, MSE is 88.3808 and SSIM is 0.6494. Compared to existing algorithms, the proposed fusion based algorithm significantly improves the visual quality of the brain image. This observation also holds with the 9% noisy brain data (Table 1). These results also suggest that the Perona Malik's de-noising algorithm and RDWT based de-noising algorithm provide complementary information and the fusion approach combines the globally de-noised images such that the fused information provide better quality image. An interesting observation is related to the time taken to de-noise the image. With Perona Malik's algorithm, time to de-noise the image is very much dependent on the amount of noise present in the image. With RDWT based de-noising algorithm, computational requirement is reduced because of inherent advantages of shift invariance and able to tolerate noise. For fusion based approach, the computational time includes time to globally de-noise the brain image and to fuse the de-noised images. Although the computational time for fusion approach is higher than constituent algorithms but the visual quality is significantly increased, thereby making it applicable to medical applications. Next, correct classification accuracy is used to evaluate the segmentation algorithm. Figure 5 shows a close view of the segmentation result. Visually, the results are encouraging and preserve both the region and edge information. Since the Brainweb database provides the ground truth, correct classification accuracy quantitatively represents the performance of the segmentation algorithm. For the six categories or regions, Table 4 shows that the proposed algorithm provides the accuracy in the range of 91.9-94.8%. In comparison with the existing SVM based segmentation algorithm [21], the proposed algorithm yields similar results. However, the main advantage is with computational time. With the proposed algorithm, the time taken to segment the regions of 3D brain volume is 5.37 seconds (at an average) whereas with the SVM based algorithm, it is 37.22 seconds. Further, in another experiment, we segment the noisy brain data (Figure 5). It is clear from this result that the segmentation of noisy images yield erroneous results. However, when the brain image is first de-noised and then segmented, the results show clear and correct segmentation. Furthermore, visual results were shown to eminent medical professionals and they asserted that the proposed de-noising and segmentation algorithms provide better information compared to existing algorithms.

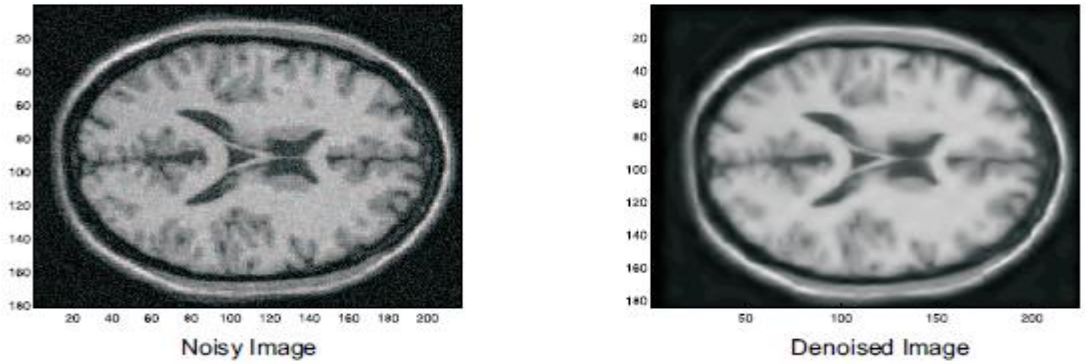

Fig. 8: De-noising medical data using RDWT based algorithm.

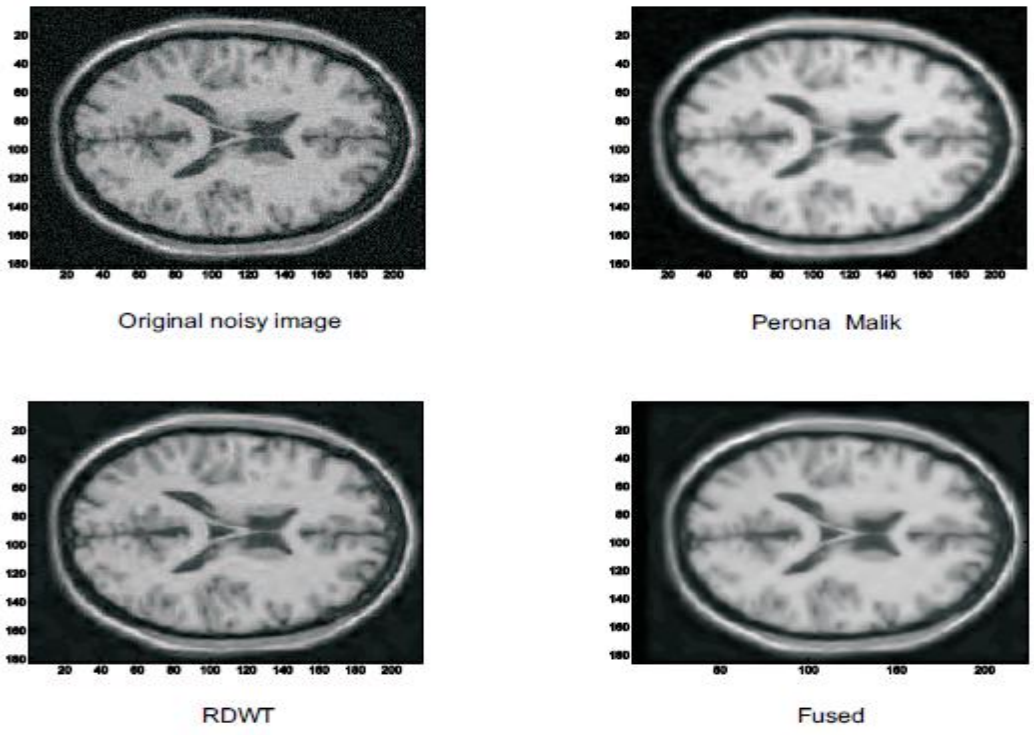

Fig. 9: Comparison of Denoising algorithms

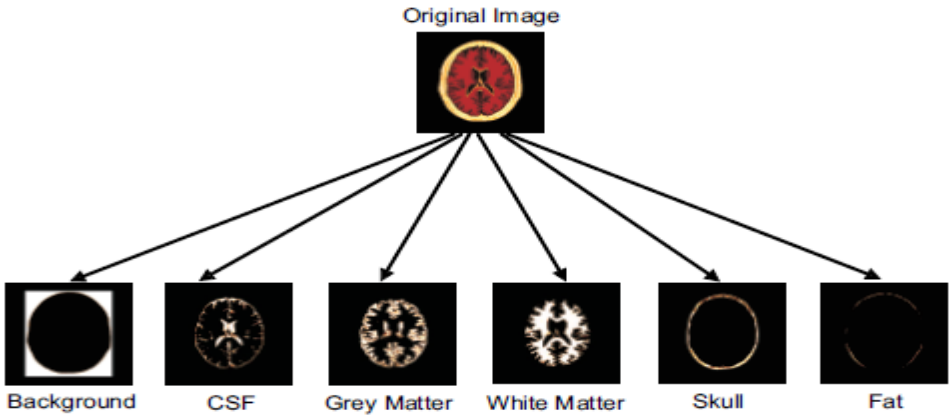

Fig. 10: Training data used for training the clustering algorithm.

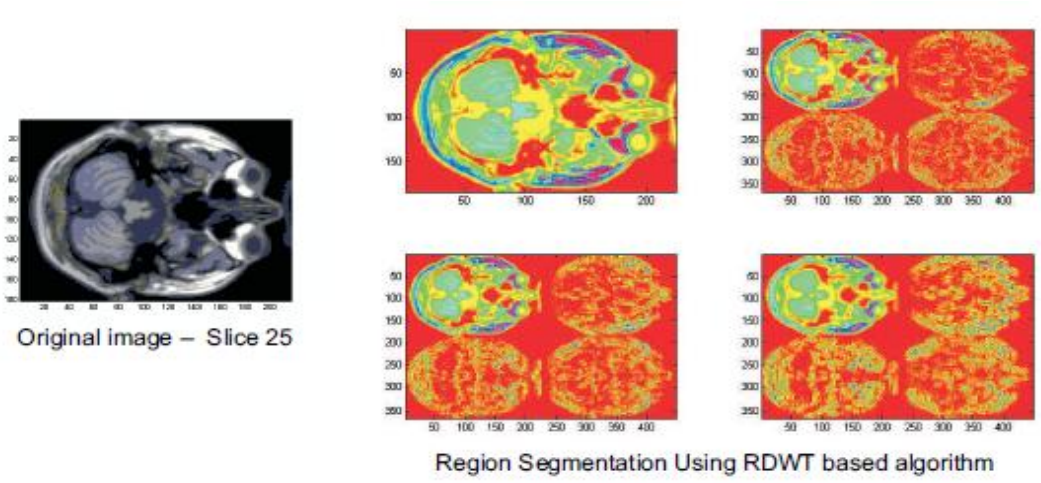

Fig. 11: Segmentation using RDWT based algorithm.

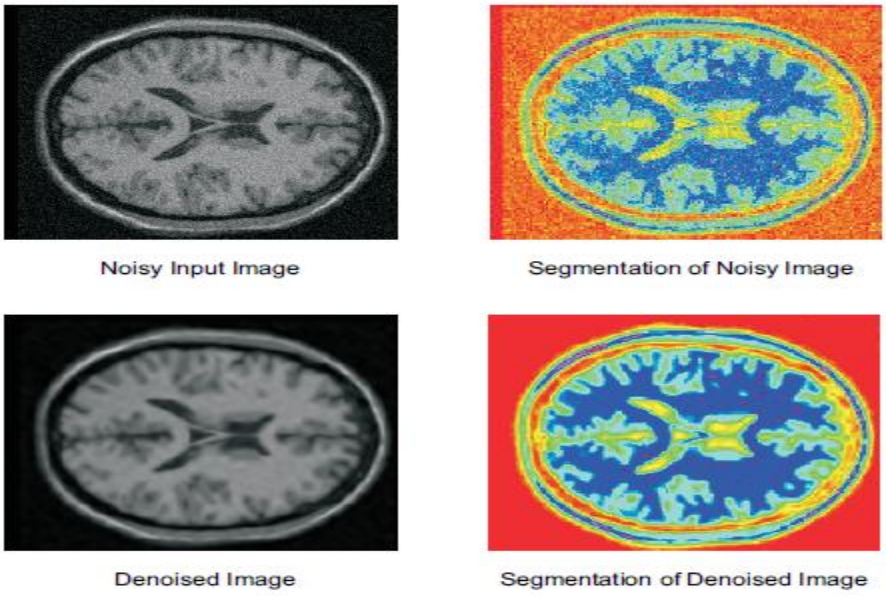

Fig. 12: Segmentation of noisy and de-noised brain image.

XV. DISCUSSION AND CONCLUSION

This paper presented a fully-automated blockwise version of the Non Local (NL) means filter with sub-bands wavelet mixing. Experiments were carried out on the Brain Web dataset [6] and real data set. The results on phantom shows that the proposed Optimized Blockwise NL-means with sub-bands wavelet mixing filter outperforms the classical implementation of the NL-means filter and the optimized implementation presented in [7, 8], in terms of PSNR values and computational time. Compared to the classical NL-means filter, our implementation (with block selection, blockwise implementation and wavelet sub-bands mixing) considerably decreases the required computational time (up to a factor of 20) and significantly increases the PSNR of the de-noised image. The comparison of the filtering process with and without wavelet mixing shows that the sub-bands mixing better preserves edges and better enhances the contrast between the tissues. This multi resolution approach allows to adapt the smoothing parameters along the frequencies by combining several de-noised images. The comparison with well-established methods such as NLD filter and TV minimization shows that the NL-means-based restoration produces better results. Finally, the impact of the proposed multi resolution approach based on wavelet sub-bands mixing should be investigated further, for instance when combined to the Non Linear diffusion filter [19] and the Total Variation minimization [21]. Computer assisted diagnosis and therapy, in general, require image processing operations such as de-noising and segmentation. Sophisticated imaging techniques such as MRI and CAT scanning provide abundant information but require preprocessing techniques so that 3D image/volume can be optimally used for diagnosis. This paper presents fusion based de-noising algorithm and RDWT entropy based region segmentation algorithm. Using the 3D Brainweb database,

the proposed algorithms show significant improvement over existing algorithms. In future, fusion based de-noising algorithm and segmentation will be extended with the non-linear learning approach for further reducing the errors.

XVI. ACKNOWLEDGEMENTS

The authors are thankful to Mr.Saikat Maity and Dr.Chandan Konar for preapering this paper.

REFERENCES

[1] D. Barash. A fundamental relationship between bilateral filtering, adaptive smoothing, and the nonlinear diffusion equation. IEEE Transactions on Pattern Analysis and Machine Intelligence, 24(6):844–847, June 2002.
[2] M.J. Black and G. Sapiro. Edges as outliers: Anisotropic smoothing using local image statistics. In Scale-Space Theories in Computer Vision, Second International Conference, Scale-Space'99, Corfu, Greece, September 26-27, 1999, Proceedings, pages 259–270, 1999.
[3] J. Boulanger, Ch. Kervrann, and P. Bouthemy. Adaptive spatio-temporal restoration for 4D fluoresence microscopic imaging. In Int. Conf. on Medical Image Computing and Computer Assisted Intervention (MICCAI'05), Palm Springs, USA, October 2005.
[4] A. Buades, B. Coll, and J. M. Morel. A review of image denoising algorithms, with a new one. Multiscale Modeling & Simulation, 4(2):490–530, 2005.
[5] A. Buades, B. Coll, and J.-M. Morel. Image and movie denoising by nonlocal means. Technical Report 25, CMLA, 2006.
[6] D.L. Collins, A.P. Zijdenbos, V. Kollokian, J.G. Sled, N.J. Kabani, C.J. Holmes, and A.C. Evans. Design and construction of a realistic digital brain phantom. IEEE Transactions on Medical Imaging, 17(3):463–468, 1998.
[7] P. Coup´e, P. Yger, and C. Barillot. Fast Non Local Means Denoising for 3D MR Images. In R. Larsen, M. Nielsen, and J. Sporring, editors, 9th International Conference on Medical Image Computing and Computer-Assisted Intervention, MICCAI'2006, volume 4191 of Lecture Notes in Computer Science, pages 33–40, Copenhagen, Denmark, October 2006. Springer.
[8] O. Rioul and M. Vetterli, "Wavelets and signal processing," IEEE Signal Processing Magazine, vol. 8, no. 4, pp. 14–38, 1991. G. Beylkin, "On the representation of operators in bases of compactly supported wavelets," SIAM Journal of Numerical Analysis, vol. 29, pp. 1716–1740, 1992.
[9] G. Strang and T. Nguyen, Wavelet and filter banks. Wellesly- Cambridge Press, 1996.
[10] P. Perona and J. Malik, "Scale-space and edge detection using anisotropic diffusion," IEEE Transaction on Pattern Analysis and Machine Intelligence, vol. 12, no. 7, pp. 629–639, 1990.
[11] E. Angelini, A. Laine, S. Takuma, J. Holmes, and S. Homma, "LV volume quantification via spatio-temporal analysis of real-time 3D echocardiography," IEEE Transactions on Medical Imaging, vol. 20, pp. 457–469, 2001.
[12] Y. Jin, E. Angelini, P. Esser, and A. Laine, "De-noising SPECT/PET images using cross-scale regularization," Proceedings of the Sixth International Conference on Medical Image Computing and Computer Assisted Interventions, vol. 2879, no. 2, pp. 32–40, 2003.
[13] D. Donoho, "De-noising by Soft-thresholding," IEEE Transaction on Information Theory, vol. 41, no. 3, pp. 613–627, 1995. Http://www.bic.mni.mcgill.ca/brainweb/.
[14] D. H. Ballard and C. Brown, Computer vision. Prentice Hall, 1982.
[15] A. Laine and J. Fan, "Frame representation for texture segmentation," IEEE Transaction on Image Processing, vol. 5, no. 5, pp. 771–780, 1996.
[16] M.Kass, A.Witkin, and D.Terzopoulus, "Snakes: Active contour models,"International Journal of Computer Vision, vol. 1, no. 4, pp. 321– 331, 1988.
[17] R. O. Duda, P. E. Hart, and D. G. Stork, Pattern classification. Willey, 2000.
[18] Z. Wang, A. C. Bovik, B. R. Sheikh, and E. P. Simoncelli, "Image quality assessment: From error visibility to structural similarity," IEEE Transaction on Image Processing, vol. 13, pp. 500 512, 2004.
[19] L. Guo, X. Liu, Y. Wu, W. Yan, and X. Shen, "Research on the segmentation of MRI image based on multi classification support vector machine," Proceedings of the 29th Annual International Conference of the IEEE Engineering in Medicine and Biology Society, pp. 6019–6022, 2007.
[20] W. Souidene, A. Beghdadi, and K. Abed-Meraim. Image denoising in the transformed domain using non local neighborhoods. volume 2, pages II–II, 2006.
[21] C. Tomasi and R. Manduchi. Bilateral filtering for gray and color images. In ICCV '98: Proceedings of the Sixth International Conference on Computer Vision, page 839, Washington, DC, USA, 1998. IEEE Computer Society.
[22] D. Tschumperl´e. Curvature-preserving regularization of multi-valued images using pde's. In 9th European Conference on Computer Vision (ECCV'06), pages 428–433, Graz, 2006.
[23] J. van deWeijer and R. van den Boomgaard. Local mode filtering. In CVPR '01: IEEE Computer Society Conference on Computer Vision and Pattern Recognition, 8-14 December, Kauai, HI, USA, pages 428–433, 2001.
[24] G. Winkler, V. Aurich, K. Hahn, A. Martin, and K. Rodenacker. Noise reduction in images: Some recent edge-preserving methods. Pattern Recognition and Image Analysis, 9:749–766, 1999.

American Journal of Engineering Research (AJER)
e-ISSN : 2320-0847 p-ISSN : 2320-0936
Volume-03, Issue-01, pp-222-232
www.ajer.org

Research Paper Open Access

An Evolutionary Transition of conventional n MOS VLSI to CMOS considering Scaling, Low Power and Higher Mobility

Md Mobarok Hossain Rubel[1], Muhammad Minhazul Haque Bhuiyan[2]
[1]*Electrical and Electronic Engineering, Leading University, Sylhet, Bangladesh)*
[2]*(Computer Science and Engineering, Leading University, Sylhet, Bangladesh)*

Abstract: **-** This paper emphasizes on the gradual revolution of CMOS scaling by delivering the modern concepts of newly explored device structures and new materials. After analyzing the improvements in sources, performance of CMOS technology regarding conventional semiconductor devices has been thoroughly discussed. This has been done by considering the significant semiconductor evolution devices like metal gate electrode, double gate FET, FinFET, high dielectric constant (high k) and strained silicon FET. Considering the power level while scaling, the paper showed how nMOS VLSI chips have been gradually replaced by CMOS aiming for the reduction in the growing power of VLSI systems.

Keywords: **-** *Dielectric, Electrostatic, Low power Design, Moore's Law, Microelectronics, Nanowire, Nanotechnology, VLSI, Work function.*

I. INTRODUCTION

Early 1970 was an era when various methods of scaling MOS devices were explored and it was found that if the voltages with lithoographic dimensions were scaled, benefits of scaling like faster, low energy consumption and cheaper gates would be made easily. Semiconductor industry has been so successful that Semiconductor Industry Association (SIA) has published roadmaps [1] for semiconductor technology since 1992. The only objective of the roadmap incorporating the industries in many developed nations was to pursue with Moore's law [2], which is generally known as the doubling of transistors performance and quadrupling of the number of devices on a cheap every three years. As the MOSFET's power performance was improved, it literally followed the evolution of CMOS technology which was introduced in the late 1970. Power FET technologies use depreciated CMOS basics, with the leading edge with a time delay in the order of feature size as $1\mu m$, $0.8\mu m$, $0.5\mu m$, $0.35\mu m$, $0.25\mu m$, $0.18\mu m$ etc. The outstanding progress signified by Moore's law leaded VLSI circuits to be used in electronic applications like computing, portable electronics and telecommunications [3].

But it is a matter of disgrace that no hypothesis can last forever and recently scaling has been diverged from its ideal characteristics that were assumed before. The problem was found critical when it was seen that all device voltages can not scale; since kT/q does not scale and leakage currents are set by the transistor's threshold voltage, certainly there was a limit to how transistor's V_{th} can be made. Fixing V_{th}, changing V_{dd} simply trades off energy and performance.

Shrinking the conventional MOSFET beyond 50-nm-technology node requires innovations to circumvent barriers due to the fundamental physics that constraints the conventional MOSFET.

Unreliable power scaling, combined with previously applied aggressive performance scaling strategy has made power the most vital problem in modern chip design. Manufacturers can no longer focus on creating the highest performance chips just because of uncertainty whether the chips will dissipate more power. The limitations must be included with quantum mechanical tunneling of carriers through the thin gate oxide, quantum mechanical tunneling of carriers from source to drain and drain to the body of the MOSFET, control of the density and location of the dopant atoms in the MOSFET channel and source/drain region to provide a high on-off current

ratio and finally the finite subthreshold slope. These predominant limitations led semiconductor industries to pessimistic predictions of the significant end of technological progress [1].

The organization of this paper is first to address opportunities for the silicon MOSTFET that usually deviate from conventional scaling techniques like doping profile control and thin silicon dioxide gate dielectrics. Later discussions include high dielectric constant gate dielectric, metal gate electrode, double gate FET and strained silicon FET. Following the fact, the paper also shows the difference between conventional microelectronics technology and the more predefined nanotechnology.

II. EARLY MOSFETs AND THE DEVELOPMENT IN THE FIELD

The first generation of macrocell power MOSFET transistors were double diffused MOSFET (DMOS) which was introduced by International Rectifier into the market. This was simply known as planer power MOSFET. The second generation of macrocell technology TrenchFET introduced by Siliconix became popular in the 1990. This actually offered improved switch resistance. This technology was more advantageous than the previous one as it was designed for a drain voltage capability lower than 100V. However, soon the switching loss that was assumed to be very important in switch mode power supply (SMPS), remain the main hindrance. Transient response has become the burning question to be improved as well as the converter's switching frequency. Macrocell power MOSFET recently introduced by Texas Instruments, NexFETTM technology offers a specific R_{DSON} competitive to the TrenchFET which is in the order to reduce the input and Miller capacitances significantly. This new generation MOSFET reduces switching losses in SMPS applications and enables operation at high switching frequencies. It has been proved to be promising at 30V and below which is desirable for distributed bus architecture prevalent in today's end systems.

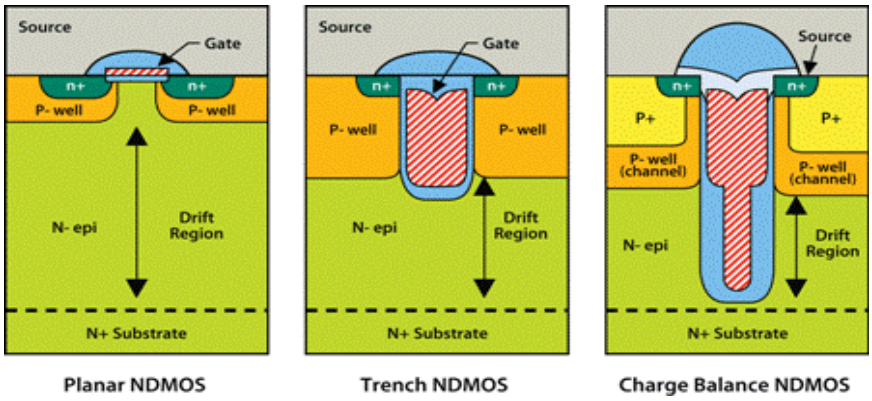

Fig. 1: Comparison of planar DMOS and TrenchFET device structures

III. SILICON GROWTH AND INSTABILITY AND MOSFET

The main problem of electron transport in SiO_2 was high field electron transport in polar insulators which was demonstrated by Karel Throbner in 1970 when he was pursuing his PhD thesis with Richard Feynman. Experimental observations do not show predicted run-away at $2-3MV/cm$ and as a result, Umklapp scattering with acoustic phonons keeps electron energy under control.

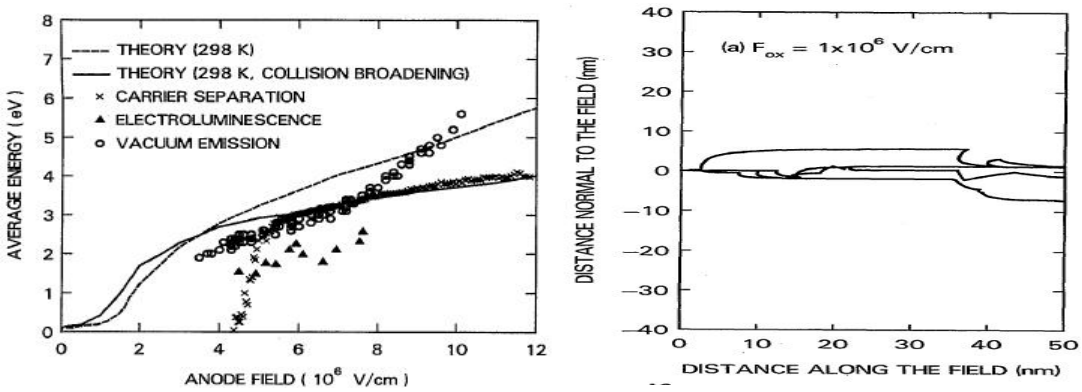

Fig. 2: LO-phonon scattering run-away connected to dielectric breakdown and Small polaron of time-of-flight experiments

Although there few drawbacks for which the consequences of injecting hot electrons in constant voltage scaled MOSFET were in the highlights. The two main problems understood the origin/spectrum of hot carrier and the nature/process of damage generation. Practical problems were also revealed pointing the unnecessary and expensive burn in and Wall Street big glitch in 1994. For some digital circuits, a figure of merit for MOSFET's for unloaded circuit is CV/I, where C the gate capacitance is, V is the voltage swing and I is the current drive of the MOSFET. For the loaded circuits, the current drive of the MOSFET is of paramount importance. Historical data indicate the scaling the MOSFET channel length improves circuit speed as suggested by scaling theory. Figure 1 shows how the injection of electrons affects the scattering runaway to dielectric breakdown. The off-current specification for CMOS has been rising rapidly to keep the speed performance high. While $1nA/\mu m$ was the maximum off-current allowed in the late 1990's, off currents in excess of $100nA/\mu m$ are proposed today.

Keeping in mind both CV/I metric and the benefits of a large current drive, we note that device performance maybe improved by 1) inducing a larger charge density for a given gate voltage drive; 2) enhancing the carrier transport by improving the mobility, saturation velocity o ballistic transport; 3) ensuring device scalability to achieve a shorter channel length and 4) reducing parasitic capacitances and parasitic resistances.

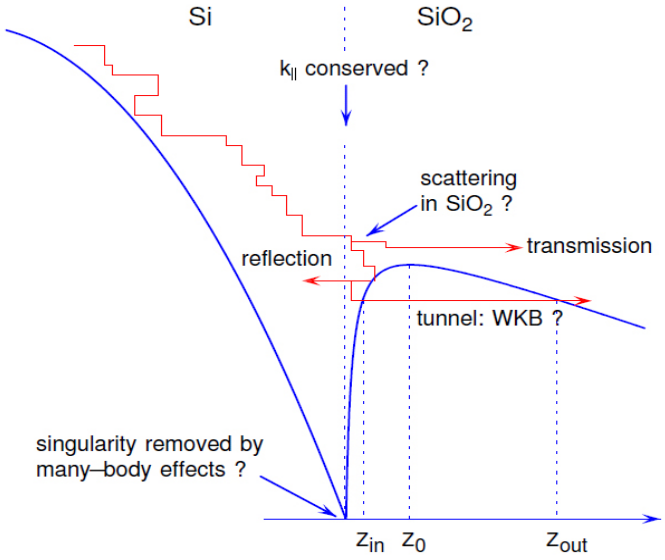

Fig. 3: Electron injection in SiO_2

IV. MOSFET GATE STACK

The reduction in the gate dielectric thickness is required for continuous device scaling. This has actually two different considerations: controlling the short channel effect and achieving a high current drive by keeping the amount of charge induced in the channel large as the power supply voltage decrease. It is the electrical thickness that is significant. The electrical inversion is determined by the series combination of three capacitances in the gate stack: the depletion capacitance of the gate electrode, the capacitance of the gate dielectric and the capacitance of the inversion layer in the silicon.

In the contrast, the direct tunneling current through the gate dielectric grows exponentially with decreasing physical thickness of the gate dielectric [7]. The tunneling current has a direct impact on the standby power of the chip and puts a lower limit on unabated reduction of the physical thickness of the gate dielectric. It is likely that tunneling currents arising from silicon dioxides (SiO_2) thinner than $0.8nm$ cannot be tolerated, even for high performance systems [8]. High dielectric constant gate dielectrics and metal gate electrodes were explored through the introduction of new materials. Figure 4 shows the depletion capacitance of the electrode, the capacitance of the gate dielectric, and the capacitance of the inversion layer in the silicon.

V. HIGH k GATE DIELECTRIC

A gate dielectric with a dielectric constant k substantially higher than that of SiO_2 (k_{ox}) will achieve a smaller equivalent electrical thickness (t_{eq}) than the SiO_2, even with a physical thickness (t_{phys}) larger than that of the SiO_2 (t_{ox}): $t_{eq} = (\frac{k_{ox}}{k})t_{phys}$

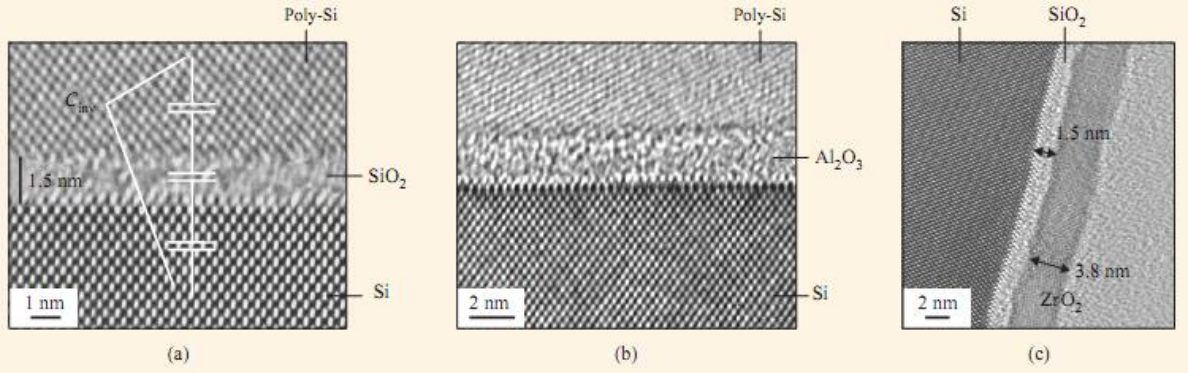

Fig 4. a) Transmission electron micrograph (TEM) of a conventional silicon dioxide (oxynitride) with a physical thickness of $1.5nm$. b) TEM of a $2.2nm$ Al_2O_3 with an equivalent electrical thickness of $1nm$. C) TEM of a $3.8nm$ ZrO_2 on an $1.5nm$ interfacial silicon dioxide. Adapted with permission from Gusev et al. 2001 IEEE.

It is not that simple to replace SiO_2 with a material having the same dielectric constant. Thermal stability with respect to silicon is more important consideration, since high temperature anneals are generally employed to activate dopants in the source/drain as well as the polysilicon gate. Although many binary and ternary oxides are predicted to be thermally stable with respect to silicon [9], recent research on high dielectric constant gate insulators have focused primarily on metal oxides such as Ta_2O_5, Al_2O_3, La_2O_3, HfO_2 and GdO_3 and their silicates [10]. Large silicon to insulator energy barrier height is exponentially dependent on the square root of the barrier height [11]. Hot carrier emission into the gate insulator is also related to the same barrier height [12]. The high k material should therefore not only have a large bandgap but also have a band alignment which results in a large barrier height.

VI. METAL GATE ELECTRODE

Metal gate electrode has numbers of advantages compared to the doped polysilicon gate used almost exclusive today. Due to the depletion of the doped polysilicon gate capacitance degrades for $0.4-0.5nm$ of the equivalent oxide thickness of the total gate capacitance at inversion. Considering the gate equivalent oxide of less than $1.5nm$ at inversion, substantial amount like sub $50nm$ CMOS is required. Thermal instability may require the use of a low thermal budget process after the gate dielectric deposition. From a device design point of view, the most important consideration for the gate electrode is the work function of the material. When the polysilicon gate technology has somehow got locked in the gate work functions to values close to the conduction band and the valence band of silicon, the use of the metal gate material opens up the opportuinity to choose the work function of the gate and the redesign the device to achieve the best combination of work function and channel doping. A mid gap work functions results in either a threshold voltage that is too high for high performance applications or compromised short channel effects since the channel must be counterdroped to bring the threshold voltage down. For double gate FET's where the short channel effects are controlled by the device geometry, the threshold voltage is determined mainly by the gate work function [13-15]. Therefore, for double gate FET, the choice of the gate electrode is particularly important.

The requirements of a low gate dielectric/silicon interface state density and low gate dielectric fixed charges imply that a damage free metal deposition process like CVD instead of sputtering is required. The deposition process must not introduce impurities like traces of the CVD precursor materials into the gate stack. The thermal stability of the metal electrode must withstand the thermal anneals required to passivate at the silicon/gate dielectric interface after the metal deposition as well as the thermal processing of the back end metallization processes. Moreover, it is likely to be expected to have a low resistivity at least similar to

conventional silicides such as $CoSi_2$, although this requirement may be relaxed by strapping the gate electrode of the proper work function with a lower resistivity material on top.

In the replacement gate technology [16], a dummy gate material is used for the formation of the self aligned gate to source/drain structure. As a result, the dummy gate material is removed and replaced with the desired gate dielectric and electrode [16]. In the other hand, the metal gate electrode may be etched in a way similar to the polysilicon gate technology. In addition, thermal stability issues from the source/drain dopant activation anneal must be addressed. In both of the cases, if metals with two different work functions are employed for n-FET and p-FET, respectively the integration of n-FET and p-FET in a CMOS process remains a challenge. Since 1) the deposition of the metals for n-FET and p-FET must be done separately and 2) one must find a way to strap the two different metals in a compact way to connect the n-FET and p-FET gates.

VII. DOUBLE GATE FET (DGFET) AND ELECTROSTATIC

In the early 1980's, double gate FET was introduced for the first time. Many groups explored the concept both experimentally and theoretically [18]. The Monte Carlo and drift diffusion modeling work by Fiegna at al. [17] and Frank at al. [19] clearly showed that a DGFET can be scaled to a very short channel thickness about 15nm while achieving the expected performance derived from scaling. Although the initial work focused on the better scalability of DGFET, current researches suggest that the scalability advantage may not be as large as previously envisioned [20, 21], but the carrier transport benefits may be substantial.

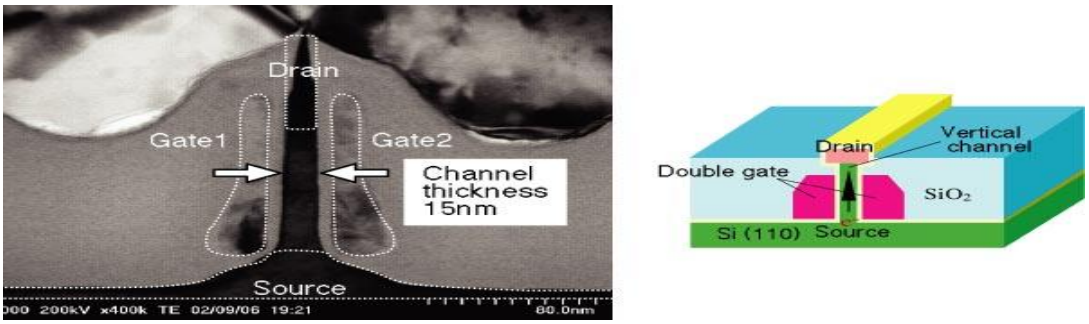

Fig. 5: Scaling- Electrostatic integrity: Double gate FET

DGFET has the unique features like [24] 1) short channel control effects by device geometry,a s compared to bulk FET where short channel effects are controlled by doping and 2) a thin silicon channel leading to tight coupling of the gate potential with the channel potential. These features provide potential DGFET advantages like reduced 2D short channel effects leading to a shorter allowable channel length to bulk FET and a sharper subthreshold slope like $60mV/dec$ compared to > $80mV/dec$ for bulk FET which allows for a greater gate override for the same power supply and the same off current and better carrier transport as the channel doping is reduced. When the channel doping is reduced, it relieves a significant scaling limitation due to the drain to body band to band tunneling leakage current. Hence, there is more current drive per device area, and this density improvement critically depends on the specific fabrication methods employed and is not intrinsic to the device structure. DGFET can be switched with its two gates simultaneously. The one gate can be switched only and another one is used to apply bias to dynamically alter the threshold voltage of the FET [22, 23]. A thin gate dielectric at the nonswitching gate reduces the voltage required to specify the threshold voltage and preserves the drain field shielding advantage of the double gate device structure. Moreover, a thinner gate dielectric also means extra capacitance that does not contribute to channel charge for switching. To evaluate the scalability of FET's, the concept of the "scale length" for a MOSFET is useful [24, 25, 26]. The electrostatic potential of the MOSFET channel can be approximated by analytically solving the 2D Laplace equation using the superposition principle and the short channel behavior can be described by a characteristic "scale length." [27]. By the amount of 2D short channel effects, the minimum gate length can be determined. From the figure 7, it can be seen that the trend of these 2D effects as the channel length is decreased with respect to the scale length of the MOSFET. With the same scaling formation, figure 6 shows the electrostatic integrity of Si nanowire transistors where 10nm Al_2O_3 blocking layer has been injected. SiO_2 layer is still present for the predetermined presence of nanowires expressing the 2D electrostatic behavior. With typical tolerance of 20-30% gate length variation, an L/λ of 1.5 is required. Conventional short channel effect theory [28] correlates the junction depth to the shorter channel effects. For DGFET, consideration of junction depth is moot, since the 2D electrostatic behavior is controlled by the thickness of the silicon channel instead of the junction depth.

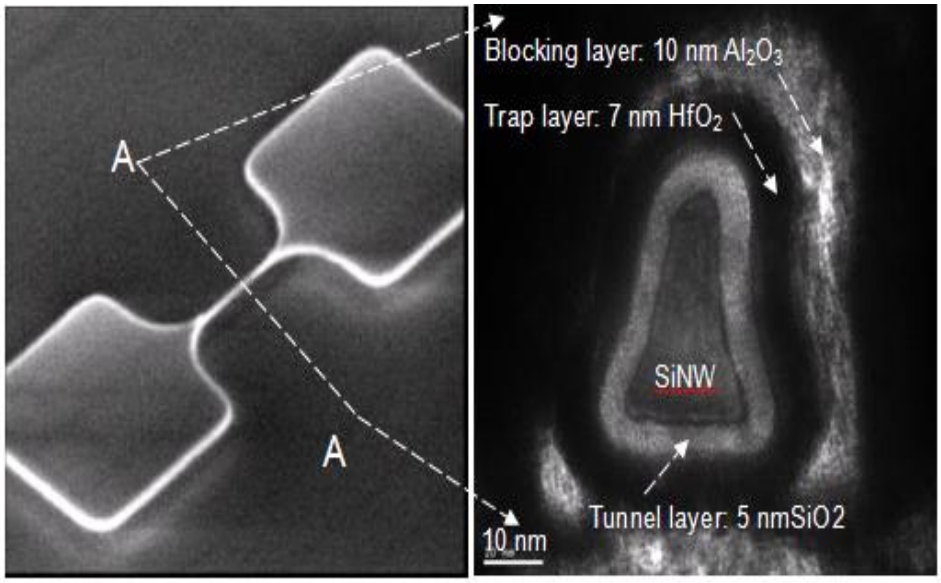

Fig. 6: Scaling- Electrostatic integrity: Si Nanowire Transistors

But the steepness of the source/drain junction is still an important consideration as in the case of bulk FETs [21]. Figure 7 illustrates the threshold voltage roll-off characteristics of the DGFET with lateral junction profile gradients of 2, 4 and 6 nm which is known as Gausian analytical profile.

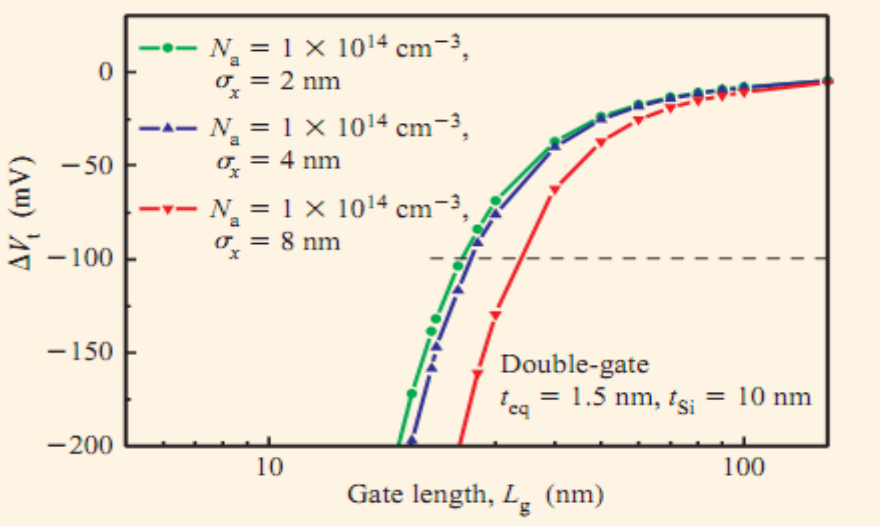

Fig. 7: Threshold voltage roll-off characteristics of double gate FET with different junction gradients, illustrating the importance of maintaining a sharp doping profile for DGFET even though the junction depth is no longer important for DGFET. The silicon channel thickness t_{Si} is 10nm and the equivalent gate dielectric thickness t_{eq} is 1.5 nm.

VIII. SCALING kT/q AND THE PROBLEM:

It took the first power crisis in the 1980 while CMOS technology was invented, caused VLSI chips to switch from nMOS which during the late 1970s was the dominant VLSI technology. During the period V_{dd} was fixed to 5V, and was not scaling with technology to maintain system compatibility. The depletion thresholds for the nMOS loads did not scale rapidly, so the current per minimum gate scaled only slowly. The power of the chips started to grow with the complexity and chips rapidly went from a watt to multiple watts with the final nMOS VLSI chips dissipating over 10W [29]. While the peak currents in CMOS were as large as nMOS, since they were transients that lasted roughly 1/20 of a clock cycle, a CMOS processor ran at roughly 10x lower power than a similar nMOS chip. Figure 8 uses microprocessor data to track CMOS technology scaling since

the mid 1980 to today. Through four generations of technology, from the $2\mu m$ generation in the early 1980s to the $0.5\mu m$ generation in the mid 1990s, the power savings from switching to CMOS was large enough that V_{dd} did not need to scale and was kept constant at 5V.

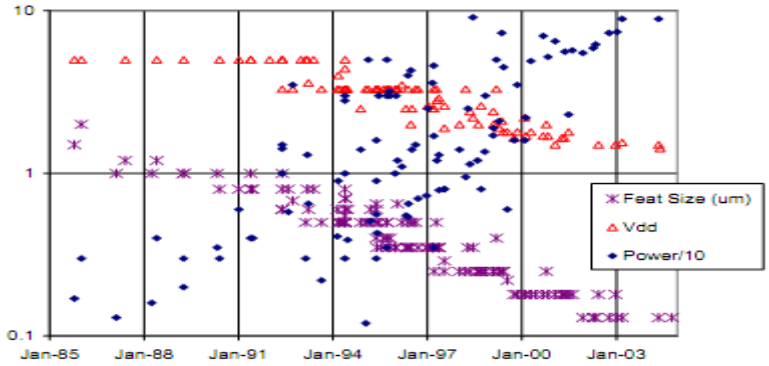

Fig. 8: Microprocessor V_{dd}, Power/10, and feature size versus year from 1994 to today V_{dd} has roughly tracked feature size

Power continued to increase during this time. Part of this increase in power was due to increase in area but power density increased by 30x during this period as well. This was due to the performance optimizations such as improved circuit design, better sizing optimization and deeper pipelines.

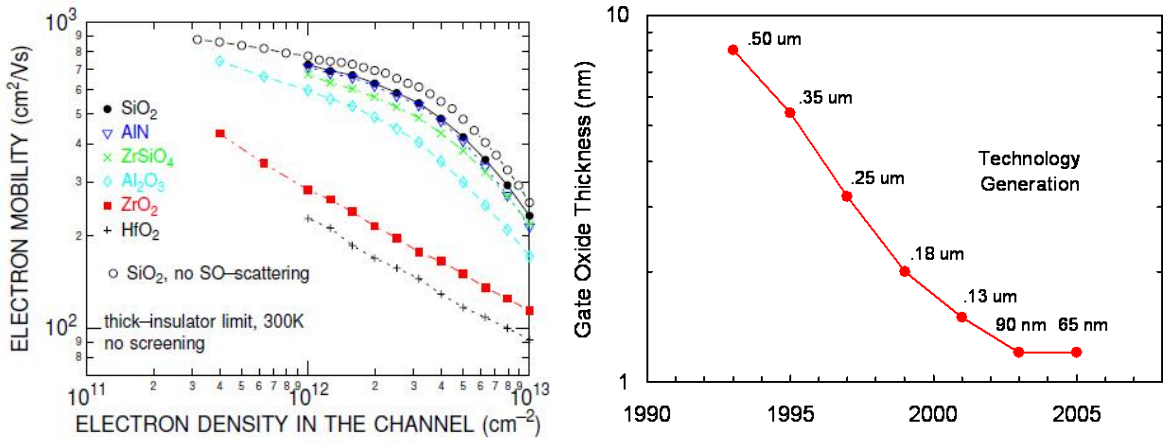

Fig. 9: a) Scaling- reduce leakage, low mobility in high k MOS systems scattering with interfacial optical phonons, b) Scaling- reduce leakage: gate oxide scaling at Intel

Figure 9 (a) illustrates the accepted value of off-leakage increasing for $I_{off} / I_{on} \approx 10^{-4}$ for the 32nm mode and the electrostatic integrity stands for junction leakage and gate leakage. For the gate leakage high k insulators such as HfO_2, ZrO_2, Al_2O_3 etc, electron mobility decreases as the electron density increases. Figure 9 (b) shows the variation of gate oxide thickness as the generations meet up their new challenges through years.

IX. INCREASED IMPROVMNETS IN SCALING AND HIGHER MOBILITY

The double gate FET carrier transport pointed out its importance of a low doped channel for carrier transport in DGFET. A higher carrier mobility and saturation velocity can be found through the choice of material for the FET channel. Fischetti and Laux [89] compared the performance of several semiconductors that have high carrier mobilities and saturation velocities including Ge, InP, InGaAs, GaAs etc. These materials provide a significantly higher carrier mobility which give only a moderate performance advantage over a lower mobility material such as silicon. The band structure which determines the density of states like the inversion capacitance [30] and the carrier scattering rates at high carrier energies are just as important as the carrier mobility.

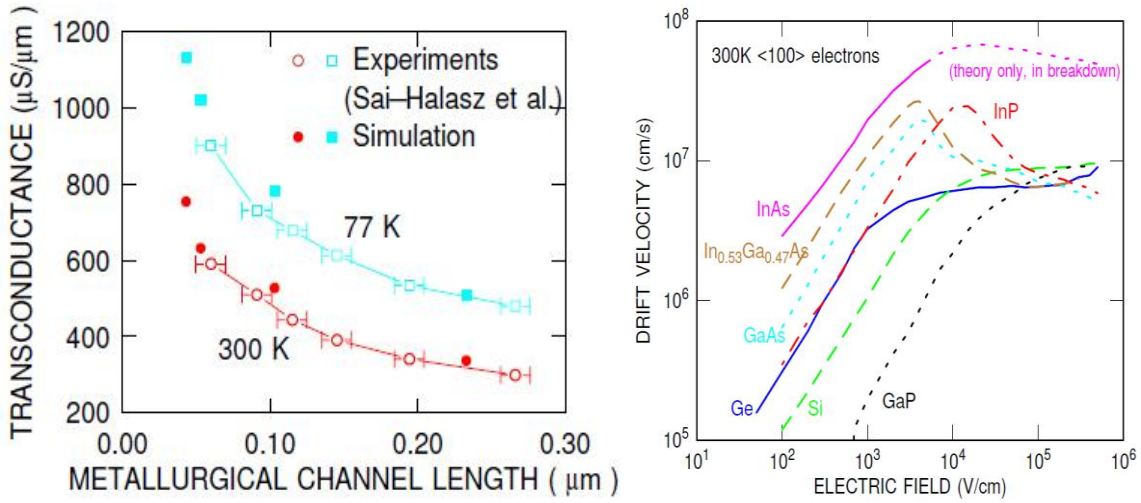

Fig. 10 a) Scaling improve performance – transconductance varies with the temperature with channel length, b) high velocity and low effective mass semiconductors

The carrier mobility in silicon under biaxile tensile strain is enhanced. [31-36]. The most commonly cited reason for electron mobility enhancement in strained silicon is that under the biaxile tensile strain, the sixfold degeneracy of the conduction band of silicon is lifted, raising the higher effective mass fourfold degenerate ellipsoids. The use of strained silicon provides a trustworthy trade off between moderate levels of performance enhancement over silicon an ease of fabrication and integration with silicon as compared to other higher mobility materials such as Ge, InGaAs, InAs, GaAs and InP that has been shown in figure 10 (b). Recent work provided promising experimental evidence that introducing the biaxial tensile strained silicon through a layer of relaxed SiGe may provide adequate performance gains for incorporation into conventional CMOS technologies.

Another improvement can be made by stretching the silicon atoms beyond their normal interatomic distance. This can be done by putting the layer of silicon over a substrate of silicon germanium (SiGe). In the silicon layer atoms align with atoms underlying silicon germanium layer, so the links between the silicon atoms become stretched thereby approach to the formation of strained silicon. Figure 11 shows the scaling improves performance with strained silicon that has been performed to make IBM 32nm strained silicon nFET on silicon germanium virtual substrate and Intel 45nm strained silicon pFET.

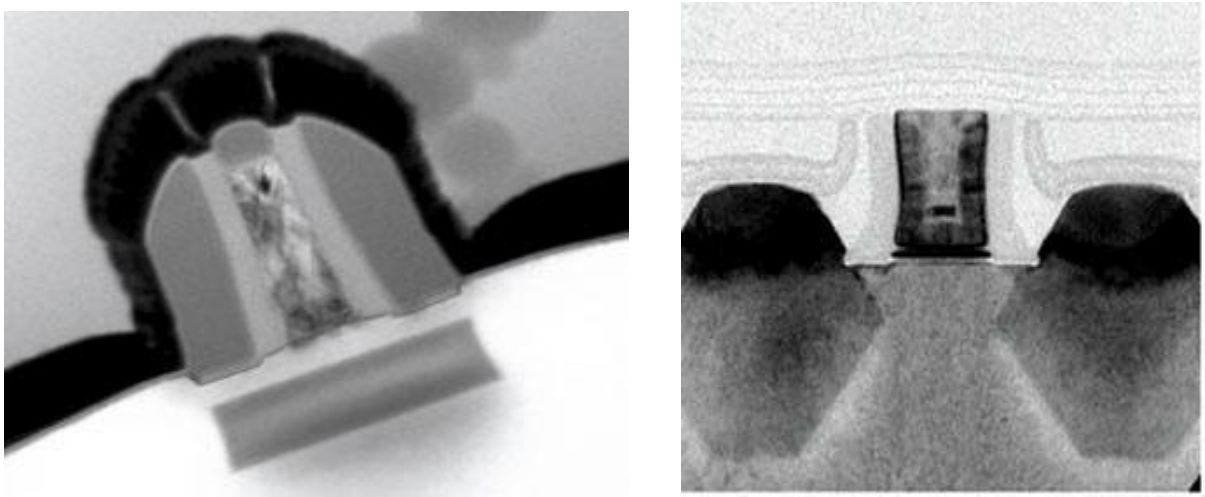

Fig. 11: Scaling- Improve performance: Strained Si a) IBM 32 nm strained (tensile) Si nFET on SiGe virtual substrate, b) Intel 45 nm strained (compressive) Si pFET with regrown SiGe S/D

X. OPTIMIZATION PERSPECTIVE

Let us assume that there is an attempt to try all the different ways to build a unit using all possible transistor sizes, circuit methods and supply and threshold voltages. The optimal design point depends on the

application constraints like maximum power or minimum performance requirements, but will always lie on the lower right edge of the feasible set that forms the Pareto optimal points.

Figure 12 (a) shows the result of plotting all of the solutions on a graph with performance on one axis and the energy consumed for a single operation on the other. Figure 12 (b) estimates the energy performance trade offs using published microprocessor data. While a complete optimizer does not exist, tools that optimize a subset of the parameters exist. The result of a tool is a sized circuit, and the optimal values of V_{dd} and V_{th} to use for the circuit. Table 1 shows the optimal result of the voltages with respective sensitivity.

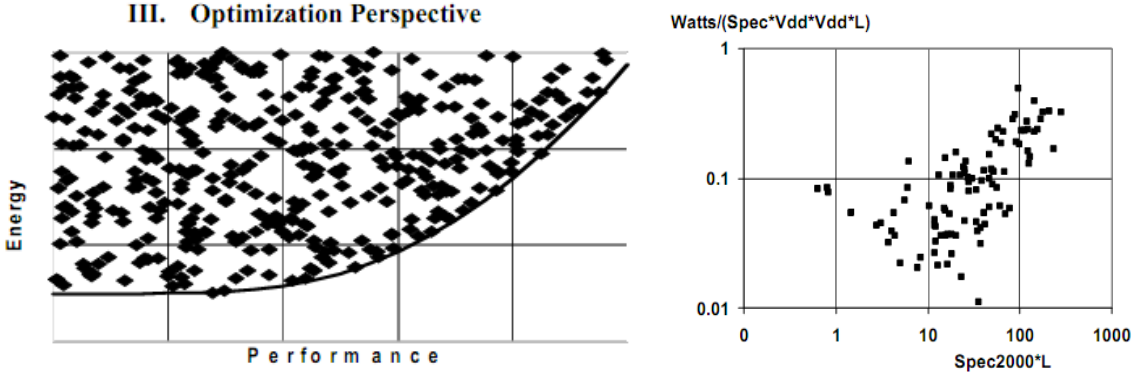

Fig. 12 a) The optimal curve is the boundary of the space of all possible solutions in the Energy Performance plane, b) Energy consumed per operation for CMOS processors built during the past 20 years.

V_{dd}	nMOS V_{th}	Sensitivity $\frac{\partial E}{\partial V_{dd}} \Big/ \frac{\partial Perf.}{\partial V_{dd}}$
550 mV	321 mV	0.031
700 mV	189 mV	0.194
850 mV	183 mV	0.7633
1 V	182 mV	1.8835

Table 1: Optimal V_{dd} , V_{th} and sensitivity for a 90 nm inverter at $80^0 C$ with 20% activity factor driving a fixed capacitive load.

XI. LOW POWER CIRCUITS AND ARCHITECTURE

A technique with moderate performance cost might be well suited for a low speed machine with a large marginal delay cost per unit energy, but would actually make the power higher if it was applied to a fast machine with a small marginal delay cost for lower energy consumption. The energy reduction technique generally involves problem reformulation or algorithmic changes that allow the desired task to be accomplished with less computation than before. These techniques can change the power required for a task by orders of magnitude [37], more than any other method. Before power became a critical problem, designers were rarely concerned whether a unit was doing useful work; they were only concerned about functionality and performance. The larger output reductions come from applying this idea at the system level. Subsystems often support different execution states, from powered off, to ready-to-run. Modern PCs use an interface called ACPI to allow the software to deactivate unused units so that they don't dissipate power [38]. The reducing of energy with no performance cost are techniques that improve performance with no energy cost. For applications with data parallelism, it is possible to use two functional units each running at half rate rather than using a single unit running a full rate. As the energy per operation is lower as one decreases performance, this parallel solution will dissipate less power than the original solution. Most of the remaining low power techniques are really methods of dealing with application, environmental or fabrication uncertainty, so the energy cost of variability should be considered.

XII. CONCLUSION

In the scaling, power has always been a concern. Rise in the power levels of nMOS VLSI chips in the 1980s caused the industry to switch to CMOS. In the early 1990, power became the issue of talking in designing

of CMOS; many approaches were there to reduce the growing power of VLSI systems. Energy efficiency of technology scaling, and system level optimization were the most successful approaches for reduction in the reduced computation. One thing should be kept in mind that power and performance are integrally connected for reducing chip power. By reducing the performance, power can be lowered but the technique is to lessen the energy without affecting the circuit's performance. Power growth must be addressed by application specific system level optimization. Unless they become impractical, conventional devices and materials will continue to be used. In this paper, we review the approaches to circumvent or surmount the barriers to device scaling. Discussing the new materials and new device structures, we showed innovations of materials for the gate stack and transistor channel. Double gate FET structure has also been shown. Gradually approaching the facts of dopant profile control and contact formation, unconventional to conventional technologies have been employed. In the silicon microelectronics technology, as nanotechnology may be seen successful, it is proven that it will be many years before nanotechnology can reach the level of maturity of the current silicon technology. As been seen, in the near future, there will be a gigantic shift of microelectronics to nanotechnology, hence, at present; it is somehow exposed by recent researches to make plenty of applications for the continuous technological progress.

REFERENCES

[1] *International Technology Roadmap for Semiconductors, 1999 Edition, Semiconductor Industry Association (SIA)*, Austin, Texas: SEMATECH, USA, 2706 Montopolis Drive, Austin, Texas 78741; http://www.itrs.net/ntrs/publntrs.nsf.

[2] G. Moore, "Progress in Digital Integrated Electronics," *IEDM Tech. Digest*, pp. 11–13 (1975)

[3] R. Dennard, F. H. Gaensslen, H. N. Yu, L. Rideout, E. Bassous, and A. R. LeBlanc, "Design of Ion-Implanted MOSFET's with Very Small Physical Dimensions," *IEEE, J. Solid State Circuits* SC-9, 256 (1974).

[4] B. Hoeneisen and C. A. Mead, "Fundamental Limitations in Microelectronics—I MOS Technology," *Solid State Electron*. 15, 819 (1972).

[5] S. Asai and Y. Wada, "Technology Challenges for Integration Near and Below 0.1 nm," *Proc. IEEE* 85, 505 (1997).

[6] H.-S. P. Wong, D. Frank, P. M. Solomon, H.-J. Wann, and J. Welser, "Nanoscale CMOS," *Proc. IEEE* 87, 537 (1999).

[7] S.-H. Lo, D. Buchanan, Y. Taur, and W. Wang, "Quantum-Mechanical Modeling of Electron Tunneling Current from the Inversion Layer of Ultra-Thin-Oxide nMOSFETs," *IEEE Electron Device Lett*. 18, 209–211 (1997)

[8] D. Frank, R. Dennard, E. Nowak, P. Solomon, Y. Taur, and H.-S. Wong, "Device Scaling Limits of Si MOSFETs and Their Application Dependencies," *Proc. IEEE 89*, 259 –288 (2001).

[9] HR. W. Keyes, "Fundamental Limits of Silicon Technology," *Proc. IEEE 89*, 227–239 (2001).

[10] K. Hubbard and D. Schlom, "Thermodynamic Stability of Binary Oxides in Contact with Silicon," *J. Mater. Res. 11*, 2757 (1996).

[11] E. Gusev, D. Buchanan, E. Cartier, A. Kumar, D. DiMaria, S. Guha, A. Callegari, S. Zafar, P. Jamison, D. Neumayer, M. Copel, M. Gribelyuk, H. Okorn-Schmidt, C. D'Emic, P. Kozlowski, K. Chan, N. Bojarczuk, L.-A. Rannarsson, P. Ronsheim, K. Rim, R. Fleming, A. Mocuta, and A. Ajmera, "Ultrathin High-k Gate Stacks for Advanced CMOS Devices," *IEDM Tech. Digest*, pp. 451– 454 (2001).

[12] J. Robertson, "Band Offsets of Wide-Band-Gap Oxides and Implications for Future Electronic Devices," *J. Vac. Sci. Technol*. B 18, 1785–1791 (2000).

[13] J. Hauser, "Gate Dielectrics for Sub-100 nm CMOS," in IEDM Short Course: Sub-100 nm CMOS, M. Bohr, Ed., *IEDM Tech. Digest* (1999)

[14] Y.-S. Suh, G. Heuss, H. Zhong, S.-N. Hong, and V. Misra, "Electrical Characteristics of TaSi, Ny Gate Electrodes for Dual Gate Si-CMOS Devices*," Symposium on VLSI Technology, Digest of Technical Papers*, 2001, pp. 47– 48.

[15] D.-G. Park, K.-Y. Lim, H.-J. Cho, T.-H. Cha, J.-J. Kim, J.-K. Ko, I.-S. Yeo, and J.-W. Park, "Novel Damage-Free Direct Metal Gate Process Using Atomic Layer Deposition," *Symposium on VLSI Technology, Digest of Technical Papers*, 2001, pp. 65– 66.

[16] A. Chatterjee, R. Chapman, G. Dixit, J. Kuehne, S. Hattangady, H. Yang, G. Brown, R. Aggarwal, U. Erdogan, Q. He, M. Hanratty, D. Rogers, S. Murtaza, S. Fang, R. Kraft, A. Rotondaro, J. Hu, M. Terry, W. Lee, C. Fernando, A. Konecni, G. Wells, D. Frystak, C. Bowen, M. Rodder, and I.-C. Chen, "Sub-100 nm Gate Length Metal Gate NMOS Transistors Fabricated by a Replacement Gate Process*," IEDM Tech. Digest*, pp. 821– 824 (1997).

[17] C. Fiegna, H. Iwai, T. Wada, T. Saito, E. Sangiorgi, and B. Ricco, "A New Scaling Methodology for the 0.1– 0.025nm MOSFET," *Symposium on VLSI Technology, Digest of Technical Papers*, 1992, p. 33.

[18] F. Balestra, S. Cristoloveanu, M. Benachir, J. Brini, and T. Elewa, "Double-Gate Silicon-on-Insulator Transistor with Volume Inversion: A New Device with GreatlyEnhanced Performance," *IEEE Electron Device Lett*. 8,410 (1987)
[19] D. Frank, S. Laux, and M. Fischetti, "Monte Carlo Simulation of a 30nm Dual-Gate MOSFET: How Far Can Si Go?," *IEDM Tech. Digest*, p. 553 (1992).
[20] D. Frank, R. Dennard, E. Nowak, P. Solomon, Y. Taur, and H.-S. Wong, "Device Scaling Limits of Si MOSFETs and Their Application Dependencies," *Proc. IEEE* 89, 259 –288 (2001)
[21] Y. Taur, C. Wann, and D. J. Frank, "25 nm CMOS Design Considerations," *IEDM Tech. Digest*, pp. 789 –792 (1998).
[22] I. Yang, C. Vieri, A. Chandrakasan, and D. Antoniadis, "Back-Gated CMOS on SOIAS for Dynamic Threshold Voltage Control," *IEEE Trans. Electron Devices* 44, 822 (1997).
[23] H.-S. Wong, D. Frank, and P. Solomon, "Device Design Considerations for Double-Gate, Ground-Plane, and Single-Gated Ultra-Thin SOI MOSFET's at the 25 nm Channel Length Generation," *IEDM Tech. Digest*,p. 407 (1998).
[24] R. Yan, A. Ourmazd, and K. Lee, "Scaling the Si MOSFET: From Bulk to SOI to Bulk*," IEEE Trans. Electron Devices* 39, 1704 (1992)
[25] K. Suzuki, T. Tanaka, Y. Tosaka, H. Horie, and Y. Arimoto, "Scaling Theory for Double-Gate SOI MOSFET's," *IEEE Trans. Electron Devices* 40, 2326 (1993).
[26] D. Frank, Y. Taur, and H.-S. P. Wong, "Generalized Scale Length for Two-Dimensional Effects in MOSFET's," *IEEE Electron Device Lett*. 19, 385 (1998).
[27] C. Y. Chang and S. M. Sze, Eds., ULSI Devices, Wiley, New York, 2000, Ch. 3
[28] S. M. Sze, Physics of Semiconductor Devices, Wiley, New York, 1981
[29] M. Forsyth, W.S. Jaffe, D. Tanksalvala, J. Wheeler, and J. Yetter, "A 32-bit VLSI CPU with 15-MIPS Peak Performance," *IEEE Journal of Solid-State Circuits*, Oct. 1987.
[30] S. Takagi, M. Takaytanagi-Takagi, and A. Toriumi, "Accurate Characterization of Electron and Hole Inversion-Layer Capacitance and Its Impact on Low Voltage Operation of Scaled MOSFETs," *IEDM Tech. Digest*, pp. 619 – 622 (1998)
[31] T. Vogelsang and H. R. Hofmann, "Electron Transport in Strained Silicon Layers on Six Gex Substrates," *Appl. Phys. Lett*. 63, 186 (1993)32.
[32] D. Nayak, J. Woo, J. Park, K. Wang, and K. MacWilliams, "High-Mobility p-Channel Metal-Oxide-Semiconductor Field-Effect Transistors on Strained Si," *Appl. Phys. Lett.* 62, 2853–2855 (1993)
[33] J. Welser, J. Hoyt, S. Takagi, and J. Gibbons, "Strain Dependence of the Performance Enhancement in Strained-Si n-MOSFETs," *IEDM Tech. Digest, pp*. 373– 376 (1994).
[34] M. Fischetti and S. Laux, "Band Structure, Deformation Potentials, and Carrier Mobility in Strained Si, Ge, and SiGe Alloys," *J. Appl. Phys*. 80, 2234 (1996).
[35] S. Tiwari, M. Fischetti, P. Mooney, and J. Welser, "Hole Mobility Improvement in Silicon-on-Insulator and Bulk Silicon Transistors Using Local Strain," *IEDM Tech. Digest*, pp. 939 –941 (1997)
[36] K. Rim, J. Hoyt, and J. Gibbons, "Transconductance Enhancement in Deep Submicron Strained-Si n-MOSFETs," *IEDM Tech. Digest*, p. 707 (1998)
[37] N. Zhang and R. Brodersen, "The cost of flexibility in systems on a chip design for signal processing applications," http://bwrc.eecs.berkeley.edu/Classes/EE225C/Papers/arch_design. doc, 2002.
[38] "*Advanced Configuration and Power Interface Specification*," Hewlett-Packard Corp., Intel Corp., Microsoft Corp., Phoenix Technologies Ltd., and Toshiba Corp., http://www.acpi.info/ DOWNLOADS/ACPIspec30.pdf, Sept. 2004.

American Journal of Engineering Research (AJER)
e-ISSN : 2320-0847 p-ISSN : 2320-0936
Volume-03, Issue-01, pp-233-244
www.ajer.org

Research Paper Open Access

Study of Physical-Spatial Effects of High-Rise Building

Mohammad Rahim Rahnama, Mohammad Hossein, HeraviTorbati,
(Case Study: Sajad Blvd. and N.-S. JanbazBlvd. Trading Corridors, Mashhad)
Associate Professor, Geography and Urban Planning Department, Ferdowsi University of Mashhad
Student of Ph.D. in Geography and Urban Planning, Ferdowsi University of Mashhad

Abstract: - The process of high rise building in Mashhad has been considerably increased during the last years. Despite of solving the problem of shortage of land and housing, this caused many problems in different environmental, physical-spatial, functional, social, and demographic aspects. In fact, loading of land-use intensity (plot ratio) affects different aspects of urban environment. In the present study, the aim is to discuss plot ratio and high rise building policies in Mashhad, and its physical-spatial effects. This study is conducted on Sajad Blvd. and North-South Janbaz Blvd. trading corridors, as a sample of tall buildings erected on the trading corridor in Mashhad, in which the growth of high rise building during the recent years in these two corridors has been strictly increased. Then, it analyzes plot ratio indices through documentary and library studies and field approach. Finally, SWOT method is used in order to evaluate advantages and disadvantages of high rise building in both corridors. The results from the studies conducted show that current plot ratio and high rise building policies, in terms of physical-spatial effects, have caused damages to access network and aesthetics, and only has a considerable financial contribution economically.

Keywords: -*Plot ratio, High Rise Building, Physical-Spatial System, Sajad and N.-S. Janbaz Trading Corridor.*

I. INTRODUCTION

Today, most of the cities in the world, especially metropolises, encounter the phenomenon of high rise building. The idea of high rise building was first developed in order to use the estates of the downtown, following paying attention to the city economy, because, on one hand, tendency to plot ratio and concentration of firms, had increased the demand for land in the downtown and, on the other hand, land supply was limited at this area of the city. As a result, increase in land-use intensity (plot ratio) was provided as a solution for increasing built area under use. In fact, the phenomenon of high rise building was a response to living and activity in cities with high rise building, and today in most of the world cities, high rise buildings are an integral part of urban life.

Erecting tall buildings in the modern way stated first in American metropolises and then in the Europe. After some decades, it emerged in developing countries as well. In Iran also, it is nearly half a century that we witness the presence of tall buildings. In fact, in addition to the human's responding to shortage of space, mentioned first, this phenomenon is a tool by which states are able to boast about their economic powers. However, towers began to take on residential role in addition to trading one, so that in the next decades, residential towers have had a more percentage of trading-office towers.

There are three viewpoints on the issue of high rise building; the advocates know tall building construction as a type of realism, and always emphasize its advantages. Indeed, they consider tall building construction as a response against shortage of urban lands, control of urban development, need for housing, and the available demand. On the contrary, the opponents of tall building construction believe that construction of such buildings reduces quality of urban life, and causes disadvantages for living in cities through trampling on the values and traditions. But, the third viewpoint on this issue is a middle position. The owners of this viewpoint accept high rise building under certain conditions (adapted from Golabchi, 2010).

Although construction of tall buildings in Iran is not the result of functional, cultural, social and even developmental need, and this has been in imitation of the world's metropolises, today, given certain conditions and the existing needs in some cities, one witnesses increasing extension of high rise buildings. This

phenomenon is extended in the western countries as more quickly as possible; but, in the West, while using high rise buildings, certain regulations and standards are applied, causing less negative effects. In Iran, however, in spite of responding to high demand for housing and, due to violating the necessary regulations and rules in the performance of high rise building phenomenon, this causes important problems in urban spaces. The fact is that the phenomenon of high rise building is not problematic, in itself, as we see in the western countries, there are less problems than Iran, in spite of more extension of this phenomenon over there. These problems in Iran are caused by the weakness of regulations (Azizi, 1999).

II. STATEMENT OF THE PROBLEM

Following physical extension of cities and the subsequent problems, addressing the phenomenon of plot ratio is high on the agenda of urban planning, as the most important solution of the problems of urban development. Here, plot ratio control is considered as an effective device for controlling the problems due to urban developments. Generally, the goals of plot ratio control can include establishing a logical balance between the activity produced by buildings and the surrounding spaces outside, as well as creating an environment with better quality. Increased plot ratio or vertical urban development in the recent years has become one of the most important strategies and urban plannings. However, this phenomenon, with several advantages, will have negative effects on qualitative indices of urban environment, in case of weak planning. Today, the indiscriminate and unplanned process of high rise building in Mashhad, has resulted in excess consequences and effects on different aspects of the urban environments. The aim of the present study is to identify physical-spatial aspects and components of urban environments influenced by high rise building. By identifying negative effects and examining positive effects of high rise building in terms of physical-spatial effects, this study takes step towards knowing this category as best as possible and assisting optimal use of this problem and, as a result, creating a high-quality environment.

1. Theoretical Fundamentals

1.1 Concept of Tall Building and Its Types

According to the definition of Ministry of Housing and Urban Development, high rise buildings refer to those with 6 stories or more. High rise buildings emerged in Tehran after the 1340s, and multiplied following the 1360s (Karimi, 2004).

Although high rise buildings in Iran refer to the buildings with more than 6 stories, on the strength of the regulations and codes of Iran Supreme Council for Architecture and Urban Planning, approved in 1998, this definition is used for the buildings having more than 12 stories, in accordance with Detailed Plan of Tehran, approved in 2007 (the original document of Detailed Plan of Tehran, approved in 2007).

Urban planners often know buildings with ten or more stories as tall buildings, and believe that a high rise building is characterized by a designed facing indicating number of its stories. In other words, an exhibition, factory and or any building with a high height is excluded from this definition. In Iran's domestic regulations, according to the executive guideline for building protection against fire (Journal 112 issued by the State Plan and Budget Organization), the minimum stories of a high rise building is known to be 8, although this figure can be increased to 12, given the advance in facilities (Shakeri, 2010).

The main problem of defining high rise buildings from urban perspective is that this definition is not adequately flexible, because "tall buildings" have a relative concept, which in addition to its heights, other things should be considered as well. For this reason, defining tall buildings with respect to urban problems can be a combination of qualitative and quantitative variables. For example, in some parts of the UK, tall buildings are defined depending on the height, their effect on the surrounding environment or major impact on the sky line. If a building has one of these conditions, it constitutes a high rise building. With these conditions, for example, a building with a middle height can be considered as a high rise building on condition that it has impact on the sky line or the surrounding environment (KarimiMoshaver, 2010).

The following criteria can define a tall building regardless of its height or stories:

1. Special land-use intensity (plot ratio): The ratio of total built area to area of the land on which building erected, is high relative to the neighbouring properties.
2. Mechanical systems (usually lift) are used for vertical movements.
3. Use of special construction and management systems and methods differs from the systems used in low rise constructions (Farhoodi, 2001).

High rise buildings have different types, which can be categorized based on diferent occupancies (residential, trading, office and …), size and scale (narrow, high, massive, elongated and …), distribution (single, cluster) and plot ratio (low rise, high rise and …) (Golabchi, 2010).

1.2 History of High Rise Building in the World

High rise building in the world is a phenomenon which has emerged since the late 19th century and in the early 20th century, when the first steps were taken towards producing skyscrapers about 1880-1900 in Chicago (Sadoughian, 1992). At the turn of the nineteenth century, steel structure began to substitute for heavy masonry structures in construction of multi-storey buildings. Coincided with the Industrial Revolution (accompanied by urbanization and rapid population growth), mass building was common.

Chicago School: Chicago School is a term used in the framework of evolutions made in the city of Chicago after the big fire occurred in this city in 1871. This school moved in line with modernism movement of the 19th and 20th centuries (Sadoughianm 1992). This school was among the first viewpoints encouraging high rise building and the use of tall buildings for residential purposes, and in its development process, it made International School of Modernism emerged (Poormohammadi, 2004).

Table 1. Theories of Chicago School (Adapted from Poormohammadi, 2004)

Theories of Chicago School	Use technical developments of construction
	Reject the old traditions in decorating buildings
	Use simple and pure forms and make the structure prominent

School of Modernism or Functionalism: This school which was emerged between the World War I and the World War II, and reached full flowering one decade after the World War II, played more role in vertical growth of cities during the 20th century than other intellectual movements, but was criticized.Aspirations of the followers of this school are manifestedinthe AthensCharter. It can be said that in the Modernism, high rise building and separation of performances are the main base of urban planning (Poormohammadi, 2004).

Table 2. Theories of School of Modernism (Adapted from Poormohammadi, 2004)

Theories of School of Modernism	Generalities in urban planning
	Spatial separation of urban functions
	Economic saving in construction, mass building, and low land use
	Emphasize high rise building to achieve sunlight, fresh air and green space
	Use tall buildings for different occupancies (trading, office, residential)

School of Human Spatial Planning or Humanism: As urban planning experiences of Modernism were developed and criticized, the necessity of considering the human and his/her social relations in the process of planning was taken into account, thus making emerged an approach known as Humanism or School of Human Spatial Planning. The followers of this school believe that urban planning is a thing beyond architecture and an interdisciplinary activity.

Mumford and Jacobs are two followers of this school, whose studies indicate that desired plot ratio from the viewpoints of humanists is a condition between suburb-oriented status and excessive concentration of urban centers, so that it can meet the needs of balanced and organic human. This approach is derived from culture-oriented thinking about city, as seen in the works of Cit, Havard, and Geddes as well (Poormohammadi, 2004).

Table 3. Theories of School of Humanism (Adapted from Poormohammadi, 2004)

Theories of School of Humanism	Limit city size and population density to improve social relations
	Organize distributed suburbs into a balanced community
	Decreased plot ratio of metropolis through vacating part of population and use its place for service occupancy
	Create a compressed urban texture to provide diversity and improve urban performance

Postmodernism: Extended criticism of the modernists' performance in different cultural, social and environmental aspects resulted in the movement of Postmodernism in different sciences including urban planning. This movement attempts to review the principles of modernism to improve environmental quality of cities. In fact, in postmodernism, two historic culture-oriented and future-oriented approches, which, with criticism of industrial city emerged and sought to solve urban problems from two different perspectives, approached each other and reached a relative equilibrium (Poormohammadi, 2004).

Table 4. Theories of School of Postmodernism (Adapted from Poormohammadi, 2004)

Theories of School of Postmodernism	Value the historic continuity of urban space and finally emphasize street, square, and short buildings
	Emphasize partial organizing cities rather than fully designing them
	Underline the importance of mixing land uses
	Encourage pedestrian movement and relatively control vehicles in urban space

After postmodernism, when sustainable development approach was posed in the late 20th century, theories of the postmodernists continue in the framework of sustainable urban development theory, with highlighting the role of environmental issues (Poormohammadi, 2004). The discussions about sustainable urban development made more coherent the viewpoints on evolution and improvement of modern city, resulting in new ideas appeared in urban planning. Among these ideas, the idea focusing on increased urban plot ratio and using it in urban planning is the idea of "compressed city", attempting to provide more sustainability through developing the components of physical form of the city (Ghorbani, 2004).
Although, the idea of compressing urban spaces in the framework of urban planning thinkings dates back to more than a century, what is posed in the process of compressing has two essential differences with the first theories:

1. Economic-social and environmental results of energy generation and consumption for development, were not properly understood in the first approaches of the followers of compressed city.
2. Global effects and effects of globalization of environmental issues were not posed.

Therefore, it can be said that compressing in the last decade is a response to going to extremes of high rise buildings and suburb-oriented low rise buildings, to achieve an equilibrium based on social and environmental values in urban planning (Poormohammadi, 2004).

1.3 History of High Rise Building In Iran

The phenomenon of high rise building in Iran commenced from the middle current century in Tehran and then, became practical in metropolises, and gradually spread to other parts of the country. The history of modern high rise building in Iran dates back to about the 1330s. During these years (1949-1951), the first 10-storey high rise building was constructed in western style in Jomhouri St. (the former Nader St.), Tehran. The structure of this building was made of reinforced concrete. The building was equipped with two lifts, still being used (HosseinzadehDalir, 2011). During the years of the 1350s, construction of high-rise residential buildings, mostly in the north and north west of Tehran flourished. Location and type of these buildings show that the policy on encouragement of high rise building resulted in increased price of high-rise residential buildings for low-income or middle-income classes. With the outbreak of the Islamic Revolution, high rise building stopped for more than ten years. There was a new wave of high rise building during the late 1360s, due to increased price of land and when Tehran Municipality began to sell land-use intensity (plot ratio), coverings all parts of Tehran (Safavi, 2001).

1.4 Positive and Negative Effects of High Rise Building

Like other human-made artifacts, high rise buildings have both positive effects and advantages and negative effects and disadvantages obtained from their construction in urban environments. Negative effects of high rise building can be studied in different environmental, traffic, social, aesthetical and … categories. In addition, positive effects of tall buildings can be known as such things as reduced cost, visual aspects and … In the following tables, positive and negative effects of high rise buildings are classified and provided:

Table 5. Negative effects of high rise building (adapted from HosseinzadehDalir, 2011)

Negative Effects of High Rise Building	
Environmental	- Destroy nature and environment in case of incorrect location - Environmental pollutions due to vehicle congestion - Tall buildings block fresh air circulation and sunlight
Traffic	- Increased traffic volume due to increased plot ratio of tall buildings - Increased distance between place of occupants, because of erected tall residential complexes as mass building projects
Social	- Decreased health social relations among occupants of tall buildings due to their scale and nature - Social degeneration, social isolation and alienation in tall residential complexes
Cultural	- Incompatibility of ideology and culture of occupants of tall buildings with their spaces - Spatial limitation of tall buildings prevents activities rooted in Iranian Islamic culture from accomplishing - Priority of high rise buildings over low rise ones

Safety	- Vulnerability of tall buildings relative to low rise buildings against accidents such as earthquake - In cases where such accidents as fire occur, the fire will spread - Possibility of accidents including falling down the stairs and falls from height
Health	- Pressure from weight of tall building breaks soil layers and interferes sewage networks with groundwater supplies - Existence of car parking lots in a closed space in tall buildings makes pollution stable.
Aesthetical	- Erection of tall buildings near each other prevents natural perspectives such as sunrise and sunset, from being seen from low rise buildings - Mass building of tall blocks causes the environment to be drab

Table 6. Positive effects of high rise building (adapted from HosseinzadehDalir, 2011)

Negative Effects of High Rise Building	
Reduced Cost	- Save costs of construction and reduced cost of residential units - Use tall buildings decreases land price per capita, street cost per capita, and cost of underlying facilities - Compressed cities decrease volume of infrastructures of cities and reduce costs
Perspective	- Due to visual highlight, high rise buildings can help orientation of cities - Possible creation of cozy and relaxed atmosphere far from crowdedness; urban perspective
Prevention of Horizontal Extension	- Decreased suburban development and decreased damage to environment - A suitable model for housing in cities facing limited physical horizontal extension
Social	- Possible creation of suitable space for improving social facilities and urban services

1.5 Criteria for High Rise Buildings

Although designing a tall building is the final result of a complicated process whose elements interact with each other, and multiple factors including cultural, social and economic features affect it, by compliance with the principles and criteria obtained from fundamental and applied studies on architectural design, structure and urban planning (if accompanied by formulating and implementing the policies needed in other areas), the possibility of properly using tall buildings is provided. In general, given special conditions of the current century, proper and conditional use of tall buildings can be considered a realistic and desired solution for accommodating people and meeting other needs related to social and economic activities in metropolises (Golabchi, 2001). In fact, tall buildings can properly satisfy, under appropriate conditions, the needs and necessities of the environment, if some main criteria are considered when planning and desiging them. General criteria with respect to erecting tall buildings can be classified as shown in the following table:

Table 7. Criteria for Tall Buildings (adapted from English Heritage, 2007)

Relationship between building and location conditions	Includes natural topography, scale, height, urban texture, its facing in street, and quality of construction, open space, river and waterway, important facings, perspective and view, and its effect on the horizon line. Tall buildings must have a correct relationship with the factors associated with topography and other buildings.
Effect on historic texture of city	Historic buildings, sites, urban facings, and horizon line should be preserved. Design of tall buildings do not must affect historic buildings.
How to access to vehicles	Includes limitations of air transportation, particularly public transportation capacity, quality of site routes and possible improvement of conditions. Existence of vehicles due to continuous and excess use, specially with respect to tall buildings is very important.
Quality of building in terms of architecture	Includes scale, frame, size, proportion, design, materials, and its relationship with other structures. High rise building, due to its effect on the horizon line, is very important. Basic design of a tall building also influences the appearance of the street and the surrounding perspectives.
Role of building in space and public services	This means internal and external development of a tall building including the multi-purpose nature of the building particularly in ground floor and its capacity as a part of public domain. This development should interact with other buildings of the street, and help safety, diversity, life, social interaction and its sense.
Effect on the surrounding environment	Includes micro climate, its effect on other buildings, facing of the building at night, vehicles and environment and welfare of the neighbors.
Effect on permeability	A site and a more extensive area, an opportunity for availability and in a suitable place will improve the situation and more extensive perspective of the city.

III. METHODOLOGY OF RESEARCH

The present study is of analytic-descriptive type, and given the descriptive objectives, a documentary method is used. The documents and evidence in local organizations including urban development plans, satellite images, books, and specilized journals have been the most important sources used by this strudy.
SWOT method, as one of the most suitable techniques of planning and data analysis, is used in order to evaluate physical-spatial effects of high rise building. SWOT method includes environmental examinations (both internal and external environments), formulating a strategy (long-term or strategic planning), implementing the strategy, evaluating and control (Chase, 2001). This model is one of the strategic tools for comparing in-house strengths and weaknesss with opportunities and threats outside the organization, as an abbreviation forthe words of Strength (S), Weakness (W), Opportunity (O), and Threat (T) (Earabi, 1384: 12).
By investigating the principles and criteria of urban planning in high rise building, the factors affecting determination urban plot ratio and the regulations and codes of tall buildings, and by overlapping their components, the main determinants of the study approach were obtained, each having some sub-criteria, as shown in Table 8.

Table 8. Determinants of Physical-Spatial Effects of High Rise Building (Author)

Determinants under Survey		
Physical-Functionals	Aesthetical	Access
Human Scale	Sky Line	Relation with occupancies and service activities
Mixed Occupancies	Proportion	Access to parking
Number of Stories		Traffic Volume
		Passage Width

The area study is Sajad Blvd. and N. Janbaz Blvd. corridors, located at the western middle area of Mashhad. Physical-spatial effects of high rise building in these two corridors will be discussed in detail in the framework of the above criteria.

Introduction to the Area Study:

In terms of antiquity and history, Mashhad is a 1200-year-old city, whose special religious place and spiritual richness of the Holy Shrine of Imam Reza (peace be upon him) in the Islamic world and national and international applications cause Mashhad to annually receive millions of pilgrims and tourists. The dominant economic role of Mashhad is tourism, by which about 15 to 20 millions of pilgrims and travelers per annum come to Mashhad, playing an important role in economic, social, cultural, and physical life of this metropolis.
High rise building in Mashhad, during the recent decade, has grown increasingly, influencing the tendencies for construction in the city. Currently, the average stories of a building in Mashhad ranges from 2 to 3. High complexes in the form of tall buildings with more than 7 stories and or more than 20 meters are considered high rise buildings, which are located sometimes in cluster (e.g., Alton Trading Tower and Baran Residential Tower) and or in localized form in an axes (trading towers located in Sajad Blvd.).

IV. INTRODUCTION TO THE CORRIDORS UNDER SURVEY

(Sajad Blvd., N. and S. Janbaz Blvd. Trading Corridors)

Sajad corridor and N. and S. Janbaz one locate at districts 1 and 2, Mashhad, respectively. These two corridors are connected each other through Janbaz square. The area study in this research is Sajad-Janbaz corridor, as one of the most important trading corridors in Mashhad, on which characteristic elements such as Proma Trading Complex and Caspian Mode Trading Complex locate, that serving in urban scale. The first core of tower making on north Janbaz corridor begins from Proma Trading Complex (around Janvas Sq.). This process, during the recent years, is growing increasingly, so that construction policies in this area move towards construction of tall trading and office towers. New constructions have been made in the form of high rise buildings, especially on the edge of these corridors, because of shortage of undeveloped land and expensive land, as the most important reasons. On the other hand, increased economic role and performance of the area in Mashhad decrease residential construction and increase construction of new occupancies (office and business use).

Most of the area study has a checked regularly texture. Grading plots in this areas is middle, mass and space have a linear order, and networking the passages is also regular and in checkerboard shape. Occupation surface of the plots in trading towers in Sajad Blvd., sometimes reach to 80% even. In the area study (Sajad-Janbaz corridor), powerful presemce of Azadi Blvd., as one of the important accesses of Mashhad, with a high traffic load, is obviously seen. Janbad and SajadBlvds., as two main corridors of Mashhad, play the main collecting and distributing role, that connect with Azadi and Ferdowsi streets. The role of Janbaz and Sajad streets is their social availability, which is implemented due to business uses.

V. ANALYSIS OF FINDINGS

Explain and analyze the determinants discussed in the study:

4.1 Physical-Functional:

4.1.1 Human Scale: Scale is a combination of the ratio of height to street width, relative distance of human from building, permeability in textute and sense of glory or glandeuror personal intimacy with the space. Therefore, this scale depends on intensity of plot ratio because high rise spaces have usually taller buildings (Seddigh, 2010).

The area study (Sajad corridor and Janbaz corridor), due to proper width of both corridors, high rise buildings do not prevent human scale from being observed and even, the same high rise buildings in summer and the heat from it cause shading and climatic welfare alongside both corridors, and increase individuals' feeling of being present, strengthening pedestrian-orientation.

4.1.2 Mixed Occupancy: In the area study, most of high rise buildings have business uses, including banks, trading complexes, shopping centers and … It can be said that, currently, in these complexes and high rise buildings, there is no mixed occupany, and indeed, they all are single-purpose.

Fig. 1 Pasargad Bank, Sajad Blvd.

Fig. 2 Proma Trading Complex, Janbaz Blvd.

4.1.3 Number of Stories: Status of number of stories in the corridors under survey is shown in the following diagram. The studies show that in Sajad Blvd., buildings with 4 to 8 stories have 37% of total buildings in this area, while in Janbaz Blvd., high rise buildings are formed as spot, and most of high rise buildings are being constructed.

Fig. 3 High Rise Buildings Being Constructed in Janbaz Blvd

Fig. 4 High Rise Buildings Already Constructed in Sajad Blvd.

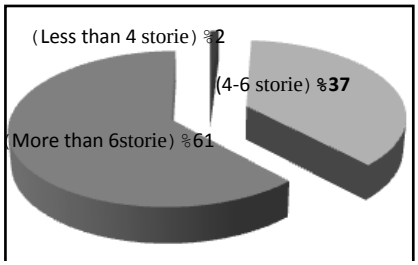

Diagram 1. Percentage of Number of Stories of Janbaz's Buildings

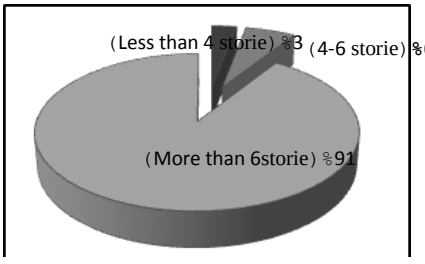

Diagram 2. Percentage of Number of Stories of Sajad's Buildings

4.2 Aesthetics:

`4.2.1 Sky Line: Sky line, which constitutes one of the basic and important elements of a street landscape, refers to separation limit of pyhsical wall of the street from the sky. This physical element includes total volumes existing in combined roofs of buildings and or is visible in combination with taller buildings located behind the wall. Physical element of the sky line manifests form combination in street body and presents order or diversity in street landscape (Armanshahr Consulting Engineers, 2007).

Fig. 5 Sajad's Wall

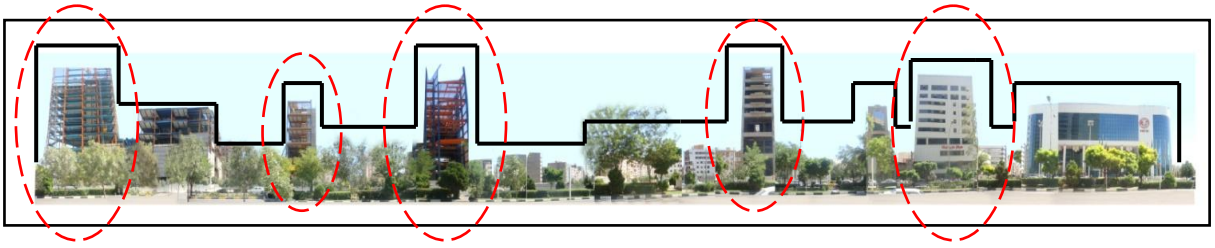

Fig. 6 Janbaz's Wall

As shown by the panoramic images provided, in Sajad Blvd. most of buildings have 2 to 3 stories, and the existence of tall buildings in this corridor causes fractures in sky line of the walls. For example, however, in Fig. 6, the symmetry among high rise buildings is evaluated to be positive in examining sky line of the wall. In the panoramic image of Janbaz's wall, it is also seen that the existence of high rise buildings already constructed and or being constructed beside low rise buildings has caused a sky line with many fractures, which have been decreased in some parts through planting trees.

4.2.2 Visual Proportion: Body of each street forms the original part of the street body. In fact, this element specifies street space and gives it environmental concept. Facings can be admired in terms of visual richness, and in different distances from building, the eyes' need for seeing should be met. In various scales, the details should be taken into account. Design elements in the wall include theme, rhythm,similar row, continuity, street architecture, proportions, turn, and corner (Armanshahr Consulting Engineers, 2007).

Fig. 7 Disproportion of Extensions

Fig. 7, disproportion in billboards installed on the building and the disproportion between them in terms of color and dimensions also result in visual disturbance. It should be considered that in high rise buildings, due to their height, they usually have different activities in their stories. So, it should be noted that

any extension and billboard installed on them with respect to size, color and location, must be proportioned and create no sense of irregularity for pedestrians.

5.3 Access

Criterion of communication networks can be analyzed in the framework of different things such as spatial relation of the network with occupancies and activities as well as traffic issues. Effects of changed plot ratio and population density on communication network and access, due to high rise building construction can be studied in traffic volume, traffic jams and communication networks per capita. The relationship of any network with land uses and activities can also be of the essential issues of this criterion (Mashhoudi, 1996).

5.3.1 Traffic Volume: high rise buildings will result in population density. This population is the people living in or passing in a certain hour peak. If the tower is residential, the population is the occupants and, if it is trading or office, presence of the people in towers will be passing and at a certain time.

In the area study, most of the towers located at Sajad Blvd. and Janbaz Blvd. have some clients at a certain time peak. These clients themselves are the reason for increased traffic volume at certain times. In Sajad Blvd., traffic jamsexistein Bozorgmehr-Sajad intersection, and the existence of tall buildings such as Caspian Mode, Tandis, and Bank Melli attract many persons from all parts of the city, which in turn are the main reasons for traffic in this area.

In S. Janbaz Blvd., there is no traffic jam, and traffic is flowing, while in N. Janbaz Blvd., there is traffic jam at peak hours (in the evening and at night) in front of Proma Trading Complex, because of high volume of vehicles of the users ofProma Trading Complex.

Fig. 9 High Volume of Traffic in Sajad Blvd. (Source: Author)

5.3.2 Access to Parking Lot: One of the important criteria for studying access is proper access to parking. In the area study (Sajad Blvd.), the existence of trading and office towers doubles this necessity, because the users of these towers often face difficulties with parking their cars. Because most of trading and office towers in Sajad Blvd., such as Bank Melli, Tandis Trading Tower, Bank Pasargad, Caspian Mode Shopping Center lack public parking lots, and their users have to use fringe parking (with No Parking sign or Prohibitory Traffic sign) or use Sajad's subsidiary streets for parking purpose.

In Janbaz Blvd., as the second area study, the existence of Proma public parking provides the possibility of access to public parking for the users.In the other parts of Janbaz Blvd. such as Kondoz and Poonak take-aways (fast food restaurants), there are public parking lots with a low capacity of vehicles. There are still fringe parking lots, often problematic.

Fig. 10 Fringe Parking in Sajad Blvd. (Source: Author)

5.3.3 Width of Passages: Given type and function of the land uses around, width of passages should be in proportion with them to prevent such problems as traffic congestion. In Sajad Blvd., the land uses adjacent to the main street are often trading complexes and offices, as tall towers distributed all over Sajad Blvd., while the width of Sajad Blvd. is 45 m, with a middle island for separation round trips in the street. Width of Sajad Blvd. relative to type and scale of the adjacent land uses, often serving extra-local level and the city surface, is

proportional, and in cases where vehicles fail to stop unnecessarily and do not use fringe parking, ir can be said that there will no traffic jam in the street, and the traffic from Khayyam Crossing to Azadi Blvd. will be flowing easily. Janbaz Blvd. also is 50 meter wide. The land uses adjacent to it are all trading complexes and offices, scale level of which is extra-local. Example is Proma Trading Complex. The studies suggest that the width of Janbaz Blvd. is proportional to the land uses adjacent to it.

Drawing 1. Width of Passages in the Area Study (Source: Author)

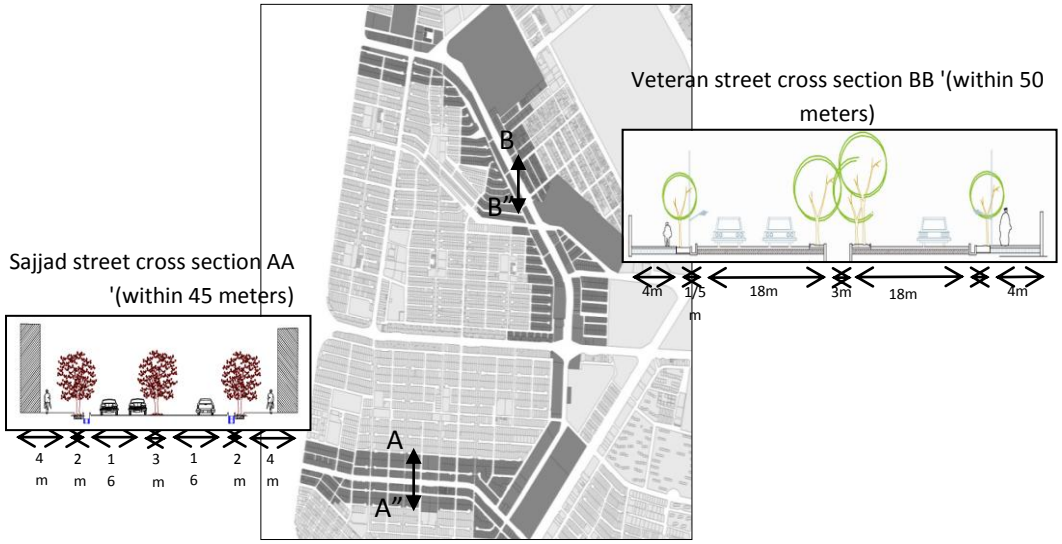

Summarizing

Given the above, it can be said that high rise building in the area study (Sajad and Janbaz) has many negative and positive effects. In order to achieve these effects, SWOT tables are used, so that indentifying strengths and weaknesses of high rise building in the area, ongoing opportunities and threats can be presented.

Table 2. Analysis of Strengths, Weaknesses, Opportunities and Threats (SWOT) in the Area Study (Source: Author)

	Strength	Weakness	Opportunity	Threat
Physical-Functional	1. Follow human scale for the purpose of proportion of passage width 2. Desirable proportion (one by one) of main streets and high rise buildings 3. Mixed land uses alongside Janbaz Blvd. (existence of high rise buildings with business and office use) 4. Proportion of number of stories (high rise buildings) in Janbaz corridor	1. Visual disturbances due to disproportion of number of stories in Sajad Blvd. 2. Lack of mixed land use in high rise buildings and their sigle function 3. Lack of following human scale and improper capture in Sajad's subsidiary streets.	1. Possible use of furniture and accessories in order to adjust human scale in subsidiary streets of the area 2. Possible creation of mixed occupancies in high rise buildings 3. Possible adjustion of status of number of stories through adjusting plot ratio in the area studies	1. Increased single functional tall buildings 2. Increased captured in subsidiary streets due to non-systematic growth of high rise building in the area 3. Increased visual disturbances in cases where disproportion process continues in number of stories of Sajad Blvd.

Aesthetical	1. Readable corridors because tall buildings are indicators 2. Tall buildings in both corridors are often of high quality, because they are new-built.	1. Fracture in sky line due to high rise buildings 2. Lack of visual continuity in walls because of disproportion between color and type of materials used in buildings 3. Lack of equilibrium and rhythm and joint row in the wall because of not neutral line moves 4. Existence of uncoordinated billboards on high rise buildings in Sajad	1. Possible decrease of sky line fractures through planting trees in Sajad Blvd. 2. Possible creation of visual continuity in the wall through proportion of materials used 3. Establish a unit system for installing accessories on tall buildings	1. Increased process of high rise building in Janbaz Blvd. to make a uniform and dull wall in this corridor 2. Create visual disturbance due to disproportion between extensions of tall buildings in Sajad Blvd.
Access	1. Existence of multi-storey car parks in Proma Trading Complex in order to faciliate access to the services therein 2. Easy access to local and extra-local services due to access ways 3. Proportional width of main passages given the land uses adjacent to the same 4. Proportional width of passages given dominant role of trading corridors	1. Lack of public parking in Sajad Blvd. 2. High volume of traffic in the area studies and disturbing citizens' welfare 3. Existence of traffic jams in front of trading towers in Sajad and Janbaz 4. Existence of fringe parking lots in Sajad and disturbed traffic of vehicles	1. Possible erection of public parking lots in Sajad and Janbaz 2. Possible improvement of public transportation in main streets 3. Possible disturbance of occupancies in high rise buildings and decreased accesses	1. Increased traffic load due to lack of public parking 2. Increased fringe park due to lack of public parking lots

VI. CONCLUSION

Tendency to high rise building in metropolises of the country such as Mashhad is one of the consequences of urban development. This can have effective contributions to failure to uncontrolled expansion of metropolises. However, regardless of its postitive effects, it can have negative and harmful impacts on urban space and the land uses, if not properly considered. By the studies conducted in the process of this research, bad effects of high rise building on urban environment are identified, which in addition to negative effects mentioned earlier, it has positive effects as well, including strengthening city landscape, prevention of uncontrolled horizontal growth, saving in land use and urban infrastructure, and solving some housing problems. By considering criteria of high rise building and its effects on urban environment, it can be concluded that tall buildings require a detailed design process and understanding its main principles with respect to homogeneous and integrated architectural design, urban planning and environmetal management. Design by such a characteristic originated from general-oriented design see tall building as a part of a larger environment, which should be seen by a general view, so that its effects on the environment remain high on the agenda.

Suggestions:

Now, given the criteria obtained in this study, some solutions and suggestions are provided in order to decrease negative effects of high rise building on urban environment:

1. Any permit for plot ratio in result of high rise building should be issued only if urban transportations per capita are supplied, because in the area study, most of high rise buildings have business use, attracting excess urban trips.
2. To create more desirable and humanistic view for a tall building, it is more advisable that an open space around it (particularly around high rise buildings in Sajad Blvd.) are considered.

3. To prevent overlooking, tall buildings should not be erected in the proximity of each other or near low rise ones. Their distance from each other must be proportional in this regard.
4. The urban spaces existed or suggested should not be captured only by tall buildings. It is advisable that urban space is captured by buildings with human dimensions and scale, and tall buildings are taken farther.
5. Some standards can be formulated for painting tall buildings to be proportional to its occupancy, culture and etc., so that while creating a visual beauty, the building will become proportional to the surrounding buildings.
6. To prevent changed scale and disproportion of urban appearances, seen in Sajad Blvd., it is suggested that in combination of high rise buildings with low rise ones, middle scales and stages are used, or a separation space between both tall and short sizes are considered in the form of green and open space.
7. Erect public parking in the area study (Sajad and Janbaz) in order to facilitate access for the users and businesmen is a must.
8. Create an open public space and green space defined alongside trading towers in order to create soft space in Sajad Blvd.
9. Determine some criteria for protruded tall buildings along with margine of sidewalk in order to sunlight reach to the street and sidwalk is a must.
10. Diversity and mixing high rise buildings in order to render services will facilitate accesses.
11. Provide public transportation services in otder to facilitate accesses and decrease traffic jam, are all examples of suggestions for access system of the area study.

VII. REFERENCES

[1] Approved original document of Tehran Detailed Plan, 2007.
[2] Farhoodi, Rahmatollah; Mohammadi, Alireza, "Effect of Erecting High Rise Buildings on Urban Uses", Journal of Geographic Researches, Issue No. 41, March 2002, p. 75.
[3] Ghorbani, Rassoul, "Plot Ratio and Organizing Urban Spaces (Case Study: Tabriz)", Doctoral Thesis, Supervisor: Mohammad Reza Poormohammadi, Geography and Urban Planning, Spring 2004.
[4] KarimiMoshaver, Mehrdad; Mansouri, Amir; Adibi, Ali Asghar, "Relationship between Quality of High Rise Building Location and City Landscape", YaghNazar Journal, Issue No. 13, Spring 2010, 7th Year, p. 92.
[5] Golabchi, Mahmoud, "Criteria for Design and Construction of Tall Buildings", Journal of Beautiful Arts, Issue No. 9, 2010.
[6] Shakeri, Eghbal; SamadiVaghefi, Omid, "High Rise Building: A Response for Decreased Compressed and Old Urban Regions", 2010.
[7] Sadoughian, Minoush, "High Rise Building and Urban Space", University of Tehran, 1992.
[8] Seddigh, Morteza, "Basic Concepts of Urban Design", 2008.
[9] Safavi, Yahya, "Guidance on High Rise Building in Tehran", Journal of Geography Education, 2001.
[10] "Urban Design Plan in Ahmadabad Ave., Mashhad", Armanshahr Consulting Engineers, 2007.
[11] Azizi, Mohammad Mahdi, "Plot Ratio in Urban Plans", Journal of Beautiful Arts, Issue No. 2, 2007.
[12] Azizi, Mohammad Mahdi; Moeini, Marjaneh, "Analysis of Relationship between Environmental Quality and Plot Ratio", Journal of Beautiful Arts, Issue No. 45, Spring 2011.
[13] Azizi, Mohammad Mahdi, "Evaluation of Physical-Spatial Effects of Tower Building in Tehran (Case Study: Farmanieh and Kamranieh Quarters), Journal of Beautiful Arts, Issue Nos. 4 and 5, Winter 1999.
[14] HosseinzadehDalir, Karim; Heidari, Mohammad Javad, "Analysis of High Rise Building and Its Disadvantages in Iran", Journal of Geography Education, Edition 25, Issue No. 4, Summer 2011.
[15] CABE and English Heritage, "Guidance on Tall Buildings", July 2007.
[16] Chase, M, "How SWOT Audits. Analysis and Action Planning Can Help Your Town", 2001.

American Journal of Engineering Research (AJER)
e-ISSN : 2320-0847 p-ISSN : 2320-0936
Volume-03, Issue-01, pp-245-250
www.ajer.org

Research Paper Open Access

Comparison Of Some Numerical Methods For The Solution Of First And Second Orders Linear Integro Differential Equations.

Taiwo, O. A., + Jimoh, A. K . and Bello, A . K.
Department Of Mathematics,University Of Ilorin, Ilorin, Nigeria.
+ Department Of Statistics And Mathematical Sciences, Kwara State University, Malete, Nigeria.

Abstract: - This paper deals with the comparison of some numerical methods for the solutions of first and second orders linear integro differential equations. Two numerical methods employed are Standard and Perturbed Collocation using, in each case, power series and canonical polynomials as our basis functions. The results obtained for some examples considered show that the perturbed Collocation method by Canonical Polynomials proved superior over the Perturbed Collocation method by power series and the Standard Collocation method by power series and canonical polynomials respectively. Three examples are considered to illustrate the methods.

Keywords: - *Integro-Differential Equations, Standard and Perturbed Collocation, Power series Canonical Polynomials*

I. INTRODUCTION

Integro differential equation is an important aspect of modern mathematics and occurs frequently in many applied fields of study which include Chemistry, Physics, Engineering , Mechanics, Astronomy, Economics, Electro – Statics and Potential.

In recent years, there has been growing interest in the mathematical formulation of several risk phenomena and models. It is found that most of the models if not all, have always assumed integral or integro differential equations. As reported in literature, integro differential equations are very difficult to solve analytically (See [1]) and so numerical methods are required.

Several research works have been carried out in this area in recent years. Among the popular methods used by most numerical analyst are wavelet on bounded interval [2] , semiorthogonal Spline Wavelets [3], Orthogonal Wavelets [4], Wavelet-Galerkin Method [5] and Multi-Wavelet Direct Method [6] . Other methods include Quadrature Difference Method [7] , Adomain Decomposition Method [8] , Homototpy Analysis Method [9], Compact Finite Difference Method [10], Generalised Minimal Residual [11] and Variational Iteration Method [12].

Without loss of generality ,we consider the general second order linear integro-differential equation defined as:

$$P_o\, y(x) + P_1\, y'(x) + P_2\, y''(x) + \int_a^b k(x,t)\, y(t)\, dt = f(x) \qquad (1)$$

With the boundary conditions

$$y(a) + y'(a) = A \qquad (2)$$

And,

$$y(b) + y'(b) = A \qquad (3)$$

Where P_0 , P_1 , P_2 are constants, $k(x,t)$ and $f(x)$ are given smooth functions and $y(x)$ is to be determined.

Remark: In case of first- order Integro –Differential Equation considered, P_2 in equation (1) is set to zero with initial condition given as

$$y(a) = A \qquad (3a)$$

II. METHODOLOGY AND TECHNIQUES

In this section, we discussed the numerical methods mentioned above based on power series and canonical polynomials as the basis function for the solution of equations (1)—(3)

III. STANDARD COLLOCATION METHOD BY POWER SERIES (SCMPS)

We used this method to solve equations (1)—(3) by assuming power series approximation of the form:

$$y_N(x) = \sum_{r=0}^{N} a_r x^r \qquad (4)$$

Where , a_r $(r \geq 0)$ are the unknown constants to be determined. Thus, equation (4) is substituted into equations (1), (2) and (3), we obtained

$$P_o y_N(x) + P_1 y'_N(x) + P_2 y_N ''(x) + \int_a^b k(x,t) y_N(t) dt = f(x) \qquad (5)$$

together with the boundary conditions

$$y_N(a) + y'_N(a) = A \qquad (6)$$

and,

$$y_N(b) + y'_N(b) = A \qquad (7)$$

Equation (5) is re-written as

$$P_0 \sum_{r=0}^{N} a_r x^r + P_1 \sum_{r=0}^{N} r a_r x^{r-1} + P_2 \sum_{r=0}^{N} r(r-1) a_r x^{r-2} + \int_a^b k(x,t) \sum_{r=0}^{N} a_r t^r dt = f(x) \qquad (8)$$

Hence ,further simplification of equation (8), we obtained

$$\sum_{r=0}^{N} [P_0 a_r + P_1 (r+1) a_{r+1} + P_2 (r+1)(r+2) a_{r+2}] x^r + \int_a^b k(x,t) \sum_{r=0}^{N} a_r t^r dt = f(x) \qquad (9)$$

The integral part of equation (9) is evaluated and the left -over is then collocated at the point $x = x_k$, we obtained

$$\sum_{r=0}^{N} [P_0 a_r + P_1 (r+1) a_{r+1} + P_2 (r+1)(r+2) a_{r+2}] x_k^r + \int_a^b k(x_k,t) \sum_{r=0}^{N} a_r t^r dt = f(x_k) \qquad (10)$$

Where,

$$x_k = a + \frac{(b-a)k}{N}, \; k = 1, 2, 3, \ldots, N-1 \qquad (11)$$

Thus, equation (10) gives rise to (N-1) algebraic linear equation in (N+1) unknown constants. Two extra equations are obtained using equations (6) and (7) . Altogether, we have (N+1) algebraic linear equations in (N+1) unknown constants. These (N+1) algebraic linear equations are then solved by Gaussian elimination method to obtain the (N+1) unknown constants which are then substituted back into equation (4) to obtain the approximate solution.

IV. PERTURBED COLLOCATION METHOD BY POWER SERIES (PCMPS)

We used the method to solve equations (1)—(3) by substituting equation (4) into a slightly perturbed equation (1) to get

$$P_o y_N(x) + P_1 y'_N(x) + P_2 y''_N(x) + \int_a^b k(x,t) \sum_{r=0}^{N} a_r t^r dt = f(x) + \tau_1 T_N(x) + \tau_2 T_{N-1}(x) \qquad (12)$$

Where, τ_1 and τ_2 are two free tau parameters to be determined along with the constants $a_r (r \geq 0)$ and $T_N(x)$ is the Chebyshev polynomial of degree N in [a,b] defined by

$$T_{N+1}(x) = 2\left(\frac{2x-a-b}{b-a}\right) T_N(x) - T_{N-1}(x), \qquad N \geq 0 \qquad (13)$$

Hence, further simplification of equation (12), we obtained

$$\sum_{r=0}^{N} [P_0 a_r + P_1 (r+1) a_{r+1} + P_2 (r+1)(r+2) a_{r+2}] x^r + \int_a^b k(x,t) \sum_{r=0}^{N} a_r t^r dt = f(x) + \tau_1 T_N(x) + \tau_2 T_{N-1}(x) \qquad (14)$$

The integral part of equation (14) is evaluated and the left-over is then collocated at the point $x = x_k$, we obtained

$$\sum_{r=0}^{N} [P_0 a_r + P_1(r+1)a_{r+1} + P_2(r+1)(r+2)a_{r+2}]x_k^r + \int_a^b k(x_k,t)\sum_{r=0}^{N} a_r t^r dt = f(x_k) + \tau_1 T_N(x_k) + \tau_2 T_{N-1}(x_k) \quad (15)$$

where,

$$x_k = a + \frac{(b-a)k}{N}, \; k = 1,\ 2,\ 3,\ \ldots\ N-1 \quad (16)$$

Thus, equation (15) gives rise to (N+1) algebraic linear equations in (N+3) unknown constants. Two extra equations are obtained using equations (6) and (7). Altogether, we have (N+3) algebraic linear equations in (N+3) unknown constants. These (N+3) algebraic linear equations are then solved by Gaussian elimination method to obtain the (N+1) unknown constants a_r (r ≥0) together with the parameters τ_1 and τ_2 which are then substituted back into equation (4) to obtain the approximate solution.

V. STANDARD COLLOCATION METHOD BY CANONICAL POLYNOMIALS (SCMCP)

We used the method to solve equations (1)-(3) by assuming canonical polynomial approximation of the form

$$y_N(x) = \sum_{r=0}^{N} a_r \Phi_r(x) \quad (17)$$

Where, x represents the independent variables in the problem, $a_r (r \geq 0)$ are the unknown constants to be determined and $\Phi_r(x)(r \geq 0)$ are canonical polynomials which should be constructed.

Thus, equation (17) is substituted into equations (1)-(3), we obtained

$$P_0 \sum_{r=0}^{N} a_r \Phi_r(x) + P_1 \sum_{r=0}^{N} a_r \Phi_r'(x) + P_2 \sum_{r=0}^{N} a_r \Phi_r''(x) + \int_a^b k(x,t)\sum_{r=0}^{N} a_r \Phi_r(t)dt = f(x) \quad (18)$$

Together with the conditions

$$\sum_{r=0}^{N} a_r \Phi_r(a) + \sum_{r=0}^{N} a_r \Phi_r'(a) = A \quad (19)$$

and

$$\sum_{r=0}^{N} a_r \Phi_r(b) + \sum_{r=0}^{N} a_r \Phi_r'(b) = B \quad (20)$$

Equation (18) is re-written as

$$P_0 a_0 \Phi_0(x) + P_0 a_1 \Phi_1(x) + \cdots + P_0 a_N \Phi_N(x) + P_1 a_0 \Phi_0'(x) + P_1 a_1 \Phi_1'(x) + \cdots + P_1 a_N \Phi_N'(x) + P_2 a_0 \Phi_0''(x)$$
$$+ P_2 a_1 \Phi_1''(x) + \cdots + P_2 a_N \Phi_N''(x) + \int_a^b k(x,t)\sum_{r=0}^{N} a_r \Phi_r(t)dt = f(x) \quad (21)$$

Hence, further simplification of equation (21), we obtained

$$[P_0\Phi_0(x) + P_1\Phi_0'(x) + P_2\Phi_0''(x)]a_0 + [P_0\Phi_1(x) + P_1\Phi_1'(x) + P_2\Phi_1''(x)]a_1 + \cdots + [P_0\Phi_N(x) +$$
$$P_1\Phi_N'(x) + P_2\Phi_N''(x)]a_N + \int_a^b k(x,t)\sum_{r=0}^{N} a_r \Phi_r(t)dt = f(x) \quad (22)$$

The integral part of equation (22) is evaluated and the left-over is then collocated at the point x = x_k , we obtained

$$[P_0\Phi_0(x_k)+P_1\Phi_0^{'}(x_k)+P_2\Phi_0^{''}(x_k)]a_0+[P_0\Phi_1(x_k)+P_1\Phi_1^{'}(x_k)+P_2\Phi_1^{''}(x_k)]a_1+\cdots+[P_0\Phi_N(x_k)+P_1\Phi_N^{'}(x_k)$$
$$+P_2\Phi_N^{''}(x_k)]a_N+\int_a^b k(x_k,t)\sum_{r=0}^{N}a_r\Phi_r(t)dt=f(x_k) \quad (23)$$

where

$$x_k = a + \frac{(b-a)k}{N},\ k=1,\ 2.,3.,\ldots,N-1 \quad (24)$$

Thus, equation (23) gives rise to (N-1) algebraic linear equations in (N+1) unknown constants. Two extra equations are obtained using equations (19) and (20). Altogether, we have (N+1) algebraic linear equations in (N+1) unknown constants. These (N+1) algebraic linear equations are then solved by Gaussian elimination method to obtain the (N+1) unknown constants which are then substituted back into equation (17) to obtain the approximate solution.

VI. PERTURBED COLLOCATION METHOD BY CANONICAL POLYNOMIALS (PCMCP)

We used the method to solve equations (1)-(3) by substituting equation (17) into a slightly perturbed equation (1) to get

$$P_o\,y_N(x)+P_1\,y'_N(x)+P_2\,y_N''(x)+\int_a^b k(x,t)\sum_{r=0}^{N}a_r\Phi_r(t)\,dt=f(x)+\tau_1T_N(x)+\tau_2T_{N-1}(x) \quad (25)$$

Where, τ_1 and τ_2 are two free tau parameters to be determined along with the constants $a_r\,(r\geq 0)$ and $\Phi_r(x)$ is the canonical polynomial of degree N.

Hence, further simplification of equation (25), we obtained

$$[P_0\Phi_0(x)+P_1\Phi_0^{'}(x)+P_2\Phi_0^{''}(x)]a_0+[P_0\Phi_1(x)+P_1\Phi_1^{'}(x)+P_2\Phi_1^{''}(x)]a_1+\cdots+[P_0\Phi_N(x)+P_1\Phi_N^{'}(x)+P_2\Phi_N^{''}(x)]a_N$$
$$+\int_a^b k(x,t)\sum_{r=0}^{N}a_r\Phi_r(t)dt=f(x)+\tau_1T_N(x)+\tau_2T_{N-1}(x) \quad (26)$$

The integral part of equation (26) is evaluated and the left-over is then collocated at the point x = x_k , we obtained

$$[P_0\Phi_0(x_k)+P_1\Phi_0^{'}(x_k)+P_2\Phi_0^{''}(x_k)]a_0+[P_0\Phi_1(x_k)+P_1\Phi_1^{'}(x_k)+P_2\Phi_1^{''}(x_k)]a_1+\cdots+[P_0\Phi_N(x_k)+P_1\Phi_N^{'}(x_k)$$
$$+P_2\Phi_N^{''}(x_k)]a_N+\int_a^b k(x_k,t)\sum_{r=0}^{N}a_r\Phi_r(t)dt=f(x_k)+\tau_1T_N(x_k)+\tau_2T_{N-1}(x_k) \quad (27)$$

where

$$x_k = a + \frac{(b-a)k}{N+2},\ k=1,\ 2,\ 3\ ,\ \ldots.\ N+1 \quad (28)$$

Thus, equation (27) gives rise to (N+1) algebraic linear equations in (N+3) unknown constants. Two extra equations are obtained using equations (19) and (20). Altogether, we have (N+3) algebraic linear equations in (N+3) unknown constants. These (N+3) algebraic linear equations are then solved by Gaussian elimination method to obtain the (N+1) unknown constants $a_r(r\geq 0)$ together with the parameters τ_1 and τ_2 which are then substituted back into equation (17) to obtain the approximate solution.

VII. CONSTRUCTION OF CANONICAL POLYNOMIALS

The canonical polynomials denoted by $\Phi_r(x)$ is generated recursively from equation (1) as follows:

Following [13], we define our operator as:

$$L \equiv P_2\frac{d^2}{dx^2}+P_1\frac{d}{dx}+P_0$$

Let $L\Phi_r(x)=x^r$

Thus, $Lx^r=P_2r(r-1)x^{r-2}+P_1rx^{r-1}+P_0x^r$

Implies, $L\{L\Phi_r(x)\}=Lx^r\equiv P_2r(r-1)x^{r-2}+P_1rx^{r-1}+P_0x^r$

$$L\{L\Phi_r(x)\}=P_2r(r-1)L\Phi_{r-2}(x)+P_1rL\Phi_{r-1}(x)+P_0L\Phi_r(x)$$

We assumed that L^{-1} exists, then

$$x^r = P_2 r(r-1)L\Phi_{r-2}(x) + P_1 rL\Phi_{r-1}(x) + P_0 L\Phi_r(x)$$

Implies,

$$\Phi_r(x) = \frac{1}{P_0}\left\{x^r - P_2 r(r-1)\Phi_{r-2}(x) - P_1 r\Phi_{r-1}(x)\right\};\ r \geq 0,\ P_0 \neq 0 \qquad (29)$$

Hence, equation (29) is our constructed recursive canonical polynomials used in this work.

Remarks:

i. First order linear Integro-Differential Equation: For the purpose of our discussion, we set $P_2=0$ in equation (1) and this resulted to first order linear Integro-Differential equation considered in this work together with the initial condition y(a)=A (30)

ii. Errors: For the purpose of this work, we have defined maximum error used as

Maximum Error = $\max_{a\leq x\leq b}|y(x) - y_N(x)|$

8. Numerical Examples

Examples 1: Consider the first order linear integro-differential equation

$$y'(x) + 2y(x) + 5\int_0^x y(t)dt = 1 \qquad (31)$$

with initial condition

y(0)=0

The exact solution is given as $y(x) = \frac{1}{2}e^{-x}\sin(2x)$.

Table 1: Absolute maximum errors for example 1

N	Standard Collocation Method by Power Series (SCMPS)	Standard Collocation Method by Canonical Polynomials(SCMCP)	Perturbed Collocation Method by Power Series (PCMPS)	Perturbed Collocation Method by Canonical Polynomials (PCMCP)
4	3.30842E-4	8.01922E-2	2.80105E-5	9.84836E-4
6	1.77942E-5	3.48756E-4	5.48351E-6	1.91790E-6
8	7.34987E-6	5.78564E-6	2.78564E-7	9.23458E-8

Example 2:

Consider the first order linear integro differential equation

$$y'(x) = y(x) - Cos(2\pi x) - 2\pi Sin(2\pi x) - \frac{1}{2}Sin(4\pi x) + \int_0^1 Sin(4\pi x + 2\pi t)\, y(t)\, dt \qquad (32)$$

together with the initial condition

$$y(0) = 1$$

The exact solution is given as:

$$y(x) = Cos(2\pi x)$$

Table 2: Absolute maximum errors for example 2.

N	Standard collocation method by Power series(SCMPS)	Standard collocation method by canonical polynomials(SCMCP)	Perturbed collocation method by Power series(PCMPS)	Perturbed collocation method by canonical Polynomials(PCMCP)
4	7.48300E-2	1.86680E-3	8.83939E-3	9.37068E-4
6	1.52471E-2	3.16809E-4	6.39096E-3	2.13246E-5
8	8.76953E-3	1.67845E-5	3.67589E-4	1.03421E-6

Example 3: Consider the second-order linear integro-differential equation

$$y''(x) = 9y(x) + \frac{e^{-15} - 1}{3} + \int_0^5 y(t)dt \qquad (33)$$

together with the boundary conditions

$y(0) = 1 \quad and \quad y(1) = e^{-3}$

The exact solution is given as

$y(x) = e^{-3x}$

Table 3: Absolute maximum errors for example 3.

N	Standard Collocation Method by Power Series (SCMPS)	Standard Collocation Method by Canonical Polynomials(SCMCP)	Perturbed Collocation Method by Power Series (PCMPS)	Perturbed Collocation method by Canonical Polynomials(PCMCP)
4	4.86680E-2	2.02310E-2	1.86433E-3	2.13172E-4
6	1.16878E-2	5.16037E-3	2.17081E-4	2.05136E-5
8	8.45834E-3	1.67452E-4	7.45801E-5	1.89561E-7

VIII. DISCUSSION OF RESULTS AND CONCLUSION

Integro – Differential equations are usually difficulty to solve analytically. In many cases, it is required to obtain the approximate solutions. In this work, we proposed perturbed Collocation by Canonical polynomials for first and second orders linear In tegro Differential Equations and comparison were made with the Standard Collocation Method by Power Series and Canonical Polynomials as the the basis functions.

The comparison certifies that Perturbed Collocation Method gives good results as these are evident in the tables of results presented.

REFERENCES

[1] Hussein, J., Omar A. and S. Al-Shara, (2008) Numerical solution of linear integro-differential equations. J. Math and Stat. 4(4): 250 - 254.

[2] Goswani, J. C., A. K. Chan and C. K. Chui(1995) On solving first-kind integral equations using wavelets on a bounded interval. IEEE Transactions on Antennas and Propagation, 43, 614 – 622.

[3] Lakestani, M., M. Razzaghi and M. Dehghan (2006) Semi-orthogonal spline wavelets approximation for Fredholm integro-differential equations. Mathematical problems in Engineering, vol. 2006, Article ID96184, pp:12.

[4] Neveles, R. D., J. C. Goswani and H. Tehrani(1997) Semi-orthogonal versus orthogonal wavelet basis sets for solving integral equations. IEEE Trans. Antennas Propagat., 45(9): 1332 – 1339.

[5] Chrysafinos, k.,(2007) Approximations of parabolic integro-differential equations using wavelet-Galerkin compression techniques. BIT Numerical Mathematics, 47: 487 – 505.

[6] Abbasa, Z., S. Vahdatia K. A. Atanb and N. M. A. NikLonga, (2009) Legendre multi-wavelets direct method for linear integro-differential equations. Applied Mathematical Sciences, 3(14): 697 -700.

[7] Fedotov, A. I (2009) Quadrature-difference method for solving linear and nonlinear singular integro-differential equations. Nonlinear Anal., 71: 303 - 308.

[8] S. M. El-Sayed, M. R. Abdel-Aziz (2003) Comparison of Adomians decomposition method and wavelet-Galerkin methods for solving integro- differential equations. Appl. Math. Comput. 136, 151 -159.

[9] Liao, S. J. (2004) On the Homotopy analysis method for nonlinear problems. Applied Math. Comput., 147: 499 – 513.

[10] Zhao, J. and R. M. Corless (2006) Compact finite difference method for integro-differential equations. Applied Math. Comput., 177: 325 – 328. DOI:10.1016/j.amc.2005.11.007.

[11] Aruchunan, E. and J. Sulaiman, (2010) Numerical Solution of second- order linear Fredholm integro-differential equation using Generalized Minimal Residual Method. American Journal of Appl. Sciences. 7(6): 780 – 783.

[12] Wang, S. and J. He(2007) Variational Iteration Method for solving integro-differential equations. Phys. Lett. A, 367: 188 -191.

[13] Taiwo, O. A. and Onumanyi, P. (1991). A collocation approximation of singularly perturbed second – order differential equation, Computer mathematics, vol. 39 pp 205 – 211.

American Journal of Engineering Research (AJER)
e-ISSN : 2320-0847 p-ISSN : 2320-0936
Volume-03, Issue-01, pp-251-257
www.ajer.org

Research Paper Open Access

Stochastic Analysis of Concrete Strength In An Ongoing Construction

Onwuka D.O.[1] and Sule, S.[2]
[1]*Department of Civil Engineering Federal University of Technology, Owerri, Imo State.*
[2]*Department of Civil and Environmental Engineering, University of Port Harcourt, P.M.B 5323 Port Harcourt, Rivers State - Nigeria.*

Abstract: - Structural safety evaluation is a task of paramount importance at every stage of a building process. In this paper, the result of stochastic analysis of concrete strength in an ongoing construction is discussed. Convolution theory was employed in the reliability estimation. The parameters used in the stochastic analysis were obtained from the schmidt hammer test carried out on the Laboratory Block at College of Continuing Education, University of Port Harcourt, Rivers State, Nigeria. The strength parameters were assumed to be random and stochastic. The obtained geometric index was found to be 2.97 which is less than the target safety index of 4.5 for slabs, 4.9 for beams in bending or flexure, 3.6 for beams in shear and 3.9 for columns under dead and live load combination. Also, the failure probability corresponding to the estimated geometric index (1.49E-3) when compared with the tolerable risk levels (10^{-3}) for structures in society showed that the structure is not safe and can lead to a very serious accident which may result in loss of lives and damage of properties on collapse.

Keywords: *- structural safety, building process, stochastic analysis, convolution theory, reliability estimation*

I. INTRODUCTION

Building failures in Nigeria has led to loss of lives and damage of properties. As a result reliability appraisal of structures becomes a necessity at every stage of a building process as a guide against structural failure and eventual collapse of structures [1-3]. Structural deterioration is a common reason for structural appraisal [4]. Condition assessment of a building is a necessity at every stage of a building construction rather than sitting down and watch the building collapse [5]-[6]. According to Afolayan [5-6], once the nature of the risk has been recognized the next step is the determination and implementation of measures to reduce the risk or reduce the effect of the loss or both at an economical cost. Eventually, the need for loss financing will be reduced in most instances and losses will be avoided or reduce to the bearest minimum.

Application of safety factors in the conventional design cannot guarantee structural safety as the applied loads are probabilistic in nature.

The best way to assess the safety of an existing or deteriorating structure is by probability of failure [8]. In structural design, structural loading and intensities cannot be predicted with certainty and probabilistic concept has become an important tool for any realistic, quantitative and rational analysis and any conceivable condition is necessarily associated with a numerical measure of the probability of its occurrence. It is by this measure alone that the structural significance of a specified condition can be assessed. Since it is not possible to achieve absolute reliability in the uncertain world, a probabilistic approach to the evaluation of structural safety becomes a sensible solution [9]. According to Afolayan [10], it has been the directional effort of the engagement of probabilistic thinking to systematically assess the effect of uncertainty on structural performance. The probabilistic concept may not provide answers to all issues of unknown but has played a very important role in the integrity appraisal of many engineering structures.

This paper highlights the use of probabilistic concept to assess the structural integrity of an ongoing construction. The probabilistic model is simple and straightforward and can be manually achieved.

II. FORMULATION OF STOCHASTIC MODEL

Let X and Y be the applied stress random variable and allowable stress random with statistical properties described by first and second moment, (μ_x, σ_x) and (μ_y, σ_y) respectively.

The limit state function is given by:

$$Z = X - Y \tag{1}$$

According to equation (1),
Violation of limit state occurs when:

$$z > 0, \tag{2}$$

Again, using equation (1), the probability of failure is given by:

$$P_f = \int_0^{\infty} g(z)dz. \tag{3}$$

The capacity demand are assumed to statistically independent.

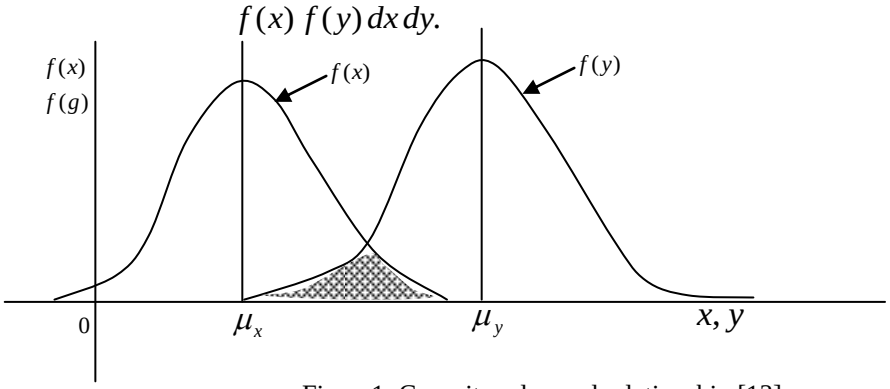

Figure1: Capacity –demand relationship [13]

Using equation (1), the joint density function of capacity and demand is transformed as:

$$f(x)\, f(x-z)\, dx.dz. \tag{4}$$

Using equation (1) and applying convolution theorem, the probability density function of Z given by:

$$g(z) = \int_a^b f(x)\, f(x-z)\, dx\, dz \tag{5}$$

where a *and* b represent the structural stress limits.

From Figure 1, X *and* Y are assumed to be normally distributed. Therefore, the probability density functions are given by equations (6) and (7) respectively [13].

$$f(x) = \frac{1}{\sigma_x \sqrt{2\pi}} \exp\left[-\frac{1}{2}\left(\frac{x-\mu_x}{\sigma_x} \right)^2 \right] \quad (-\infty,\ \infty), \tag{6}$$

$$f(y) = \frac{1}{\sigma_y \sqrt{2\pi}} \exp\left[-\frac{1}{2}\left(\frac{y-\mu_y}{\sigma_y} \right)^2 \right] \quad (-\infty,\ \infty), \tag{7}$$

Substituting for $f(x)$ *and* $f(x-z)$ using equation (6) and (7) gives:

$$g(z) = \int_{-\infty}^{\infty} \frac{1}{2\pi\sigma_x\sigma_z} \exp\left[-\frac{(x-\mu_x)^2}{2\sigma_x^{\,2}} - \frac{(x-z-\mu_y)^2}{2\sigma_y^{\,2}} \right] dx \tag{8}$$

Let the expression in the bracket be denoted by λ.
Therefore,

$$\lambda = -\frac{(x-\mu_x)^2}{2\sigma_x^{\,2}} - \frac{(x-z-\mu_y)^2}{2\sigma_y^{\,2}} \tag{9}$$

Multiplication of top and bottom of equation (9) by $\sigma_x^2+\sigma_y^2$ gives:

$$\lambda=\frac{\sigma_x^{\ 2}+\sigma_y^{\ 2}}{2\sigma_x 2\sigma_y^{\ 2}}\left(\frac{-2\sigma_y^{\ 2}(x-\mu_x)^2-2\sigma_x^{\ 2}(x-z-\mu_y)^2}{\sigma_x^{\ 2}+\sigma_y^{\ 2}}\right) \tag{10}$$

Simplification of bracketed terms in equation (10) gives equation (11).

$$\lambda=\frac{\sigma_x^{\ 2}+\sigma_y^{\ 2}}{2\sigma_x^{\ 2}\,2\sigma_y^{\ 2}}\left[\frac{x^2-2x(\mu_x\sigma_z^{\ 2}+z\sigma_x^{\ 2}+\mu_y\sigma_x^{\ 2})}{\sigma_x^{\ 2}+\sigma_y^{\ 2}}\right.$$
$$\left.+\mu_x^{\ 2}\sigma_y^{\ 2}+\frac{(z^2+\mu_y^{\ 2}+2z\mu_z).\sigma_x^{\ 2}}{\sigma_x^{\ 2}+\sigma_y^{\ 2}}\right]. \tag{11}$$

Multiplying the top and bottom of the last term of equation (11) by $\sigma_x^{\ 2}+\sigma_y^{\ 2}$ gives:

$$\lambda=-\frac{\sigma_x^{\ 2}+\sigma_y^{\ 2}}{2\sigma_x^{\ 2}\,2\sigma_y^{\ 2}}\left\{\frac{x^2-2x(\mu_x\sigma_y^{\ 2}+(z+\mu_y)\sigma_x^{\ 2}]}{\sigma_x^{\ 2}+\sigma_y^{\ 2}}\right.$$
$$\left.+\frac{\mu_x^{\ 2}\sigma_x^{\ 2}\sigma_y^{\ 2}+(z^2+2z\mu_y+\mu_y^{\ 2})\sigma_x^{\ 4}+\mu_x^{\ 2}\sigma_y^{\ 4}+(z^2+2z\mu_y+\mu_x^{\ 2})\sigma_x^{\ 2}\sigma_y^{\ 2}}{(\sigma_x^{\ 2}+\sigma_y^{\ 2})^2}\right\} \tag{12}$$

According to Haugen [13], separation of the two middle terms of the last fraction of equation (12) from the other two terms followed by addition and subtraction of expression

$$\frac{2\mu_x(z+\mu_y)\sigma_x^{\ 2}\sigma_y^{\ 2}}{(\sigma_x^{\ 2}+\sigma_y^{\ 2})^2}$$

transforms equation (12) to:

$$\lambda=\frac{\sigma_x^{\ 2}+\sigma_y^{\ 2}}{2\sigma_x^{\ 2}\sigma_y^{\ 2}}\left[x^2-2x\frac{\mu_x\sigma_y^{\ 2}+(z+\mu_y)\sigma_x^{\ 2}}{\sigma_x^{\ 2}+\sigma_y^{\ 2}}\right.$$
$$+\frac{\mu_x^{\ 2}\sigma_y^{\ 4}+2\mu_x(z+\mu_y)\sigma_x^{\ 2}\sigma_y^{\ 2}+(z+\mu_y)^2\sigma_x^{\ 4}}{(\sigma_x^{\ 2}+\sigma_y^{\ 2})}$$
$$\left.+\frac{\mu_x^{\ 2}-2\mu_x(z+\mu_y)+(z+\mu_y)^2}{(\sigma_x^{\ 2}+\sigma_y^{\ 2})^2}\sigma_x^{\ 2}\sigma_y^{\ 2}\right. \tag{13}$$

Also, multiplying the last term of equation (13) by $-\frac{\sigma_x^{\ 2}+\sigma_y^{\ 2}}{2\sigma_x^{\ 2}\sigma_y^{\ 2}}$ transforms equation (13) to:

$$\lambda=-\frac{\sigma_x^{\ 2}+\sigma_y^{\ 2}}{2\sigma_x^{\ 2}\sigma_y^{\ 2}}\left(x-\frac{\mu_x\sigma_y^{\ 2}+z+\mu_y)\sigma_x^{\ 2}}{\sigma_x^{\ 2}+\sigma_y^{\ 2}}\right)^2-\frac{(z+\mu_y-\mu_x)^2}{2(\sigma_x^{\ 2}+\sigma_y^{\ 2})} \tag{14}$$

Using equation (14), equation (8) now becomes:

$$g(z)=\frac{1}{\sqrt{2\pi(\sigma_x^{\ 2}+\sigma_y^{\ 2})}}\exp\left\{-\frac{\sigma_x^{\ 2}+\sigma_y^{\ 2}}{2\sigma_x^{\ 2}y^2}\left[x-\frac{\mu_x\sigma_y^{\ 2}+(z+\mu_y)\sigma_x^{\ 2}}{\sigma_x^{\ 2}+\sigma_y^{\ 2}}\right]\right.$$
$$\left.-\frac{(z+\mu_y-\mu_x)^2}{2(\sigma_x^{\ 2}+\sigma_y^{\ 2})}\right\}dx, \tag{15}$$

Let

$$\alpha = \int_{-\infty}^{\infty} \frac{\sqrt{\sigma_x^{\,2} + \sigma_y^{\,2}}}{\sqrt{2\pi\sigma_x\sigma_z}} \exp\left\{ \frac{-\sigma_x^{\,2} + \sigma_y^{\,2}}{2\sigma_x^{\,2}2\sigma_z^{\,2}} \left[\frac{x - \mu_x\sigma_y^{\,2} + (z + \mu_y)^2}{\sigma_x^{\,2} + \sigma_y^{\,2}} \right]^2 \right\} dx \tag{16}$$

Equation (15) now becomes:

$$g(z) = \frac{1}{\sqrt{2\pi(\sigma_x^{\,2} + \sigma_y^{\,2})}} \exp\left[-\frac{(z + \mu_y - \mu_x)}{2(\sigma_x^{\,2} + \sigma_y^{\,2})} \right] \alpha, \tag{17}$$

From equation (14), let

$$t = \frac{\sqrt{\sigma_x^{\,2} + \sigma_y^{\,2}}}{\sqrt{\sigma_x\sigma_y}} \left[x - \frac{\mu_x\sigma_y^{\,2} + (z + \mu_y)\sigma_x^{\,2}}{\sigma_x^{\,2} + \sigma_y^{\,2}} \right], \tag{18}$$

Differentiating t with respect to x in equation (18) yields:

$$dt = \frac{\sqrt{\sigma_x^{\,2} + \sigma_y^{\,2}}}{\sigma_x\sigma_y} dx, \tag{19}$$

Substituting for t and dx in equation (16), we have:

$$\alpha = \int_{-\infty}^{\infty} \frac{1}{2\pi} e^{-(t^2/2)} dt \tag{20}$$

From statistics and probability,

$$\int_{-\infty}^{\infty} pdfdx = 1 \tag{21}$$

Therefore, equation (15) now transforms to:

$$g(z) = \frac{1}{\sqrt{2\pi(\sigma_x^{\,2} + \sigma_y^{\,2})}} \exp\left[-\frac{1}{2} \frac{(z + \mu_y - \mu_x)^2}{(\sigma_x^{\,2} + \sigma_y^{\,2})} \right], \tag{22}$$

From Figure 1, Z is a normally distributed random variable. The mean and standard deviation are therefore:

$$\mu_z = \mu_x - \mu_y, \tag{23}$$

$$\sigma_z = \sqrt{\sigma_x^{\,2} + \sigma_y^{\,2}} \tag{24}$$

The probability that the structure fulfils the intended purpose is structural reliability defined by:

$$\text{Reliability} = \int_0^{\infty} g(z)\, dz. \tag{25}$$

Again, let $$t = \frac{z + \mu_y - \mu_x}{\sqrt{\sigma_x^{\,2} + \sigma_y^{\,2}}}; \tag{26}$$

Differentiation of equation (26) with respect to x yields:

$$dt = \frac{d_z}{\sqrt{\sigma_x^{\,2} + \sigma_y^{\,2}}} \tag{27}$$

Using equation (27), equation (25) now transforms to:

$$\text{Reliability} = \int_0^{\infty} g(z)dz = \int_0^{\infty} \frac{\mu_y - \mu_x}{\sqrt{\sigma_x^{\,2} + \sigma_y^{\,2}}} \frac{1}{2\pi} e^{-(t/2)}\, dt \tag{28}$$

Using equation (28), the transformation which relates μ_x, μ_y and standard normalized variable z is given by:

$$z = \frac{\mu_y - \mu_x}{\sqrt{\sigma_x^{\ 2} + \sigma_y^{\ 2}}} \quad (29)$$

Applied stress = 0

Therefore,

$$y = \mu_y = \sigma_y = 0 \quad (30)$$

Using equation (29) now reduces to:

$$z = \frac{|\mu_x|}{\sigma_x} \quad (31)$$

Let σ_{cu} *and* x represent the concrete cube strength and strength of concrete in an ongoing construction respectively.

According to BS8110 [11], the mean design strength is given by:

$$\mu_x = 0.67\sigma_{cu} \quad (32)$$

To cater for error in the formulated reliability mode, errors due to test procedures and errors due to in-batch variabilities of concrete strength reinforcement strength and dimensional variability, the resultant coefficient of variation of concrete strength is given as:

$$COV_{\text{Re sul tan t}} = \left(COV_y^2 + COV_{testing}^2 + COV_{in-batch}^2\right)^{1/2} \quad (33)$$

Where:

μ_x, σ_x = mean value and standard deviation of structural capacity respectively.

COV_y is a function of the mix design

According to Ranganathan [2], $COV_{testing} = COV_{in-batch} = 0.10$.

Structural failure occurs when $X < \sigma_{all}$. Therefore, the probability of failure (P_{fi}) for a particular structural member is given as:

$$P_{fi} = P(X_i < \sigma_{all}) \quad (34)$$

Where:

P, σ_{all} represents probability operator and allowable concrete stress in axial compression respectively.

According to BS8110 [11]

$$\sigma_{all} = 0.33\sigma_{cu} \quad (35)$$

Assuming X to be normally distributed, the probability of failure is the structure is given by:

$$P_f = \phi\left(\frac{\sigma_{all} - \mu_x}{\sigma_x}\right) \quad (36)$$

Using equations (32) and (35), equation (36) can be written as:

$$P_f = \phi\left(\frac{0.33\sigma_u - 0.67\sigma_{cu}}{COV_{\text{Re sul tan t}}(0.67\sigma_{cu})}\right), \left(\sigma_x = COV_{\text{Re sul tan t}} \times 0.67\sigma_{cu}\right) \quad (37)$$

According to Ranganathan [2], the probability of structural failure can be approximated as:

$$P_f \approx \phi(-\beta) \quad (38)$$

Where:

$\phi(.)$ is the standard Gaussian cumulated function and

$$\beta = \min \| u \| = \left(\sum_{i=1}^{n} X_i^{\ 2}\right)^{1/2}$$

$||u||$= minimum distance between the origin and the failure surface in the normalized coordinate

u_{ii} represents an appropriate probabilistic transformation.

III. RESULTS AND DISCUSSION

Table 1: Results of Schmidt hammer test on concrete [1].

S/No	Location	Rebound Hammer readings	Average Rebound	Concrete Strength from Rebound Test (y)
1	Middle panel	23,23	23	18
2	Edge panel	23,23	23	18
3	Beam 2	20,20	20	14
4	Slab 2	24,24	24	20
5	Slab 1	18, 19	19	8
6	Beam 1	12,12	12	5
7	Staircase	23.3, 19	21.2	15
8	Middle column	35,27	31	29
9	Corner column	27,27	27	2.5
10	Column footing	12.5,6	9	4
				$\mu_y = \sum_{i=1}^{10} \frac{y_i}{10} = 15\,N/mm^2$

Table 2: Stochastic model [2].

Variable	Mix	Specified strength	Mean (μ_y) (N/mm^2)	Std deviation $\sigma_y\,(N/mm^2)$	COV (σ_y) (%)	Probability distribution	Quality control
Cube strength	Grade 15	15	17.56	2.69	15.33	Normal	Design mix

From Table 2, $\mu_{\sigma cu} = 17.56\,N/mm^2, \sigma_{\sigma cu} = 2.69 N/mm^2$ $and\, COV_y = 0.1533.$

Using equation (33),

$$COV_{Resultant} = (0.1533^2 + 0.10^2)^{1/2} = 0.18$$

From equation (32),

$$\mu_x = 0.67\sigma_{cu} = 0.67 \times 17.56 = 11.76\,N/mm^2$$

$$\sigma_x = COV_{Resultant}\,(0.67\sigma_{cu}) = 0.67 \times 0.18 \times 17.56 = 2.24\,N/mm^2$$

From equation (35),

$$\sigma_{all} = 0.34\,\sigma_{cu} = 0.34 \times 15 = 5.10\,N/mm^2$$

From equation (37), the probability of failure of concrete is structure is:

$$P_f = \varphi\left(\frac{5.10 - 11.76}{2.24}\right) = \varphi(-2.97) = 1.49\,x10^{-3}$$

IV. DISCUSSION OF RESULTS AND CONCLUSION

The results of stochastic appraisal of an ongoing construction using convolution theory has been presented. From Table 1, it can seen that the average strength of concrete in the as constructed structure is about 15N/mm^2. The as-constructed safety appraisal gave a geometric index value of 2.97 which is below the target value of 4.9 for beams in bending or flexure, 3.6 for beams in shear, 4.5 for slabs, and 3.9 for columns subjected to both dead and live load combination.

In conclusion, the structure cannot perform satisfactorily in service and can cause serious accident and serious damage to properties on collapse. The structure is therefore, recommended for careful demolition to give rise to a new structure and more stringent supervision should be carried out Also, reliability prediction using convolution theory gave the same result (geometric index = 2.97) as those of the previous models showing the effectiveness of the convolution theory in the reliability prediction of an ongoing construction.

REFERENCES

[1] Sule, S. "Probabilistic Approach to Structural Appraisal of a Building during Construction." Nigerian Journal of Technology, Vol. 30, No.2, 2011, pp 149-153.

[2] Ranganathan, R. *Structural Reliability, Analysis and Design,* Jaico Publishing House, Mumbai, 1999.

[3] Theft-Christensen P. and Baker M.J. Structural Reliability and Theory and its Applications, Springer-Verlag, Berlin, 1982.

[4] Mori Y. and Ellingwood B.R. "Reliability-Based Service Life Assessment of Aging Concrete Structures." *Journal of Structural Engineering*, Vol. 119, No.5, 1993, pp. 1600-1621.

[5] Villemeur, A. "*Reliability, Maintenance and Safety Assessment."*Vol.2, 1992, (John Wiley), Chichester.

[6] Wilkinson, S. *Physical Control of Risk,* (Witherby), London, 1992.

[7] Afolayan, J.O. "Probability based design of glued thin-webbed timber beams." *Asian Journal of Civil Engineering (Building and Housing)* Vol.6, Nos. 1-2, 2005, pp. 75-84.

[8] Melchers, R. *Structural Reliability Analysis and Prediction.* Second Edition, John Wiley and Sons, 1999.

[9] Freudenthal, A.M. "Safety and Probability of Structural Failure." *Transactions, ASCE,* Vol. 121, 1956, pp. 1337-1375.

[10] Afolayan, J.O. "Cost-Effectiveness of Vibration Criteria for Wooden Floors." *Asian Journal of Civil Engineering (Building and Housing),* Vol. 5, Nos. 1-2, 2004, pp. 57-67.

[11] BS: 81100. *British Standard Code of practice for Plain and Reinforced Concrete (3rd Revision)* Indian Standards Institution, London, 1985, pp. 2-7.

[12] CIRIA. Rationalization of Safety and Serviceability in Structural Codes, Report No. 63, Construction Industry Research and Information Association, London.

[13] Haugen, E.B. Probabilistic Approach to Design, John Wiley, New York, 1986.

American Journal of Engineering Research (AJER)
e-ISSN : 2320-0847 p-ISSN : 2320-0936
Volume-03, Issue-01, pp-258-267
www.ajer.org

Research Paper Open Access

RF Propagation Measurement and Modelling to SupportAdept Planning of Outdoor Wireless Local Area Networks in 2.4 GHz Band

J. Isabona, and K.Obahiagbon
[1]*Department of Basic SciencesBensonIdahosa University, PMB.1100, Benin City, Nigeria*
[2]*Department of Mathematics and Computer Sciences*

Abstract: -Radio Frequency (RF) propagation is the study of how radio waves broadcast over distances. One of the main problems in mobile radio communication is the loss of propagated RF signal power at the receiver due to fading. When the fading is very strong, the signal is blocked. Modeling of the signal propagation loss is an important element of the design and performance analysis of wireless communication systems.The initiative of RF propagation modeling is to devise a model that can predict the signal coverage of an access point placed at a certain location in an environment.Propagation models help network planner to estimate the signal coverage and pathloss for a given deployment plan, as well as perform automated placement of access points. This paper presents a measurement based Log-distance propagation model for effective planning of outdoorWLAN in the 2.4 GHz Band. Measurements were carried out over a distance to determine various received power levels from a fixed WLAN access pointtransmitter; these values were applied to some path loss model equations to obtain the mobile radio planning parameters such as the path loss exponent, the mean path loss intercept and AP cell range. The results obtained show that path loss exponent was 1.85 while the mean path loss intercept was mean path loss intercept 84. Hence the log model for the design of a mobile radio link in the test bed area is
PL(dB) = 84+ 1.85log (d). In general, results show that the obstructions in the environment considered here had little effect (not much) on radio signals.

Keywords: -*RF propagation modeling, Log Distance Pathloss model, WLAN radio link design*

I. INTRODUCTION

The far-reaching demand for wireless communicationtechnologies is ever increasing in all the human-life activities and this has boosted the development of Wireless Local Area Networks (WLANs).Among the WLAN standards, the IEEE 802.11 [1] is the most popular one. A Schema of the IEEE 802.11 standard is represented in figure 1. The IEEE 802.11 standard defines both the physical (PHY) and medium access control (MAC) layers of the network.The basic network building block defined by the standard is the infrastructure Basic Service Set (BSS) which is composed of a single Access Point (AP) connected to a wired backbone network providing wireless connectivity to a bunch of mobile users.Thus, Aps, normally routers, are base stations for the wireless network.

However, it is no easy task to decide on the number and locations where these APs have to be fixed in an outdoor or indoor environment so as to provide not only coverage but ensure minimum signal strength at all node points, requisite bandwidth, in the presence of obstructions, reflections and signal interference. Design of this nature is very complex and needs proper modeling and formulating the problem as an optimization problem with several constraints.

Thus, the development of efficient transmission, operation and management WLAN technologies requires a greater precision on the estimations of the system signal coverage, which is given by propagation pathloss models. This is usually done in order to obtain "total coverage" with which the operator attempts to assure the quality of service.Propagation models to help network designer estimate the signal coverage and pathloss for a given deployment plan, as well as perform automated placement of access points. For this reason a precise and flexible prediction methodologies of signal coverage with easy implementation is needed.

This paper presents Measurement-based RF propagation modellingfor efficient WLAN radio link design. Measurements were carried out over a distance to determine various received power levels from a fixed WLAN access pointtransmitter; this enables to develop a precise path loss modelfor itsefficient RF design.

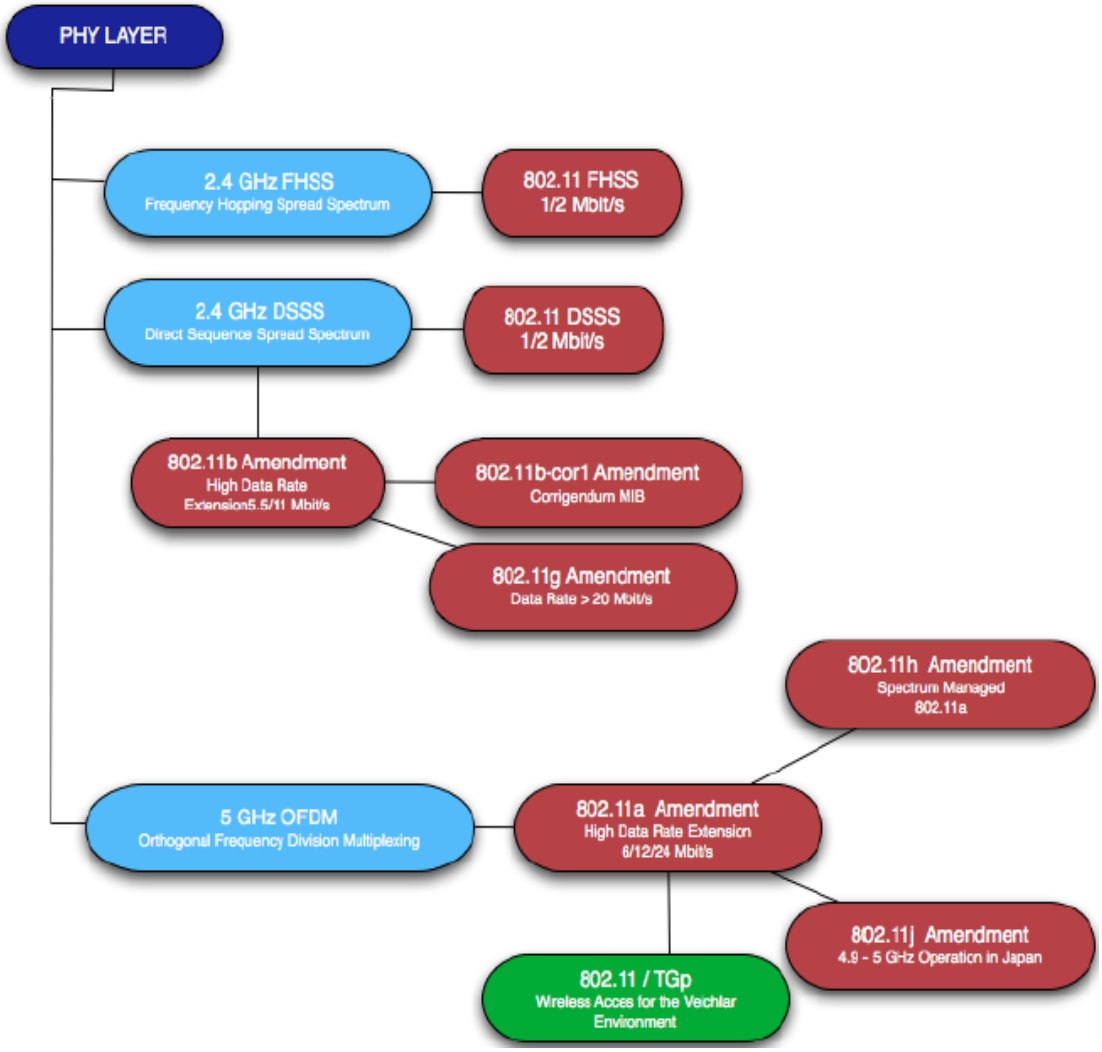

Figure 1.Schema of the IEEE 802.11 standard

II. MOTIVATION AND GOAL

Wireless communication systems are used everywhere, both in indoor and outdoor environments. In these environments, customers demand a good coverage and quality of service. Operator deployment provisionsmust classically guarantee coverage, with certain quality requirements, of a minimum percent of the geographical area and population (e.g., 90-95 % of the geographical area and population covered). Today the challenge is how to accurately predict the propagationsignal coverage and path loss at the cellular frequency of 2.4 GHz in outdoor terrain. There are several empirical propagation models which can precisely calculate up to 2 GHz. But beyond 2 GHz, there are few reliable models which can be referred for the WLAN context. So far, WLAN propagation studies are more tuned to the indoor communications; however, WLAN outdoor networks may also play a role in the wireless communications.Even more so, there had been no upkeep of path loss modeling for the 2.4 GHz frequency, which holds a dominant role in indoor wireless networks (802.11b/g/n) and will continue to be of importance as next-generation networks come into the forefront. Also, the possibility of using WLAN communications for long ranges can therefore be an important feature to add to the WLAN list of exciting potentials.

Therefore, the development of efficient transmission, operation and management of outdoor WLAN technologies and a progressive reduction in the size of the cells requires a greater precision on the estimations of the system coverage, which is given by propagation losses, in order to obtain “total coverage” with which the operator attempts to assure the quality of service. For this reason a precise and flexible prediction methodologies of coverage with easy implementation is needed.

In this paper, our goal is to devise a RF propagation pathloss model that can effectivelypredict the signal coverage of theWLAN access point deployedin the studied location and similar environment.

III. MATERIALS AND METHODS

In planning any radio system, a fundamental task is to predict the coverage of a proposed system and to determine whether the intended service objectives are met. Over the years a wide variety of approaches have been developed to predict coverage using propagation models. Propagation in this context simply means the transfer or transmission of signals from the transmitter to the receiver. Radio propagation modeling is the most complicated aspect of any wireless network planning. This is due to multi-path propagation characteristics that could vary substantially from environment to environmentwith distance as well as with time.

Explicitly, by propagation or radio-channel modelling, what is meant is that the amount of propagation pathloss obtainable within a specified environment is estimated and put forward for (future) estimation/prediction purposes, in addition to characterizing the propagation channel's impulse response. It is an empirical mathematical formulation for the characterization of radio wave propagation as a function of frequency, distance, and other dynamic factors. In view of that, propagation models are developed with the goal of formalizing the way radio waves propagate from one place to another; such models typically predict the path loss along a link or the effective coverage area of the transmitter. A single model is usually developed to predict the behaviour of propagation for all similar links under similar constraints. An understanding of radio propagation is essential for coming up with appropriate design, deployment, and management strategies for wireless networks. In effect, it is the nature of radio channel that makes wireless networks more complicated than their counterparts wired networks. According to Rappaport [2] propagation models are not only needed for installation guidelines, but they are a key part of any analysis or design that strives to mitigate interference. A (potentially) much more accurate method of determining coverage, bandwidth and other parameters uses RF propagation modeling to analyze the RF environment, and predict the signal strength contours at all points within the environment. From the signal strength contours, the path loss, throughput, error rate, etc. can be deduced.

Several models have been developed to model the propagation characteristics of radio waves under differentscenarios. Each of these models attempt to predict signal strength at various locations for a given access point position. On the basis of scale, the models can be categorized into two - Large scale propagation model and Small scale fading model. The large scale propagation attempts to model the average signal intensity for arbitrary distances between transmitter and receiver. These models can estimate coverage area of a given transmitter, and are therefore used for coverage planning purposes. On the other hand, variations in signal strength over short distances or over short time periods are modeled by small-scale fading models. For small-scale fading models, multipath effects dominate and the distance-based attenuation is considered to be constant. In this paper, we deal mostly with large-scale propagation models as they are useful for coverage planning purposes.

3.1. BasicRF Propagation model

We begin the discussion by introducing the basic propagation model that plays role in deciding signal coverage of a given transmitter. In telecommunication, the most basic propagation model is free space model – the transmitted signal is attenuated only according to the inverse square distance RF radiation law. Free-space path loss (FSPL) is the loss in signal strength of an electromagnetic wave that would result from a line-of-sight path.The FSPL, also known as Friis propagation model [[2], calculates the average radio signal attenuation over distance, d.Friis described the physics of electromagnetic wave behavior in free space using the correlation between the power radiated by the transmitting antenna and the power received by the receiving antenna.

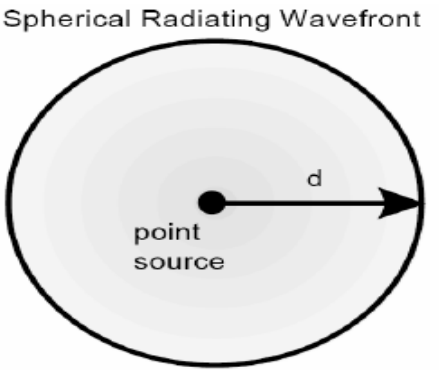

Figure 2: Free space radiating point source

Assuming that the radiating source as shown in figure 2 radiates energy at 360° with a fixed power forming an ever increasing sphere, the power flux at the transmitter is,

$$P_r = A_{er}\langle w(t)\rangle \quad (1)$$

defined as the product of average power received by the antenna's load, and the time average power density at the antenna, and is called effective area. The average power density for the far-field and effective area of the receiving antenna is defined by [3],

$$\left|\langle w(t)\rangle\right| = \frac{|E_0|^2}{2\eta} \quad (2)$$

and

$$A_{er} = \frac{\lambda^2}{4\pi} G_r \quad (3)$$

where G_r is the directive gain of the Hertzian dipole. Equation (3) shows that the receiving antenna's effective area is independent of its length and inversely proportional to the square of the carrier frequency. At this point one can realize that the term frequency dependent propagation loss is not the effect of wave propagation but the receiving antenna itself. The average power density in terms of radiated power, transmitter gain, G_t and the distance *r* can be written as,

$$\langle w(t)\rangle = \frac{P_{rad}\ G_1}{4\pi d^2} \quad (4)$$

Considering the equations (2), (3) and (4) in (1) yield the following formula:

$$P_r = P_{rad}\, G_1 G_r \left(\frac{\lambda}{4\pi d}\right)^2, \quad (5)$$

Equation (5) is called the Friis transmission formulaand gives a relation between the power radiated by the transmitting antenna and the power received by the receiving antenna. The Pathloss for the free space in dB then can be written as follows:

$$PL(dB) = 10\log\frac{P_{rad}}{P_r} = -10\log\left[\frac{G_1 G_r \lambda^2}{(4\pi)^2 d^2}\right] \quad (6)$$

The far-field (Fraunhofer) distance depends on the maximum linear dimension D of the transmitter antenna, R_f

$$R_f = \frac{2D^2}{\lambda} \quad (7)$$

For the distance to be in the far-field zone it should also satisfy $R_f >> D$ and $R_f >> \lambda$.

Free space path loss is the spreading loss in signal between two isotropic antennas ($G_1 = 1, G_r = 1$), and it can be expressed as:

$$PL(dB) = -10\log\left[\frac{d^2}{(4\pi)^2 d^2}\right] = -10\log\left(\frac{\lambda}{4\pi d}\right)^2 \quad (8)$$

Equation (8) shows that free-space path loss is proportion to the square of the distance between the transmitter and receiver, and also proportional to the square of the wavelength of the radio signal. Substituting (λ (in km) = 0.3/f (in MHz)), the generic free space path loss formula is stated in equation (9):

PL (*dB*) = 32.5 + 20 log10 (*d*) + 20 log10 (*f*) (9)

3.2. Log-distance Propagation model

The Log-distance model is an empirical approach for deriving radio propagation models and it is based on fitting curves or analytical expressions that recreate a set of measured data. Adopting this approach has the advantage of taking into account all the known and unknown phenomena inchannel modeling. In this model, power decreases logarithmically with distance. The average loss for a given distance is expressed using a Path Loss Exponent, n. The Log-distance propagation model is the path loss model that will be used in this research.There also exist many studies that use a variation of the Log-distance Path Loss model [4, 5]. For calculating the received power based on this model, we first calculate the received power at a reference distance

using the Friis formula and then, we incorporate the effect of path loss exponent. The Log-distance Path Loss model, PL (d) is represented below:

$$PL(d) \alpha \left(\frac{d}{do}\right)^{-n} \quad (11)$$

$$PL(d) = PL(d_o) + 10n\log\left(\frac{d}{do}\right) \quad (12)$$

$PL(d_o)$ is the free path loss in decibels which is usually determined at some specific reference distance, d_o from the transmitted signal; d is the distance between the transmitter and receiver in meters,n is a path loss exponent and it value depend on specific propagation environment. For free space n=2 and when obstruction are present n will have a larger value. The reference distance, d_o(typically 1m, 100m, or 1km depending on the environment [6])should always be in the far field of the antenna so that near field effects do not alter the reference path loss. In this study, d_0 is set to1m.

According to many studies which used the model or a variation of this model, the Log-distance Path Loss model is accurate and simple to use [4, 7]. The Log-distance Path Loss model also will work in our environment and could be used in the development of our signal strength monitoring system.

IV. EXPERIMENTAL DATA COLLECTION METHODS

Our method of data collection is based on site survey. Site survey is a method to survey Wi-Fi signal strength route by route within its coverage area [12]. It also involves measuring network performance at various locations and finding coverage and performance issues.

These experiments were carried out at the outdoor area surrounding of library buildings of our university, Benson Idahosa University (BIU), Benin City, Edo State, Nigeria. It is a story building with three 3 floors. However, the access point used for data collection was installed in the ground floor of the building.

For the field propagation measurement using site survey, an Acer laptop equipped with a wireless card, running on Microsoft windows XP platform with net surveyor software installed was used to collect Received Signal Strength Indicator (RSSI); the software has the ability to sniff any wireless LAN within the test area. In the Network Surveyor interface, the wireless adapter has the ability to scans all Wi-Fi channels of interest and then makes measurements of the RSS along the routes from the access point. Measuring tape of a longer distance calibrated in meters was used to measure the distance of received signal strength from the access point. On each of these paths, test points were manually measured at a 5m interval using the measuring tape to a 65m mark from the AP. Figure 1 shows a snap shot of net surveyor taken during data collection at library building. When taking measurement, the receiving antenna was visible to the transmitting antenna without or with very minimal obstruction. The sources of attenuations were basically from the movement of people and vehicles across the transmission path and attenuation due to the author's body.

Care has been taken that laptop was all the time oriented towards Access Point (TP-LINK router). For the purpose of this work, the measurements of radio signal strength are limited to consider path attenuation loss and analysis. Table 1and 2 describes measurement setup parameters for transmitter-receiver and the measured RSSI data.

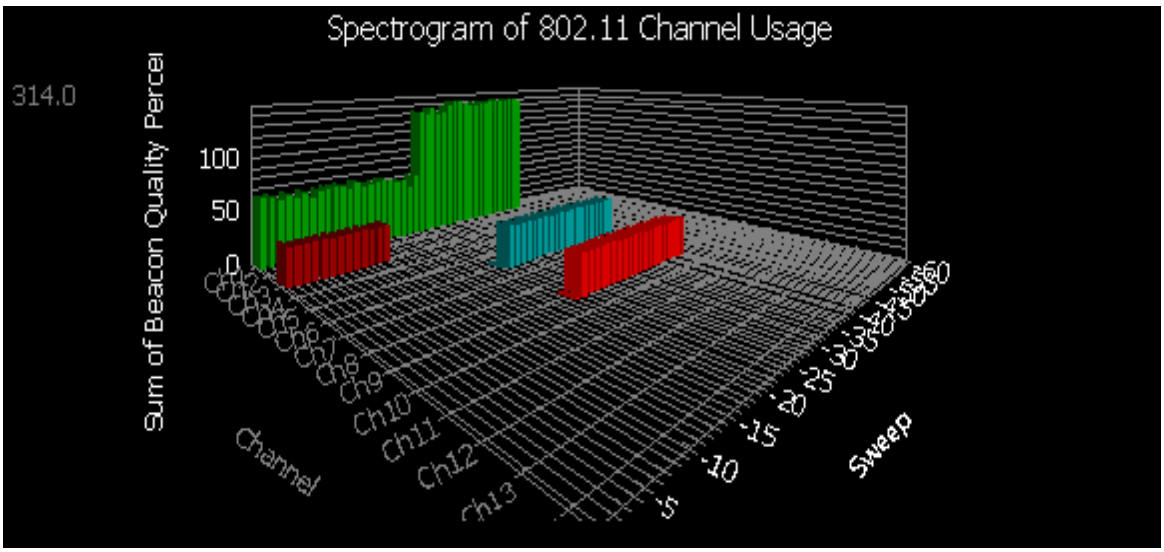

Figure 3: A spectrogram of measured RSSI data using Net surveyor

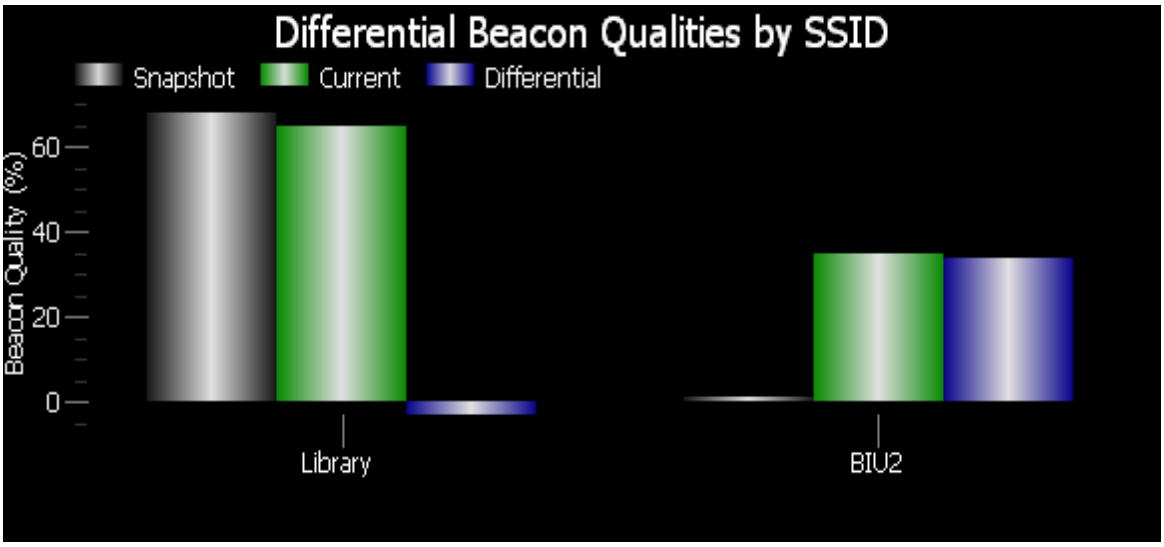

Figure 4: A snapshot of measured RSSI quality (%) using Net surveyor

RSSI is an indication of the power level being received by the antenna. Therefore, the higher the RSSI number the stronger the signal.

Table 1: T-R Measurement setup parameters

No.	Measurement setup	
	Name	Amount
1	Carrier Frequency (GHz)	2.4
2	Bandwidth (MHz)	20
3	Transmit Power (dBm)	30
4	Transmit antenna gain (dB)	6
4	Tx antenna height (m)	7
5	Rx antenna height (m)	1.5
6	Maximum data rate per stream(Mbit/s)	54
7	protocol	802.11g
8	Radio type	OFDM

V. RESULTS AND DATA ANALYSIS

Having known that the close-in reference distance (d_o), the path loss exponent(n) statistically describe the path loss model of an arbitrary location; to truly characterize propagation path loss for the environment (location), values should be establish for these parameters PL, n, and d_o,. The path loss exponent n which characterizes the propagation environment is obtained from the measured data by the method of linear regression (LR) analysis [8].

From field measurement, at close-in distance, (d_o) of 0.001 km, Lp (d_o) = 84 dB. Estimates or Predicted values of Path Loss at specified distances are calculated as follows:

At d_i = 0.001km = d_o,

Lp (d_i) = 84 + 10n log = 84

At d_o = 0.001km and r_i = 0.015km,

Lp (d_i) = 84 + 10n log = 56 + 1.8n

Subsequent evaluations were carried out in the same manner and the results are given in table 3.

Using LRanalysis the difference between the measured and predicted path loss values are minimized in a mean square sense, the sum of the squared errors is given by [8].

$$E(e) = \sum_{i=1}^{N} (PL - P\acute{L})^2 \quad (13)$$

$$E(e) = \sum_{i=1}^{N} [(PL - PL(d_o) + 10n\log(\frac{d}{do})]^2 \quad (14)$$

Where PL is the measured path loss and PĹ is the modeled path loss obtained using equation (2). The value of n which minimizes the mean square error e (n) is obtained by equating the derivative of equation (4) to zero and solving for n. Table 2 shows the measured path loss values while table 3 summarizes the regression analysis of measured data.

Table 2: Measurement Results

T-R separation distance, d(m)	RSS (dBm), Route 1	RSS (dBm), Route 2	RSS (dBm), Route 3	Average RSS (dBm)	PL(dB)
1	-54	-44	-45	-48	84
5	-62	-52	-61	-58	94
10	-63	-67	-70	-67	103
15	-68	-63	-75	-69	105
20	-71	-73	-83	-76	112
25	-62	-55	-81	-66	102
30	-76	-72	-80	-76	112
35	-67	-72	-81	-73	109
40	-66	-71	-83	-73	109
45	-77	-80	-86	-81	117
50	-79	-74	-82	-78	114
55	-80	-79	-88	-82	118
60	-79	-81	-89	-83	119
65	-81	-82	-100	-88	124

Table 3: Regression Analysis

Distance, r (m)	PL (dB)	PĹ	PL- PĹ	$(PL- PĹ)^2$
1	84	84	0	0
5	94	84+6.99n	10-6.99n	$100-139.8n+48.86n^2$
10	103	84+10.00n	19-10n	$361-380n+100n^2$
15	105	84+11.76n	21-11.76n	$441-246.96n+493.92n^2$
20	112	84+13.01n	28-13.01n	$784-728.56n+169.26n^2$
25	102	84+13.97n	18-13.97n	$324-502.92n+195.16n^2$
30	112	84+14.77n	28-14.77n	$784-827.12n+218.15n^2$
35	109	84+15.44n	25-15.44n	$625-722n+238.39n^2$
40	109	84+16.02n	25-16.02n	$625-801n+256.64n^2$
45	117	84+16.53n	33-16.53n	$1089-1090.98n+273.24n^2$
50	114	84+16.98n	30-16.98n	$900-1018.8n+288.32n^2$
55	118	84+17.40n	34-17.40n	$1156-1183.2n+302.76n^2$
60	119	84+17.78n	35-17.78n	$1225-1244.6n+316.13n^2$
65	124	84+18.13n	40-18.13n	$1600-1450.4n+328.70n^2$

The value of n, which minimizes the mean square error, is obtained by equating the derivative of equation (15) to zero, and when solving for n.

Therefore the value of the mean square error from the table gives:

$E(e) = \sum_{i=1}^{N} (PL - PĹ)^2 = 10014.00-10633.30n+2873.91n^2$ (15)

Differentiating equation (5) and equating it to zero gives the value for n.

$\frac{dE(e)}{(dn)} = \frac{d(10014.00-10633.30n+2873.91n2\ )}{(dn)} = 0$ (16)

n=1.82

Substituting the above calculated path loss exponent n into the model in equation (12) gives the model that describes the design parameters of a mobile link in that location. Therefore, the resultant path loss model is

PL(dB) = 84 + 10(1.85) log (d) (17)

The model expressed in equation (17) reveals that the corresponding environment has path loss exponent almost equal to that of free space (having n = 2). In general, results show that the obstructions in the environment considered here had little effect (not much) on radio signals. This may well be as a result of the way in which the measurements have been taken; precisely, during the measurements, the transmitting and receiving antennas were, more often than not, in direct sight.

Figure 5shows the relationship between Path loss and distance; as the distance increases the signals fading (path loss) increases.

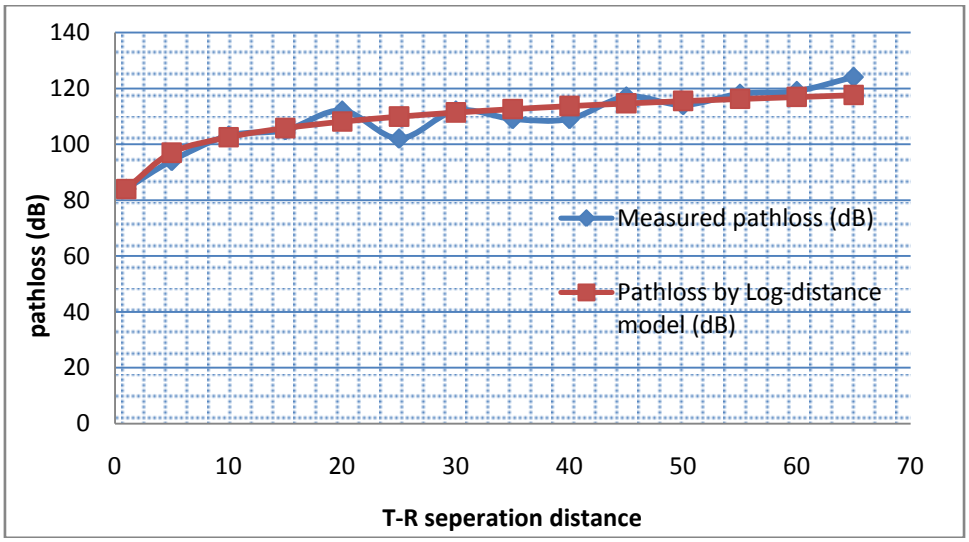

Figure 5: Log-distance model at n=1.85 and measured data.

VI. CELL RANGE AND COVERAGE AREA ESTIMATION

One critical problem in communication network design is the determination of the cell range or radius [9].As a client device moves farther away from the access point, the declining received signal power level forces thecommunication link to operate at successively lower data rates, until the signal or SNR is too low for communication at the lowest data received rate. See figure 6for illustration.

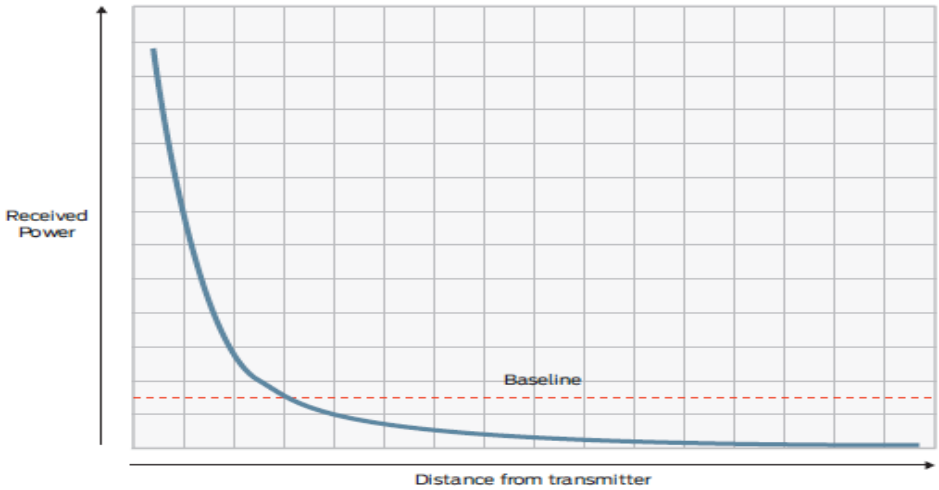

Figure 6: Signal Strength and distance

Thus, cellrange is the greatest distance from an access point (AP) at which the minimum data rate can be demodulated with an acceptable SNR or packet error rate or probability of error per bit (or bit error rate, BER); where it is assumed that there are no co-channel or adjacent-channel radiators in the vicinity. Coverage applies to moderate- size or large cellular deployments and is a measurement of the resulting cell size, or square meters per AP. Range, coverage and rate-weighted coverage are strongly influenced by transmit power, receiver sensitivity, noise and interference, as well as the physical environment. By analyzing, understanding and managing those parameters, WLAN system designers can greatly affect the overall performance of the system [10]. The underestimation of the cell radius leads to an overestimation of the number of access points (Aps) required to provide service in a specific area, and hence excessive deployment investment costs. This is obviously bad news for the business of the network operator. On the other hand, an overestimation of the cell radius results in the installation of fewer APs than needed, and then in shadow areas in also in turn create dead signal spots. This means the network operator provides bad Quality of Service (QoS) in terms of coverage, and customers will complain. This problem is more critical in wireless networks due to its susceptibility to traffic load in a given cell. When traffic increases, the cell radius decreases. Once cell range has been estimated, it can then be used to conduct optimization to obtain a cost-efficient network.

Here, similar to work by [11],the radius of a studied site or an AP determined from the pathloss model for optimal network performance by:

$r = 10^{(P_T - P_{min} - FM\sigma - A)/B}$ (18)

where A is the intercept of the optimised path loss model in dB, $B$is the propagation slope, $P_T$is the BS total transmit power, $P_{min}$is the minimum required signal strength (signal threshold) at the receiver and $FM\sigma$- is the fade margin. Fade margin is the amount of amount of extra signal, above the minimum receiver threshold level added to the path loss budget to account for signal fluctuations for the purpose of ensuring that the required quality of service is maintained at the cell edge. $FM\sigma$, that ensures the desired cell edge reliability, can be work out as [11]:

$FM_\sigma = \sigma Q^{-1}(1-P_{cov})$ (19)

where σ represents the composite variation due to two primary factors: lognormal fading and measurement error;P_{cov} is the probability the signal strength measured throughout the cell will meet or exceed a desired threshold (e.g. 75%).

The value of σ determined from equation (20) by

$\sigma(dB) = \sqrt{(\sum_{i=1}^{N} (PL - P\acute{L})^2/k)}$ (20)

where n=1.82 and k=14. Therefore substituting these values in equation (18) gives

σ(dB)=3.59

For

$FM_\sigma = 75\%$ (i.e., $FM\sigma = 0.675\sigma$) =2.43

$FM_\sigma = 90\%$ (i.e., $FM\sigma = 1.29\sigma$) = 4.62

$FM_\sigma = 95\%$ (i.e., $FM\sigma = 1.64\sigma$) = 5.74

For 75% cell edge reliability the estimated radius is

$r = 10^{-(30--75+2.43-84)/18.2)} = 0.05km$

Similarly, the radius for 90% cell edge reliability is given by

$r = 10^{-(30--75+4.62-84)/18.2)} = 0.04km$

And 95% cell edge reliability the estimated radius is

$r = 10^{-(30--75+5.74-84)/18.2)} = 0.03km$

The coverage area of the AP is also a critical factor in link budget analysis. Coverage of a serving AP represents the region around it, which it can reliably serve. It directly determines the number of and the separation between APs that must be set up to work together to serve a larger service area or customer base.

The next step is to determine the number of access points (AP) to ensure coverage. Given the cell range, the coverage area can be calculated. Coverage area is defined as an area where all network quality requirements are met. Any location outside the coverage region or of very limited coverage and it is called dead spot or zone.

A cell site is normally dimensioned using a hexagonal shape as shown figure 7. The cell area (shaded area) is given by:

$$Area_{cell} = \ 2 \ \text{x area of } \Delta ABC = 2x(\frac{1}{2} xpx \frac{l}{2}) = \frac{pl}{2} \quad (21)$$

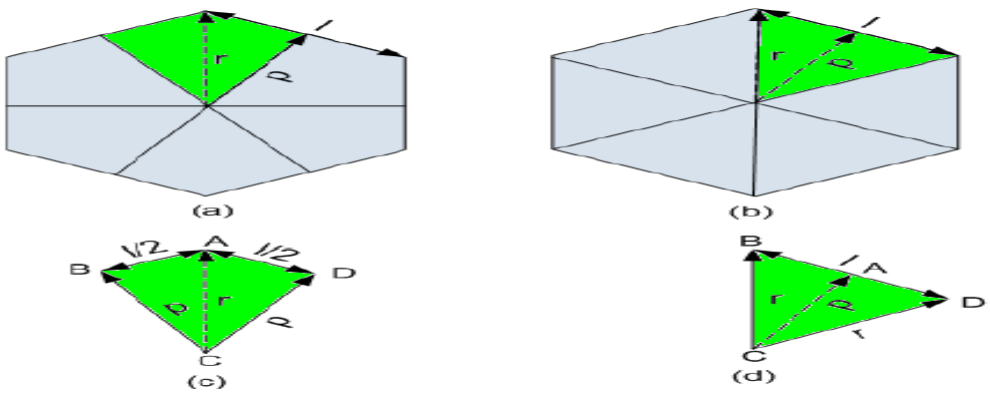

Figure 7: Cell Dimensioning

From the right angled triangle ABC,

$$p = \sqrt{r^2 - (l/2)^2} \quad (22)$$

If the hexagon is regular, i.e., the side length l and the radius r are equal, then $p = \frac{\sqrt{3}}{2} r$.

Now, looking at one of the equilateral triangles:

$$\text{Area of a triangle} = \frac{1}{2}\text{ x base x height } = \frac{1}{2}x\frac{\sqrt{3}}{2}r \text{ x } r = \frac{3\sqrt{3}}{4}r^2$$

and

$$The\ area\ of\ the\ hexagon = \frac{\sqrt{3}}{4}r^2x6 = \frac{3\sqrt{3}}{2}r^2x6$$

Thus the cell area,

$$Area_{cell} = \frac{3\sqrt{3}}{2}r^2 \qquad (13)$$

Therefore, the number of access points required for coverage is estimated by the expression in equation (14)[13]

$$N_{AP} = \frac{C_{total}}{Area_{cell}} \qquad (14)$$

Where N_{AP} is the number of access points required for coverage, C_{total} is the total cell area to be covered, and $Area_{cell}$ is the coverage of a single access point based on maximum power.The location where this research took is a medium-sized university campus and it the campus covers an area approximately 3260 square-metre(i.e C_{total}=3260 square-metre)of plane land [12].

VII. CONCLUSION

Propagation modeling is an effort to predict what happens to signals en route from the transmitter to the receiver. The accurate qualitative understanding of the radio propagation using path loss model as a function of distance from where the signal level could be predicted is essential for reliable mobile wireless system network plan.If network planning is carried out with the help of a network planning system then coverage planning, frequency planning, capacity planning, interference analysis, dominance analysis, handover analysis, etc. rely on the propagation predictions. The process of deciding AP placement can be greatly simplified with the use of propagation modeling tools. These tools use various modeling techniques to predict the signal coverage corresponding to a given placement of access point, enabling the network designer to try out various placements right on his desktop. Accordingly, the accuracy of the path loss models is of critical importance with regard to the design and implementation of wireless LAN.

This paper presents a Log Distance Model for signal path loss prediction in WLAN and the model reveals that the channel path loss exponent and the mean pathloss intercept are 1.82 and 84dB respectively. In summary, results show that the obstructions in the environment considered here had little effect (not much) on radio signals.

REFERENCES

[1] IEEE 802.11 Working Group: http://grouper.ieee.org/groups/802/11/

[2] Rappaport T.S., Wireless *Communications: Principles and Practice*, Prentice Hall PTR, New Jersey, 1996.

[3] Akkaşl, C (2009). Methods for Path loss Prediction, M.Sc Thesis, School of Mathematics and Systems Engineering, Vaxjo University.

[4] Pahlavan, K. and Levesque, A. H. "Wireless Information Networks". Wiley-Interscience. New York, NY, 1995. 73-112.

[5] Tipper, D. "Wireless Communication Fundamentals". University of Pittsburgh lecture. 2005. 40-42.

[6] J. B. Anderson, T.S. Rappaport, and S. Yoshida, "Propagation Measurements and Models for Wireless Communications Channels," IEEE Communications Magazine, January 1995, pp.42 – 49.

[7] Vig, J. "ISM Band Indoor Wireless Channel Amplitude Characteristics: Path Loss vs. Distance and Amplitude vs. Frequency". M.S. Thesis, Ohio University, 2004.

[8] Oguejiofor O.S, Oleka C.V, Ejiofor H.C, Okumbor N.A (2013). Mobile Radio Link Design Using Path Loss Model, International Journal of Engineering and Advanced Technology (IJEAT), Vol. 2, Issue-6, pp 421-424.

[9] Figueras, P. A., Salcedo-Sanz, S., Klaus, D. H., ´Opez-Ferreras, F. L., and Esteve-Asensio, G. (2009). Novel Heuristics for Cell Radius Determination in WCDMA Systems and Their Application to Strategic Planning Studies.*EURASIP Journal on Wireless Communications and Networking*, Vol. 2009, pp 1-14.

[10] Yee, J and Hossain, P. E. (2002). Understanding Wireless LAN Performance Trade-Offs, Communication System Design,pp 32-35.Available at www.CommsDesign.com.

[11] Bernardin, P., Yee, M., and Ellis, T.,(1997) "Estimating the Cell Radius from Signal Strength Measurements," 6th WINLAB Workshop, March, 20-21,

[12] Isabona, J andK. Obahiagbon(2013) ''APractical-Based Radio Channel Site Survey Approach for OptimalDeployment of a Campus WLAN'',Africa Journal of Computing and ICT, vol. 6, No 4, pp 133-146

[13] Isabona. J. (2013). Performance Optimisation of CDMA2000 Networks in South-South, Nigeria, Ph.D Thesis, Department of Physics, University of Benin, Benin City, Nigeria.

American Journal of Engineering Research (AJER)
e-ISSN : 2320-0847 p-ISSN : 2320-0936
Volume-03, Issue-01, pp-268-271
www.ajer.org

Research Paper Open Access

Properties of Concrete on Replacement of Coarse Aggregate and Cementitious Materials with Styfoam And Rice Husk Ash Respectively

Ananya Sheth[1], Anirudh Goel[2], B.H.Venkatram Pai[3]
[1,2,3]*Department of Civil Engineering, Manipal Institute of Technology / Manipal University, India*

Abstract: **-** This paper reports an experimental investigation on the influence of Rice Husk Ash (RHA)and Expanded Poly Styrene (EPS) on the mechanical properties and the properties of fresh concrete of the produced RHA and EPS blended concrete. EPS aggregates were used to replace coarse aggregates by volume with an aim to decrease the unit weight. Locally produced RHA was used to replace cement by its weight with an aim to increase workability.
Mixture proportioning was performed to produce target strength of 65 MPa. Past researches regarding complete replacement of coarse aggregates with EPS aggregates have shown strength of less than 10 MPa. Hence, our aim is to achieve strength of 25-30 MPa thereby utilizing environmentally sustainable concrete in the rapidly developing low cost housing sectors of developing countries.

Keywords: **–** *environment, sustainable concrete, expanded polystyrene, rice husk ash, low cost housing, concrete, 25 MPa, 4 more key words.*

I. INTRODUCTION

Medium weight concrete is the choice of designers owing to lighter and more economic structures. Medium weight concrete is produced by introducing air inside the concrete; either by using gassing and foaming agent or using lightweight aggregate such as natural aggregate (pumice, shale, slate) or industrial by-product (palm oil clinker, sintered fly ash) or plastic granules (Styrofoam or polymer materials). The high porosity of such industrial by-product and natural aggregates would cause adsorption of water and would prove disadvantageous in terms of shrinkage and permeability.

Styrofoam is popularly used as a good thermal insulation material in building construction. Besides, it is widely used in the packaging industry especially as a damping agent to protect soft goods from vibrations and damage during transportation. It has no secondary use and is treated as a waste product. Its is difficult to recycle which as a whole is not a fundamental process in developing countries. We propose the use of Styrofoam cubes in concrete to replace by weight, a percentage of coarse aggregate (grit) with a purpose to make our concrete lighter. The Styrofoam aggregate has a closed cell structure consisting essentially of 98% air. Due to the porosity and buoyancy, the lightweight aggregates in fresh concrete tend to float on the concrete surface.

Rice husk is an agro-by product which is produced in large quantities in agrarian countries. Approximately, 20 Kg of rice husk is obtained from 100 Kg of rice. Rice husk is constituted by 80% organic and 20% inorganic substances. When rice husk is combusted, the ash obtained can be termed Rice Husk Ash (RHA). It contains a high amount of amorphous phase content such as silicon dioxide which is the primary constituent of Portland cement. Therefore, RHA may be used as a constituent material in lime-pozzolana and/or a replacement for both cement as well as silica fumes.

Concrete samples were synthesized by mixing ordinary Portland cement, sand and coarse aggregate (grit) where some part of grit and cement was replaced (by weight), with Styrofoam aggregates and RHA respectively. A comprehensive range of samples having various permutations of density and compressive strength were obtained by proportioning the replacements.

II. EXPERIMENTAL DETAIL

2.1 MATERIALS.

2.1.1 CEMENT.

Ordinary Portland Cement - Grade 42

2.1.1.1 CHEMICAL COMPOSITION.

Silicon dioxide (SIO2) 21.00; Aluminium oxide (AL2O3) 5.30; Ferric oxide (FE2O3) 3.30; Calcium oxide (CAO) 65.60; Magnesium oxide (MGO) 1.10; Sulphur tioxide (SO3) 2.70; Loss of ignition (LOI) 0.90; Tricalcium silicate (C3S) 60.00; Dicalcium Silicate (C2S) 15.00; Tricalcium aluminate (C3A) 8.05; Tricalcium alumino ferrice (C4AF) 9.76.

2.1.1.2 PHYSICAL AND MECHANICAL PROPERTIES.

Blain CM2/GR 3.250, Autoclave expantion 0.02, Initial setting time (VICAT) 105 minutes, Final setting time (VICAT) 135 minutes.

2.1.2 SAND.

Fine sundried sand passing through 475 micron sieve was selected as the most appropriate to make a uniform and homogeneous binding matrix of the concrete to be produced.

2.1.3 COARSE AGGREGATE.

The coarse aggregate selected were 20mm down sized crushed granite aggregates.

2.1.4 STYROFOAM AGGREGATE.

The Styrofoam aggregate were 10 x 10 x 10 mm. cubes, cut from waste EPS (Expanded Polystyrene) sheets.

2.1.5 FLY ASH.

Fly ash material solidifies while suspended in the exhaust gases and is collected by electrostatic precipitatorsor filter bags. Since the particles solidify while suspended in the exhaust gases, fly ash particles are generallyspherical in shape and range in size from 0.5 μm to 100 μm. They consist mostly of silicon dioxide (SiO2), which is present in two forms: amorphous, which is rounded and smooth, and crystalline, which is sharp, pointed and hazardous; aluminium oxide (Al2O3) and iron oxide (Fe2O3). Fly ashes are generally highly heterogeneous, consisting of a mixture of glassy particles with various identifiable crystalline phases such asquartz, mullite, and various iron oxides. For the concrete mix so produced we use Class F flyash.

2.1.6 RICE HUSK ASH (RHA).

Rice milling generates husk as its by-product. About 78 % of weight is that of the rice grain, broken rice and bran. The remaining 22 % weight is husk. This husk is used as fuel in the rice mills to generate steam for the boiling process. Husk contains about 75 % organic volatile matter and the balance 25 % weight is converted into ash during the firing process. This is known as rice husk ash (RHA). RHA contains around 85 – 90 % amorphous silica. Therefore, for every 1000 kgs of paddy milled, about 220 kgs (22%) of husk is produced. This husk when combusted in boilers, generates about 55 kgs (25 %) of RHA.

India is a major producer of rice, and the husk generated during milling is mostly used as a fuel in the boilers for processing paddy , producing energy through direct combustion and / or by gasification . About 20 million tonnes of RHA is produced annually in India. Generally, RHA is dumped in a landfill and thereby causes damage.

The particle size of the cement is about 35 microns, which is why it can reduce the amount of cement in the concrete mix. RHA is a good super-pozzolana.

There is a growing demand for fine amorphous silica in the production of special cement and concrete mixes, high performance concrete, high strength-low permeability concrete, for use in bridges, marine environments , nuclear power plants etc. This is where RHA finds an extensive use.

2.1.7 SUPER PLASTICIZER

Poly carboxylate ether based super-plasticizer, “algihyperplast-n” claims to be a recommended product for batching plant mixed concrete of M50, M60 or higher grade concrete and where very high water reduction of 30-40% early and final strength is required or where colourless superplasticizer is required. It claims application

in mix M60 where collapse slump is need at w/c of 0.3. It claims to improve cohesive properties of concrete, reduce segregation and bleeding, save cement through economy in mix design, allow early demoulding. Also speed up construction.

Super plasticizer was added to the concrete mix in the ratio of 100-400ml for 50 kg of cement. Field trials are recommended to determine the optimum ratio.

2.2 Mix Design And Proportions.

Table 1: Mixture proportions of the synthesized concrete.

W/C RATIO	FLY ASH	CEMENT	FA	CA
0.3	0.6875	1	1.32	5.28

Table 2: Mix and replacement proportions.

Mix. No.	RHA Replacement by weight of the total cementitious material.	STYRO FOAM Replacement by volume of CA.	WATER (mL)	CEMENT (g)	FINE AGGREGATE (g)	COARSE AGGREGATE (g)	FLY ASH (g)	RHA (g)	STYRO FOAM (g)
C11	10 %	20 %	1260	1450	1600	5600	900	260	16.65
C12	10 %	25 %	1470	1450	1600	5250	900	260	20.80
C13	10 %	30 %	1260	1450	1600	4550	900	260	29.10
C21	20 %	20 %	1260	1280	1600	5600	750	520	16.65
C22	20 %	25 %	1260	1280	1600	5250	750	520	20.80
C33	30 %	30 %	1470	1120	1600	4550	700	780	29.10

A fixed amount of super plasticizer i.e. 7ml per 1kg of cementitious material was added. After that, it was tested for the fresh concrete properties of workability (the vee-bee test) and then moulded into cubical specimens of dimensions 15X15X15cm and tested to the simple compressive strength, water absorption by immersion. The tests had been carried through with ages of 7 days with curing in humid chamber.

III. RESULT

3.1 Workability.

The workability, measured in VB degrees is shown in Table 3. The results show that higher amounts of RHA replacement give a very high flow mix which causes segregation and the cement sand matrix settles down causing a failure to set and harden.

Table 3: Workability, measured in VB Degrees.

Mix. No.	C11	C12	C13	C21	C22	C33
VB-Degrees (s)	19	17	5	6	17	10

3.2 Water Absorption.

The results indicate that higher substitution amounts results in lower water absorption values, this occurs due to the fact that RHA is finer than cement. Adding 10% of RHA to the concrete, a reduction of 38.7% in water absorption is observed, but the presence of styrofoam results in a certain higher percentage of water retention because the water is filled in the voids of the styrofoam so used.

3.3 Simple Compressive Strength.

The compressive strength is shown in Table 4. The addition of RHA caused an increment in the compressive strength due to the capacity of the pozzolana to fix the calcium hydroxide; generated during the hydration of cement. All samples which contained RHA showed increased compressive strength. However, the addition of styrofoam reduced the strength of the concrete. Greater percentage replacement of styrofoam rendered lesser strength owing to the inherent lower compressive strength of the polymer as compared to granite aggregates. Micro-cracks were developed after the hydration process near the styrofoam – cement paste joints.

Table 4: Simple Compressive Strength.

Mix. No.	C11	C12	C13	C21	C22	C33
Compressive Strength (MPa)	26.55	20.55	23.55	20	18.2	15.55

IV. CONCLUSION

The use of RHA in civil construction, besides reducing the environmental pollutants factors, may bring several improvements for the concrete characteristics. With the addition of RHA to concrete, a decreasing in water absorption was verified. According to the results of compressive strength test, all the replacement degrees of RHA researched showed an increase in the compressive strength to a particular level of replacement, but decreased if replaced to a higher degree.

Greater surface area of the aggregate provides a larger area for bonding contact with the cement paste. Therefore, the strength of the concrete matrix will be higher. A smaller sized aggregate would yield greater surface area and hence would provide more surface for coating with binders. Thus, the usage of smaller size aggregates of styrofoam is preferable. Moreover, due to the structure of the Styrofoam cubes, the compressive strength at the corners was observed to be stronger and the faces notably remained soft.

The highest compressive strength was obtained using minimum RHA content with the minimum Styrofoam content of size roughly 10 cubic mm. However, all the Styrofoam concrete series exhibited lower strength compared to the standard concrete mixture referring to the available literature. The concrete mixes under consideration produced strength in the range of 17-26 MPa at 7-days which is beyond the minimum requirement for structural lightweight applications, therefore this series is economical, lighter in weight and suitable for structural use.

ACKNOWLEDGEMENTS

We would like to acknowledge the faculty and staff of Manipal Institute of Technology's Material Testing Laboratory and Civil Engineering Laboratory for allowing us to conduct the experiments and use their facility for the purpose of this paper. We would also like to thank the staff of the library for allowing us to borrow from their large database of books and journal papers.

REFERENCES

A reference list **MUST** be included using the following information as a guide. Only *cited* text references are included. Each reference is referred to in the text by a number enclosed in a square bracket (i.e., [3]). References **must be numbered and ordered according to where they are first mentioned in the paper,** NOT alphabetically.

Journal Papers:

[1] V.I.E Ajiwe, C.A Okeke, F.C Akigwe, A preliminary study of manufacture of cement from rice husk ash, *Bioresource Technology ,ELSEVIER, Volume 73,Issue 1,May* 2000,37-39.

[2] Raoul Jauberthie, Frank Rendell, Seni Tamba, Ibrahima Khalil Cisse, Properties of Cement – rice husk mixture, Construction and building Materials, ELSEVIER, Volume 17, Issue 4, June 2003, 239-243.

[3] Muhammad Shoaib Ismail, A.M. Waliuddin, Effect of Rice husk ash on high strength concrete, Construction and building Materials, ELSEVIER, Volume 10, Issue 7, October 1996, 521-526.

[4] European Union – Brite EuRam III, A rational mix design method for lightweight aggregate concrete using typical UK materials, EuroLightCon, Document BE96-3942/R5, January 2000.

[5] Standard practice for selecting proportions for structural lightweight concrete, ACI 211.2-81.

[6] Irving Kett, Engineered Concrete: Mix Design and Test Methods, Second edition, New Developments in Portland Cement Concrete (PCC) Technology, 182-184.

[7] Kevin J. Simons, Affordabe Lightweight High Performance Concrete (ALWHPC) – Expanding the envelope of concrete mix design, University of Nebraska – Lincoln.

Web data dases:

[8] www.ricehuskash.com/publications.htm

[9] www.ricehuskash.com/details.htm

[10] http://www.lightconcrete.com/images/LightConcrete.pdf

American Journal of Engineering Research (AJER)
e-ISSN : 2320-0847 p-ISSN : 2320-0936
Volume-03, Issue-01, pp-272-279
www.ajer.org

Research Paper Open Access

Impact of Transmission Distance on the Strength of Received Signals within the Vicinity of Four Base Stations

Adegboyega Gabriel A., FapohundaKofoworola O., Famoriji John O*.
Department of Electrical and Electronic Engineering, Federal University of Technology, P. M. B. 704,Akure, Nigeria.

Abstract: *-*Signal propagation is an essential part of communication system. The achievement of a complete communication system involves the source where the signal is been generated from, the medium and the destination. This research work concentrated on radio broadcasting stations where the source of reference is mainly the radiating antenna, free space as channel and receivers as the destination. The broadcast signal strength measurements were carried out around radiating antennas for four different radio broadcasting stations situated in different locations. It was therefore established that the radio broadcast signal strength decreases as the line-of-sight distance increases except along a transmission path where metal-poles were found.

Keywords*: -Radio, Signal Strength, Line-of-Sight.*

I. INTRODUCTION

An observation was made that clear radio signals were not regularly received and as such this paper was borne out of the inquisitiveness to know what was responsible for this and to be able to determine how distance (nature of path inclusive) can affect the signals received. Eric Cheng-Chung L.O. (2007) [1] reported: Electronic communication is the currency of our time, which lies on communicating information at certain rate between geographically separated locations reliably. Figure 1 shows the process taking to transmit and receive a message electronically.

Figure1: Communication Process [1]

Also, the ionospheric radio propagation has a strong connection to space weather. A sudden ionospheres' disturbance or shortwave fadeout is observed when the x-rays associated with a solar flare ionize the ionosphere D-region. Enhanced ionization in that region increases the absorption of radio signals passing through it. Whenever we experience the strongest solar flares, complete absorption of virtually all ionospherically propagated radio signals in the sunlight hemisphere can occur. These solar flares can distrupt HF radio propagation and affect the GPS accuracy [2]. Since radio propagation is not 100% predictive, services such as the emergency locator transmitters in flight communication with ocean crossing aircraft as well as some television broadcasting have been moved to communication satellites because a satellite link though expensive can offer highly predictable and stable line of sight coverage of a given area.
The inverse square law is a principle that describes the way radiant energy propagates through space and it states that the power intensity per unit area from a point source, if the rays strike the surface at a right angle, varies inversely according to the distance from the source.

II. PATH LOSS MODEL

A transmission via a radio channel will be affected by path loss (average signalpower attenuation), which is largely depending on the distance between thetransmitting and receiving radio antennas. Further,

characteristics of objectsin the radio channel, particularly in the vicinity of the receiving MS, such asterrain, buildings and vegetation may also have a significant impact on thepath loss.

The prediction of the expected mean value of the received signal power,PRx, is crucial in the planning-phase of a cellular mobile radio network. Theknowledge of the expected coverage area for each base station in a cellular network isvery important in order to estimate the minimum acceptable reuse distanceof the carrier frequencies [3]. In CDMA radio access systems, such as IS-95,the BS coverage area will dictate the PN sequence reuse scheme that has tobe put in place [3].In a simple propagation model, the mean path loss is proportional to thedistance, d, to the power of the path loss exponent, γ, as$L \propto d$ (1)where γ indicates the rate at which the path loss increases with distance. Inthe logarithmic domain, this relationship may be expressed as:

$$L[dB] = A + B\,\gamma \log10(d) \qquad (2)$$

where the terms A and B are variables that depend on multiple parameters,as will be shown in later sections. The variable γ depends on terrain andtopographical features and may take on values from 2 (free space) up to 6for strong attenuation. For guided wave phenomenon, which may occur intunnels, street canyons, or corridors inside buildings, even values below 2 arepossible. Some of the models developed over the years are: Okumura Model, COST231-Hata model, Egli Model, Friis Model etc [4-10].

III. RESEARCH METHODOLOGY

The general survey and physical planning of the propagation environment was done first. This was to ensure that the best routes for the research were taken in order to ensure that the environmental factors (both natural and manmade) to be considered for all the stations are not totally the same. The battery of the GPS and the field strength meter were charged. GPS 72 Germin (Plate 1) was used to determine the elevation, longitude and the latitude of the locations where measurements were taken. This was also used to measure the Line Of Sight (LOS) distance (in meters) from the transmitting antenna. In situations where 150m distance could not be obtained before a major obstacle, the distance from the base of the transmitting antenna to the obstacle was first taken and added to the width of the obstacle measured at its end. The total was recorded as obstacle distance and the new point after the obstacle was taken as the reference point (Fig. 2). At approximately 10m separating distance, the signal strength measurementwas taken in dBμ using a BC1173 DBC field strength meter of 50 ohm (Plate 2) at different observation point (Fig. 3). Data comparism was done by plotting the graph of signal strength against distance for each station. This is as summarized in figure 2.

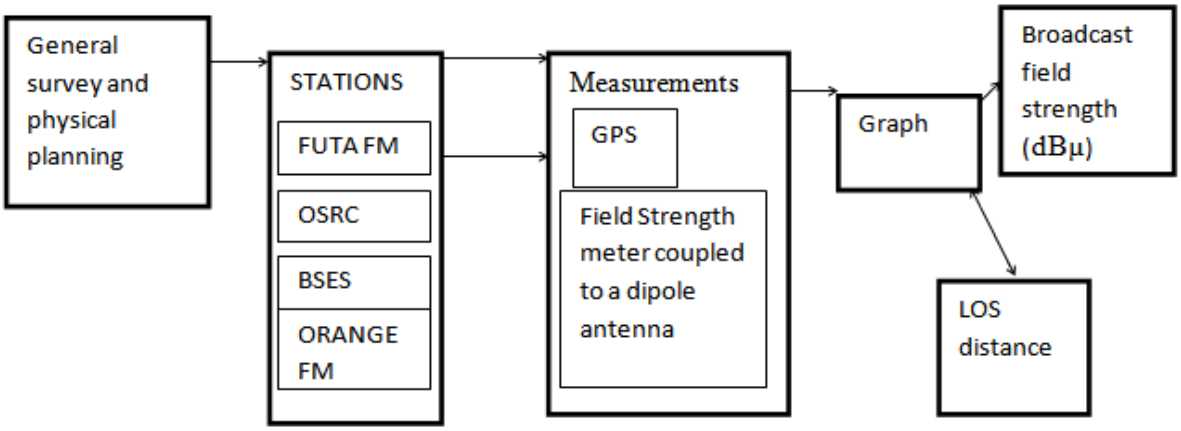

Figure 2: Research Performance matrices

Plate 1: Field Strength Meter **Plate 2: GPS**

The propagation measurement environment of this study was performed within 150m line of sight distance from the reference point by considering only one path for each base station. The FM stations considered are:

- Ondo State Radio vision Corporation (OSRC) 96.5MHz
- Broadcasting Service of Ekiti State (BSES) 91.5MHz
- FUTA Radio Station 93.1MHz
- Orange Radio Station 94.5MHz

Figure 3: Observation Point

IV. RESULTS AND DISCUSSION

Table 1: Measurement taken at OSRC from the Reference point to a Distance of 150m

LOS DISTANCE (m)	Nº	Eº	ELEVATION (m)	ACCURACY (m)	AVERAGE SIGNAL STRENGHT READING (dBµV)
0.00	07.30345	005.16122	395.2	14.5	82.4
10.13	07.30353	005.16114	395.6	18.0	81.65
20.08	07.30340	005.16164	394.4	16.6	80.01
30.14	07.30293	005.16098	397.1	9.9	78.85
40.19	07.30285	005.16096	393.5	8.5	76.89
50.01	07.30273	005.16091	396.5	9.4	75.84
60.14	07.30266	005.16089	392.1	8.8	74.86
70.00	07.30259	005.16084	394.8	8.3	73.87
80.16	07.30249	005.16082	392.6	9.3	71.06
90.10	07.30240	005.16078	393.1	9.9	70.63
100.09	07.30233	005.16074	394.1	8.1	69.21
110.32	07.30223	005.16071	394.2	7.1	68.82
120.14	07.30215	005.16067	391.3	8.1	67.58
130.33	07.30208	005.16062	389.7	9.9	66.84
140.06	07.30198	005.16060	390.8	8.1	65.99
150.03	07.30188	005.16055	392.1	8.3	64.86

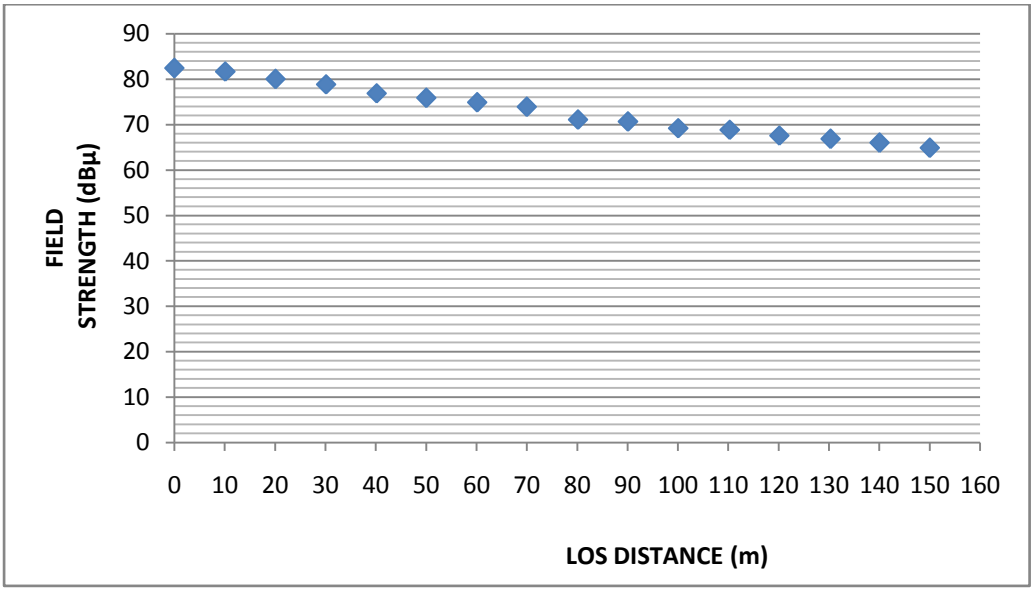

Figure 4: Propagation Profile of OSRC Radio Station (96.5 FM)

Table 1 shows the results of measurements taken with OSRC Radio Station where Fig. 4 shows the relationship between signal field strength. It could be observed that the field strength decreases with increasing distance from the reference point and also from the base station. This obeys "inverse square law" of radio wave propagation. But at certain points, the attenuation was not much; this could be as a result of the short range of distance considered.

Table 2: Measurement taken at BSES from the reference point to a distance of 150m

LOS DISTANCE (m)	N°	E°	ELEVATION (m)	ACCURACY (m)	AVERAGE SIGNAL STRENGHT READING (dBμV)
0.00	07.67551	005.24690	383.7	9.4	82.3
10.06	07.67553	005.24678	388.9	9.0	79.73
20.15	07.67555	005.24670	388.0	7.2	79.03
30.04	07.67558	005.24661	388.7	8.1	76.87
40.09	07.67562	005.24651	387.3	8.2	70.07
50.10	07.67564	005.24643	391.9	8.9	69.26
60.24	07.67566	005.24634	390.9	8.5	68.84
70.06	07.67570	005.24626	392.6	7.4	66.87
80.18	07.67575	005.24614	399.7	7.8	65.48
90.61	07.67577	005.24605	396.3	8.6	63.78
100.49	07.67578	005.24597	391.9	8.2	61.98
110.72	07.67581	005.24588	395.5	9.1	60.03
120.26	07.67585	005.24581	396.9	7.8	58.45
130.06	07.67587	005.24572	393.0	8.0	56.84
140.22	07.67591	005.24565	394.5	7.0	54.19
150.48	07.67594	005.24557	394.3	9.2	52.83

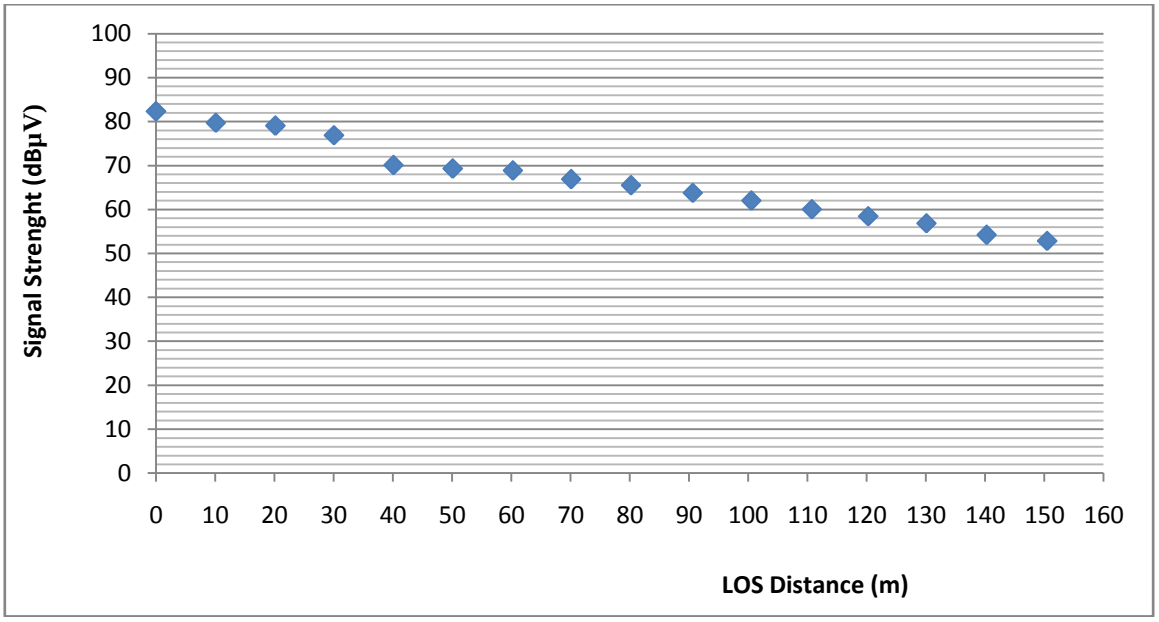

Figure 5: Propagation profile of BSES Radio Station (91.5 FM)

Table 2 shows the results obtained at the BSES Radio Station and Fig. 5 shows the relationship that exists between the two measured parameters. It could be observed that, signal strength decreases as the line-of-sight distance increases. It also obeys the "inverse square law".

Table 3: Measurement taken at ORANGE FM from the reference point to a distance of 150m

LOS DISTANCE (m)	Nº	Eº	ELEVATION (m)	ACCURACY (m)	SIGNAL STRENGHT AVERAGE READING(dBµV)
0.00	07.28979	005.19405	378.1	11.0	94.4
10.07	07.28976	005.19395	379.6	9.5	93.85
20.07	07.28990	005.19398	378.9	8.2	92.08
30.05	07.28996	005.19381	378.9	9.1	91.65
40.35	07.29002	005.19375	377.0	10.1	90.43
50.26	07.29008	005.19361	379.6	14.3	88.87
60.01	07.29014	005.19355	380.3	10.4	87.59
70.07	07.29019	005.19349	380.0	8.9	85.84
80.06	07.29025	005.19342	381.7	10.2	84.01
90.13	07.29030	005.19332	383.5	8.3	82.75
100.08	07.29033	005.19325	381.8	8.7	80.89
110.26	07.29032	005.19313	384.2	8.7	78.54
120.04	07.29034	005.19307	382.0	8.9	76.68
130.25	07.29037	005.19297	381.3	8.7	74.87
140.06	07.29038	005.19287	381.2	9.0	72.54
150.12	07.29040	005.19275	385.1	10.2	70.34

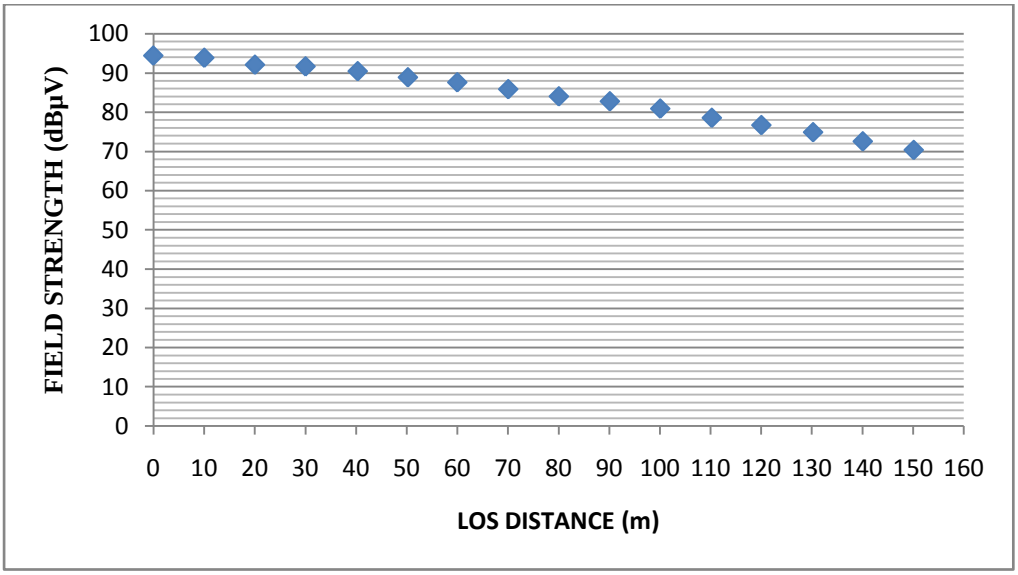

Figure 6: Propagation Profile of Orange Radio Station (94.5 FM)

Table 3 shows the results obtained with Orange Radio Station and Fig. 6 shows the relationship that exist between measured signal strength and line-of-sight distance. It could be observed that, signal strength decreases as the line-of-sight distance increases. It also obeys the "inverse square law" which states that the signal field strength is inversely proportional to the square of the line-of-sight distance.

Table 4: Measurement taken at FUTA Radio from the reference point (antenna base) to a distance of 150m

LOS DISTANCE (m)	N°	E°	ELEVATION (m)	ACCURACY (m)	SIGNAL STRENGHT AVERAGE READING (dBµV)
0.00	07.30240	005.13887	391.5	16.6	90.64
10.16	07.30235	005.13876	392.0	10.3	86.73
20.57	07.30224	005.13874	389.9	7.9	85.7
30.03	07.30217	005.13871	383.7	8.9	83.89
40.07	07.30202	005.13870	387.8	10.2	80.21
50.04	07.30195	005.13868	390.5	8.0	84.06
60.11	07.30180	005.13867	388.3	10.0	84.01
70.22	07.30172	005.13863	390.7	8.7	85.52
80.17	07.30177	005.13860	389.9	11.3	71.83
90.08	07.30168	005.13858	391.1	7.3	69.94
100.12	07.30159	005.13859	387.8	9.7	67.57
110.19	07.30145	005.13858	389.0	9.4	65.72
120.07	07.30136	005.13855	390.2	10.4	64.03
130.10	07.30126	005.13854	389.5	9.6	62.68
140.04	07.30120	005.13853	390.2	10.5	60.55
150.06	07.30109	005.13852	387.3	9.5	59.87

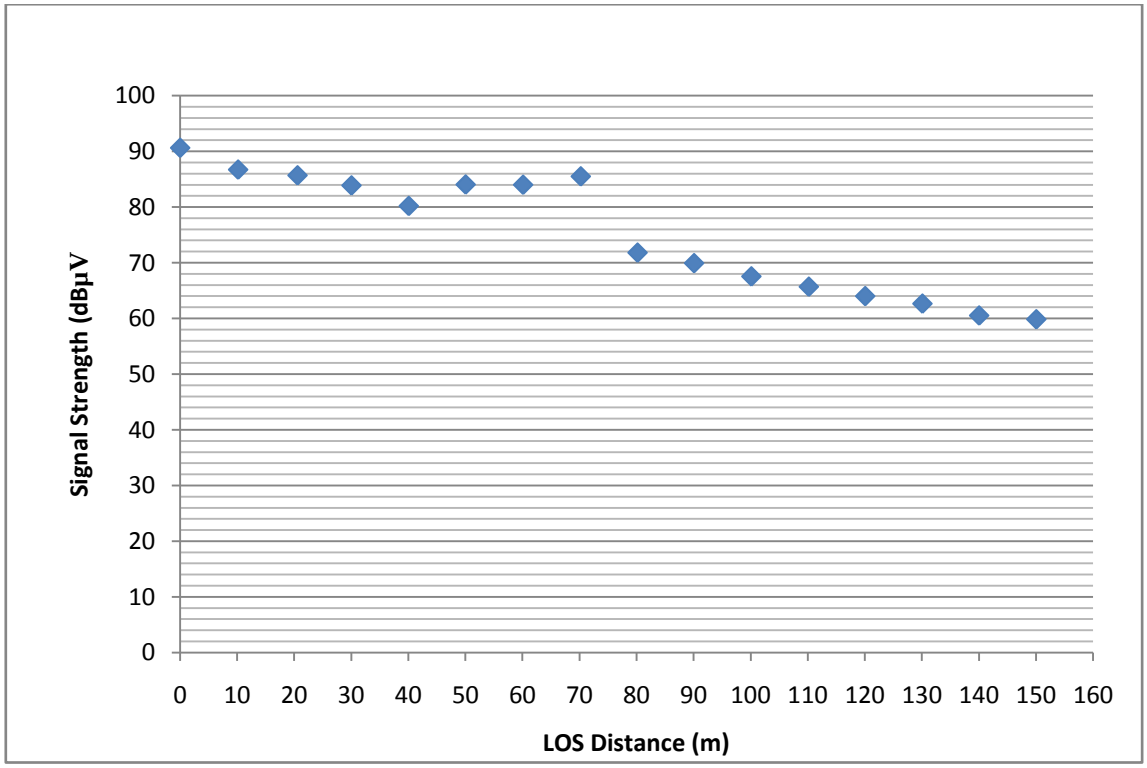

Figure 7: Propagation Profile of FUTA Radio Station (93.1 FM)

Results obtained with FUTA radio station is presented in Table 4 while Fig. 7 indicates the relationship that exists between signal strength and line-of-sight distance. It was observed that the graph did not completely obey "inverse square law" (decrease in signal strength as a result of increase in distance) this was because there were metal poles situated at some points along the transmission path taken (plates 3); these poles acted as signal strength booster there by increasing the strength of the signals towards them. Comparing the graphs obtained from this research to an ideal situation where there are no boosting antennas, the signal strength would decrease as the transmission distance increases and vice versa with reference to the base station.

Plates 3: Image of Metal Poles found along the Path taken.

V. CONCLUSION

Based on the work done so far, it was generally observed that signal strength reception is a function of distance, natural and man-made environment of the transmission path taken by the signal. Attenuation of radio waves increases with increasing transmission line-of-sight distance as well as the number of absorbers situated along the path taken but increases whenever reflectors are encountered.

REFERENCES

[1] Eric Cheng-Chung L.O. (2007), An investigation of the impact of signal strength on Wi-Filink through propagation measurement, A dissertation submitted to the University of Technology, Auckland.

[2] Frank Kleijer, (2004) Troposphere modelling and filtering for precise GPS levelling Ph.D Thesis, Department of mathematical Geodesy and positioning, University of Technology, Delft.

[3] ITU-R Recommendation P.370-7, "VHF and UHF propagation curvesfor the frequency range from 30 MHz to 1000 MHz," October 1999.

[4] J. D. Parsons, *The Mobile Radio Propagation Channel*. Chichester,England: John Wiley & Sons Ltd., 2000.

[5] H. Demuth and M. Beale, *Neural Network Toolbox*, MATLAB, Natick,MA, USA, January 2003.

[6] TIA/EIA/IS-95, "Mobile station-base station compatibility standard fordual-mode widebandspread spectrum cellular system," TelecommunicationsIndustry Association, July 1993, Washington, USA.

[7] E. ¨Ostlin, H.-J. Zepernick, and H. Suzuki, "Evaluation of the new semi-terrainbased propagation model Recommendation ITU-R P.1546," in*IEEE Semiannual Vehicular Technology Conference*, vol. 1, Orlando, FL,USA, October 2003, pp. 114–118.

[8] "Macrocell radio wave propagation prediction using an artificialneural network," in *IEEE Semiannual Vehicular Technology Conference*,vol. 1, Los Angeles, CA, USA, September 2004, pp. 57–61.

[9] E. ¨Ostlin, H. Suzuki, and H.-J. Zepernick, "Evaluation of the propagationmodel Recommendation ITU-R P.1546 for mobile services in rural Australia," *IEEE Transactions on Vehicular Technology*, vol. 57, no. 1,pp. 38–51, January 2008

[10] ITU-R Recommendation P.1546, "Method for point-to-area predictionsfor terrestrial services in the frequency range 30MHz to 3000MHz," October2001.

[11] ITU-R Recommendation P.1546-1, "Method for point-to-area predictionsfor Terrestrial services in the frequency range 30MHz to 3000MHz," April2003.

American Journal of Engineering Research (AJER)
e-ISSN : 2320-0847 p-ISSN : 2320-0936
Volume-03, Issue-01, pp-280-291
www.ajer.org

Research Paper Open Access

Processing Of Fe - 1%Tic and Fe - 2%Tic Composites & Densification Behaviour Including Mechanical Properties

[1] Mrs. S. K. Pandey, [2] K. S. Pandey
[1] *Director, National Institute of Technology, Karaikaal, Puducherry, India.*
[2] *Professor, Department of Metallurgical and Materials Engineering, National Institute of Technology, Tiruchirappalli –620 0 15, Tamil Nadu, India.*

Abstract: - Present investigation pertains to evaluate the densification mechanism/s exhibiting the influence of initial preform geometries and the composition as well as to assess the mechanical properties of hot forged discs and square cross–section (~14mm x ~14mm) bars with an approximate lengths of 100±05mm at 1150 ± 10^0C of Fe -1%TiC and Fe–2.0%TiC systems. These compacts of the above systems were prepared on a 1.0MN capacity UTM, in the relative density range of 0.84 ± 0.01 by taking accurately pre-weighed powder blends for all aspect ratios, namely, 0.25, 0.50, 0.75 and 1.24 respectively by applying pressures in the range of 435 ± 20 M Pa using a suitable die, punch and the bottom insert. Ceramic coated compacts were sintered in an electric muffle furnace at 1150±10^0C for a period of 100 minutes. Sintered compacts of first three initial aspect ratios were axially hot upset forged to different height strains, whereas, the fourth one were hot forged to square cross - section bars of the above dimensions. Ten such bars were forged. Analysis of experimental data and the calculated parameters has shown that the lower aspect ratio preforms densified more rapidly compared to the higher aspect ratio preforms. Mechanical properties such as yield strength, tensile and fracture strengths including percentage elongation and percentage area reduction were obtained by conducting uniaxial tensile tests. Further homogenization step has improved the above properties. Thus, the present investigation opens up a new area of research.

Keywords: - *ceramic coating, Composite, densification, forged***,** properties, relative density,

I. INTRODUCTION

World wide popularity of Powder Metallurgy lies in the ability of this technique to produce complex metal shapes to exact dimensions at high rate and at extremely economical prices, and, thus, providing technical achievements to improve quality composite materials. These are produced with care from the various complex multi-phase powder particles via compaction, sintering and forging. Powder is compacted to desired shape of sufficient strength in lubricated dies after initial powder characterization. Lubrication reduces friction effects and provides strength and ease of ejection after pressing. Proper compacting at required pressures, the compacts attain sufficient strength to withstand ejection from the tools and subsequent handling unto the completion of sintering without breakage or damage. Thus sintering is an important step in powder metallurgy by which the required properties like strength, densification and dimensional controls are attained. Sintering temperature is normally taken in the range of 0.7 to 0.9 times of the absolute melting point of the highest melting major element taken in the investigation [1]. However, in order to achieve near full densification, a forging step is involved. This process gives the material its almost full strength, i.e., the material has attained near to full density [2].

Growing demand for materials to meet high temperature engineering applications present a serious problem to design engineers and to the metallurgist and thus a structural material which can be used at elevated temperatures is a boon today. This resulted in the quest for new materials, which demand greater efficiency in steam engines to aircraft and to missiles. The major requirements of such materials are high temperature resistance with increasing temperatures, high wear resistance, minimal oxidation and scaling rates [3]. Thus, structural materials can be divided in four classes namely, metals, ceramics, polymers and composites respectively. Composites, in general, consist of two or more separate materials combined in a macroscopic

structural unit and are made from various combinations of metals, ceramic and polymers. Composites are generally used because they possess desirable properties which could not be achieved by either of the single constituents alone. Particles, flakes or fiber reinforcements are used. The matrix in the larger unit which holds the reinforcements and protects them from external damage transfers and distributes loads to fibers [4]. A composite is considered to be a multiphase material with a combination of properties. A strong material is relatively dense with increased strengths and stiffness but at a substantial loss of impact strength. Cermets are examples of ceramic – metal composites. Most common cermets is the cemented carbide which is composed of extremely hard particles of refractory carbide ceramic such as tungsten or titanium carbide embedded in a matrix of a metal. These composites are utilized as cutting tools for hardened steels. The hard carbide particles provide the cutting surface, but, being extremely hard, they are embedded in a matrix of a metal. They are as inclusions in a ductile metal matrix which isolates the carbide particles from one another and prevent particle to particle crack propagation [5]. However, the performance of composites depends upon the materials of which the constituents are composed, i.e., the form, structural arrangement of the constituents and the interaction among the constituents [4].

Iron based composites have been used widely spelled out structural applications in aircraft, missiles, engine components etc. With iron as a matrix imparts better high temperature softening resistance, a much better anti-seizure property and a higher wear resistance [6]. However, titanium carbide imparts wear resistance and hardness to the matrix phase. The electrical conductivity is found to be decreasing with increase in titanium carbide addition [7]. These tool materials with titanium carbide can be machined and are corrosion, oxidation and wear resistant. In addition, they are light weight and have high elastic modulus and vibration damping capacity. Apart from these titanium carbide is a cheap, easily available material with a high thermodynamic stability [8].

I.1 Manufacture of composites

Fabrication methods involve processing the metal either in a molten or in a solid state. Components can also be formed either by direct combination of matrix and the reinforcements or by the production of a precursor composite which in the form of composite wires, sheets, and laminates that are used to build up the component. Subsequently, the assemblage of piles must be consolidated and bonded in later processes.

In liquid – metal techniques, composites are prepared by infiltrating mats or fiber preforms with liquid metals or under carefully controlled conditions by physically mixing the reinforcements and the liquid metal together. A pseudo-liquid route is offered by plasma or flame spraying in which metal powder particles are heated above their melting point and are sprayed onto an array of fibers on a thin sheet of the same matrix metal. The resulting sheet of fiber-reinforced metal can then be stacked with other sheets and consolidated in subsequent operation. The simplest solid – state preparation route is to mix short fibers or particulates with metal powder. Alternatively, the metal can be coated onto the reinforcement by electrochemical or chemical vapour deposition method [9]. Few methods described in literature [9-13] for the manufacture of composites are liquid metal infiltration, squeeze casting, stir casting or compo-casting, consolidation and bonding methods, semi-solid slurry processing, co-spraying, press molding techniques, filament winding techniques, electrochemical co-deposition and powder metallurgy techniques.

Some of the processes adopted to produce particular composites include electro-deposition of zirconnia in a copper matrix [13], in-situ preparation of titanium base composites reinforced matrix by titanium boride single crystals by using P/M technique [14], manufacture of aramid fiber reinforced nylon-12 by dry powder impregnation [15], manufacture and properties of polyethylene homo-composites [16], combined process of coating and hybridizing for the fabrication of carbon – fibers reinforced aluminium matrix composites [17], manufacturing and applications of structural sand-witch components [18], silicon carbide particulates reinforced aluminium matrix composite rods and wires produced by new continuous casting route [19]. Pressure less sintering of and characterization of alumina (Al_2O_3) platelets reinforced barium-magnesium alumino-silicate glass composites [20] and carbon-fiber reinforcement on glass [21] are some of the examples quoted.

I.2 Porosities in Composites

Composites made by P/M route and conventional casting methods contained good amount of porosities and were not well eliminated and the distribution of reinforcements were not greatly improved. The presence of considerable amount of porosities means the occurrence of incomplete bonding between the matrix and the reinforcements, i.e., poor wetting. However, in the Pressure less state, a great enhancement in wetting between the melt and the reinforcements is feasible. Therefore, a prominent improvement in tensile properties can be obtained because of the interfacial bonding in this type of composite which renders it superior to conventional composites [22]. However, the porosities in these composites can be reduced considerably by mechanical working such as extrusion, swaging, forging and rolling etc. [23]. The plastic deformation contribution to the

overall densification is a function of the deformation behaviour of the different components in the powder composites [25].

I.3 Mechanism of Deformation

Production of parts by conventional P/M route involves compaction and sintering which has a substantial fraction of voids which limit its use to less than heavy duty applications. One method to enhance properties of sintered materials involves deformation process which densifies and develops final desired shape. Powder preform forging is particularly attractive because it blends the cost and material saving advantages of conventional press and sinter powder compacts with the higher production rates and property enhancement due to forging which has enhanced the density. Investigation of densification of a porous material is facilitated by consideration of deformation of material element containing a void. It is well known that from the theory of plasticity analysis of a thick walled sphere that it is impossible to completely close a hole purely by the application of hydrostatic loading of a finite magnitude. However, the pressure (P) required for a plastic deformation of a sphere containing a hole is given by:

$$P = 2\sigma_o \ln (r_0/r_f) \quad \ldots\ldots\ldots (1)$$

Where "σ_o" is the flow stress of the material, "r_0" is the outside radius (equivalent to mean space between the voids), "r_f" is the hole radius (equivalent to void radius). It is clear that voids of larger diameter (large, r_f) requires less pressure for densification, but, for smaller void radius the pressure required is high to close down is unbounded. Under hydrostatic pressure, void simply changes size, but, not the shape as the pressure is equal in all direction [26]. Now, therefore, the pores play a role in limiting the mechanical properties is obvious. Voids act as sites for initiation of fractures and provide an easy path for crack propagation [27]. Hence, the elimination of pores in the preform by deformation processing is imperative for achievement of high performance properties [2]. In compacting metal powders, the total porosity of the compact decreases rapidly at first and then more and more slowly with increasing compacting pressure. The total porosity of a powder compact cannot be changed without affecting the pore size distribution (28).

Forging denotes a family of processes by which the plastic deformation of the work-piece is carried out by compressive forces. Forging is one of the oldest metal working processes known. Forging can be carried out at room temperature and is called cold working or at elevated temperatures called warm and hot forging depending upon the temperature. However, forging is classified as;

1. Open die forging, and,
2. Close die forging.

Open die forging generally involves placing a porous cylindrical work piece between the two flat die (platens) and reducing the height of the porous cylinder by compressing and this operation is also known as upsetting. Specimen can develop a barrel shape and this barreling is caused primarily by frictional forces at the die and the work-piece interfaces that oppose the outward flow of the materials and the pores at these interfaces. Barreling also occurs in upsetting the hot work pieces in between the flat, but, cool dies. The material at and near the interfaces cool rapidly, while the rest of the specimen is relatively hot. Since strength decreases with temperature, the ends of the specimen in contact with the die surfaces offer a greater resistance than do the free ends [2].

The theory of plasticity is applicable for conventional incompressible materials, whereas, to predict flow of a porous material, the simultaneous decrease of volume must be incorporated. Production forging of powder preforms is normally carried out in closed dies with the aim of achieving full density. However, upsetting between flat dies is applicable as a model for the initial stage of closed die forging until the lateral flow of the preform material forces against the die walls. The modes of initial material flow are an important consideration in the choice of preform and die geometries. Dead zones created during initial deformation in which densification lags behind other regions which are difficult to compact them later on when they are enclosed by a shell of denser and stronger material [24]. Comparison of forging from wrought bar stock production route, the forging of P/M preforms can be referred elsewhere [30 – 35]. Some Industrial applications of powder forging and the powder preform forging routes are shown in fig. 1 [29]. Some important literature on a number of automotive parts, e.g., diesel engine tappets, automotive valve caps, and certain soft magnetic parts are being produced by cold forging of P/M preforms. P/M structural parts finding their applications in automobiles, but, their use has rapidly spread into the fields of house hold appliances, farm and garden equipment, business machines, power tools etc. The present investigation has been undertaken because the steels which are recognized as the foundation of the engineering industry is susceptible to oxidation at high temperatures and corrodes under the hostile environment. Thus, with the new era of composites the present investigation is aimed at developing an iron based – titanium carbide dispersed composites for high temperature structural needs. The compositions chosen were Fe–1%TiC and Fe-2%TiC. Literature has shown that titanium carbide containing composites exhibited high hardness and ductility along with the good property of wear

resistance. Possible area of applications is for engine wear resistant parts, tool and die making and high temperature furnace appliances [30-35].

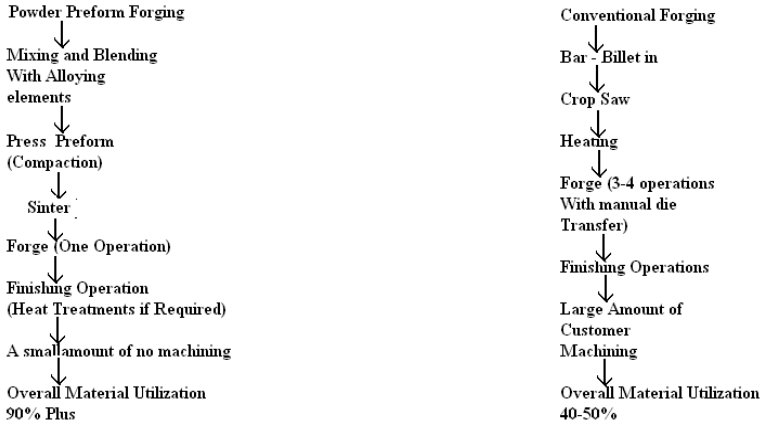

Figure 1 Powder and Conventional Forging Details [29]

II. EXPERIMENTAL DETAILS

Materials required and their characterization including sieve size analysis, apparent densities, flow rates, compressibility for iron, Fe - 1%TiC and Fe - 2%TiC were assessed. The compaction of powder blends, ceramic coating of compacts and subsequent sintering and forgings are detailed.

II.1 Materials Required

Material required were iron and titanium carbide powders, graphite powder of 3-5um for lubrication and linseed oil as quench ant for quenching after forging. Suitable die, punch and bottom insert were required for compacting powder blends of Fe-1%TiC and Fe-2%TiC respectively, ceramic coating, furnace for sintering the ceramic coated compacts, a suitable Chromel / Alumel thermocouple along with the temperature indicator cum – controller, a Universal Testing machine for compacting and Friction screw press for forging were also required. Atomized iron powder of -180µm was obtained from M/s Hoaganaes Corporation, Hyderabad, Andhra Pradesh, India. However, titanium carbide powder of -.37µm was procured from M/s. Ghrishma Speciality Powders, Mumbai, Maharashtra, India. Further, the graphite powder of 3-5um was obtained by courtesy, Ashby Inc., USA. Chemical purity of atomized iron powder was 99.63 per cent with remaining 0.37 per cent insoluble impurities.

II.2 Powder and Powder Blend Characterization

Since the main ingredient powder was iron its sieve size analysis was carried out and is reported in Table 1. However, the other properties such as apparent .densities, flow rates and compressibility were recorded. for iron powder, Fe-1%TiC and Fe-2%TiC powder blends and the same are reported in Table 2

Table 1: Sieve Size Analysis of Iron Powder

Wt. % Powder Retained	Sieve Size, µm									
	+150	+125	+106	+90	+75	+63	+53	+45	+37	-37
Wt.% Ret.	10.100	21.942	9.460	2.100	20.100	12.112	11.100	5.70	0.320	7.00
Cum. Wt.% Ret.	10.100	32.042	41.502	43.602	63.702	75.814	86.914	92.614	92.934	99.934

Table 2 Properties such as Apparent Density, Flow Rate and Compressibility of Iron, Fe – 1%TiC and Fe-2%TiC Blends

S. No.	Systems Selected	Apparent Density, g/cc	Flow Rate, S/50g. (by Hall Flow Meter)	Compressibility, g/cc, at a pressure of 400±10 M Pa
1.	Iron	2.961	26.151	6.594
2.	Fe- 1.0%TiC	2.897	20.151	6.550
3.	Fe-2.0%TiC	2.994	21.307	6.517

II.2 Powder Blend Preparation

In order to carry out the blending of the required amounts of iron and titanium carbide powders in two proportions by weight, a pot mill was used. Required amounts of iron and titanium carbide powders in two sets were taken and placed inside stainless steel pots and these pots were securely tightened on the mill after tightly closing their lids. Blending operation ensures uniform distribution of powder ingredients. In these two cases, the powder mixes to ball (10 – 15 mm diameters) ratio by weight was maintained at 1.2:1. After a run time of an hour, nearly 100g of powder mixes from each pot were taken out for the measurements of flow rates and apparent densities. Immediately after the completion of measurements, the powder mixes were returned back to their respective pots and the pots were securely fixed on the mill after tightening their lids, and, then the mill was operated again. This test has been repeated periodically after the lapse of every one hour. The pot mill was switched off, once the last three measurements for flow rates and apparent densities were consistent. Thus, the blending time of 24 hours was found to be ideal for both the systems.

II.3 Compaction of Iron and Powder Blends

Powder blends were compacted in compacting die of 26+0.1 mm diameter and a height of 140 mm with a wall thickness of 37mm. The punch height was 150 mm and its diameter was $26^{-0.1}$mm with a bottom insert of 20 mm height and $26^{-0.1}$ mm diameter. Thus the compact diameter was fixed to be $26^{-0.1}$mm and only

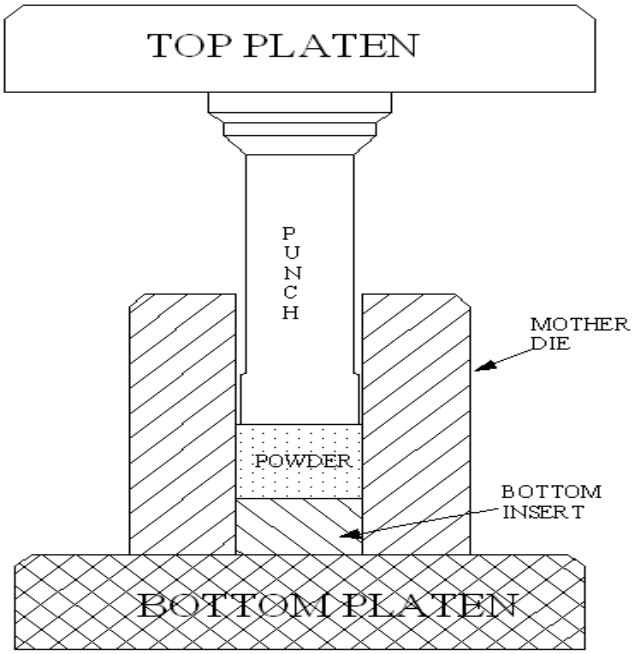

Figure 2 Schematic Diagram of compaction Assembly

option was to vary the height to get initial aspect ratios of the compacts as 0.25, 0.50, 0.75 and 1.24 respectively. This was attained by taking pre-weighed powder and applying controlled pressures in the range of 420±10 M Pa respectively for initial aspect ratios of 0.25, 0.50, 0.75 and 1.24 respectively. Thus the density was obtained in the range of 84±1 per cent of theoretical. An external lubricant, molybdenum-di-sulphide was used as a lubricant during compaction.

II.4 Ceramic Coating and Drying

The burrs on the compact edges were filed off. Indigenously developed ceramic coating was applied on the entire surfaces of the compacts of all compositions and all aspect ratios. These surface coated compacts were allowed to dry under ambient conditions for a period of sixteen hours. A second coat was applied on the already coated compacts in the direction 90^0 to the previous coating and this coating was once again allowed to dry for a further period of sixteen hours under the aforementioned conditions.

II. 5 Sintering of Ceramic Coated Compacts

Sintering process is an important step prior to forging. Therefore, sintering must result in a strong bond formation between the particles and thereby enhancing density and as a consequence of the same, the strength. Sintering, in general, is carried out in the range of 0.7–0.9 times the absolute melting point of the base component in a multi-component system. The ceramic coated and dried compacts were sintered at 1150610^0C for a period of ninety minutes in a Kanthal wound muffle furnace. However, preheating of the compacts was carried out at 600610^0 C for a period of 120 minutes so as to avoid bursting of compacts during sintering due to entrapped gaseous release. Chromel / Alumel thermocouple was used along with a temperature indicator cum controller. Prior to sintering operation, the compacts were kept in a ceramic tray of 180 mm length and 150 mm X 150 mm cross-section. This tray was kept in a square cross – section (200 mm x 200 mm) furnace chamber with a depth of 240 mm. Now after sintering schedule was over, the sintered compacts were ready to be forged.

II. 6 Hot Upset Forging to Discs and Square Cross-Section Bars

Sintered preforms were hot forged at 1150610^0C to various deformation levels on a friction screw press of 1.0 MN capacity using flat dies. Immediately after forging, the forged compacts were transferred to an oil bath (linseed oil bath) kept at room temperature to retain the forged structure and to avoid any oxidation after forging. This whole process of forging and transferring to oil bath took around 15 – 20 seconds. The sintered compacts with initial preform aspect ratios of 0.25, 0.50, and 0.75 respectively were axially hot forged to different height strains in order to enable evaluation of densification mechanisms. However, the cylindrical compacts of initial aspect ratio of 1.24 were hot upset forged from two sides to square cross – section (~14mm x 14mm) bars of 100±05 mm. These were used to evaluate the tensile properties.

II. 7 Removal of Residual Ceramic Coating

Residual ceramic coatings from the forged compacts were removed by mild grinding and manual filing then these specimens were smoothened using fine emery papers for measuring density and forged dimensions. This procedure of removing the residual ceramic coating was done uniformly to all forged compacts.

II. 8 Dimensional Measurements

Figure–3 shows the initial and the deformed sintered compacts. Dimensional measurements were made

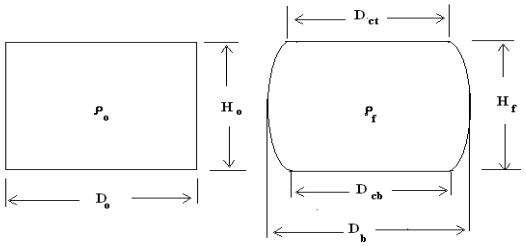

(a) (b)

Figure 3 Initial (a) Sintered Preform, and, (b) Sintered, but, Forged Disc.

for initial height and initial diameter. In case of forged compacts, the dimensional measurements such as forged height, contact (top and bottom) diameters and the bulging diameter were carried out. From these measurements true height and true diameter strains were calculated along with the forged aspect ratios.

II.9 Densities of all forged compacts

Density Measurements were evaluated following Archimedes principle. Weight in air was taken on an electronic balance with a sensitivity of 10^{-4} g. A very thin, but, mild mustard oil film was applied on the entire surfaces of the forged compacts prior to measuring the weights in water so as to avoid the penetration of water during measuring the weight in water. The density was measured as:

$$\rho_f = W_{air} / (W_{air}-W_w) \times \text{Density of water} \ldots\ldots\ldots \textbf{(2)}$$

Where, ρ_f is the forged density in g/cc, W_{air} is the weight of the forged compact in air and W_w is the weight of the forged compact in water.

II.10 Tensile Tests

Standard tensile test specimens were prepared from the square cross-section bars to be tested on a 2,000 Kg capacity Hounsfield Tensometer. While conducting the tensile tests observations are made on the

elongation of the specimen and the area of cross section where necking started and grew up unto fracture. Tensile test is ultimately used for the following considerations.

1. fundamental mechanical properties assessment for the use in designing parts or components, and,
2. Establishes the basis for the selection of the values for engineering design Apart from the above, the fractured surfaces were used to obtain SEM fractographs to assess the mode of fracture.

III. RESULTS AND DISCUSSIONS

III.1 Compressibility Test Results

Compressibility of powder refers to the ability of the powders to be compacted under the application of load. However, the compressibility is a function of various parameters such as powder shape, size and their distribution. Moreover, it is also dependent on the inter particle friction. Once the die cavity is uniformly filled with the metal powders, it gives rise to certain packing density, but, some amount of pores is also formed. First densification occurs on the application of load through the punch, it sets the particle movement and rearrangements causing improved packing density. When the pressure is further increased the clean particles close together and adhere to each other [1]. The compressibility plots are drawn between the percentage fractional theoretical density and the applied pressure. These plots are shown in figs. 4(a) and 4(b) respectively. The observation of these plots indicate that as the compacting pressure is raised the compact density, too, has gone up. However, after certain load, the further application of load showed a flattening of these curves indicating the saturation of pore density inside the compact in agreement with others [9]. Figure 4(a) represents for Fe-1%TiC and 4(b) represents Fe-2%TiC composites.

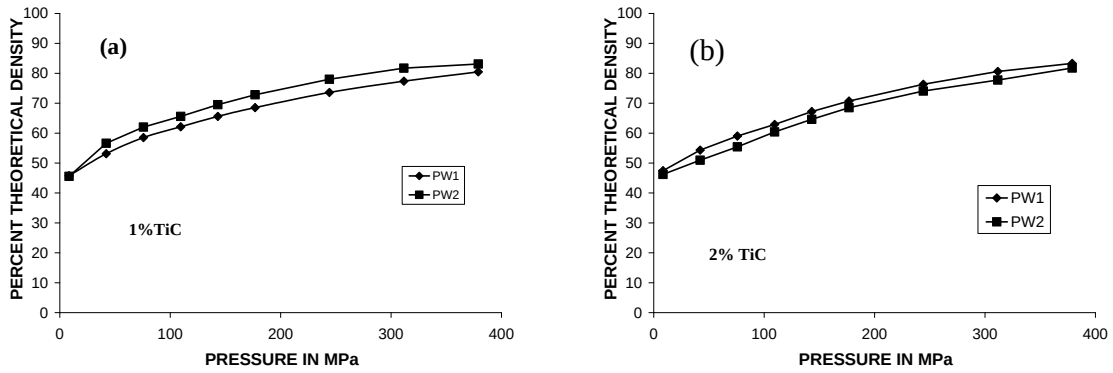

Figure 4 Compressibility Plots for Iron-Titanium Carbide Blends

III.2 Deformation and Densification

Figs. 5(a) and 5(b) have been drawn between the fractional theoretical density (ρ_f/ρ_{th}) and the true height strains (ln (Ho/Hf) for Fe-1%TiC and Fe-2%TiC composites during hot forging respectively. These plots indicate the influence of preform geometry on densification mode for a given percentage of titanium carbide addition. Examining these two figures 5(a) and 5(b), it is, observed that the rate of densification is comparatively steep in the beginning followed by a virtual steady state and ultimately at higher strain levels the curves exhibiting flattening pattern. Further observation shows that the preforms with lower initial aspect ratios have densified more rapidly than the higher initial aspect ratio preforms. This behaviour has been true irrespective of titanium carbide addition. This means that the preforms of initial aspect ratio of 0.25 always remained above the other two plots drawn for initial preform aspect ratio of 0.50 and 0.75 respectively. This behaviour is attributed to the fact that there is a rapid and uniform load transfer all across the deforming compact of 0.25 initial aspect ratio compared to the one with higher aspect ratio preforms. Due to mild damping effect in pore volumes (i.e., higher H/D ratios), higher order of inhomogeneity in deformation becomes the route cause for poor densification. In addition to this, the pores tending to move towards the free surfaces of the deforming preform coalesce just before reaching to the free surfaces and open out as cracks. While examining figs. 5(a) and 5(b), the common feature of these curves are that they exhibit similar characteristic nature, and, further these curves are found to correspond to a third order polynomial between dependent variable (ρ_f/ρ_{th}) and the independent variable ln (H_o/H_f) where, ln (H_o/H_f) = εh, ρ_f is the forged density and ρ_{th} is the theoretical density of the system. H_o is the initial height and H_f is the forged height. The third order polynomial to which these curves conform to is of the form:

$$(\rho_f/\rho_{th}) = A_0 + A_1\varepsilon h + A_2\varepsilon h^2 + A_3\varepsilon h^3 \quad \ldots\ldots\ldots (3)$$

Where, 'A_0', 'A_1', 'A_2' and '$A'_3$are empirically determined constants and are dependent upon the preform geometries and the compositions of the composite systems investigated. The values of 'A'_1 are in close vicinity of the initial preform density, and, therefore, do not contribute to densification. Whereas, 'A'_1 is always positive and, therefore, contributes to densification linearly while 'A'_2 possesses always negative value of low magnitude and hence moderates the densification in the final stages of densification little more effectively than does in the initial stages. The values of these constants are listed in Table 3. However, the value of 'A'_3 is mostly positive except in one case when 'A'_3 is negative then 'A'_2 is positive. Thus, they compensate for each other. Since the values of regression coefficient, '$R^{2'}$ for each aspect ratio is very much close to unity, and, therefore, the relationship given in (3) stands justified.

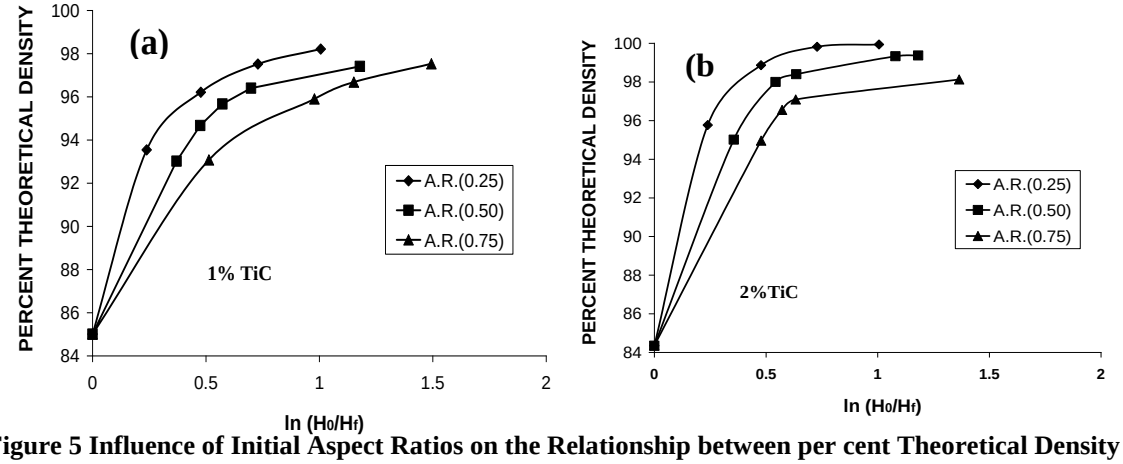

Figure 5 Influence of Initial Aspect Ratios on the Relationship between per cent Theoretical Density and the Height Strain

Table 3 Coefficients of 3rd Order Polynomial of the Form: $(\rho_f/\rho_{th}) = A_0+A_1\varepsilon_h+A_2\varepsilon_h^2+A_3\varepsilon_h^3$

Composition	Aspect Ratio	A_3	A_2	A_1	A_0	R^2
Fe-1%Tic	0.25	0.295	- 0.645	0.481	0.85	0.998
	0.50	0.075	-0.271	0.320	0.849	0.994
	0.75	0.072	-0.0245	0.289	0.850	0.999
Fe-2%Tic	0.25	0.428	-0.932	0.659	0.844	0.997
	0.50	0.269	-0.667	0.541	0.843	0.999
	0.75	-0.208	0.276	0.112	0.843	0.995

III.4 Relationship between True Diameter and True Height Strains

Figs. 6(a) and 6(b) are drawn between the true diameter and the true height strains for both the systems, i.e., Fe-1%TiC and Fe-2%TiC respectively. These two figs. reveal that all data points corresponding to each aspect ratio irrespective of the composition, remain below the theoretical line under ideal conditions, and, in the plastic region, the ideal value of Poisson's ratio would be 0.5, and, therefore, the theoretical line has the slope of 0.5. Since, all the data points remain below the theoretical line, confirming to the fact that the Poisson's ratio for porous materials in plastic deformation will always remain less than 0.5, meaning thereby, that the ratio of true diameter strain to true height strain (which of course, is the Poisson's ratio) can attain a value of 0.5 in the near vicinity of the theoretical density. Further, it is noticed that the curves corresponding to lower aspect ratio preforms are nearest to the theoretical line than the curves corresponding to higher aspect ratio preforms which goes to suggest that the Poisson's ratio is influenced by the geometry of the preforms as well as the compositions of the system investigated. Mathematically, it has been established that the curves shown in figs. 6(a) and 6(b) conform to a third order polynomial of the form:

$$\ln (D_f/D_0) = B_0 + B_1 \ln (H_0/H_f) + B_2 [\ln (H_0/H_f)]^2 + B_3 [\ln (H_0/H_f)]^3 \quad \text{----------} \quad (4)$$

Table 4 Coefficients of 3rd Order Polynomial between $\ln (D_f/D_o)$ and $\ln (H_o/H_f)$ For Fe-1%TiC and Fe-2%TiC Composite Steel during Hot Forging

Composition	Aspect Ratio	B_3	B_2	B_1	B_0	R^2
Fe-1%Tic	0.25	-1.1246	1.8009	-0.2133	-0.0017	0.999
	0.50	0.2892	0.6152	0.1575	-8E-05	0.9999
	0.75	0.1669	+0.5397	0.0427	-0.0002	0.9999
Fe-2%Tic	0.25	-0.853	1.342	-0.063	-0.008	0.971
	0.50	-0.461	0.948	-0.028	0	0.999
	0.75	-0.408	-1.066	-0.261	3E-05	0.998

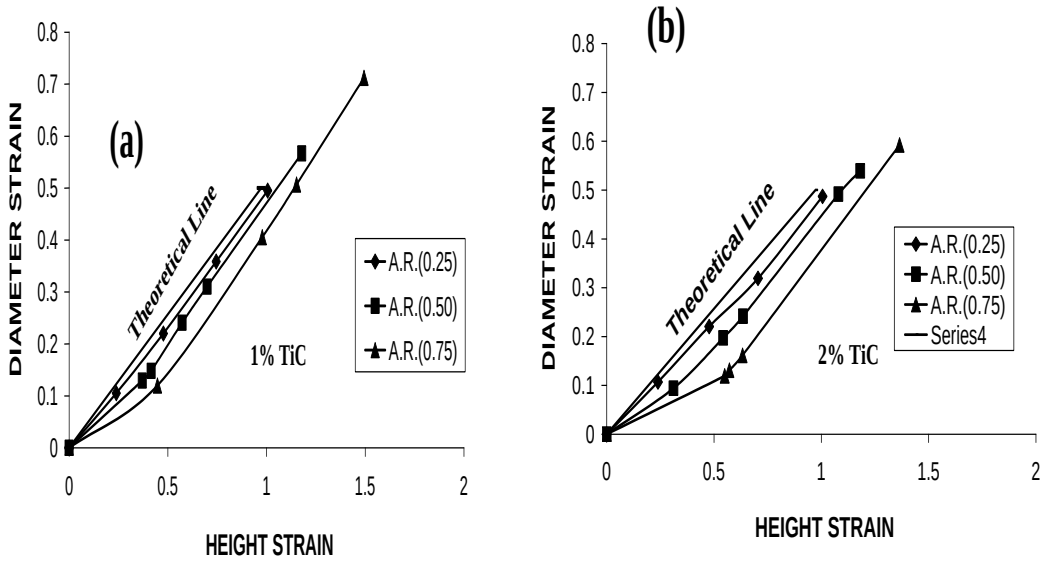

Figure 6 Influences of Initial Aspect Ratios on the Relationship between True Diameter and True Height Strains

Where, B_0, B_4, B_2, and B_3 are empirically determined constants and are found to depend upon the initial aspect ratios of the preforms and the compositions of the systems investigated. Further ln (D_f/D_o) is the true diameter strain (ϵ_d) and ln (H_0/H_f) is the true height strain (ϵ_h).

III. 5 Poisson's Ratio and Densification

Figs. 7(a) and 7(b) are drawn between the Poisson's ratio and the per cent theoretical density attained during hot forging of sintered preforms of Fe-1%TiC and Fe-2%TiC composites respectively. These plots also

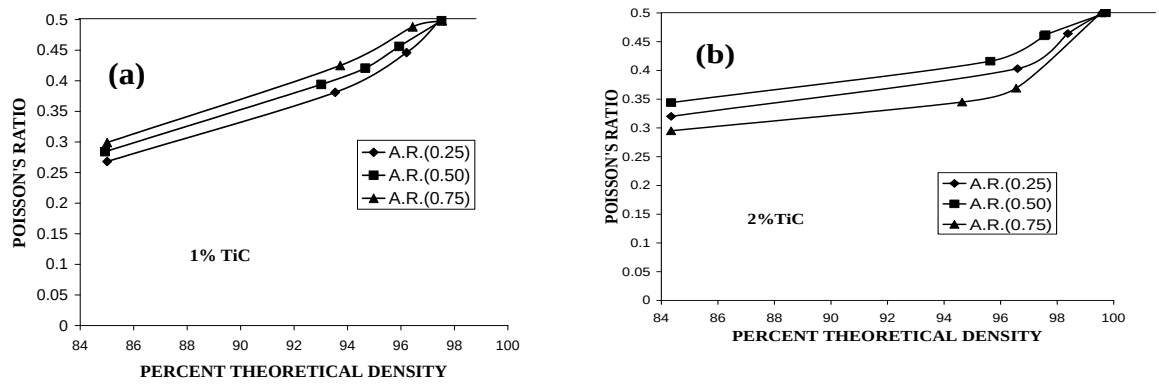

Figure 7 Influences of Initial Aspect Ratios on the Relationship between Poisson's Ratio and Per cent Theoretical Density

exhibit the influence of preform geometry on the Poisson's ratio variation with respect to attained densities. While examining these two figs. 7(a) and 7(b), it is, observed that the curves corresponding to lower aspect ratio preforms remained above the other two curves corresponding to higher aspect ratio preforms. This phenomenon is true irrespective of the compositions investigated. Apart from these, the curves in these two figs. 7(a) and 7(b) indicate the tendency to approach to a limiting value of Poisson's equaling to 0.5 in the near vicinity of the theoretical density. It is also observed that the nature of curves corresponding to higher aspect ratios tended to deviate compared to the lower aspect ratio preforms irrespective of the compositions. Therefore, this behaviour is attributed to the number of pores, their size and its distribution apart from their total volume present in the preforms and their mode of deformation during hot forging. But, their salient features remained more or less same. These curves can be divided into two distinct zones-the first zone involves higher rate of densification, but, low rise in the values of Poisson's ratio. Whereas, in the second zone high rise in the values of Poisson's ratio, but, least increase in densification. This zone is a confirmation of the fact that the flow of material and pores tend to become simultaneous.

III. 6 Mechanical Properties

Bars of square cross-section (~14 mm x ~14 mm) with a length of 100±05mm were machined to standard tensile specimens and the tension test has been conducted on a Hounsfield Tensometer. Tensile properties such as tensile and fracture strengths, per cent area reduction and per cent elongation were found out. These values are tabulated in Table–4. This table shows that iron with 2%TiC forming a composite has exhibited a nominal increase in tensile and fracture strengths. The value of % area reduction for this composite dropped from 39.41(for Fe-1%TiC) to 28.41 per cent whereas, elongation dropped marginally from 23.73 (for Fe-1%TiC) to 20.39 per cent. Fractographs shown in figures 8(a) and 8(b) indicate mostly ductile and partly brittle fractures. Fractographs show sufficiently high number of dimples, but, failure was facilitated due to particle de-lamination.

Table 4 Mechanical Properties of as Sintered and Forged Iron and Fe-1%TiC, and Fe-2%TiC Composites.

SYSTEM	T.S. (M Pa)	F.S. (M Pa)	% Elongation	% Area Reduction
Fe	410	720	28.92	47.33
Fe-1%TiC	490	767	23.73	39.41
Fe-2%TiC	580	770	20.39	28.41

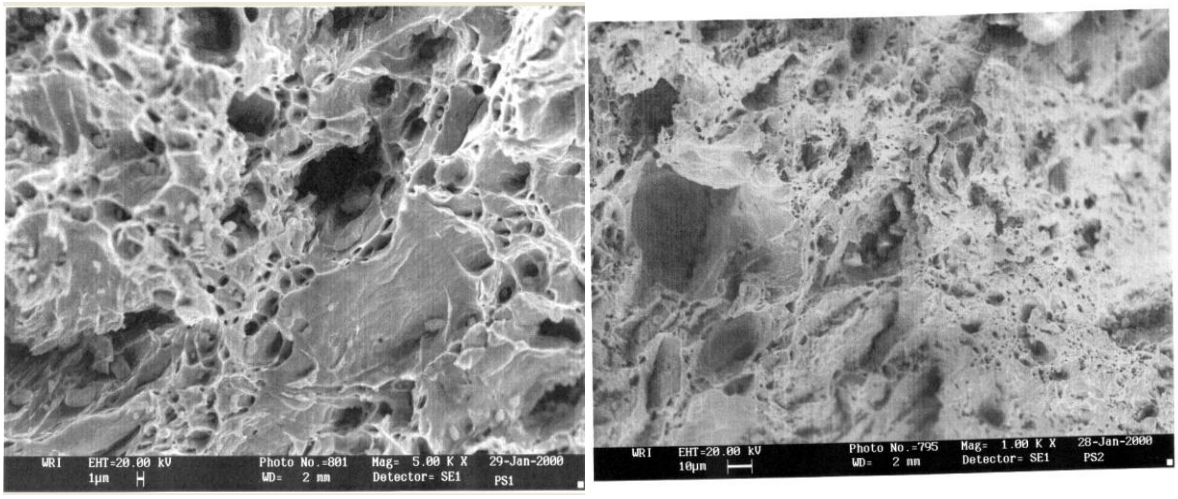

(a) **(b)**

Figure 8 SEM Fractographs of Fe-TiC Composites, (a) Fe-1%TiC and (b) Fe-2%TiC.

IV. CONCLUSIONS

Based on the analysis of the experimental data, calculated parameters and various plots drawn, the following main conclusions were arrived at:

1. The Relationship between the fractional theoretical density (ρ_f/ρ_{th}) and the true height strains ($\ln (H_o/H_f) = \varepsilon h$) on hot forging was found to correspond to a third order polynomial of the type: $(\rho_f/\rho_{th}) = A_0 + A_1\varepsilon h + A_2\varepsilon h^2 + A_3 Ch^3$; where, '$A_0$', '$A_1$', '$A_2$' and '$A_3$' are empirically determined constants which are found to depend upon the initial preform aspect ratio and their composition,
2. Poisson's ratio with respect to percent fractional theoretical density was found to be a function of initial preform aspect ratios and the compositions of the systems investigated. This presentation of data and calculated parameters for Poisson's ratio and the per cent fractional theoretical density tended to approach to a limiting value of 0.5, which is a theoretical value attainable in the near vicinity of theoretical density,
3. Tensile and fracture strength values for both the systems have been on the higher side, but, both systems showed high values of per cent elongation and per cent area reduction. These high values of elongation and per cent area reduction indicate that both the systems were equally tough.

REFERENCES

[1] A.K. Sinha, "Powder Metallurgy, Dhampat Rai Publications (P) Ltd., New Delhi, pp-1-3, 1997.
[2] Howard. A. Kuhn, "Manufacturing methods for composites – An Overview", Concise Encyclopedia of Composite Materials, Ed. By Antbony Kelly, pp 99-134, 1986.

[3] Donal S. Clark and Wilbur. R. Varney, "Physical Metallurgy for Engineers", Van Nostrand Co. Inc. pp 347-349, 1973.

[4] Ronald. L. Gibson, "Principles of Composite Materials Mechanics", McGraw Hill Inc. pp 1-11, 1994.

[5] William D. Callister. Jr., "Materials Science and Engineering – An Introduction", Composites, 3rd Edn. pp 513-540, 1994.

[6] D. Dutta, G. Mohan, B. Chatterjee and C.G. Krishnadas, " Indigenous Development and Manufacture of Aircraft Friction Materials by Powder Metallurgy," Transaction of Powder Metallurgy", PMAI, Vol.13, pp 12-20, 1986.

[7] A. Pathak, A.N. Tiwari and T.R. Ramamohan, "Sintered Cu-TiC Particulate Composites", Transactions of PMAI, Vol. II, pp 9-11, 1984.

[8] G. Suresh and G.S. Upadhyaya, "Sintering of High Speed Steel Bonded TiC Particulate Composites", Transactions of PMAI, Vol. II, pp 9-11, 1984.

[9] D.H. Bowen, Manufacturing Methods for Composites – An overview" Concise Encyclopedia of Composite Materials, Ed. By Anthony Kelly, pp 182-183, 1986.

[10] K.G. Satyanarayana, B.C. Pai, K. Sukumaran and S.G.K. Pillai, "Synthesis and Properties – A Hand Book of Ceramics and Composites", Vol. I, ED. By Nicholas, P. Chereemerinoff, pp 339-382, 19--.

[11] K.G. Satyanarayana, R.M. Pillai and B.C. Pai, "Aluminium cast matrix composites", A Handbook of ceramics and composites", Vol. I, Ed. By Nicholas P. Cheremerinoff, pp 555-599, 19--.

[12] Zhang Zhy, "A Literature Survey on Fabrication Methods of Cast Reinforced Metal Composites", Proceedings of the International Symposium on Advances in Cast Reinforced Metal Composites, Ed. By Fishman and A.K. Dingra, pp 93-100, 1999.

[13] Benea Lida, "Electro-deposition of Zirconia Particles in Copper Matrix", Materials and Manufacturing process, Vol.4, No.2, pp 231=242, March 1999.

[14] Gorsse. S., Chaminade. J.P., Le Peticorps.Y, "In Situ Preparation of Titanium Based Composites Reinforced by TiB Single Crystals by Using Powder Metallurgy Technique", Composites – Part – A: Applied Science and Manufacturing, Vol.29, No.9, pp 1229-1234, 1998.

[15] Rath. M. Kreuzbegfe, S. Hinrichsen.G., "Manufacture of Aramid Fiber Reinforced Nylon-12 by Dry Powder Impregnation", Composites Part A: Applied Science and Manufacturing, Vol.29, No.8, pp 933-938, 1998.

[16] Mosleh M. Suh N.P. Arinez. J., "Manufacture and properties of polyethylene Homo Composite", Composites Part A: Applied Science and Manufacturing, Vol.29, No.5-6, pp 611-617, 1998.

[17] Wang Juven, Hong Zao, Geyang Li, Pengxing Li, "Combined Process of Coating and Hybridizing for the Fabrication of Carbon Fibres Reinforced Aluminium Matrix Composites", Composites, Part A: Applied Science and Manufacturing, Vol.28, No.11, pp 943-948, 1997.

[18] F. Kickikalson, Thomas, B. Astrom, "Manufacturing and Applications of Structural Sandwitch Components", Composites Part A: Applied Science and Manufacturing, Vol.28, No.2, pp 97-111, 1997.

[19] A. Mclean, H. Soda, Q. Xia, et.al,: "SiC Particulate Reinforced Aluminium Matrix Composite Rods and Wires Produced by Continuous Casting Route", composites part A: Applied Science and Manufacturing, Vol.28, No.2, pp 153-162, 1997.

[20] R. Aldo Boccacuni, H.D. David Peare, A. Paul Trusty, "Pressureless sintering and characterization of Alumina Platelets Reinforced Barium-Magnesium Aluminosilicate Glass-Ceramic Composite", Composites Part A: Applied Science and Manufacturing, Vol.28, No.5, pp 505-570, 1997.

[21] Endang Zhang, P. Derch Thompson, "Carbon-Fibre Reinforcement on the Fibre Glass, Composites Part A; Applied Science and manufacturing, Vol.28, No.6, pp 581-586, 1997.

[22] Kon Bae Lee, Youn Su Kim and Houn Kwon, "Fabrication of Al-3Wt% Mg Matrix composities Reinforced with Al_2O_3 and SiC Particulates by Pressureless Infiltration Technique", Metallurgical and Materials Transacions A, Volume 294, pp 3087-3095, Dec.1998.

[23] R. H. Baskey, G. F. Davis and A.D.Sewope, "Fibre Reinforced Sintered Composites" * Vol.2, pp 332-338. 1965.

[24] G. Bocksteigel and O. Stevenson, "The Influence of Lubrication, Die Material and Tool Design Upon Die Near in the Compacting of Iron Powders", Modern developments in Powder Metallurgy, Ed. By Henery H. Hausner, Vol.4, pp 87-114, 1970.

[25] B. N. Singh, "Pressure less Densification of Powder Composites" , Powder Metallurgy, Vol.14, No.28, pp 277-280, 1971.

[26] N. D. Sopchak and W.Z. Misiolek, "Multilayer Compaction of Iron Powders", Advanced processing techniques in Powder Metallurgy and Particulate Materials, Compiled by Chaman Lall & Alberts J. Neupaver, Vol.6, pp 21-23, 1994.

[27] F. Thummbler and W. Thomma "Investigation of Sintering Process During Formation of Solid Solutions", Modern Developments in Powder Metallurgy, Vol.3, Ed by H. H. Hausner, pp 361-375, 1965.

[28] C. J. Leadbeater, I. Northcott and F. Hargarveas, "Some properties of Engineering Iron Powders", Iron powder Metallurgy, Vol.3, Ed. By Henery H. Hansner, K.H. Roll and P.K. Johnson, pp 117-118, 1968.
[29] B. Avitzur and P. Blum, "Forging and Extrusion of Powder Metallurgy Preforms", Modern Developments in Powder Metallurgy, Ed. By Henery H. Hausner and Walter E. Smith, Vol.7, pp 90-93, 1973.
[30] Richard W. Hertzberg, "Deformation and Fracture Mechanics of Engineering Materials", 4th Edn. John wiley and Sons, Inc., New York, pp 380-386, 1996.
[31] Gerhard Bocksteigel, "Relations Between Pore Structure and Densification in Compacting Iron Powders", Iron Powder Metallurgy, Ed. By Henery H. Hausner, K H. Roll and P.K. Johnsons, Vol.3, pp 54-57, 1968.
[32] H. F. Fischmeister, B. Aren, K. E. Easterling, "Deformation and Densification of Porous Preforms in Hot Forging", Powder Metallurgy, Vol.14, pp 144-153, 1971.
[33] G.T. Brown and P.K. Jones, "Experimental and Practical Aspects of the Powder Forging Process", Modern Developments in Powder Metallurgy, Ed. By Henery H. Hausner, Vol.4, pp 368-383, 1971.
[34] H. N. Tewari and R. Sharan, "Forging of Iron and Steel Powder Preforms – A" critical Review, PMAI. Newsletter, A Quarterly Publication of the P/M Association of India, Vol.12, No, pp 15-18, March 1986.
[35] www.micronmetals.com/titanium Carbide.Html from AEE Home page.
[36] K. H. Roll, "Challenges and Opportunities for Powder Metallurgy in Structural Applications", Powder Metallurgy, Vol.25, pp 159-165, 1982.
[37] G.S. Upadhyaya, "Extending Role of Powder Metallurgy in Advanced Ceramics", A Quarterly Publication of Powder Metallurgy Association of India, Vol.13, No.4, pp 26-29, Sept.1987.
[38] Kunal Ghosh, Tom Troczynski and Asoke C. Chaklader, "Processing of Composite Al/Sic Powders for Plasma Spraying", International Journal of Powder Metallurgy, Vol.35, No.2, pp 27-33, March 1999.
[39] R. K. Galgali, H. S. Ray and A.K. Chakrabarti,"Preparation of TiC Reinforced Steel Composites and Their Characterization", Materials Science and Technology, Vol.15, pp 431-442, April 1999.
[40] Mujin Yang and Randall M. German, "Defect Formation and Densification Analysis of Particulate Materials, Ed. By Chaman Lall and Albert J. Neupaver pp 95-108, 1994Cemented Carbides Made by Powder Metallurgy Injection Molding", Advances in Powder Metallurgy.

American Journal of Engineering Research (AJER)
e-ISSN : 2320-0847 p-ISSN : 2320-0936
Volume-03, Issue-01, pp-292-298
www.ajer.org

Research Paper Open Access

Some Aspects of Hot Forging Characteristics Of Sintered Ultra – High Strength Ring Preforms

Sunil Pandey[1] & Dr. K.S. Pandey[2]
[1] *System Administrator, Computer Centre, National Institute of Technology, Raipur, Chhattisgarh, India.*
[2] *Professor, Department of Metallurgical and Materials Engineering, National Institute of Technology, Tiruchirappalli - 620015, Tamil Nadu, India.*

Abstract: - Present investigation pertains to assess the hot upset mode of forging characteristics of sintered P/M ring preforms of iron and AISI 4340 P/M steels containing 0.80, 1.20 and 1.60 percent chromium. P/M rings of iron and AISI 4340 grade of blended powders were prepared using suitable die set assembly on a 1.0 MN capacity hydraulic press. The ring geometries were maintained to outer Diameter: Inner Diameter: Height:: 8:4:2 and density in the range of 86 ±1 per cent of theoretical by employing controlled pressure in the range of 480 ±10 MPa and taking pre-weighed powders. These ring preforms were coated with indigenously developed ceramic coating to protect them against oxidation during sintering. These preforms were sintered in an electric muffle furnace at 1150^0 $\pm 10^0$C for a period of 100 minutes and subsequently hot upset forged to different height strain levels and quenched in linseed oil. Residual ceramic coating was gently machined off followed by dimensional and density measurements. Analysis of the experimental data has revealed that the rate of densification followed the second order polynomial of the form: $Y = a_0 + a_1X + a_2X^2$; Where, Y = fractional theoretical density achieved, i.e., (ρ_f/ρ_{th}), X = the fractional height deformation. The values of 'a_0', 'a_1' and 'a_2' were dependent upon the composition. Further, the effect of chromium content in AISI 4340 steel was negligibly small on the relationship between per cent decrease in I.D. and the per cent height reduction.

Keywords: - *AISI 4340, Coated, Deformation, Geometries, Hot, Muffle Furnace, Preforms, Sintered, Ring, Upset,*

I. INTRODUCTION

Ring compression test was technically developed to characterize the lubricants during metal forming operations. This test involves in the measurement of the change in inner diameter of a ring of specific O.D.: I.D.: Ht. geometry during axial deformation and the same is employed to assess the friction factor and the effectiveness of lubrication [1]. Therefore, a complex mode of measuring forces is not necessarily required instead inward or outward flow of ring material during compression is of a great significance. Inward or outward flow of the ring material with respect to the inner diameter would depend upon the lubricating conditions prevalent between the die and the ring preforms contact surfaces. However, Male and Pierre [2] extended the ring test for the determination of flow stresses of cent per cent dense materials. But, Dulton et.al [3] have attempted the ring test on porous materials while considering the complexities in densification of rings during compression due to intricate nature of the shrinkages of pores their closure mechanisms and their movement kinetics. Few research publications [4-6] on P/M ring deformation with emphasis on densification mechanisms are available Rao and Pandey [7] have developed a relationship between density and the geometric parameters of a ring preforms initial and final parameters inclusive of their initial and final densities. Further, Han et.al [8] had also studied the deformation behaviour of rings under compression and developed the following relationships for plastic Poisson's ration (γ_p) and density change as given underneath:

$$\gamma_p = -[(d_0-dr_i) / (r_0 - r_i)]/(dh/h) \text{ ----- ----- -------- (1), and,}$$
$$(d\rho/\rho) = - [\{2(r_0dr_0-r_idr_i) / (r_0^2-r_i^2)\} + (dh/h)] \text{ ------ ------ ------ (2)}$$

It has been reported elsewhere [9-12] that initial geometric ratio of the ring preforms and lubrication affected densification during cold compression of sintered Al – Cu rings. Rao and Pandey [5] have reported that the application of graphite as lubricant during cold axial compression of Al – Cu sintered ring preforms led to decrease in inner diameter (flow reversal) which is an indication of pore flattening and their collapse. However, the ring preforms under compressive forces would experience frictional shear forces along the lateral direction –directed radially inward which help the pores to flatten out. Rao and Pandey [5, 6] have reported that the rings of higher geometric ratios have shown enhancement in densification rate and crushing strengths. Deformation behaviour of P/M rings dealing with the prediction of friction and its evaluation, a mathematical and finite elemental analysis, influence the flow stresses and friction upon characteristic behaviour of metal flow are described elsewhere [13-25] in detail.

The present investigation is an attempt to evaluate the upset mode of ho forging characteristics of iron and AISI 4340 P/M steels containing 0.80, 1.20 and 1.60 per cent chromium. Attempt is also made to evaluate the densification mechanism and its dependence upon the chromium addition in AISI 4340 steel.

II. EXPERIMENTAL DETAILS

II.1 Materials Required

Atomized iron powder of -180µm was obtained from m/s Hoeganaes India Limited Hyderabad, Andhra Pradesh, India and the graphite powder of 3-5µm was supplied by m/s Ashbury Graphite Mills Inc., Ashbury Warren County, New Jersey, USA. Chromium powder (-37µm), molybdenum powder (-37µm), nickel powder (-37µm) were obtained from m/s Ghrishma Specialty powder Materials, Mumbai, India and silicon powder (-37µm) was procured from the m/s The Metal Powder Company, Thirumangalam, Madurai, Tamil Nadu, India. The chemical analysis of chromium, molybdenum, manganese, and nickel including silicon powder yielded 99.59, 99.57, 99.85, and 99.33 percent respectively. Remaining 0.41, 0.43, 0.62, 0.15 and 0.67 per cent respectively were the insoluble impurities in them individually. The basic characteristic of iron powder and AISI 4340 steels with 0.80, 1.20 and 1.60 per cent chromium contents independently prepared as blends are given in Table 1 along with the sieve size analysis of the base iron powder.

Table 1 Characteristics of Iron Powder, AISI 4340 [**] with 0.8, 1.20 and 1.60 Percent Chromium Separately.

Sl. No.	Property	Systems			
		Iron	AISI4340-0.80Cr	AISI4340-1.20Cr	AISI4340-1.60Cr
1.	Apparent Density, g/cc	2.93	2.91	2.87	2.87
2.	Flow rate by Hall Flowmeter, Sec/50g	25.00	26.30	27.25	28.00
3.	Compressibility, g/cc at a pressure of 480±10Mpa	6.652	6.665	6.672	6.678

4. Sieve Size Analysis of Iron Powder

Sieve Size in µm	-180 +150	-150 +125	-125 +106	-106 +90	-90 +75	-75 +63	-63 +53	-53 +45	-45 +38	-38
Wt % Ret.	1.43	13.40	8.08	1.22	22.28	13.59	13.22	6.75	1.63	19.35
Cum, Wt. % Ret.	1.43	14.83	22.91	23.13	45.41	59.00	72.22	78.97	80.60	99.95

AISI 4340[**] standard composition: Fe- 0.4%C – 0.25%Si – 0.75%Mn – 0.25%Mo – 1.90%Ni – 0.80%Cr.

II.2 Powder Blending

Three powder mixes corresponding to final compositions as given below were prepared on a potmill by taking pre-weighed elemental powders for each compositions corresponding to P, Q and R respectively:

P=Fe-0.4%C–0.25%Si–0.75%Mn–0.25%Mo–1.90%Ni–0.80%Cr,
Q=Fe-0.4%C-0.25%Si–0.75%Mn–0.25%Mo–1.90%Ni–1.20%Cr,
R= Fe-0.4%C–0.25%Si–0.75%Mn–0.25%Mo–1.90%Ni–1.60%Cr.

Three different compositions of steels as stated above were taken separately in stainless steel pots with the powder mix weights to porcelain balls (10-15mm diameters) weights ratio of 1.2:1.0 and the same was fixed on the pot mill after securely tightening their lids. The blending operation was carried out for a period of 30 hours.

The homogeneity of the powder blends were established by conducting hourly tests for flow rates and apparent densities by taking out separately approximately 100±10g of powder mixes from each pot and returning the same back to respective pots after carrying out the aforementioned tests and re-tightening the lids, the pots were fixed on the potmill and the blending operation was continued. Once the flow rates and apparent densities for respective blends were found to be consistent in the last three tests, the blending operation was discontinued. Thus, the blending time turned out to be 36 hours which was good enough to attain homogeneity in the respective powder blends.

II.3 Green Compacts Preparation and Application of Ceramic Coating

Green compacts of ring geometry, i.e. O.D.: I.D.: Height as 8:4:2 were prepared from iron powder and powder blends P, Q and R respectively on a 1.00MN capacity Universal Testing Machine using suitable die, hollow punch, core rod and bottom inserts. The powder compaction assembly is shown in figure-1. The initial ring preform

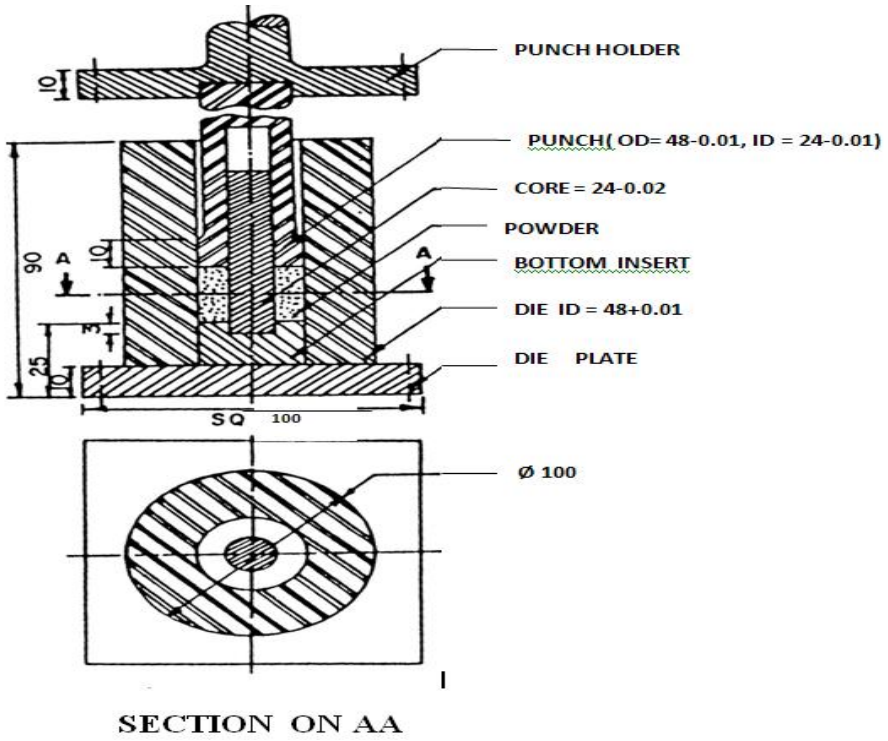

Figure 1 Die Assembly for Compaction of Powder Preforms

densities were maintained in the range of 86±1 per cent of theoretical by employing a pressure in the range of 480±10M Pa. The inner,, outer, the top and bottom ring surfaces were coated by indigenously developed ceramic coating [26] in order to protect the ring preforms during sintering against oxidation. However, the applied ceramic coating was dried under the ambient conditions for a period of sixteen hours followed by recoating the ring preform 90^0 to the previous coating. The second coating was dried for a further period of sixteen hours under the ambient conditions. During compaction specially prepared graphite paste with acetone was used as lubricant to avoid powder sticking but for easy ejection so as to obtain damage free ring compacts.

II. 4 Sintering of the Ceramic Coated Ring Compacts and Hot Upset Forging

Ceramic coated ring compacts of each system were separately sintered in an electric muffle furnace for a period of 100 minutes in the temperature range of 1150 ± 10^0 C. The sintering schedule included pre-heating of the compacts 1n the temperature range of 750 ± 10^0 C and holding them at this pre-heat temperature for a period of nearly 60 minutes in order to avoid any accidental bursting of ring compacts during actual sintering operation in accordance with the reported results elsewhere [27]. Immediately after the completion of pre-heating operation, the furnace temperature was raised to 1150 ± 10^0 C and was retained at this temperature for a period of 100 minutes. A minimum of eleven (11) ring preforms were sintered for each system. Ten out of eleven sintered P/M ring preforms were hot upset forged to different height strains and the same were quenched in linseed oil. One sintered ring of each composition was cooled to room temperature inside the furnace itself by switching off the furnace. All forged and oil quenched rings were cleaned off oil, and, subsequently the residual ceramic

coatings were removed by mild rubbing with emery papers are fine files so as to use them for dimensional and density measurements. Three main measurements were required and they were namely, deformed inner diameters, outer diameters and the forged heights. In some rings negative barreling was observed. Density measurements of sintered rings were carried out by finding out the mass in air and the volume by geometrical calculations where as the density of forged rings were found out by employing Archimedian principle by adopting the technique described elsewhere [28]. Using the initial and the dimensions of the forged rings, various parameters were calculated and used to plot different plots.

III. RESULTS AND DISCUSSION

III. 1 Axial Hot Upset Forging and Densification

Figure-2 has been drawn in order to evaluate the relationship between fractional theoretical density (ρ_f/ρ_{th}) and fractional height reduction. While observing this figure-2 it is found that curve corresponding to iron

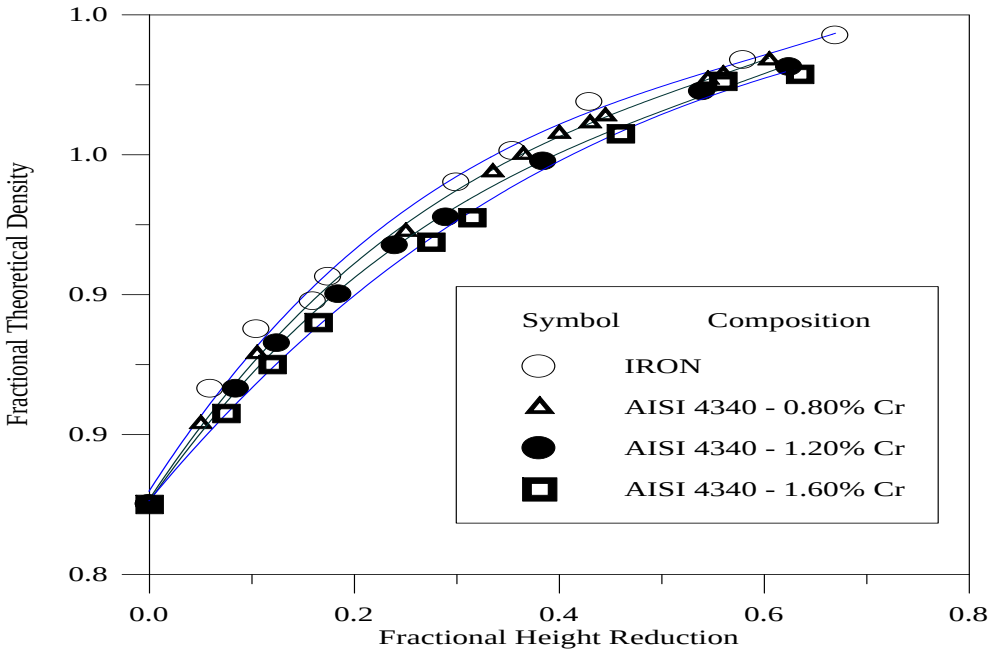

Figure 2 Relationship Between Fractional Density and the Fractional Height Reduction During Hot Forging of Sintered P/M Steel Ring Preforms of Initial Preform Geometry.

has densified at the much faster rate compared to all other compositions of AISI4340, namely, AISI 4340 with 0.80%CrAISI 4340 with 1.20%Cr and AISI 4340 with 1.60%Cr steels respectively. Further, it is found that the curve corresponding to AISI 4340 with 1.60%Cr densified at the least rate compared to other chromium additions, namely, 0.80% and 1.20% respectively. The characteristic natures of these curves are found to be similar,and, they mathematically conformed to a second order polynomial of the form:

$$(\rho_f/\rho_{th}) = a_0 + a_1 (\Delta H/H_0) + a_2 (\Delta H/H_0)^2,$$

Where, 'a_0', 'a_1' and 'a_2' are found to be empirically determined constants. These constants are tabulated in Table 2.

Table 2 Coefficient of the second order polynomial of the form:
$(\rho_f/\rho_{th}) = a_0 + a_1 (\Delta H_f/H_0) + a_2 (\Delta H_f/H_0)^2$

Sl. No	System	Coefficients			Regression Coefficient R^2
		a_0	a_1	a_2	
1	Iron	0.86360	0.45610	-0.62653	0.99498
2	AISI 4340-0.8%Cr	0.86120	0.44250	-0.59682	0.999451
3	AISI 4340-1.2%Cr	0.86070	0.41571	-0.54453	0.999422
4	AISI 4340-1.6%Cr	0.86095	0.35201	-0.31813	0.99861

The values of 'a_0' are found to be in very much close proximity to the initial preform densities, and, hence, they do not contribute to densification, whereas, the constant 'a_1' is positive and linearly multiplied to

the fractional height reduction and, therefore, contributes linearly to densification. However, the constant 'a_2' is always negative and of very low magnitude and the same is multiplied by the square of the fractional height reduction, i.e., $(\Delta H/H_0)^2$ and thus, the term $a_2(\Delta H/H_0)^2$ becomes a value of very low magnitude and plays a role in plateaueing the curves in their final stages of densification. Since in all cases, the value of the regression coefficient 'R^2' is in extremely close proximity to unity, and, hence, the second order polynomial's correspondences to the actual data points are justified. Further, it can be safely said that the constants 'a_0', 'a_1' and 'a_2' depend upon the initial preform geometry and their composition, i.e., the composition of each system independently. However, the values of the regression coefficient (R^2) in each case are found to be much beyond 0.99, i.e., in close proximity to unity. Therefore, the relationship exhibiting a second order polynomial stands justified.

III.2 Relationship Between $(\Delta Di/Di)$ and $(\Delta H/H_0)$

Figure-3 is a plot drawn between the fractional decrease in inner diameter ($\Delta Di/Di$) and fractional height reduction during hot upset forging of sintered iron, and AISI 4340 steel ring preforms with 0.80%Cr, 1.2%Cr and1.6%Cr addition independently. The fig.3 further shows that the characteristic nature of each curve is similar to each other, and, therefore, they can be represented by a similar type of mathematical expressions.

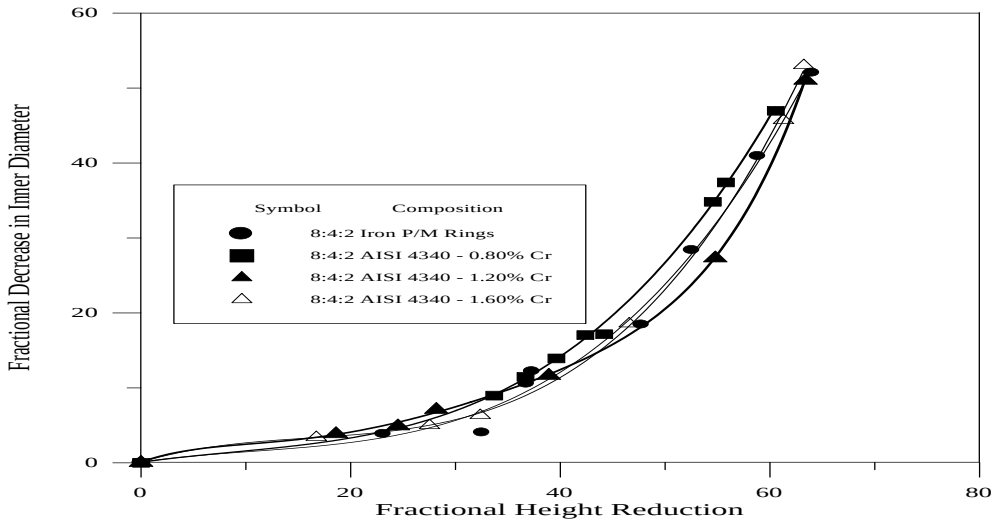

Figure 3 Relationship between Fractional Inner Diameter Decrease and Fractional Height Reduction of 8:4:2 Ring geometry Preforms of Sintered P/M Steels during Hot Upset Forging

Hence, an attempt has been made to evaluate each of these curves, and, it has been found out that the best fitting expression is a third order polynomial of the form:

$$(\Delta Di/Di) = b_0 + b_1(\Delta H/H_0) + b_2(\Delta H/H_0)^2 + b_3(\Delta H/H_0)^3 \quad \text{---- ------ ------ (3)}$$

Where, 'b_0', 'b_1', 'b_2' and 'b_3' are found to be empirically determined constants and they also were observed to depend upon the steel compositions. The addition of chromium in different proportions, i.e., 0.80%, 1.2%, and 1.6% separately in AISI4340 steel revealed the mixed response as far as the relationship between fractional decrease in inner diameter and the fractional height reduction is concerned. These constants 'b_0', 'b_1', 'b_2' and 'b_3'are tabulated in Table-3. Since the values of regression coefficient in each case was found to be beyond 0.99, and, therefore, the curve fitting has been done accurately and reliably.

Table 3 Coefficient of the Third order polynomial of the form:
$(\Delta Di/Di) = b_0 + b_1(\Delta H/H_0) + b_2(\Delta H/H_0)^2 + b_3(\Delta H/H_0)^3$

Sl. No.	System	Coefficient of the polynomial				Regression Coefficient, R^2
		b_0	b_1	b_2	b_3	
1.	Iron	0.2452	0.20537	-0.009725	0.00030105	0.9921
2.	AISI 4340-0.8%Cr	0.0077	0.19923	-0.000751	0.000283	0.9985
3.	AISI 4340-1.2%Cr	0.0024	0.52108	-0.047373	0.00235	0.9948
4.	AISI4340-1.6%Cr	0.00730605	0.42307	-0.020566	0.0004258	0.9993

IV. CONCLUSIONS

Based on the experimental data and calculated parameters and various plots constructed and their critical analysis has led to the following main conclusions:

1. Visual observation has established that up to sixty per cent (60%) of height reduction of the rings, there was no appearance of any surface cracks irrespective of the compositions investigated.
2. Fractional theoretical density and fractional height reduction were related with each other by a second order polynomial of the form: $(\rho_f/\rho_{th}) = a_0 + a_1 (\Delta H/H_0) + a_2 (\Delta H/H_0)^2$, where, '$a_0$', '$a_1$' and '$a_2$' are found to be empirically determined constants. These constants were found to depend upon the compositions of the systems. 'a_0' did not contribute to densification as the same was found to be almost the initial density of ring preforms, whereas, the constant 'a_1' contributed to densification linearly, and, the low negative values of 'a_2'assisted in flattening the densification curves in their final stages. Nearly unity was the regression coefficient (R^2) which has clearly established the perfect curve fittings.
3. Addition of chromium exhibited the mixed response on the relationship between fractional I.D. decrease and the fractional height reduction. However, these curves were found to conform to a third order polynomial exhibiting best curve fit.

Thus, the finding of the present investigation can be successfully utilized for forging of sintered rings for ball-bearing races and spur gears with appropriate tool design economically.

REFERENCES

[1] T. Tabata et.al, "Determination of Coefficient of Friction in Forging of Porous Metals from Ring Compression", International Journal of

[2] Mechanical Science, Vol. 20, pp. 475 – 481, 1978.

[3] V. De Pierre and A.T. Male, "Mathematical Calibration of the Ring Test for Friction Studies in Flat Forging Operation", AFML – TR 69-28, 1969.

[4] R.E. Dutton et.al, "The Ring Test for P/M Materials, Transactions of American Society of Mechanical Engineers, Journal of Engineering Materials Technology, Vol.120, pp. 764 – 769, Nov.1998.

[5] R.J. Dower and G.I. Miles, "The Production of Mild Steel Rings by a Combined Powder Metallurgy and Cold Forging Process", Powder Metallurgy, Vol.19, No.3, pp. 141-152, 1976.

[6] T.S. Rao and K.S. Pandey, "Axial Cold Pressing of Sintered Al – 4%Cu Disc and Ring Preforms", Journal of Material Processing Technology, Vol.39, pp. 319 – 326, 1993.

[7] T.S. Rao and K.S. Pandey, "Aluminium Ring Preform Deformation Behaviour and Rupture Tests", Key Engineering Materials, Vol. 29-31, pp.351 – 364, 1989.

[8] T.S. Rao and K.S. Pandey, "Development of Theoretical Relations during Deformation of Disc and Ring Shaped Preforms", Transactions of Powder Metallurgy Association of India, Vol.15, pp.15-22, 1998.

[9] Han et.al, "Elastoplastic Finite Element Analysis for Porous Metals", Powder Metallurgy, Vol. 37, No. 2, pp. 140-146, 1994.

[10] T. S. Rao and K.S. Pandey, "Material Behaviour during Cold Upsetting of Sintered Al and Al-Cu Ring Preforms", Quarterly International Journal of Powder Metallurgy Science and Technology, Vol.5, No.2, pp.13-24, Jan.1994.

[11] J.Y. Liu, "An Analysis of Deformation Characteristics and Interfacial Friction Conditions in Simple Upsetting of Rings", Transaction of A.S.M.E., Journal of Engineering Industry, Vol. 94, pp. 1149 – 1156, 1972.

[12] S. Biswas and F.W. Travis, "Deformation Patterns of Annular Rings of Varying Geometry Subjected to Static and Dynamic Axial Compression", Inst. J.M.T.D.R., Vol.11, pp. 235 – 249, 1971.

[13] C.H. Lee and T. Altan, "Influence of Flow Stress and Friction upon Metal flow in Upset Forging of Rings and Cylinders", Transaction of A.S.M.E., Journal of Engineering Industry, pp.775 – 782, 1972.

[14] M. Kunogi, " On Plastic Deformation of Hollow Cylinders under axial Compressive Loading", Journal of Scientific Research Institute, Vol. 30, No.2, 1956, pp. 215 – 218.

[15] T. Tabata, S. Masaki and K. Hosokama, "A Compression Test to Determine the Coefficient of Friction in Forging P/M Preforms", International Journal of Powder Metallurgy, Vol. 16, No.2, pp. 149 – 156, 1980.

[16] A.T. Male and M.G.Cockcroft, "A Method for the Determination of the Coefficient of Friction of Metals under the Conditions of Bulk plastic Deformation", Journal of Institute of Metals, pp. 38-46, 1964.

[17] V. Nagpal, G.D. Lahoti and T. Altan, " A Numerical Method for Simultaneous Prediction of Metal Flow and Temperatures in Upset forging of Rings", Transactions of A.S.M.E. , Journal of Engineering for Industry, Vol. 100, pp.413 – 420, 1978.

[18] T. Tabata and S. Masaki, "Determination of the Coefficient in Forgings of Porous Metals from Ring Compression", International Journal of Mechanical Science, Vol.20, pp.475 – 481, 1978

[19] V. De Pierre, F. Gruney and A.T. Male, "Mathematical Calibration of the Ring Test with Bulge Formation", AFML-TR-72-37.

[20] B. Avitzur, "Bulges in Hollow Discs Forging", AFML-TR-69-261, 1969.
[21] Yhu Jen Hwn, "Measurement of Friction and Flow Stress of Steel at room and Elevated Temperatures by Ring Compression Test", Journal of Materials Processing Technology, Vol.37, pp.317-335, 1993.
[22] Aun Arban, "A Prediction of the Influence of Friction in the Ring Test by FEM", Proceedings of the Seventh NAMRC Conference, pp. 151-158, 1979.
[23] M. Burgdorf, "Investigation of Fiction values for Metal Forming Process by the Ring Compression Test", Industrie Auzeiger, Vol89, pp.799 – 807, 1967.
[24] J. Van Sant, "Mathematical Analysis for Axial Compression of a Flat Ring", Journal of Institute of Metals, Vol. 95, pp.125 – 127, 1967.
[25] H.N. Han, H.S. Kim, K.H. Oh and D.N. Lee, " Analysis of Coefficient of Friction in Compression of Porous Metal Rings", Powder Metallurgy, Vol.37, No.4, pp. 259 – 263, 1994.
[26] A.T. Male, "Variation in Friction Coefficient of Metals during Compressive Deformation", Journal of Institute of Metals, Vol. 94, pp. 121-125, 1966.
[27] K.S. Pandey, "Special High Temperature Ceramic Coating – Indigenously Developed to Protect Against Oxidation During Sintering", Regional Engineering College, Tiruchirappalli – 620 015, T.N., India.
[28] K.S.Pandey, "Salient Characteristics of High Temperature Forging of Ferrous Preforms", Key Engineering Materials, Vol. 29-31, pp. 465-486, Trans. Tech. Publications, Switzerland, 1989.
[29] N. Ponnusamy, K.S.Pandey and P. Aravindam, "Effect of Manganese Addition in Sintered Fe-1.0%C Hyper Eutectoid Steel during Hot Forging", National Conference on Quality Concept in Metallurgical Industries Conf. Proc., September 29-30, 1999 at PSG College of Engineering, pp. 496-503, 1999.

American Journal of Engineering Research (AJER)
e-ISSN : 2320-0847 p-ISSN : 2320-0936
Volume-03, Issue-01, pp-299-304
www.ajer.org

Research Paper Open Access

Extraction of Valuable Substances from E-Waste

P.I. Okwu[1] and I.N. Onyeje[2]
[1]*Deputy Director, Electronics Development Institute (ELDI) Awka, Nigeria*
[2]*Department of Electrical/Electronic Engineering, Anambra State University, Uli Nigeria*

Abstract: - Globally, e-waste is the fastest growing waste stream due to rapid growth in technology, planned obsolesces in electronics industry and increased desire for new electronic products. E- waste has the ugly and good sides because it contains substances that can be classified as hazardous and non-hazardous. This paper focuses on the good side-extraction of valuable substances by means of recycling. Millions of dollars of gold, silver and other precious metals are hidden away e-waste landfills because electronic machines use so much precious metals and their waste can be recovered in the process called urban mining. E-waste now contains precious metal deposits that are 40 to 50 times richer than ores mined from the ground. The processes involved in e-waste recycling are: collection, dismantling, pre-processing, end processing and final metal recovery. To achieve environmental sustainability, the trend in e-waste management is green computing.

Keywords: - *e-waste, green computing, precious metals, recycling, urban mining*

I. INTRODUCTION

The Information and Communication Technology (ICT) has gradually but steadily permeated virtually every facet of our lives through the emergence of new technologies that have made it possible to produce a wide range of electronic products at relatively affordable prices. Consequently, there are ever increasing demands for electronic items leading to alarming rate in waste generation.

E-waste is the shortened form of the term electronic waste and is the waste material generated from electronic products. It is also called e-garbage, e-scrap and Waste Electrical and Electronic Equipment. [1] E-waste therefore refers to electrical or electronic materials that are unwanted, discarded, and obsolete and are broken. Some of the sources of this category of waste include: radio and television sets, computers, monitors, all types of phones, fax machines and copiers, personal digital assistants and electronics from industrial sources.

1.1 E-waste Generation

The rapid e-waste generation witnessed globally today is attributed to some factors. People have discovered the ability of electronic products to make life more convenient and therefore have developed almost insatiable craving for them, resulting in the growth of electronic waste. Furthermore, technologies are rapidly changing positively and prices of electronic products are now lower and thus users can conveniently do away with their old electronics. Again, manufacturers have tactically planned obsolesce of their electronic and electrical products by rapidly introducing new ones with better features. Equally, users of electronic products have observed that it is often cheaper and more convenient to buy new electronics than to upgrade the old ones. That is not all; liquid crystal display (LCD) screens have now replaced cathode-ray tube (CRT) monitors because they are smaller and have energy economy resulting in massive dumping of CRT monitors. Very importantly, manufacturers have embarked on aggressive marketing resulting in consumers' cravings for electronic products.

1.2 E-waste Statistics

Statistics on e-waste is frightening. According to Causes International, 20- 50 million tons of e-waste are generated worldwide annually. [3] Also, the USA is seen as the world leader in e-waste generation, producing about 3 million tons annually. [4] In addition, according to Greenpeace International in the developing countries, the lifecycle of mobile phones is less than two years. [5].

1.3 Electronic Waste Substances

The composition of e-waste differs from one product to another. Some of them are found in large quantities. There are some elements that are found in small amounts, while others are in trace amounts. [4]

1.3.1 Elements found in trace amounts

Americium, antimony, arsenic, barium, bismuth, boron, cobalt, europium, gallium, germanium, gold, indium, lithium, manganese, nickel, niobium, palladium, rhodium, ruthenium, selenium, silver, tantalum, terbium, thorium, titanium, vanadium and yttrium. [4]

1.3.2 Elements found in small amounts

Cadmium, mercury and thallium.[4]

1.3.3 Substances found in large quantities

Epoxy resins, fibre glass, PCBs, PVC, thermosetting plastics, lead, tin, copper, silicon, beryllium, carbon, iron and aluminium., [4]

1.4 The Dark and Bright Sides of E-waste

Like two side of a coin, electronic waste has the ugly and the good sides. Being a highly complex waste stream e-waste contains both very scarce and valuable as well as highly toxic components.

1.4.1 Ugly Side

Electronic materials contain substantial amounts of lead and other substances which are harmful to the body.. Unfortunately, they are either dumped at landfills or burnt. Worst still, some of the developed countries have been sending large amounts of e-waste to developing countries such as China, India, and Nigeria where there are poor environmental standards. By so doing, they are indirectly converting them to waste dump sites for the developed countries.

1.4.2 Economic Perspective

As e-waste also contains valuable substances, it also serves as source of secondary raw materials or wealth when properly treated. This achieved through recycling to extract precious materials from he e-waste stream.

The objectives of this study are to gain an understanding of e-waste, its substances and associated hazards; to review the various e-waste management options and to stress that e-waste contains several precious materials that can be extracted through recycling. This paper is divided into five chapters. Of course, chapter one is the introduction. In chapter two, there is a review of e-waste management efforts. Chapter three deals extensively on processes employed in extracting gems from e-waste. The emerging trends in e-waste threats and opportunities are handled in chapter four while chapter five is the conclusion.

II. REVIEW OF E-WASTE MANAGEMENT OPTIONS

Generally, in waste management, waste materials are collected, transported, disposed or possibly processed and recycled with the view to reducing their negative impacts on health, the environment or aesthetics. It is also carried out in order to recover resources from it. Some of the methods used in managing e-waste include the following.

2.1 Disposal to Landfill

In this method, which is one of the most widely used methods of waste disposal, e-waste is buried. Mining voids or borrow pits can be used in land filling. [4] However, this has the disadvantages of uncontrolled fires which can release toxic fumes and also that toxic components of e-waste may contaminate ground water and pollute the environment.

2.2 Incineration

Here, the waste materials are burnt in incinerators at high temperatures. When e-waste is incinerated, there is a reduction in the waste volume and the energy content of combustible materials can be utilised. However, this method results in pollution, more so because most e-wastes contain some quantities of lead-tin solders and therefore should not be encouraged..

2.3 Re-use Method

In this method the original equipment is put into second hand use or use after modifications. This method equally has an advantage of reducing the volume of e-waste generation.

2.4 Avoidance and Reduction Methods

Waste reduction or prevention involves the prevention of e-waste from being created. This method is good in waste management because it is only when waste is generated that it has associated waste management costs. In addition, it helps in resources conservation.

2.5 Extended Producer Responsibility (EPC)

Usually producers push the responsibility for the end-of-life product management to the general public. However, this method places it appropriately on the shoulders of the producers and all entities involved in the product chain. With this in mind, product designers are challenged to ensure that at every stage of products lifecycle, there is minimisation of impact on human health and the environment.

2.6 Legislation

The issue of e-waste has sparked off a number of initiatives around the world with the aim of promoting the reuse of electronic devices and mandating manufacturers to use safer substances in their products. For instance, in some states in the USA developed policies banning cathode ray tubes from landfills due to the fear that the heavy metals contained in them would contaminate ground water. Also in Europe, legislation has been drafted to deal with the problem. [4]

2.7 Export to Developing Countries

Some developed countries have adopted a method of exporting e-waste to developing countries like China, India and Nigeria under the guise of sale or donation of second hand electronics. [6] These countries have gradually become their e-waste dump sites extensions. The exporting countries carry out their illegal business because they see it as less expensive than normal disposal.

2.8 Recycling

The best method of e-waste management is to recycle the equipment. Recycling is the process of extracting resources of value from e-waste. Here the equipment is disassembled and the valuable components are recovered and are used for manufacturing new products. This method is extensively treated in the next chapter.

III. GEMS EXTRACTION FROM E-WASTE

It has been explained earlier that, when properly managed, e-waste can be a source of wealth and employment because it contains several precious materials. Thus, e-waste recycling is a rapidly thriving business in the developed world today. In fact, during the first e-Waste Academy held in Accra Ghana, the organisers revealed that electronic goods contain 40 t0 50 times the amount of gold and other precious metals mined from the ground. [7][11] It was an eye-opener to what is now called urban mining.

3.1 Urban Mining

Usually, mining involves digging out ores from the ground in remote areas. These ores are refined and used to make, among other things, electronic products. With the astronomical rise in the consumption of electronic products, the demand for precious substances used in their manufacture is simultaneously on the increase. An initiative, known as “Solving the E-waste Problem” (StEP) found out that 320 tons of gold and 7,500 tons of silver are required annually for global electronic goods production. Also, a financial estimate on urban mining of e-waste provided by experts from United Nation University is challenging. According to them, e-waste could generate $21 annually. [7][11] This makes urban mining imperative.

Generally, urban mining refers to resources in the cities that can be recycled and reused and in particular, recycling electrical and electronic equipment. [8] The term, urban mining, derives from the fact that, these days, cities have become mines that are rich in valuable substances but located above the ground. [9] Actually, most of these substances end up in cities where actual mining does not usually take place but are locked up in e-waste waiting to be mined. Electronic wastes are now other electronic gold mines. Thus, the process of reclaiming gems from e-waste in urban areas is known as urban mining. This new terminology was coined by John S. Shegerian of Electronics Recycling, Inc. [10] There are now urban mining recycling plants whose function is turn trash into treasure.

3.2 Gems E-waste

E-waste usually contains various precious metals which are of high economic value thereby turning recycling of these wastes into an economic opportunity. [12] The gems include gold and silver which are good conductors of electricity and commonly found in printed circuit boards. Germanium, indium and gallium are needed in semiconductor devices. There are tin and lead that are useful for soldering and coating of component leads. Mercury serves a useful purpose in fluorescent tubes. Aluminium, being a good conductor is a good heat sink while zinc is used in paintings for steel parts. [4][13]

3.3 Informal and Formal Recycling

Recycling of e-waste is done in both formal and informal ways. Informal recycling is found more in developing countries and usually involves large workforce requiring manual operation and intensive labour. Though it is a profitable e-waste management method, it lacks skills and technologies to manage e-waste in an environmentally friendly manner and substantial resource recovery. [14][15]

Informal recyclers can be found in scrap metal yards, dumpsites or in recycling sites around second hand markets. Here, e-wastes are disassembled, assorted and sold. In most cases, these recyclers are only interested in copper, aluminium, lead and steel. To liberate copper, cables and other plastics are incinerated while high grade printed circuit boards are separated and sold. At times, fire is used to reduce waste volume. [15] On the other hand, formal recyclers have the capacity to manage e-waste in a more environmentally friendly way and enhanced resource recovery. [15]

3.4 E-waste Recycling Processes

The factors that affect the selection of the recycling process are type and complexity of material, metal content and volume. There are several methods and technologies that are involved. However, to extract valuables from e-waste, it has to go through a basic process: collection, dismantling, pre-processing, and end processing and final metal recovery. This is illustrated in Fig.1.

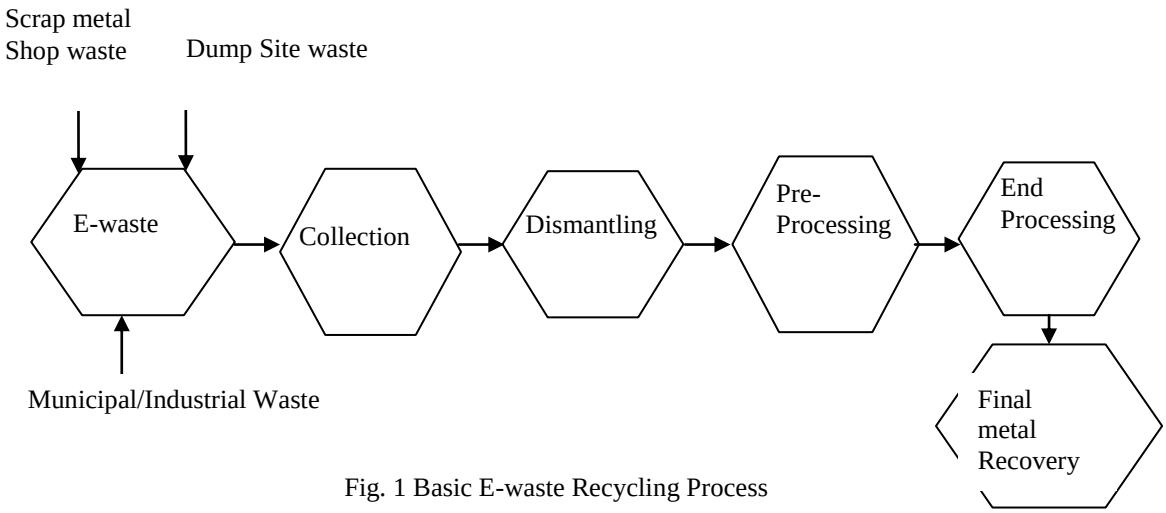

Fig. 1 Basic E-waste Recycling Process

The figure shows that e-waste for recycling can come from various sources such as dump sites, scrap metal shops and municipal and industrial wastes.

3.4.1 Collection

This is the first and crucial step in the recycling process because if no wastes are collected, it will be impossible to establish a recycling chain. Furthermore, collection mechanism of e-waste is very important because it is the determinant of the quantity of waste that is available for recovery through recycling and the amount that is lost in the process of storage. Several collection programmes exist; however their efficiencies are functions of place and recycling technologies in use.

In the developed countries, for instance, there are municipal collection points where consumers are obliged to hand in electronic wastes. On the other hand, in the developing countries there is an informal method where collectors go house-to-house and pay money to consumers in order to be allowed to pick e-waste.[15][16] Furthermore, the materials are classified, evaluated and separated according to metal content and recoverability. [12]

3.4.2Dismantling

The next step is the removal of some functioning or valuable components such as copper cables, memories, drives, batteries, capacitors and so on for re-use. The non-functioning components are dismantled and sorted according to their main functions while the hazardous substances are removed and are either stored or treated safely [15][16]. This step is sometimes called enrichment because critical materials are removed to avoid dilution or contamination with toxic substances. [12] Two methods are employed here; one is mechanical shredding and sorting, while the other is manual dismantling and sorting.[15] Simple tools are used in the second method and thus they can be carried out by unskilled workers. This method is preferable in the developing countries with lower wages. Mechanical shredding method is economically preferred in the developing countries. [12][18]

3.4.3 Pre-processing

Dismantling and pre-processing are interwoven; the slight difference is that pre-processing activities are last activities before end processing. For instance, in air conditioners and refrigerators, a very important pre-processing step is de-gassing stage because the refrigerants like CFC have to be removed with care in order to avoid emission. Also before end processing of appliances that contain CRT such as monitors and TVs, coatings in the panel glass are removed. Usually circuit boards and motherboards are manually removed before shredding to prevent losses of precious and special metals. [16] [18]

3.4.4 End Processing:

Some of the outputs of pre-processing are: steel scraps, aluminium scraps, structural components of drives, high grade precious metals fractions like contacts, copper cables and plastics. [15] These outputs are sent to end-processing operations that are capable of achieving efficient material recovery in an eco-friendly way. For instance, steel are sent to steel plants to produce secondary steel items while aluminium are sent to smelters. As for high- grade metal fractions, they are sent to pyrometallurgical and hydrometallurgical refineries for precious metal recovery. [15]

A very important component of end-processing is mechanical processing. Usually, this is an industrial operation that gives rise to greater percentage of concentrates of recyclable material. Typical mechanical processing plants have the following components: shredders, magnetic separators, eddy- current separators and air separators. [12]

Precious metals are extracted by means of chemical stripping using acids usually cyanides. This method strips the metal content from the material surface into solution. To reach metals embedded in components, the material is first finely milled. For instance, to mine gold from hard drives and motherboards, they are left in acid bath and left until they are fully dissolved. Other chemicals are then added to precipitate gold. [12][17]

Similar to chemical stripping is leaching. In this operation, useful materials are extracted by dissolving the solid waste in liquids. [12][18]

3.5. E-waste Recycling Plants

Several e-waste recycling plants are available. Characteristically, they combine best component dismantling and increased capacity to process large amount of e-waste in a cost effective way. It usually starts with feeding e-waste materials into a hopper from where it travels up a conveyor and dropped into a mechanical separator. Following this a series of screening and granulating machines. Expectedly, the whole system is enclosed and usually employs a dust collection system to ensure eco-friendliness.[1]

IV. EMERGING TRENDS IN E-WASTE THREATS AND OPPORTUNITIES

Nowadays households and businesses are generating electronic wastes like never before resulting in ever-increasing mountains of e-waste in urban areas and mounds of the same waste in rural areas. Up till now several developing countries are stilling undergoing their technological revolutions leading to rise in living standard and demand for electronic products.[19]

E-waste is a global threat. The trend is to ban the importation of e-waste and also preventing the use of toxic materials in computers and other electronics. The challenge is having a global standard on e-waste. What exists are regulations or laws in some states like California (USA) and other countries [20] The implication therefore is that any region that that lacks regulation turns itself into a global collection centre for e-waste. [21] Interestingly, some voluntary organizations are rising up to the occasion. For instance, Green Electronics Council has launched a program, Electronic Product Environment Assessment Tool (EPEAT). EPEAT was designed to provide standards for greener computers and also to keep e-waste out of landfills. [20] It encourages the manufacture of environmentally friendly electronics. This has resulted in the reduction of mercury but adopting a technology that eliminates mercury and uses light emitting diodes (LEDs) in computer screens. [20]

Another interesting trend focuses on packaging of products making them lighter than before and leading to decrease in the amount waste that goes to the landfills. [22]

Furthermore, there is an increasing awareness of the potential value of resources in e-waste thereby making it a business opportunity. E-waste recycling market has therefore received a boost, however with some challenges. For instance, to recover precious metals from e-waste, heavy investments are required and this tends to discourage investors [21]

V. CONCLUSION

E-waste cannot be eliminated as long as there is global population growth and increased dependence on electrical and electronic equipment that generate mountains of wastes. Recycling has remained the best option in e-waste management. Researches should be focused on developing technologies that enhance efficient e-waste

recycling /valuable materials extraction and greener electronics and green computing. This e-waste management option is both eco-friendly and wealth generating. Many people seem to be uneducated concerning e-waste; there should therefore be increased awareness on the dangers in this waste material and the business opportunities in urban mining. Finally, International standards are urgently needed in order to control this global menace and encourage recyclers.

REFERENCES

[1] I.N. Onyeje. Creating Wealth from e-waste in the Third World countries, The Heartland Engineer, .4, (1),2009, 10-14

[2] (2013) Electronic Waste Management **[**Online] Available: http://epa.ohio.gov/ocapp/p2/mercury_pbt/ewaste/index.aspx

[3] (2013) E-Waste Facts **[**Online] Available: http://www.causesinternational.com/ewaste/e-waste-facts

[4] (2013) Electronic waste **[**Online] Available: http://en.wikipedia.org/wiki/Electronic_waste

[5] (2013) The e-waste problem [Online] Available: http://www.greenpeace.org/international/en/campaigns/toxics/electronics/the-e-waste-problem/

[6] (2013) Unfair e-Waste Trade in Africa [Online] Available: http://www.ncbi.nlm.nih.gov/pmc/articles/PMC1440802/

[7] (2013) Welcome To The Age Of Urban Mining [Online] Available: http://www.forbes.com/sites/trevorbutterworth/2012/07/17/welcome-to-the-age-of-urban-mining/

[8] (2013) Urban mining: revitalized recycling that goes beyond electronics [Online] Available: http://martinasblogs.blogspot.com/2013/06/urban-mining-revitalized-recycling-that.html

[9] (2013) Urban Mining in Ubiquitous Cities of Gold [Online] Available: http://ourworld.unu.edu/en/urban-mining-in-ubiquitous-cities-of-gold

[10] (2013) Urban Mining: An Emerging Industry for Recycling Electronics [Online] Available: http://voices.yahoo.com/urban-mining-emerging-industry-recycling-electronics-12113837.html

[11] M. Iyer (2012) E -waste contains $21 billion worth gold and silver: Experts [Online] Available: http://timesofindia.indiatimes.com/business/international-business/E-waste-contains-21-billion-worth-gold-and-silver-E

[12] (2013) NEW Precious Metal Recovery from E-Waste & I-Waste [Online] Available: http://goldmachinery.com/machinery/i-waste.htm

[13] EMPA (2013) Valuable Substances in e-waste [Online] Available: http://ewasteguide.info/node/220

[14] L. Raghupathy, M. GTZ , C. Krüger, A. Chaturvedi, G.ASEM, R. Arora, G. ASEM , M. P. Henzler, " E-Waste Recycling In India – Bridging The Gap Between The Informal And Formal Sector ",

[15] A. Manhart ,O. Osibanjo, A. Aderinto and S. Prakash Informal e-waste management in Lagos, Nigeria – socio-economic impacts and feasibility of inter-national recycling co-operations, 2011, Final report of component 3 of the UNEP SBC E-waste Africa Project , Lagos & Freiburg.

[16] United Nations Environment Programme Recycling-From E-waste to Resources, 2009, Final Report, Sustainable Innovation and Technology Transfer Industrial Sector studies, Berlin, Germany.

[17] (2013) How to mine for gold in your television set and computer keyboard [Online] Available: o9.com/5895071/how-to-mine-for-gold-in-your-television-set-and-computer-keyboard

[18] N. Dickinson (2013) How to Extract Precious Metals From Computers [Online] Available http://www.ehow.com/how_6642677_extract-precious-metals-computers.html

[19] (2013) Current e-waste Trends [Online] Available: http://electronicrecyclers.com/historyofewaste_currenttrends.aspx

[20] D. Bello (2013) New E-Waste Standards: Junking Electronic Gadgets without Trashing the Planet [Online] Available: http://www.scientificamerican.com/article.cfm?id=new-ewaste-standards

[21] (2013)New Regulations in Asia-Pacific to Help Boost E-waste Recycling Market [Online] Available:

[22] http://www.environmentalleader.com/2013/06/13/new-regulations-in-asia-pacific-to-help-boost-e-waste-recycling-market/

[23] J. Kantor (3013) Latest Trends in Recycling for the Future [Online] Available

[24] http://www.greenconduct.com/news/2013/07/25/latest-trends-in-recycling-for-the-future/